

INTEGRATED, MULTI-SCALE CHARACTERIZATION OF IMBIBITION AND
WETTABILITY PHENOMENA USING MAGNETIC RESONANCE AND WIDE-BAND
DIELECTRIC MEASUREMENTS

Final Report

February 4, 2004 – September 30, 2007

By

Mukul M. Sharma, Steven L. Bryant, and Carlos Torres-Verdín

and

George Hirasaki

September 2007

Work Performed under Contract No. DE-FC26-04NT15518

Prepared by

Department of Petroleum and Geosystems
Engineering
One University Station, Mail Stop C0300
The University of Texas at Austin
Austin, Texas 78712
Phone: 512 471 3257
Fax: 512 471 9605
e-mail: msharma@mail.utexas.edu

Rice University
Chemical Engineering Dept., MS-362
P.O. Box 1892
Rice University
Houston, TX 77251-1892
e-mail: gjh@owlnet.rice.edu

Chandra Nautiyal
Project Manager
U. S. Department of Energy
National Petroleum Technology Office
Tulsa, Oklahoma

DISCLAIMER

This report was prepared as an account of work sponsored by an agency of the United States government. Neither the United States government nor any agency thereof, nor any of their employees, makes any warranty, express or implied, or assumes any legal liability or responsibility for the accuracy, completeness, or usefulness of any information, apparatus, product, or process disclosed, or represents that its use would not infringe privately owned rights. Reference herein to any specific commercial produce, process or service by trade name, trademark, manufacturer, or otherwise does not necessarily constitute or imply its endorsement, recommendation or favoring by the United States government or any agency thereof. The view and opinions of authors expressed herein do not necessarily state or reflect those of the United States government or any agency thereof.

ABSTRACT

The petrophysical properties of rocks, particularly their relative permeability and wettability, strongly influence the efficiency and the time-scale of all hydrocarbon recovery processes. However, the quantitative relationships needed to account for the influence of wettability and pore structure on multi-phase flow are not yet available, largely due to the complexity of the phenomena controlling wettability and the difficulty of characterizing rock properties at the relevant length scales. This project brings together several advanced technologies to characterize pore structure and wettability. Grain-scale models are developed that help to better interpret the electric and dielectric response of rocks. These studies allow the computation of realistic configurations of two immiscible fluids as a function of wettability and geologic characteristics. These fluid configurations form a basis for predicting and explaining macroscopic behavior, including the relationship between relative permeability, wettability and laboratory and wireline log measurements of NMR and dielectric response. Dielectric and NMR measurements have been made show that the response of the rocks depends on the wetting and flow properties of the rock. The theoretical models can be used for a better interpretation and inversion of standard well logs to obtain accurate and reliable estimates of fluid saturation and of their producibility.

The ultimate benefit of this combined theoretical/empirical approach for reservoir characterization is that rather than reproducing the behavior of any particular sample or set of samples, it can explain and predict trends in behavior that can be applied at a range of length scales, including correlation with wireline logs, seismic, and geologic units and strata. This approach can substantially enhance wireline log interpretation for reservoir characterization and provide better descriptions, at several scales, of crucial reservoir flow properties that govern oil recovery.

EXECUTIVE SUMMARY

This report presents a summary of the work conducted under DOE Contract No. DE-FC26-04NT15518 at The University of Texas at Austin and Rice University to better understand the relationships between core scale rock properties, such as relative permeability and wettability, to the NMR and broadband dielectric response of rocks.

Chapter 2 shows how profiles of T2 relaxation time distributions can be generated by implementing the rapid acquisition with relaxation enhancement (RARE) pulse sequence. RARE experiments were performed on a vuggy Yates core sample. Generation of a T2 map revealed a slight heterogeneity even within a core sample with a height of 1 inch. A porosity profile constructed from the RARE results yielded a porosity of 0.146 which was in good agreement with the gravimetric porosity (0.147) and the porosity determined via CPMG.

In Chapter 3 we revisit random-walk methods to simulate the NMR response of fluids in porous media. By simulating longitudinal and transversal magnetizations for specific bulk fluid properties and fluid/solid boundary geometries, the random-walk approach can be used to generate parametric multidimensional T1/T2/D NMR maps to improve the characterization of pore structures and saturating fluids from NMR.

Chapters 4 and 5 introduce a new geometrical concept to simulate DC electrical conductivity phenomena in arbitrary rock models. The assumed geometry considers 3D grain and pore objects that include intragranular porosity, clay inclusions, non-wetting fluid blobs, thin films, and pendular rings. This provides a simple way to parameterize the three-dimensional space and to simulate the electrical conductivity of porous media saturated with two immiscible fluid phases. This work emphasizes the importance of thin films, pendular rings and snap-offs to capture the correct electrical behavior of dense media using granular models. We introduce a new approach to quantify the effects of pore geometry and connectivity on the kHz-GHz frequency dispersion of dielectric permittivity and electrical conductivity of clay-free porous rocks. The simulation procedure provides a systematic method to assess the sensitivity of a multitude of pore-scale properties to the macroscopic wide-band dielectric dispersion of saturated rocks.

In Chapter 6 a comprehensive pore-scale numerical framework is introduced that incorporates explicit geometrical distributions of grains, fluids and clays constructed from core pictures, and that reproduces the WBEM saturated-rock response on the entire kHz-GHz frequency range. WBEM measurements are verified to be primarily sensitive (a) in the kHz range to clay amounts and wettability, (b) in the MHz range to pore morphology (i.e., connectivity and eccentricity), fluid distribution, salinity, and clay presence, and (c) in the GHz range to porosity, pore morphology and fluid saturation. Our simulations emphasize the need to measure dielectric dispersion in the entire frequency spectrum to capture the complexity of the different polarization effects. In particular, it is crucial to accurately quantify the phenomena occurring in the MHz range where pore connectivity effects are confounded with clay polarization and pore/grain shape effects usually considered in dielectric phenomena. These different sensitivities suggest a strong complementarity between WBEM and NMR measurements for improved assessments of pore size distribution, hydraulic permeability, wettability, and fluid saturation.

Chapters 7 and 8 present the results of electrical impedance measurements made over a broad spectrum of frequencies (10 Hz to 10 MHz) with fully brine saturated rock samples of varying permeability (grain size). It is shown that a systematic shift in loss tangent (both peak frequency and magnitude) occurs as the grain size is varied. This suggests that the loss tangent, derived from broadband dielectric measurements, may be used to measure the formation grain size and hence estimate the permeability.

TABLE OF CONTENTS

| | |
|--|-------|
| DISCLAIMER | i.i |
| ABSTRACT | i.ii |
| EXECUTIVE SUMMARY | i.iii |
| CHAPTERS | |
| 1. INTRODUCTION..... | 1.1 |
| 2. NMR 1-D PROFILING | |
| 2.1 INTRODUCTION | 2.1 |
| 2.2 OUTLINE OF CHAPTER..... | 2.2 |
| 2.3 FREQUENCY-ENCODING GRADIENTS..... | 2.2 |
| 2.4 BASIC SPIN ECHO (SE) IMAGING PULSE SEQUENCE | 2.3 |
| 2.5 IMAGE CONTRAST | 2.3 |
| 2.6 T_2 PROFILING VIA RAPID ACQUISITION WITH RELAXATION ENHANCEMENT (RARE)..... | 2.4 |
| 2.7 EFFECT OF DIFFUSION | 2.5 |
| 2.8 SELECTION OF RARE PARAMETERS..... | 2.7 |
| 2.8.1 Sample Size and Position..... | 2.8 |
| 2.8.2 Gradient Strength..... | 2.8 |
| 2.8.3 Dwell Time | 2.9 |
| 2.9 NUMBER OF ACQUISITION POINTS..... | 2.10 |
| 2.9.1 Selection Criteria | 2.11 |
| 2.9.2 Profile Averaging..... | 2.14 |
| 2.10 APPLICATIONS | 2.15 |
| 2.11 CONCLUSIONS..... | 2.16 |
| 2.12 REFERENCES | 2.17 |

| | | |
|-------|--|------|
| 3. | A RANDOM-WALK TECHNIQUE FOR SIMULATING NMR MEASUREMENTS AND 2D NMR MAPS OF POROUS MEDIA WITH RELAXING AND PERMEABLE BOUNDARIES | |
| 3.1 | INTRODUCTION | 3.1 |
| 3.2 | MACROSCOPIC THEORY | 3.3 |
| 3.3 | MICROSCOPIC RANDOM-WALK RESOLUTION | 3.5 |
| 3.3.1 | Diffusion of Equivalent Magnetic Dipoles | 3.6 |
| 3.3.2 | Magnetization Formulations A and B..... | 3.6 |
| 3.3.3 | Treatment of Local Surface Relaxation | 3.8 |
| 3.3.4 | Transfer Probability of Permeable Membranes | 3.9 |
| 3.4 | SIMULATION RESULTS IN BULK FLUID | 3.10 |
| 3.4.1 | Effect of Volume Sampling and Pulse Width on Echo Amplitude | 3.10 |
| 3.4.2 | Multi-Component Fluids with Multiple Wait-Time Acquisitions | 3.11 |
| 3.4.3 | Decay in an Inhomogeneous Background Magnetic Field | 3.12 |
| 3.5 | SIMULATION RESULTS IN SATURATED POROUS MEDIA | 3.12 |
| 3.5.1 | Fast Diffusion Limit..... | 3.12 |
| 3.5.2 | Two-Dimensional NMR Maps of Gas/Water and Oil/Water Mixtures in Saturated Rocks..... | 3.13 |
| 3.6 | CONCLUSIONS..... | 3.15 |
| 3.7 | REFERENCES | 3.16 |
| 3.8 | APPENDIX: ANALYTICAL CALCULATIONS OF THE TIME-EVOLUTION MATRIX EXPONENTIALS IN BLOCH'S EQUATION..... | 3.20 |
| 4. | AN OBJECT-ORIENTED APPROACH FOR THE PORE-SCALE SIMULATION OF DC ELECTRICAL CONDUCTIVITY OF TWO-PHASE SATURATED POROUS MEDIA | |
| 4.1 | INTRODUCTION | 4.1 |
| 4.2 | OBJECT-ORIENTED GEOMETRY | 4.3 |
| 4.2.1 | Integrating Grain Morphology and Pore-scale Fluid Distribution as Geometrical Objects..... | 4.3 |
| 4.2.2 | Fluid Distribution Model and Capillary-Pressure Hysteresis | 4.6 |

| | | |
|-------|---|------|
| 4.2.3 | Random-Walk Simulation of DC Electrical Conductivity | 4.9 |
| 4.3 | SIMULATION RESULTS | 4.12 |
| 4.3.1 | Single-phase Saturation with Clustered Grains and Clay Inclusions... | 4.12 |
| 4.3.2 | Two-phase Saturation with Water-wet Grains (Saturation Cycles 1 to 3)..... | 4.13 |
| 4.3.3 | Two-phase Saturation with OW Solid and Microporous Grains (Saturation Cycles 1, 4, 5)..... | 4.14 |
| 4.4 | DISCUSSION | 4.15 |
| 4.5 | CONCLUSION..... | 4.17 |
| 4.6 | ACKNOWLEDGEMENTS | 4.17 |
| 4.7 | REFERENCES | 4.18 |
| 5. | TWO-DIMENSIONAL PORE-SCALE SIMULATION OF WIDE-BAND ELECTROMAGNETIC DISPERSION OF SATURATED ROCKS | |
| 5.1 | INTRODUCTION | 5.2 |
| 5.1.1 | Maxwell-Wagner Interfacial Polarization Process | 5.2 |
| 5.1.2 | Dielectric Mixing Laws and Other Polarization Models | 5.3 |
| 5.1.3 | Objectives and Methodology | 5.5 |
| 5.2 | NUMERICAL METHOD FOR THE CALCULATION OF EFFECTIVE CONDUCTIVITY AND DIELECTRIC PERMITTIVITY | 5.6 |
| 5.2.1 | Scatterer Geometry | 5.6 |
| 5.2.2 | Internal Electric Fields | 5.7 |
| 5.2.3 | Inversion of Effective Conductivity and Dielectric Permittivity | 5.9 |
| 5.3 | CONNECTIVITY EFFECTS IN DILUTE CONCENTRATIONS OF BRINE INCLUSIONS..... | 5.11 |
| 5.3.1 | Effective Medium Approximation with Depolarization Factor l | 5.11 |
| 5.3.2 | Statistical Significance of Sigmoid Dispersions | 5.12 |
| 5.3.3 | Consistency of the Simulation Results | 5.13 |
| 5.3.4 | Finite Volume Scaling | 5.15 |
| 5.3.5 | Impact of Clustering and Connectivity | 5.16 |

| | | |
|-------|---|------|
| 5.4 | DISCUSSION | 5.17 |
| 5.4.1 | Porosity and Scaling | 5.17 |
| 5.4.2 | Pore Connectivity..... | 5.18 |
| 5.4.3 | Generalization | 5.19 |
| 5.5 | CONCLUSIONS..... | 5.20 |
| 5.6 | ACKNOWLEDGEMENTS..... | 5.20 |
| 5.7 | APPENDIX A: ACCURACY OF THE NUMERICAL SOLUTION OF THE ELECTRIC FIELD INTEGRAL EQUATION WITH A 2D FFT-MOM METHOD | 5.21 |
| 5.8 | APPENDIX B: PRACTICAL IMPLEMENTATION OF THE MINIMIZATION PROBLEM..... | 5.22 |
| 5.9 | REFERENCES | 5.23 |
| 6. | IMPROVING PETROPHYSICAL INTERPRETATION WITH WIDE-BAND ELECTROMAGNETIC MEASUREMENTS | |
| 6.1 | INTRODUCTION | 6.1 |
| 6.2 | REVIEW OF WIDE-BAND ELECTROMAGNETIC BEHAVIOR OF SATURATED ROCKS | 6.3 |
| 6.2.1 | Origins of Wide-Band Dispersion | 6.3 |
| 6.2.2 | Power-Laws, Double-Layers, and Fractal Geometries..... | 6.5 |
| 6.2.3 | WBEM for Quantifying Petrophysical Properties | 6.7 |
| 6.3 | DEVELOPMENT OF A GENERALIZED 2D WBEM NUMERICAL FRAMEWORK..... | 6.9 |
| 6.3.1 | Geometrical Pore-Scale Framework | 6.9 |
| 6.3.2 | Inclusion of Clays | 6.10 |
| 6.3.3 | Inclusion of Immiscible Fluids and Wettability..... | 6.10 |
| 6.4 | ASSESSING ROCK MORPHOLOGY FROM SINGLE-PHASE WBEM MEASUREMENTS..... | 6.11 |
| 6.5 | ASSESSING WETTABILITY AND FLUID SATURATION..... | 6.12 |
| 6.6 | CONCLUSIONS..... | 6.14 |

| | | |
|-------|--|------|
| 6.7 | APPENDIX A: QUANTITATIVE INCORPORATION OF ELECTRICAL DOUBLE LAYERS..... | 6.15 |
| 6.8 | APPENDIX B: CONSTRUCTION OF A WBEM MODEL TO QUANTIFY WBEM MICROPOROSITY EFFECTS | 6.17 |
| 6.9 | ACKNOWLEDGEMENTS..... | 6.19 |
| 6.10 | REFERENCES | 6.19 |
| 7. | EXPERIMENTAL MEASUREMENTS OF THE DIELECTRIC RESPONSE OF BRINE SATURATED ROCKS | |
| 7.1 | METHOD 1: DIELECTRIC FIXTURE..... | 7.1 |
| 7.1.1 | Dry Berea Measurements..... | 7.1 |
| 7.1.2 | Air Measurements..... | 7.2 |
| 7.1.3 | Fully Saturated Berea Measurements | 7.3 |
| 7.1.4 | Berea Measurements—Non-Contacting Method..... | 7.4 |
| 7.1.5 | Discussion of Method 1 | 7.5 |
| 7.2 | METHOD 2: MODIFIED DIELECTRIC FIXTURE..... | 7.5 |
| 7.2.1 | De-Ionized Water Measurement..... | 7.6 |
| 7.2.2 | Toluene Measurements | 7.6 |
| 7.2.3 | Circuit Measurements | 7.6 |
| 7.2.4 | Fully Saturated Berea Measurements | 7.7 |
| 7.2.5 | NaCl Brine, 1% and 3%..... | 7.7 |
| 7.2.6 | De-Ionized Water..... | 7.8 |
| 7.2.7 | NaCl Brine, 0.45% and 2.15%..... | 7.9 |
| 7.2.8 | Discussion of Method 2 | 7.9 |
| 7.3 | METHOD 3: MODIFIED DIELECTRIC FIXTURE AND COATED ELECTRODES | 7.10 |
| 7.3.1 | Gold Sputter Coating | 7.10 |
| 7.3.2 | Physical Vapor Deposition (PVD) of Gold | 7.12 |
| 7.3.3 | Sandwich Method | 7.12 |
| 7.3.4 | External Field Method | 7.13 |

| | |
|--|------|
| 7.3.5 Silver Plating Powder | 7.13 |
| 7.3.6 Discussion of Method 3 | 7.14 |
| 7.4 METHOD 4: FOUR-ELECTRODE METHOD..... | 7.14 |
| 7.4.1 Circuit Measurements | 7.15 |
| 7.4.2 Berea Measurements..... | 7.16 |
| 7.4.3 Berea Measurements with Large Cylindrical Sample | 7.17 |
| 7.4.4 Discussion of Method 4 | 7.17 |
| 7.5 METHOD 5: NON-CONTACTING METHOD (REVISITED)..... | 7.17 |
| 7.5.1 Air Gap Method | 7.18 |
| 7.5.2 Discussion of Method 5 | 7.18 |
| 7.5 DISCUSSION OF METHODS..... | 7.19 |
| 7.6 DISCUSSION OF RESULTS..... | 7.20 |
| 7.6.1 Changing Grain Size | 7.20 |
| 7.6.2 Changing Saturating Fluid Salinity..... | 7.21 |
| | |
| 8. DIELECTRIC MEASUREMENT RESULTS FOR PARTIALLY SATURATED ROCKS | |
| 8.1 HIGH RESOLUTION X-RAY CT SCAN | 8.1 |
| 8.2 SCAN RESULTS..... | 8.2 |
| 8.3 PARTIAL SATURATION MEASUREMENT RESULTS | 8.3 |
| 8.4 CONCLUSIONS..... | 8.4 |

CHAPTER 1. INTRODUCTION

The objective of this study was to better understand the relationships between core scale rock properties such as relative permeability, wettability, laboratory and log measurements of NMR, broadband dielectric response of rocks and pore-scale structures and fluid distributions. This required obtaining realistic configurations of immiscible fluids as a function of wettability and geologic characteristics and using these fluid configurations as a basis for predicting macroscopic rock properties. The ultimate objective is to measure dielectric and NMR responses in a range of sedimentary rocks and to use state-of-the-art multi-scale modeling to interpret these measurements to quantify wettability and relative permeability at the core and log scales.

Chapter 2 discusses how the 1-D NMR response of rocks can provide information about pore structure and wettability. Chapter 3 of this report presents numerical simulations of the NMR response of realistic pore and pore fluid configurations transformed into 2D NMR diffusion maps and standard T2 distributions as a function of inter-echo times for a variety of pulse sequences. In turn, the simulations are contrasted against actual NMR measurements performed on rock core samples. This comparison provides a solid quantitative basis to validate the numerical simulation approach and to quantify the sensitivity of the data to wettability in complex pore structures and fluid distributions.

The low frequency and high frequency (dielectric) response of rocks (in the DC to 10MHz range) is highly sensitive to surface phenomena at the rock-fluid interface. Since dielectric measurements are made using both MWD and wireline tools, this relationship can be used to describe the distribution of wettability at the core, log and geologic flow unit length scales. Pore scale models are presented in Chapters 4 and 5 that simulate the dielectric response of rocks under different pore geometries and wettability conditions. Comparisons with experiments show good quantitative agreement.

Different methods are presented for making dielectric measurements on core samples in Chapter 7. These measurements are particularly challenging in low resistivity (high salinity) brines. A set of experimental data is provided for the complex impedance of cores saturated with NaCl brine from 10 Hz to 10 MHz (Chapter 8). Core samples with a range of

permeabilities were used. The dielectric relaxation time (which is sensitive to the specific surface area) is shown to vary systematically with the permeability. On the other hand the in-phase conductivity scales with the porosity. This allows us a possible way of obtaining a measure of the permeability from the in-phase and out-of-phase dielectric measurements.

CHAPTER 2. NMR 1-D PROFILING

Profiles of T_2 relaxation time distributions can be generated by implementing the rapid acquisition with relaxation enhancement (RARE) pulse sequence. The RARE sequence is a multi-echo imaging sequence where each echo is used to construct a one-dimensional profile. Experimental parameters, such as sample size, gradient strength and duration, and the number and spacing of the acquired data points, must be selected to ensure that useful information can be extracted from the profiles. The gradient strength relates the precession frequency to sample position. Attenuation due to diffusion is dependent on the product of gradient strength (g) and duration. The dwell time (DW), or spacing between acquired data points, needs to be selected so that the sample plus a small region above and below is resolved by the experiment. Image resolution is dependent upon the product of the number of data points collected per echo and the dwell time directly, and the acquisition time ($SI * DW$) is limited by δ . Interdependence exists between these parameters; subsequently, they should be chosen in concert such that diffusion attenuation is minimized while maximizing image resolution. RARE experiments were performed on a vuggy Yates core sample. Generation of a T_2 map revealed a slight heterogeneity even within a core sample with a height of 1 inch. A porosity profile constructed from the RARE results yielded a porosity of 0.146 which was in good agreement with the gravimetric porosity (0.147) and the porosity determined via CPMG (0.148).

2.1 INTRODUCTION

Magnetic resonance imaging (MRI) relies on the fundamental principles of nuclear magnetic resonance (NMR) to extract spatial information about a given sample. While standard NMR techniques, such as CPMG, tend to look at either the whole sample or only a thin slice, MRI can be implemented in order to study the configuration of fluids within a core. Spatial resolution of properties such as magnetization and relaxation times will allow for the determination of saturation profiles and sample heterogeneities, such as changes in local porosity or pore size distribution. However, these experiments are typically limited to imaging or high field spectrometers. Applications in this study will focus on the use of a

low-field instrument (2 MHz Maran Ultra) to determine sample heterogeneities in one dimension (1-D) by generating T_2 profiles.

2.2 OUTLINE OF CHAPTER

This chapter is broken into several sections, each of which pertains to an essential topic for the successful generation of 1-D NMR profiles. First, the ability to spatially encode an NMR signal using frequency-encoding gradients will be addressed. Then, the basic spin echo imaging pulse sequence will be examined, and the concept of image contrast introduced. Next, the concept of collecting multiple echoes with the rapid acquisition with relaxation enhancement (RARE) sequence to extract a spatial resolved T_2 distribution will be introduced. Finally, two systems, an ideal layered water/oil sample and a vuggy carbonate core sample, will be characterized using the RARE sequence.

2.3 FREQUENCY-ENCODING GRADIENTS

Frequency encoding is a standard MR technique used to detect spatial information from a desired sample. In a uniform magnetic field, protons precess at the same frequency, known as the Larmor frequency.

$$g_L = \frac{\gamma}{2\pi} B_0 \quad (1)$$

When a magnetic gradient is applied, the intensity of the magnetic field and subsequently, the precession frequency varies with spatial position. For instance, under the application of a linear gradient field, the spatially dependent precession frequency can be represented by

$$f(x) = \frac{\gamma}{2\pi} (B_0 + g_x x) \quad (2)$$

or

$$f(x) = f_L + \frac{\gamma}{2\pi} g_x x, \quad (3)$$

where g_x designates the gradient strength and x denotes position. Therefore, spatial information can be extracted from the sample's various precession frequencies. Consequently, g_x is referred to as a frequency-encoding gradient (Bernstein et al., 2004).

2.4 BASIC SPIN ECHO (SE) IMAGING PULSE SEQUENCE

This sequence is comprised of two gradient pulses, the prephasing and readout pulses, which are separated by a refocusing RF pulse. The prephasing gradient pulse prepares the system for an echo to occur later. The prephasing gradient pulse causes the magnetic field to be stronger at one position than another resulting in non-uniform precession frequencies throughout the sample. Therefore, spin isochromats, regions of constant precession frequency, will begin to precess at different rates and thus get out of phase with the other isochromats. Then, the RF refocusing pulse flips all of the spins by 180° . The subsequent readout gradient pulse plays a similar role as the prephasing gradient pulse, causing different isochromats to gather phase at different rates. The application of the readout gradient pulse after the 180° RF pulse causes the spins to refocus resulting in the formation of an echo (Bernstein et al., 2004).

The temporal location of the echo does not depend on the spacing of the RF pulses, but on the duration and magnitude of the gradient pulses. When the area under the readout pulse equals the area under the prephasing pulse, the echo will reach its maximum amplitude (Bernstein et al., 2004). A one-dimensional profile is then attained by performing a fast Fourier transform (FFT) reconstruction of the acquired signal (Liang and Lauterbur, 2000). For instance, a collected echo is depicted in Figure 2 and its corresponding one-dimensional profile in Figure 3. Note that the scale of the ordinate in Figure 3 is in centimeters and not Hertz; the conversion between the two is made via the linear relationship described in Equation (4).

$$f - f_{Larmor} = \frac{\gamma}{2\pi} G(x - x_{Larmor}), \quad (4)$$

where x_{Larmor} corresponds to the sample height at which $f = f_{Larmor}$.

2.5 IMAGE CONTRAST

Image contrast is a technique used to stress either the T_1 or T_2 component of relaxation. Three types of contrast methods are readily applicable to this pulse sequence: spin-density, T_1 -weighting, and T_2 -weighting. The easiest way to understand how to generate an image with the desired contrast method is to consider the magnetization equation and how

it may apply to a system with two vastly different relaxations times (e.g., squalane layered on top of water). For the previously described basic spin echo imaging pulse sequence, the magnetization is described by Equation (5).

$$M = M_0 \left[1 - \exp\left(\frac{-T_R}{T_1}\right) \right] \left[\exp\left(\frac{-T_E}{T_2}\right) \right], \quad (5)$$

where T_E is the time at which the echo center occurs and T_R is the repetition time between scans (Liang and Lauterbur, 2000). The parameters T_E and T_R can be selected in such a manner so that the profile is representative of M_0 or is either weighted by the T_1 or T_2 terms. Therefore, image contrast can be used to help differentiate fluids with varying relaxation times as in the squalane/water example. Guidelines for selecting T_E and T_R for a given method of contrast are given.

For T_1 contrast, selection of T_R should allow for one fluid to be fully polarized while the other is only partially polarized. Similarly, for T_2 contrast, the proper choice of T_E allows for greater relaxation of one fluid than the other. The difference between the various contrast methods are illustrated in Figures 4 through 6. All profiles are of the same layered water ($T_2 = 2.80$ sec) and squalane ($T_2 = 120$ msec) system, and the only parameters varying are T_E and T_R . Figure 4 represents a spin-density image. The two phases cannot be distinguished from one another, because both water and squalane have similar hydrogen indexes. On the other hand, the squalane layer in a T_1 -weighted image (Figure 5) has a much larger amplitude, because it is allowed to fully polarize between scans while the water is not. Finally, Figure 6 is an illustration of a T_2 -weighted image in which both phases are allowed to fully polarize between scans. Therefore, a long T_E results in greater relaxation in the oil phase and, subsequently, greater amplitude of the water phase. However, the longer T_E will also result in relaxation due to diffusion if the gradient is too large.

2.6 T_2 PROFILING VIA RAPID ACQUISITION WITH RELAXATION ENHANCEMENT (RARE)

The rapid acquisition with relaxation enhancement pulse sequence (RARE) is a CPMG-style extension of the one-dimensional profile measurement first proposed by Henning et al., 1986. It is commonly used for clinical imaging, but modifications to the

sequence must be made in order to accommodate the use of a MARAN. Figure 7 is a schematic of the pulse sequence created for the MARAN.

In Figure 7, the first gradient pulse is known as the pre-phasing pulse and all subsequent gradient pulses are referred to as readout or imaging pulses. Both pulses play analogous roles as their counterparts in the one-dimensional profiling pulse sequence, with one significant exception. As in the profiling sequence, the temporal location of the echo occurs when the area of the readout pulse is equivalent to the area under the prephasing pulse. Therefore, the remainder of the readout pulse acts as a prephasing pulse for the next echo. Resulting from this fact stems a careful balance between the two gradient pulses. In other words, the readout pulse should have twice the area of the prephasing pulse. In Figure 7, note that $2g_1\delta_1 = g_2\delta_2$.

The Fourier transform can be taken for each individual echo to obtain a series of one-dimensional profiles. The attenuation in the signal is also observable in the profiles. Therefore, the goal behind using such a sequence is to take advantage of the frequency encoding gradients and extract T_2 information as a function of position within the sample. A series of profiles with an increasing amount of T_2 relaxation generated by the RARE sequence is shown in Figure 8.

2.7 EFFECT OF DIFFUSION

Due to the presence of multiple gradient pulses, attenuation due to diffusion can become significant. Therefore, it is necessary to develop a suitable model describing the attenuation in terms of the relevant parameters of the pulse sequence. Callaghan (1991) suggests that one method which can be used to determine the effect of self-diffusion is the application of the Bloch-Torrey equations. In the rotating reference frame, the effect of self-diffusion and velocity on the transverse magnetization, M_T , can be represented by (Torrey, 1956):

$$\frac{\partial M_T}{\partial t} = -i\gamma\mathbf{r} \cdot \mathbf{g}M_T - \frac{M_T}{T_2} + D\nabla^2 M_T - \nabla \cdot \mathbf{v}M_T, \quad (6)$$

with the solution (Stejskal and Tanner, 1965):

$$M_T(\mathbf{r}, t) = A(t) \exp \left[-i\gamma \mathbf{r} \cdot \int_0^t \mathbf{g}(t') dt' \right] \exp \left(\frac{-t}{T_2} \right). \quad (7)$$

At the echo center, $\int_0^t \mathbf{g}(t') dt'$ is equal to zero. Therefore, Equation (7) reduces to

$$M_T(\mathbf{r}, t) = A(t) \exp \left(\frac{-t}{T_2} \right). \quad (8)$$

Substituting Equation (8) into Equation (6) yields an expression for A(t).

$$\frac{\partial A(t)}{\partial t} = -D\gamma^2 \left(\int_0^t \mathbf{g}(t') dt' \right) \exp \left(\frac{-t}{T_2} \right) \quad (9)$$

$$A(t) = \exp \left[-D\gamma^2 \int_0^t \left(\int_0^{t'} \mathbf{g}(t'') dt'' \right)^2 dt' \right] \exp \left[i\gamma \mathbf{v} \cdot \int_0^t \left(\int_0^{t'} \mathbf{g}(t'') dt'' \right) dt' \right] \quad (10)$$

If there is no flow, this expression can be reduced to

$$A(t) = \exp \left[-D\gamma^2 \int_0^t \left(\int_0^{t'} \mathbf{g}(t'') dt'' \right)^2 dt' \right] \quad (11)$$

This formulation neglects the presence of RF pulses. However, the effect of the RF pulses can be accounted for by examining the “effective gradient”. When a π pulse is applied, the phase shift due to the presence of the gradient is flipped. This is equivalent to applying a gradient pulse with the opposite polarity. Therefore, the effective gradient, g^* , can be thought of as gradient pulses required to refocus the signal in the absence of 180° RF pulses, and is represented in Figure 9 for the RARE sequence.

Or the effective gradient, $g^*(t)$, can be defined as

$$\begin{aligned} 0 & \quad \text{when} \quad 0 < t < d \\ -g_1 & \quad \text{when} \quad d < t < d + \delta_1 \\ 0 & \quad \text{when} \quad d + \delta_1 < t < d + \Delta_1 \\ g_2 & \quad \text{when} \quad d + \Delta_1 < t < 2\tau + \delta_2/2 \end{aligned}$$

$$\begin{aligned}
0 & \quad \text{when} \quad 2\tau + \delta_2/2 < t < 4\tau - \delta_2/2 \\
-g_2 & \quad \text{when} \quad 4\tau - \delta_2/2 < t < 4\tau + \delta_2/2 \\
0 & \quad \text{when} \quad 4\tau + \delta_2/2 < t < 6\tau - \delta_2/2 \\
g_2 & \quad \text{when} \quad 6\tau - \delta_2/2 < t < 6\tau + \delta_2/2 \\
\dots & \\
-g_2 & \quad \text{when} \quad 2n\tau - \delta_2/2 < t < 2n\tau + \delta_2/2,
\end{aligned}$$

where n , the number of echoes, is even.

Using these facts and imposing the stipulation that $g_1 = g_2 = g$ and $2\delta_1 = \delta_2$, $A(t)$ takes the form

$$A(t) = \exp \left[-D\gamma^2 g^2 \delta_1^2 \left(2(n-1)\tau + \Delta_1 - \frac{(n-1)}{3} \delta_2 \right) \right] \quad (12)$$

Therefore, the magnetization at the echo center of the RARE sequence can be described by

$$\frac{M}{M_0} = \exp \left[-D\gamma^2 g^2 \delta_1^2 \left(2(n-1)\tau + \Delta_1 - \frac{(n-1)}{3} \delta_2 \right) \right] \exp \left(\frac{-t}{T_2} \right), \quad (13)$$

where n is the number of echoes. A comparison of this equation to experimental results can be seen in Figure 10 and Figure 11. Water was used as the sample. The blue curve represents the CPMG decay, the green curve is the decay of the RARE profiles at the specified sample location, and the red curve is the calculated behavior.

2.8 SELECTION OF RARE PARAMETERS

The generation of NMR 1-D profiles is highly dependent upon the selected experimental parameters such as the sample size and location, gradient strength (g) and duration (δ), dwell time (DW), and number of acquisition points (SI). Choosing experimental parameters is not a trivial task since an interdependence of the parameters exists. For example, a long acquisition time will yield a higher resolution image, but will require longer gradient pulses ultimately causing greater diffusion attenuation. This section discusses the

relevant parameters, their impact on the quality of the collected image, and proposes a selection method.

2.8.1 Sample Size and Position

The sample should be located within the sweet spot of the NMR and centered about f_{Larmor} . In order to determine the size and location of the sweet spot, a series of FID experiments were performed with water. The water sample has a height of 0.5 cm and was moved in 0.5cm increments through the probe; an FID was performed at each location. The results are illustrated in

Figure 12. From these results, it was determined the sweet spot was about 5 cm long. Therefore, for all subsequent measurements, the sample will be located within the sweet spot and have a height of 4 cm.

2.8.2 Gradient Strength

Gradient pulses are necessary in order to generate MRI images, and subsequently a range of viable gradient strengths exists. On one hand, the presence of multiple gradient pulses results in a greater amount of attenuation due to diffusion. One way to reduce diffusion attenuation is to use weaker gradient pulses. Therefore, it is necessary to properly characterize the behavior of the gradient over a range of values. For instance, at very low gradients, the expected behavior deviates from what is observed. This deviation marks the lower range of reliable gradient strengths, g_{min} .

On the other hand, the maximum gradient strength, g_{max} , depends on the probe's bandwidth as well as the height of the sample. Profile rounding can occur when the range of encoded frequencies, Δf , takes up a large portion of the probe's bandwidth.

$$\Delta f = \frac{\gamma}{2\pi} g h_s \quad (14)$$

Figure 14 demonstrates profile rounding. In this plot, the range encoded is about 30 kHz, and a slight rounding is noted at the top and bottom of the sample. Selection of g_{max} should limit the range of encoded frequencies so that rounding does not occur.

$$g_{\max} = \frac{2\pi \Delta f_{\max}}{\gamma h_s} \quad (15)$$

Where Δf_{\max} is the maximum allowable frequency range. Δf_{\max} has been set to 30 kHz for the subsequent calculations.

2.8.3 Dwell Time

The dwell time (DW), or the spacing between the acquired data points, governs the length of investigation by the imaging experiment. Therefore, DW should be selected to acquire data over the length of the sample plus a small distance beyond. If the dwell time is too short, the distance which the measurement can identify is much longer than the length of the sample (Figure 15).

The largest, useable dwell time, DW_{\max} , can be determined from the size of the sample and the strength of the gradient pulses applied. Equation (17) gives a means of calculating an appropriate DW_{\max} . This equation is based on the Nyquist sampling theorem, which states that the sampling rate, SR , should be at least twice the maximum frequency encoded in the signal where the maximum encoded frequency, f_{\max} , corresponds to half the sample height plus a small distance outside for a centered sample (Bernstein et al., 2004). If this criterion is not met, aliasing can occur.

$$SR_{\max} = \frac{1}{DW_{\max}} = 2f_{\max} \quad (16)$$

$$DW_{\max} = \frac{1}{2f_{\max}} = \frac{1}{2\left(\frac{\gamma}{2\pi} g_x \frac{h_s + h_\epsilon}{2}\right)} = \frac{2\pi}{\gamma g_x (h_s + h_\epsilon)}, \quad (17)$$

where h_s is the sample height and h_ϵ is the length outside of the sample to be measured. For example, Figure 16 depicts a profile in which the dwell time has been chosen so that the sample plus about half a centimeter above and below the sample is resolved. Note that only the DW has changed between Figure 15 and Figure 16.

2.9 NUMBER OF ACQUISITION POINTS

The number of acquisition points (SI) is also a vital parameter when performing a profiling measurement. While DW determined the range of frequencies resolved, SI governs the number of points spanning that range. Therefore, the product of SI and DW directly impact image resolution.

$$resolution \left[\frac{points}{cm} \right] = \frac{SI}{h_s + h_e} \quad (18)$$

$$(h_s + h_e) = \frac{2\pi}{\gamma g DW} \quad (19)$$

$$resolution \left[\frac{points}{cm} \right] = \frac{\gamma g DW SI}{2\pi} \quad (20)$$

However, acquisition must occur under a gradient and is therefore limited by the readout gradient duration (δ_2). Therefore, the duration of the gradient pulse must be greater than or equaled to the product of SI and DW . Increasing the gradient duration to accommodate more points will increase resolution at the cost of greater attenuation due to diffusion.

$$\delta_2 \geq SI(DW) \quad (21)$$

Furthermore, it is desirable to keep SI as a power of 2 (i.e., 2^n where n is an integer), because the FFT algorithm is fastest for powers of 2.

$$SI = 2^n \quad (22)$$

By collecting as many points as possible, Equation (21) can be rearranged to give

$$SI = \frac{2\delta_1}{DW} \quad (23)$$

Combining Equations (22) and (23) yields

$$2^n = \frac{2\delta_1}{DW} \quad (24)$$

Taking the logarithm of Equation (24) allows for one to solve for which power of 2 will be used to determine SI .

$$n \ln(2) = \ln\left(\frac{2\delta_1}{DW}\right) \quad (25)$$

Solving for n yields Equation (26).

$$n = INT \left[\frac{\ln\left(\frac{2\delta_1}{DW}\right)}{\ln(2)} \right] \quad (26)$$

The operation $INT(x)$ rounds the value x down to the nearest integer. Rounding the value down ensures that Equation (7) is satisfied. Therefore, SI can be expressed as

$$SI = 2^{\left[\frac{\ln\left(\frac{2\delta_1}{DW}\right)}{\ln(2)} \right]} \quad 27$$

2.9.1 Selection Criteria

Various parameters can affect the results of a RARE experiment. For instance, the gradient pulse strength (g) and durations (δ_1 , δ_2) influence the attenuation due to diffusion, while SI and DW dictate the measurement's resolution. In order to best select experimental parameters, understanding how these parameters will affect the experiments results is necessary.

The equation below describes the signal attenuation due to both diffusion and relaxation.

$$\exp\left(\frac{-t}{T_2^\#}\right) = \exp\left(-D\gamma^2 g^2 \delta_1^2 \left(2(n-1)\tau + \Delta_1 - \frac{(n-1)}{3}\delta_2\right)\right) \exp\left(\frac{-t}{T_2}\right) \quad (28)$$

The above equation is only valid for the case where $g = g_1 = g_2$ and $2\delta_1 = \delta_2$. Equation (28) can be rearranged to show the contribution due to diffusion.

$$\frac{1}{T_2} - \frac{1}{T_2^\#} = -\frac{D\gamma^2 g^2 \delta_1^2}{t} \left(2(n-1)\tau + \Delta_1 - \frac{(n-1)}{3}\delta_2\right) \quad (29)$$

Since $t = 2n\tau$, this can be rewritten as

$$\frac{1}{T_2} - \frac{1}{T_2^\#} = -D\gamma^2 g^2 \delta_1^2 \left(\frac{2(n-1)\tau}{2n\tau} + \frac{\Delta_1}{2n\tau} - \frac{(n-1)}{3(2n\tau)} \delta_2 \right) \quad (30)$$

As n , or the number of echoes, becomes larger, $(n-1)/n$ will approach unity and $\Delta_1/(2n\tau)$ will tend to zero since $1/n$ approaches zero as n tends to infinity. Therefore, the difference between the relaxation rates can be estimated by

$$\frac{1}{T_2} - \frac{1}{T_2^\#} \approx -D\gamma^2 g^2 \delta_1^2 \left(1 - \frac{\delta_1}{3\tau} \right), \quad n \rightarrow \infty \quad (31)$$

Therefore the ratio of $T_2^\#$ to T_2 can be expressed as

$$\frac{T_2^\#}{T_2} = \left[1 + DT_2 \gamma^2 g^2 \delta_1^2 \left(1 - \frac{\delta_1}{3\tau} \right) \right]^{-1}, \quad n \rightarrow \infty \quad (32)$$

However, when selecting parameters for the RARE sequence, image resolution must also be taken into consideration. Image resolution also depends on the gradients strength, in addition to the dwell time (DW) and number of acquisition points (SI).

$$resolution \left[\frac{points}{cm} \right] = \frac{\gamma g SI DW}{2\pi} \quad (33)$$

For a given g , the maximum resolution occurs when data is acquired during the entire readout gradient, or

$$2\delta_1 = SI DW \quad (34)$$

Substituting Equation (34) into Equation (33) demonstrates that resolution is also a function of g and δ_1 .

$$resolution \left[\frac{points}{cm} \right] = \frac{\gamma g \delta_1}{\pi} \quad (35)$$

Figure 18 shows the resolution as function of g and δ_1 (Equation (35)). Also plotted on the graph are lines of constant $(T_2^\#/T_2)$. For these calculations, τ was chosen so that there would be 1 millisecond between the end of a gradient pulse and the subsequent RF pulse (Equation (36)).

$$\tau = \delta_1 + 1 \text{ msec} \quad (36)$$

Figure 18 demonstrates that for a given $T_2^\# / T_2$, the corresponding image resolution changes only slightly. Therefore, by selecting an acceptable amount of attenuation due to diffusion, the image resolution is set, and a trade off between resolution and $T_2^\# / T_2$ ensues. For example, if it is desired to have $T_2^\# / T_2 = 0.95$ for a 4 cm water sample, then the resulting image will have a resolution of about 9 points cm^{-1} . In order to generate a higher resolution image, the RARE signal will undergo more attenuation due to diffusion.

By selecting the $T_2^\# / T_2$, possible g and δ_1 pairs can be determined. These pairs correspond to the lines of constant $T_2^\# / T_2$ in Figure 18. However, not all of the gradient strengths (g) can be used to produce meaningful profiles; a minimum and maximum gradient strength exist for each measurement

Adding g_{\min} and g_{\max} to the resolution plot limits the range of possible g and δ_1 (Figure 19). However, a broad range of g and δ_1 pairs still exist for a given $T_2^\# / T_2$. The minimum T_2 value to be resolved for the measurement can be used in selecting only a single pair. Since the gradient pulses are between the π -pulses, the echo spacing is limited by the gradient duration:

$$\delta_1 < \tau \quad (37)$$

However, the echoes must be spaced close enough in order to resolve the fast relaxing components:

$$2\delta_1 < 2\tau \ll \min(T_2) \quad (38)$$

If a minimum ratio between echo spacing and $\min(T_2)$ is established, a relationship between δ_1 and $\min(T_2)$ can be constructed using Equations (36) and (38). Equation (39) represents an arbitrary ratio between δ_1 and $\min(T_2)$.

$$\frac{2\tau_{\max}}{\min(T_2)} \leq \frac{1}{10} \quad (39)$$

Combining equations (38) and (39),

$$2\delta_1 < 2\tau_{\max} \leq \frac{1}{10} \min(T_2) \quad (40)$$

Substituting equation (36) into (40),

$$\delta_1 \leq \frac{1}{20} \min(T_2) - 1 \text{ msec} \quad (41)$$

Using the largest δ_1 will allow for the longest echo train and, subsequently, the broadest resolution of relaxation times. Therefore, Equation (42) is used as the relationship between the minimum T_2 and the gradient duration.

$$\delta_1 = \frac{1}{20} \min(T_2) - 1 \text{ msec} \quad (42)$$

With a $T_2^{\#}/T_2$ selected, use of Equation (42) should yield a suitable g and δ_1 pair. If, however, this pair lies outside the bounds set by the g_{\max} and g_{\min} lines, then the selected g and δ_1 pair will correspond to the intersection of the $T_2^{\#}/T_2$ curve and the nearest vertical bound (either g_{\max} or g_{\min}). Similarly, if Equation (42) produces a negative value, then the g and δ_1 pair will correspond to the intersection of the $T_2^{\#}/T_2$ curve and the g_{\min} line. In this situation, the fastest relaxing components may not be well resolved. Choosing a value of $T_2^{\#}/T_2$ closer to unity should produce a better measurement of the fastest relaxation times (image resolution should be reduced). Figure 20 shows the selected g and δ_1 pair for a water sample.

Once a g and δ_1 pair have been selected, DW and SI can be determined using Equations (17), (27), and (34). Collection should occur for the entire duration (27), and SI should remain an integer power of 2 (34). Presented below are plots for SI and DW corresponding to $\delta_1 = 3.06$ msec. The red dot indicates the appropriate choice for SI and DW .

2.9.2 Profile Averaging

The profiles collected via the RARE sequence for bulk fluids have consistently demonstrated a noisy plateau. In order to reduce the noise, a 3-point weighted average is implemented.

$$\bar{S}(x_i) = w_1 S(x_{i-1}) + w_2 S(x_i) + w_3 S(x_{i+1}), \quad (43)$$

where $S(x_i)$ is the signal amplitude at the height x_i , $\bar{S}(x_i)$ is the weighted signal average and w_i are the weights used to perform the average. Note that $w_1 + w_2 + w_3 = 1$.

Figure 23 shows this averaging performed on a layered water/squalane system with $w_2 = 0.5$ and $w_1 = w_3 = 0.25$. In Figure 23, the points represent the profile data prior to averaging while the lines identify the averaged profiles. The profiles become slightly more rounded at the corners and oil/water interface after the averaging is performed. This is evident in Figure 24, which depicts the profile acquired from the 16th echo.

T_2 distributions were found from the RARE profiles before and after averaging. Note that for both calculations, the regularization parameters was kept constant ($\alpha = .75$). The T_2 profiles presented in Figure 25 and Figure 26 are generated from the data before and after averaging, respectively. Both profiles show the same basic features. However, the averaged data appears to yield a more consistent T_2 profile over the two phases, especially the oil phase. The oil spot in the un-averaged profile shows demonstrates a lack of uniformity at higher relaxation times (the right edge, Figure 25). This does not appear to be the case for the averaged profiles (Figure 26). Therefore, by applying a weighted average to noisy profiles, T_2 profiles with a greater uniformity can be produced.

2.10 APPLICATIONS

The RARE sequence can be applied to a system in order to generate a map of T_2 distributions as a function of sample position. Figure 26 is an example of a T_2 map for a layered water/squalane system. While this is a simplistic system, the two phases are clearly distinguishable in the T_2 map due to their distinct relaxation times. However, RARE can be extended to examine systems with greater heterogeneity.

Core samples can have complex pore structures. Implementation of the RARE sequence yields a greater insight into the core's heterogeneity than the standard CPMG measurement due to the spatial resolution of the imaging experiment. Both CPMG and RARE experiments performed on a Yates vuggy carbonate core sample, denoted A3, revealed a bimodal pore size distribution. However, the RARE results give a much clearer picture of the core sample's heterogeneity. Even though the sample is only 1 inch in

diameter and 1 inch in height, Figure 27 clearly shows that there is a larger fraction of microporosity in the upper half of the sample.

After generating a T_2 map, porosity profiles can be constructed by comparing the RARE profiles of the brine saturated core sample and a bulk brine sample. A profile of intrinsic magnetization was generated by extrapolating the first 15 profiles for both the rock and brine sample. The brine sample had the same dimensions as the core sample. The porosity was calculated using the equation below. Note the brine's intrinsic magnetization, $M_{0,brine}$, and slice volume, $V_{slice,brine}$, will be constant throughout the sample. Therefore, the denominator of Equation (44) takes on a constant value.

$$\phi_{RARE}(x) = \frac{M_{0,core}(x) / V_{slice,core}}{M_{0,brine} / V_{slice,brine}} \quad (44)$$

Figure 28 depicts the porosity profile for A3. The porosity obtained from the RARE measurement was compared to the porosity measured gravimetrically as well as the NMR porosity obtained from the intrinsic magnetization of a CPMG experiments. Table 2 summarizes these results and illustrates that all three measurement techniques are in very good agreement. Figure 28 shows that the core's porosity doesn't change very much across the sample. This is expected, since the core sample is only 1 inch in height. However, while the overall porosity does not vary very much, the T_2 map indicates that the upper region of the core has a large fraction macroporosity.

2.11 CONCLUSIONS

In closing, the application of MRI principles can be applied while using an ultra-low field spectrometer to generate 1-D NMR profiles. Profiling a sample is a valuable tool enabling for the determination of inherent spatial characteristics. When parameters are properly selected, useful information can be extracted from NMR profiles. These parameters include the gradient strength, dwell time, and the number of acquisition points. Proper parameter selection is not straight forward since an interdependence of the parameters exists. The gradient imparts spatial resolution upon the measurements, but can also cause

attenuation due to diffusion. The proposed method of selecting parameters is based on trying to minimize the attenuation due to diffusion while maximizing the image resolution.

Furthermore, by taking advantage of differing relaxation times within a sample, images with different types of contrast, such as spin-density, T_1 -weighted, and T_2 -weighted, can be generated. By comparing several images which have undergone various amounts of relaxation, T_2 can be calculated as a function of time. The rapid acquisition with relaxation enhancement (RARE) pulse sequence can be used to generate multiple profiles, each with a different amount of T_2 -weighting. Experiments have been performed with a vuggy carbonate core sample. The resulting T_2 map illustrates indicates a slight heterogeneity within the core sample; a larger fraction of macropores appear to exist near the top of the core than at the bottom. Also, a porosity profile can be constructed from the T_2 map. The porosity profile of the Yates core sample had an average value of 0.146, which corresponded very well with porosity measurements achieved gravimetrically and via a CPMG measurement.

2.12 REFERENCES

1. Bernstein, M.A., King, K.F., & Zhou, X.J. (2004). Handbook of MRI pulse sequences. Amsterdam: Elsevier Academic Press.
2. Callaghan, P.T. (1991) Principles of nuclear magnetic resonance microscopy. New York: Oxford University Press, Inc.
3. Henning, J., Nauerth, A., & Friedburg, H. (1986). RARE imaging: A fast imaging method for clinical MR. *Magnetic Resonance in Medicine*, 3, 823-833.
4. Liang, Z.P., & Lauterbur, P.C (2000). Principles of magnetic resonance imaging: A signal processing perspective. New York, NY: IEEE Press.
5. Stejskal, E.O., & Tanner, J.E. (1965). Spin diffusion measurements: Spin-echoes in the presence of a time-dependent field gradient. *The Journal of Chemical Physics*, 42(1), 288-292.
6. Torrey, H.C. (1956). Bloch equations with diffusion terms. *Physical Review*, 104(3), 563-565.

Table 1 Parameters for desired image contrast (Liang & Lauterbur, 2000) **T_A : relaxation time of fast relaxing component** **T_B : relaxation time of slow relaxing component**

| Method of Contrast | T_E | T_R |
|---------------------------|-------------------------|-------------------------|
| Spin Density | $T_E \ll T_A < T_B$ | $T_A < T_B \ll T_R$ |
| T_1 -weighted | $T_E \ll T_A < T_B$ | $T_A < T_R < T_B$ |
| T_2 -weighted | $T_A < T_E < T_B$ | $T_A < T_B \ll T_R$ |

Table 2: Summary of porosity measurements for A3

| Method | ϕ |
|----------------|--------------------------|
| Gravimetric | 0.147 |
| CPMG | 0.148 |
| RARE (average) | 0.146 |

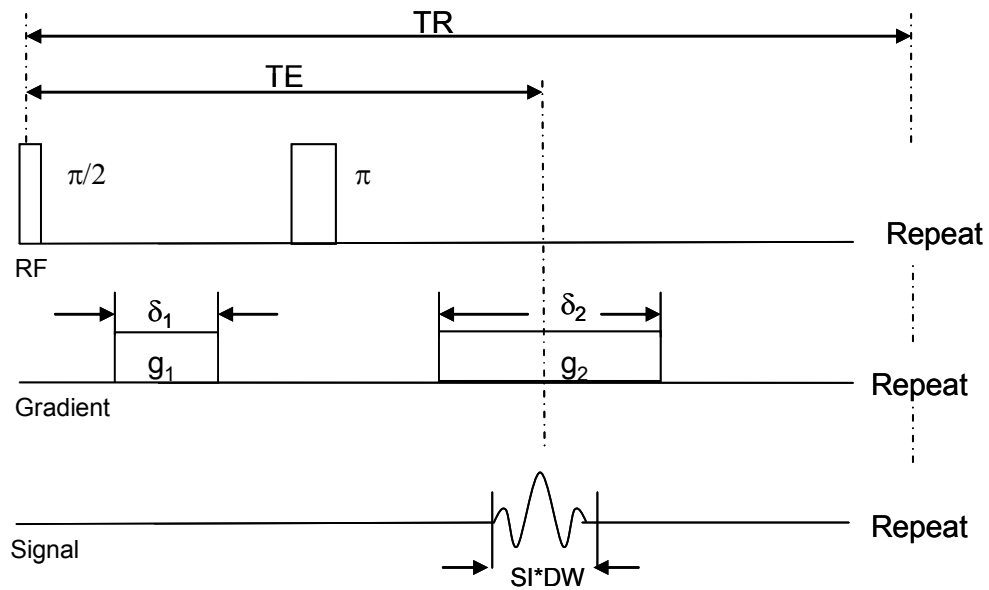


Figure 1 One Dimensional Profiling Pulse Sequence (PROFILE)
(Liang & Lauterbur, 2000)

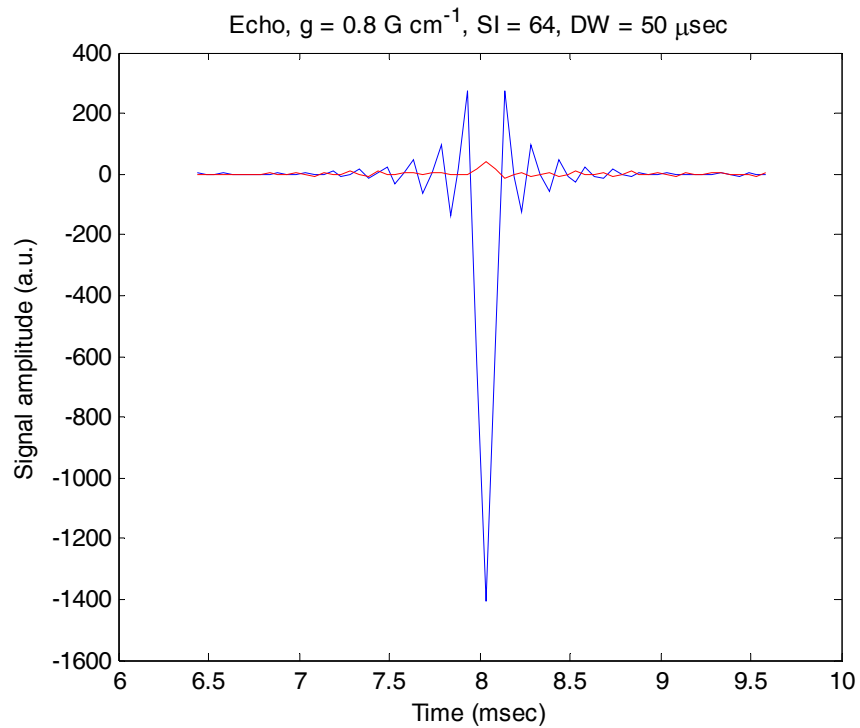


Figure 2 Collected Echo for a Water Sample with a height of 4 cm.

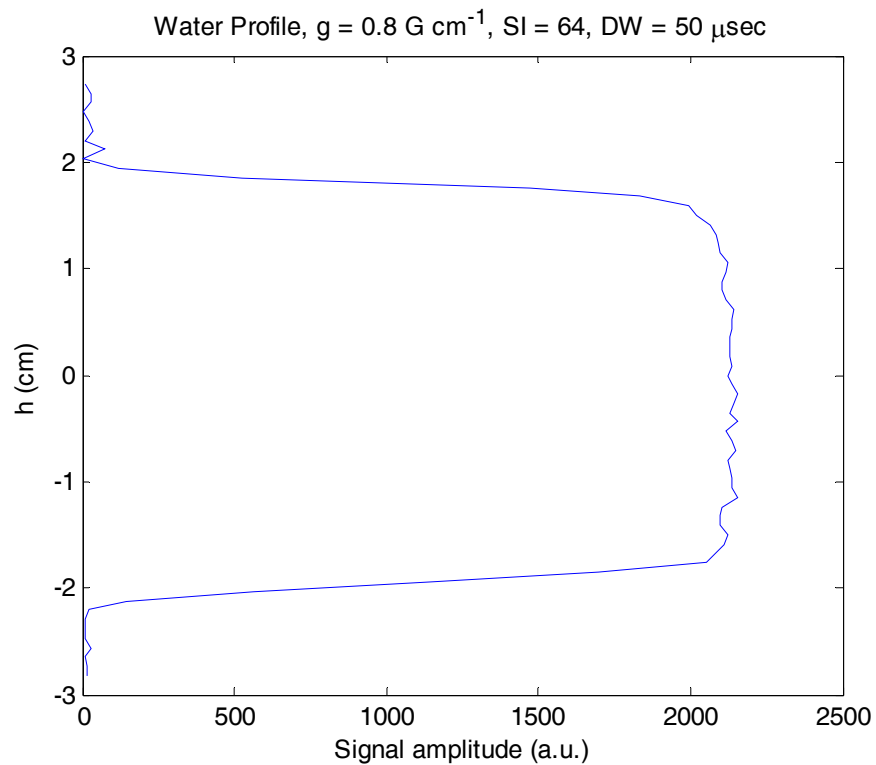
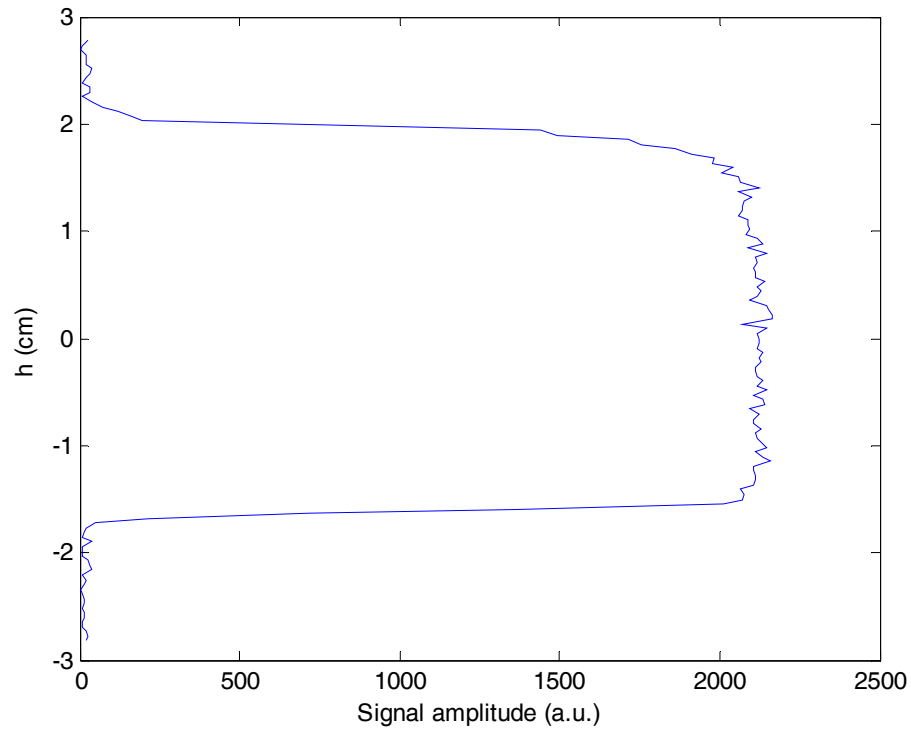
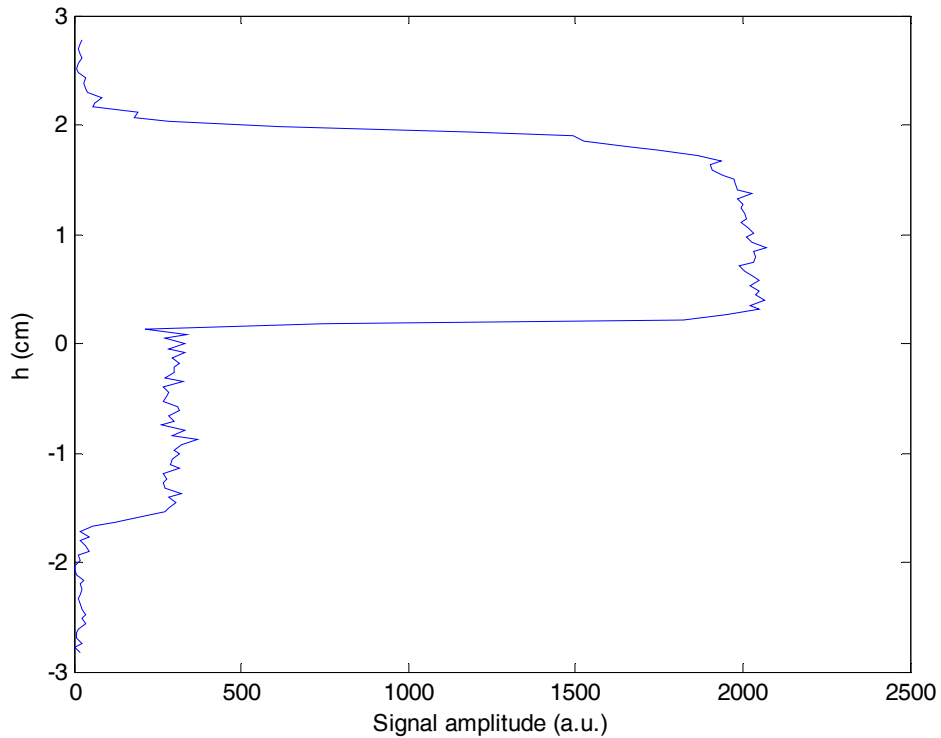
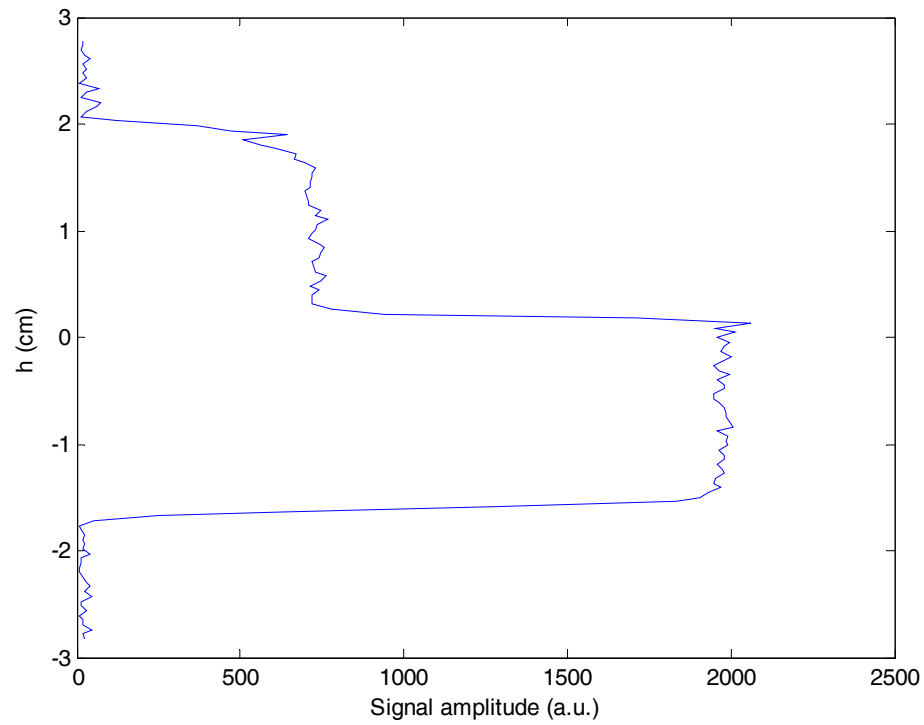
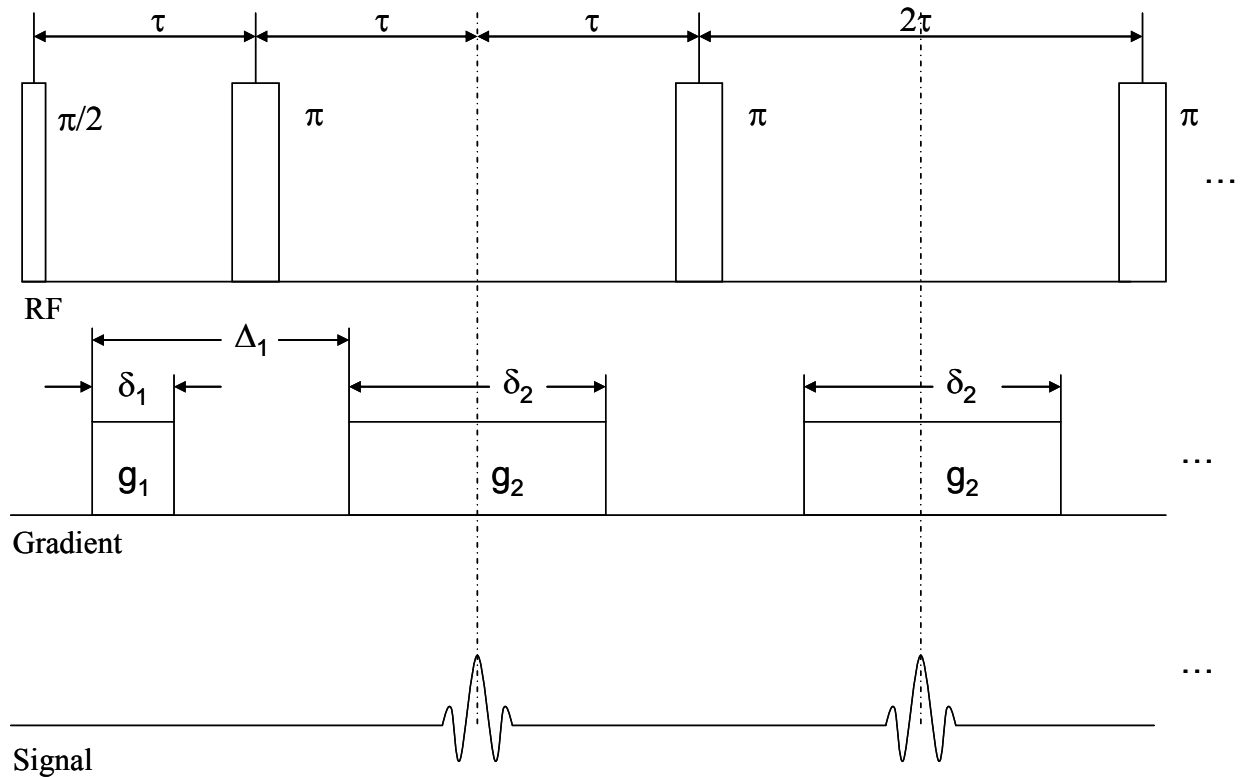


Figure 3 Profile of 4 cm water sample generated after FFT reconstruction of the collected echo.

Spin Density Image of a Layered Water-Squalane Sample ($T_E = 8$ msec, $T_R = 15,000$ msec)**Figure 4** Spin Density image of a layered water and squalane system T_1 -Weighted Image of a Layered Water-Squalane Sample ($T_E = 8$ msec, $T_R = 714$ msec)**Figure 5** T_1 -weighted image of a layered water and squalane system

T_2 -Weighted Image of a Layered Water-Squalane Sample ($T_E = 140$ msec, $T_R = 15,000$ msec)**Figure 6** T_2 -weighted image of a layered water and squalane system**Figure 7** RARE Pulse Sequence Diagram (Bernstein et al, 2004)

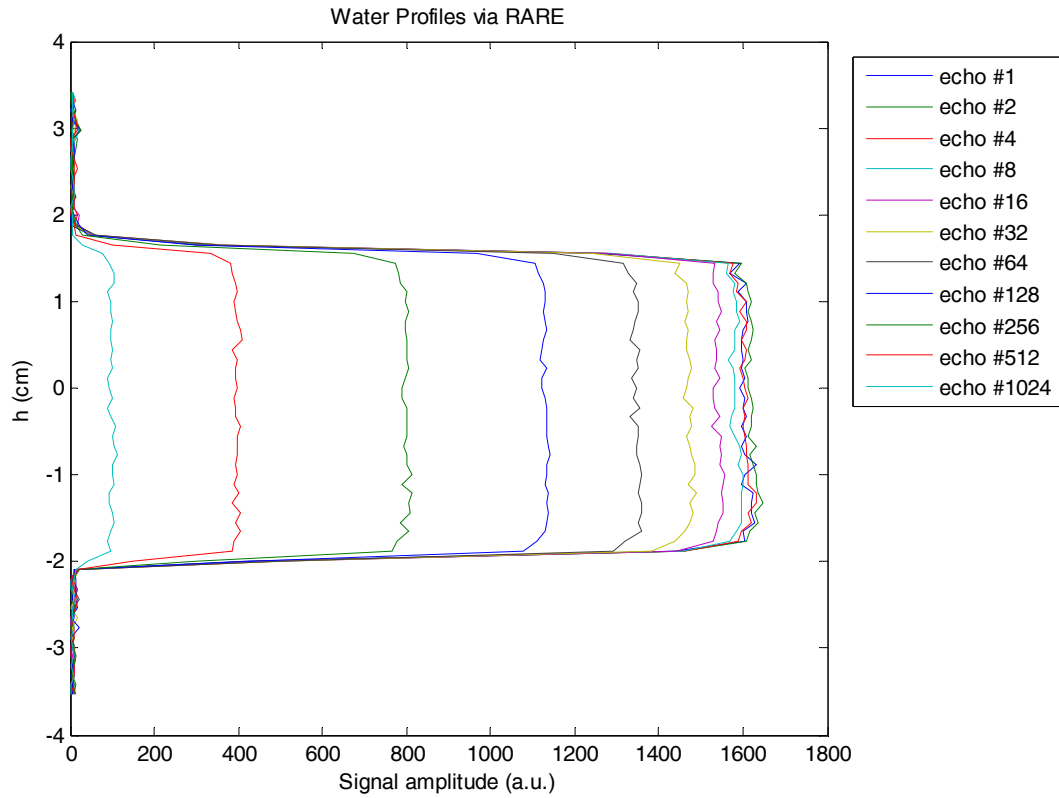


Figure 8 RARE Profiles of a water sample with a 4 cm height. $g_1 = g_2 = 0.800 \text{ cm}^{-1}$,
 $\delta_1 = 1.30 \text{ msec}$, $\tau = 3.00 \text{ msec}$, $DW = 40.0 \text{ msec}$, $SI = 64$

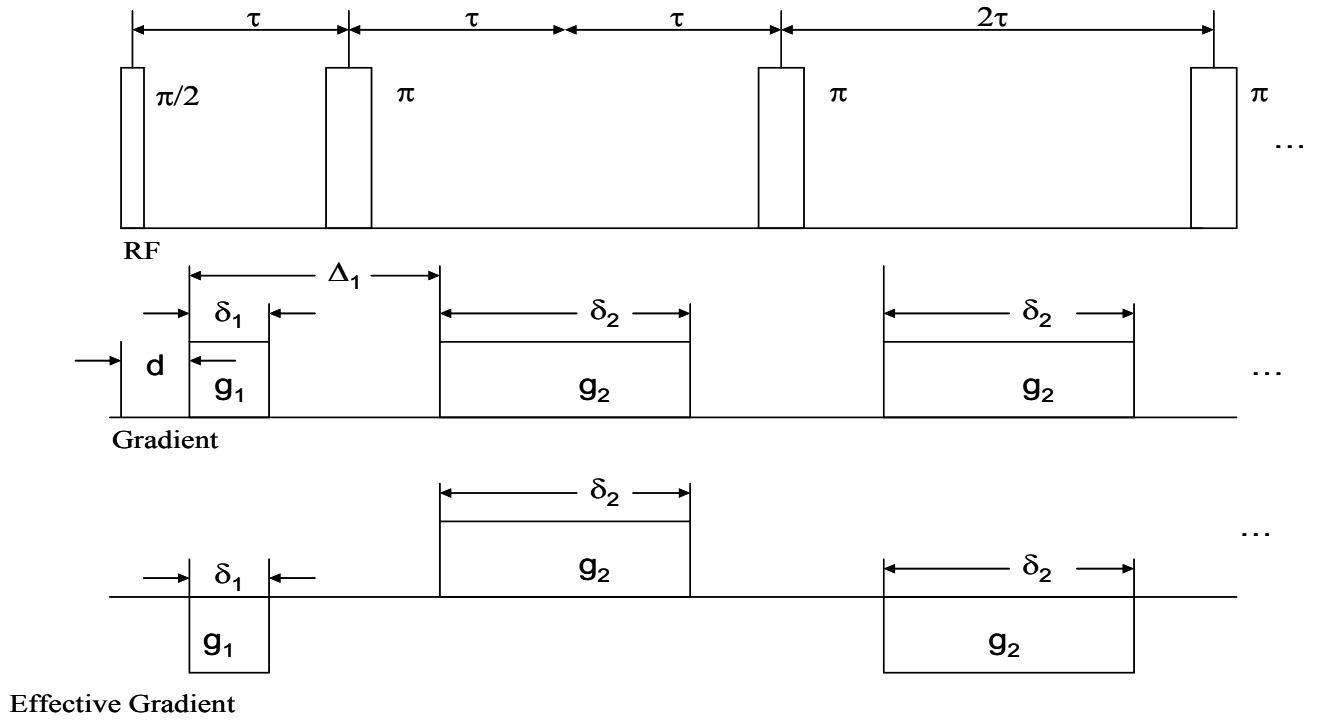


Figure 9 Representation of the effective gradient, g^* , in the RARE sequence.

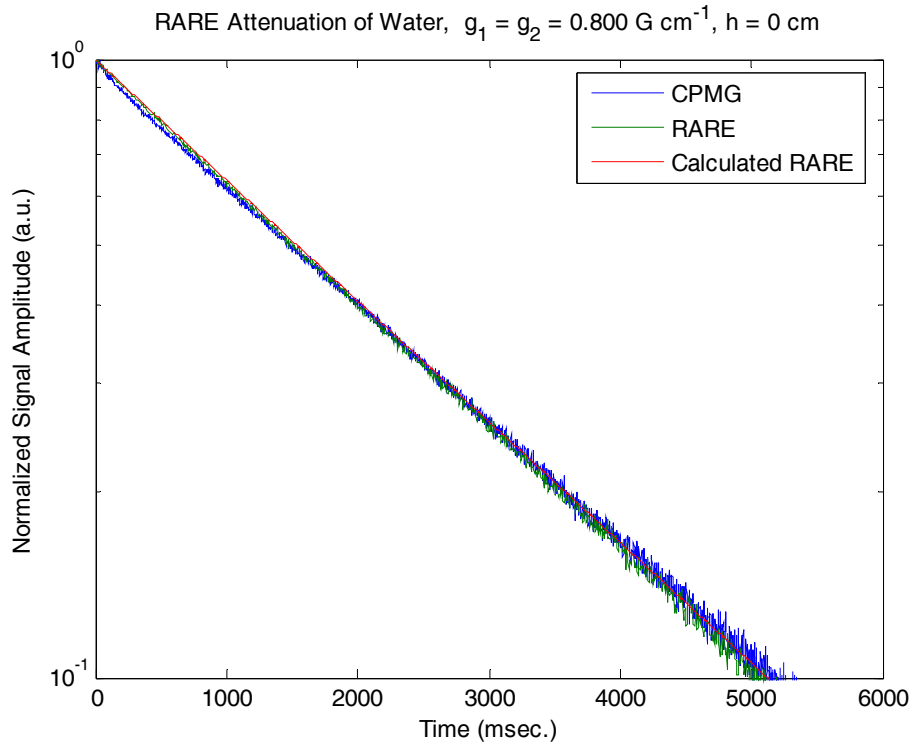


Figure 10 Normalized signal amplitude versus time.

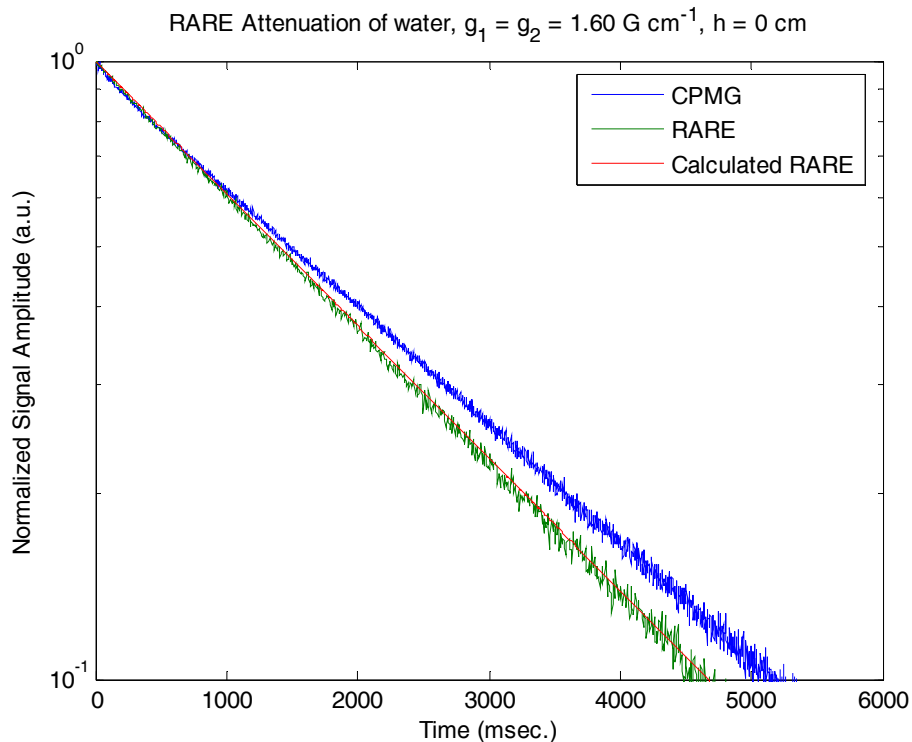


Figure 11 Normalized signal amplitude versus time.

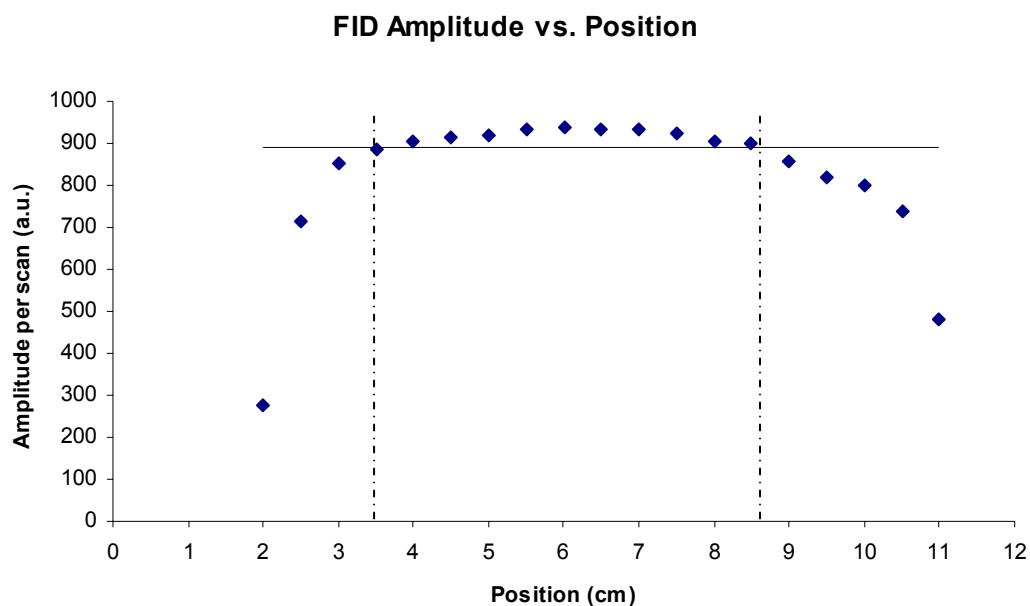


Figure 12 Results of a series of FID experiments performed on a 0.5 cm sample of water used to determine the sweet spot of the MARAN-M. The horizontal line denotes a 5% percent deviation from the maximum amplitude.

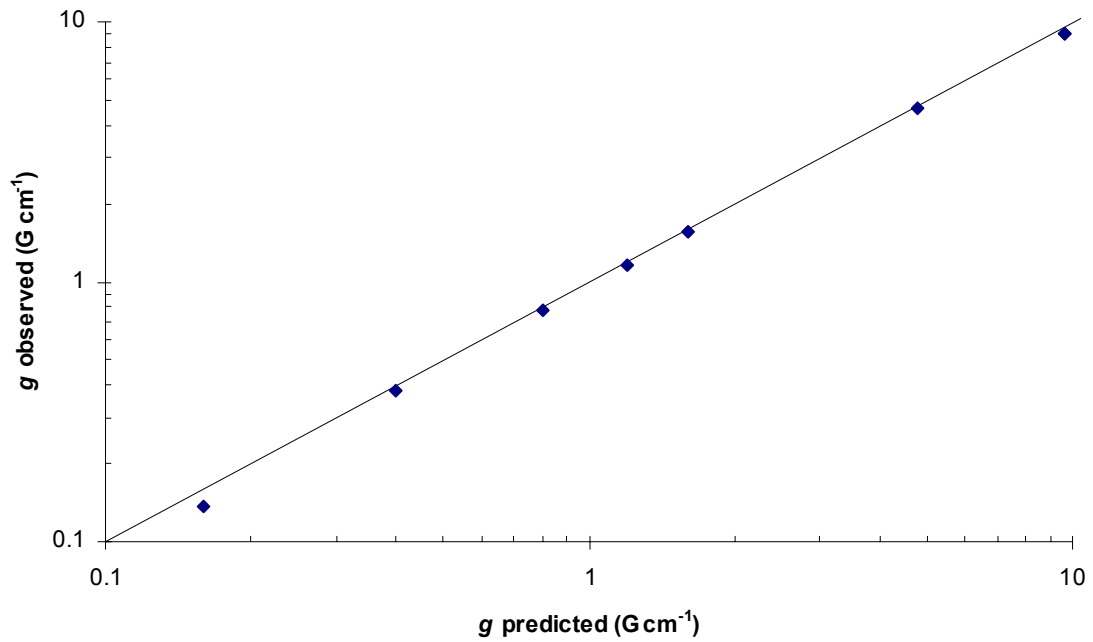


Figure 13 Observed vs. Predicted behavior of the MARAN-M's gradient. Deviations are observed at very low values of g .

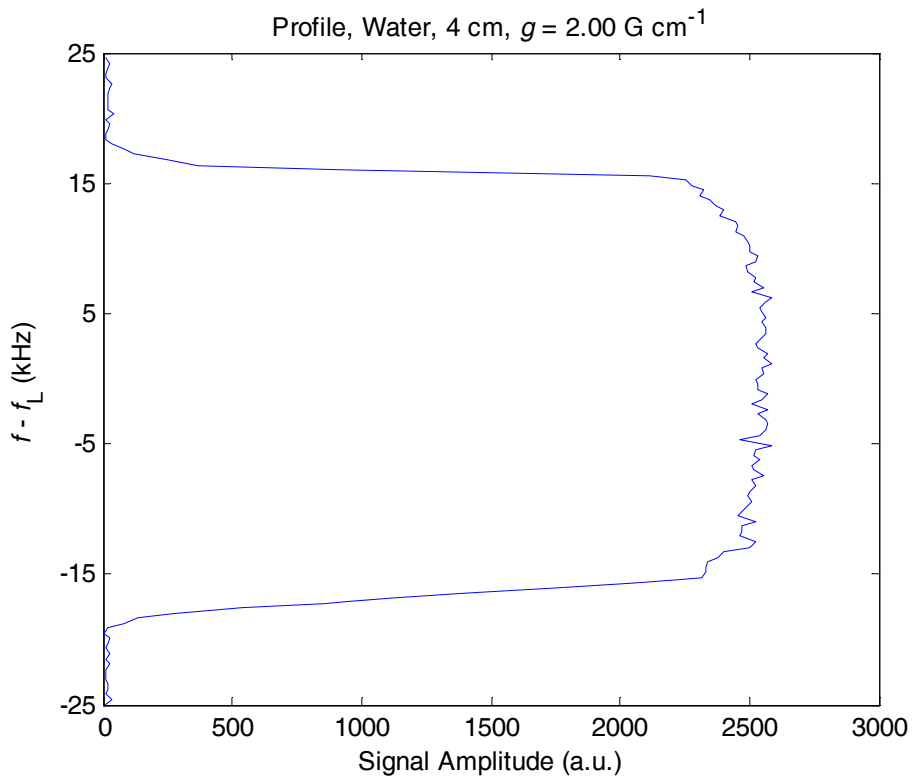


Figure 14 Demonstration of profile rounding due to a large Δf

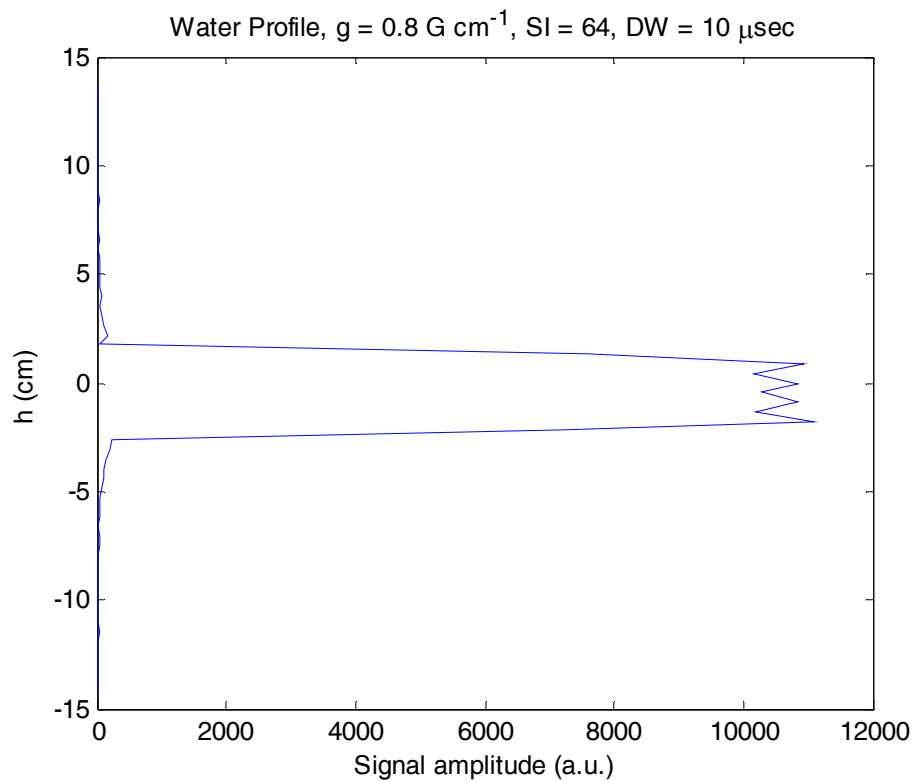


Figure 15 Improper selection of DW. The measurement resolved a length much greater than the sample height.

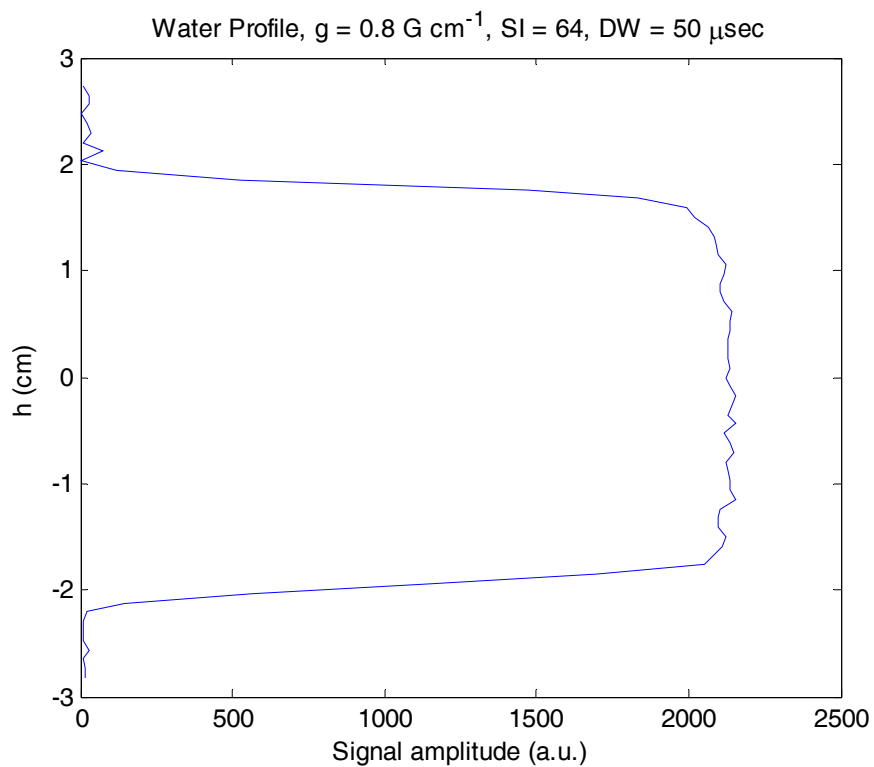


Figure 16 Dwell time selected so that the sample plus an excess of about half a centimeter above and below the sample is measured. All other parameters remain the same as the profile depicted in Figure 15.

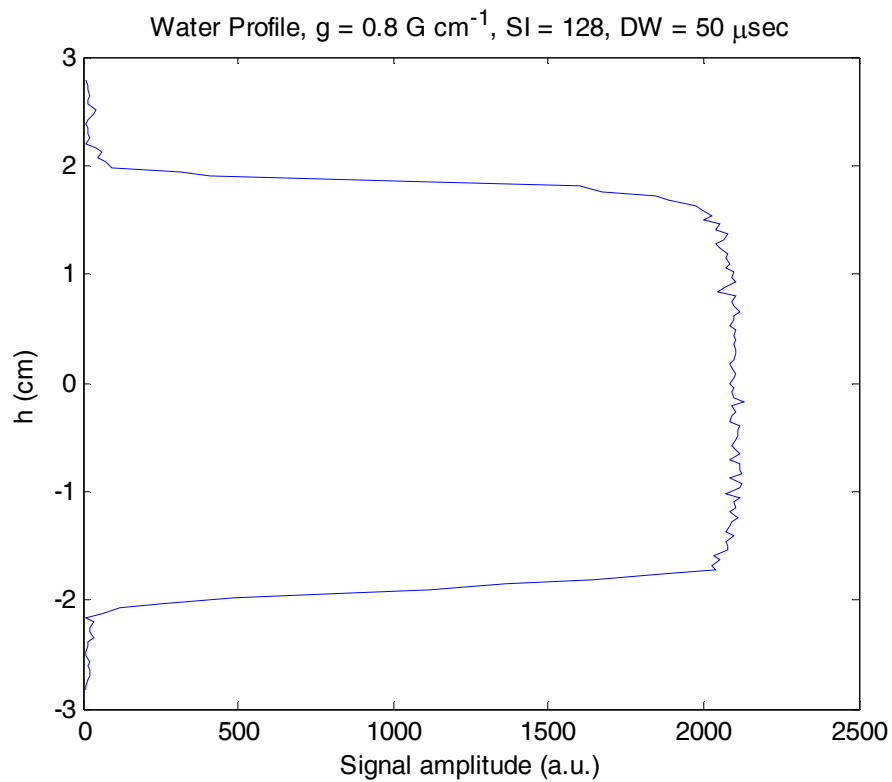


Figure 17 Increasing SI increases the resolution of the profile. The only parameter changed from Figure 16 to this figure was SI from 64 (Figure 16) to 128. Resolution has been increased from $2.2 \text{ points cm}^{-1}$ (Figure 16) to $4.4 \text{ points cm}^{-1}$.

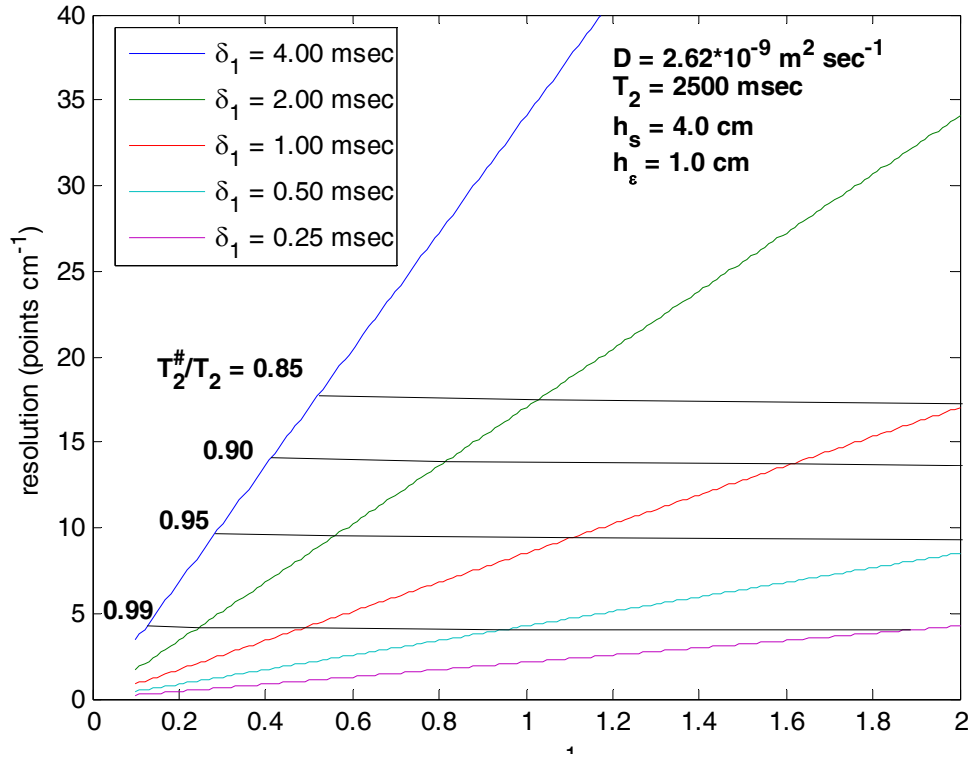


Figure 18 Measurement Resolution based on Equation 4.

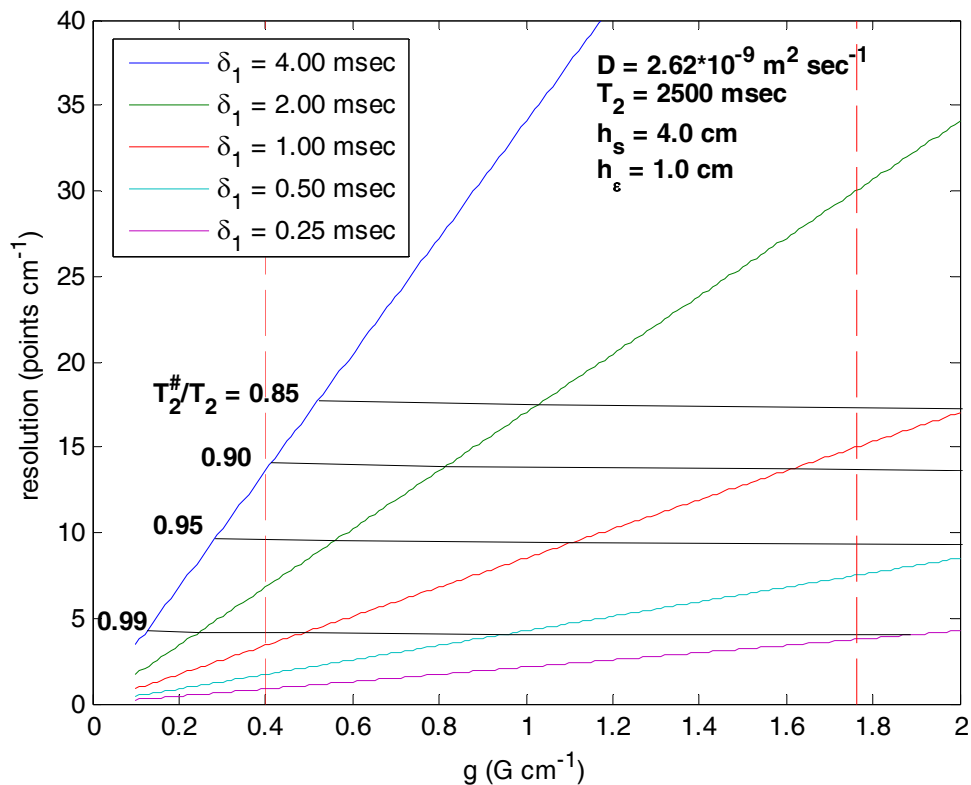


Figure 19 Measurement Resolution based on equation 4 with g_{\min} and g_{\max} denoted by the red, vertical dashed lines

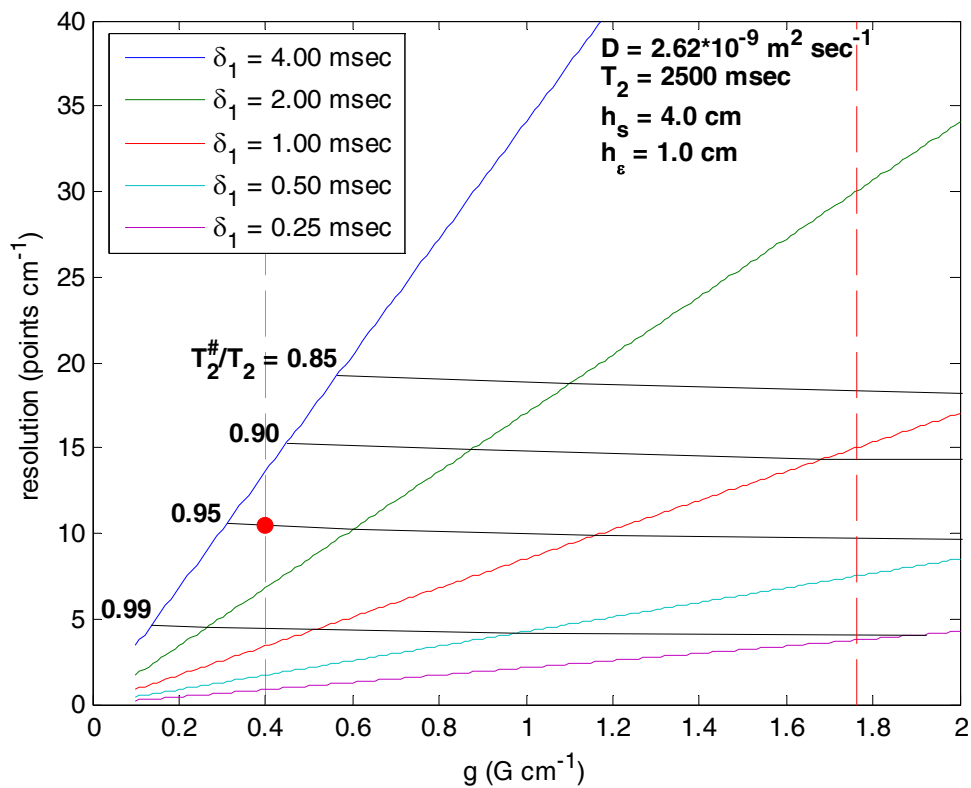


Figure 20 Measurement resolution based on Equation 4 with g_{\min} and g_{\max} denoted by the red, vertical dashed lines. Red dot corresponds to selected g and δ_1 pair ($g = 0.40 \text{ G cm}^{-1}$, $\delta_1 = 3.06 \text{ msec}$).

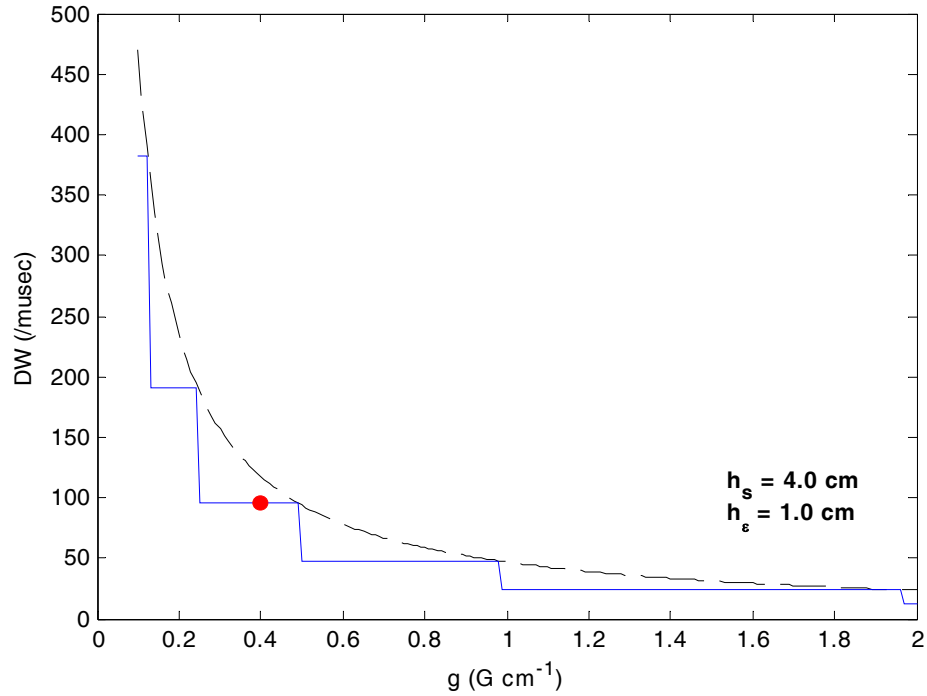


Figure 21 Dwell time as a function of g for $\delta_1 = 3.06$ msec. The dashed line represents the maximum DW determined by g , h_s , and h_e .

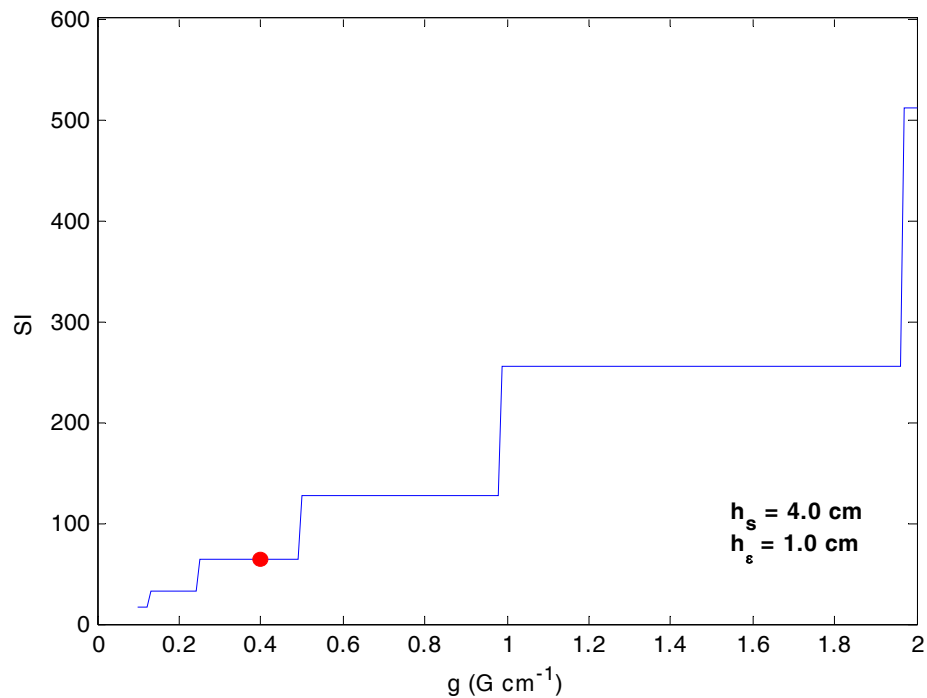


Figure 22 SI as a function of g for $\delta_1 = 3.06$ msec.

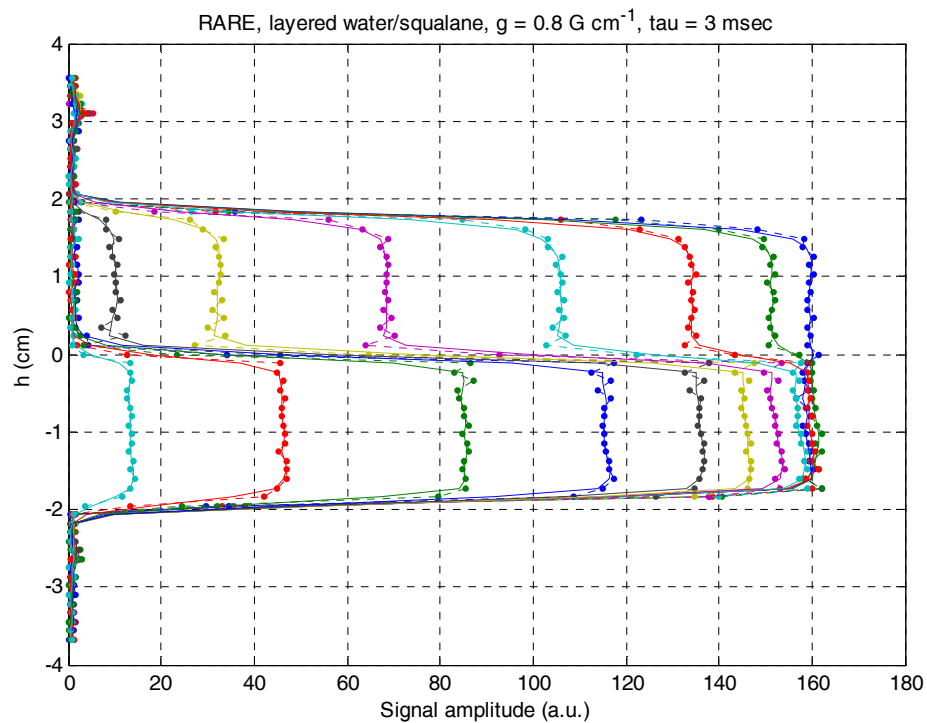


Figure 23 RARE profiles of a water/squalane system. The points represent the un-averaged data while the line indicates the profiles after averaging has been performed.

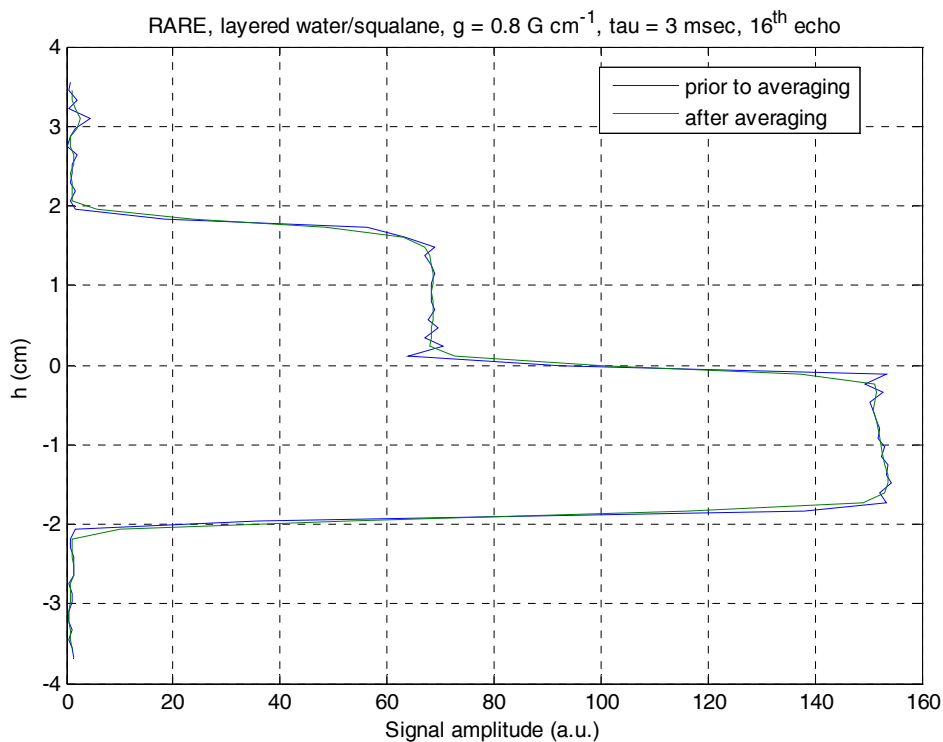


Figure 24 RARE profile (16th echo) of a water/squalane system. The blue line corresponds to the profile prior to averaging. The green line indicates the resulting profile after averaging.

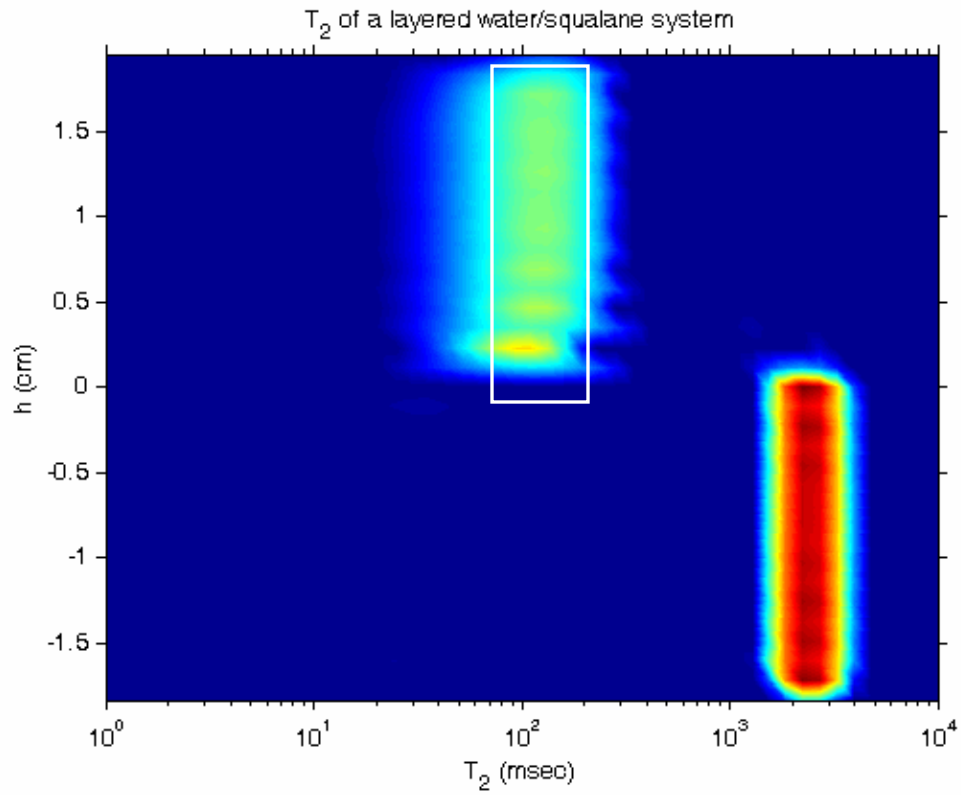


Figure 25 T_2 profile of a water/squalane system using the un-averaged data.

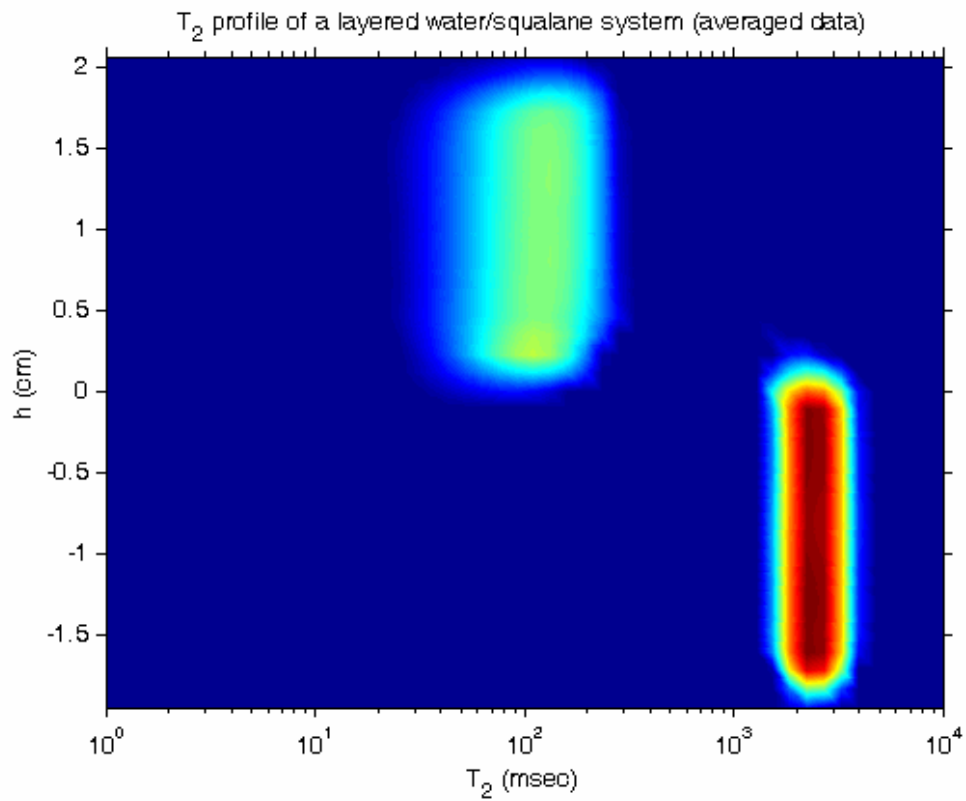


Figure 26 T_2 profile of a water/squalane system using the averaged data.

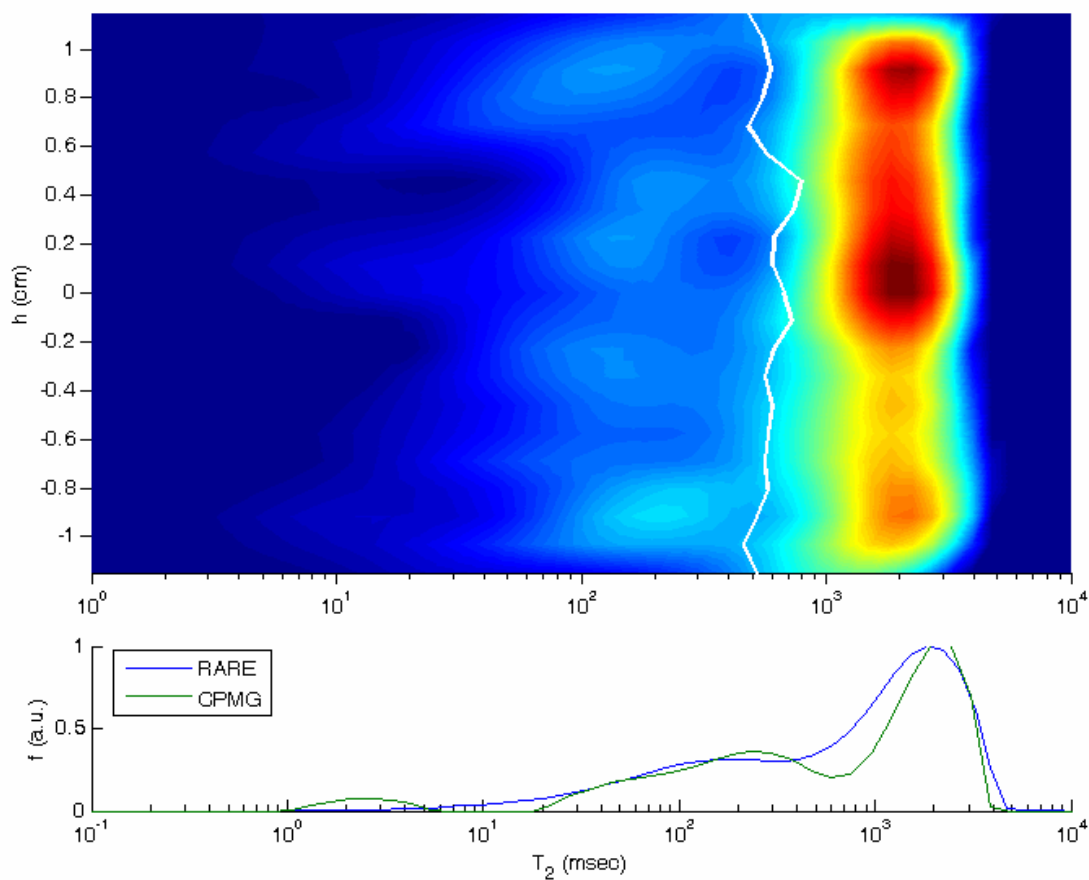


Figure 27 T_2 map for A3. The white line indicates the $T_{2, \log\text{mean}}$

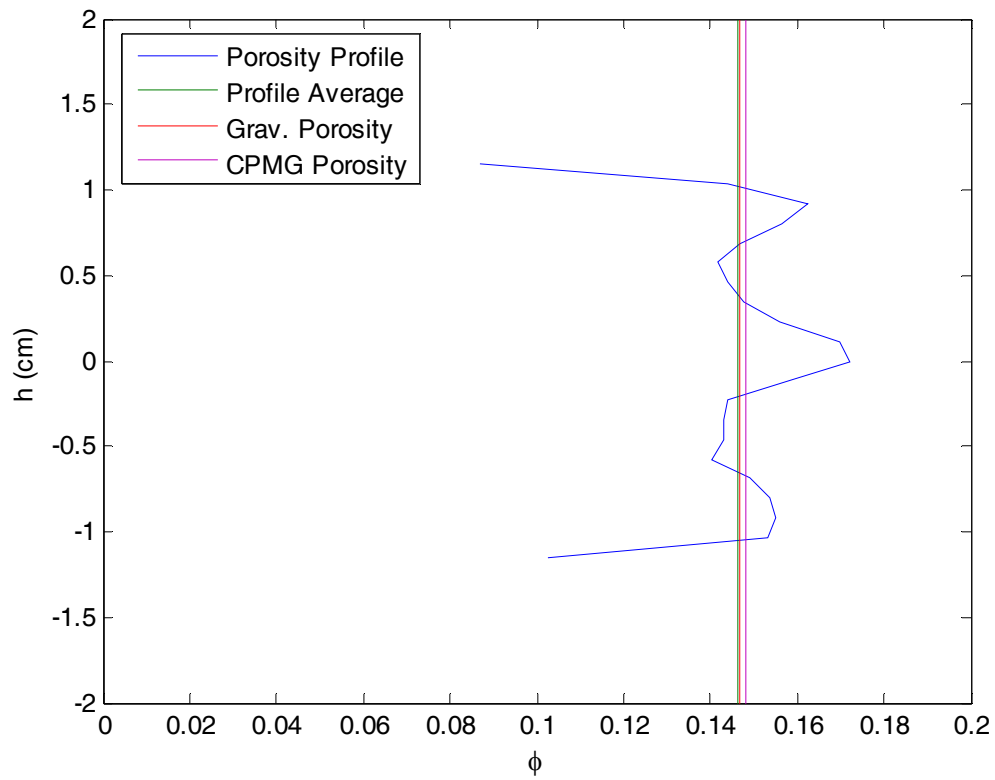


Figure 28 Porosity Profile for A3

CHAPTER 3. A RANDOM-WALK TECHNIQUE FOR SIMULATING NMR MEASUREMENTS AND 2D NMR MAPS OF POROUS MEDIA WITH RELAXING AND PERMEABLE BOUNDARIES

We revisit random-walk methods to simulate the NMR response of fluids in porous media. The simulations reproduce the effect of diffusion within external inhomogeneous background magnetic fields, imperfect and finite-duration \mathbf{B}_1 pulses, T_1/T_2 contrasts, and relaxing or permeable boundaries. This approach generalizes existing NMR numerical methods used in biology and engineering into a single formulation that expands on the magnetic-dipole equivalent of spin packets. When fluids exhibit low T_1/T_2 contrasts and when CPMG pulse sequences are used to acquire NMR measurements, we verify that classic NMR numerical models neglecting T_1 effects accurately reproduce surface magnetization decays of saturated granular porous media. However, when fluids include several components or when magnetic fields are strongly inhomogeneous, we show that simulations obtained with the complete set of Bloch's equations differ substantially from those of classic NMR models. Our random-walk formulation accurately reproduces the magnetization echoes stemming from fundamental spin dynamics calculations in arbitrary spatial distributions of background magnetic field. By simulating longitudinal and transversal magnetizations for specific bulk fluid properties and fluid/solid boundary geometries, the random-walk approach can be used to generate parametric multidimensional $T_1/T_2/D$ NMR maps to improve the characterization of pore structures and saturating fluids from NMR.

3.1 INTRODUCTION

The application of NMR measurements for pore-size characterization of porous and permeable media is motivated by two relationships between measurable quantities and the pore surface-to-volume ratio S/V of porous media saturated with a single fluid phase. Firstly, longitudinal and transversal relaxation times of a fluid (T_1 and T_2 , respectively) are related to the product $\rho(S/V)$, where ρ is the relaxivity of the pore surface. This relationship remains valid in the fast-diffusion limit (1) when paramagnetic centers are present at the pore wall

surface. Secondly, the short-time asymptotic behavior of the effective fluid diffusivity D is directly related to S/V (2-3). Practical limitations exist when applying these two relationships to the interpretation of NMR measurements of porous media. Specifically, it is normally assumed that (1) pores are well defined and isolated, and (2) inversion techniques can reliably and accurately estimate the distribution of surface-to-volume ratios. Experimental evidence shows that pores spanning different length scales can be connected and, therefore, that the estimated values of S/V could be interpreted in an average sense in the presence of low surface relaxivity, such as in certain carbonate rocks(4). In addition, effective pore values of S/V sensed by protons in a fluid phase depend on the relative saturation of that phase within the pore: when several fluid phases are present in the same pore space, such as in the case of mixed-wettabilities, the actual and effective values of S/V for that pore may differ substantially. Models used in biological applications to study the influence of membrane permeability on NMR signals also over-simplify the pore structure of biological systems because of the lack of efficient numerical simulation techniques (5-8).

Recently, special acquisition techniques have been developed to improve the accuracy of NMR measurements to assess fluid types (9-11) using (a) suites of magnetic pulse sequences of different magnitudes, orientations, and characteristic times, e.g. CPMG-like sequences with different echo-times and wait-times, and (b) multi-dimensional inversion of the measured magnetization decays in the form of intensity maps in T_1 , T_2 and D domains. Despite these efforts, ambiguities remain when the saturating fluids exhibit similar characteristics, such as light oil and water in water-wet and mixed-wet rocks, because the inversion process is sensitive to fluid diffusivity contrasts, restricted diffusion, surface relaxation, and wettability of the porous medium.

Modern NMR applications require simulation and interpretation methods that can incorporate the complexity of real porous media and multiphase fluid saturation at the pore scale. Accurate simulation methods have been proposed based on a quantum mechanical framework for bulk fluids (12), or based on analytical diffusion propagators for the case of periodic porous microstructures (13). However, the disordered nature of most biological and mineral porous media demands more sophisticated approaches for numerical simulation.

The objective of this study is to develop an accurate and efficient algorithm for the simulation of NMR measurements of saturated microporous media. Specifically, the algorithm is designed to account for known distributions of (a) pore boundaries and surface characteristics (i.e. geometry and surface relaxation ρ and/or diffusion permeability P), (b) static and susceptibility-induced magnetic fields, (c) fluid phases and their bulk properties, and (d) corresponding velocity fields superimposed to the diffusive Brownian motion in the case of ionic displacement (14) or hydraulic motion (15). After motivating the need for a microscopic description of the pore space to construct quantitative NMR numerical models, we develop the algorithm for the solution of Bloch's equations along the continuous diffusion paths of random walkers. This approach remains valid when the magnetization coupling between spins in a fluid is governed by constant longitudinal and transversal bulk relaxations, and when Bloch's equations remain valid to describe spin magnetization, i.e., both in the low-field NMR measurement of spin $\frac{1}{2}$, and in the high-field ^1H measurements of water. Next, we compare the results of our approach with a more conventional resolution method that neglects the 3D dipole precession in bulk fluid magnetization. We emphasize the ability of our approach to simulate the NMR response of mono- and multi-phase fluids in porous media and to synthesize models of parametric multidimensional NMR maps from pore-scale arguments.

3.2 MACROSCOPIC THEORY

Macroscopically, it is usually considered that three independent processes affect the relaxation time of the measured NMR magnetization: (1) bulk fluid relaxation, with characteristic longitudinal and transversal times T_{1B} and T_{2B} , mainly due to dipole-dipole interactions between spins within the fluid; (2) surface relaxation, characterized by effective relaxation times T_{1s} and T_{2s} , which occurs because of the proximity with paramagnetic centers at interfaces between pore fluids and grain solids; and (3) relaxation due to the presence of background magnetic field heterogeneities, T_{2D} . The measured longitudinal and transversal relaxation times measured for a fluid-saturated sample are equal to the harmonic averages (16):

$$\frac{1}{T_1} = \frac{1}{T_{1B}} + \frac{1}{T_{1S}}, \quad (1)$$

and

$$\frac{1}{T_2} = \frac{1}{T_{2B}} + \frac{1}{T_{2S}} + \frac{1}{T_{2D}}. \quad (2)$$

Bulk and surface relaxation times are intrinsic properties given by fluid, porous medium and thermodynamic state. Bulk relaxations are usually in the form (17-18)

$$T_{1B,2B} = a \frac{T}{\eta} = f(P, T) D_B \quad (3)$$

where a is a fluid-specific constant, f a thermodynamic function, and P , T , η and D_B the pressure, temperature, viscosity and bulk diffusivity of the fluid, respectively. The surface decay times T_{1S} and T_{2S} are proportional to S/V (1):

$$\frac{1}{T_{1S,2S}} = \rho_{1,2} \frac{S}{V} \quad (4)$$

as long as the diffusion-relaxation problem is controlled by diffusion, i.e., in the fast-diffusion limit $\rho R/D_B < 1$ (R being the pore radius). T_{2D} , on the other hand, is an experimentally controllable quantity affected by fluid diffusivity, internal fields induced by porous medium magnetic heterogeneities, and instrument configuration. For instance, using a CPMG sequence with constant echo time TE and an applied magnetic gradient G , we have

$$\frac{1}{T_{2D}} = \frac{(\gamma G TE)^2 D}{12}, \quad (5)$$

where γ is the hydrogen gyromagnetic ratio.

The intrinsic bulk and surface relaxation times affect the time-space evolution of the macroscopic magnetization $\mathbf{M} = (M_x, M_y, M_z)^T$ of a given volume of fluid according to the Bloch-Torrey Equation (19) in the rotating frame $\Sigma = (\hat{\mathbf{x}}', \hat{\mathbf{y}}', \hat{\mathbf{z}})$:

$$\frac{d\mathbf{M}}{dt} = D_{bulk} \nabla^2 \mathbf{M} + \gamma \mathbf{B} \times \mathbf{M} - \frac{M_x}{T_2} \hat{\mathbf{x}}' - \frac{M_y}{T_2} \hat{\mathbf{y}}' - \frac{M_z}{T_1} \hat{\mathbf{z}} + \frac{\mathbf{M}_0}{T_1}. \quad (6)$$

In this equation, $\mathbf{M}_0 = M_0 \hat{\mathbf{z}}$ is the equilibrium magnetization aligned with the background magnetic field \mathbf{B}_0 , and $\mathbf{B} = (B_x, B_y, B_z)^T$ is the total magnetic field that affects the spins in Σ . \mathbf{B} varies as a function of time and space because of (a) inhomogeneous tool background field maps such as modeled in Figure 1, (b) susceptibility contrasts between fluid and porous matrix which distort the background field map (13, 20), and (c) additional background field gradients used to enhance the NMR decay due to diffusivity contrasts between fluids in low-field applications, or to encode the spin position in high-field MRI applications as illustrated in Figure 2. When an RF pulse sequence is used to enforce spin refocusing and echo forming, \mathbf{B}_1 magnetic pulses superimpose to \mathbf{B}_0 for finite durations t_θ . This duration quantifies the amount of magnetization tilting ($\theta = \gamma \|\mathbf{B}_1\| t_\theta$) they create through the curl term in Equation (6) – usually $\pi/2$ or π for the entire pulse duration. For instance, regular CPMG pulse sequences take the form of a $\pi/2$ -pulse of duration t_{90} along the $\hat{\mathbf{x}}'$ axis, followed by a series of π -pulses of duration t_{180} along the $\hat{\mathbf{y}}'$ axis separated by the inter-echo time $TE = 2\tau$. Spin echoes are stimulated between two successive π pulses. Together with the proximity of relaxing surfaces which affect the relaxation of the spin packets captured by Equation (6), this variation of \mathbf{B} with both time and space suggests a microscopic treatment where such constraints can be explicitly enforced.

3.3 MICROSCOPIC RANDOM-WALK RESOLUTION

Random walkers reproducing the diffusive motion of spins have proved to be a reliable and flexible approach to simulate the NMR responses in a variety of porous medium geometries, including fractal or 3D disordered granular porous media (22-23). Diffusion random-walks, on the other hand, readily lend themselves to distributed computer environments thereby considerably reducing computation times. Such algorithms simulate the projection of spin packets in the transversal plane of the rotating frame, i.e., in the plane of measurement of an NMR tool antenna, and describe either surface relaxation effects (4, 24) or diffusion effects (20, 25). In this section, we introduce a unified formulation for the

simulation of NMR measurements acquired in a wide range of engineering and biological applications.

3.3.1 Diffusion of Equivalent Magnetic Dipoles

We use a classical continuous random walk, whereby an equivalent magnetic dipole is displaced within the pore space attributed to a given fluid of self-diffusion D and bulk relaxation times T_{1B} and T_{2B} . Following an initial location randomly determined within that fluid volume, at each time step of infinitesimal duration δt a vector of normally distributed random numbers $\mathbf{n} = (n_x, n_y, n_z)^T$ is generated with unit variance and zero mean. The walker is then spatially displaced in the Cartesian geometrical reference by a vector

$$\delta \mathbf{r}_D = (6 D_B \delta t)^{1/2} \mathbf{n} / \|\mathbf{n}\|. \quad (7)$$

In the presence of velocity drift \mathbf{v} applied to the molecule, an additional drift displacement $\delta \mathbf{r}_V = \mathbf{v} \delta t$ is added to $\delta \mathbf{r}_D$. In so doing, δt is dynamically adapted along the walk so that (a) it is smaller than any magnetic field pulse duration, (b) the amplitude of the displacement, $\|\delta \mathbf{r} = \delta \mathbf{r}_D + \delta \mathbf{r}_V\|$, is several times smaller than surrounding geometric features (such as pore throats restricting the passage from pore to pore, wetting film thickness, etc.), (c) the value of the total magnetic field resulting from \mathbf{B}_0 and \mathbf{B}_1 in the rotating frame can be considered constant during each step, and (d) all walkers are synchronized at the onset and offset of magnetic pulses as well as at the time of echo acquisition.

3.3.2 Magnetization Formulations A and B

We use diffusing random walkers to simulate NMR signals under the assumption that each walker carries a magnetic dipole equivalent to that of a hydrogen spin packet. Equation (6) is adapted along each 1-dimensional segment by neglecting its convection term in ∇^2 and by defining the evolution matrix \mathbf{A} given by

$$\mathbf{A} = \begin{bmatrix} -\frac{1}{T_2} & \gamma B_z & -\gamma B_y \\ -\gamma B_z & -\frac{1}{T_2} & \gamma B_x \\ \gamma B_y & -\gamma B_x & -\frac{1}{T_1} \end{bmatrix}, \quad (8)$$

and the reduced magnetization

$$\mathbf{M}' = \mathbf{M} + \mathbf{A}^{-1} \cdot \mathbf{M}_0 / T_1. \quad (9)$$

Equation (6) is integrated as

$$\mathbf{M}'(t) = e^{\mathbf{A}t} \cdot \mathbf{M}'(0), \quad (10)$$

where $\mathbf{M}'(0)$ is the reduced magnetization at the onset of each integration interval. New appropriate values for B_x , B_y and B_z are used on each random-walk segment. The relaxation times T_1 and T_2 are also locally adjusted to account for the proximity of a relaxing boundary. Consequently, for each step i spanning the time interval $[t_i, t_i + \Delta t_i]$, the spin carried by the random walker is subject to a new evolution matrix \mathbf{A}^i and longitudinal relaxation time T_1^i . This calculation yields the magnetization **formulation A**:

$$\mathbf{M}^i = e^{(\mathbf{A}^i)\Delta t} \cdot \left\{ \mathbf{M}^{i-1} + (\mathbf{A}^i)^{-1} \cdot \frac{\mathbf{M}_0}{T_1^i} \right\} - (\mathbf{A}^i)^{-1} \cdot \frac{\mathbf{M}_0}{T_1^i}. \quad (11)$$

The total NMR signal is the sum of all \mathbf{M} vectors for all diffusing magnetic dipoles, sampled at the same rate. Hydrogen indices weight the magnetization contribution of each walker in the presence of multiple fluid phases with different hydrogen index. The Appendix provides analytical solutions for the matrix exponential of \mathbf{A} . Tracking the projections of that total magnetization \mathbf{M} onto \mathbf{z} and $\hat{\mathbf{y}}'$ with time yields the magnetization polarizations and decays illustrated in Figure 3. This figure shows the responses of both bulk water and water within relaxing porous medium simulated with CPMG pulse sequences and different values of wait times (TW) and echo time (TE).

Previously developed NMR simulation algorithms focused exclusively on reproducing surface relaxation or diffusion within inhomogeneous fields. The latter effect was usually treated in a manner similar to the one described above, except that Bloch's equation is just solved in the $(\hat{\mathbf{x}}', \hat{\mathbf{y}}')$ projection of Σ by substituting \mathbf{M} in Equation (6) with a complex magnetization $M^* = M_x + i M_y$ (26). That magnetization is subsequently solved in finite-difference grids (27) or without convection term along random-walk trajectories (20, 25). This approach neglects surface as well as longitudinal relaxation effects. RF pulses could not be accurately reproduced, and only $(\pi)_y$ pulses could be modeled as a sign change in the phase of M^* with the axis of $\hat{\mathbf{y}}'$ (20), which makes the method amenable to CPMG sequences exclusively. The NMR signal was then considered equal to the sum of the cosine of the spin phase shifts, where the phase shifts were equal to the same rotation angle as in the evolution matrix for 3D calculations (see the Appendix), i.e., $\phi = \gamma B \delta t$. For comparison purposes, we also implemented this resolution in $(\hat{\mathbf{x}}', \hat{\mathbf{y}}')$ space as **formulation B**.

3.3.3 Treatment of Local Surface Relaxation

While the walker remains away from a fluid boundary, the relaxation times T_1 and T_2 that affect the equivalent magnetic dipole of the random walker are equal to the bulk fluid longitudinal and transversal relaxation times T_{1B} and T_{2B} . However, once the walker is located within one step of a fluid boundary of surface relaxivities ρ_l (longitudinal) and ρ_2 (transversal), the magnetization decay is locally enhanced to include this surface relaxation effect at the microscopic level. If the displacement achieved during the interval $[t, t + \delta t]$ comes within a distance δr of a fluid boundary, the boundary equation

$$D_{bulk} \frac{\partial \mathbf{M}}{\partial \hat{\mathbf{n}}} + \begin{bmatrix} \rho_2 & & \\ & \rho_2 & \\ & & \rho_1 \end{bmatrix} \cdot \mathbf{M} = 0 \quad (12)$$

governs the behavior of the relaxation, where the unit vector $\hat{\mathbf{n}}$ describes the normal direction to the surface boundary. For a locally flat boundary, Equation (12) is solved on a square lattice (28) or for continuous random walks (24) to define a probability of

instantaneously ‘killing’ the spin when it reaches the boundary. Bergman *et al.* (24) solved the boundary condition by integrating diffusion propagators and related that ‘killing’ probability p to surface relaxivity ρ as

$$p = \frac{2}{3} \frac{\rho \delta r}{D_B} \times 0.96. \quad (13)$$

In our model, we consider that each time the walker reaches a relaxing boundary then the magnetization decreases by a factor $(1-p)$, or $\exp[-\delta t / (p / \delta t)]$ since $p \ll 1$. Therefore, the total relaxation rate for that step becomes $1/T_{1,2} = 1/T_{1B,2B} + \delta t / p$ for that step. Equivalently, the relaxation times used on each segment of the random walk become

$$\frac{1}{T_{1,2}} = \frac{1}{T_{1B,2B}} + \varepsilon \frac{\delta r}{3.84 \rho_{1,2}}, \quad (14)$$

where $\varepsilon = 1$ when the walker is located within a step of the relaxing boundary, and 0 otherwise.

3.3.4 Transfer Probability of Permeable Membranes

The case of permeable barriers between pore volumes can be approached in a similar fashion to the case of relaxing surfaces. A boundary exchange rate k_j is defined as the proportionality factor between diffusion flux and concentration difference across a boundary j . If bulk and surface relaxations can be neglected, then the macroscopic magnetization balance of a compartment bounded by permeable membranes is given by (7-8)

$$\frac{\partial \mathbf{M}}{\partial t} = D_B \nabla^2 \mathbf{M} + \gamma \mathbf{B} \times \mathbf{M} - \sum_{\text{outwards}} k_j \mathbf{M} + \sum_{\text{inwards}} k_j \mathbf{M}^{(j)}, \quad (15)$$

where $\mathbf{M}^{(j)}$ is the magnetization within a neighboring compartment j . The sum over outward boundaries acts as a surface sink term whereas the one over inward boundaries acts as a surface source term. Since the surface sink term in Equation (12) acts as the relaxation decay terms in Equation (1), the following equivalence holds:

$$\frac{1}{T_2} \equiv \sum_{\text{outwards}} k_j. \quad (16)$$

Furthermore, in the fast diffusion limit we have $1/T_{2S} = \rho(S/V)$ (1); similarly, $k_j = P_j(S/V)$ (7), where P_j is the membrane permeability in units of count per unit time and unit surface. It is then straightforward to solve for surface permeability using Bergman *et al.*'s treatment of surface relaxation: when the walker comes within one step of distance δr from a permeable boundary k , we define a probability of transfer equal to

$$g_k = \frac{2 P_k \delta r}{3 D_B} \times 0.96. \quad (17)$$

If g_k is honored, then the walker crosses the boundary; if not, it bounces back into its original compartment while the clock time is incremented by δt . It is remarkable that both fluid/rock surface relaxation (29) and biological membrane permeability (7) exhibit the same range of values between 0.5 and 30 $\mu\text{m/s}$. This similarity suggests that the parallel treatment of relaxing or permeable boundaries remains valid on the same range of fluid types and pore sizes.

3.4 SIMULATION RESULTS IN BULK FLUID

3.4.1 Effect of Volume Sampling and Pulse Width on Echo Amplitude

Dispersion of magnetic field strength – and therefore of Larmor frequencies – throughout the volume enhances the precession decay and the formation of echoes due to the RF π -pulses of a CPMG sequence. When the duration of these RF pulses increases, then the measurable echo amplitude decreases. Background field maps can therefore be optimized to maximize the signal obtained during acquisition. These remarks are illustrated in Figure 4, where the formation of echoes in 1 cm^3 of water is simulated with our random-walk method (formulation A) through spin refocusing between two π -pulses, for different pulse widths and two permanent magnetic field maps. As the duration of the RF pulses increases, the quality of the echoes degrades through lower amplitudes and larger spread. In these tests, the

field map shown in Figure 1 generates higher echo amplitudes, hence higher signal, than that of a homogeneous magnetic gradient. When the spread of Larmor frequencies decreases, e.g., by reducing the sampling volume (Figure 5) or the magnitude of the magnetic gradient, the signal remains maximal.

Hürlimann and Griffin (12) quantified the relative amplitude variation of the stimulated echo (produced by the energy stored during the initial $(\pi/2)_x$ pulse) and of the first spin echo (refocused by the first CPMG $(\pi)_y$ pulses) with spin dynamic calculations for given field maps and pulse durations. In Figure 6 we show that similar results are obtained with the random-walk technique. The differences between the results of Reference (12) and our simulations can be attributed to differences in field map details and homogeneity of the background magnetic field. In all cases, the amplitude of the first echo is remarkably lower than that of the second echo for $TE < 5$ ms, and becomes larger when TE increases. As suggested by Figure 5, the shapes and relative amplitudes of any echo beyond the first two can also be simulated using random walks.

The magnetization decays considered in the rest of this paper are taken as the envelopes of maximal values reached at each M_y echo.

3.4.2 Multi-Component Fluids with Multiple Wait-Time Acquisitions

It is customary to consider that the NMR decay obtained for a fluid after repolarization of the duration TW is equal to the decay at full polarization (i.e. starting from $\mathbf{M} = \mathbf{M}_0$, or $TW \rightarrow \infty$) weighted by the value $(1 - \exp(-TW/T_1))$. Figure 7 shows that this is appropriate for a simple-component fluid such as 7-cp oil with unimodal bulk relaxation time (200-ms peak value in laboratory conditions), but not for a 300-cp multi-component heavy oil (40-ms peak value, distribution shown in insert of Figure 7). For a known distribution of bulk relaxations of the multi-component fluid, each walker accounts for a molecule of one miscible component of that fluid, and was stochastically assigned a bulk relaxation time so that the T_2 distribution is honored over the entire population of random walkers. The walker was also assigned a diffusivity which relates to this relaxation time via existing correlations (17-18).

3.4.3 Decay in an Inhomogeneous Background Magnetic Field

We now compare the decays generated by the presence of background magnetic gradients between (1) random-walk formulation A, (2) random-walk formulation B, and (3) the normalized analytical decay $M = \exp[-t(1/T_{2B} + 1/T_{2D})]$. Because the M_y signal in formulation A is decreased by large sampling volumes and imperfections in the magnetic field distribution, all its simulated decays were normalized at the time origin. Decays simulated with formulation B required no normalization. Figure 8 shows results for two values of homogeneous gradients, $G_z = 12$ G/cm and 29 G/cm, three echo times, $TE = 0.3, 1,$ and 3 ms, and two sampling volumes, 1 mm^3 and 1 cm^3 . Formulation B yields the same decays regardless of the sample volume, which exactly match the analytical decays. Likewise, Formulation A perfectly fits the analytical results for the smaller sampling volume, but entails substantial differences for the larger volume. This effect is due to the distribution of the energy acquired during the different RF pulses, as mentioned in section 4.1, and cannot be accounted for by formulation B or by standard analytical expressions.

3.5. SIMULATION RESULTS IN SATURATED POROUS MEDIA

We now study how the incorporation of a porous medium exhibiting surface relaxation affects the quality of the simulation results. Different relaxation types are incorporated simultaneously to generate parametric multidimensional NMR maps with the purpose of characterizing pore size, wettability, fluid type and volumetric fraction in the context of saturated rock-core analysis and in-situ oilfield exploration.

3.5.1 Fast Diffusion Limit

We now test our algorithm in the classic context of an isolated spherical pore of radius R , where $S/V = 3/R$. Figure 9 shows the results of simulations performed with different sphere sizes from $0.4 \text{ }\mu\text{m}$ to 4 mm and for different values of surface relaxivity. In all the cases, the simulation decays obtained with both formulations A and B perfectly match the analytical decays as long as $\rho R/D_B < 1$. This is due to the fact no ρ_1/ρ_2 contrast was enforced, as encountered in natural systems – for example, it is usually observed that this contrast usually does not exceed 1.5 in water-saturated rocks (29). If this contrast were to

reach several units, however, differences in apparent decay times would appear between formulations A and B. The deviation from the analytical expression, Equation (4), is captured by the random-walk model precisely at $\rho R/D_b = 1$, when the fast-diffusion assumption is no longer valid, especially at large values of ρ . Even though no gradient is applied in this simulation set, we observe a deviation between the results obtained for the two formulations A and B similar to the one observed in Figure 8 when the pore size reaches the mm range. Identical results were obtained in the 3D star-shaped pores formed by the void space fraction existing within a dense packing of overlapping spherical grains with different compaction coefficients.

As a result, for most dense porous media with low values of gradient and sub-millimeter pore size, both formulations A and B yield similar results for CPMG-like sequences. However, in the presence of internal fields created by dia- or paramagnetic material in the medium, the value of gradients can locally increase to hundreds of G/cm (13). In these conditions, it is expected that formulations A and B will yield different magnetization signals for any pore size and standard analytical expressions will fail. Work is currently underway to quantify these internal field effects using the random-walk algorithm described in this paper

3.5.2 Two-Dimensional NMR Maps of Gas/Water and Oil/Water Mixtures in Saturated Rocks

In oil exploration and rock/fluid characterization, the fluids measured by in-situ NMR logging tools include brine, single- and multi-component oil, gas, and water-based or oil-based drilling-mud filtrate which leaked into a freshly drilled porous rock formation. Multidimensional NMR techniques are currently based on the simultaneous inversion of suites of CPMG-like sequences with multiple values of TE and/or TW which allow different degrees of spin repolarization between successive CPMG RF sequences (Figure 3). The fluid phases are distributed in the pore space of a disordered grain pack (Figure 10) according to geometrical models in agreement with thermodynamic capillary equilibrium (30) or with more complex principles of drainage, imbibition, and electrical properties (31). In these models, the fluid phases are distributed at the pore level as overlapping blobs which are

truncated by grain surfaces, as shown in Figure 11. Two examples of rock/fluid systems were simulated to illustrate the methodology in disordered packs of overlapping spheres exhibiting 20% void space, uniform distribution of pore sizes, and enforcing a homogeneous gradient with $G_z = 16$ G/cm.

The first example was simulated for a mixture of 30% water and 70% gas in arbitrary reservoir conditions, whose bulk properties are shown in Table 1. Wait times varying logarithmically from 1 ms to 10 s were applied during the simulations of CPMG decay with 0.2 ms echo time, and the corresponding magnetization decays were processed with a T_1/T_2 inversion algorithm (11). The left panel of Figure 12 shows the resulting intensity T_1/T_2 map, where the water peak located at $T_1 = T_2 = 100$ ms is affected by surface decay. The small echo time has negligible influence on the T_2 response of the low-diffusivity water, however it significantly reduces the apparent T_2 value of the large-diffusivity gas with respect to its intrinsic T_1 value. In this case, inversion of the T_1 dimension efficiently discriminates the signals from the two fluids. We also synthesized magnetization decays for multiple- TE diffusion sequences for D/T_2 inversion and mapping. This was done by considering full polarization ($TW \rightarrow \infty$) and values of TE equal to 0.2, 1, 3, 9 and 16 ms for a homogeneous gradient $G_z = 16$ G/cm. Focusing on the same water/gas mixture saturating our porous rock model, we obtain the D/T_2 map shown in the right-hand panel of Figure 12. In this plot, as in subsequent D/T_2 maps, the diagonal line characterizes a D/T_2 correlation existing for live hydrocarbons at specific conditions of pressure and temperature, Equation (3). In this plot, water and gas are distinguishable on both the D and T_2 dimensions.

Our second example consists of a mixture of 60% water and 40% 7-cp oil at ambient conditions (see Table 1) within the same rock model, and illustrates the simulation of wettability effects at the rock surface. The same diffusion sequences were implemented, and the simulation results were inverted into the D/T_2 maps shown in Figure 13. The water-wet case (left-hand panel) exhibits a water peak at the intersection of the bulk water diffusivity (2.10^5 m²/ms) and the surface relaxation time previously observed in Figure 13 (100 ms). The oil peak, however, can be recognized as such for lying along the D/T_2 hydrocarbon correlation line. The (D, T_2) coordinates of that peak along that line enable the assessment of oil viscosity and possibly water-wettability. Upon wettability alteration, it is usually

considered that the water film existing between oil and rock surface ruptures under different chemical and thermodynamic conditions (32-33), while the least attainable zones of the pore space remain water-wet (see Figure 11). The right-hand panel of Figure 13 shows simulation results obtained where such microscopic geometries are included in the model. When oil is considered as the wetting fluid phase, it is affected by surface relaxation and the spread of its D/T_2 peak increases along both the D and T_2 dimensions. Simultaneously, the relaxation time of the water peak increases because some relaxing water/rock surfaces have disappeared, and some of the water now relaxes in bulk mode. Because of the low T_{1B}/T_{2B} contrasts for water and oil, the low gradient value, and because of the choice of CPMG acquisition sequence, Formulation B was computationally efficient in this particular case. We insist, however, that Formulation A would be required for more general RF sequences or in the presence of stronger magnetic field gradients.

The random walk algorithm developed in this paper can be used to quantify the impact on NMR measurements of the combined effects of fluid content, fluid viscosity, saturation history of the porous medium, and rock wettability. For instance, Refs. (30) and (31) study the quality of D/T_2 2D NMR interpretation to accurately assess hydrocarbon content and rock properties under the assumption of specific fluid displacement mechanisms within the pore space.

3.6. CONCLUSIONS

The simulation algorithm described in this paper consolidates existing NMR numerical simulation methods used in diverse areas of biology and engineering into a single formulation that incorporates both diffusion within inhomogeneous magnetic fields and surface effects, including magnetization relaxivity and membrane permeability. Other than the magnetic dipole approximation, our formulation is constrained by none of the assumptions required for analytical models concerning the statistical distribution of spin phase shifts, spin density, field homogeneity, or fast-diffusion limit. In addition, the simulation algorithm described in this paper extends NMR simulation capabilities beyond those of single-phase periodic media, which are so far the only type of porous media that can be accurately described with analytical techniques.

Previously described NMR simulations techniques neglected longitudinal effects; while it is expected that those techniques would not accurately reproduce the NMR response of molecules with substantial T_1/T_2 contrasts, we showed that the solution of the complete set of Bloch's equations is necessary to accurately reproduce echo amplitudes in strongly inhomogeneous magnetic fields, for arbitrary pulse sequences, and even for large sampling volumes (larger than 1 mm^3 for water) for the case of valued of field gradient. The simulation algorithm described in this paper was successfully validated against the limits of macroscopic models, when fluids include multiple components, or at the limit of fast-diffusion regime.

We considered suites of longitudinal and transversal magnetizations for multiphase fluid mixtures saturating models of porous media for different values of wait time and echo time. These synthetic magnetizations can be subsequently inverted into parametric multidimensional intensity maps cross-plotting T_1 , T_2 and D for improved characterization of pore structure, wettability and fluid types. Such a methodology provides new opportunities to study quantitative relationships between NMR measurements and properties of economic interest that cannot be directly measured in-situ (28). Moreover, the accurate simulation of magnetization decay opens the possibility of optimizing new NMR pulse acquisition sequences for specific applications in porous media in the presence of local variations of fluid distributions and internal fields.

3.7. REFERENCES

1. Brownstein, K.R., and Tarr, C.E.: Importance of Classical Diffusion in NMR Studies of Water in Biological Cells, *Phys. Rev. A* 19 (1979) 2446.
2. Latour, L.L., Mitra, P.P., Kleinberg, R.L., and Sotak, C.H.: Time-Dependent Diffusion Coefficient of Fluids in Porous Media as a Probe of Surface-to-Volume Ratio, *J. Magn. Res. A* 101 (1993) 342-346.
3. Song, Q.: Determining Pore Sizes Using an Internal Magnetic Field, *J. Magn. Res.* 143 (2000) 397-401.
4. Ramakrishnan, S., Schwartz, L.M., Fordham, E.J., Kenyon, W.E., and Wilkinson, D.J.: Forward Models for Nuclear Magnetic Resonance in Carbonate Rocks, *Log Analyst* 40 (1999) 260-270.

5. von Meerwall, E., and Ferguson, R.D.: Interpreting Pulsed-gradient Spin-echo Diffusion Experiments with Permeable Membranes, *J. Chem. Phys.* 74 (1981) 6956-6959.
6. Pfeuffer, J., Dreher, W., Sykova, E., and Leibfritz, D.: Water Signal Attenuation in Diffusion-weighted ^1H NMR Experiments During Cerebral Ischemia: Influence of Intracellular Restrictions, Extracellular Tortuosity, and Exchange, *Magn. Res. Imag.* 16 (1998) 1023-1032.
7. Stanisz, G.J., Szafer, A., Wright, G.A., and Henkelman, R.M.: An Analytical Model of Restricted Diffusion in Bovine Optic Nerve, *Magn. Res. Med.* 37 (1997) 103-111.
8. Zientara, G.P., Freed, J.H.: Spin-echoes for Diffusion in Bounded, Heterogeneous Media: A Numerical Study, *J. Chem. Phys.* 72 (1980) 1285-1292.
9. Hürlimann, M.D., and Venkataramanan, L.: Quantitative Measurement of Two-Dimensional Distribution Functions of Diffusion and Relaxation in Grossly Inhomogeneous Fields, *J. Magn. Res.* 157 (2002) 31-42.
10. Sun, B. and Dunn, K.-J.: Probing the Internal Field Gradients of Porous Media, *Phys. Rev. E* 65 (2002) 051309.
11. Sun, B. and Dunn, K.-J.: A Global Inversion Method for Multi-dimensional NMR Logging, *J. Magn. Res.* 172 (2005) 152-160.
12. Hürlimann, M.D., Griffin, D.D., and Spin, D.D.: Dynamics of Carr-Purcell-Meiboom-Gill-like Sequences in Grossly Inhomogeneous B_0 and B_1 Fields and Application to NMR Well Logging, *J. Magn. Res.* 143 (2000) 120-135.
13. Dunn, K.-J.: Enhanced Transverse Relaxation in Porous Media Due to Internal Field Gradients, *J. Magn. Res.* 156 (2002) 171-180.
14. Johnson, Jr., C.S., and He, Q.: Electrophoretic Nuclear Magnetic Resonance, in: J.S. Waugh (Ed.), *Advances in Magnetic Resonance* 13, Academic Press, London, 1989, pp. 131-159.
15. Caprihan, A., Fukushima, A. and Fukushima, E.: Flow Measurements by NMR, *Physical Reports* 198 (1990) 195-235.

16. Fukushima, E., and Roeder, S.B.W.: Experimental Pulse NMR: A Nuts and Bolts Approach, Addison-Wesley, Reading, Massachusetts, 1981.
17. Lo, S.-W., Hirasaki, G.J., House, W.V., and Kobayashi, R.: Mixing Rules and Correlations of NMR Relaxation Time with Viscosity, Diffusivity, and Gas/oil Ratio of Methane/hydrocarbon Mixtures, SPE paper 77264, SPE Journal 7(2002) 24-34.
18. Winkler, M., Freeman, J.J., and Appel, M.: The Limits of Fluid Property Correlations Used in NMR Well-logging: An Experimental Study of Reservoir Fluids at Reservoir Conditions, Petrophysics 46 (2005).
19. Torrey, H.: Bloch Equations with Diffusion Terms, Phys. Rev. 104 (1956) 563-565.
20. Weiskoff, R.M., Zuo, C.S., Boxerman, J.L., and Rosen, B.R.: Microscopic Susceptibility Variation and Transverse Relaxation: Theory and Experiment, Magn. Res. Med. 31 (1994) 601-609.
21. Sun, B., Dunn, K.-J., LaTorraca, G.A., and Wilson, D.M.: NMR Imaging with Diffusion and Relaxation, Paper SCA2003-19 presented at the 2003 SCA International Symposium, Pau, France, Sept. 22-24.
22. Schwartz, L.M., and Banavar, J.R.: Transport Properties of Disordered Continuum Systems, Phys. Rev. B 39 (1989) 11965-11970.
23. Wilkinson, D.J., Johnson, D.L., and Schwartz, L.M.: Nuclear Magnetic Relaxation in Porous Media: The Role of the Mean Lifetime $\tau(\rho, D)$, Phys. Rev. B 44 (1991) 4960-4973.
24. Bergman, D.J., Dunn, K.-J., Schwartz, L.M., and Mitra, P.P.: Self-diffusion in a Periodic Porous Medium: A Comparison of Different Approaches," Phys. Rev. E 51 (1995) 3393-3400.
25. Gudbjartsson, H., and Patz, S.: NMR Diffusion Simulation Based on Conditional Random Walk, IEEE Trans. Med. Imag. 14 (1995) 636-642.
26. Slichter, C.P.: Principles of Magnetic Resonance, Springer, New York, 1992.

27. Sen, P., André, A., and Axelrod, S.: Spin Echoes of Nuclear Magnetization Diffusing in a Constant Magnetic Field Gradient and in a Restricted Geometry, *J. Chem. Phys.* 111 (1999) 6548-6555.
28. Mendelson, S.: Continuum and Random-walk Models of Magnetic Relaxation in Porous Media, *Phys. Rev. B* 47 (1993) 1081-1083.
29. Kenyon, W.E.: Petrophysical Principles of Applications of NMR Logging, *Log Analyst* 38 (1997).
30. Toumelin, E., Torres-Verdín, C., Sun, B., and Dunn, K.-J.: A Numerical Assessment of Modern Borehole NMR Interpretation Techniques, Paper 90539 presented at the 2004 Annual Technical Conference and Exhibition of the Society of Petroleum Engineers, Houston, Texas, Sept. 26-29.
31. Toumelin, E., Torres-Verdín, C., Devarajan, S., and Sun, B.: An Integrated Pore-scale Approach for the Simulation of Grain Morphology, Wettability, and Saturation-history Effects on Electrical Resistivity and NMR Measurements of Saturated Rocks, paper presented at the 2006 International Symposium of the Society of Core Analysts, Trondheim, Norway, Sept. 12-16.
32. Hirasaki, G.: Wettability: Fundamentals and Surface Forces, *SPE Formation Eval.* 6 (1991) 217-226.
33. Kovscek, A.R., Wong, H., and Radke, C.J.: A Pore-level Scenario for the Development of Mixed Wettability in Oil Reservoirs, *AIChE Journal* 39 (1993) 1072-1085.

3.8 APPENDIX: ANALYTICAL CALCULATIONS OF THE TIME-EVOLUTION MATRIX EXPONENTIALS IN BLOCH'S EQUATION

The total magnetic field applied to the spin $\mathbf{B} = \mathbf{B}_0 + \mathbf{B}_1$ is either $\mathbf{B} = \mathbf{B}_0 = B_0 \hat{\mathbf{z}}$ between RF pulses, $\mathbf{B} = B_1 \hat{\mathbf{x}} + B_0 \hat{\mathbf{z}}$ during x' -pulses, or $\mathbf{B} = B_1 \hat{\mathbf{y}} + B_0 \hat{\mathbf{z}}$ during y' -pulses. This approach makes no approximation on the quality of magnetic pulses because the actual dispersion of Larmor frequencies is honored across the spin population and the spin diffusion is fully accounted for during the enforcement of \mathbf{B}_1 .

Between \mathbf{B}_1 pulses, the only magnetic field present is the background field, and the effective relaxation times for that step are given by Equation (14). It then follows that

$$\mathbf{A}\Delta t = \begin{bmatrix} -\frac{\Delta t}{T_2} & \gamma B_z \Delta t & 0 \\ -\gamma B_z \Delta t & -\frac{\Delta t}{T_2} & 0 \\ 0 & 0 & -\frac{\Delta t}{T_1} \end{bmatrix}, \text{ and therefore}$$

$$e^{\mathbf{A}\Delta t} = \begin{bmatrix} e^{-\frac{\Delta t}{T_2}} \cos(\gamma B_z \Delta t) & e^{-\frac{\Delta t}{T_2}} \sin(\gamma B_z \Delta t) & 0 \\ -e^{-\frac{\Delta t}{T_2}} \sin(\gamma B_z \Delta t) & e^{-\frac{\Delta t}{T_2}} \cos(\gamma B_z \Delta t) & 0 \\ 0 & 0 & e^{-\frac{\Delta t}{T_1}} \end{bmatrix}. \quad (\text{A1})$$

During $\mathbf{B}_1 (\pi/2)_x$ pulses, the product $\mathbf{A}\Delta t$ takes on the form

$$\mathbf{A}\Delta t = \begin{bmatrix} -\frac{\Delta t}{T_2} & \gamma B_z \Delta t & 0 \\ -\gamma B_z \Delta t & -\frac{\Delta t}{T_2} & \gamma B_x \Delta t \\ 0 & -\gamma B_x \Delta t & -\frac{\Delta t}{T_1} \end{bmatrix}. \quad (\text{A2})$$

The three eigenvalues λ_i of $\mathbf{A}\Delta t$ are found by solving the characteristic polynomial given by

$$\begin{aligned}
P_x(\lambda) &= \det(\lambda \mathbf{I} - \mathbf{A}\Delta t) \\
&= \lambda^3 + \lambda^2 \left(\frac{2\Delta t}{T_2} + \frac{\Delta t}{T_1} \right) \\
&\quad + \lambda \left(\frac{2(\Delta t)^2}{T_2 T_1} + \frac{(\Delta t)^2}{T_2^2} + (\gamma B_x \Delta t)^2 + (\gamma B_z \Delta t)^2 \right) \\
&\quad + \left(\frac{(\Delta t)^3}{T_2^2 T_1} + \frac{(\Delta t)^3 (\gamma B_x)^2}{T_2} + \frac{(\Delta t)^3 (\gamma B_z)^2}{T_1} \right)
\end{aligned}$$

which we solve using Cardan's method:

$$\begin{cases}
\lambda_1 = \sqrt[3]{(s-q)} - \sqrt[3]{(s+q)} - \frac{a}{3} \\
\lambda_2 = \frac{1}{2} \left(\sqrt[3]{(s+q)} - \sqrt[3]{(s-q)} \right) - \frac{a}{3} + \frac{i\sqrt{3}}{2} \left(\sqrt[3]{(s+q)} + \sqrt[3]{(s-q)} \right) \\
\lambda_3 = \frac{1}{2} \left(\sqrt[3]{(s+q)} - \sqrt[3]{(s-q)} \right) - \frac{a}{3} - \frac{i\sqrt{3}}{2} \left(\sqrt[3]{(s+q)} + \sqrt[3]{(s-q)} \right)
\end{cases}, \quad (\text{A3})$$

with $p = \frac{1}{3} \left(b - \frac{a^2}{3} \right)$; $q = \frac{1}{2} \left(c - \frac{ab}{3} + \frac{2a^3}{27} \right)$; $s = \sqrt{q^2 + p^3}$, and

$$\begin{aligned}
a &= \left(\frac{2\Delta t}{T_2} + \frac{\Delta t}{T_1} \right); \quad b = \left(\frac{2(\Delta t)^2}{T_2 T_1} + \frac{(\Delta t)^2}{T_2^2} + (\gamma B_x \Delta t)^2 + (\gamma B_z \Delta t)^2 \right) \\
c &= \left(\frac{(\Delta t)^3}{T_2^2 T_1} + \frac{(\Delta t)^3 (\gamma B_x)^2}{T_2} + \frac{(\Delta t)^3 (\gamma B_z)^2}{T_1} \right)
\end{aligned} \quad (\text{A4})$$

A matrix of eigenvectors corresponding to the above eigenvalues can be calculated as

$$\mathbf{U} = \begin{bmatrix} \frac{\gamma B_z \Delta t}{\lambda_1 + \frac{\Delta t}{T_2}} & \frac{\gamma B_z \Delta t}{\lambda_2 + \frac{\Delta t}{T_2}} & \frac{\gamma B_z \Delta t}{\lambda_3 + \frac{\Delta t}{T_2}} \\ 1 & 1 & 1 \\ -\frac{\gamma B_x \Delta t}{\lambda_1 + \frac{\Delta t}{T_1}} & -\frac{\gamma B_x \Delta t}{\lambda_2 + \frac{\Delta t}{T_1}} & -\frac{\gamma B_x \Delta t}{\lambda_3 + \frac{\Delta t}{T_1}} \end{bmatrix},$$

whereupon,

$$e^{\mathbf{A}\Delta t} = \mathbf{U} \cdot \begin{bmatrix} e^{\lambda_1} & 0 & 0 \\ 0 & e^{\lambda_2} & 0 \\ 0 & 0 & e^{\lambda_3} \end{bmatrix} \cdot \mathbf{U}^{-1}.$$

During $\mathbf{B}_1 (\pi)_y$ pulses, $\mathbf{A}\Delta t$ takes on the form:

$$\mathbf{A}\Delta t = \begin{bmatrix} -\frac{\Delta t}{T_2} & \gamma B_z \Delta t & -\gamma B_y \Delta t \\ -\gamma B_z \Delta t & -\frac{\Delta t}{T_2} & 0 \\ \gamma B_y \Delta t & 0 & -\frac{\Delta t}{T_1} \end{bmatrix}.$$

Upon replacing B_x with B_y in Equation (A4), it is readily found that the eigenvalues of this last matrix are identical to those of Equation (A3). The corresponding eigenvectors are included in matrix \mathbf{U} as

$$\mathbf{U} = \begin{bmatrix} 1 & 1 & 1 \\ -\frac{\gamma B_z \Delta t}{\lambda_1 + \frac{\Delta t}{T_2}} & -\frac{\gamma B_z \Delta t}{\lambda_2 + \frac{\Delta t}{T_2}} & -\frac{\gamma B_z \Delta t}{\lambda_3 + \frac{\Delta t}{T_2}} \\ \frac{\gamma B_y \Delta t}{\lambda_1 + \frac{\Delta t}{T_1}} & \frac{\gamma B_y \Delta t}{\lambda_2 + \frac{\Delta t}{T_1}} & \frac{\gamma B_y \Delta t}{\lambda_3 + \frac{\Delta t}{T_1}} \end{bmatrix}.$$

The computation of $e^{\mathbf{A}\Delta t}$ follows directly from the above expressions.

Table 1 Bulk properties of the fluids used in the numerical simulation of NMR measurements of saturated rocks

| Fluid | Hydrogen index | Bulk relaxation times: $T_1 \approx T_2$ | Bulk diffusivity D_B |
|----------|----------------|--|-----------------------------------|
| Water | 1.0 | 3 s | $2.10^{-5} \text{ cm}^2/\text{s}$ |
| Gas | 0.3 | 4.5 s | $1.10^{-3} \text{ cm}^2/\text{s}$ |
| 7-cp oil | 1.0 | 0.2 ms | $1.10^{-6} \text{ cm}^2/\text{s}$ |

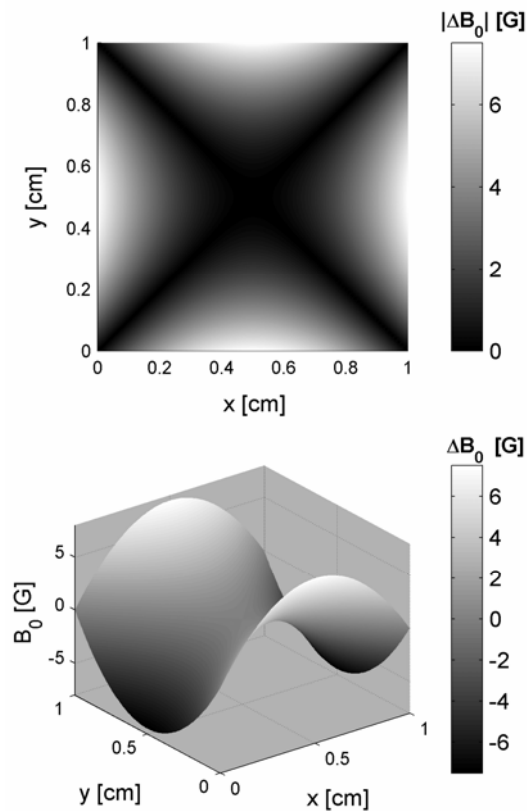


Figure 1 Magnetic field map representing an approximation of tool background magnetic field adapted from Reference (12), assuming \mathbf{B}_0 of the elliptical form

$\mathbf{B}_0 = \left(-(x/c - 0.5)^2 + (y/c - 0.5)^2 \right) \times 30 \hat{\mathbf{z}}$ [Gauss], where $c = 1$ cm and x and y are the Cartesian locations of the random walker in the geometrical reference.

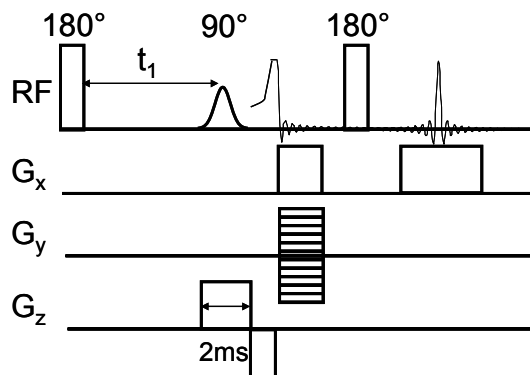


Figure 2 Example of T_1 MRI pulse sequence synchronizing \mathbf{B}_1 RF pulses and 3D pulsed background magnetic gradients. G_x , G_y and G_z are the projections of ∇B_0 on the axes of the rotating frame (adapted from Reference (20)).

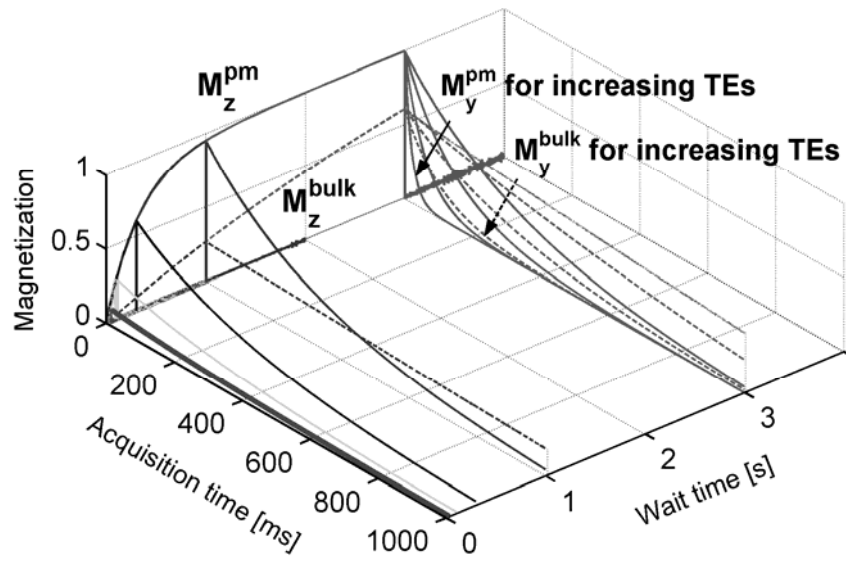


Figure 3 Amplitude of the mean M_z and M_y magnetizations simulated for 1-second CPMG pulse acquisitions taking place after different wait times for bulk water (dashed curves) and in the relaxing porous medium (continuous curves, noted $^{\text{pm}}$) formed by the void fraction of a disordered grain packing. Surface relaxivity ($\rho_1 = \rho_2 = 20 \mu\text{m/s}$) and pore size ($30 \mu\text{m}$) were considered uniform. Each magnetic dipole is initially depolarized ($M_z = 0$ and M_y randomly distributed with zero mean), then M_z increases freely for a wait time TW (no RF pulse).

Dipoles collectively generate an exponential build-up of the form $1 - \exp(-t/T_1)$. The CPMG RF pulse sequence is then turned on, M_z is tilted by the first $(\pi/2)_x$ pulse into M_y which becomes non-zero and subsequently decays. Next, dipoles collectively generate a macroscopic magnetization in the exponential form $\exp(-t/T_2)$ following the subsequent $(\pi)_y$ refocusing pulses. The results plotted above were simulated for $TE = 0.3$ ms at $TW = 0.03, 0.1, 0.3,$ and 1 s, and $TE = 0.3, 1, 4$ and 16 ms for $TW = 3$ s.

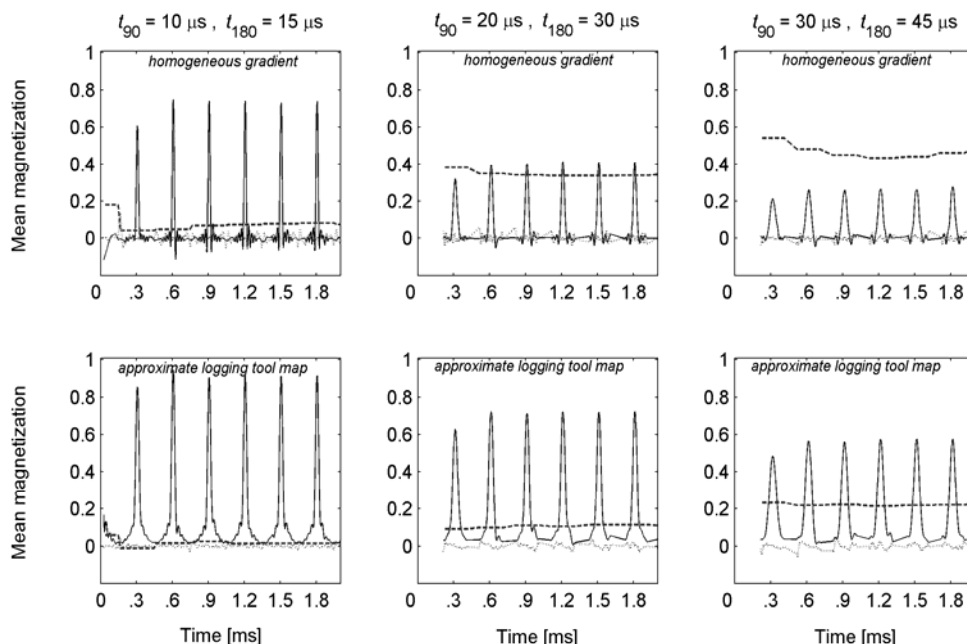


Figure 4 Normalized amplitude of the projections of the mean NMR magnetization simulated with 20,000 walkers in 1cm^3 of water, for a 300- μs echo-time CPMG sequence, for different \mathbf{B}_0 maps, and for different values of t_{90} and t_{180} . Plain curves: M_y projection (signal); dotted curves: M_x projection (out-of-phase noise); dashed curves: M_z projections. Top row: simulations performed with a homogeneous permanent gradient $dB_0/dz = 20 \text{ G/cm}$. Bottom row: simulations performed with the field map described in Figure 1.

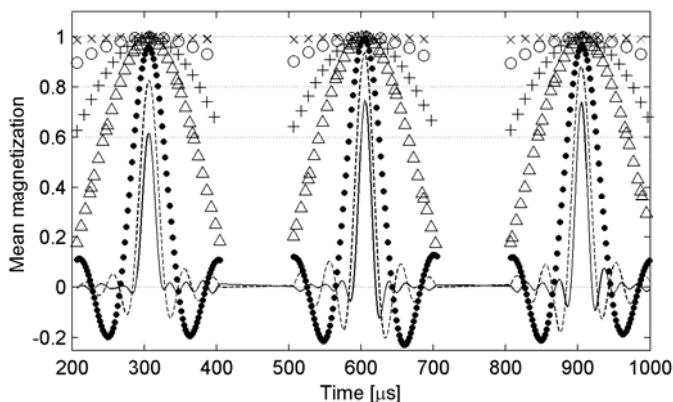


Figure 5 Normalized amplitude of the mean M_y magnetization of 20,000 random walkers generating the first three CPMG echoes ($TE = 300 \mu\text{s}$) for different volume sizes. Each series of markers represents a different sampling cube size: 10 mm (—), 6 mm (---), 3 mm (●), 1 mm (Δ), 0.6 mm (+), 0.3 mm (○) and 0.1 mm (x). The size of the sampling volume affects both the spread and the maximum amplitude of the echoes when it is larger than 1 mm^3 .

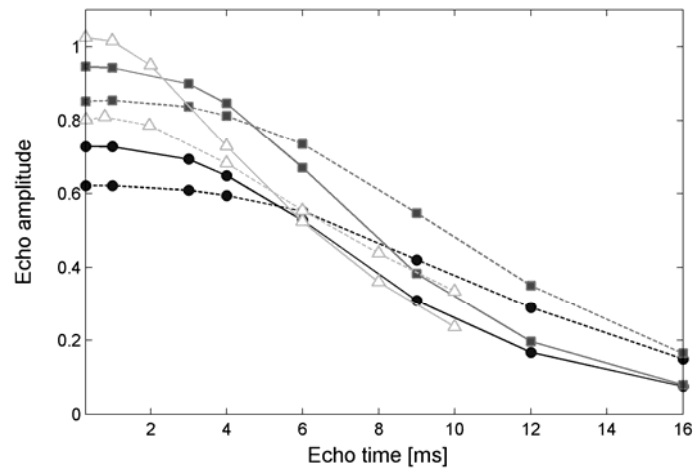


Figure 6 Amplitudes of the first (dash) and second (plain) CPMG echoes simulated as a function of echo time for 1cm^3 of bulk water volume. Curves with square and circle markers identify the mean M_y signal simulated with 10,000 random walkers in the background magnetic field map of Figure 1, for different \mathbf{B}_1 pulse widths (square markers: $t_{90} = 10\ \mu\text{s}$, $t_{180} = 15\ \mu\text{s}$; circle markers: $t_{90} = 20\ \mu\text{s}$, $t_{180} = 30\ \mu\text{s}$). Calculations reported in Reference (12) for a similar field map are plotted with open triangle markers.

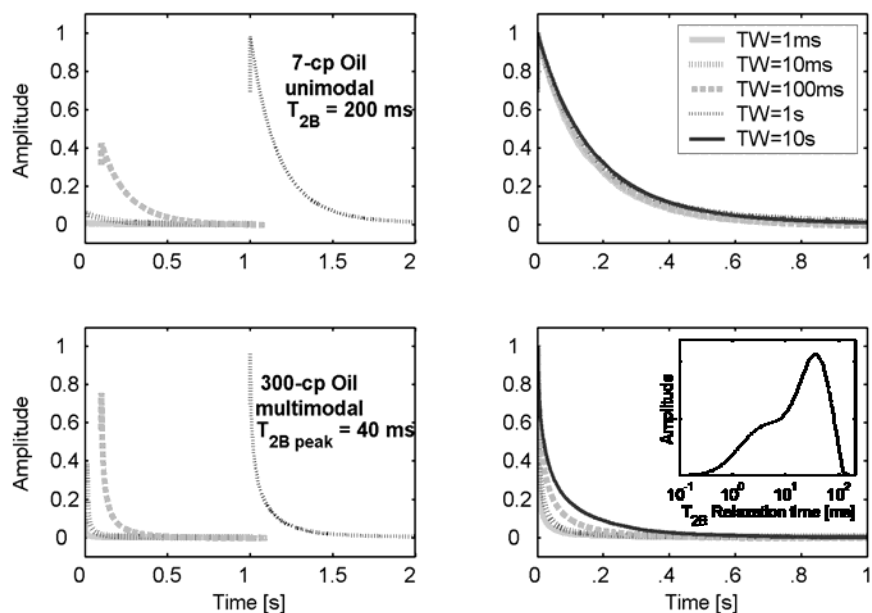


Figure 7 NMR magnetization decays of bulk fluids simulated for different values of wait time (left panels), and same decays normalized in amplitude at time $t = 0$ (right-hand panels). The same legend applies to all panels. For simple fluids with unimodal distribution of bulk relaxation times (top-right panel), all curves scale with TW and overlap with canonical form $(1 - \exp(-TW/T_1)) \times \exp(-t/T_2)$. For multi-component hydrocarbons (bottom right-hand panel), such normalized curves do not overlap. The insert describes the distribution of bulk relaxation times for the 300-cp heavy oil measured in laboratory conditions, and is used as input to the simulation algorithm.

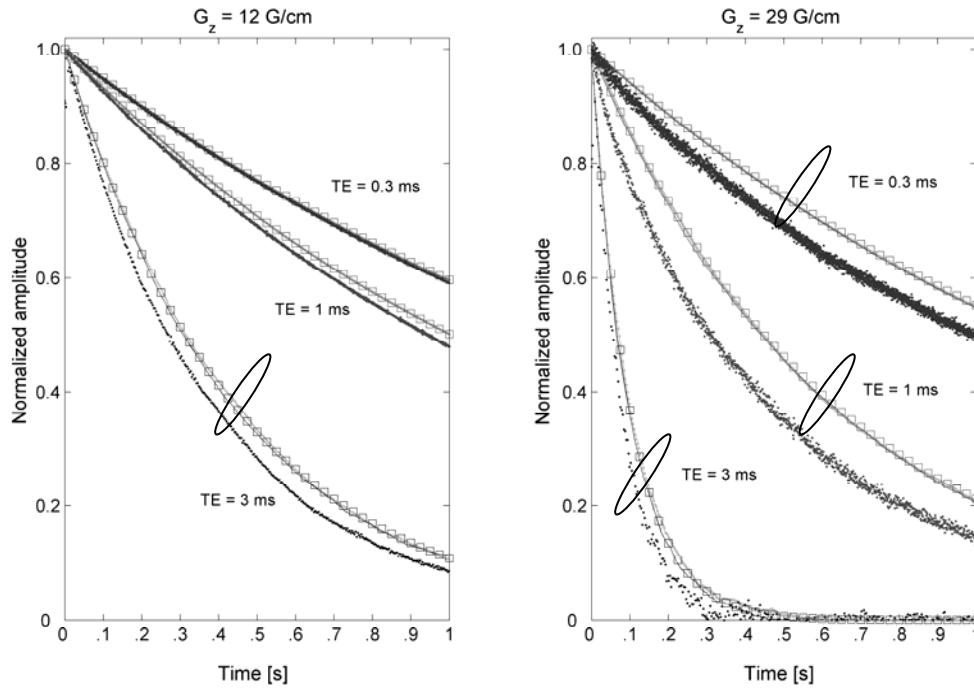


Figure 8 NMR decay for CPMG pulse acquisition of bulk water in a homogeneous background magnetic gradient G_z for different values of TE and for magnetization formulations A and B. Open square markers describe the analytical solution; lines (dots) describe the simulation results of Formulation A for 1 mm^3 (1 cm^3) sampling of water. For each value of TE and sampling volume, Formulation B yields results that exactly match the analytical solution.

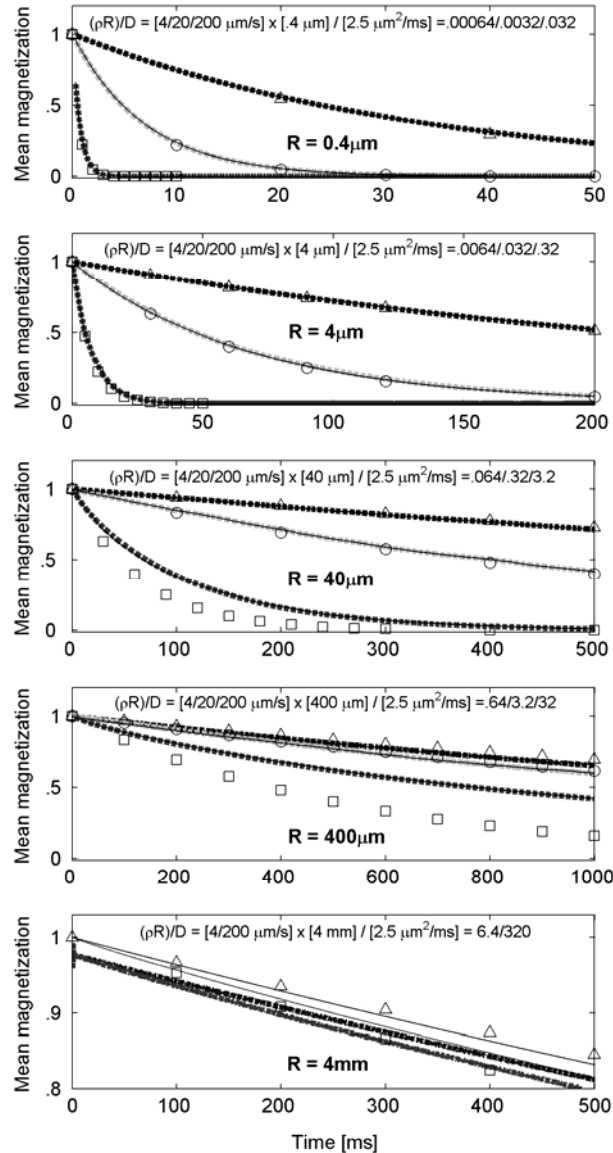


Figure 9 Decay curves simulated for water ($D_{bulk} = 2.5 \mu\text{m}^2/\text{ms}$, $T_{2B} = 3 \text{ s}$) in a single spherical pore with no background magnetic gradient. The pore radius R varies logarithmically from $0.4 \mu\text{m}$ (top panel) to 4 mm (bottom panel), while for each radius the surface relaxivity ρ at the pore wall is equal to $4 \mu\text{m/s}$ (triangles), $20 \mu\text{m/s}$ (circles) or $200 \mu\text{m/s}$ (squares). Results simulated with formulation A are plotted in thick lines; those simulated with formulation B use thin lines, while the analytical decays for a sphere (where $1/T_2 = 1/T_{2B} + 3\rho/R$) are plotted with markers. The ratio $\rho R/D_B$ is computed within the panels for each combination of R and ρ .

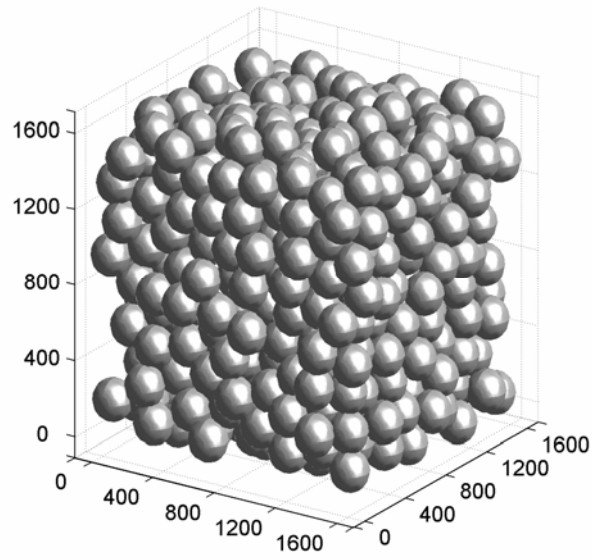


Figure 10 Example of disordered packing of identical grains used as rock model to generate the 2D NMR maps of Figs. 12 and 13. The spherical grains are overgrown until the void fraction reaches 20% of the bulk volume.

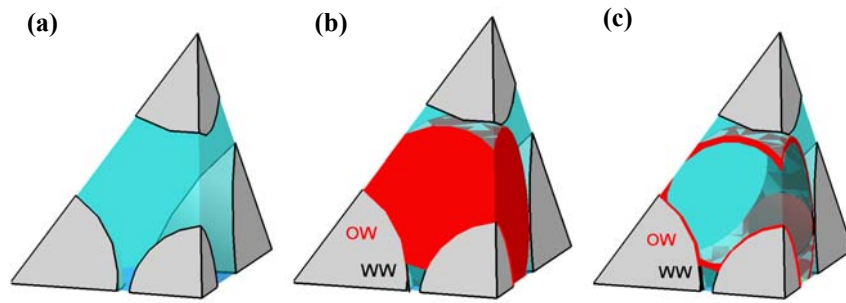


Figure 11 Examples of fluid distributions implemented at the pore scale. Each tetrahedron is centered on a pore from the void space of the grain packing (Figure 10), and is limited by sets of four-closest grains (in gray). Blue represents the water-filled pore space, red the oil-filled pore space. (a) Water fills the pore. (b) An oil blob centered on the pore under the double assumption of oil-wettability (OW) of the grain surface within the radius of the oil blob, and water-wettability (WW) of the grain surface in the least-accessible pore regions. (c) A thin film of wetting oil and bridging oil lenses are left in the oil-wet region of the pore after invasion by water. The random-walk step is adjusted within each fluid zone.

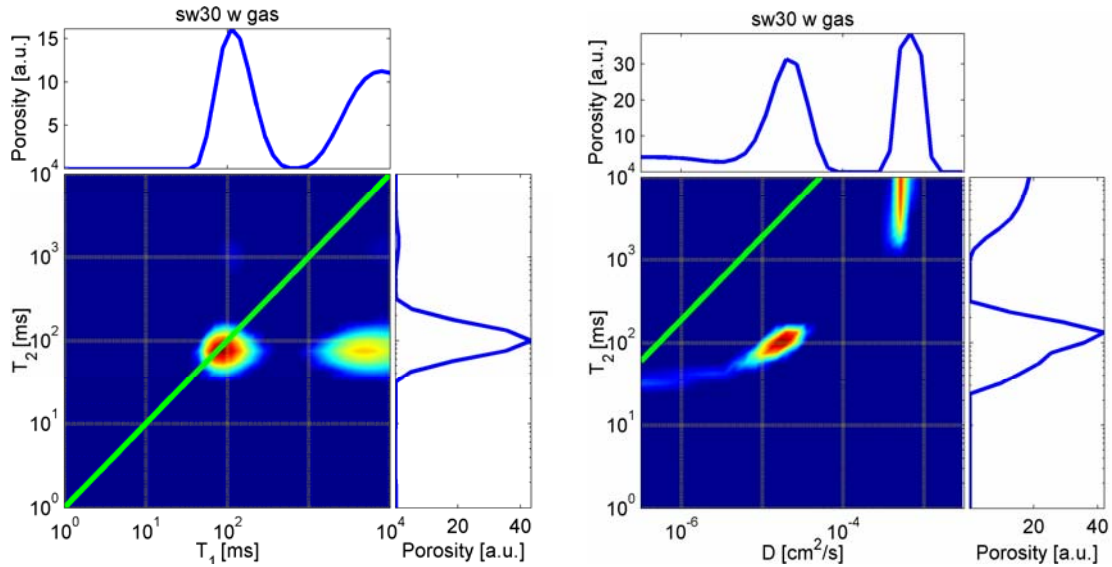


Figure 12 T_1/T_2 (left) and D/T_2 (right) NMR maps simulated for a 2-phase immiscible mixture of 70% gas and 30% water in the grain packing of Figure 10. The diagonal line in the left-hand panel represents the $T_1=T_2$ line. The diagonal line in the right-hand panel represents the D/T_2 correlation characterizing hydrocarbons in the conditions assumed for the simulations (after Ref (29)).

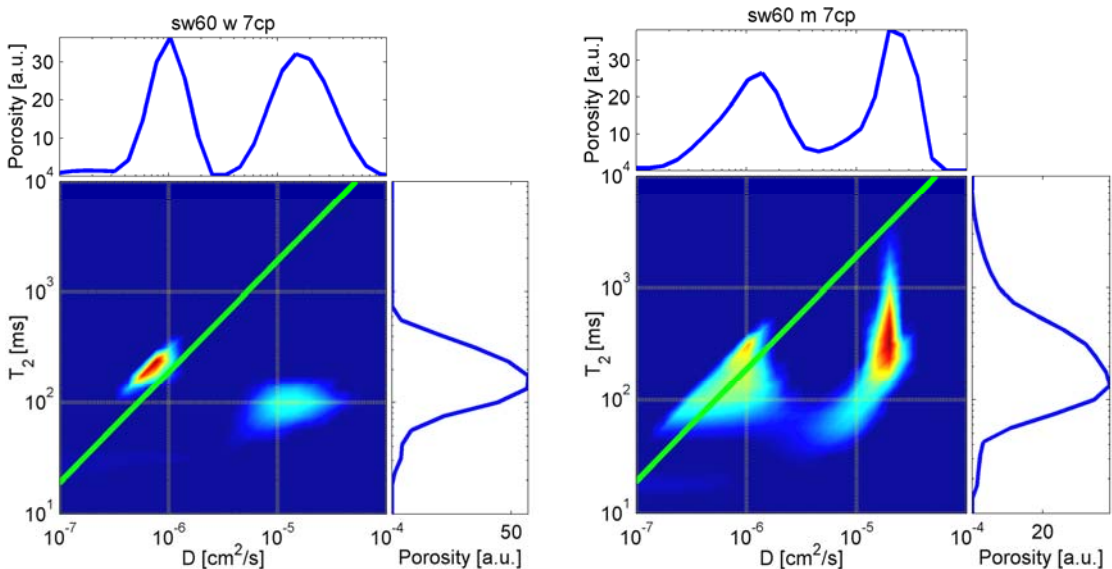


Figure 13 D/T_2 NMR maps simulated for a 2-phase immiscible mixture of 60% water and 40% 7-cp oil in the grain packing of Figure 10, for water-wet (left-hand panel) and oil-wet (right-hand panel) configurations. The diagonal line in the two panels represents the D/T_2 correlation characterizing hydrocarbons in the conditions assumed for the simulations (after Reference (29)).

CHAPTER 4. AN OBJECT-ORIENTED APPROACH FOR THE PORE-SCALE SIMULATION OF DC ELECTRICAL CONDUCTIVITY OF TWO-PHASE SATURATED POROUS MEDIA

We introduce a new geometrical concept to simulate DC electrical conductivity phenomena in arbitrary rock models. The assumed geometry considers 3D grain and pore objects that include intragranular porosity, clay inclusions, non-wetting fluid blobs, thin films, and pendular rings. These objects are distributed following simple heuristical principles of drainage/imbibition that honor capillary-pressure curves. They provide a simple way to parameterize the three-dimensional space and to simulate the electrical conductivity of porous media saturated with two immiscible fluid phases by way of diffusive random-walks within the brine-filled pore space. We show that grain surface roughness, microporosity, clays double-layers and wettability can be simultaneously incorporated using this geometrical framework to quantitatively reproduce measured conductivity behaviors for both water-wet and hysteresis-dominated oil-wet porous rocks. Our work emphasizes the importance of thin films, pendular rings and snap-offs to capture the correct electrical behavior of dense media using granular models.

4.1 INTRODUCTION

In-situ quantification and monitoring of water saturation in hydrocarbon formations is usually performed using open-hole and time-lapse cased-hole well-log measurements of electrical conductivity in the kHz range. The traditional basis for quantification of water saturation from low-frequency resistivity measurements, water salinity, and rock porosity, is established by the well-known Archie's relations (1942) and by their calibration to core measurements. These empirical relations relate a fully water-saturated electrical formation factor F_R and a partially-water-saturated electrical resistivity index I_R to power-laws of porosity, ϕ , and water saturation, S_w . Letting ρ be the value of electrical resistivity, such relations are written as

$$F_R = \frac{\rho_{S_w=100\%}}{\rho_{brine}} = \frac{a}{\phi^m} \text{ and } I_R = \frac{\rho_{S_w<100\%}}{\rho_{S_w=100\%}} = \frac{1}{S_w^n}, \quad (1)$$

where a defines the so-called tortuosity factor, m the lithology (or cementation) exponent, and n the saturation exponent. Similar power laws have been derived for shaly sands with exponents corrected for the presence of clay double-layer electrical conduction, as reviewed by Argaud et al. (1989).

With the resistivity measurements published by Sweeney and Jennings (1960) on oil-wet carbonate samples, or by Wei and Lile (1991) on siliciclastic cores successively imbibed and drained with water and kerosene, it has been recognized that Archie's relations only apply to rocks that are strongly water-wet and exhibit homogeneous granular morphology. For instance, complex rock morphology such as vugular and intragranular porosity, clay cation-exchange surfaces, and oil-wetting films at the grain surface affect the values of m and n in conflicting fashion over the entire water saturation range (Stalheim et al., 1999; Fleury, 2002). Fluid distribution, recovery, and multiphase flow displacement are also directly affected by the degree of water-wettability in reservoir rocks (Hirasaki, 1991).

The factors that influence the electrical response of saturated rocks are so varied that pore-scale models are required to describe – and, in some simple cases, quantitatively predict – these measurements. Models based on site and bond percolation theories (Zhou et al., 1997) seem very efficient to reproduce the electrical behavior of generic rocks, including in oil-wet conditions; however, it is out of their scope to incorporate grain morphology information. At the other end of the spectrum of pore-scale models, pore networks extracted from high-resolution rock tomography (Oren and Bakke, 2003) or reconstructed stochastically (Liang et al., 2000) aim to honor accurate grain topology but reach practical limitations due to limited voxel resolution, simplified pore throat and body shapes, and inability to include cation exchange clay surfaces. An alternative way to compute electrical conductivity from such digital rocks is to mesh the pore volume of a nominal bulk rock volume with finite elements (Adler et al., 1992) and solve the Laplace equation for the electrical potential at steady-state. However, the computation requirements of such applications remain prohibitive for several millions voxels. Complex multi-scale issues also

arise when dealing with nanometer-thin wetting films in pores as large as tens or hundreds of microns.

Therefore, can one consider a different numerical approach that incorporates explicit grain morphology description, including microporosity and clays, that overcomes resolution limitations, and that can be run without a complex parallel computation algorithm? This paper introduces the use of diffusive random walks and a simple grain- and pore-based geometrical model as a viable solution to circumvent such problems for the simulation of DC electrical conductivity in porous media with two-phase fluid saturation. We illustrate the flexibility of the method for single-phase, two-phase WW and two-phase OW granular rocks, before discussing the practical implications of the model.

4.2 OBJECT-ORIENTED GEOMETRY

Over the years, diffusive random walks have been successfully used to simulate single-phase measurements of nuclear magnetic resonance, electrical conductivity and hydraulic permeability in fully-saturated soils and rocks for a variety of pore geometries (Schwartz and Banavar, 1989; Kim and Torquato, 1990; McCarthy, 1990a and 1990b; Kostek et al., 1992; Ioannidis et al., 1997; Ramakrishnan et al., 1999). No attempt, however, has been reported to use the same principles applied to electrical conduction effects due to multiphase fluid saturations, saturation history, and variable wettability.

4.2.1 Integrating Grain Morphology and Pore-scale Fluid Distribution as Geometrical Objects

Following Schwartz's geometrical simulation models (Johnson et al., 1986; Schwartz and Banavar, 1989; Ramakrishnan et al., 1999), we define porous rocks as disordered packings of solid or microporous spherical grains which limit the free diffusion of random walkers in the pore space. Once a pack of given grain-size distribution is constructed, the grains are homogeneously overgrown to replicate the effects of rock diagenesis, overburden pressure, and cementation. As illustrated in Figure 1, pore units are defined by the void space left between each tetrahedral group of the four-closest grains. A Quickhull algorithm (Barber et al., 1996) is used to partition the bulk volume into a Delaunay tessellation of such conforming tetrahedra (Bryant and Pallatt, 1996). In Figure 1, we consider a consolidated

version of Finney's pack of monodisperse grains (Finney, 1970). For simplicity, the size of each pore size is assimilated to the size of the largest sphere that can be positioned between the four surrounding grains; each pore shape, however, remains accurately defined by the 3D asymmetric star-shaped volume complementary of the four surrounding grains. Likewise, pore throats between two neighboring tetrahedra are assigned the size and center of the largest disc that can be positioned between the three grains of the corresponding triangular section, while they retain their exact 2D star shape. This strategy ensures that the entire pore space remains encoded by only the position and size of each grain with no compromise on the actual pore and throat shapes probed by the random walkers. Finally, pendular rings of wetting fluid are defined where the grains meet in the pore space.

We increase the complexity of the tortuous diffusion pathways within the granular model with intragranular porosity features controlled by the type of grains used in the packing. Figure 2 illustrates the different grain objects available in our approach. Solid grains (type 1) are just made of spheres at the contact of which the random walkers rebound. Microfractured grains (type 2) feature unidirectional slit-type micro-fracture along the direction of maximal overburden stress across the packing, and passage of random walkers within the slit. Microporous grains (types 3-4) capture purely geometrical intragranular rock microporosity (as encountered in carbonate micrites or microporous cherts) and are approximated with consolidated cubic-centered packings of micrograins. If that microporosity is openly connected to the intergranular pore space, it is then deemed "coupled" following the work by *Ramakrishnan et al. (1999)*; on the contrary, if the microporosity is isolated from the intergranular porosity by cement or crystal overgrowth, it is then considered "uncoupled."

Clay-bound micro-porosity is approached in a different manner. Because the pore size between clays is extremely small and because of the presence of exchange surface charges and cation double-layers, we assign effective wet-clay volumes with an equivalent electrical conductivity. The value of this equivalent "clay conductivity" may differ from that of pore brine depending on brine ionic content and clay type. Several publications have described this dual conductivity approach: *Argaud et al. (1989)* considered the macroscopic effect of the ratio of "excess conductivity associated with the clay conductor" and the bulk brine conductivity in pores. They measured the ratio between both conductivities to be in the range 0.02-2 for a variety of sandstones and brine salinities. *De Lima and Sharma (1990, 1992)*

used explicit dual distributions of conductivities in a formulation based on effective-medium theory to account for the effect of dispersed and coating clays on electrical conduction. We use similar concepts to distributing effective wet-clay conductivity as dispersed micron-thick shells surrounding the grains (grain type 5 in Figure 2) or as structural clay amalgamates (grain type 6). Johnson et al. (1986) first used the coating-clay geometry (grain type 5) in combination with diffusive random walks to replicate the non-linear effect of clay-coating electrical conduction for single-phase, cubic-centered grain packs.

Next, 3D pore objects describe the distribution of two fluid phases within the pore space explicitly left between the grains objects. These pore objects idealize the pore archetypes advanced by Kovscek et al. (1993). Figure 3 represents in three dimensions the volume occupied by oil within one partially-saturated pore as delimited by a sphere concentric with the pore and of radius equal to the pore size R multiplied by a given factor α_o . Although simplistic, this pore geometry has the advantage of capturing the complexity of immiscible fluid geometry at the pore level with only one parameter per pore, α_o . The pore described in Figure 3 also assumes the oil blob does not wet the grain surface, thereby allowing a water film of thickness T_w at the grain surface. Figure 4 recapitulates the four possible states described in our approach as pore objects characterized by blob size, film type and thickness. The resolution of the thermodynamic and chemical processes affecting wettability at the pore scale is out of the scope of this paper; however if one postulates that wettability is altered from WW to OW, then an oil film of thickness T_o replaces the water film at the grain surface. The pendular rings at the intersection between the overlapping grains now include irreducible water where the oil blob of radius $R.\alpha_o$ does not extend. Finally, Figure 4 also represents the result of water invasion in an OW pore. Figure 5 illustrates how thicker wetting films capture the excess electrical conduction due to high surface roughness between the grain surface and the non-wetting fluid phase.

It is important to realize that random-walk trajectories of water particles are defined across both pore objects and microporous grain objects through (a) water-filled pore throats, (b) wetting water films, (c) pendular rings, and (d) microporous grains (including clays).

4.2.2 Fluid Distribution Model and Capillary-Pressure Hysteresis

For the purpose of demonstration of our methodology, we distribute the pore objects described above across the entire pore space according to simple drainage and imbibition heuristics. Elaborate fluid-flow algorithms could be used interchangeably, such as the one developed by Gladkikh and Bryant (2005). For the purpose of generality, we use simple displacement heuristics to model the electrical response of the saturated medium.

Specifically, we consider two mechanisms of pore-to-pore piston-like propagation and film-growth in agreement with the scenarios suggested by Knight (1991) and implemented by Kovscek et al. (1993). The two mechanisms are known to alternate depending on capillary number, therefore on flow rate, fluid viscosity and porous medium properties (Lenormand and Zarcone, 1988; Lenormand et al., 1988; Vizika et al., 1989). Kovscek et al. (1993) assume that only a film-growth mechanism takes place during imbibition in the presence of asphaltenic oil and subsequent alteration of grain surface wettability into oil-wet. We model this main assumption for comparison purposes. Unlike Kovscek et al.'s mixed-wettability model whereby a size cut-off discriminates populations of smaller OW pores from larger WW pores, we enforce the additional physical constraint that pores must be hydraulically connected to allow fluid displacement from pore to pore. We implement six saturation cycles of drainage and imbibition, whether alternate or successive. In what follows, drainage refers to the displacement of the dominant wetting phase by the non-wetting phase and imbibition refers to the opposite; this notion becomes ambiguous in the presence of mixed-wet pores after wettability alteration. We illustrate these saturation mechanisms in Figure 6, while resulting hysteretic loops of pseudo-capillary pressure (PCP) are shown in Figure 7 for the piston-like displacement cycles and compared to the analytical results from Kovscek et al. (1993).

- Cycle 1: drainage of the WW medium model through pore-to-pore piston-like oil propagation (Figure 6c-d). Starting from the inlet face of the simulation domain ($x = 0$ in Figure 1a), we assume oil blobs (pore type 2, Figure 4) that invade the pores on a neighbor-to-neighbor basis, using nested conditional loops which test the two following criteria: (i) the oil blob reaches the throat that separated the two pores, and (ii) the size of

that throat is larger than a given throat-size threshold (TST). Once the outlets faces other than those at $x = 0$ are reached, the distribution of pore types 1 and 2 within the pore space defines the fluid geometry for the random walkers at a given value of water saturation. Drainage continues by decreasing the TST. Figure 8 illustrates the propagation of non-wetting phase, tetrahedron by tetrahedron, for a non-wetting phase saturation equal to 22%. At each saturation stage, the PCP is calculated from the inverse of the TST while water saturation S_w is obtained by counting the proportion of randomly generated points in the water phase. Depending on the value of α_o , S_w reaches a critical value (irreducible saturation) below which the PCP increases sharply, as shown in Figure 9. The value of α_o is therefore calibrated to meet objective irreducible water saturation located in the pendular rings and the least accessible pores that cannot be reached by the oil blobs. In this example, the value of α_o is considered homogeneous for all the pores and is set at 2.25 to reach 13% irreducible water saturation. Before each subsequent cycle, the TST is reset to a large value.

- Cycle 2: imbibition of the WW medium through pore-to-pore water propagation (Figure 6d-e). Water is now injected from the inlet face $x = 0$ (pores of type 2 revert back to type 1) and propagates from pore to pore when a new TST is met between two pores. The inverse of the imbibition TST is now subtracted from the PCP at the imbibition onset (point B) to yield new values of PCP for this cycle. This TST is decreased until S_w remains constant (point C). Irreducible oil saturation is located within type-2 snapped-off pores trapped between type-1 pores. Figure 10 shows the evolution of the number of snap-offs with TST. The hysteresis ABC of Figure 7a agrees very well with the capillary-pressure hysteresis expected for a homogeneous rock.
- Cycle 3: imbibition of the WW medium through film thickening (Figure 6f-h). This cycle is an alternate of Cycle 2 and models the fluid distribution resulting from incremental growth of the wetting films by thickness T_w (Kovscek et al., 1993). As the films grow, the non-wetting phase features increasingly elongated shapes. A parameter β_w is defined to account for a possible truncation of these elongated shapes as T_w increases, such that the radius of the blob is reduced by $\beta_w T_w$. Starting from point B (Figure 7a) at 30 nm, T_w and S_w increase in similar relative proportions (Figure 11) while the blob radius decreases in

the connected pores. When T_w becomes as large as the pore throats, the NW phase is snapped-off and becomes isolated from the inlet; the NW phase is now trapped and films stop thickening in those pores. T_w continues to increase in the pores where oil remains connected to the inlet. The coefficient β_w controls the maximal water saturation of the cycle (i.e., the saturation of snapped-off oil or gas). For the 20%-porosity Finney pack, values of β_w were distributed homogeneously amid the pores; values equal to 0.5 and 1 yielded irreducible oil saturation values of 27% and 13%, respectively. The simulation results presented in this paper use $\beta_w = 0.5$. Film thickness and PCP are not immediately related, whereupon capillary pressure during Cycle 3 is not represented in Figure 7a.

- Cycle 4: drainage of the OW medium through pore-to-pore piston-like water displacement after assumed wettability alteration, following the completion of Cycle 1 (Figure 6i-k). All the type-2 pores are arbitrarily converted into type-3 pores, then water is put into contact with the inlet face $x = 0$. The process is similar to that of Cycle 1, except that pores change from type 3 to type 4 as water advances across the pore space. The only criterion for water propagation across a pore throat is that its size meets a new TST. The PCP derived for this cycle is taken equal to the onset PCP (point B) minus the inverse of TST. In Figure 7a, Cycle 4 describes the segment BDE and reaches PCP = 0 at point D. The endpoint E almost reaches $S_w = 100\%$ because the only oil volume left in the rock is formed by the 30-nm thin films. Oil-wet, oil-filled pendular rings would be required in the model to reach the curvature and the irreducible oil saturation obtained by Kovscek et al. in Figure 7b.
- Cycle 5: imbibition of the OW medium through oil film thickening (Figure 6k-l). This displacement process is identical to Cycle 3 by defining a new blob shrinkage coefficient $\beta_o = 0.5$ equivalent to β_w in the WW case. Likewise, no PCP is derived for this cycle. The segment EF represented in Figure 7a only illustrates the transition between Cycles 4 and 6.
- Cycle 6: secondary drainage of the OW medium through pore-to-pore piston-like water displacement. This cycle starts from a configuration where most pores are filled with thick oil films and with water left at their center, disconnected from the inlet (point F in Figure 7a). Water is again put into contact with the inlet face and propagates pore by pore

as long as a new TST is met, thus reconnecting the snapped-off water to the bulk water. The PCP for this cycle is taken equal to the inverse of that TST (segment FG). Overall, The OW segments BDE and FG agree well with Kovscek et al.'s results (Figure 7b), despite the absence of significant irreducible oil saturation in our model.

4.2.3 Random-Walk Simulation of DC Electrical Conductivity

Having described the brine-filled pore space in a manner consistent with displacement mechanisms and capillary pressure, we now review how diffusive random walkers are used to compute formation factor and resistivity index for arbitrary porous media. If one defines by σ the locally homogeneous DC electrical conductivity in a sub-region and $\nabla\Phi$ the gradient of electrical potential across that region, then macroscopically the Laplace equation for the electric potential Φ is verified across the entire volume considered, i.e.

$$\nabla \cdot (\sigma \nabla \Phi) = 0. \quad (2)$$

The macroscopic conductivity value that satisfies equation (2) for the apparent electrical gradient taken across the entire volume is σ_{eff} . In a similar manner, the material balance for a diffusing species of locally homogeneous self-diffusivity D across a sub-region of local concentration gradient ∇C macroscopically satisfies the equation

$$\nabla \cdot (D \nabla C) = \frac{\partial C}{\partial t}. \quad (3)$$

The macroscopic diffusivity value that satisfies equation (3) for the apparent concentration gradient taken across the entire volume is D_{eff} . In the steady-state limit ($t \rightarrow \infty$) where C converges asymptotically, the diffusion problem of equation (3) is equivalent to the DC electrical conduction problem of equation (2) by setting D , C and D_{eff} as equivalents of σ , Φ and σ_{eff} .

Simultaneously, the diffusion problem can be solved in three dimensions with random walkers reproducing thermal agitation: particles within a fluid phase of self-diffusion coefficient D describe trajectories through iterative microscopic displacements of length δr and duration δt related by Einstein's equation (Einstein, 1956):

$$(\delta r)^2 = 6D \delta t. \quad (4)$$

If \mathbf{r} is the position vector of a walker in the pore space, and t is the walk time, the effective diffusivity of the fluid is then related to the mean-square displacement over all walkers, i.e.,

$$D_{eff}(t) = \frac{\langle \|\mathbf{r}(t) - \mathbf{r}(0)\|^2 \rangle}{6t}. \quad (5)$$

The effective conductivity across the porous medium is therefore proportional to the long-time asymptote of effective diffusivity of the conductive phase calculated with random walkers across the porous medium.

From this equivalence, it can be shown (Rasmus, 1986; Clennell, 1997) that the formation factor F_R and resistivity index I_R defined in equation (1) are proportional to the following diffusivity ratios:

$$F_R(S_w) = \frac{\sigma_{water}}{\sigma_{S_w=100\%}} = \frac{1}{\phi} \frac{D_{water}}{D_{S_w=100\%}(t \rightarrow \infty)} \quad (6)$$

and

$$I_R(S_w) = \frac{\sigma_{S_w=100\%}}{\sigma_{S_w<100\%}} = \frac{1}{S_w} \frac{D_{S_w=100\%}(t \rightarrow \infty)}{D_{S_w<100\%}(t \rightarrow \infty)}, \quad (7)$$

where σ_{water} and D_{water} refer to the electrical conductivity and diffusivity of the bulk electrolyte, and σ_{S_w} and D_{S_w} refer to the effective values across the porous medium saturated with water saturation equal to S_w .

Given the scale contrasts between the relevant length scales of rock and fluid (nm-thick films, sub- μm micropores, μm -scale pores, sub-mm grains, mm-scale vugs), we dynamically adjust the step size to be smaller than the smallest surrounding length scale (e.g. the throat size of an occupied pore or the film thickness within a wetting water film). Once a walker is determined to belong to the pore volume formed by one of the grain or pore objects defined previously, distances are calculated between random-walker location and pore center and grain centers. The length of a random-walk step is equal to the smallest quantity between $1/20^{\text{th}}$ of the pore radius and $1/5^{\text{th}}$ of the smallest open throat size of that pore, while that

within a wetting film is equal to $T/3$. To optimize the number of random walkers necessary to determine the asymptote $D_{S_w}(t \rightarrow \infty)$, we perform the simulations sequentially with series of 10 to 50 walkers. The resulting long-time effective diffusivities are averaged across as many series of walkers as needed to obtain a smooth time decay curve, and for simulation times long enough (10^5 to 10^7 ms equivalent diffusion time, for $D_{water} = 2 \mu\text{m}^2/\text{ms}$) to reach asymptotic convergence within $\pm 5\%$ error. Lower error values can be reached at low computational expenses for high S_w values. However, exponentially increasing simulation times prevent higher accuracy for values of S_w lower than about 30% or in the presence of intragranular microporosity (grain type 3) where pore size is at least 10 times smaller than intergranular pore size. Figure 12 shows the time decay of effective water diffusivity computed in the consolidated Finney pack described in Figure 1a, for different values of S_w .

Inclusion of conductive clays in the model (grain types 5 and 6) implies conductivity contrasts (i.e., diffusivity contrasts for random-walk purposes) between pore water and clay volumes, as shown in Figure 2. Each time a random walker reaches such an interface between pore water and conductive clay volume, it is subject to a probability of passage adapted from McCarthy's work (1990a; 1990b):

$$p = D_{clay} / (D_{water} + D_{clay}). \quad (8)$$

If that probability is honored, then the random walker crosses the interface and its self-diffusivity value is changed thereby affecting the clock increment δt for a given step size δx , after equation (4). If not, then the random walker bounces back in the original region. However, no rigorous demonstration exists for that probability of passage (McCarthy, 1990a) so that any probability that honors the limits

$$p \rightarrow 0 \text{ when } D_{clay} \rightarrow 0, \quad (9a)$$

and

$$p \rightarrow 1/2 \text{ when } D_{clay} \rightarrow D_{water} \quad (9b)$$

should be acceptable. Equation (8) precisely differs from McCarthy's by a factor of 2, for his expression of p tends to 1 in condition (9b); we think p should on the contrary be unbiased (tend to $1/2$) when clay volumes are as conductive as pore water. Equation (8), however, is not

acceptable when clay becomes more conductive than pore water ($D_{clay} > 2D_{water}$) for yielding values of $p > 1$, as clay electrical double-layers expand with decreasing brine salinity. Further investigation is under process to correctly calibrate clay-coating thickness, D_{clay} and p in pore-scale models with respect to electrical conductivity measurements in shaly sands (Jin et al., 2007).

4.3 SIMULATION RESULTS

4.3.1 Single-phase Saturation with Clustered Grains and Clay Inclusions

We uniformly overgrow the Finney pack from Figure 1a to reduce its porosity from 39 to 7%. As shown in Figure 13, the values of formation factor derived from the random walk (RW) simulation via equation (6) compare very well to those obtained using a pore network (PN) with the same Finney pack, and also to published measurements in clay-free sandstones. For porosities above 15%, however, uniform overgrowth underestimates the formation factor of real rocks. This phenomenon can be explained by comparing micrographs of fused-glass-bead pack and sandstones. Figure 14 shows that grains tend to form clusters in relatively high-porosity rocks while packs of spherical grains (fused glass bead packs) exhibit no such clustering. At low values of porosity, however, the clustered structure of squashed rock grains is no longer apparent and the sample acquires the same morphology as a tight packing of fused beads. If we regard the Finney pack as a good approximation of a fused glass bead pack, this observation explains why the corresponding formation factor agrees well with sandstone measurements at low values of porosity but not at high values of porosity. Three grain packs numbered 1 to 3 are constructed with a more realistic normal grain diameter distribution in the range of 50 to 320 μm (Figure 15). We define attracting grains within the pack and then enforce grain clustering by displacing all other grains toward those attractors by a distance a/r^2 , where a is a constant and r is the distance between the grains and the attractors. Figure 16 shows that for grain packs 1 to 3, characterized by increasing values of a , calculated values of F_R ensue closer to those measured in real 20%-porosity rocks. Similar results could be obtained by growing the grains on a cluster basis, instead of homogeneously, during the porosity reduction process.

We also consider distributions of grain-coating clay randomly distributed in the Finney pack. Thirty percent of the grains are assigned a 3- μm clay coat (as described in the type-4 grains of Figure 2), so that the corresponding clay volume amounts to 2% of total solids in the synthetic sample. The porosity is reduced by homogeneously growing all the grains while maintaining the 3- μm clay coat. We consider contrasts between effective clay conductivity and pore brine conductivity, $D_{\text{clay}}/D_{\text{water}}$, equal to 1:1000, 1:10 and 1:1, which correspond to decreasing brine salinities. Figure 17 shows the resulting plot of formation factor vs. porosity, whose slope reads as the apparent lithology exponent m (Clavier et al., 1984). Formation factor can substantially decrease for lower values of conductivity contrast: when clays become as conductive as the pore brine (a situation that is common in low-salinity shaly sands), m decreases to 1.5 for the Finney grain pack model.

4.3.2 Two-phase Saturation with Water-wet Grains (Saturation Cycles 1 to 3)

Figure 18 shows the resistivity index curve simulated as a function of S_w from equation (7) for Cycle 1. Archie's n saturation exponent appears as the negative slope of the bilogarithmic plot assuming a constant tortuosity factor $a = 1$. Simulation results agree well with measurements made on a 20%-porosity clay-free sandstone sample (core T1 from Argaud et al., 1989). Moreover, RW simulations yield a smoother resistivity index curve around $S_w = 50\%$ than PN simulations because the latter neglect presence of wetting films (Bryant and Pallatt, 1996).

Let us now turn to the issue of grain surface roughness. It is well known that n decreases as S_w decreases in the presence of substantial surface roughness. For instance, Diederix (1982) reports measurements of clay-corrected resistivity indices of shaly sandstones that exhibited an abnormal decrease of n from 2.1-2.2 to 1.3-1.5 below a critical water saturation $S_{w\text{crit}}$ close to 55%. The conductivity enhancement occurring below $S_{w\text{crit}}$ was explained by Diederix as a consequence of the roughness created by the coating clay texture at the grain surface, which was supported by experiments on smooth and rough water-wet glass-bead samples. As illustrated in Figure 5, substantial roughness created by clay flakes at the grain surface causes an effective increase of the thickness of the brine film between water-wet rock and oil. The same argument justifies the choice of a thickness of 30 nm brine at the surface of our smooth spherical grains to represent *some* grain roughness, instead of the

5 to 10 nm thickness expected (for instance) for a flat rock/water/oil interface (Hirasaki, 1991). Because clay conductivity was deemed negligible in the salt-saturated formation, we simulate these measurements with the 20% Finney pack of Figure 1a and increase the thickness of the brine wetting film from 30 to 300 nm during drainage (Cycle 1). Figure 19 shows the corresponding simulation results for I_R along with the experimental trends measured by Diederix (1982). Moreover, in Figure 19 we include the results obtained by Zhou et al. (1997) with their percolation simulation approach for a generic rock model. All the measured and simulated curves agree extremely well for sharing identical values of S_{wcrit} (around 55%) and n (around 1.3). Given the absence of morphological description of the rocks, this negative curvature of I_R vs. S_w due to grain roughness can therefore be treated as a wetting effect.

Next, we consider the imbibition processes integrated in our model (Cycles 2 and 3). Figure 20 shows that the adoption of either imbibition process after drainage (Cycle 1 endpoint) yields a distinct resistivity index hysteresis. The hysteresis formed by Cycles 1 and 2 is hardly noticeable and remains within the range of numerical simulation error with a constant n value equal to 2.1. The other hysteresis formed by Cycles 1 and 3 exhibits values of n higher than 2 for $S_w < 25\%$ and down to 1 for $S_w > 30\%$. Even though measured values of n rarely reach such low values, it is not unusual to encounter values of n lower than 2 depending on experimental conditions (Knight, 1991; Longeron et al., 1989; Grattoni and Dawe, 1998). An imbibition resulting from a combination of the phenomena described by Cycles 2 and 3 could explain why these measurements exhibit values of n lower than 2.

4.3.3 Two-phase Saturation with OW Solid and Microporous Grains (Saturation Cycles 1, 4, 5)

Depending on the pH, thermodynamic conditions, and chemical oil composition, the grain surface can become OW. Figure 21a shows the resistivity index curves calculated along saturation Cycles 4, 5 and 6 for the 20%-porosity Finney pack, side by side with Zhou et al.'s (1997) percolation simulation results in a generic porous medium (Figure 21b). The results of both models exhibit striking similarities, including a constant slope $n = 3$ during drainage Cycle 4 and a sudden increase of n as S_w decreases below a critical value S_{wcrit} about 40% during imbibition Cycle 5. These models reproduce quite well the measurements by Wei and

Lile (1991), shown in Figure 21c, whereby a succession of resistivity index hysteresis appears between Cycles 4, 5 and 6. The value of S_{wcrit} constitutes the main difference between simulation results ($S_{wcrit} = 40\%$) and measurements ($S_{wcrit} = 55\%$). It is remarkable that rock porosity and morphology substantially influence the value of S_{wcrit} , as indicated by the following panels of Figure 21. Simulations performed on an overgrown 7%-porosity Finney pack constructed with solid grains exhibit a higher value of $S_{wcrit} = 60\%$ (Figure 21d). On the other hand, a 22%-porosity microporous pack constructed from a 14%-porosity overgrown Finney pack with 30% solid grains and 70% microporous grains yields both a high value of irreducible water saturation (45%), a negative curvature of n for decreasing values of S_w , and a high value of $S_{wcrit} = 72\%$ (Figure 21e). This last simulation case agrees very well with the resistivity-index measurements performed by Sweeney and Jennings (1960) on oil-wet carbonates, shown in Figure 21f.

4.4 DISCUSSION

Despite the simplicity of the geometrical model introduced in this paper, quantitative comparison of our results against those obtained using other approaches reveals interesting properties. In particular, the coincidence of our results in the 20%-porosity Finney pack with Zhou et al.'s (1997) percolation results suggests that our pore-object approach was able to capture the effect of fluid distribution on electrical conductivity in a *generic* dense porous medium. By using the grain objects described previously and varying the model porosity, we added morphological information that was missing in the percolation approach to describe the net effect of rock structure and fluid distribution (including wettability) on electrical measurements.

We can compare our simulation results to those obtained by other methods using grain packs to emphasize the importance of thin films, pendular rings and snap-off phenomena for conductivity modeling. Earlier PN models of WW granular media (Bryant and Pallatt, 1996) ignored the presence of thin conductive films but did allow full electrical conduction between hydraulically disconnected pores owing to common pendular rings. Those assumptions for WW medium are similar to our assumptions for OW medium, except for the fact we enforce constriction of the electrical pathways at the pendular rings. The jump of resistivity index observed around $S_w = 13\%$ between (a) Bryant and Pallatt's (1996) PN

results at Cycle 1's endpoint (Figure 18) and (b) our simulation results at the onset of Cycle 4 (Figure 21a) can therefore be attributed to the constriction of pendular rings. Regarding the results shown in Figure 18, it is remarkable that almost exactly the same values of resistivity index are obtained in the WW case using the two simulation approaches (absence of wetting films but connection through pendular rings, vs. presence of wetting films and constriction of pendular rings).

Snap-offs form important elements in pore-scale immiscible displacement. In addition, our model explains the high values of resistivity index obtained for OW media at low values of water saturation (Cycles 5 and 6) based on the existence of snap-offs. It might therefore seem contradictory that Gladkikh and Bryant (2005) concluded that snap-off phenomena had no impact on immiscible displacements in the Finney pack. To reach that conclusion, Gladkikh and Bryant performed calculations of the interface curvatures and determined the onset of fluid displacement and snap-offs from the geometrical coalescence of fluid menisci and nearby pendular rings. Their calculations, however, assume (1) perfect grain curvature, which for a given contact angle constrains the meniscus curvature at the interface between the two fluid phases, and (2) clear determination of pendular ring sizes and locations in the pore space. Based on these restrictive assumptions, it is unclear to what extent their approach should be generalized to real subsurface conditions. This point also questions the universality of grain packs to simulate transport processes through dense, compacted soils and rocks.

Our modeling philosophy is different. Rather than accurately simulating the displacement processes occurring in smooth bead packs, we consider the grain packs as *proxies* for grain arrangements in real subsurface conditions. The object-oriented approach is intended to reproduce trends known to take place in rocks in order to simulate the DC electrical conductivity resulting from the superposition of complex grain morphologies, saturation history, and wettability effects. Segmentation of high-resolution rocks tomographies into grain packs (Saadatfar et al., 2005) offers new possibilities to quantitatively compare and calibrate our object-based approach to more detailed, but computationally impractical, voxel-based simulation techniques. In particular, such experiments would help assign distributions of the parameters α_o , β_w and β_o within the pore

space that would conform to observations in real rocks, not just match calculations in ideal sphere packs.

4.5 CONCLUSION

This work demonstrated the value of simple geometrical models to explain the complex electrical behavior of saturated rocks. Specifically, complex grain morphologies, clay inclusions and fluid configurations were considered as pore-scale objects which we simply defined with a few geometrical parameters in consistency with capillary-pressure curves and Kovscek et al.'s thermodynamic model. By enforcing simple drainage and imbibition mechanisms, we could quantitatively reproduce the resistivity hysteresis of two-phase saturated rocks and describe abnormal non-Archie behavior in oil-wet rocks as the combined effect of saturation history, wettability, and rock morphology.

This paper showed that the accuracy of the algorithm used to distribute the fluids at the pore scale is contingent upon the objective of the simulation model. For electrical conductivity calculations, both grain surface roughness, thin films, pendular rings and snap-offs need to be consistently incorporated in the model geometry.

Finally, the random-walk technique used in conjunction with the object-oriented geometry described in this paper offers unique opportunities to study the time-domain transient behavior of electrical conductivity in porous rocks beyond the asymptotic DC value. Specifically, following the approach of Cortis and Knudby (2006) adopted for hydraulic permeability, we expect that the random-walk approach could be used to simulate both time-domain induced polarization and electrical conductivity frequency dispersion in rocks, at the pore scale.

4.6 ACKNOWLEDGEMENTS

We express our gratitude to S. Bryant for many useful discussions, as well as to O. Vizika and M. Knackstedt for their insightful review of a paper presented at the 2006 annual symposium of the Society of Core Analysts. We also thank J.L. Finney for providing access to the dataset of the so-called Finney pack. Funding for the work reported in this paper was provided by the US Department of Energy, contract no. DE-FC26-04NT15518, and by UT

Austin's Research Consortium on Formation Evaluation, jointly sponsored by Anadarko, Aramco, BP, Baker Atlas, BHP, British Gas, Chevron, ConocoPhillips, ENI E&P, ExxonMobil, Halliburton Energy Services, Hydro, Marathon Oil Corporation, Mexican Institute for Petroleum, Occidental Oil and Gas Corporation, Petrobras, Schlumberger, Shell International E&P, Statoil, Total, and Weatherford.

4.7 REFERENCES

1. Adler, P.M., Jacquin, C.G., and Thovert, J.-F.: The Formation Factor of Reconstructed Porous Media, *Water Resources Research*, **28**, 1571–1576, 1992.
2. Archie, G.E.: The Electrical Resistivity Log as an Aid to Determining Some Reservoir Characteristics, *Transactions of the AIME*, **146**, 54-62, 1942.
3. Argaud, M., Giouse, H., Straley, C., Tomanic, J., and Winkler, K.: Salinity and Saturation Effects on Shaly Sandstone Conductivity, SPE paper 19577 presented at the 64th SPE Annual Technical Conference and Exhibition, 1989.
4. Barber, C.B., Dobkin, D.P., and Huhdanpaa, H.T.: The Quickhull Algorithm for Convex Hulls, *ACM Transactions on Mathematical Software*, **22**, 469-483, 1996.
5. Bryant, S., and Pallatt, N.: Predicting Formation Factor and Resistivity Index in Simple Sandstones, *Journal of Petroleum Science and Engineering*, **15**, 169-176, 1996.
6. Clavier, C., Coates, G.R., and Dumanoir, J.L.: Theoretical and Experimental Bases for the Dual-water Model for the Interpretation of Shaly Sands, *SPE Journal* (April issue), 153-168, 1984.
7. Clennell, M.B.: Tortuosity: A Guide Through the Maze, in M.A. Lovell and P.K. Harvey (eds.), *Developments in Petrophysics*, Geological Society Special Publication 122, 299-344, 1997.
8. Cortis, A., and Knudby, C.: A Continuous Time Random Walk Approach to Transient Flow in Heterogeneous Porous Media, *Water Resources Research*, **42**, W10201, 2006.

9. Diederix, K.M.: Anomalous Relationships Between Resistivity Index and Water Saturations in the Rotliegend Sandstone (The Netherlands), paper X presented at the SPWLA 23rd Annual Logging Symposium, 1982.
10. Doyen, P.: Permeability, Conductivity and Pore Geometry of Sandstones, *Journal of Geophysical Research*, **93** (B7), 7729-7740, 1988.
11. Einstein, A.: Investigation on the Theory of the Brownian Movement, Dover, New York, 1956.
12. Finney, J.L.: Random Packings and the Structure of Simple Liquids. I. The Geometry of Random Close Packing, *Proceedings from the Royal Society of London*, **A 319**, 1539, 1970.
13. Fleury, M.: Resistivity in Carbonates: New Insights, SPE paper 77719 presented at the Society of Petroleum Engineers 77th Annual Technical Conference and Exhibition, 29 Sept.-2 Oct., San Antonio, Texas, 2002.
14. Gladkikh, M., and Bryant S.: Prediction of Imbibition in Unconsolidated Hranular Materials, *Journal of Colloid and Interface Science*, **288**, 526-539, 2005.
15. Grattoni, C.A., and Dawe, R.A.: The Effect of Differences of Multiphase Spatial Distributions on the Electrical Properties of Porous Media, *The Log Analyst*, **39**, 47-59, 1998.
16. Hirasaki, G.J.: Wettability: Fundamentals and Surface Forces, *SPE Formation Evaluation*, **6**, 217-226, 1991.
17. Ioannidis, M.A., Kwiecien, M.J., and Chatzis, I.: Electrical Conductivity and Percolation Aspects of Statistically Homogeneous Porous Media, *Transport in Porous Media*, **29**, 61-83, 1997.
18. Jin, G., Torres-Verdín, C., Devarajan, S., Toumelin, E., and Thomas, E.C.: Pore-scale Analysis of the Waxman-Smiths Shaly-sand Conductivity Model, *Petrophysics*, **48**, 104-120, 2007.

19. Johnson, D.L., Koplik, J., and Schwartz, L.M.: New Pore-size Parameter Characterizing Transport in Porous Media, *Physical Review Letters*, **57**, 2564-2567, 1986.
20. Kim, I.C., and Torquato, S.: Determination of the Effective Conductivity of Heterogeneous Media by Brownian Motion Simulation, *Journal of Applied Physics*, **68**, 3892-3903, 1990.
21. Knight, R.: Hysteresis in the Electrical Resistivity of Partially Saturated Sandstones, *Geophysics*, **56**, 2139-2147, 1991.
22. Kostek, S., Schwartz, L.M., and Johnson, D.L.: Fluid Permeability in Porous Media: Comparison of Electrical Estimates with Hydrodynamical Calculations, *Physical Review B*, **45**, 186-195, 1992.
23. Kovsky, A.R., Wong, H., and Radke, C.J.: A Pore-level Scenario for the Development of Mixed Wettability in Oil Reservoirs, *AIChE Journal*, **39**, 1072-1085, 1993.
24. Lenormand, R., and Zarcone, C.: Physics of Blob Displacement in a Two-dimensional Porous Medium, *SPE Formation Evaluation*, **3**, 271-275, 1988.
25. Lenormand, R., Touboul, E., and Zarcone, C.: Numerical Models and Experiments on Immiscible Displacements in Porous Media, *Journal of Fluid Mechanics*, **189**, 165-187, 1988.
26. Liang, Z., Ioannidis, M.A., and Chatzis, I.: Permeability and Electrical Conductivity of Porous Media **Form** 3D Stochastic Replicas of the Microstructure, *Chemical Engineering Science*, **55**, 5247-5262, 2000.
27. De Lima, O.A.L., and Sharma, M.M.: A Grain Conductivity Approach to Shaly Sandstones, *Geophysics*, **55**, 1347-1356, 1990.
28. De Lima, O.A.L., and Sharma, M.M.: A General Maxwell-Wagner Theory for Membrane Polarization in Shaly Sands, *Geophysics*, **57**, 431-440, 1992.

29. Longeron, D.G., Argaud, M.J., and Feraud, J.-P.: Effect of Overburden Pressure and the Nature and Microscopic Distribution of Fluids on Electrical Properties of Rock Samples, *SPE Formation Evaluation*, **4**, 194-202, 1989.
30. McCarthy, J.J.: Effective Permeability of Sandstone-shale Reservoirs by a Random Walk Method, *Journal of Physics A*, **23**, L445-L451, 1990.
31. McCarthy, J.J.: Effective Conductivity of Many-component Composites by a Random-walk Method, *Journal of Physics A*, **23**, L749-L753, 1990.
32. Øren, P.E., and Bakke, S.: Reconstruction of Berea Sandstone and Pore-scale Modeling of Wettability Effects, *Journal of Petroleum Science and Engineering*, **39**, 177-199, 2003.
33. Ramakrishnan, T.S., Schwartz, L.M., Fordham, E.J., Kenyon, W.E., and Wilkinson, D.J.: Forward Models for Nuclear Magnetic Resonance in Carbonate Rocks, *The Log Analyst*, **40**, 260-270, 1999.
34. Rasmus, J.C.: A Summary of the Effects of Various Pore Geometries and Their Wettabilities on Measured and In-situ Values of Cementation and Saturation Exponents, paper PP presented at the SPWLA 27th Annual Logging Symposium, 1986.
35. Saadatfar, M., Turner, M.L., Arns, C.H., Averdunk, H., Senden, T.J., Sheppard, A.P., Sok, R.M., Pinczewski, W.V., Kelly, J., and Knackstedt, M.A.: Rock Fabric and Texture from Digital Core Analysis, paper ZZ presented at the SPWLA 46th Annual Logging Symposium, New Orleans, Louisiana, June 26-29, 2005.
36. Schwartz, L.M., and Banavar, J.R.: Transport Properties of Disordered Continuum Systems, *Phys. Rev. B*, **39**, 11965-11970, 1989.
37. Stalheim, S.O., Eidesmo, T., and Rueslåtten, H.: Influence of Wettability on Water Saturation Modelling, *Journal of Petroleum Science and Engineering*, **24**, 243-253, 1999.
38. Sweeney, S.A., and Jennings, H.Y.: Effect of Wettability on the Electrical Resistivity of Carbonate Rock from a Petroleum Reservoir, *Journal of Physical Chemistry*, **64**, 551-553, 1960.

39. Vizika, O., and Payakates, A.C.: Parametric Experimental Study of Forced Imbibition in Porous Media, *Physicochemical Hydrodynamics*, **11**, 187-204, 1989.
40. Wei, J.-Z., and Lile, O.B.: Influence of Wettability on Two- and Four-electrode Resistivity Measurements on Berea Sandstone Plugs, *SPE Formation Evaluation*, **6**, 470-476, 1991.
41. Wong, P.-z., Koplik, J., and Tomanic, J.P.: Conductivity and Permeability of Rocks, *Physical Review B*, **30**, 6606-6614, 1984.
42. Zhou, D., Arbabi, S., and Stenby, H.: A Percolation Study of Wettability Effects on the Electrical Properties of Reservoir Rocks, *Transport in Porous Media*, **29**, 85-98, 1997.

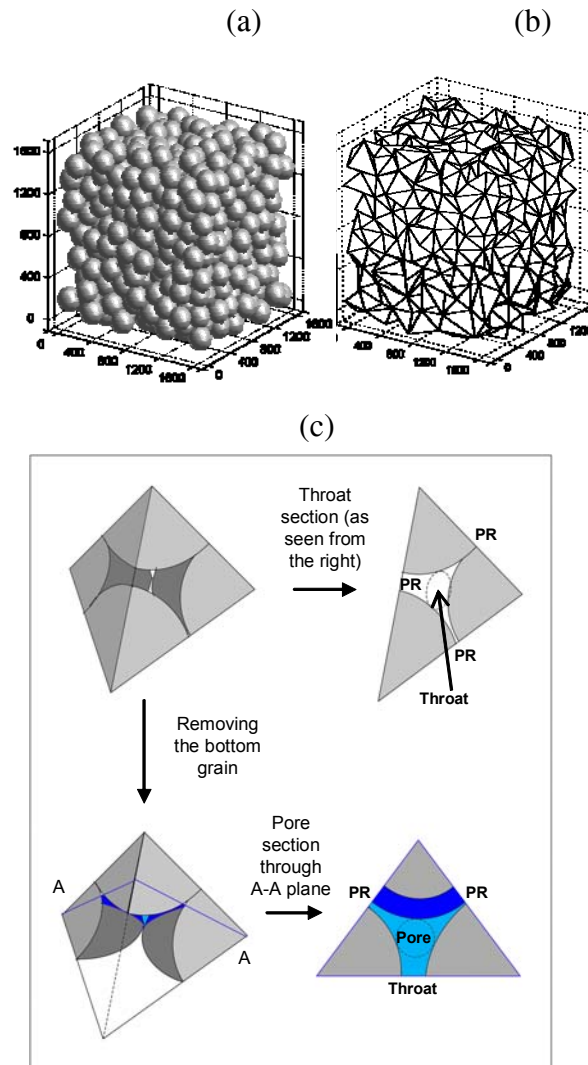


Figure 1 (a) Example of a 1000-grain cubic subset from the Finney pack constructed with $200\text{-}\mu\text{m}$ -diameter grains and uniformly consolidated to reach 20% porosity.
 (b) Corresponding Delaunay tessellation. All dimensions are given in μm .
 (c) Graphical description of one cell which defines one pore, four throats, and six pendarular rings (PR).

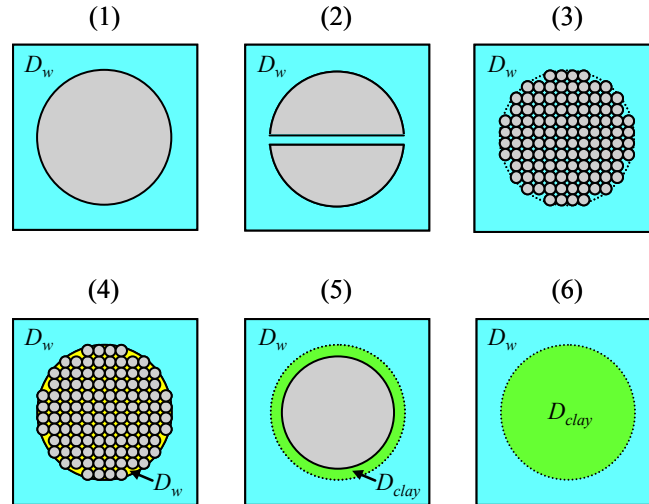


Figure 2 Description of the six grain types constructed in the geometrical framework of this paper. Color is used to code the diffusivity values enforced during random walk by zones (blue: D_w ; yellow: D_w – disconnected from the blue connected brine; green: D_{clay}). Dotted lines: passage allowed via probability of passage, equation (8). Plain lines: surface rebound of the random walker.

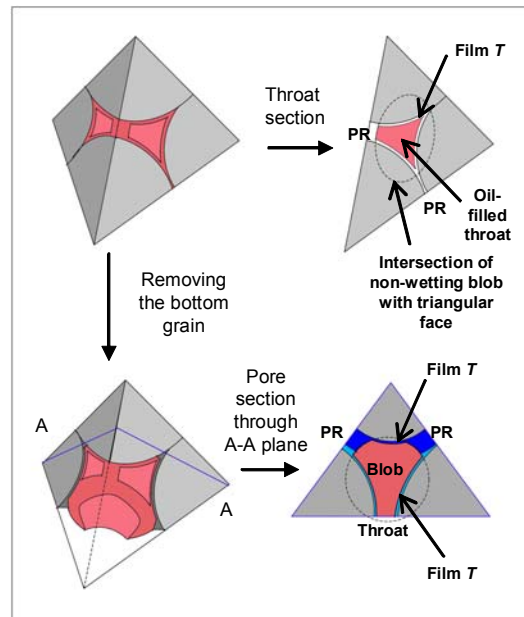


Figure 3 Description of the geometry of two-phase fluid saturation in a Delaunay tetrahedron. A non-wetting blob occupies the intersection between the pore space and a sphere of radius R_o concentric with the pore shown in Figure 4. Thin wetting films of thickness T are included between the blob and the grains.

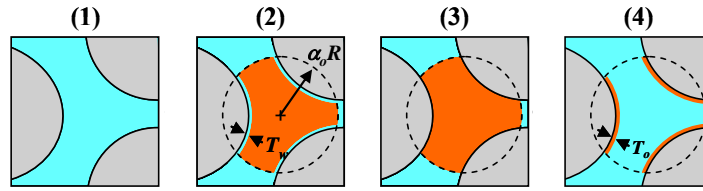


Figure 4 Illustration of the 4 pore types: (1) WW, water-saturated; (2) WW (water films of thickness T_w), invaded with hydrocarbons; (3) OW, oil-saturated; (4) OW (oil films of thickness T_o), invaded with water.

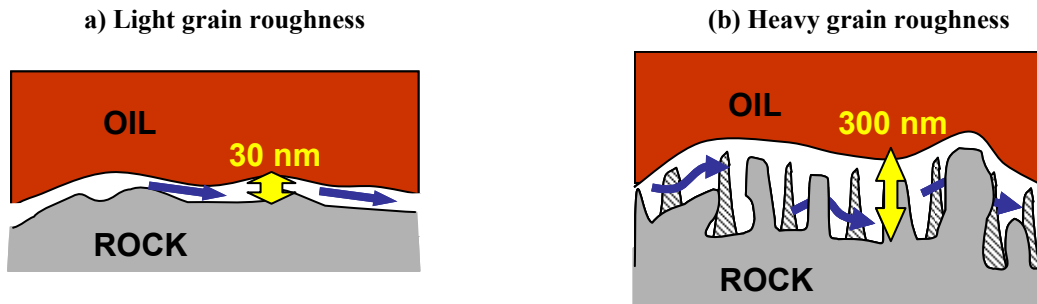
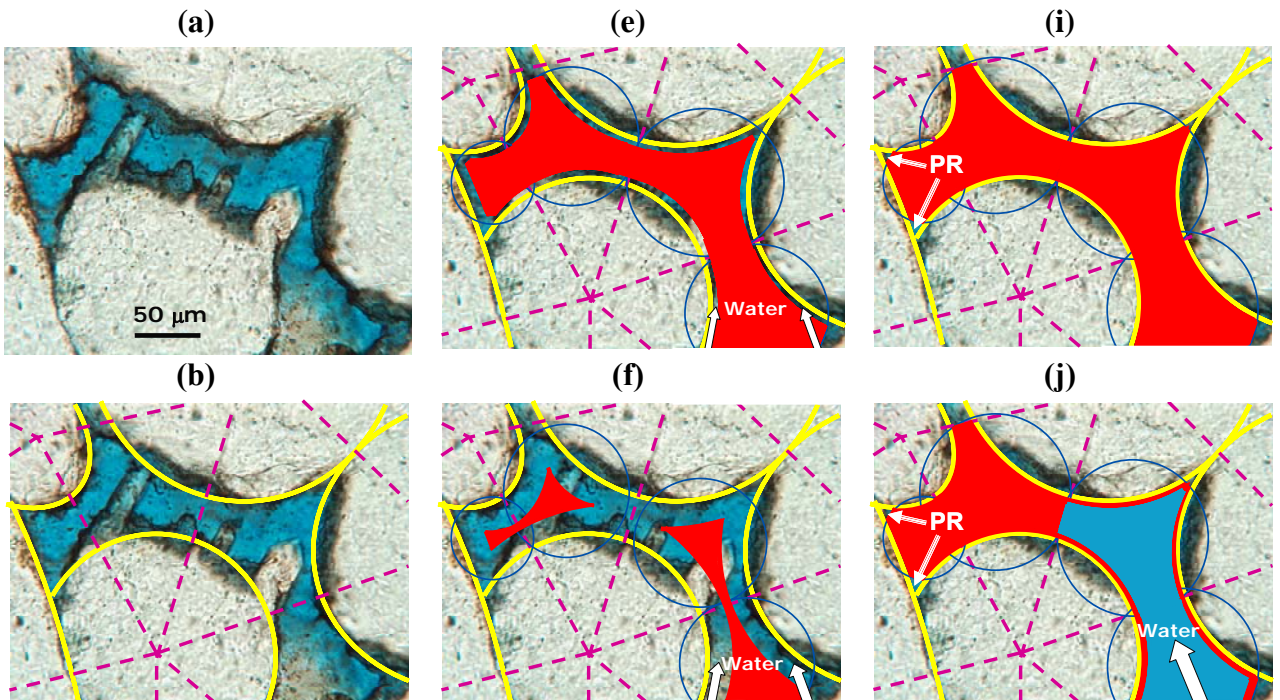


Figure 5 Effect of surface roughness on the effective thickness of the brine wetting film for an equivalent smooth surface: (a) relatively smooth grain surface; and (b) rough grain surface. Single-headed arrows identify conduction currents through the brine film.



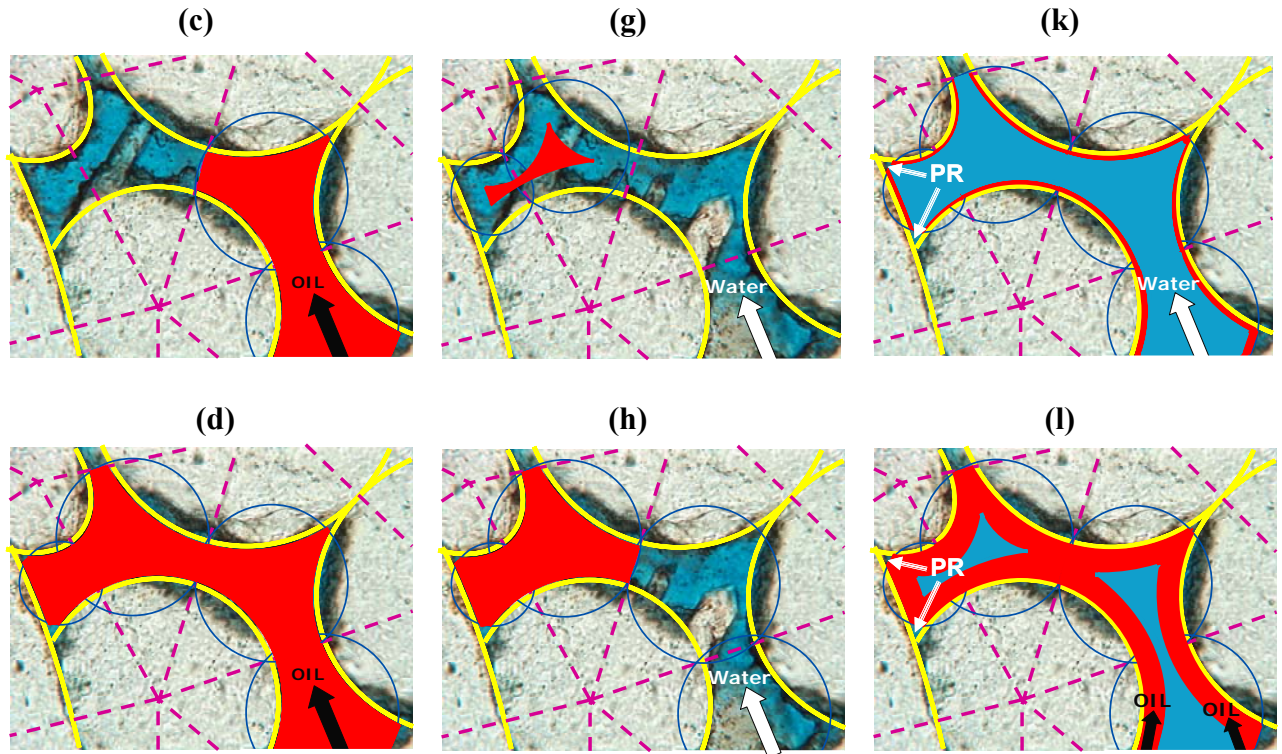


Figure 6 Two-dimensional description of the saturation mechanisms implemented in this paper. (a) Real rock topology from a thin section (white is quartz and blue is pore space). (b) Model idealization including the grains (yellow circles) and the Delaunay cells (dashed triangles). (c)-(d) Successive stages of drainage (Cycle 1). Sphere (blue circles) of radius $R_o = \alpha_o R$, delimit the oil-saturated volume within each pore of size R . (e) Result of imbibition through piston-like displacement of the oil blobs (Cycle 2) starting from stage (d) and leading to irreducible oil saturation in the top-left corner of the pore space. (f)-(h) Successive stages of imbibition through incremental growth of the water films (Cycle 3) starting from stage (e); in (g), snap-off occurred between the non-wetting phase inlet and blobs to the left of the pore space yielding irreducible oil saturation in (h). (i-k) Alternatively from Cycles 2 and 3, Cycle 4 assumes wettability alteration of stage (d) and successive drainage by piston-like displacement of water blobs. (l) Imbibition of the OW medium through oil film growth (Cycle 5) starting from stage (k). Note the evolution in connectivity of the pendular rings (PR) to the inlet water during Cycles 4-5.

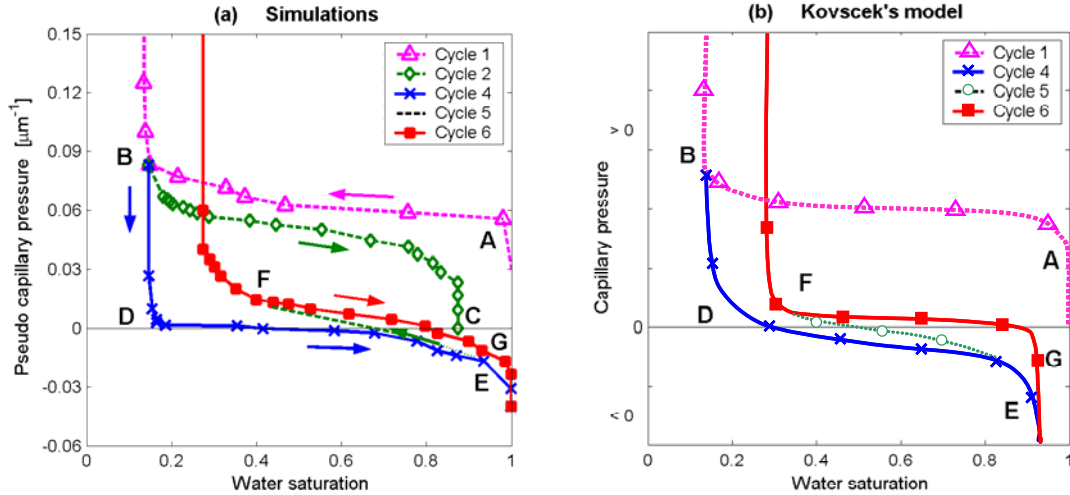


Figure 7 Comparison between (a) the pseudo-capillary pressure curves simulated with our model and (b) the theoretical mixed-wet capillary pressure curves derived by Kovscek et al. (1993), for identical values of irreducible water saturations reached after Cycles 1 (13%) and 5 (23%).

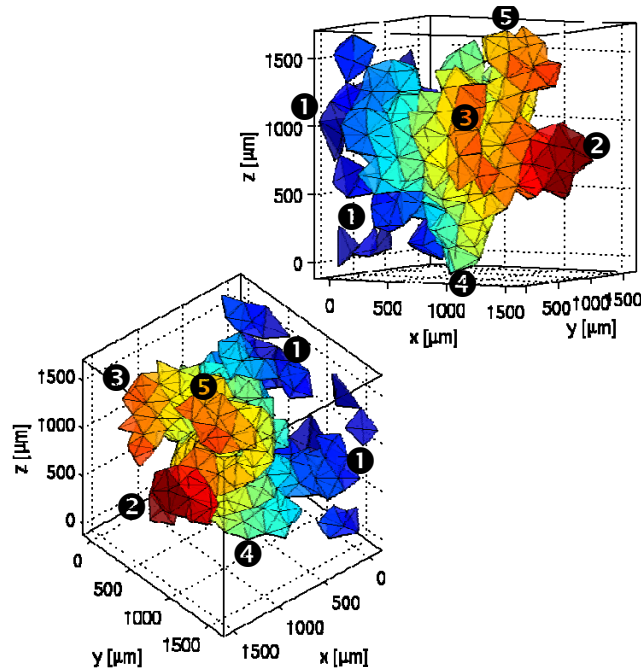


Figure 8 Visualization of the Delaunay tetrahedra invaded by oil during Cycle 1 to reach 22% oil saturation for the pack of 100- μm grains shown in Figure 1 (17 μm throat size threshold). The oil inlets are located at face $x=0$ (circled 1's). Breakthrough is reached at faces $x=1600 \mu\text{m}$ (circled 2), $y=0$ (circled 3), $z=0$ (circled 4) and $z=1600 \mu\text{m}$ (circled 5). The color scale describes the x-coordinate of the pore centers.

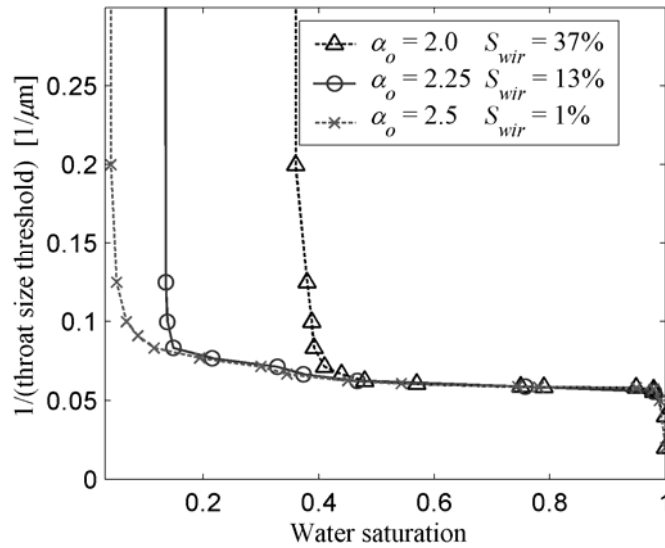


Figure 9 Pseudo-capillary-pressure curves for primary drainage in the pack of Figure 1. The curves describe pseudo-capillary pressure values as a function of water saturation for different non-wetting blob-size factors α_o involving different values of irreducible water saturation, S_{wir} .

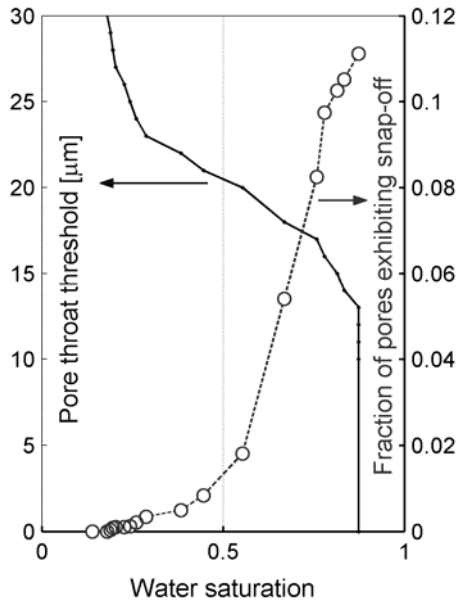


Figure 10 Evolution with water saturation of throat size threshold and fraction of oil-saturated snapped-off pores where snap-off occurs during Cycle 2.

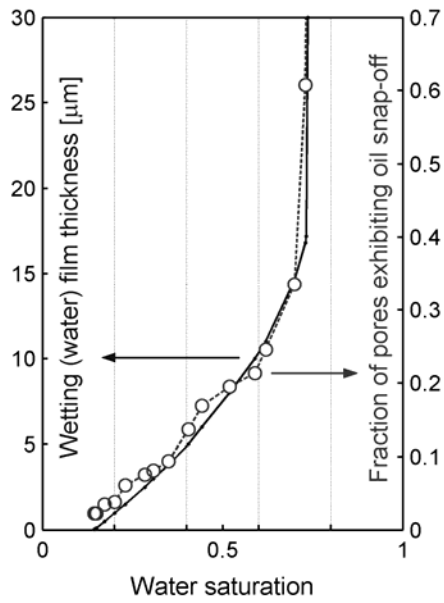


Figure 11 Evolution with water saturation of incremental water film thickness and fraction of oil-saturated snapped-off pores during Cycle 3.

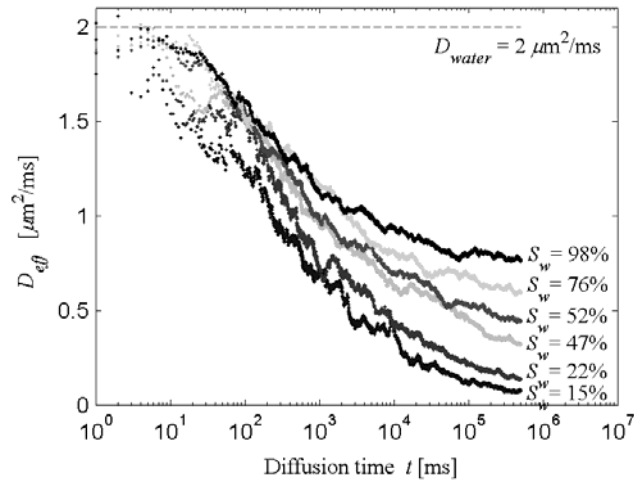


Figure 12 Examples of diffusivity time decays simulated for water molecules at different values of water saturation S_w , in the grain pack shown in Figure 1.

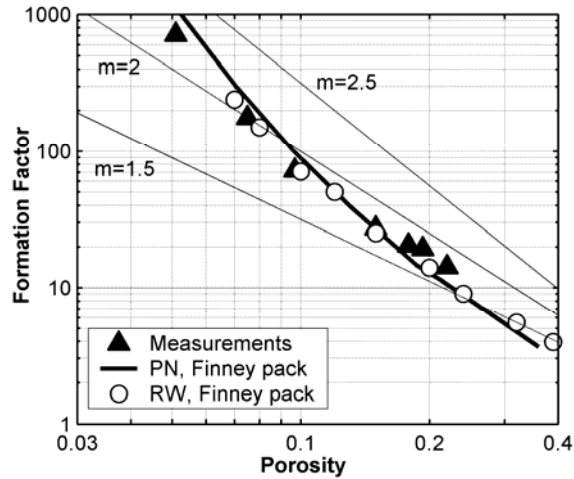
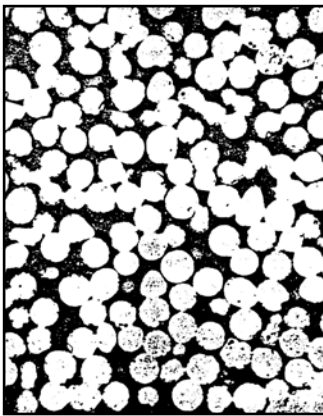


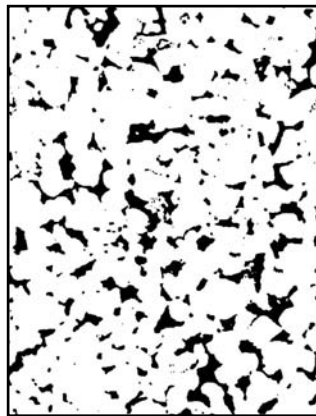
Figure 13 Comparison of formation-factor/porosity crossplots measured in clay-free sandstones (Doyen, 1988) and simulated with a pore network (PN) (Bryant and Pallatt, 1996) and random-walk (RW) techniques. Archie's lithology exponent m is equal to the negative slope of the bilogarithmic plot.

(a) 32 p.u. fused glass bead pack



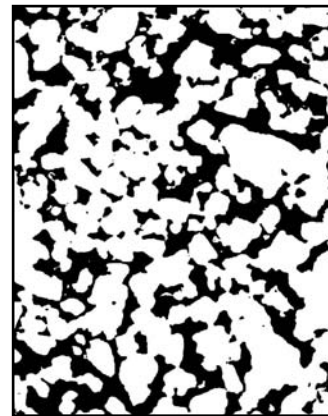
Adapted from Wong et al. (1984)

(b) 9.7 p.u. sandstone



Adapted from Doyen (1988)

(c) 22 p.u. sandstone



Adapted from Doyen (1988)

Figure 14 Micrographs of fused packs of glass beads and rocks exhibiting different values of porosity.

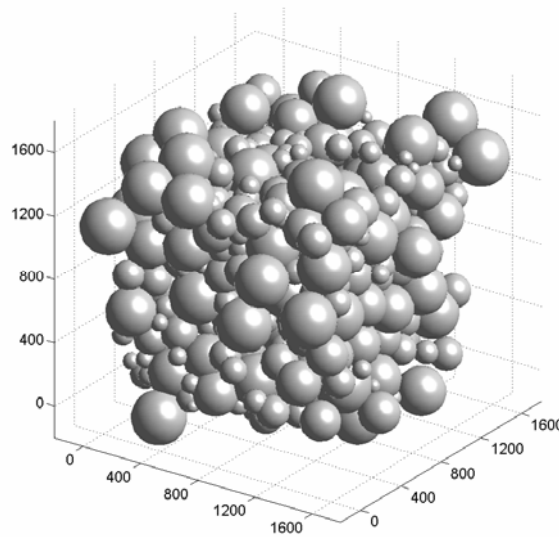


Figure 15 Three-dimensional view of one of the clustered grain packs used for the calculations of formation factors shown in Figure 16.

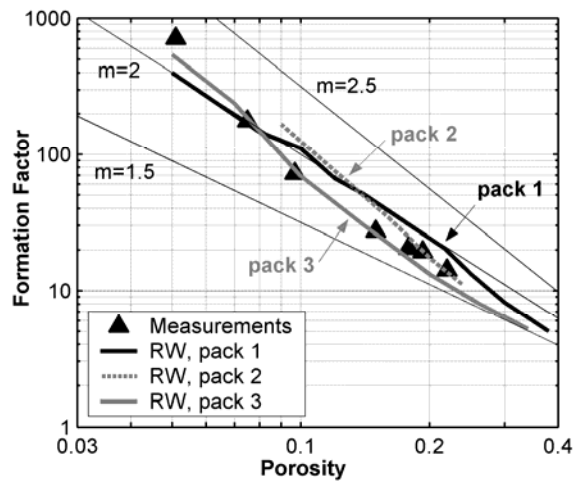


Figure 16 Cross-plot of formation factor and total porosity values measured in clay-free sandstones (Doyen, 1988) and formation factors simulated with random-walks (RW) for packs of normally distributed grain sizes and different degrees of grain clustering (pack 1 is the least clustered and pack 3 is the most).

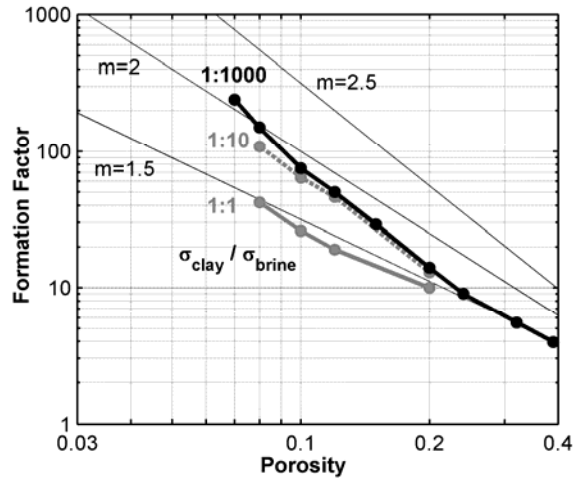


Figure 17 Cross-plot of formation factor vs. total porosity for the clay-coated rock model exhibiting different contrasts of clay-to-brine electrical conductivity.

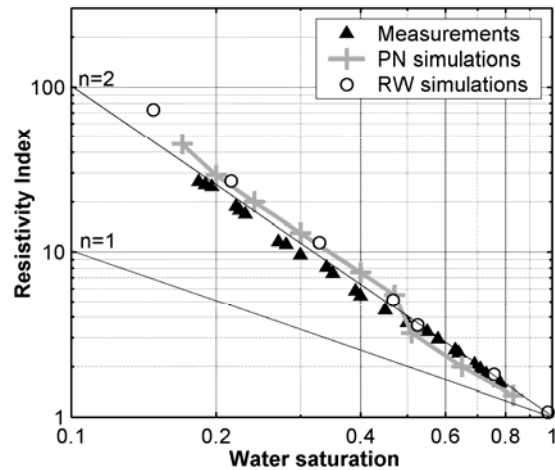


Figure 18 Comparison of primary-drainage resistivity-index curves measured in clay-free sandstone (Argaud et al., 1989) and simulated with PN (Bryant and Pallatt, 1996) and RW techniques with the Finney pack shown in Figure 1.

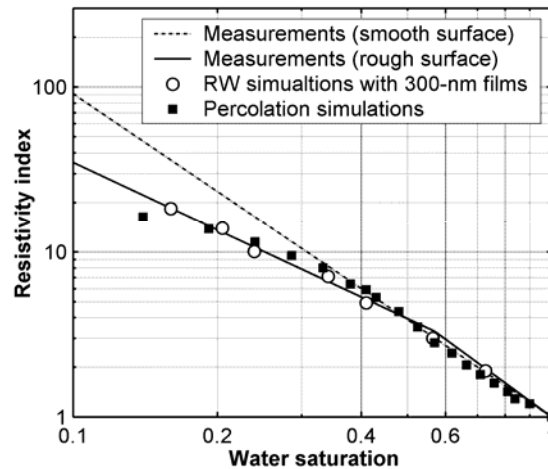


Figure 19 Influence of surface roughness on the resistivity index drainage curve: comparison between the RW simulation results and thick 300-nm films, percolation simulations (Zhou et al., 1997), and well-log measurements of salt-saturated shaly sandstones containing smooth grains (as in Figure 5a: Well 4 data from Diederix, 1982) and rough grains (as in Figure 5b: Well 1 data from Diederix, 1982).

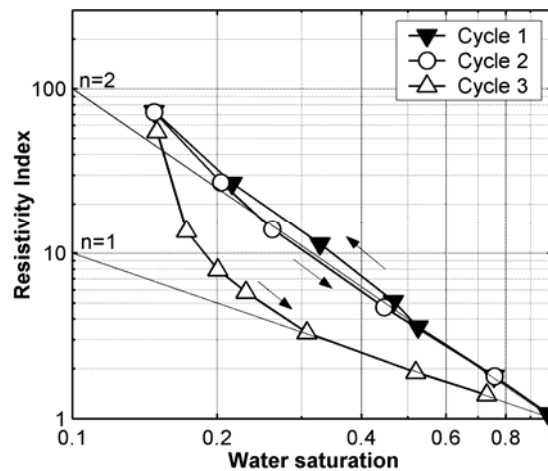
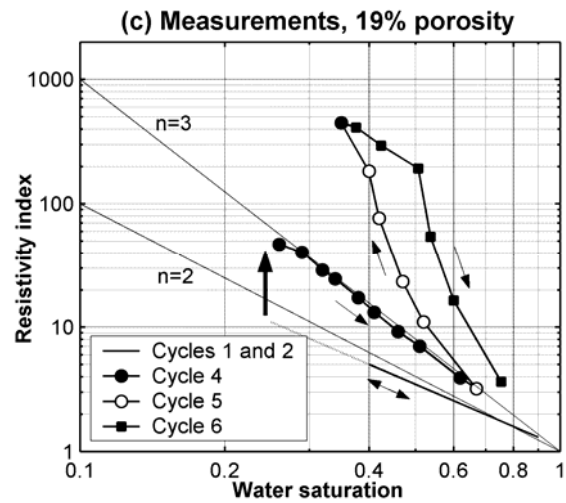
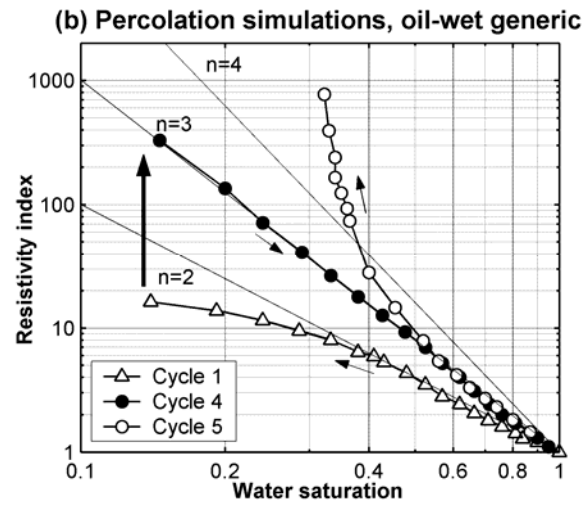
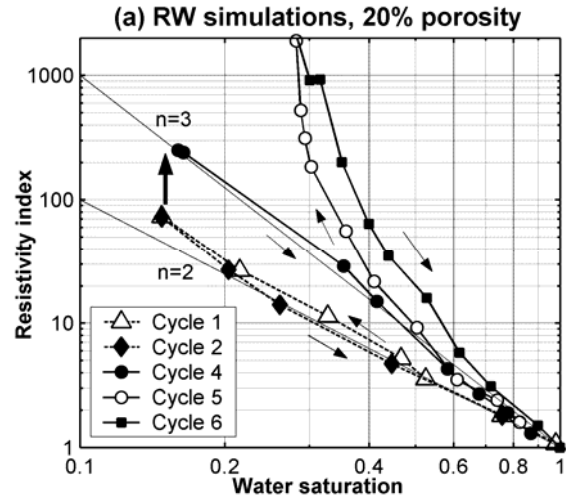


Figure 20 Resistivity index hysteresis due to drainage and imbibition cycles for the 20%-porosity WW Finney pack with 13% irreducible water saturation.



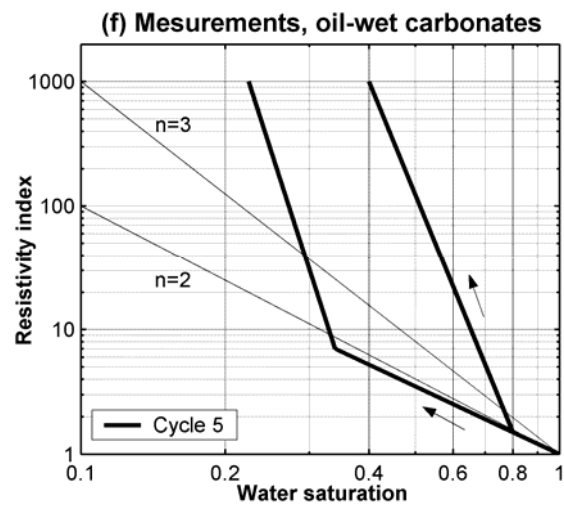
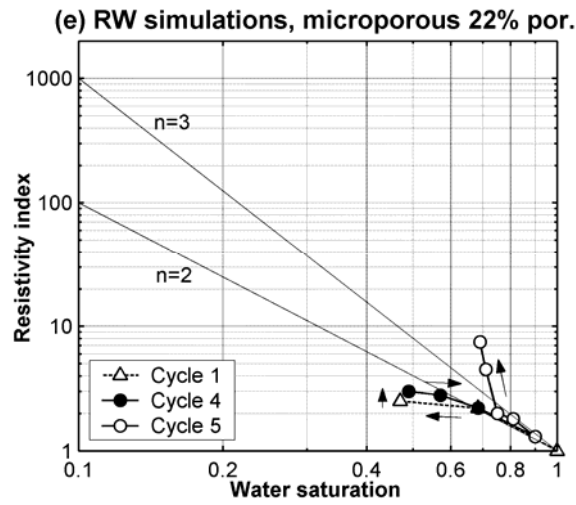
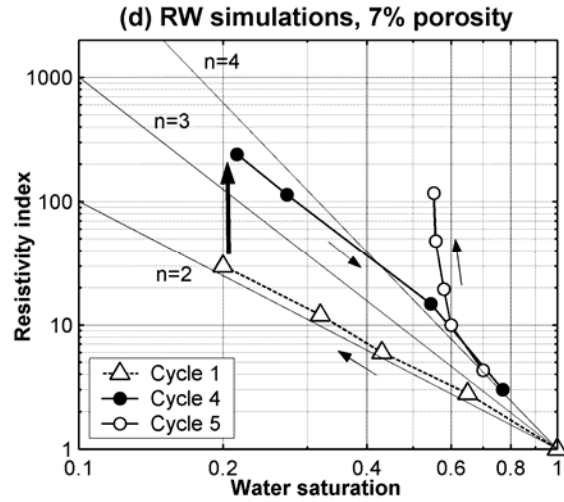


Figure 21 Comparison of resistivity-index curves: (a) simulated in 20%-porosity solid Finney pack with random walks; (b) simulated in a generic rock model with percolation simulations (Zhou et al., 1997); (c) measured in 19%-porosity. Sandstone sample (Wei and Lile, 1991); (d) simulated in 7-p.u. solid Finney pack with random walks; (e) simulated in 22%-porosity microporous Finney pack with random walks; (f) measured in preserved oil-wet carbonate samples (Sweeney and Jennings, 1960). Vertical arrows identify increases of resistivity due to wettability alteration between Cycles 1 and 4.

CHAPTER 5. TWO-DIMENSIONAL PORE-SCALE SIMULATION OF WIDE-BAND ELECTROMAGNETIC DISPERSION OF SATURATED ROCKS

Effective-medium theories (EMTs) are routinely used to interpret multi-frequency dispersions of dielectric permittivity and electrical conductivity of saturated rocks. However, EMTs exhibit limitations which substantially restrict their use for petrophysical interpretation. For instance, pore connectivity is of significant interest in the study of subsurface reservoirs, but no existing EMT includes it as an explicit property in the current analysis of kHz-GHz-range dielectric measurements.

We introduce a new approach to quantify the effects of pore geometry and connectivity on the kHz-GHz frequency dispersion of dielectric permittivity and electrical conductivity of clay-free porous rocks. This approach is based on the numerical solution of the internal electric fields within submicron-resolution pore maps constructed with grain and rock pixels. The discrepancy between the internal fields and electrical currents calculated for a homogeneous scatterer and those calculated for a given pore map is minimized to yield the effective electrical conductivity and dielectric constant for that pore map. This minimization is performed independently for each frequency and is verified to implicitly agree with Kramers-Kronig causality relationships.

We show that EMTs only predict an average dispersion for given microscopic geometrical parameters (e.g., porosity, pore eccentricity) while individual realizations honoring the same parameters are associated with dispersion about average values predicted by EMTs. Unlike any EMT prediction, we show that pore connectivity plays a major role in both the shape and amplitude of wide-band electromagnetic property dispersions. The simulation procedure introduced in this paper provides a systematic method to assess the sensitivity of a multitude of pore-scale properties on the macroscopic wide-band dielectric dispersion of saturated rocks.

5.1 INTRODUCTION

5.1.1 Maxwell-Wagner Interfacial Polarization Process

The complex electrical impedance measured across a saturated rock is in some ways analogous to a parallel resistor/capacitor model. Geometrically normalized measurements of conductance and capacitance yield the effective conductivity σ_{eff} and dielectric permittivity ϵ_{eff} of the rock sample, both real quantities. Electrical conductivity quantifies dissipation of energy whereas dielectric permittivity quantifies energy storage. If the rock sample is regarded as a conductor of complex conductivity $\bar{\sigma}^*$ subject to monochromatic excitation of frequency f and radian frequency $\omega = 2\pi f$, $\bar{\sigma}^*$ can be expressed in terms of the measured values of σ_{eff} and ϵ_{eff} with the expression

$$\bar{\sigma}^* = \sigma_{eff} - i\omega\epsilon_{eff}, \quad (1)$$

where the $e^{-i\omega t}$ time harmonic convention is adopted for the exciting electric field and t is time. Similarly, if the rock sample is regarded as a capacitor of complex dielectric permittivity $\bar{\epsilon}^*$ under the same conditions, $\bar{\epsilon}^*$ is equal to

$$\bar{\epsilon}^* = i\bar{\sigma}^*/\omega = \epsilon_{eff} + i\sigma_{eff}/\omega. \quad (2)$$

The dielectric constant κ of the medium is the ratio of effective dielectric permittivity to that of vacuum, $\epsilon_0 = 8.854 \times 10^{-12}$ Farad/m. The conductivities and permittivities of pure charge-free isolated rock and bulk hydrocarbons are constant over the entire kHz-GHz frequency range. For increasing values of frequency, salty water begins to exhibit frequency dependence about 1 GHz (for simplicity, in this paper we assume that the dielectric properties of water remain constant over the entire kHz-GHz frequency range). In the case of rock-fluid mixtures, electric charges accumulate at the interface between brine and rock (or oil). Within these charged surfaces, brine polarizes in the form of a macroscopic dipole, which can give rise to frequency-dependent macroscopic polarization. At low frequency, macroscopic dipoles reach equilibrium before the incident field has notably changed, hence giving rise to polarization build-up. When frequency increases, the orientation of macroscopic dipoles cannot follow the applied field due to the viscosity of the fluid, thereby

resulting in energy dissipation, increased electrical conductivity, and reduced dielectric permittivity. This behavior, summarized by Bona et al. (1998, 2002), is known as the Maxwell-Wagner phenomenon, and describes the Debye-relaxation behavior of complex effective permittivity of composite material as a function of frequency, namely,

$$\bar{\varepsilon}^*(\omega) = \bar{\varepsilon}^*(\omega \rightarrow \infty) + \frac{\Delta\bar{\varepsilon}^*}{1+i\omega\tau} \quad (3)$$

In this equation, $\Delta\bar{\varepsilon}^*$ is the difference between the asymptotic values of the composite permittivity at zero and at infinite frequencies, and τ is the dielectric relaxation time of the equivalent dipole formed by brine pores. The relaxation time τ is a complex function of pore shape factor, pore isotropic orientation, and rock/brine permittivities (Sillars, 1937). Variants of equation (3) exist with adjustable exponents introduced to match experimental data (Bona et al., 2002). Other models adapt equation (3) for distributions of pore geometries (Lysne, 1983) that include several inflection points in a single dielectric dispersion curve.

5.1.2 Dielectric Mixing Laws and Other Polarization Models

Dielectric mixing laws based on effective medium theory and polarization averaging also yield sigmoidal frequency-dispersion curves. The books by Choy (1999) or Sihvola (2002) summarize the assumptions and limitations of existing dielectric effective medium theories. Starting from Maxwell-Garnett's mixing formula, strictly valid for isolated inclusions, a family of models was developed to describe the behavior of dense composites, including Bruggeman's, coherent potential, Looyenga's, Sen-Scala-Cohen's (Sen et al., 1981), and Mendelson-Cohen's (1982) effective medium approximation (EMA). In particular, Choy (1999) provides a thorough description of the Maxwell-Garnett and Bruggeman averages from a theoretical viewpoint and compare the two approaches and their limitations. In similar fashion to Maxwell-Wagner type descriptions, effective-medium models account for (a) contrasts of electrical properties between the components and (b) eccentricities and anisotropic distributions of brine-filled zones (or, similarly, of grains and resistive oil blobs), regardless of pore or grain size. Sihvola (2002) also describes a family of power-law dielectric models where the effective complex permittivity of the mixture taken to some power, $(\bar{\varepsilon}^*)^{1/N}$, is equal to the volumetric average of $(\bar{\varepsilon}^*)^{1/N}$ for each component.

These models include the popular complex refractive index method (CRIM) with $N = 2$, which have been widely applied as convenient phase volumetric averages in the GHz range; CRIM also forms the basis for ongoing efforts to include grain morphology in the prediction of the dielectric constant of inhomogeneous carbonate rocks in the 100 MHz-1 GHz frequency range (Seleznev et al., 2005).

The mixing laws summarized above shed much theoretical insight on the relaxation processes taking place in saturated rocks. Unfortunately, they scarcely provide *practical* petrophysical information either because they fail to accurately fit laboratory measurements (as in Kenyon, 1984), or because they use parameters that are difficult to determine (e.g., those of Sillars' model) without direct observation (or spatial imaging) of the sample. Their physical consistency, as well as their assumptions, are also sometimes questionable (Sihvola, 2002), so that one is left to wonder which mixing laws are applicable to which specific cases – if any. Díaz et al. (1998) provided a 14-point summary list of both conceptual and practical issues related to the application of dielectric mixing laws. A major failure of these mixing laws based on electric field-averaging is that they implicitly neglect both the duality of Maxwell's equations and the electromagnetic (EM) coupling between brine bodies within rocks. This limitation was overcome by del Río and Whitaker (2000a, 2000b), who enforced the *dual* averaging of electric and magnetic fields simultaneously, and mathematically demonstrated the limits of *single*-field averaging results. A similar duality is at the basis of the numerical approach developed in this paper for the calculation of the effective conductivity and dielectric permittivity of digital composite media, as discussed in a subsequent section.

Finally, attention is called to the remarkable but rarely mentioned Stroud-Milton-De (SMD) analytical model (Stroud et al., 1986), based on Bergman's analytic model for a 2-component composite. The strength of the SMD model is to capture the pore space geometrical information as a cascade of gamma functions of porosity and DC conductivity, as long as the contact area between grains remains smaller than that of rock/fluid interfaces. Generality of the SMD model was supported by excellent data fitting with dielectric dispersions measured on a variety of rock samples between 10 MHz and 1 GHz. A similar analytical approach based on the single-mode decomposition of rock dielectric permittivity spectrum was developed by Díaz et al. (1998), who captured the geometry of a dielectric

composite with a single percolation threshold. The main problem that remains is to assign the right percolation threshold to the rock sample for proper geometrical description.

5.1.3 Objectives and Methodology

The analytical models described above suggest strong ties between grain and pore geometry, DC conductivity, and percolation ability of the water phase within the rock. However, much work remains to relate dielectric frequency dispersions with pore connectivity at the small scale, and with rock hydraulic permeability at the large scale. Therefore, it is appropriate to quantify the respective contributions of pore or grain eccentricity on dielectric dispersion as collective objects or clusters, versus the contribution of pore connectivity regardless of eccentricity at a macroscopic scale. The objective of this paper is twofold: (a) to develop a numerical method that enables the accurate simulation of dielectric dispersion effects at the pore scale on a frequency range wider than allowed by existing methods, and (b) to quantify the influence of *explicit* pore connectivity on the dielectric dispersion of 2D digital rock models. We specifically target our analysis to the range 10 kHz-1 GHz, which corresponds to the frequency band of borehole measurements acquired with open-hole logging resistivity and induction (10-200 kHz), logging-while-drilling propagation (2 MHz) and EM propagation (1 GHz) instruments.

We introduce a numerical framework consisting of two-dimensional (2D) digital pore maps that distribute sub- μm brine and rock/oil pixels of variable complex conductivities included in realistic pore and throat geometries. Frequency-dependent dispersions of upscaled effective conductivity, σ_{eff} , and dielectric constant, κ_{eff} , for disc-shaped pore maps are estimated based on EM propagation principles. Specifically, the electric fields induced by a monochromatic EM excitation and the corresponding internal currents are computed within the pore maps and compared to those that would be excited by the same incident plane wave in a homogeneous cylindrical scatterer of given conductivity and dielectric constant. The conductivity and dielectric constant of the homogeneous cylinder that minimize the misfit between the internal fields and electrical currents in the pore map and in the homogeneous medium become the best-fit effective properties of the pore map. Without loss of generality, the developments presented in this paper assume macroscopic isotropy of the rock models

when using an isotropic homogeneous cylinder to calculate the effective values of σ_{eff} and K_{eff} .

5.2 NUMERICAL METHOD FOR THE CALCULATION OF EFFECTIVE CONDUCTIVITY AND DIELECTRIC PERMITTIVITY

5.2.1 Scatterer Geometry

The geometrical configuration adopted for the pixel-based scatterer is compatible with an existing fast analytical solution of EM scattering due to a homogeneous dielectric and lossy cylinder on a wide frequency range (kHz-GHz). Pekonen et al. (1999) apply similar principles to simulate the MHz-range response of 2D pixel-based purely dielectric mixtures bounded by a waveguide. These authors compute the effective dielectric constant of the medium from the reflection and transmission coefficients at the scatterer boundaries. The main disadvantage of the waveguide method is that it remains accurate only below 80 MHz (Pekonen et al., 1999), whereas our problem demands high numerical accuracy for frequencies as high as 1 GHz.

To circumvent the above limitation, we introduce a new estimation approach based on the cylindrical scatterer geometry shown in Figure 1. Without restriction on frequency, the medium is described as a disc populated with square pixels of contrasting conductivities and dielectric constants of grain and fluids representing the pore map. We consider transverse-magnetic (TM) excitation such that the vector components of the incident electric field are in the same plane defined by the cross-section of the 2D scatterer. This TM polarization causes the induced electrical currents to cross boundaries between pixels with contrasts of electric and dielectric properties.

Presence of corners, vertices, and irregular shapes on the boundary of the disc-shaped scatterer can cause significant fringe effects on the internal electric field. We choose a circular boundary to define the spatial extension of the pore map to mitigate this problem, to take advantage of the closed-form analytical resolution of the electric fields in a cylindrical scatterer (Balanis, 1989), and ultimately to compare simulations against measurements performed on cylindrical core data. In addition, a high-resolution pore map is necessary to

attenuate boundary effects at low frequencies for the case of resistive pixels. As shown in Figure 2, at the nm- to μm -scale resolution used in our models, pore maps with less than 400x400 pixels resolution entail substantial boundary fringing below 10 MHz for a homogeneous distribution of resistive pixels and 1 S/m background water. These numerical artifacts bias the estimation of effective properties of the scattering medium. In what follows, we show that spatial discretizations of the scattering medium larger than 400x400 pixels enable reliable estimations of effective properties of a homogeneous disc in the entire kHz-GHz range.

5.2.2 Internal Electric Fields

We assume that the individual pixel conductivities as well as the conductivity of the lossy brine background are isotropic. Equation (1) defines the complex effective conductivity for each pixel. Similarly, the complex effective conductivity of the water background is given by

$$\bar{\sigma}_b^* = \sigma_b - i\omega\epsilon_0\kappa_b, \quad (4)$$

where σ_b is the brine effective conductivity and κ_b is its dielectric constant. If $\mu_0 = 1.257 \times 10^{-6}$ H/m is the vacuum magnetic permeability, the wave number k_b of the background is defined as

$$k_b^2 = i\omega\mu_0\bar{\sigma}_b^*. \quad (5)$$

The pore map is regarded as a complex scatterer where each element interacts with the incident wave, and where the cross-coupled response (or cross-scattering) of all the elements gives rise to the overall EM response of the saturated rock. The Fast-Fourier Transform Method of Moments (FFT-MoM) (Wang, 1991; Catedra et al., 1995; Avdeev et al., 2002) was implemented in 2 dimensions to solve Maxwell's equations and compute the complex electric field values in each pixel of the pore map. We selected this method over other numerical methods for several reasons: (a) it is formulated in the same frequency domain as the closed-form analytical homogeneous solution used for effective property inversion; (b) it explicitly honors the scatterer boundaries and does not require implementing special

boundary conditions; and (c) it accurately and efficiently handles large contrasts in material electrical properties (as encountered at the water/grain interface).

All the calculations are performed in the (x, z) 2D Cartesian coordinate frame described in Figure 1. We numerically solve the general integral equation for the electric field \mathbf{E} at location $\mathbf{r} = (x, z)$ given by

$$\mathbf{E}(\mathbf{r}) = \mathbf{E}_b(\mathbf{r}) + \int_{\mathbf{r}' \in V_{scat}} i\omega\mu_0 \vec{\mathbf{G}}(\mathbf{r} - \mathbf{r}') \cdot \Delta\sigma^*(\mathbf{r}') \cdot \mathbf{E}(\mathbf{r}') dV, \quad (6)$$

where \mathbf{E}_b is the background field normalized by the $e^{-i\omega t}$ time-harmonic variation imposed by a TM incident plane wave that forms a counter-clockwise angle ϕ with the x axis, i.e.,

$$\mathbf{E}_b(\mathbf{r}) = \begin{bmatrix} -e^{ik(-x\cos\phi+z\sin\phi)} \sin\phi \\ 0 \\ -e^{ik(-x\cos\phi+z\sin\phi)} \cos\phi \end{bmatrix}. \quad (7)$$

The scatterer consists of rock and fluid pixels of effective complex conductivity $\bar{\sigma}^*$ occupying the volume V_{scat} . We solve equation (6) as the Riemann sum of the scattering due to all the pixels forming V_{scat} . For each pixel, $\Delta\sigma^*$ is the electrical conductivity contrast tensor between the scatterer and the water background. The tensor $\Delta\sigma^*$ is assumed isotropic at the pixel level and, following equations (1) and (4), becomes the complex scalar $\Delta\bar{\sigma}^* = \bar{\sigma}^* - \bar{\sigma}_b^*$. Finally, in equation (6) $\vec{\mathbf{G}}(\mathbf{r}, \mathbf{r}')$ is the dyadic Green's tensor for the electric field. This tensor quantifies the cross-interaction of two scatterers located in the (x, z) plane of the pore map at positions \mathbf{r} and \mathbf{r}' , respectively, and is defined as the solution of the dyadic wave equation

$$\nabla \times \nabla \times \vec{\mathbf{G}}(\mathbf{r}, \mathbf{r}') - k_b^2 \vec{\mathbf{G}}(\mathbf{r}, \mathbf{r}') = \vec{\mathbf{I}} \delta(\mathbf{r} - \mathbf{r}'), \quad (8)$$

i.e.,

$$\vec{\mathbf{G}}(\mathbf{r}, \mathbf{r}') = \left(\vec{\mathbf{I}} + \frac{1}{k_b^2} \nabla \nabla \right) g(\mathbf{r}, \mathbf{r}'). \quad (9)$$

In equation (9), g is the scalar Green's function that satisfies the wave equation with a point source excitation,

$$\nabla^2 g(\mathbf{r}, \mathbf{r}') + k_b^2 g(\mathbf{r}, \mathbf{r}') = -\delta(\mathbf{r} - \mathbf{r}'). \quad (10)$$

In the process of discretizing equation (6), $\vec{\mathbf{G}}(\mathbf{r}, \mathbf{r}')$ is integrated on the rectangular area of each pixel of the pore map using the analytical expressions derived by Gao et al. (2005). Appendix A quantifies the accuracy with which the fields are determined within a homogeneous cylinder when using this method of solution.

Figure 3 shows an example of internal currents distributed within a pore map that consists of brine ellipses ($\sigma_w = 1$ S/m, $\kappa_w = 70$) embedded in a rock-like host ($\sigma_{host} = 0$, $\kappa_{host} = 2$) for two cases of perpendicular plane-wave TM excitation. At 100 MHz, the out-of-phase dielectric effects are more significant than the in-phase conductivity effects. Consequently, the internal currents induced across the scatterer are normal to the incoming electric field, i.e., parallel to the incoming TM wave according to the nomenclature of Figure 1. A variation of the scale of the current amplitudes in Figure 3 emphasizes two main phenomena. First, the distribution of low-current amplitudes (middle panels) shows the directionality of the internal currents and describes how the currents bypass the ellipsoidal inclusions that block the passage of the incident waves. Second, the distribution of high-current amplitudes (right-hand panels of Figure 3) show that electrical current becomes maximum in the brine inclusions that are normal to the incident waves (parallel to the incident electric fields), while the amplitude of currents decreases in the inclusions parallel to the incident wave.

5.2.3 Inversion of Effective Conductivity and Dielectric Permittivity

From the viewpoint of EM propagation, we define the effective conductivity and dielectric constant of the composite pore map as the conductivity σ_h and dielectric constant κ_h of a homogeneous and isotropic scatterer that reproduces as closely as possible the scattered field due to the pore map. These conditions include angle of incidence, frequency and amplitude of the exciting EM wave, and scatterer shape. Hence, the estimation of σ_h and κ_h is consistent with Maxwell's equations and can be approached as a minimization problem.

It follows from equation (6) that the electrical field propagated to *any* location in space is a weighted function of the currents \mathbf{J} inside the scatterer, i.e.,

$$\mathbf{J} = \Delta \bar{\sigma}^* \mathbf{E}. \quad (11)$$

Therefore, if one seeks to minimize the discrepancy between the electric fields scattered by the pore map and the fields scattered by a homogeneous scatterer *regardless* of the position where the fields are evaluated, the same results should be obtained if one minimizes the discrepancy of internal currents \mathbf{J} within the scatterers.

If the pore map is considered as the scatterer, $\Delta \bar{\sigma}^* = \bar{\sigma}^* - \bar{\sigma}_b^*$ varies for each pixel. For a homogeneous scatterer of real conductivity σ_h and dielectric constant κ_h , we define its complex conductivity as $\bar{\sigma}_h^* = \sigma_h - i\omega \varepsilon_0 \kappa_h$ and the conductivity contrast with respect to the background becomes $\Delta \bar{\sigma}^* = \bar{\sigma}_h^* - \bar{\sigma}_b^*$ for the entire scatterer. We minimize the discrepancy of internal currents \mathbf{J} over the entire scatterer by minimizing the cost function

$$\Psi = \left\| (\bar{\sigma}^* - \bar{\sigma}_b^*) \mathbf{E} - (\bar{\sigma}_h^* - \bar{\sigma}_b^*) \mathbf{E}_h \right\|_{L_2} = \left\| \bar{\sigma}^* \mathbf{E} - \bar{\sigma}_h^* \mathbf{E}_h - \bar{\sigma}_b^* (\mathbf{E} - \mathbf{E}_h) \right\|_{L_2}, \quad (12)$$

where \mathbf{E} is the total electric field at a given pixel of complex conductivity $\bar{\sigma}^*$, and \mathbf{E}_h is the electric field analytically calculated for the homogeneous scatterer of complex conductivity $\bar{\sigma}_h^* = \sigma_h - i\omega \varepsilon_0 \kappa_h$. Because the pore map does not exceed 1 mm², this analytical value is identical across the entire disc and we calculate it close to the disc center. The L_2 norm adopted for the cost function Ψ above enforces the quadratic misfit over the entire surface of the pore map. Therefore, the values of σ_h and κ_h for which Ψ reaches its minimum correspond to the effective, upscaled electrical properties σ_{eff} and κ_{eff} of the pore map for this frequency and this angle of excitation.

Appendix B describes the practical implementation of the minimization of equation (12) with a disc-shaped, homogeneous and isotropic 2D scatterer. In the same Appendix we emphasize that the choice of the cost function

$$\Psi_3 = \left\| \bar{\sigma}^* \mathbf{E} - \bar{\sigma}_h^* \mathbf{E}_h \right\|_{L_2} + |\bar{\sigma}_b^*| \times \left\| \mathbf{E} - \mathbf{E}_h \right\|_{L_2} \quad (13)$$

provides the widest range of accuracy, including rock conductivities as low as 1 mS/m.

We note that the approach described above for the estimation of σ_{eff} and κ_{eff} is performed frequency by frequency independently. As shown in the next sections, it is remarkable that our estimation method produces smooth dielectric dispersion curves which implicitly satisfy the Kramers-Kronig relationships (Landau and Lifschitz, 1960).

5.3 CONNECTIVITY EFFECTS IN DILUTE CONCENTRATIONS OF BRINE INCLUSIONS

5.3.1 Effective Medium Approximation with Depolarization Factor l

Mendelson and Cohen's (1982) EMA (subsequently adapted by Feng and Sen, 1985, to the case of multiphase fluid saturations) is one of the few mixing laws that are applicable to 2D media and that explicitly integrate grain or pore geometry information over a wide frequency range. An often overlooked property of the EMA in its application to interpret measurements of saturated rocks is that this approximation remains strictly valid for dilute concentrations of impurities, (in our case, lossy dielectric brine inclusions embedded into a resistive rock host). The EMA assumes an incremental refinement of the rock/water mixture where infinitesimal amounts of rock are added to the rock/water mixture of a previous step, and where the new complex conductivity of the mixture is estimated by averaging the electric fields and the electric displacements throughout the entire volume. At each step, the rock grains added to the mixture are oblong spheroids randomly oriented and individually characterized by the same geometric depolarization factor, l . The EMA then yields a relationship between the porosity ϕ of the saturated rock and the complex dielectric constants of water, $\bar{\epsilon}_w^*$, rock grains, $\bar{\epsilon}_{grain}^*$, and mixture, $\bar{\epsilon}^*$, (Mendelson and Cohen, 1982 ; Sen, 1984; Kenyon, 1984) given by:

$$\ln \phi = \frac{3l(1-l)}{1+3l} \ln \left(\frac{\bar{\epsilon}_w^*}{\bar{\epsilon}^*} \right) + \ln \left(\frac{\bar{\epsilon}^* - \bar{\epsilon}_{grain}^*}{\bar{\epsilon}_w^* - \bar{\epsilon}_{grain}^*} \right) + \frac{2(1-3l)^2}{(1+3l)(5-3l)} \times \ln \left[\frac{(5-3l)\bar{\epsilon}_w^* + (1+3l)\bar{\epsilon}_{grain}^*}{(5-3l)\bar{\epsilon}^* + (1+3l)\bar{\epsilon}_{grain}^*} \right]. \quad (14)$$

The general expression for l can be found in Landau and Lifshitz (1960). For 2D elliptic inclusions of eccentricity e , l is given by the expression (Sihvola, 2005)

$$l = \frac{\sqrt{e}}{1 + \sqrt{e}}. \quad (15)$$

The comparisons that follow are based on the pore maps A-D shown in Figure 4, where ellipses of brine ($\sigma_w = 1$ S/m, $\kappa_w = 70$) are randomly distributed in an insulating rock-like host. These ellipses share unique semi-axes values equal to 4 pixels by 48 pixels, thereby involving a constant eccentricity $e = 12$ and a depolarization factor $l = 0.776$. In all cases, the porosity formed by these brine inclusions is kept equal to 8% and enforces the assumption of dilute concentration of inclusions. Two possible dielectric constants are assigned to the host, $\kappa_{host} = 2$ and 10, that bound realistic values for rock (4.5 for quartz and 7.5 for calcite).

5.3.2 Statistical Significance of Sigmoid Dispersions

At a first stage, let us consider the random pore distributions of maps A-D shown in Figure 4. The elliptical pores are randomly distributed and exhibit different geometrical arrangements; Pores in map A and C seem more organized as local clusters, while pores in map B and D look more homogeneously distributed across the entire space. Each map includes a distribution of 401x401 pixels with a resolution of 1 μm^2 /pixel. All the simulations are performed for one angle of incidence and include two frequency samples per decade.

The EMA solution of equation (14) is plotted in Figure 5 with a depolarization factor of $l = 0.82$ for both values of κ_{host} . In this figure, EMA dispersions fit very well the average of both the dielectric and conductivity simulation results for maps sharing the same value of κ_{host} on the entire frequency band. Two conclusions stem from this result. First, the scattering that appears between the different pore map realizations and the EMA sigmoids suggest that sigmoid analytical mixing rules capture an *average* trend for the given set of porosities, material electrical properties, and l values, but does not account for the geometrical features that entail variations of σ_{eff} and κ_{eff} from one pore map to another. Second, the difference between the best-match value of l (0.82) and the theoretical value of l (0.776) is small and

possibly due to the fact that some ellipses touch each other and form clusters with overall eccentricities larger than 12.

5.3.3 Consistency of the Simulation Results

We then verify the consistency of our dilute-inclusion simulation results with respect to a volumetric dielectric power-law, brine conductivity sensitivity, Argand plots, and Kramers-Kronig relations. Figure 5 first verifies that simulation results obtained with $\kappa_{host} = 2$, $\kappa_w = 70$ and $\sigma_w = 1$ S/m fit a CRIM-like power-law behavior of exponent $N = 3$ above 30 MHz for both conductivity and dielectric constant, whereby

$$\bar{\varepsilon}^* = \left[\phi (\bar{\varepsilon}_w^*)^{1/3} + (1-\phi) (\bar{\varepsilon}_{grain}^*)^{1/3} \right]^3. \quad (16)$$

Specifically considering map A, we also verify that simulation results remain consistent when the brine conductivity is changed to $\sigma_w = 0.1$ and 10 S/m. Figure 6 confirms the trend predicted by both EMA and the power-law.

The Argand plot constructed in Figure 7 from the results of Figure 6, and from the corresponding EMA predictions is also in excellent agreement with the expected convex curvature measured in saturated rocks (Lima and Sharma, 1992). An Argand plot describes the evolution of reactance with respect to resistance of a sample for increasing values of frequency. Defining as ρ' and ρ'' as real in-phase and out-of-phase resistivities, we equate the normalized complex resistivity $\bar{\rho}^* = \rho' - i\rho''$ to the inverse of the corresponding normalized admittance $\bar{\sigma}^* = \sigma_{eff} - i\omega\varepsilon_0\kappa_{eff}$ to obtain the relationships

$$\rho' = \frac{\sigma_{eff}}{(\sigma_{eff})^2 + (\omega\varepsilon_0\kappa_{eff})^2} \quad \text{and} \quad \rho'' = \frac{-\omega\varepsilon_0\kappa_{eff}}{(\sigma_{eff})^2 + (\omega\varepsilon_0\kappa_{eff})^2}, \quad (17)$$

which are the quantities plotted in Figure 7.

Kramers-Kronig (KK) relations are normally used to verify the quantitative consistency of wide-band dielectric experimental measurements. In a general sense, the current density $\mathbf{J} = \sigma^* \mathbf{E}$ and the electric displacement field $\mathbf{D} = \varepsilon^* \mathbf{E}$ through a material assume that σ^* and ε^* are complex numbers that can be written in terms of their real and

imaginary parts as $\sigma^* = \sigma' - i\sigma''$ and $\varepsilon^* = \varepsilon' + i\varepsilon''$. As a causal physical mechanism, the KK relationship (Landau and Lifschitz, 1960) establishes the following coupling between ε' and ε'' :

$$\varepsilon'(\omega) = 1 + \frac{2}{\pi} \int_0^{\infty} \frac{\omega_0 \varepsilon''(\omega_0)}{\omega_0^2 - \omega^2} d\omega_0. \quad (18)$$

A similar relationship holds between σ' and $-\sigma''$, so that κ_{eff} at any frequency can be calculated from the dispersion of σ_{eff} in the ideal case where σ_{eff} is measured on the entire 0- ∞ frequency range. Methods have been developed to account for the frequency-range truncation implicit in laboratory measurements (Lucarini et al. 2005). We used a companion Matlab routine (publicly available from <http://www.mathworks.com/matlabcentral>) to calculate the dielectric constant κ_{eff} predicted from the σ_{eff} spectrum obtained from our simulations. Because the wide frequency band used in this work spans five frequency decades, and because such KK estimate uses data linearly and not logarithmically spaced in the frequency domain, for each numerical experiment we calculated two KK estimates of dielectric constant spectra from the simulated spectra of conductivity. A high-frequency (HF) KK dielectric spectrum was first computed for frequencies between 10 kHz and 1 GHz and interpolated every 25 kHz. As shown below, the lack of data below 1 kHz and the 25-kHz sampling interval causes this KK-derived dielectric spectrum to be invalid below the 1-MHz range. We therefore defined a second, low-frequency (LF) KK estimate of dielectric constant with lower sampling increment (2.5 kHz) to interpolate the simulated conductivities below 100 MHz assuming that the dielectric response of the composite remains constant below 10 kHz down to 10 Hz. This proxy calculation allowed the reconstruction of a consistent dielectric-constant spectrum down to the 100-kHz range and up to the MHz range. Being uniquely defined within an arbitrary constant, each of the high- and low-frequency KK reconstructions was made to honor the simulated dielectric values at a specific frequency in order to secure a unique constant in the transformation

The accuracy of our numerical simulations of effective electrical properties is therefore quantified (1) by the fit between the dielectric-constant spectrum directly simulated on each map with respect to that predicted by KK relations, and (2) by the overlap between HF and LF KK predictions. Figure 8 shows the KK results reconstructed from the effective

conductivities simulated for maps A, B and D and honored at 1 GHz for the HF KK range and at 300 kHz for the LF KK range. Results verify the accuracy criterion (1) above for all the pore maps. Criterion (2) is respected for pore maps B and D with almost perfect overlap between 1 and 60 MHz, while for map A it remains approximate with a slight shift between HF and LF KK reconstructions; nonetheless, the slopes of the reconstructed dielectric spectra correctly match those of the simulated ones. Overall, the KK relations support the accuracy and reliability of our numerical results.

5.3.4 Finite Volume Scaling

The (2D) volume considered in our pore-scale numerical model constitutes a portion of a macroscopic continuum. Unlike effective medium theories which are based on unbounded, homogeneous macroscopic media, our disc-shape numerical rock/water mixtures do not extend beyond a circular boundary. This finite geometry raises two questions with respect to the physical validity of the pore map to properly represent the behavior of binary mixtures: (1) Does the circular boundary of the pore maps affect the simulation results? (2) Is there a minimum size for the pore map to be representative of the medium? The first issue was a primary concern in the construction of the model, as the circular shape minimizes boundary fringing for homogeneous discs. Inspection confirmed that the internal fields at the boundary of the heterogeneous maps used in this paper are in the worst case only marginally affected by the vicinity of the circular rock/water disc boundary. The most noticeable case of boundary effect was encountered in homogeneous discs; even then, as discussed in Appendix A, only the few outer pixel layers of the disc were affected by the proximity of the boundary.

The issue of scaling is approached with binary map E (Figure 9), which includes the same 4x48 pixels brine ellipses and the same 1- μm resolution as discussed previously, but whose size doubles in each direction to 801x801 pixels. Figure 5 compares the simulation results for map E to those of maps A-D and to their best-fit EMA and power-law curves. Dispersions of κ_{eff} and σ_{eff} simulated for map E fit in the range determined by the 401x401-pixel-wide maps. This comparison indicates that a map size of 401x401 pixels is sufficient to capture the macroscopic geometry of such an 8%-porosity medium with inclusions smaller than 1/8th of the map diameter.

5.3.5 Impact of Clustering and Connectivity

If relative pore *geometrical arrangement* justifies the differences between the dispersions shown in Figure 4, it is remarkable that no substantial difference exists between the EM dispersions resulting from pores that tend to be regrouped (maps A and C) and those from pores that are more homogeneously distributed in space (maps B and D). To quantify a possible impact of clustering and associated pore *connectivity*, we consider pore maps with the *same* pore shapes, sizes and locations, and we enforce variable degrees of explicit connectivity between these pores. We start from map D and progressively decrease, then increase, pore connectivity to construct the maps shown in Figure 10. In map D0, we first removed the 4 connections existing between the ellipses of map D whose edges overlap and leave 4 more crossovers between other ellipses. In map D00, we also remove these crossovers so that all the ellipses are now completely different. In maps D1 to D3, we increasingly connect the brine inclusions from map D. While map D only includes 4 pairs of crossed ellipsoids out of 18 ellipses, map D1 includes 3 clusters of 4 connected ellipses each plus 2 ellipse crossovers. In map D2, a cluster of 11 interconnected ellipses is formed along with another cluster of 4 ellipses. Finally, in map D3 all the ellipses are connected except 2 at the right-hand-size medium boundary. All these modifications have marginal impact on both the total porosity and the aspect ratio of individual ellipses.

Figure 11 shows the corresponding simulated effective EM dispersions along with EMA results previously obtained for $l = 0.82$ and 0.776 . It can be noted that the spectra simulated for maps D, D0 and D00 exhibit extremely similar behavior. As soon as clustering increases in map D1, the amplitude of dielectric constant at low frequency increases from 6.3 to 9 but the conductivity remains almost identical to that of map D at 1.5 mS/m. Even close to percolation (map D2), LF conductivity doubles compared to that of maps D-D00 to 2 mS/m. On the other hand, the asymptotic dielectric constants on the intervals 10-100 kHz and 100 MHz-1 GHz remain practically identical to those of map D1, the only difference between these dispersions appears in the MHz-range where map D2 exhibits more sigmoid curvature than map D1. Maps D1 and D2 are the only maps for which the LF calculated dielectric constant is equal to the EMA prediction for $l = 0.776$. This result is quite surprising as the cases involved are those where the brine ellipses overlap into non-ellipsoidal clusters. It is only when percolation is reached in map D3 that the conductivity increases substantially

over the entire frequency range, and that the dispersion of dielectric constant reaches the maximum amplitude with $\varepsilon_{eff} = 15$ below 300 kHz. We verify in Figure 12 that the KK reconstructions of the dielectric spectra of maps D0, D1 and D3 are compatible with our simulation results. The excellent agreement between the two methods gives physical credence to our numerical simulation results and the corresponding conclusions.

5.4 DISCUSSION

5.4.1 Porosity and Scaling

More information can be gathered from higher-porosity simulations. In similar fashion to maps A-D, we generated maps F-I as 401x401-pixel random distributions of 20%-porosity pore maps including 4x48-pixel brine inclusions. For the purpose of testing the relevance of scaling at 20%-porosity, we also constructed a 801x801-pixel map with similar ellipses, map J. Figure 13 shows the corresponding pore maps F-J and Figure 14 describes the simulation results along with EMA fits. As in the 8%-porosity cases, simulation results shown in Figure 14 emphasize the different EM spectra obtained for maps F-I as well as how sigmoids capture average trends for a given porosity and host permittivity. However, Figure 14 also suggests two technical issues that did not arise with the lower porosity cases. First, EMA results for $l = 0.82$ still agree well with the simulation results for σ_{eff} in the frequency spectrum, but not for κ_{eff} below 10 MHz. Between 10 kHz and 10 MHz, the value $l = 0.875$ better fits the simulated values of κ_{eff} . The same value of l , however, does not fit the conductivity data. Thus, unlike in the 8%-porosity case, at 20% porosity it is not possible to reproduce the wide-band electrical dispersion of these 2D rock models with a single value of l and the EMA theory. This observation is in agreement with the fact that such mixing laws assume finite dilutions of impurities in hosts (i.e., brine inclusions in rock), and confirms the inaccuracy of extrapolations of mixing laws to explain the behavior of non-dilute mixtures. Despite this inconsistency of the EMA at 20%-porosity, it is remarkable that the mixing-law volumetric model of equation (16) agrees well with the simulation results at 20% porosity; the agreements is as good as the one previously obtained at 8% porosity.

A second item of discussion addresses scaling. At 8% porosity, results for 801x801-pixel maps agreed with those obtained for 401x401-pixel maps and also agreed with EMA

predictions on average. At 20% porosity, however, the results for the 801x801-pixel map J hardly fall in the range determined by the results obtained with the 401x401-pixel realizations, and the simulations could not fit EMA conductivity dispersions. Nevertheless, 801x801-pixel simulations provide a conductivity dispersion that is closer to EMA predictions than the results obtained with the 401x401 pixel maps. This suggests that, as porosity increases the representative volume of the micromodel must increase to incorporate large-scale conductivity. Such a behavior would need to be confirmed with 3-dimensional (3D) simulations where the full extent of inter-pore connections would be more accurately represented. Despite this scale inaccuracy, it is remarkable that KK relations do confirm the consistency and reliability of the simulation results shown in Figure 15.

Del Río and Whitaker (2000a, 2000b) consider the coupled electric/magnetic fields averaging on both a local length scale (where most variations take place) and a macroscopic length scale dictated by the long-distance interactions between the composite elements. The parallel with our simulation results is remarkable and allows us to probe the range of those length scales. At 8% porosity, the consistency of the results obtained for 401x401 and 801x801-pixel pore maps suggests that a length scale of 401 pixels (8 times the elliptic pore size) is sufficient to capture both local and microscopic effects. At 20% porosity, however, it seems that a length scale of 801 pixels (16 times the pore size) is not yet sufficient. This question requires more work specifically directed toward studying the interaction between inclusion density, inclusion size, and the appropriate length scale that define a *homogeneous* composite.

5.4.2 Pore Connectivity

The effect of pore connectivity on dielectric dispersion confirmed at 8% porosity is quite striking: unlike what Lysne's (1983) model suggests, the inclusion shape distribution will not be the only parameters in the EM wide-band response of the medium. Instead, the degree of connectivity of these shapes, more than their arrangement, is the primary effect on dielectric dispersion. The difference obtained between the dielectric spectra simulated for maps D1 and D2 is also remarkable and suggests that near-percolation is a condition to reach single-inflection sigmoid shapes for the frequency-dispersion of dielectric constant. Comparison to other curves shown in Figure 11 supports this argument, as all the dielectric

spectra of non-percolating maps exhibit several inflection points in the 1-10 MHz range. By contrast, dielectric dispersions simulated for the 20% porosity maps F-J (Figure 14) essentially exhibit one inflection point, which could be associated with the fact these maps nearly percolate. However, given the scaling issue at higher porosities, more modeling effort is needed to establish conclusive relationships between unicity of the dielectric spectrum inflection and connectivity of the pores. The objective of such 3D simulations should be to quantify a possible relationship between the dielectric spectrum shape and large-scale pore connectivity, i.e., macroscopic hydraulic permeability in a rock sample.

5.4.3 Generalization

An approach similar to the homogeneous-cylinder method described in this paper could be used to estimate effective anisotropic tensorial electrical properties of the pore map. To that end, one could use semi-analytical scattering closed-form models for homogeneous anisotropic cylinders (Monzon and Damaskos, 1986; Wu and Yasumoto, 1997) and invert the values of electric fields and currents as effective conductivity tensor and effective permittivity tensor for the pore map in equation (6).

The 2D assumption for the rock models considered in this paper allowed us to simulate frequency-dispersion curves with relatively modest computer resources. Specifically, the FFT-MoM method allowed us to simulate frequency dispersion of 2D pore maps as large as 1 megapixel in a desktop workstation, while 3D computer simulations require larger resources not currently available to us. We chose to study TM polarization to probe the electric and dielectric contrasts within the 2D medium; however, we point out the 3D response of disordered composites will be formed by unknown combinations of both TM and TE (transversal-electric) polarization responses. Three-dimensional simulations can be performed based on the concepts presented in this paper using the closed-form field solution for homogeneous isotropic or anisotropic cylinders, and the minimization of the cost function Ψ_3 in equation (13) on the entire simulation volume instead of the cross-section of the 2D model. These 3D simulations will provide accurate estimation of LF effective properties and will quantify cross-polarization effects in 3D pore geometries.

5.5 CONCLUSIONS

This paper introduced a new method to quantify the influence of pore and grain geometry on the kHz-GHz electromagnetic response of saturated rocks. In so doing, we calculate wide-band dispersion curves of effective electrical conductivity and dielectric constant for *explicit* arbitrary rock model geometries. Unlike existing numerical methods based on reflection/transmission coefficients calculations at the medium boundary, our method remains valid on the entire kHz-GHz frequency range and is verified to honor the Kramers-Kronig relations.

We showed that effective medium theories only describe the average wide-band polarization of rocks for given porosities and pore eccentricities. In general, the wide-band electrical behavior of each rock departs from an average sigmoid curve by a factor of 2 for relatively low values of pore eccentricity (12 in our simulations), depending on pore clustering and connectivity. Although usually neglected by existing dielectric mixing laws, clustering and connectivity are demonstrated to have a significant impact on wide-band EM dispersions.

Scaling is a major issue for the pore-scale modeling of *homogeneous* properties such as conductivity and dielectric constant at all frequencies. Our work suggests a relationship between single-inflection of the dielectric spectrum and brine percolation across the model rock, however larger-scale simulations in 2 and 3 dimensions are needed to establish quantitative relationships between dielectric spectrum modes, large-scale pore connectivity, and presence of isolated pore structures in the rock skeleton.

5.6 ACKNOWLEDGEMENTS

We are thankful to Nicola Bona (ENI) and Tarek Habashy (Schlumberger-Doll Research) for stimulating discussions. Our gratitude goes to two anonymous reviewers for their constructive technical and editorial feedback. Funding for this work was provided by (a) the American Chemical Society through grant no. PRF 37519-AC9, (b) the US Department of Energy through contract no. DE-FC26-04NT15518, and (c) UT Austin's Research Consortium on Formation Evaluation, jointly sponsored by BP, Baker Atlas, Chevron, ConocoPhillips, ENI E&P, ExxonMobil, Halliburton Energy Services, Mexican Institute for

Petroleum, Occidental Oil and Gas Corporation, Marathon Oil, Petrobras, Precision Energy Services, Schlumberger, Shell International E&P, Statoil, and Total.

5.7 APPENDIX A: ACCURACY OF THE NUMERICAL SOLUTION OF THE ELECTRIC FIELD INTEGRAL EQUATION WITH A 2D FFT-MOM METHOD

We consider a homogeneous disc-shaped scatterer and analyze the numerical error between internal electric fields calculated with 2D FFT-MoM, and internal fields calculated analytically with a cylindrical expansion. The numerical approach discretizes the disc on a grid of 401x401 pixels, i.e. the disc has a radius equal to 200 pixels. We vary the frequency logarithmically from 10 kHz to 1 GHz. Electrical parameters used for this comparison are as follows: $\sigma_w = 1$ S/m, $\kappa_w = 70$, $\sigma_{disc} = 0.01$ S/m, and $\kappa_{disc} = 20$. The diameter of the disc is only 401 μm , which makes the analytical value for the internal electric field constant over the entire disc surface. In what follows, the projections of the numerical error for each pixel i are defined as:

$$error_{x,z}^i = \frac{E_{x,z}^i - E_{x,z}^a}{E_{x,z}^a}, \quad (\text{A-10})$$

where $E_{x,z}^i$ are the Cartesian projections of the internal electric field calculated for pixel i , and $E_{x,z}^a$ are the projections of the analytical internal electric field calculated close to the disc center. Figure A-1 describes the results obtained from this analysis. For all the tested frequencies, the top panels show that the numerical error within the disc lies within 10^{-2} or 1% of the analytical solution. The periphery of the white circle (zones of maximal error) illustrates the increasing importance of fringing effects for decreasing values of frequency. We employ two norms, the infinity norm L_{inf} (maximal relative error amplitude) and the L_l norm (mean relative error amplitude) to measure the overall numerical error achieved at each frequency. The bottom panel of Figure A-2 shows the results obtained by computing the errors over the complete or part of the scatterer body. A disc radius of 200 pixels stands for the entire disc discretized on the 401x401 pixel grid, whereas smaller concentric discs ignore the outmost pixels of the scattering disc where fringing occurs. The L_l norm yields less than 1% error at all frequencies regardless of fringing effects. On the other hand, the L_{inf} norm

achieves a similar accuracy when computed over the central 180-pixel disc, but it shows the degradation of field homogeneity at the disc edge when it is computed for larger radii.

5.8 APPENDIX B: PRACTICAL IMPLEMENTATION OF THE MINIMIZATION PROBLEM

Numerical experiments indicate that the estimated values of effective electric conductivity and dielectric constant obtained from the minimization of the cost function defined by equation (12) are not always consistent with the expected asymptotic behavior at low and high frequencies. To circumvent this problem, we first define the electrical field and electric-current residuals as

$$\Delta \mathbf{E} = \mathbf{E} - \mathbf{E}_h, \text{ and} \quad (\text{B-1})$$

$$\Delta \mathbf{J} = \bar{\sigma}^* \mathbf{E} - \bar{\sigma}_h^* \mathbf{E}_h, \quad (\text{B-2})$$

respectively. Moreover, we note that, according to Schwartz' inequality,

$$\Psi = \left\| \Delta \mathbf{J} - \bar{\sigma}_b^* \Delta \mathbf{E} \right\|_{L_2} \leq \left\| \Delta \mathbf{J} \right\|_{L_2} + \left| \bar{\sigma}_b^* \right| \times \left\| \Delta \mathbf{E} \right\|_{L_2}. \quad (\text{B-3})$$

We now compare the performance of three choices of cost function when inverting the conductivity and dielectric constant of a homogeneous disc-shaped pore map. These cost functions are defined as:

$$\Psi_1 = \left\| \Delta \mathbf{J} - \bar{\sigma}_b^* \Delta \mathbf{E} \right\|_{L_2}, \quad (\text{B-4})$$

$$\Psi_2 = \left\| \text{Re} \left(\Delta \mathbf{J} - \bar{\sigma}_b^* \Delta \mathbf{E} \right) \right\|_{L_2} + \left\| \text{Im} \left(\Delta \mathbf{J} - \bar{\sigma}_b^* \Delta \mathbf{E} \right) \right\|_{L_2}, \text{ and} \quad (\text{B-5})$$

$$\Psi_3 = \left\| \Delta \mathbf{J} \right\|_{L_2} + \left| \bar{\sigma}_b^* \right| \times \left\| \Delta \mathbf{E} \right\|_{L_2}. \quad (\text{B-6})$$

To assess the performance of the three cost functions defined above, we consider combinations of three values of conductivity σ_{disc} (0.001, 0.01 and 0.1 S/m) and three values of dielectric constant κ_{disc} (20, 200 and 2000) assigned to homogeneous disc-shaped pore map. We compute the internal electric fields for frequencies ranging from 1 kHz to 1 GHz, and use the three cost functions described by equations (B-4) to (B-6) to invert the effective properties σ_{eff} and κ_{eff} starting from the same forward simulation results. In all cases, the

background brine consists of 1 S/m conductivity and a dielectric constant equal to 70. Results from this exercise are shown in Figure B-1.

When σ_{disc} is at least equal to 0.1 S/m, both σ_{eff} and κ_{eff} are properly estimated with the three cost functions – with slightly better results for the case of cost function Ψ_3 compared to Ψ_1 and Ψ_2 . Incorrect results are obtained when κ_{disc} is as large as 2000 above 3 MHz – fortunately this case is not realistic in saturated rocks. When σ_{disc} is lower than 0.1 S/m, Ψ_1 overestimates κ_{eff} at low frequencies and systematically yields wrong (even negative) values for σ_{eff} . Cost function Ψ_2 yields relatively better results, always leads to the right values of κ_{eff} , but the inverted values σ_{eff} are as inconsistent as those obtained with Ψ_1 . Cost function Ψ_3 yields the most accurate and stable results in all the cases. As indicated in Figure B-1, bounds exist beyond which κ_{eff} and/or σ_{eff} are not properly inverted with cost function Ψ_3 .

For realistic cases of rock/fluid mixtures, it can be conservatively stated that the dielectric constant is never higher than 50 above 1 MHz. In this case, we expect the minimization algorithm to converge for conductivities above 0.01 S/m and for frequencies as high as 1 GHz. Similarly, we expect the minimization algorithm to converge for conductivities above 0.001 S/m and for frequencies as high as 10 MHz.

In the presence of low-frequency enhancement due to clays or other electrochemical factors, the dielectric constant might take on a value of several thousands below 1 MHz. In this case, both dielectric constant and conductivity will be correctly inverted for conductivity values as low as 0.01 S/m.

5.9 REFERENCES

1. Avdeev, D.B., A.V. Kuvshinov, O.V. Pankratov, and G.A. Newman, 2002, Three-dimensional induction logging problems, Part 1: An integral equation solution and model comparisons: *Geophysics*, **67**, 413-426.
2. Balanis, C., 1989, *Advanced Engineering Electromagnetics*: John Wiley & Sons, 608-610 and 666–667.

3. Bona, N., E. Rossi, C. Venturini, S. Cappaccioli, M. Lucchesi, and P. Rolla, 1998, Characterization of rock wettability through dielectric measurements: *Revue de l'Institut Français du Pétrole*, **53**, 771–783.
4. Bona, N., A. Orteni, and S. Capaccioli, 2002, Advances in understanding the relationship between rock wettability and high-frequency dielectric response: *Journal of Petroleum Science and Engineering*, **33**, 87–99.
5. Catedra, M.F., R.P. Torres, J. Basterrechea, J., and E. Gago, 1995, *The CG-FFT method: Application of signal processing techniques to electromagnetics*: Artech House.
6. Choy, T. C., 1999, *Effective Medium Properties, Principles and Applications*: Oxford University Press.
7. del Río, J.A. and S. Whitaker, 2000a, Maxwell's equations in two-phase systems I: local electrodynamic equilibrium: *Transport in porous media*, **39**, 159-186.
8. del Río, J.A. and S. Whitaker, 2000b, Maxwell's equations in two-phase systems II: two-equations model: *Transport in porous media*, **39**, 259-287.
9. Díaz, R.E., W.M. Merrill, and N.G. Alexopoulos, 1998, Analytic framework for the modeling of effective media: *Journal of Applied Physics*, **84**, 6815-6826.
10. Feng, S., and P.N. Sen, 1985, Geometrical model of conductive and dielectric properties of partially saturated rocks: *Geophysics*, **58**, 3236–3243.
11. Gao, G., C. Torres-Verdín, and T. Habashy, 2005, Analytical techniques to evaluate the integrals of 3D and 2D spatial dyadic Green's functions: *Progress in Electromagnetics Research (PIER)*, **52**, 47–80.
12. Kenyon, W.E., 1984, Texture effects on megahertz dielectric properties of calcite rock samples: *Journal of Applied Physics*, **55**, 3153–3159.
13. Landau, L.D., and E.M. Lifshitz, 1960, *Electrodynamics of continuous media*: Pergamon Press.
14. Lima, O.A.L., and M.M. Sharma, 1992, A general Maxwell-Wagner theory for membrane polarization in shaly sands: *Geophysics*, **57**, 431–440.

15. Lucarini, V., J.J. Saarinen, K.-E. Peiponen, and E.M. Vartiainen, 2005, *Kramers-Kronig Relations in Optical Materials Research*: Springer.
16. Lysne, P.C., 1983, A model for the high-frequency electrical response of wet rocks: *Geophysics*, **48**, 775–786.
17. Mendelson, K.S., and M.H. Cohen, 1982, The effect of grain anisotropy on the electrical properties of sedimentary rock: *Geophysics*, **47**, 257–263.
18. Monzon, J.C., and N.J. Damaskos, 1986, Two-dimensional scattering by a homogeneous anisotropic rod: *IEEE Transactions on Antennas and Propagation*, **AP-34**, 1243–1249.
19. Pekonen, O., K. Kärkkäinen, A. Sihvola, and K. Nikoskinen, 1999, Numerical testing of dielectric mixing rules by FDTD method: *Journal of Electromagnetic Waves and Applications*, **13**, 67–88.
20. Sen, P.N., 1984, Grain shape effects on dielectric and electrical properties of rocks: *Geophysics*, **49**, 586–587.
21. Sen, P.N., C. Scala, and M. Cohen, 1981, A self-similar model for sedimentary rocks with application to the dielectric of fused glass beads: *Geophysics*, **46**, 781–795.
22. Seleznev, N.V., T.M. Habashy, S.M. Luthi, G.P. Eberli, and A.J. Boyd, 2005, Dielectric properties of partially saturated carbonate rocks: submitted for publication.
23. Sihvola, A., 2002, (Ed.), *Electromagnetic Mixing Formulae and Applications*: IEE Electromagnetic Waves Series no. 47.
24. Sihvola, A., 2005, Metamaterials and depolarization factors: *Progress in Electromagnetics Research (PIER)*, **51**, 65–82.
25. Sillars, R.W., 1937, The properties of dielectrics containing semi-conducting particle of various shapes: *Journal of Institution of Electrical Engineers*, **80**, 378–394.
26. Stroud, D., G.W. Milton, and B.R. De, 1986, Analytical model for the dielectric response of brine-saturated rocks: *Physical Review B*, **34**, 5145–5153.
27. Wang, J., 1991, *Generalized moment methods in electromagnetics: formulation and computer solution of integral equations*: John Wiley & Sons.

28. Wu, X.B., and K. Yasumoto, 1997, Three-dimensional scattering by an infinite homogeneous anisotropic circular cylinder: an analytical solution: *Journal of Applied Physics*, **82**, 1996–2003.

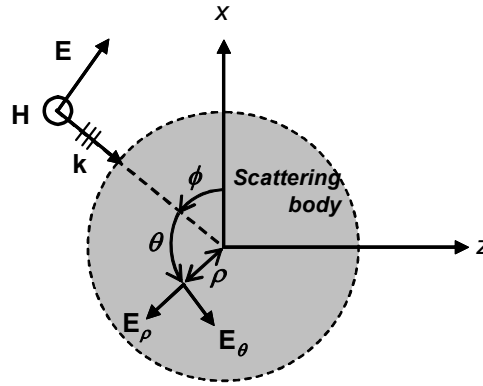


Figure 1 Description of the model geometry: incident transverse-magnetic (TM) polarized plane wave illuminating the 2-D scattering medium at an angle ϕ with respect to the x axis. \mathbf{E} : incident electric field; \mathbf{H} : incident magnetic field; \mathbf{k} : wave (propagation) vector. (ρ, θ) are the polar coordinates of a point within the scatterer, with respect to the incident plane wave and the scatterer center, and (E_ρ, E_θ) are the polar projections of the electrical field vector at that point.

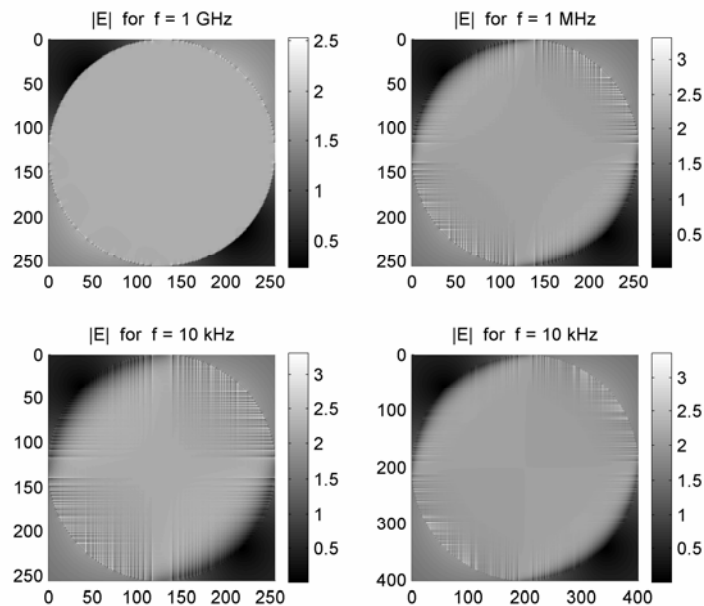


Figure 2 Illustration of the impact of frequency and map resolution on the boundary fringing distorting the internal electric fields computed within a resistive homogeneous disc. All maps include 255x255 pixel resolution except for that of the bottom right panel (401x401 pixel resolution). Electric excitation is in the form of an incident TM wave illuminating the disc in a top-right, bottom-left direction.

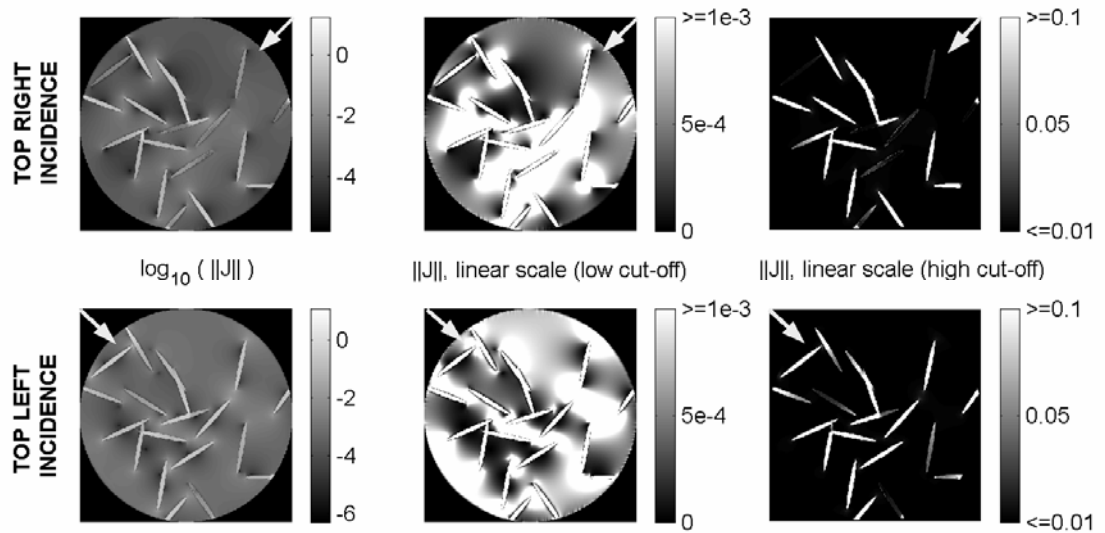


Figure 3 Graphical description of internal current amplitudes within pore map B (Figure 4) at 100 MHz for two perpendicular angles of incidence and at different scales. The arrows indicate the directions of plane-wave incidence.

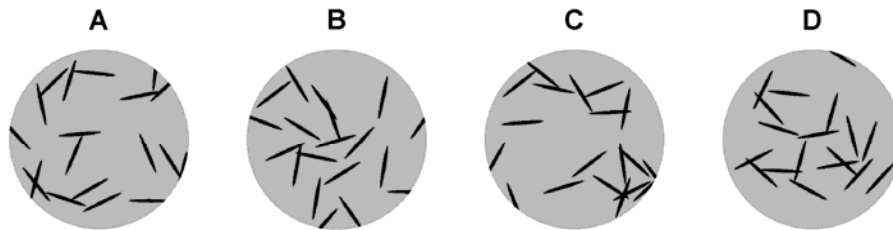


Figure 4 Pore maps exhibiting 8% porosity and measuring 401x401 pixels. The brine inclusions consist of 4x48 pixels water ellipses (black) embedded in rock host (gray).

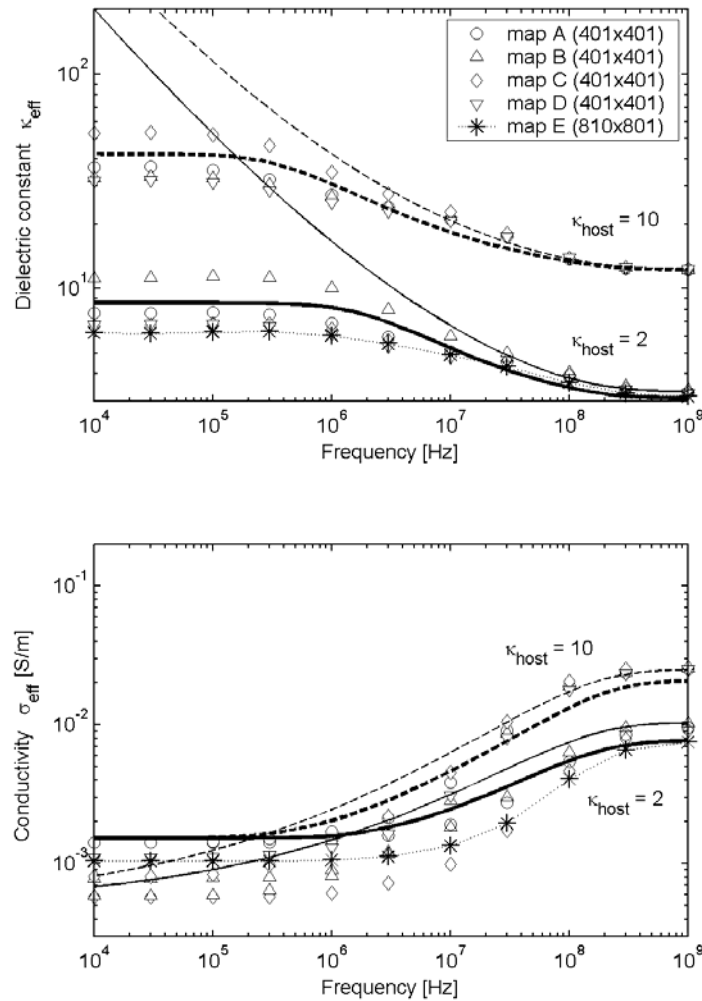


Figure 5 Frequency dispersions of effective dielectric constant (top panel) and electrical conductivity (bottom panel) for pore maps A to E. Simulation results are identified with markers for $\kappa_{\text{host}} = 2$ and 10 (only 2 for map E). Corresponding mixing-law results are identified with plain curves for $\kappa_{\text{host}} = 2$ and dashed curves for $\kappa_{\text{host}} = 10$. Thick curves identify the EMA results from equation (14) that best fit all the dielectric and conductivity dispersions simultaneously (for $l = 0.82$), while thin curves identify the power-law results from equation (16).

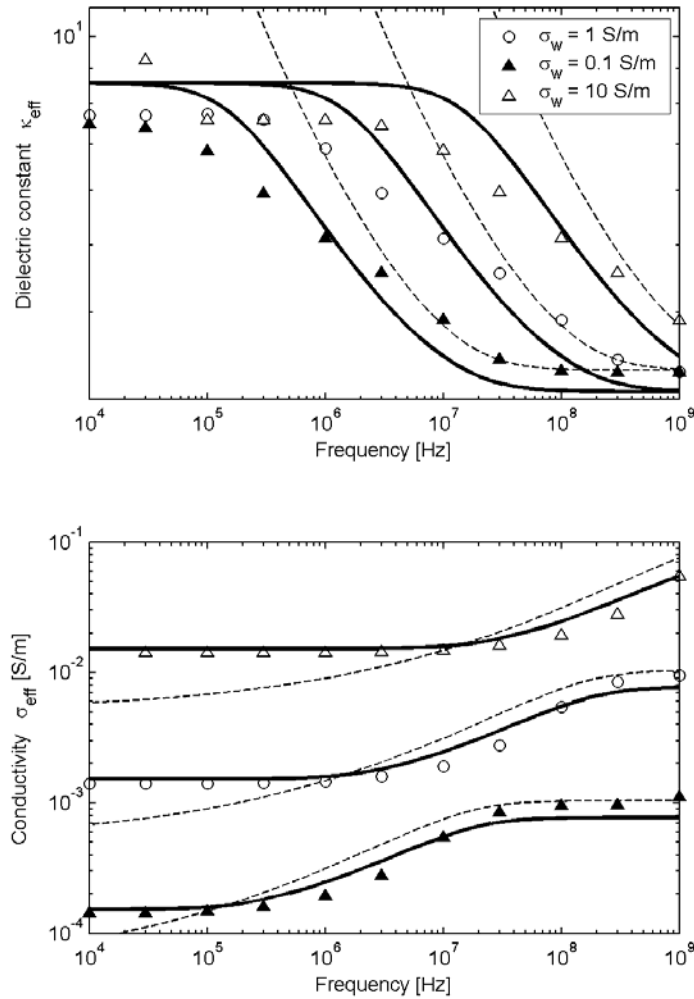


Figure 6 Frequency dispersions of effective dielectric constant (top panel) and electrical conductivity (bottom panel) for pore map A with $\kappa_{\text{host}} = 2$ and three magnitudes of water conductivity σ_w . Markers identify simulation results (starting with the ones previously plotted in Figure 5 for $\sigma_w = 1$ S/m); plain thick curves, EMA results from equation (14) with $l = 0.82$; and dashed curves, power-law results from equation (16).

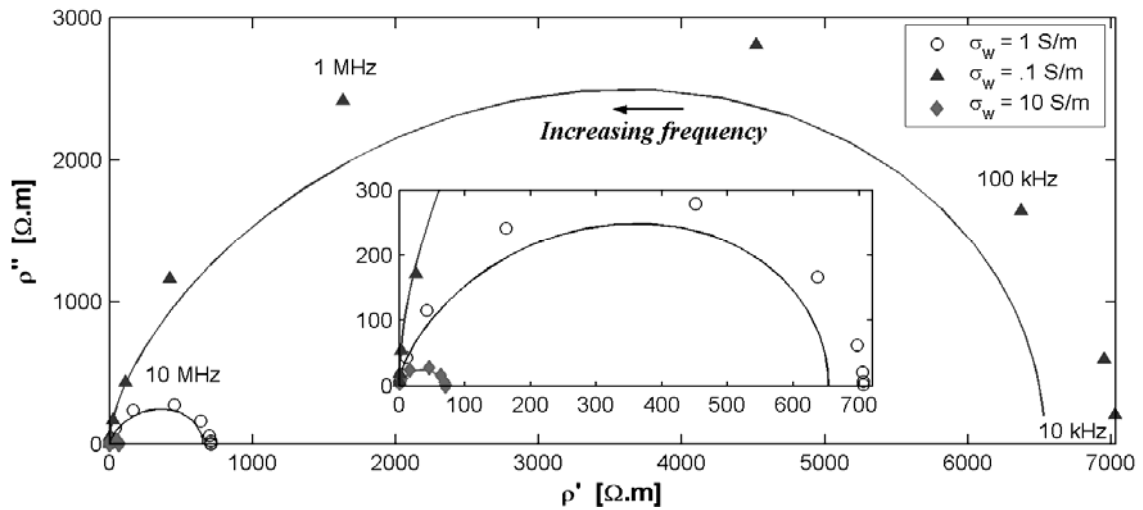


Figure 7 Argand plot of the simulation results described in Figure 6 (markers) together with the corresponding EMA results (plain curves). The insert enlarges the scale of the main plot for values of ρ' smaller than 700 $\Omega.m$.

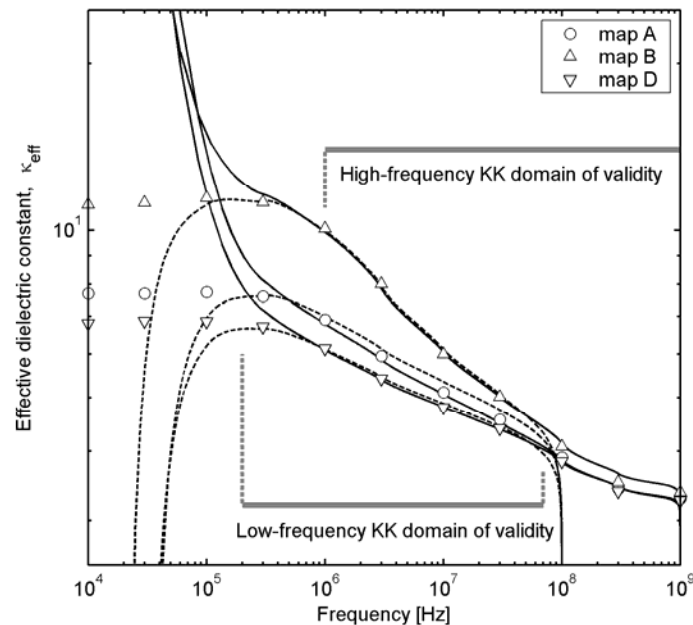


Figure 8 Comparison between the dielectric dispersions simulated for maps A, B and D in Figure 6, and the Kramers-Kronig LF and HF predictions reconstructed from the simulated conductivity dispersions. Specific additive constants for the KK reconstructions are defined at 300 kHz in the LF regime (dashed curves) and at 1 GHz in the HF regime (plain curves).

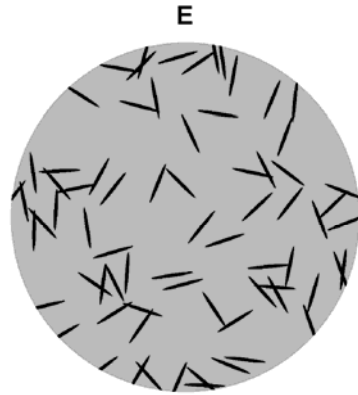


Figure 9 Pore map exhibiting 8% porosity constructed with 801x801 pixels. The brine inclusions consist of 4x48 pixels water ellipses (black) embedded in rock host (gray) in consistency with all other pore maps described in this paper.

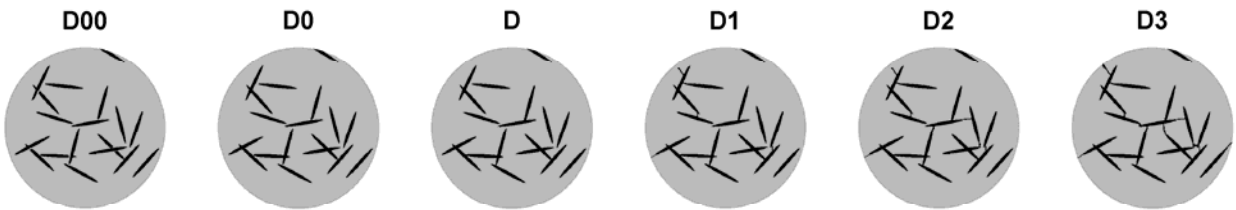


Figure 10 Pore maps modified after map D and exhibiting increasing connectivity between brine pores. Brine inclusions (black pixels) are embedded in the rock host (gray pixels).

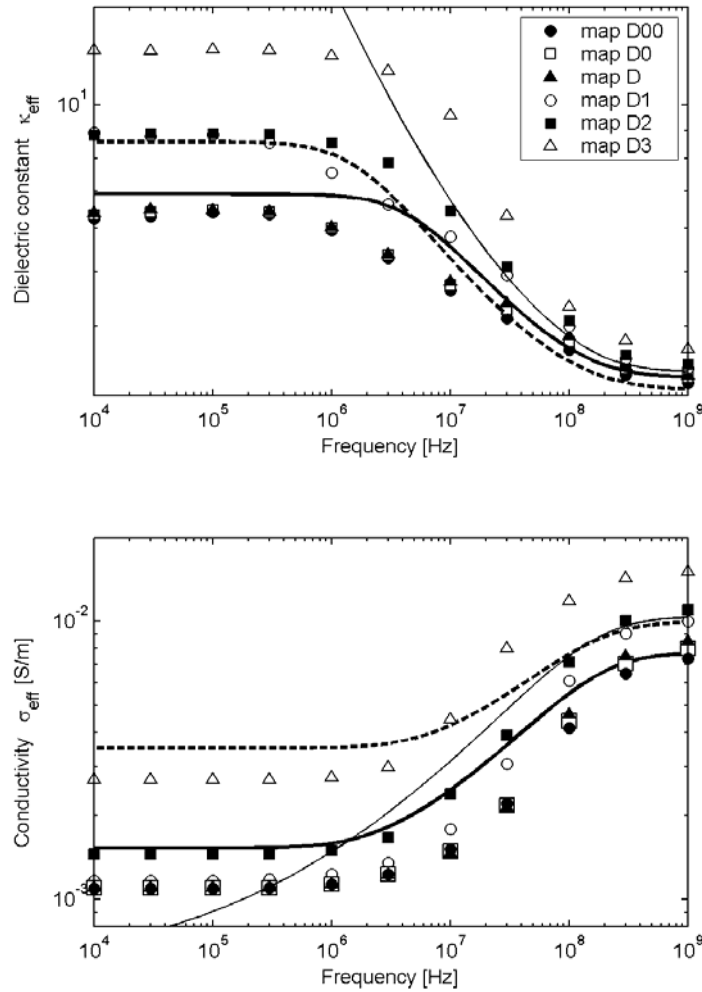


Figure 11 Frequency dispersions of effective dielectric constant (top panel) and electrical conductivity (bottom panel) for pore maps D00 to D3. Simulation results are identified with markers for $\kappa_{\text{lost}} = 2$. Thick curves identify the EMA results from equation (14) for $l = 0.82$ (plain curves) and $l = 0.776$ (dashed curves). Plain curves describe power-law results obtained from equation (16).

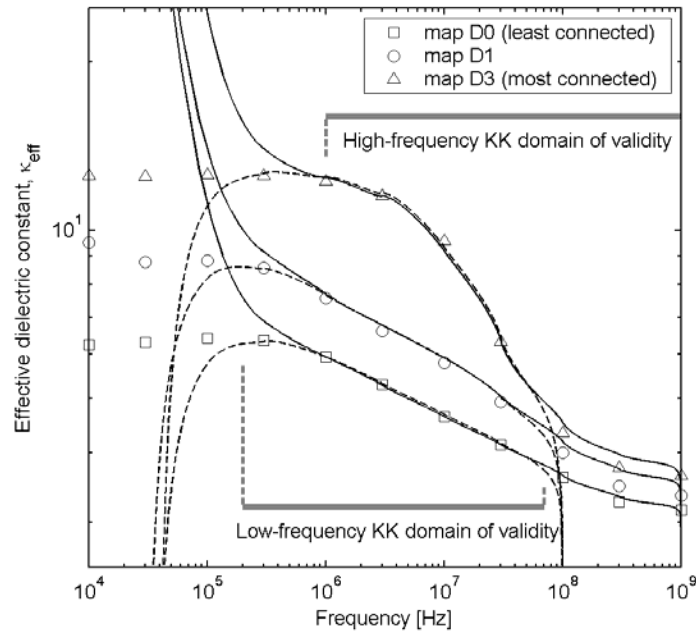


Figure 12 Comparison between the dielectric dispersions simulated for maps D0, D1 and D3 in Figure 11, and their Kramers-Kronig LF and HF predictions reconstructed from the simulated conductivity dispersions. Additive constants for the KK reconstructions are defined at 300 kHz in the LF regime (dashed curves) and at 1 GHz in the HF regime (plain curves).

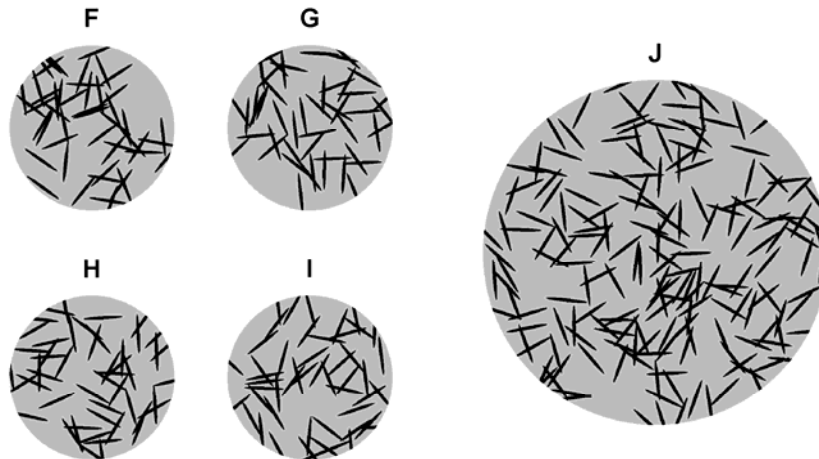


Figure 13 Pore maps exhibiting 20% porosity constructed with 401x401 pixels (F-I) and 801x801 pixels (J). Brine inclusions consist of 4x48 pixels water ellipses (black) embedded in rock host (gray) in consistency with all other pore maps described in this paper.

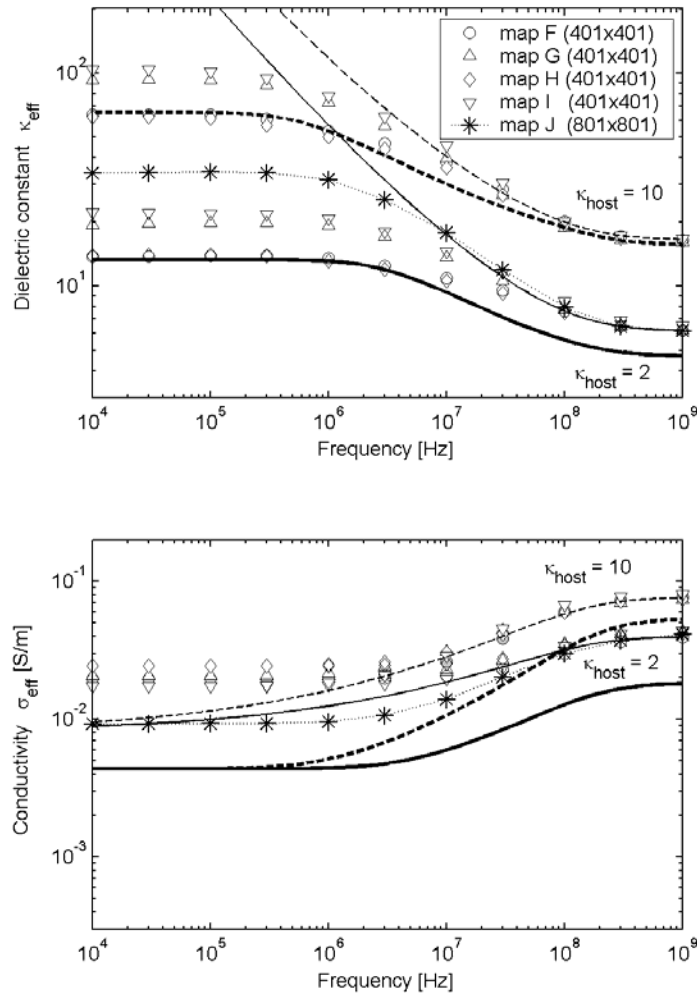


Figure 14 Frequency dispersion of effective dielectric constant (top panel) and electrical conductivity (bottom panel) for pore maps F to J. Simulation results are identified with markers for $\kappa_{\text{host}} = 2$ and 10 (only 2 for map J). Corresponding mixing-law results are represented with plain curves for $\kappa_{\text{host}} = 2$ and dashed curves for $\kappa_{\text{host}} = 10$. Thick curves identify the EMA results from equation (14) that best fit both dielectric dispersions simultaneously (for $l = 0.875$), while thin curves identify the power-law results from equation (16).

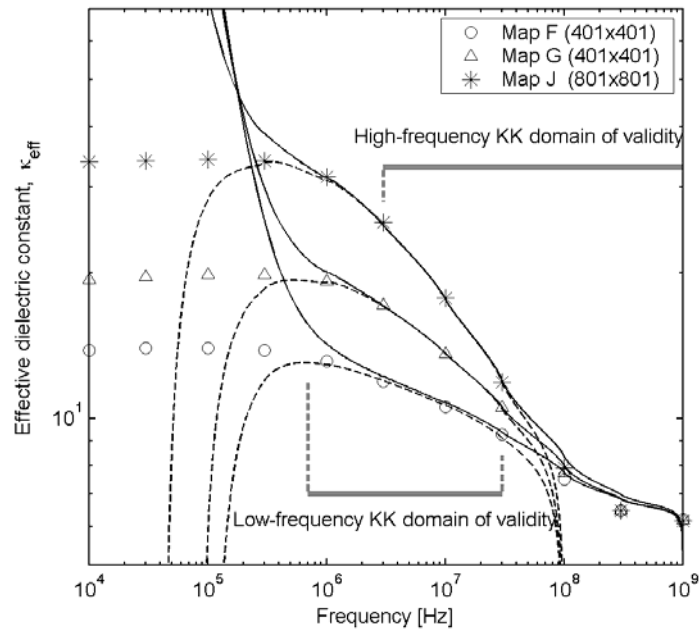


Figure 15 Comparison between the dielectric dispersions simulated for maps F, G and J in Figure 14, and the Kramers-Kronig LF and HF predictions reconstructed from the simulated conductivity dispersions. Anchors for the KK reconstructions are defined at 1 MHz in the LF regime (dashed curves) and at 1 GHz in the HF regime (plain curves).

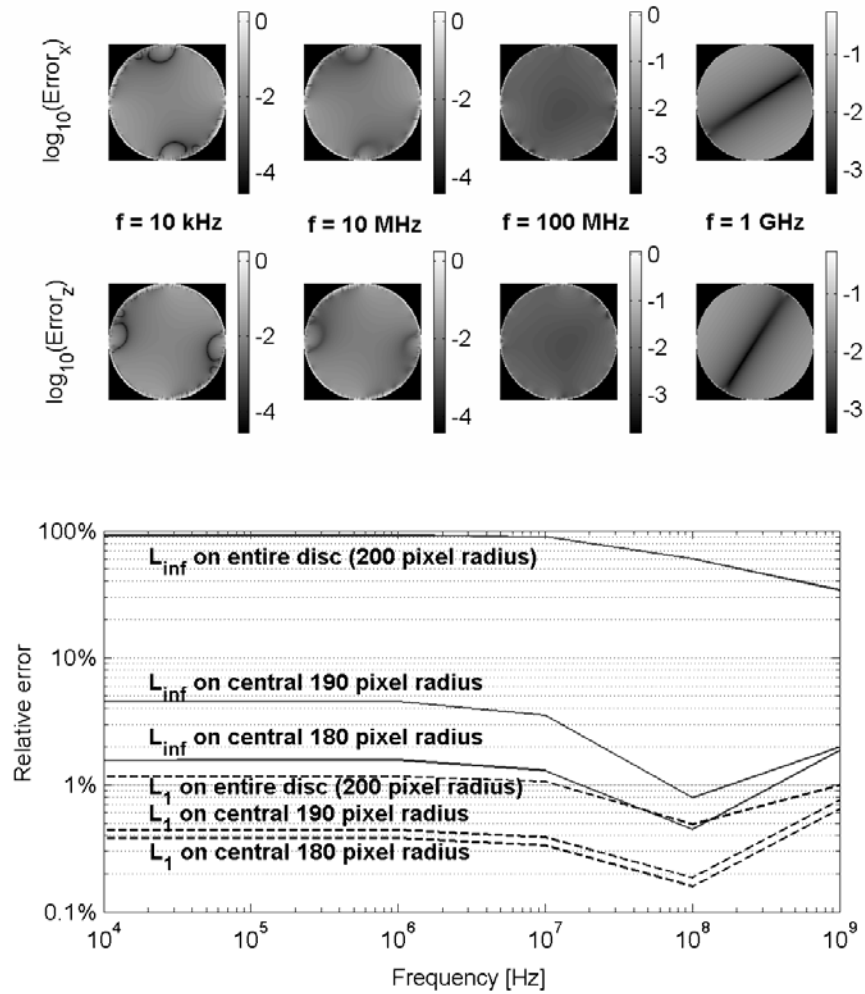


Figure A-1 Analysis of 2D FFT-MoM numerical error for the internal electric fields within a homogeneous cylinder of 401x401 pixel resolution. Top panels: distribution of the error for both x and z projections at several frequencies. Bottom panel: L_{inf} and L_1 norms of the relative error computed as a function of frequency for decreasing values of disc radius within the scatterer.

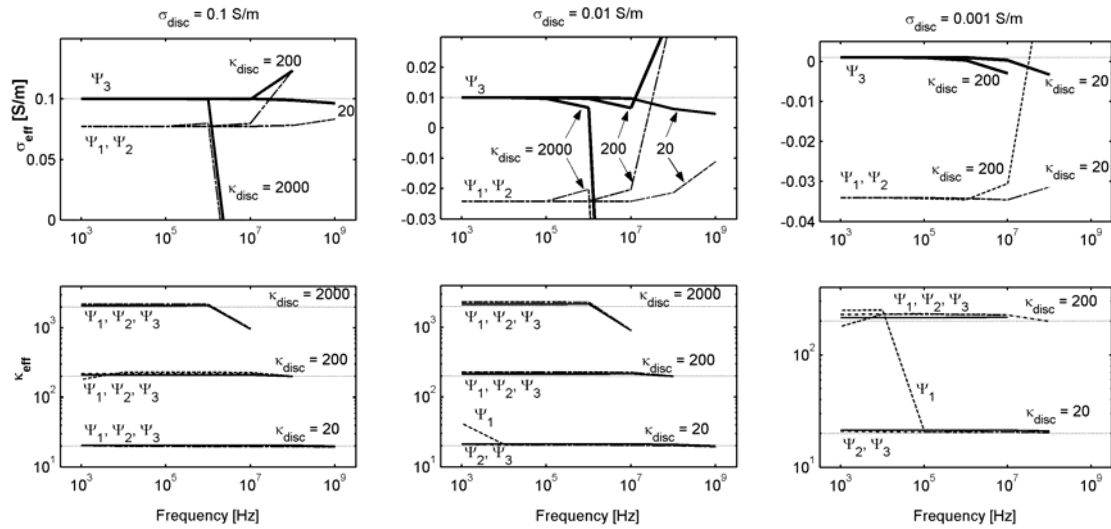


Figure B-1 Inversion results for a 501x501 pixels homogeneous disc for different combinations of effective conductivity σ_{disc} and dielectric constant κ_{disc} , with different cost functions. Dash-dotted lines: using cost function Ψ_1 ; dashed lines: Ψ_2 ; plain lines: Ψ_3 . Dotted lines indicate the true values for σ_{disc} and κ_{disc} .

CHAPTER 6. IMPROVING PETROPHYSICAL INTERPRETATION WITH WIDE-BAND ELECTROMAGNETIC MEASUREMENTS

Due to their sensitivity to ionic content and surface texture, wide-band electromagnetic (WBEM) measurements of saturated rocks exhibit frequency dispersions of electrical conductivity and dielectric constant that are influenced by a variety of petrophysical properties. Factors as diverse as fluid saturation, porosity, pore morphology, thin wetting films, and electrically charged clays affect the WBEM response of rocks. Traditional dielectric mixing laws fail to quantitatively and *practically* integrate these factors to quantify petrophysical information from WBEM measurements. This chapter advances a numerical proof of concept for useful petrophysical WBEM measurements. A comprehensive pore-scale numerical framework is introduced that incorporates explicit geometrical distributions of grains, fluids and clays constructed from core pictures, and that reproduces the WBEM saturated-rock response on the entire kHz-GHz frequency range. WBEM measurements are verified to be primarily sensitive (a) in the kHz range to clay amounts and wettability, (b) in the MHz range to pore morphology (i.e., connectivity and eccentricity), fluid distribution, salinity, and clay presence, and (c) in the GHz range to porosity, pore morphology and fluid saturation. Our simulations emphasize the need to measure dielectric dispersion in the entire frequency spectrum to capture the complexity of the different polarization effects. In particular, it is crucial to accurately quantify the phenomena occurring in the MHz range where pore connectivity effects are confounded with clay polarization and pore/grain shape effects usually considered in dielectric phenomena. These different sensitivities suggest a strong complementarity between WBEM and NMR measurements for improved assessments of pore size distribution, hydraulic permeability, wettability, and fluid saturation.

6.1 INTRODUCTION

A number of experimental and theoretical studies suggest the measurable sensitivity of WBEM to various petrophysical factors, including porosity, brine salinity, fluid saturation and wettability, clay content, surface roughness, and even pore surface-to-volume ratio.

Given the complexity of the different phenomena under consideration, practical models are designed to fit measured dielectric dispersions to ad-hoc models whose parameters are marginally supported by quantitative petrophysical concepts.

Therefore, to assess whether accurate and reliable petrophysical interpretations are possible with WBEM measurements requires an analysis that (a) incorporates pore structure, pore connectivity, multiphase saturation and electrochemical effects, and (b) quantifies the contributions of each factor in the measured WBEM dispersions. However, extracting explicit petrophysical information from WBEM responses is a difficult task. Myers (1991), for instance, illustrated the non-uniqueness of WBEM measurements when a decrease of either water saturation, porosity, or brine salinity yielded similar responses. Recent advances in NMR logging and interpretation (Freedman et al., 2004) can eliminate some of these ambiguities with adequate experimental conditions, and if rock wettability is known. Conversely, WBEM measurements could provide independent wettability assessment in the cases where NMR measurements alone reach their limits of sensitivity (for instance, the impact of fluid saturation history on wettability determination was studied by Toumelin *et al.*, 2006). Likewise, the interpretation of NMR measurements can be biased by unaccounted rock morphology (Ramakrishnan *et al.*, 1999) or by internal magnetic fields in shaly or iron-rich sands (Zhang *et al.*, 2003), whereas WBEM measurements provide independent information on overall rock overall morphology. It is therefore timely to consider integrating both technologies for improving petrophysical analysis.

The objectives of this paper are twofold: (1) Review existing results on the extraction of petrophysical information from rock WBEM measurements. (2) Establish a proof-of-concept for the necessity to integrate electromagnetic measurements on the wide frequency band from the kHz range to the GHz range, and study how WBEM techniques may yield petrophysical information unavailable from other in-situ measurements. To reach the second objective, we introduce a generalized pore-scale simulation framework that allows incorporating arbitrary rock morphology and multiphase fluid distribution.

6.2 REVIEW OF WIDE-BAND ELECTROMAGNETIC BEHAVIOR OF SATURATED ROCKS

6.2.1 Origins of Wide-Band Dispersion

As summarized by Sen and Chew (1983), two main phenomena influence the dispersion of conductivity and dielectric permittivity in saturated rocks at frequencies in the kHz-GHz range. The first effect is due to the Maxwell-Wagner polarization in the MHz range, where various pore-geometrical effects create sigmoid-type dispersions of conductivity and dielectric constant reviewed by Toumelin and Torres-Verdín (2007). The Maxwell-Wagner effect arises in the presence of bimodal lossy and dielectric compounds (such as brine/rock systems) where no surface zeta potentials (such as those encountered at clay surfaces) are present. Ions concentrate along the edges of elongated pores and create local capacitors in the pore structure whose effective capacitance and conductivity is frequency dependent. Such a behavior solely depends on structural aspect ratios regardless of size.

The second main electromagnetic phenomenon appearing in rocks consists of substantial enhancements of the dielectric constant as frequency decreases below the MHz range. In the early 1980s, when WBEM studies for petrophysical applications were in vogue, this low-frequency enhancement was regarded as measurement noise and spurious electrode polarization effects. Subsequent quantification of electrode polarization exhibited strong negative power laws of dielectric constant at kHz-range frequencies. This power-law effect has no apparent connection with Maxwell-Wagner polarization and is due to presence of static electric charges at the interface between rocks (in particularly clay minerals) and brine. The next sections of this paper review several models proposed to quantify these electrochemical effect, although none of them entirely captures the complexity of the phenomenon.

To understand the origin of low-frequency enhancement of the measured dielectric constant, let us recall fundamental postulates of electromagnetism: when an electric field E of radian frequency ω illuminates a lossy material of conductivity $\sigma^*(\omega)$ and dielectric

permittivity $\varepsilon^*(\omega)$, it generates a current density $\mathbf{J} = \sigma^* \mathbf{E}$ and an electric displacement field $\mathbf{D} = \varepsilon^* \mathbf{E}$ through that material. In general, both σ^* and ε^* are complex numbers and can be written in terms of their real and imaginary parts as $\sigma^* = \sigma' - i\sigma''$ and $\varepsilon^* = \varepsilon' + i\varepsilon''$, where $i^2 = -1$ (the minus sign in σ^* is consistent with the expressions that follow). As in the case of any causal physical mechanism, ε' and ε'' are coupled through the Kramers-Kronig relationship (Landau and Lifschitz, 1960):

$$\varepsilon'(\omega) = 1 + \frac{2}{\pi} \int_0^{\infty} \frac{\omega_0 \varepsilon''(\omega_0)}{\omega_0^2 - \omega^2} d\omega_0. \quad (1)$$

The latter relationship is generally used to verify the compatibility of experimental measurements with a complex expression of the dielectric constant (Milton *et al.*, 1997). A similar relation holds between σ' and $-\sigma''$. With the $e^{-i\omega t}$ convention for the time-harmonic electric field of radian frequency ω , the total density current $\bar{\mathbf{J}}$ enforced through the material is given by

$$\bar{\mathbf{J}} = \mathbf{J} + \frac{\partial \mathbf{D}}{\partial t} = (\sigma^* - i\omega \varepsilon^*) \mathbf{E} = \bar{\sigma}^* \mathbf{E}, \quad (2)$$

where $\bar{\sigma}^*$ is the total effective complex conductivity of the material. The above total current density can also be expressed in terms of the real effective conductivity σ_{eff} and permittivity ε_{eff} :

$$\bar{\mathbf{J}} = (\sigma_{eff} - i\omega \varepsilon_{eff}) \mathbf{E}, \quad (3)$$

so that

$$\sigma_{eff} = \text{Re}(\sigma^* - i\omega \varepsilon^*) = \sigma' + \omega \varepsilon'', \quad (4a)$$

$$\varepsilon_{eff} = \text{Re}(\varepsilon^* + i\sigma^*/\omega) = \varepsilon' + \frac{\sigma''}{\omega}, \quad (4b)$$

and the measured dielectric constant (or relative dielectric permittivity) κ_{eff} , is equal to ε_{eff} divided by the vacuum permittivity $\varepsilon_0 = 8.854 \times 10^{-12}$ Farad/m. When static charges are negligible at the rock/brine interface, the current \mathbf{J} and displacement \mathbf{D} are in phase with \mathbf{E} , and both σ^* and ε^* remain real. However, if the surface of an obstacle to the propagation of \mathbf{E} is electrically charged, then an ionic double layer develops at that interface. Complex

values of σ^* and ε^* ensue, depending on the size of the obstacle, which explains positive out-of-phase conductivity σ'' and from Equation (4b) implies an enhancement of κ_{eff} at low frequencies.

6.2.2 Power-Laws, Double-Layers, and Fractal Geometries

If σ'' varies slowly at low values of frequency, a power-law of exponent (-1) follows from Equation (4b) between dielectric constant and frequency. The power law becomes a linear relationship between κ_{eff} and frequency on a bilogarithmic scale. This very intuitive approach may justify the systematic power-law behavior experimentally observed in clay-bearing rocks (Knight and Nur, 1987; Bona et al., 1998), illustrated in Figure 1, although to date there is no conclusive physical explanation that justifies it. Different models and approaches have been used to quantify such low-frequency behavior of the dielectric constant. All these models are considered as multiscale (or, to some extent, fractal) systems.

The basic element of such multiscale constructions is the electrochemical double layer (EDL) that develops outside a charged rock surface. Hydrated sodium cations in brine solution concentrate at the surface of negatively charged rock surfaces to enforce electrical neutrality of the rock/fluid system. According to the Stern model, a fixed layer of charged cations ensues that is adsorbed to the rock surface. A second, diffusive layer of electric charge extends into the pore brine with a negative exponential profile of cation concentration. The ions in this EDL migrate under the excitation of time-varying electric field, and the EDL as a whole behaves in the form of a dipole with complex electrical properties that depend on frequency, ion mobility, pore brine salinity, surface charge, and surface geometry (Fixman, 1980; Lima and Sharma, 1992; Lesmes and Frye, 2001). Computation of the EDL potentials proceeds from the combined solution of the electrical and diffusion potentials with boundary conditions specific to the EDL (Lacey and White, 1981; Chew and Sen, 1982; Cao *et al.*, 1994).

Thevanayagam (1987) proposed an approach that posits the fractal nature of the observed power-laws between κ_{eff} and ω . Such a model is intended to capture the effective electrical properties at each rock scale. Brine chemistry and electrical properties are assumed to vary at each scale (bound fluid, clay-bound double layer, free fluid). Starting from the

smallest scale, effective electrical properties are computed at each scale from (a) the brine properties at that scale and (b) the effective properties of the next smaller scale through nested mixing-laws. Thevanayagam recognized the necessity of incorporating EDL effects at the smallest scale; however, he used arbitrary values of brine conductivity and dielectric constant at each scale. In essence, Thevanayagam's (1987) approach complements Sen *et al.*'s (1981) self-similar models using stepwise iterations of compounds whose electrical properties vary from scale to scale, instead of infinitesimal dilution of compounds that remain self-similar at all scales.

Rather than using arbitrary values of brine conductivities at each fractal level, Lima and Sharma (1992) incorporated fundamental electrochemical double-layer calculations around spherical clay grains based on Fixman's (1980) model to quantify the effective conductivity and dielectric constant for clay zones. These values were then upscaled with Sen *et al.*'s (1981) self-similar, infinite-dilution mixing law by regarding brine as the host of the mixture, rock as spherical grain inclusions, and clay as either spherical pellets or as shells coating the rock grains. In Thevanayagam's model, the latter approach constitutes a 2-step fractal process with a different mixing law. Lima and Sharma (1992), however, made no mention of power-law effects in their work. The EDL low-frequency dielectric enhancement takes the form of a sigmoid which converges at frequencies lower than 1 kHz to high values of dielectric constant, depending on clay geometry and surface charge. It can be argued that, if the sigmoid extends along several decades of frequency and if it is truncated before reaching its low-frequency asymptote, then that dielectric constant trend behaves in similar fashion to a power law. This assumption is very plausible considering the measurements of Lesmes and Frye (2001) of saturated Berea samples: as ω decreased from 1 kHz and 0.1 Hz, they measured an increase of κ_{eff} that exactly followed a power law with exponent (-1), while below 0.01 Hz κ_{eff} converged to static values in a sigmoid fashion. Such a behavior suggests that observed power laws may be formed by truncated high-amplitude sigmoids which converge outside the measurement range. This result supports the assumption of an EDL origin for the so-called dielectric low-frequency power law.

6.2.3 WBEM for Quantifying Petrophysical Properties

Previous studies examined the influence of specific petrophysical properties of interest on WBEM measurements, including clay presence, multiphase saturation, rock wettability, and pore size; however, such studies failed to quantify the influence of the same petrophysical properties on WBEM measurements. This section summarizes results from several previous studies and emphasizes their practical limitations.

Because electrochemical and geometrical phenomena affect the dielectric response of saturated rocks, Myers (1991, 1996) considered the dispersion of dielectric constant measured in the 20 MHz – 200 MHz range as the sum of (1) a clay term, where clay cation exchange capacity appears, (2) a geometric term, and (3) a vuggy porosity term. For that frequency range, Myers showed that terms (1) and (2) are sufficient to fit the dielectric dispersion of sandstones saturated with two fluid phases, while terms (2) and (3) are appropriate to fit the dielectric measurements of single-phase heterogeneous carbonates. The fitting parameters, however, have no explicit petrophysical significance and are yet to be quantitatively related to rock morphology and macroscopic petrophysical properties, such as hydraulic permeability (Myers, 1996).

Bona *et al.* (1998) used a similar superposition concept to fit dielectric rock measurements performed under partial-saturation conditions with (1) a power-law term added to (2) a Maxwell-Wagner sigmoid term, but on a broader 100 Hz – 100 MHz frequency range. As shown in Figure 1, Bona *et al.*'s (1998) measurements of water-wet Berea samples clearly exhibit power-law behavior below 1 MHz. By contrast, measurements performed on samples treated to be oil-wet at similar values of water saturation reach sigmoid-like asymptotic behavior at values of dielectric constant much smaller than for the case of water-wet samples. Although Bona *et al.* (1998) did not advance quantitative methods to calculate fluid saturation under different wettability conditions, they did emphasize the potential of WBEM measurements in the kHz-MHz range to characterize rock wettability with no need for prohibitively long Amott wettability tests.

The complex refractive index method (CRIM) is known to quantify partial fluid saturations reasonably well in the GHz range; uncertainties associated with this method are lower than those of low-frequency Archie-based conductivity calculations. However, CRIM

and similar models do not account for heterogeneous carbonate pore structure and are inaccurate to quantify fluid saturation in these conditions (Myers, 1996). CRIM also serves as a starting point for Seleznev *et al.* (2005) to derive a mixing law that corrects for the same geometrical parameters and that fits dielectric measurements of geometrically challenging carbonate rocks, even though their range of application was limited to 100 MHz – 1 GHz. Such ongoing efforts suggest that more quantitative morphologic details can be incorporated in the interpretation of WBEM measurements to improve the estimation of petrophysical properties.

Beyond their observation of power-law behaviors in the sub-MHz range, Knight and Nur (1987) also observed a correlation between measured dielectric constant and rock surface-to-volume ratio for partially saturated rocks in the range of 60 kHz – 4 MHz. However, their results lend themselves to ambiguous interpretation. The largest dispersions of dielectric constant (correlated with the highest surface-to-volume ratios) also happened to be measured in tight samples with less than 1 mD permeability, less than 8% porosity, and substantial clay content. Furthermore, these measurements were made in deionized water, which displaces the frequency range of pore geometrical effects below 1 MHz. Eventually, the exact origin of the correlation between dielectric constant and surface-to-volume ratio is difficult to determine.

Finally, Olhoeft's (1985) comprehensive review on mHz-MHz wide-band electrical phenomena in rocks cites oxidation-reduction reactions as a common brine/rock interface phenomenon. When surface reactions take place in a diffusion-limited (by opposition to kinetics-limited) fashion, the electrical response of a compound generally depends on the size of metallic bodies in the mixture. In rocks, these bodies can consist of pores coated with metallic deposits, or of metallic inclusions embedded in the rock matrix. To illustrate this argument, Olhoeft noted that suspensions of 1-mm metallic particles exhibit a 10-Hz relaxation mode in their dielectric spectrum, while suspensions of 10- μ m particles exhibit a 100-kHz mode. An adaptation of double-layer models would provide similar results, although a macroscopic model that incorporates both kinetics- and diffusion-limited reactions in saturated rocks is yet to be proposed. The possibility of inferring pore-size information from WBEM measurements becomes very attractive to validate NMR pore-size estimates.

All these approaches therefore attempt to extract petrophysical information from WBEM measurements, but remain qualitative at best for not individualizing the contributions of the processes simultaneously occurring in rocks. In order to study the interactions between the different phenomena, we develop a pore-scale model generalized from that of Toumelin and Torres-Verdín (2007) for quantifying Maxwell-Wagner geometrical polarization effects.

6.3 DEVELOPMENT OF A GENERALIZED 2D WBEM NUMERICAL FRAMEWORK

6.3.1 Geometrical Pore-Scale Framework

Toumelin and Torres-Verdín (2007) developed a numerical procedure to study the limits of dielectric mixing laws to characterize pore structures in the absence of clays and saturated exclusively with brine, in agreement with both Maxwell's equations and Kramers-Kronig relations. That model incorporates interfacial WBEM effects arising from the accumulation of charges at the boundaries between brine and grains and is based on the following procedure: (1) Build disc-shape binary pore maps where pixels represent either grain or brine in a binary fashion. (2) Assign each such pixel with DC conductivity and dielectric constant of the modeled medium (grain or brine). (3) For each given frequency between 10 kHz and 1 GHz, numerically solve Maxwell's equations with the method of moments to compute the internal electric field and electric current within each pixel of the pore map when subject to transverse-magnetic excitation. Figure 2 illustrates the distribution of internal currents obtained for different angles of incidence of the exciting wave. (4) Use the close-form analytical solution of electromagnetic scattering within a disc to determine the homogeneous DC conductivity and dielectric constant of a disc that minimize the discrepancy between the electric fields and the induced currents calculated within the pore map and within the disc.

Instead of assigning arbitrary pore shapes to the model, we extract the pore maps from rock digital pictures at different rates of magnification. Figure 3 shows an example of a digitized picture of a 24%-porosity sample, which is binarized and truncated into an appropriate disc-shape pore map (white and blue pixels). This new rock model exhibits explicit distributions of pores and throats larger than the pixel resolution of the rock image.

Extending the model in three dimensions on the binary skeleton of high-resolution rock tomography (Arns *et al.*, 2005) should shed additional insight to geometrical polarization effects in complex rock structures.

6.3.2 Inclusion of Clays

Next, we incorporate clays in the rock skeleton by arbitrarily distributing clay pixels throughout the pore map, as illustrated in Figure 3 (magenta pixels) where clay amounts to 3% of the rock volume. At each considered frequency, instead of grain or brine properties, clay pixels are assigned effective electrical properties following Lima and Sharma's (1992) treatment of an ionic double-layer around a spheroid clay grain (see Appendix A). If the grains are larger than the pixel resolution, then several pixels form one clay-coated grain and each pixel is assigned the same electrical properties. On the other hand, if the grains are smaller than the pixel resolution, then one pixel represents a group of clay-coated grains that span a surface equal to that pixel. This numerical framework therefore upscales the response of the clay-bearing rock at the pixel level regardless of mixing laws.

6.3.3 Inclusion of Immiscible Fluids and Wettability

The 2D pore map is assimilated to a cross section of 3D rock geometry, where multiphase saturations can also be distributed in the pore map as they would appear on a 2D cross-section of a 3D saturated rock. Fluid distributions described in the pore maps that follow are designed to resemble a cross-section through a rock where fluid displacement takes place in 3 dimensions. Figure 4 illustrates this concept and emphasizes the pixel-based structure of such a 2D model for a water-wet rock. In this model, a layer of 1 to 2 water pixels is preserved at the rock surface to enforce strong electrical contrast at rock/water and oil/water interfaces, while oil is assumed to invade the pore structure starting from the outside of the disc.

Simulating wettability effects on WBEM measurements is a key objective to this numerical exercise. As shown in Figure 1, large enhancements of the dielectric constant are measured at low frequencies in water-wet rocks with low values of water saturation. Continuity between thin brine films in the water-wet pores prevents any energy storage within the films; therefore, the strong enhancement of dielectric constant at low values of

frequency in water-wet rocks is primarily due to EDL effects. In strongly oil-wet conditions, these EDLs are inhibited because no cations are in contact with the charged clay surface. The activation of EDLs in the magenta pixels of Figures 3 and 4 characterizes the water wettability of the rock model depicted in Figure 3. These principles are used to construct water-wet (WW) and oil-wet (OW) multiphase pore models.

6.4 ASSESSING ROCK MORPHOLOGY FROM SINGLE-PHASE WBEM MEASUREMENTS

We now distribute the wide-band effective clay properties calculated in Appendix A into the clay pixels of Figure 3 pore maps. Pixels labeled as ‘clay’ in that pore map are successively assigned the electrical properties of (a) grain, (b) 0.1 S/m brine, and (c) 100-nm clay in 0.1 S/m brine background. Figure 5 shows the corresponding dielectric dispersions for the three cases and emphasizes the influence of rock texture in the MHz range. In that figure, conductive paths created by brine in case (b) decrease the capacity of the rock model to store energy compared to case (a). The amplitude of the dielectric dispersion at low values of frequency is lower in case (b) than in case (a). In case (c), where the inclusion of 3% dispersed clay is simulated over the entire frequency range, the dielectric dispersion is similar to that simulated for case (b) at 10 MHz, but diverges exponentially below this frequency. All cases (a) to (c) are associated with similar dielectric behavior above 10 MHz.

If we vary brine salinity in the clay-free configuration (a), then the simulated dielectric response (Figure 6) exhibits the expected scaling with brine conductivity (Kenyon, 1984; Toumelin and Torres-Verdín, 2007). On the other hand, if brine salinity is varied in the 3%-clay rock model, then the scaling of dielectric constant with conductivity disappears and the dispersion shown in Figure 7 ensues. We also note that high brine salinity preserves rock texture information in the MHz range while double-layer phenomena are prominent at lower values of frequency. By contrast, low brine salinities induce a dielectric response where both effects overlap in an undistinguishable manner. Such a numerical approach is therefore necessary to quantify – and ultimately invert for – rock morphological effects confounded with clay polarization.

The above observation appears particularly useful when other petrophysical methods fail to properly quantify pore structure and connectivity. For example, the low surface

relaxation of carbonate rocks prevents the NMR characterization of certain bimodal porosities. Appendix B describes the construction of a model for such rocks where the simulated WBEM response departs greatly from the usual sinusoidal response of sedimentary rocks (Figure 1) for exhibiting flat dispersions of both conductivity and dielectric constant across the entire kHz-GHz frequency range. Toumelin and Torres-Verdin (2007) also demonstrated that connectivity between pores of equal eccentricity affect both electrical dispersions, as recapitulated in Figures 8-9. The different inflection behavior of the dielectric spectra simulated for pore maps D1 and D2 also suggests a possible dependence of dispersion-inflection frequencies with the degree of pore isolation, as the internal electric currents distribute differently in the pore space when percolation is reached across the entire pore space. It is therefore important to quantify the contribution of pore geometry to the WBEM response in that frequency range.

6.5 ASSESSING WETTABILITY AND FLUID SATURATION

Previous simulation work (Toumelin *et al.*, 2006) emphasized the conceptual ambiguity of wettability interpretation using 2-dimensional NMR techniques for given conditions of oil viscosity and saturation history. We now conceptually confirm that WBEM techniques can circumvent these ambiguities in rocks with minimal amounts of clay. As mentioned earlier, EDL effects fully develop in water-wet cases, possibly enhanced by fractal surface roughness, while they are inhibited in oil-wet cases. Following the methodology developed above, we populate the pore map of Figures 3-4 with wetting and non-wetting fluid pixels to describe the progressive drainage of a water-wet rock by oil (Figure 10). By contrast, Figure 11 models the progressive drainage of an oil-wet rock by water.

Figure 12 shows the wide-band dispersions of dielectric constant simulated for all the pore maps described in Figures 10-11, for two values of brine conductivity, $\sigma_w = 0.1$ and 1 S/m. Each panel of Figure 12 groups the simulation results by brine conductivity or wettability type. Several remarks stem from this comparison. First, the scaling of the dielectric constant with conductivity remains present in the EDL-free OW cases regardless of fluid saturation. This scaling disappears in the WW cases, which makes saturation estimates nontrivial. Second, each panel of Figure 12 shows that the hierarchy of the dielectric dispersion curves with respect to water saturation or brine conductivity is enforced in the

GHz range regardless of the competition between geometrical and electrochemical effects at lower values of frequency. The values of dielectric constant simulated for low values of water saturation are smaller than those simulated for high values of water saturation, which honors CRIM results. Likewise, the dielectric dispersion sigmoids of the bottom right-hand panel of Figure 12 exhibit a shift to the left (lower frequencies for same values of dielectric constant) when conductivity decreases. Such a behavior is consistent with the notion of conductivity scaling introduced by Kenyon (1984). However, when frequency decreases in the MHz range where EDL effects become important, this curve hierarchy disappears as dispersion curves intersect and change order.

Simulation results described in Figure 12 exhibit a low-frequency power-law behavior for the dielectric constant of WW rock models. This power-law behavior is remarkable given the small amount of clay pixels (as low as 3% of the total number of rock pixels) and the small value of surface charge ($\beta = 11 \mu\text{C}/\text{cm}^2$) considered in the model. Simulation results agree very well with the measured trends of dielectric constant of WW rocks (Figure 1). Dielectric dispersions obtained from simulations and experiments exhibit both (a) low-frequency convergence in OW cases, (b) low-frequency exponential behavior in WW cases, and (c) dual inflection in the MHz-range in some WW cases. Quantitatively, the absolute values of simulated and measured dielectric constants differ by a factor approximately equal to 20. It is likely that larger values of clay surface charge, clay amount, or a more accurate double-layer model, would reduce this discrepancy. However, the relative wide-band behavior of WW dielectric dispersions is identical for both simulations and measurements. In the 1-MHz range, between the two inflection points of the dielectric dispersion curves, both simulations and measurements yield values of dielectric constant equal to 10 times the value of their respective high-frequency asymptotes. In the 10-kHz range, this enhancement factor becomes approximately equal to 30 for both simulations and measurements.

It is also important to note that electrical measurements in general, and water-wet dielectric low-frequency enhancements in particular, are insensitive to oil viscosity. The only assumption formulated on the saturating oil was to assign it a dielectric constant equal to 2 over the entire kHz-GHz frequency spectrum.

6.6 CONCLUSIONS

Fractal and double-layer concepts were reconciled to explain the low-frequency dielectric behavior of saturated rocks. A generalized 2D pore-scale electromagnetic model ensued, which incorporates the simultaneous dielectric effects of pore geometry, charged clays and minerals, wettability, and fluid saturations. Despite quantitative limitations due to the spatial resolution of the pore map and the double-layer model, we obtained very encouraging results when modeling explicit rock WBEM measurements independently from mixing rules or fitting parameters:

First, WBEM measurements are theoretically proven to be sensitive to both pore shape and pore connectivity. The flat dielectric dispersion simulated in the diffusively-coupled microporous rock model is an example where WBEM becomes a viable technique to characterize complex rocks where classic NMR interpretation fails to correctly predict petrophysical properties. One can envision a generalization of WBEM measurements to diagnose the presence of complex pore inhomogeneity, including micritized, oolitic, or vuggy carbonate rocks. However, WBEM measurements have no theoretical sensitivity to pore size except when EDL develops as pore surface coating.

Second, simulations reproduced WBEM measurements fairly well for partially saturated rocks. They characterized wettability trends in clay-bearing sandstones, even for clay concentrations as low as 3%, and regardless of oil grade. Wide-band EM techniques can therefore help to determine in-situ sandstone wettability and complement NMR wettability estimates which are ambiguous when oil viscosity exceeds a few cp.

A comprehensive WBEM model needs to be reliable in the presence of charged clay to perform quantitative petrophysical assessments. Clays usually form dia- or para-magnetic impurities causing internal magnetic fields which make NMR interpretation unreliable for petrophysical estimates. Consequently, WBEM techniques can improve the reliability of NMR techniques in shaly or iron-rich sands.

Table 1 summarizes the different sensitivities that are required to perform accurate petrophysical assessments of a general rock model. Pore size and connectivity are vital to assess hydraulic permeability in both clean and clayey sands. NMR measurements usually quantify pore-size distribution but not pore connectivity, unlike WBEM measurements. It is

also necessary to identify a variety of fluids to perform adequate fluid typing. NMR measurements detect medium- and light-oil grades quite well, but are riddled by acquisition and inversion problems in the presence of gas and heavy oils. Oil grades whose relaxation times and diffusivities are close to those of water within confining rocks also cause NMR interpretation problems. WBEM measurements, on the other hand, are independent of hydrocarbon type; therefore, they allow wettability assessment but not fluid typing. Table 1 emphasizes the sensitivities of NMR and WBEM techniques for these and other essential criteria. Once combined, the two measurement techniques would permit a full coverage of the sensitivity domain required to perform accurate and reliable petrophysical assessments.

6.7 APPENDIX A: QUANTITATIVE INCORPORATION OF ELECTRICAL DOUBLE LAYERS

Following de Lima and Sharma (1992), we embed the effective values of conductivity and dielectric constant for the ionic double layers of wet clay from Fixman's (1980) model. Clay particles are represented as spheres of radius a and consist of resistive core and counter-ion surface charge density β (in units of $1/\text{m}^2$). Ions in the double-layer of diffusivity D displace around the insulating sphere and build up a stationary charge. The corresponding diffusion time τ is given by the ratio

$$\tau = \frac{a^2}{2D}, \quad (5)$$

while the double-layer efficiency δ is defined by the dimensionless ratio

$$\delta = \frac{\beta}{aC}, \quad (6)$$

where C is the density of cations in the bulk water (in units of $1/\text{m}^3$). The complex conductivity associated with this double-layer $\bar{\sigma}_{DL}^*$ can be written as a function of the pore water conductivity, $\bar{\sigma}_w^*$, as follows:

$$\bar{\sigma}_{DL}^* = \frac{\delta \bar{\sigma}_w^*}{1 - \delta Y}. \quad (7)$$

In this equation, Y stands for the frequency-dependent conductivity build-up due to the time oscillation of charges around the insulating grain, and is defined by the equation

$$Y = -\frac{1 + (1-i)\sqrt{\omega\tau}}{2 + 2(1-i)\sqrt{\omega\tau} - 2i\omega\tau}. \quad (8)$$

From the above expressions, it follows that the values of real effective conductivity and dielectric constant for the clay particle and its EDL can be approximated by the equations

$$\sigma_{eff} = \sigma_{\omega} \operatorname{Re}\left(\frac{\delta}{1-\delta Y}\right) + \omega \varepsilon_0 \kappa_{\omega} \operatorname{Im}\left(\frac{\delta}{1-\delta Y}\right), \quad (9a)$$

and

$$\kappa_{eff} = \kappa_{\omega} \operatorname{Re}\left(\frac{\delta}{1-\delta Y}\right) - \frac{\sigma_{\omega}}{\omega \varepsilon_0} \operatorname{Im}\left(\frac{\delta}{1-\delta Y}\right) + \kappa_{grain}. \quad (9b)$$

The practical use of Equations (9) requires quantification of the constants β and C included in Equation (6). As noted by Glover *et al.* (1994), β depends on ion surface adsorption, brine pH, as well as electrolyte concentration. However, it is reasonable to assume a constant clay surface charge density in the order of 10-20 $\mu\text{C}/\text{cm}^2$, or 6-12x10¹⁷ ions/m², as measured by Sonon and Thomson (2005) in smectites. In this paper, we assume a conservative value of $\beta = 11 \mu\text{C}/\text{cm}^2$ or 6.9x10¹⁷ ions/m². It must be pointed out that values as high as 100 $\mu\text{C}/\text{cm}^2$ have been reported for kaolinites (Kanket *et al.*, 2005), which would make the impact of clays on the electrical response of rocks much more important than what is shown in this paper.

The brine cationic density C is linked to the electrical properties of the brine. Stroud *et al.* (1986) recapitulate existing correlations between σ_w (in S/m), κ_w , temperature T (in °C) and salinity X (in kppm) through the equations

$$\sigma_w = \frac{T + 21.67}{45.56} \left[0.0123 + \frac{3647.5}{(1000X)^{0.995}} \right]^{-1}, \quad (10a)$$

and

$$\kappa_w = \left[\frac{1}{87.69 - 0.3921T + 0.000217T^2} + \frac{2.4372X}{58.443(1000 - X)} \right]^{-1}. \quad (10b)$$

By dividing X by the molecular atomic mass of the dissolved salt and multiplying the result by the elementary charge, one obtains the expression for C .

Using the above equations (5)-(10) for different clay sizes $a = 100$ and 1000 nm, and for brines with different conductivities of 0.1 , 1 and 10 S/m, we generated the wide-band dielectric dispersions shown in Figure A-1. These results exhibit expected sinusoidal shapes whose amplitudes vary primarily with salinity. For 100 -nm clay particles, if the frequency range is limited to frequencies above 10 kHz, only brine conductivities lower than 10 S/m will affect the rock dielectric response ($\kappa_{eff} \approx \kappa_{grain}$); when clay size increases, this effect becomes more important. As salinity decreases, $\kappa_{eff} \approx \kappa_w$ for 100 -nm clay particles but $\kappa_{eff} \gg \kappa_w$ for larger clay size at low frequency. If the frequency range is truncated in the kHz range, the ascending part of the sigmoids locally fits a power-law expression between frequency and dielectric constant. Such a behavior is in agreement with discussions included in previous sections of this paper.

6.8 APPENDIX B: CONSTRUCTION OF A WBEM MODEL TO QUANTIFY WBEM MICROPOROSITY EFFECTS

Presence of diffusion coupling in microporous carbonate rocks with low surface relaxivity prevents NMR measurements from correctly quantifying pore-size distributions, bound fluid volumes, and hydraulic permeability (Ramakrishnan *et al.*, 1999; Toumelin *et al.*, 2003). In this paper, we show that WBEM measurements have the potential to reduce ambiguities on such complex rock morphologies. A WBEM geometric model is built from rock images and two-step electromagnetic upscaling in the absence of double-layer effects. We synthesized a carbonate rock model from core data, core pictures, and NMR measurements of a micritized rock sample exhibiting diffusion coupling (Sample A from Toumelin *et al.*, 2003). This sample includes a complex porosity made of dissolution vugs (amounting to 10 of the 24% porosity of the sample, with pores sizes in the $15 \mu\text{m}$ range), primary-porosity macropores (4% porosity, 5 - $15 \mu\text{m}$ range), and abundant micritized intragranular porosity (10% porosity, sub-micron range).

Following the dual-porosity structure shown by the high-resolution images of Figure B-1, Figure B-2 shows an equivalent 2-scale 2D rock model amenable to the simulation of

WBEM measurements. This figure comprises two disks with two different spatial resolutions that constitute the two steps of the upscaling method. The left disk of Figure B-2 forms a 501x501-pixel map of a low-resolution rock model (1 pixel = 0.5 μm) and captures the general dual porous structure of the micritized carbonate sample (10% intergranular and 15% intragranular porosities). However, its low spatial resolution neglects the sub-micron micropores and microthroats existing within the microporous grains. This is why we also use a higher-resolution micromodel (right disk of Figure B-2) that explicitly enforces the presence of 100-nm brine layers between micrite grains, as shown in the right disk of 501x501-pixel resolution (1 pixel = 50 nm). Once the dispersions of isotropic conductivity and dielectric constant are computed for the high-resolution micromodel, they are assigned to the grain pixels in the low-resolution rock model. The effective conductivity and dielectric constant obtained for the low-resolution model constitute the effective properties of the coupled micritized rock.

Figure B-3 illustrates the distribution of electric-current strength calculated at frequencies below 1 MHz within the low-resolution rock model after 2-step upscaling. Incorporation of the microscale model in the 2-step upscaling process plays a fundamental role in the effective response of the coupled rock model. Figure B-4 compares the wide-band dielectric dispersions calculated for the coupled model, with and without 2-step upscaling, with the frequency dispersions calculated for the generic model of Figure 3. In the absence of upscaling, the dielectric response of the coupled macromodel (left disc of Figure B-2 only) is similar to that shown in Figure 5 for the generic rock, except for the amplitudes of the dielectric constant. That amplitude is larger in the generic model than in the coupled macromodel because eccentricities and dead-ends are more prominent in the generic model. Once the micromodel (right disc of Figure B-2) is incorporated as the first step of the upscaling, the dielectric dispersion of the coupled model becomes remarkably flat. Presence of a water layer between all micrite grains effectively connects all the pores of the macromodel and eliminates the geometric dielectric enhancement of the rock. Existence of dead ends where electrical storage occurs in disconnected water zones is therefore the key to dielectric enhancement. Given these simulation results, it is likely that a rock exhibiting strong diffusion coupling will also exhibit high electrical conductivity and abnormally constant electromagnetic dispersion. Therefore, special emphasis can be placed on WBEM

measurements to characterize abnormal heterogeneous rock morphologies and refine the estimation of petrophysical properties performed with NMR measurements.

6.9 ACKNOWLEDGEMENTS

We acknowledge stimulating discussions with Dr. M. Sharma to implement the Fixman EDL model. Our sincere gratitude goes to two anonymous reviewers for their constructive technical and editorial feedback. Funding for the work reported in this paper was provided by (a) the American Chemical Society through grant no. PRF 37519-AC9, (b) the US Department of Energy through contract no. DE-FC26-04NT15518, and (c) UT Austin's Research Consortium on Formation Evaluation, jointly sponsored by Anadarko, Aramco, Baker Atlas, BHP Billiton, BP, British Gas, ConocoPhillips, Chevron, ENI E&P, ExxonMobil, Halliburton Energy Services, Hydro, Marathon, Mexican Institute for Petroleum, Occidental Oil and Gas Corporation, Petrobras, Schlumberger, Shell International E&P, Statoil, Total, and Weatherford.

6.10 REFERENCES

1. Arns, C.H., Bauget, F., Limaye, A., Sakellariou, A., Senden, T.J., Sheppard, A.P., Sok, R.M., Pinczewski, W.V., Bakke, S., Berge, L.I., Oren, P.-E., Knackstedt, M.A. 2005. Pore-Scale Characterization of Carbonates Using X-Ray Microtomography. *SPE J.* 10 (4): 475-484.
2. Bona, N., Rossi, E., Venturini, C., Cappaccioli, S., Lucchesi, M., and Rolla, P. 1998. Characterization of rock wettability through dielectric measurements. *Revue de l'Institut Français du Pétrole* 53 (6): 771-783.
3. Cao, Q.-z., Wong, P.-z., and Schwartz, L.M. 1994. Numerical studies of the impedance of blocking electrodes with fractal surfaces. *Physical Review B* 50 (8): 5771-5774.
4. Chew, W.C., and Sen, P.N. 1982. Dielectric enhancement due to electrochemical double layer: thin double layer approximation, *J. of Chemical Physics* 77 (9): 4683-4693.
5. Fixman, M. 1980. Charged macromolecule in external fields. I. The sphere. *J. of Chemical Physics* 72 (9): 5177-5186.

6. Freedman, R., Heaton, N., Flaum, M., Hirasaki, G.J., Flaum, C., and Hürlimann, M. 1990. Wettability, Saturation, and Viscosity from NMR measurements. *SPE J.* 8 (4): 317-327.
7. Glover, P.W.J., Meredith, P.G., Sammonds, P.R., and Murrell, S.A.F. 1994. Ionic surface electrical conductivity in sandstones. *J. of Geophysical Research* 99 (B11): 21635-21650.
8. Kanket, W., Suddhiprakarn, A., Kheoruenromne, I., and Gilkes, R.J. 2005. Chemical and crystallographic properties of Kaolin from ultisols in Thailand. *Clays and Clay Minerals* 53 (5): 478-489.
9. Kenyon, W.E. 1984. Texture effects on megahertz dielectric properties of calcite rock samples. *J. of Applied Physics* 55 (8): 3153–3159.
10. Knight, R.J., and Nur, A. 1987. The dielectric constant of sandstones, 60 kHz to 4 MHz. *Geophysics* 52 (5).
11. de Lacey, E.H.B., and White, L.R. 1981. Dielectric response and conductivity of dilute suspensions of colloidal particles. *J. of the Chemical Society. Faraday Transactions 2* 77: 2007-2039.
12. Landau, L.D., and Lifshitz, E.M. 1960: *Electrodynamics of continuous media*, Pergamon Press, Oxford, U.K.
13. Lesmes, D.P., and Frye, K.M. 2001. Influence of pore fluid chemistry on the complex conductivity and induced polarization responses of Berea sandstone. *J. of Geophysical Research* 106 (B3): 4079-4090.
14. de Lima, O.A., and Sharma, M.M. 1992. A generalized Maxwell-Wagner theory for membrane polarization in shaly sands. *Geophysics* 57 (3): 431-440.
15. Milton, G.W., Eyre, D.J. and Mantese, J.V. 1997. Finite Frequency Range Kramers Kronig Relations: Bounds on the Dispersion. *Physical Review Letters* 79: 3062-3064.
16. Myers, M.T. 1991. A saturation interpretation model for the dielectric constant of shaly sands. Paper 9118 presented at the SCA International Symposium, San Antonio, Texas, Aug. 21-22.

17. Myers, M.T. 1996. A pore geometry dispersion model for the dispersion of the dielectric constant. Paper 9626 presented at the SCA International Symposium, Montpellier, France, Sept. 8-10.
18. Olhoeft, G. 1985. Low-frequency electrical properties. *Geophysics* 50 (12): 2492-2503.
19. Ramakrishnan, T.S., Schwartz, L.M., Fordham, E.J., Kenyon, W.E., and Wilkinson, D.J. 1999. Forward models for nuclear magnetic resonance in carbonate rocks. *The Log Analyst* 40 (4): 260-270.
20. Seleznev, N. , T.Habashy, A. Boyd, and M. Hizem. 2006. Formation properties derived from a multi-frequency dielectric measurement. Paper VVV presented at the SPWLA Annual Logging Symposium, Veracruz, Mexico, June 4-7.
21. Sen, P.N., Scala, C., and Cohen, M. 1981. A self-similar model for sedimentary rocks with application to the dielectric of fused glass beads. *Geophysics* 46 (5): 781-795.
22. Sen, P.N., and Chew, W.C. 1983. The frequency dependent dielectric and conductivity response of sedimentary rocks. *J. of Microwave Power* 18 (1).
23. Sonon, L.S., and Thompson, M.L. 2005. Sorption of a nonionic polyoxyethylene lauryl ether surfactant by 2:1 layer silicates. *Clays and Clay Minerals* 53 (1): 45-54.
24. Stroud, D., Milton, G.W., and De, B.R. 1986. Analytical model for the dielectric response of brine-saturated rocks. *Physical Review B* 34 (8): 5145-5153.
25. Thevanayagam, S. 1997. Dielectric dispersion of porous media as a fractal phenomenon, *J. of Applied Physics* 82 (5).
26. Toumelin, E., Torres-Verdín, C., Sun, B., and Dunn, K.-J. 2006. Limits of 2D NMR interpretation techniques to quantify pore size, wettability, and fluid type: a numerical sensitivity study. *SPE J.* 11 (3): 354-363.
27. Toumelin, E., Torres-Verdín, C., Chen, S., and Fisher, D.M. 2003. Reconciling NMR Measurements and Numerical Simulations: Assessment of Temperature and Diffusive Coupling Effects on Two-Phase Carbonate Samples. *Petrophysics* 44 (2): 91-107.
28. Toumelin, E., and Torres-Verdín, C. 2007. Two-dimensional pore-scale simulation of wide-band electromagnetic dispersion in saturated rocks. *Geophysics* 72 (3): F97-F110.

29. Zhang, G.Q., Hirasaki, G.J., and House, W.V. 2003. Internal field gradients in porous media. *Petrophysics* 44 (6).

Table 1 Complementarity of the sensitivity domains of NMR and wide-band electromagnetic measurements in the kHz-to-GHz range

| Sensitivity to: | NMR | WBEM (kHz-GHz) |
|--|--|--|
| Porosity | Yes | Yes, jointly with fluid saturation |
| Pore size | Yes | Generally no (only in the presence of pore-coating paramagnetic deposits) |
| Clay volume or clay-bound-water volume (by contrast with non-clay-bound-water) | Yes | Likely in the kHz range, but difficult to assess |
| Moveable fluid volume (by contrast with non-moveable fluid) | Yes if moveable-fluid cutoffs are known | No |
| Pore connectivity and shape | No | Yes |
| Wettability type | Yes in general using 2D NMR (possible problems in the presence of vugs and due to saturation history effects) | Likely in the presence of clays and substantial grain surface roughness; unknown otherwise |
| Fluid saturation | Yes if fluids exhibit sufficient contrast in relaxation times (T_1 , T_2) and/or diffusivity | Yes, jointly with porosity |
| Brine salinity | Almost none | Yes but without influence on saturation calculations based on GHz-range measurements |
| Hydrocarbon viscosity | Yes if hydrocarbons and water exhibit sufficient contrast in relaxation times (T_1 , T_2) and/or diffusivity | No |
| Heavy oil presence (by contrast to other hydrocarbon grades) | 2D NMR may be able to quantify heavy oils in the ms-relaxation range; for heavier oil grades NMR exhibits porosity deficit | Yes (response similar to other hydrocarbons) |
| Gas presence (by contrast to other hydrocarbon grades) | Yes in general: T_2 logging sufficient in the absence of dia- or paramagnetic minerals creating internal magnetic gradients in the pore space; T_1 logging or T_2 /Diffusion logging necessary otherwise | Yes (response similar to other hydrocarbons) |

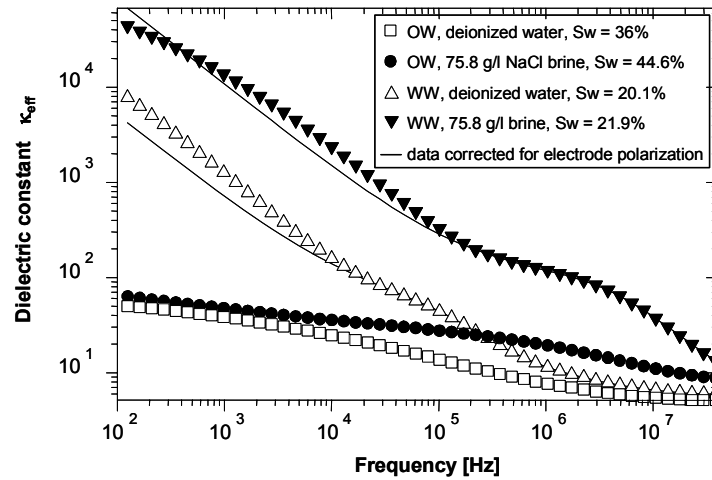


Figure 1 Wide-band dispersions of dielectric constant measured on four 22%-porosity Berea samples treated to exhibit different wettabilities and saturated with different brine salinities. OW: oil-wet samples; WW: water-wet samples. The conductivity of deionized water is 1.57×10^{-3} S/m at 100 Hz, and that of saline brine (75.8 g/l NaCl) is 9.5 S/m. After Bona *et al.* (1998), data courtesy of Nicola Bona.

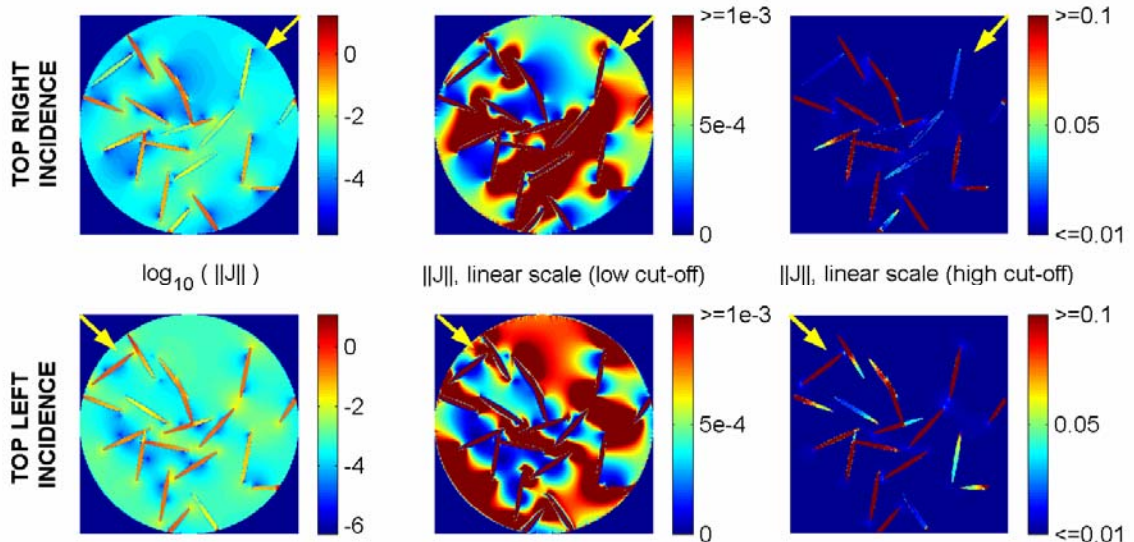


Figure 2 Amplitude distribution of internal currents J induced in a pore map exhibiting elliptic inclusions, under two perpendicular angles of incidence at 100 MHz, and using different scales. Arrows indicate the directions of plane-wave incidence.

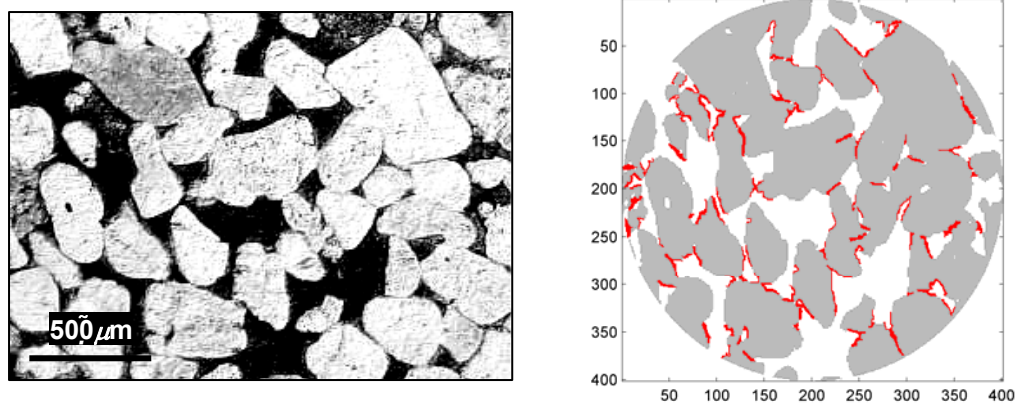


Figure 3 Sandstone micrograph (left panel; gray: grain; black: pore space) and corresponding digital pore map (right panel; gray: grain; white: pore space) scattered with arbitrary clay inclusions (red pixels). The scale on the pore map axes is given in pixels, with the pixel resolution equal to 5 μm .

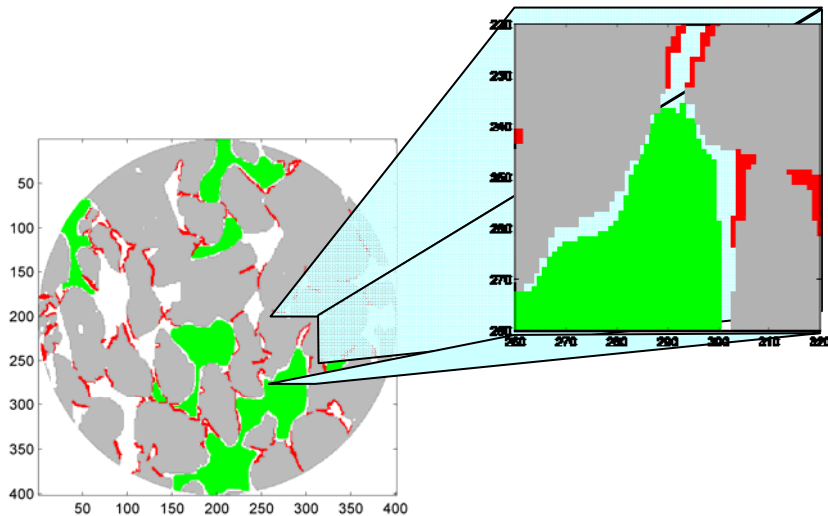


Figure 4 Graphical example of two-phase fluid distribution within the pore map of Figure 3. Colors are coded as follows: gray: grain; red: clay cements; green: non-wetting hydrocarbons; white: water-filled pore space. The local enlargement shown on the right-hand panel displays the pixel-based construction of the 2D model.

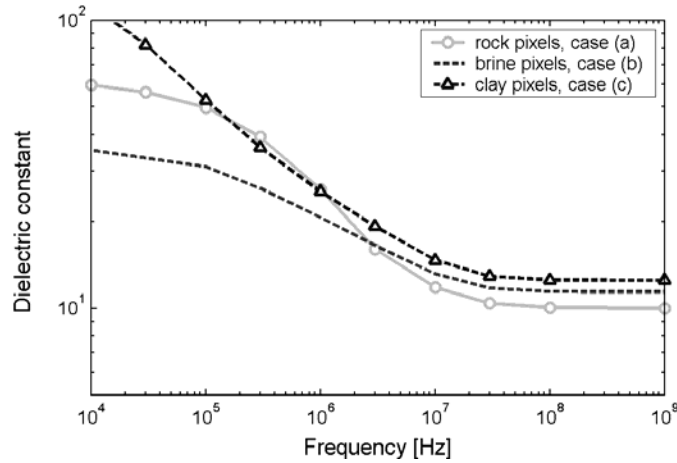


Figure 5 Frequency dispersion of dielectric constant simulated for the rock model shown in Figure 3 assigning three different textures to its red pixels. Brine conductivity is taken equal to 0.1 S/m.

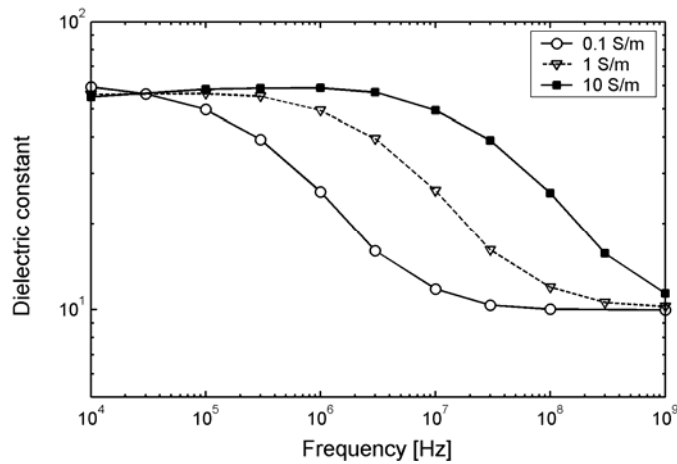


Figure 6 Frequency dispersion of dielectric constant simulated for the rock model of Figure 3 (without clay double-layers) and for three different values of brine salinity.

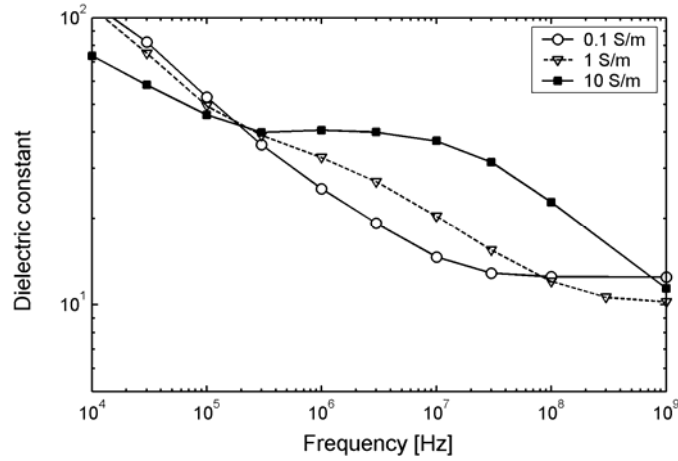


Figure 7 Frequency dispersion of dielectric constant simulated for the rock model of Figure 3 (with clay double-layers characterized in Figure A-1) and for three different values of brine salinity.

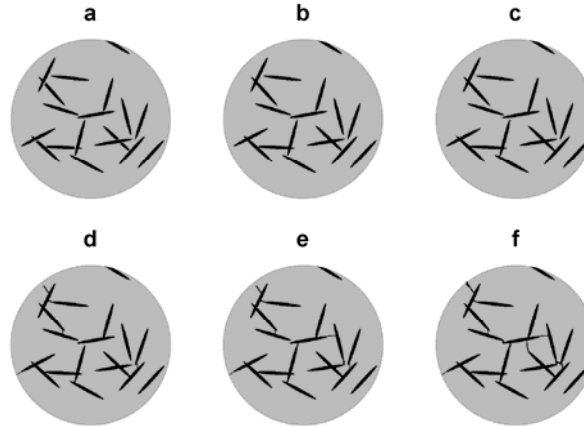


Figure 8 Pore maps modified after map D and exhibiting increasing connectivity between brine pores. Brine inclusions (black pixels) are embedded in the rock host (gray pixels).

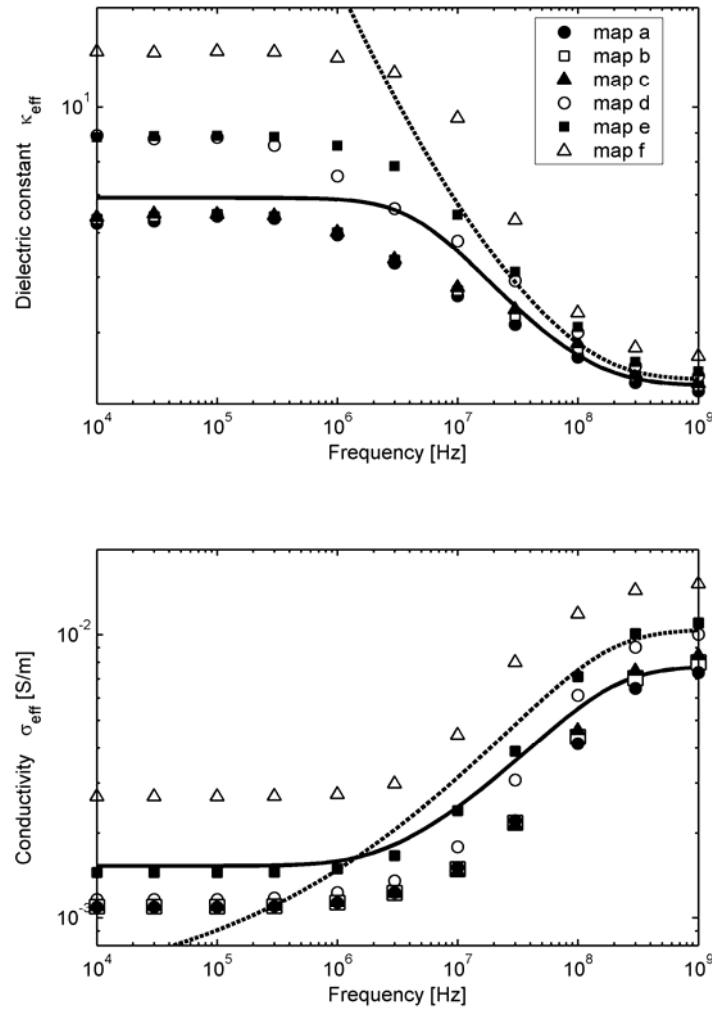


Figure 9 Frequency dispersions of effective dielectric constant (top panel) and electrical conductivity (bottom panel) for pore maps D00 to D3. Simulation results are identified with markers for $\kappa_{\text{host}} = 2$. The two continuous sigmoids identify the best matches to the simulated results obtained using two analytical approaches: Effective-Medium-Approximation in continuous curve (Kenyon, 1984) and CRIM-like powerlaw in dotted curve.

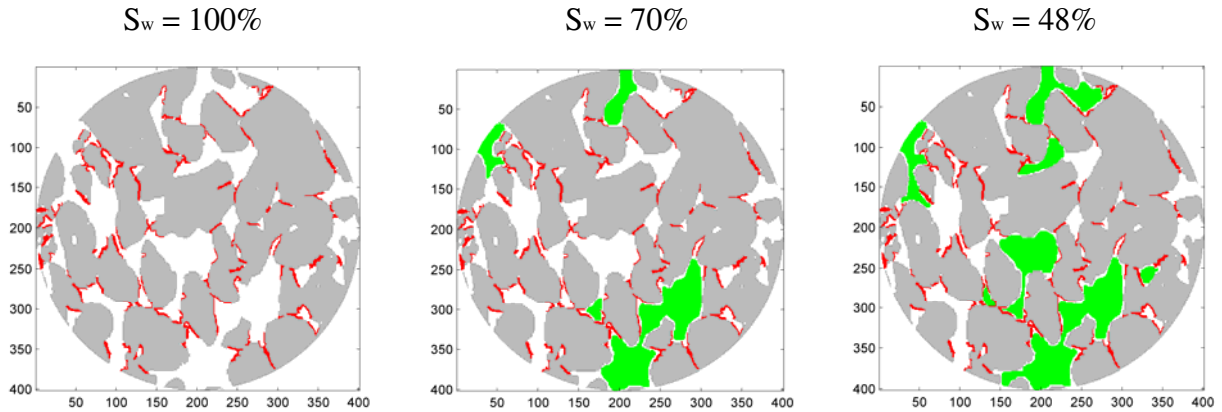


Figure 10 Fluid distribution in water-wet rock models with clays and 3 values of water saturation S_w . Gray pixels represent grain matrix, red pixels, clay, white pixels, brine-saturated porosity, and green pixels, oil-saturated porosity.

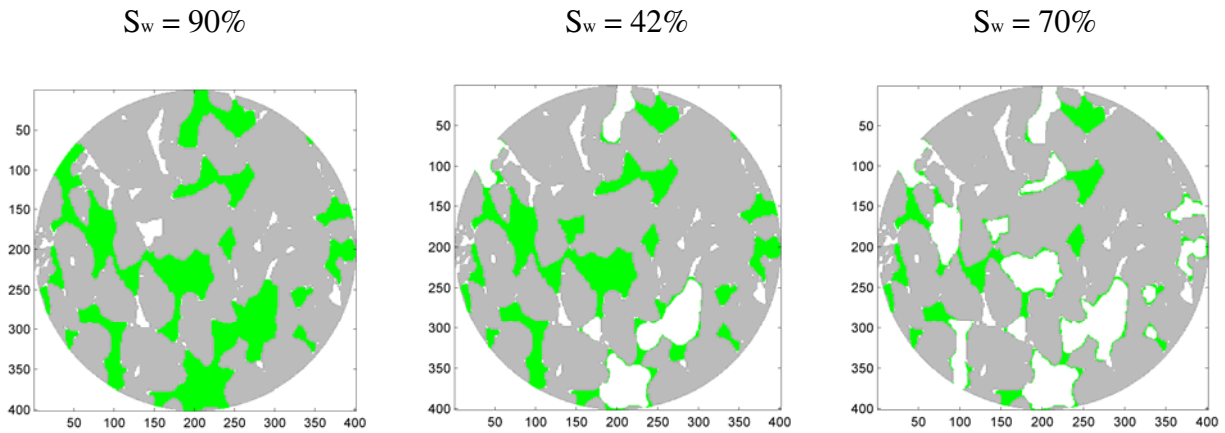


Figure 11 Fluid distribution in oil-wet rock models for 3 values of water saturation S_w . Gray pixels represent grain matrix, white pixels, water-saturated porosity, green pixels, oil-saturated porosity.

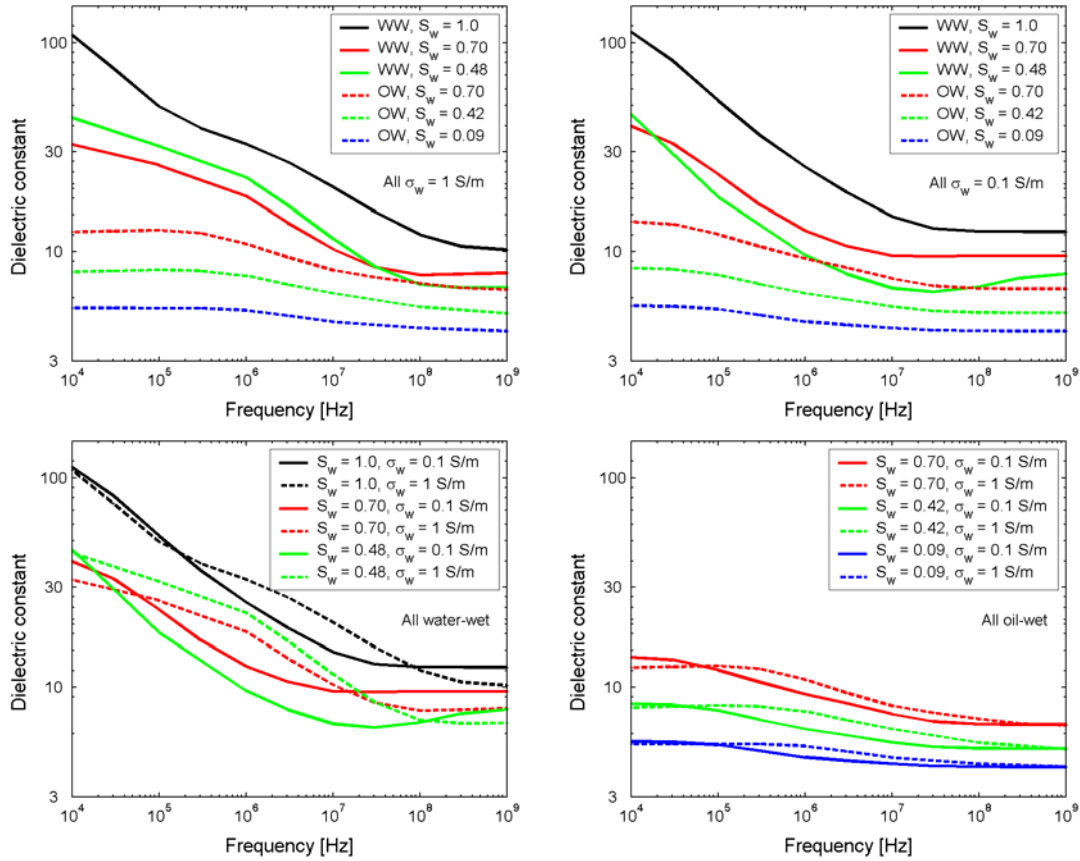


Figure 12 Frequency dispersions of dielectric constant simulated for the pore maps of Figures 10 (water-wet cases, WW) and 11 (oil-wet cases, OW), for two values of brine conductivity. Top left-hand panel: all simulation results for $\sigma_w = 1$ S/m; top right-hand panel: for $\sigma_w = 0.1$ S/m; bottom left-hand panel: all water-wet geometries; bottom right-hand panel: all oil-wet geometries.

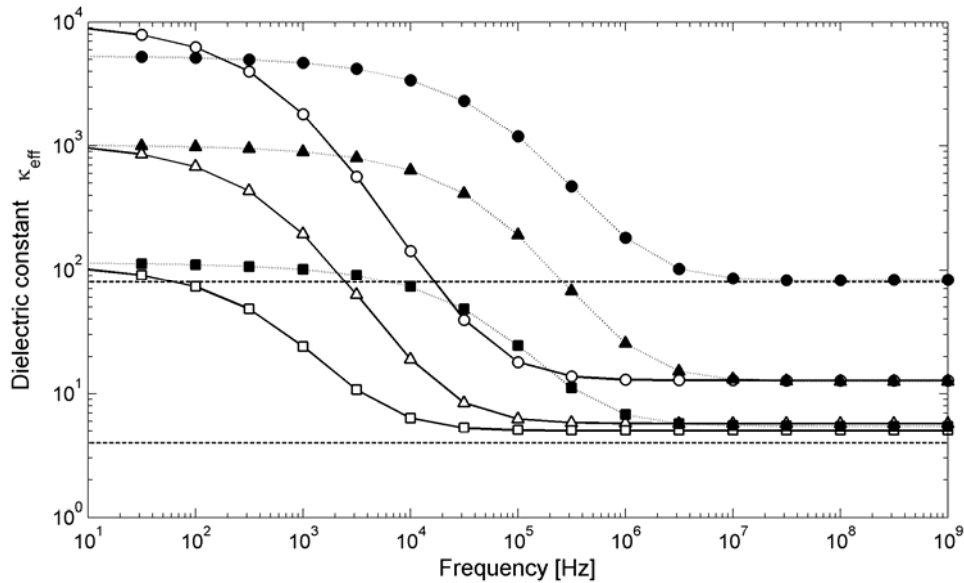


Figure A-1 Frequency dispersions of pure clay dielectric constant simulated for different values of clay size and brine conductivity via Equation (9b). Open markers: $a = 100$ nm, closed markers: $a = 1$ μm . Squares: $\sigma_w = 10$ S/m; triangles: $\sigma_w = 1$ S/m; circles: $\sigma_w = 0.1$ S/m. Dotted lines identify the bulk dielectric constant of quartz (4) and water (80). The locally-straight lines obtained between 1 kHz and 10 kHz for $a = 100$ nm and between 100 kHz and 500 kHz for $a = 1$ μm appear as power-laws of dielectric constant behavior with respect to frequency.

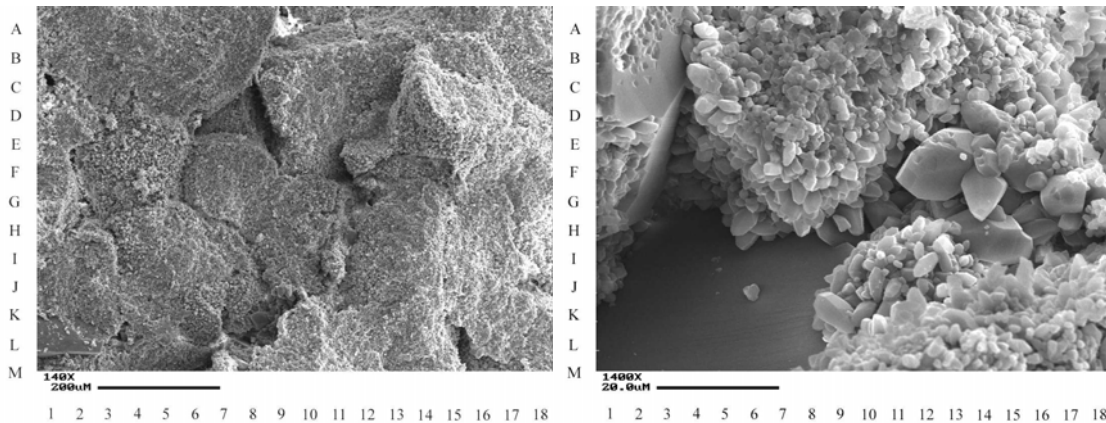


Figure B-1 High-resolution Scanning Electron Microscope (SEM) images of a carbonate sample exhibiting diffusion pore coupling at 140X (left panel) and 1400X (right panel) magnifications (Toumelin *et al.*, 2003a).

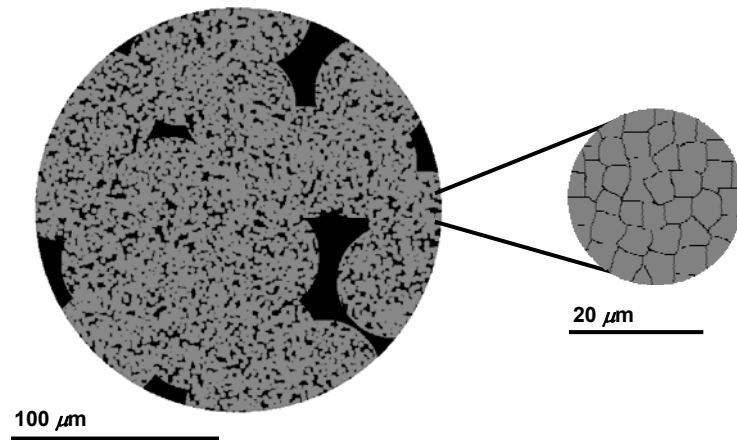


Figure B-2 Representation of the two-step 2D model of a rock designed to replicate the rock structure shown in Figure B-1.

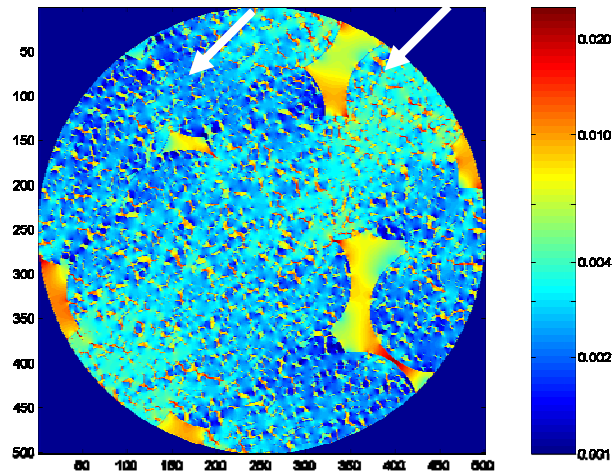


Figure B-3 Distribution of internal current amplitudes within the low-resolution microporous rock model below 1 MHz. The arrow shows the direction of polarization of the incident electric field.

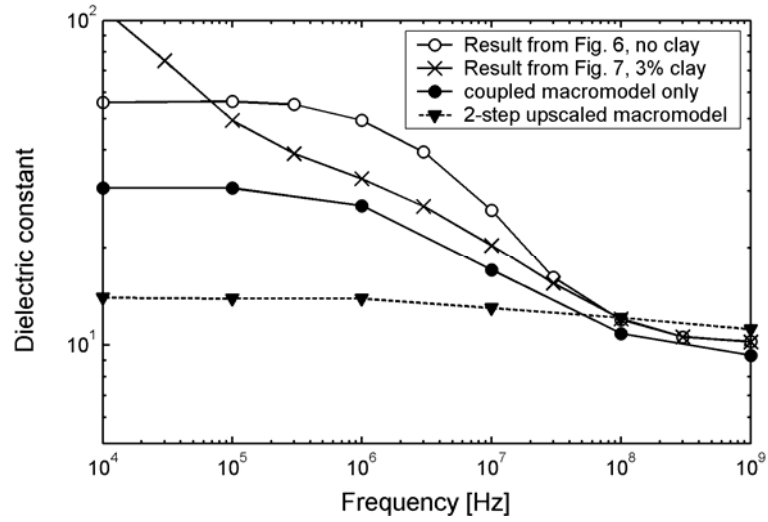


Figure B-4 Comparison of dielectric dispersions obtained for 1 S/m brine with the generic model of Figure 3 and with the coupled model of Figure B-2.

CHAPTER 7. EXPERIMENTAL MEASUREMENTS OF THE DIELECTRIC RESPONSE OF BRINE SATURATED ROCKS

This chapter describes the results of electrical impedance measurements made over a broad spectrum of frequencies (10 Hz to 10 MHz) with fully brine saturated rock samples of varying permeability (grain size). Details of the measurements can be found in Reference 1.

The Chapter first covers the different methods used to measure the dielectric properties of highly lossy materials (brine saturated rocks). Results of broad band dielectric measurements are then presented for a range of rock permeabilities.

7.1 METHOD 1: DIELECTRIC FIXTURE

Method 1 covers all the experiments conducted with an HP 4192A Impedance Analyzer, with a dielectric fixture without any electrode modifications or coatings. In the subsequent methods, modifications to the electrodes were made in order to improve the quality of the measurement results, and they are discussed in detail in the following sections.

Three different experiments were conducted using Method 1: air, dry Berea, and fully saturated Berea. The same Berea samples were used for the dry and fully saturated measurements and there were nine samples of Berea disks, two-inches in diameter and of different thicknesses.

7.1.1 Dry Berea Measurements

The first set of measurements was done on dry Berea sandstone to check the accuracy of the experimentation using the dielectric fixture and also to experiment with rock sample preparation. Berea sandstone is composed mainly of silica and, therefore, should have a dielectric constant between 1 (of air) and 5 (of silicon dioxide). Moreover, the value should be constant over the frequency range of interest because no polarization mechanism is present.

It is safe to assume that dry Berea acts as a perfect capacitor when placed between two parallel plates; therefore, the impedance of the sample approaches infinity as the frequency goes to zero. At a frequency below 10 kHz, the imaginary part of impedance

values exceeded the measurement range of the impedance analyzer and the results were only available at a higher frequency. The conductivity of dry Berea was too low to be measured accurately; therefore, these results were disregarded.

Figure 1 displays the dielectric constant measurement for dry Berea disks of different thicknesses. These samples were sliced using a circular saw that uses decane oil as a cutting fluid designed for cutting harder rocks, such as shales. The faces of the disks were not as smooth as the samples prepared by the Hillquist Thin Section Machine. It was clear that there were minute changes in dielectric constant values at different frequencies and also for different sample thicknesses. The change in frequency can be explained by the limitations and capabilities of the impedance analyzer. The change with sample thickness was believed to be caused by the contact impedance presented at the electrode-sample interfaces and had to be eliminated.

The results from Figure 1 and two more experiments were analyzed by linear adjustments and they are summarized in Figure 2. The samples prepared by the Hillquist Thin Section Machine and by the circular saw showed very similar results, although the sample surfaces treated by the two methods had different smoothnesses. Another experiment was conducted on circular saw treated samples that were left overnight in the open air, and the result had higher dielectric constant values. This was probably caused by extra moisture absorbed by the Berea sample.

Results from Figure 2 offered two conclusions. The first conclusion was that the linear adjustment worked well in dry measurements because the adjustment had eliminated two distinct parasitic impedances from two different sample surfaces. The second conclusion was that the 4192A was sensitive enough to detect extra moisture in the sample.

7.1.2 Air Measurements

Ten measurements on air with electrode separation ranging from 0.5 mm to 5 mm at 0.5 mm intervals were performed as a validity check of Method 1. Since air, a good insulating substance, has a conductivity too small to be accurately measured, as a result, discussions on the conductivity are not possible. Discussions focus on the measured dielectric constant.

Figure 3 shows the dielectric constant of all ten measurements of air. The increase in air gap thicknesses raised the dielectric constant value and this suggested that stray capacitance was most effective for larger electrode separations. Both the linear adjustment and inverse length adjustment in Figure 4 showed a good measurement result, which was within 3% of the known dielectric constant of air of 1.

7.1.3 Fully Saturated Berea Measurements

Two measurements were performed on Berea samples fully saturated with 3% NaCl brine. In the first experiment, six out of nine samples produced negative susceptances. In the second experiment, a coffee filter was used to improve the electrode/sample contact, which was thought to be the cause of problem in the prior experiment. However, all nine samples produced negative susceptances in the second run. The negative susceptance suggested either high inductive components presented in the rock sample or that faulty measurement procedures were used. The second explanation was more likely.

Table Table 1 listed two samples results from the experiment described in the previous paragraph, one for 3.18 mm and the other 3.76 mm sample thicknesses. One noticeable difference was that the 3.76 mm showed negative susceptances (B) above 200 kHz (shown in bold type) and the calculated dielectric constants were negative as well. It is also interesting to see that the conductivity for the second measurement showed a higher value, which suggested that some leakage current aided the conduction during the measurements and caused the susceptances to become negative.

As depicted in the middle sketch in Figure 5, the sample/electrode interface near the guard electrode suggests that electrical shorting occurred from electrode-A (or guarded electrode) to the guard electrode via conductive brine. When a coffee filter (placed between the MUT and the electrodes) was used in the second experiment, electrical shorting occurred much more easily than in the first experiment because the coffee filter soaked in brine had a higher conductivity than the MUT. This is the cause for negative susceptances in all nine measurements in the second experiment.

The three reasonable results from the first experiment did not show any correlations with the sample thickness. This suggested that some partial electrical shorting occurred in these measurements. These poor results are not plotted or discussed.

7.1.4 Berea Measurements—Non-Contacting Method

The non-contacting electrode method derives the dielectric constant from capacitance difference between two measurements, one with and one without the test material. The non-contacting electrode method was one of the measurement procedures suggested by the manual of the dielectric fixture. Figure 6 shows a schematic of the measurement setup and the following equation suggested by the manual was used to calculate the dielectric constant of the Berea sample:

$$\varepsilon = \frac{1}{1 - \left(1 - \frac{C_{s1}}{C_{s2}}\right) \times \frac{t_g}{t_a}}, \quad (1)$$

where ε is the calculated dielectric constant, C_{s1} is the capacitance measured with absence of the test material, C_{s2} is the capacitance measured with the presence of the test material, t_g is the distance between the two electrodes, and t_a is the thickness of the test material. Figure 6 depicts the variables used in Equation (1).

One of the benefits of using the non-contacting method was the elimination of electrode polarization. Insulating materials between the sample and electrode eliminates build up of charges on the electrode surface. Unfortunately, conductivity could not be measured accurately using this method because the conductivity for air or insulating materials was much smaller than the MUT and dominated the overall measured conductivity.

Figure 7 shows results from the non-contacting method. No linear correlations with sample thickness were found. Unexpectedly, most of the calculated dielectric constant values were negative. The best explanation for these poor results was that the extreme contrast of electrical property between the measurements with and without the conductive sample was too extreme and sensitive to measurement errors. Measurements without samples (C_{s1} in the equation) had a very small value close to the range limit of the impedance analyzer and were more susceptible to measurement errors at these low resolution ranges.

Because of the poor results, no further measurements with the non-conducting method were attempted. However, variations of the non-conducting method were attempted in later experiments.

7.1.5 Discussion of Method 1

Method 1 used the dielectric fixture and its electrode in its original configuration. This method worked perfectly on insulated materials such as dry Berea samples and air, however measurements on conductive materials such as fully brine saturated Berea samples resulted in poor and sometimes erroneous outcomes. The cause was found to be the electrical shorting from the guard electrode to electrode-A of the fixture. Method 2 in the next section modified the electrodes to overcome this problem and will be discussed next.

7.2 METHOD 2: MODIFIED DIELECTRIC FIXTURE

Method 2 covers all the experiments conducted with a modified dielectric fixture. In the previous section, Method 1 was shown to be flawed when making impedance measurements on fully saturated Berea samples due to the electrical shorting of the guard electrode. Method 2 used the same dielectric fixture but added some modifications to eliminate the electrical shorting. The modified version moved the guard electrode 1 mm away from the sample to prevent any contact with the sample. The modifications are depicted at the bottom diagram of Figure 5.

The dimensions of the MUT were limited because of the electrode modification. With the guard electrode raised, the samples were required to have the same diameter as electrode-A (or the guarded electrode). MUT of a different diameter experiences non-uniform electric field through the sample when measured, and thus resulted in inaccurate values. Another problem was that the measurements were more susceptible to stray capacitances because the guard electrode had lost its full potential in eliminating stray effects.

Samples measured with Method 2 were de-ionized water, toluene, an ideal RC electrical circuit, and Berea samples fully saturated with brine at different salinity. The first three measurements were performed to check the validity of the experiment method. The results of all four measurements are discussed in the following sub-sections.

7.2.1 De-Ionized Water Measurement

Measurement on de-ionized water was one of the three ways to check the validity of measurement Method 2. De-ionized water was injected by a pipette to the spaces between the two electrodes and was held by capillary forces from electrode faces. The separation of the two electrodes cannot extend more than 5 mm or the liquid film collapses. The measurement accuracy decreases as the electrode separation increases because the electric field is altered by the shape of the liquid meniscus. Six different gap thicknesses were measured at both 0.1 and 1.1 volt applied electrode voltages.

The results are shown in Figure 8 and Figure 9, and the raw data are displayed in Figure 10 through Figure 16. The conductivity in Figure 8 shows variations between different applied voltages, but it is uncertain whether the differences are within error since the conductivity of de-ionized water is very sensitive to any impurities in the fluid. The dielectric measurements (Figure 9) did not change much within the differences in applied electrode voltage. However, the result (85-88) was higher than 78, the known dielectric constant of water. Dielectric enhancement was experienced below 10 kHz.

7.2.2 Toluene Measurements

Dielectric constant measurements on toluene (methylbenzene or phenylmethane) are shown in Figure 17. Toluene is an aromatic hydrocarbon commonly used as a solvent and has a dielectric constant of 2.4. Two measurements were performed, one at 0.74 mm and the other at 2.75 mm electrode separations. Both measurements showed that the dielectric constant is constant within the frequencies of interests. The larger electrode separation measurement had a higher dielectric constant than the smaller separation measurement which suggested that some stray capacitances was measured. Dielectric measurements did not show any enhancements at lower frequency because toluene is non-conductive.

7.2.3 Circuit Measurements

An electrical RC circuit was measured using the dielectric fixture by replacing the electrodes with resistors and capacitors in parallel. Four measurements of different resistor/capacitor combinations were made. Figure 18 shows the measured impedances of the

four circuits. The measured values matched the specified values at low frequencies but did not match the specified values at high frequencies. The differences were caused by the limitation of the capacitors used in the circuit. All capacitors have frequency limitations and are unable to function properly at high frequency. In this experiment, the three capacitors acted as resistors at high frequency and, therefore, the measured values stayed flat. The match at low frequency shows that the instrument 4192A functions properly. This also suggests that the dielectric enhancements in rock core experiments are caused by the electrodes and other factors.

7.2.4 Fully Saturated Berea Measurements

Fully saturated Berea measurements were made on samples 1.5 inches in diameter. Two sets of Berea samples were used. The first set was saturated with 1% and 3% NaCl brine while the second set was saturated with de-ionized water, 0.45%, and 2.15% NaCl brine.

7.2.5 NaCl Brine, 1% and 3%

Twenty Berea disks 1.5 inches in diameter and of different thicknesses were used. Ten disks were saturated in 1% NaCl brine, the rest with 3% NaCl brine. A circular coffee filter of 1.5 inch in diameter was also used during the experiment. The filter was placed in between the Berea sample and the electrodes to enhance electrical contact between them. Since the guard electrode has been modified, the coffee filter did not make electrical contact with the guard electrode.

Figure 19 and Figure 20 show the results of the Berea measurements. The single measurements for 3.39 mm and 3.36 mm thickness samples shown in Figure 19 experienced low conductivity (or high resistivity) at the low frequency range. The result analyzed by linear adjustment inverted the outcome and showed high conductivity. Ideally, the conductivity should be constant at these frequencies and the decrease at low frequency was likely caused by some parasitic impedance such as electrode polarization, which created a more resistive layer on the electrode surface.

The inversion of conductivity at a low frequency after linear adjustment was caused by the use of the coffee filter for two reasons. The first reason was that the coffee filter filled

with brine was more conductive than the MUT and the second explanation was that later tests without the use of coffee filter did not have this inversion. The formation factor (FF) shown in the figure also suggested that the linear adjustment results were more accurate. The FF for Berea is known to be about 16 at full saturation.

The dielectric measurements are displayed in Figure 20. Inverse length adjustment created some negative values which were caused by the presence of stray capacitances, as suggested by the deviation in conductivity at these frequencies. The data analyzed by linear adjustment showed dielectric enhancement at frequencies below 1 MHz. The slope of the line at low frequency on a log-log scale is between -1.5 to -2.

Figure 21 through Figure 34 display the measured raw data that were used to calculate results in Figure 19 and Figure 20. The raw data are plotted in measured parameters (such as resistivity, reactance) against measured frequency. Argand diagram is also included as one of the figures. One of the main purposes for plotting these raw data is to serve as a reference for any future studies.

Figure 35 shows a single measurement made by covering a Berea sample saturated with NaCl brine 1% in plastic wrap. The plastic wrap was placed between the sample and the electrodes and functioned similarly to the non-contacting method. The figure shows that dispersion in the measured dielectric constant was observed at around 1 kHz and 1 MHz. The dielectric constant of 600 between the two dispersions was too high and the measurement was very sensitive to the thickness of the plastic wrap. A closer look at the validity of this method is detailed in Method 5.

7.2.6 De-Ionized Water

Eight Berea disks of 1.5 inches in diameter were used. Four of the samples were coated with a thin layer of epoxy at the circumference of the disk to prevent evaporation during measurements. Coffee filter were used to ensure good electrical connectivity between the electrode surfaces and the sample. Two different voltages were applied to the electrodes by the 4192A to check for any changes in the measurements due to applied voltage.

Figure 36 shows the conductivity for these samples corrected by linear adjustment. One can easily see that the differences of applied voltage did not affect the outcome of the

measurement, while the epoxy on the sample lowered the conductivity by almost half. The epoxy used was non-conductive and because it was used at the circumferences of the samples, some interference by the epoxy cannot be avoided. However, the changes due to epoxy were not conclusive because the conductivity of de-ionized water was very small and sensitive and minute changes could have caused the conductivity to vary. The FF was not calculated because the resistivity of de-ionized water was too large to be measured accurately.

Figure 37 and Figure 38 show the dielectric constant after linear and inverse length adjustment, respectively. There were very little variations caused by changes in both applied electrode voltage and the application of epoxy. Dielectric enhancement still existed, but at a lower value and at lower frequency than measurements made with brine saturated samples. The slope on a log-log scale also decreased to nearly -1 compared with brine saturated sample measurements. Figure 39 through Figure 52 show the raw measured data in different parameters.

7.2.7 NaCl Brine, 0.45% and 2.15%

The four samples that were covered with epoxy in the previous de-ionized water experiment were further tested for higher salinity brine. The de-ionized water was replaced with NaCl brine 0.45% and 2.15% in separate. Figure 53 and Figure 61 display the adjusted results of the measurement with NaCl brine 0.45% and 2.15%, respectively. In both figures, there appeared to be a change in the slope at 1 kHz and this was more prominent in the higher salinity measurement in Figure 61. The higher salinity caused both the measured dielectric constant and conductivity to increase. The FFs for both figures were reasonable, but on the low side. Figure 54 through Figure 60 and Figure 62 through Figure 68 show the raw data of the measurements.

7.2.8 Discussion of Method 2

Method 2 eliminated the electrical leakage problem that occurred in Method 1, but also enhanced the stray capacitance effect. Another problem with Method 2, which was not discussed in previous sections, was that the brines reacted chemically with the surface of the electrodes. Under alternating currents, the free ions in the brine bombarded the electrode

surface and the brine changed color as a result. This caused extra impedances and limited the accuracy of the measurements.

The stray capacitance can be determined by the adjustment methods discussed in Reference 1. The presence of stray capacitance causes the inverse length adjustment results to become negative, as shown in Figure 20. The linear adjustment, however, can only partially eliminate some of the stray capacitances. The problem with electrode surface chemical reaction needed to be solved mechanically. In other words, a coating that is chemically inert while maintaining good electrical conduction was required to cover the electrode surfaces. Method 3 covers experimentations using coatings on the electrodes.

7.3 METHOD 3: MODIFIED DIELECTRIC FIXTURE AND COATED ELECTRODES

As described in the previous section, electrode-A used by the dielectric fixture underwent chemical reactions on the surface (with brine) under alternating electrical fields. This created additional impedances that were difficult to calculate. Several coatings were applied to the electrode surfaces to adjust for this corrosion effect. Details on the electrode surface treatments are covered in Reference 1. This section shows the results obtained with each treatment and discusses the effectiveness of the treatments.

7.3.1 Gold Sputter Coating

To combat corrosion on the electrode surfaces, sputter coating gold onto the electrode surfaces was first attempted. Gold is a stable metal and should be able to contain the chemical reactions due to free moving ions in the saturating fluid. More details on sputter coating are discussed in Reference 1.

Several sputter coating sessions were attempted. Both the guarded and the unguarded electrode surfaces were cleaned by sonication and alcohol before being sputter coated. The first sputter coating lasted for 50 seconds and the electrode surfaces showed a light brown color. Figure 62 and Figure 70 show the conductivity and dielectric constant measured after the first coating. Figure 71 through Figure 77 show the raw data for these measurements. Some parasitic impedance still existed, causing the conductivity to drop at low frequency and

dielectric enhancement below 100 kHz. Both effects were similar to measurements made using previous methods.

Measurements were also made with only de-ionized water and NaCl brine 0.9% and these are shown in Figure 78 and Figure 79. The raw measured data for de-ionized water are shown in Figure 80 through Figure 86 while the raw data for NaCl brine 0.9% are shown in Figure 87 through Figure 93. It is clear that the dielectric enhancement increased both in magnitude and frequency range at higher conductivity. Figure 79 shows the conductivity measurement on 0.9% brine. The low conductivity or high resistivity below 10 kHz suggests that some parasitic impedance is present, probably from chemical reaction.

Figure 94 shows a measurement on a 2.5 mm thick Teflon disk. According to the DuPont website, Teflon has a dielectric constant of 2.01 up to 10 MHz at room temperature. This experiment conducted with modified dielectric fixture yielded a dielectric constant of 2.1 above 500 Hz, which was within 5% and the differences could have been caused by stray capacitances.

The conductivity measurement on 0.9% NaCl brine in Figure 79 suggested that the first gold coating session of 50 seconds was not enough to cover the electrode surfaces (at least on a molecular scale). A second coating was made for about 3 minutes on top of the first gold film of 50 seconds. Figure 95 and Figure 96 display the new measurements, but they showed results similar to previous measurements. Figure 97 through Figure 110 show the raw data of these measurements.

The results from experiments conducted with sputter coated electrodes did not seem to diminish the parasitic effects, and in some cases the treated electrodes enhanced these effects. It was later found that sputter coating yielded only a few angstroms per minute, which was insufficient to cover all the surface roughness of at least hundreds of angstroms on the electrode surfaces. The use of physical vapor deposition covers the electrode surface roughness effectively and at a much faster rate and is described in the next section.

7.3.2 Physical Vapor Deposition (PVD) of Gold

Gold vapor deposition was attempted after the sputter coated electrodes had failed. Unfortunately, the gold film on the PVD treated electrodes partially peeled off before any measurement was made.

Measurements were made with the partially protected electrodes. Figure 111 shows the results obtained for the same Berea sample used with the sputter coated electrode experiments. The results showed almost identical curves for both dielectric constant and conductivity measurements. Figure 112 through Figure 118 show the raw data of the results in Figure 111.

Other tests were made with the partially coated electrodes by changing the experimental methods and they are reported in the following subsections.

7.3.3 Sandwich Method

Like the non-contacting method and the method using plastic wrap, the sandwich method places the MUT between two non-conducting disks to limit the build-up of charges on the electrode surface.

The dielectric constant calculation for the sandwich method was different from the non-contacting method. The sandwich method calculation is based on a volume average of the dielectric constant. In other words, the dielectric constant of the sample is derived from the measured dielectric constant of the sample plus non-conducting disks subtracted by the volume average of the dielectric constant of non-conducting disks. The equation used is provided below:

$$\epsilon_m = \frac{\epsilon_t t_t - 2\epsilon_d t_d}{t_m}, \quad (18)$$

where ϵ_m is the dielectric constant of the measured material, ϵ_t is the measured (total) dielectric constant, t_t is the distance between the two electrodes, ϵ_d is the dielectric constant of the acrylic disks, t_d is the thickness of the acrylic disk, and t_m is the thickness of the sample.

The first experiment was conducted on Berea samples, 2 inches in diameter, as pictured in Figure 119 along with the measurement results. A dielectric constant of 10.9 was calculated for frequencies above 100 Hz. If we assume that the dielectric constant of Berea samples with zero porosity is 4.5 and that of water is 78, then by volume average calculation the porosity of the Berea sample should have been less than 9%, which was not the case.

A second experiment was attempted on Berea samples, 1.5 inches in diameter. Figure 120 shows the measurement configurations and the results. As in previous experiments, the dielectric value was constant above 100 Hz, but too low to be the volume average of water and the Berea samples. A strong correlation of the dielectric constant with sample thickness suggested that stray capacitance was important.

7.3.4 External Field Method

This method attempts to eliminate any free moving ions in the Berea samples. An external field was applied orthogonal to the measuring electric field with the goal of forcing the free moving ions to accumulate at the circumferences of the Berea sample. This setup is depicted at the bottom of Figure 121. A pair of curved copper strips was placed at the circumference of the Berea sample. An electric field was applied across the copper strips (up to 54 volts).

The result showed no changes due to the applied external field. Measurements at 10, 30, and 54 volts showed the same results for all frequencies. No further attempts were made with this method.

7.3.5 Silver Plating Powder

After the failed attempts of gold PVD, Cool-Amp silver plating powder was used to protect the electrode surfaces. Details on this application are described in Reference 1. The silver plating powder can be applied easily and does not require any equipment, so it was applied at the beginning of each experiment.

Methanol and de-ionized water measurement results are shown in Figure 122 and Figure 123. Dielectric enhancement still existed for both measurements and was more pronounced for methanol. The known dielectric constant of methanol is 32.6, which is

consistent with the measurements shown in Figure 122 above 20 kHz. The conductivity of methanol measured was also affected by parasitic effects below 1 kHz. The de-ionized water results are very similar to these measured by the gold coated electrodes. The increase in conductivity with frequency in Figure 123, however, is contrary to the measurements shown in Figure 8. Since the conductivity of de-ionized water is very small and prone to change and cause measurement errors, the conductivity results are less reliable.

Several measurements were made with different samples fully saturated in de-ionized water (shown in Figure 146, Figure 147, Figure 148, and Figure 149). Descriptions of the sample are covered in Reference 1. These samples includes the three sintered bead samples of different grain size, Berea sandstone, Boise sandstone, Texas cream limestone, and Arco-China Shale.

7.3.6 Discussion of Method 3

Method 3 focused on the coating material used on the electrode surfaces. Three approaches were used: gold sputter coating, gold physical vapor deposition, and silver plating powder application. All three approaches showed very similar results. The silver powder application was chosen for use in all future experiments because it can be applied and reapplied easily.

Dielectric enhancement was experienced in all measurements and was caused by electrode polarization. Details of electrode polarization are discussed in Reference 1. The four-electrode method in the next section combats electrode polarization problems and these measurement results are described in Method 4.

7.4 METHOD 4: FOUR-ELECTRODE METHOD

The four-electrode setup is described in Reference 1. This method allows the voltage and current electrodes to be separated so that the measured voltage is not affected by free ion buildup at the current electrodes. An electrical RC circuit was measured using the four-electrode setup to check the methods validity. The instrumentation was then used to make measurements on large Berea samples with ring electrodes.

7.4.1 Circuit Measurements

An electrical RC circuit was measured to check the validity of the 4-electrode method. Figure 124 to Figure 134 shows the measurement methods listed in Table 2. Measurements #7 and #13 were unable to make any measurements. Each figure also shows the circuit diagram of the measurement.

The results are expressed in parallel conductances (G_p) and susceptances (B_p) in Siemens because conductivity and dielectric constant cannot be obtained without any physical dimensions. The conductance corresponds to conductivity, or the real part of the admittance, while the susceptance corresponds to the dielectric constant, or the imaginary part of the admittance. A calculated value is also displayed in hollow points to show what the instrument should measure.

Measurement #1 in Figure 124 simulated three identical samples placed between the four electrodes. The conductance deviated after 100 kHz while the susceptance only matched the correct value from 1 kHz to 2 MHz. Measurement #2 (Figure 125) changed the capacitor value for the middle circuit to a smaller one. By lowering the capacitor value, the conductance increased the accuracy range, but the accuracy of susceptance decreased. Measurement #4 (Figure 127) used an even smaller capacitor and showed results similar to Measurement #2.

Other circuit configurations were attempted. For example, the capacitors were replaced with an extremely large one in Measurement #3 (Figure 126), large resistors were added to the outside in Measurement #5 (Figure 128), and certain parts of the circuits were grounded in Measurement #6, #7, #12, and #13. However, the results were unsatisfactory.

Experiment #9 (Figure 131) used a larger resistor for the middle circuit and the result was not perfect, but it was much better than the other configurations. This result suggests that the sample between the voltage electrodes needs to be thicker than the ones on the outside in between the current and voltage electrodes.

Figure 133 shows RC circuit measurements by the two-electrode method. The conductance measured with the two-electrode method only matched the calculated values up to 20 kHz. The susceptance was quite accurate for most of the frequency range.

7.4.2 Berea Measurements

Berea samples fully saturated with NaCl brine 0.9% measured using the four-electrode method showed very poor results in Figure 135. From 5 kHz to 200 kHz frequency range, both the conductivity and dielectric constant showed strange values. Dielectric enhancement still exists at low frequency so electrode polarization has not been eliminated by the four-electrode method. The cause of these abnormal values was investigated in the electrical circuit measurements. It was found from the circuit measurement that the resistance between the current and voltage electrodes needs to be smaller than the resistance between the two voltage electrodes in order to obtain reasonable values. Later Berea sample experiments followed this procedure.

Figure 136 shows the result of the Berea sample measurement after the electrical circuit measurements were performed. The results were very similar to measurements on the exact same Berea samples by the dielectric fixture but there were a few subtle differences. The slope of dielectric enhancement on a log-log scale did not change in the four-electrode method whereas in Figure 111, the slope changed at around 500 Hz. Another difference was that the conductivity started dropping at high frequency although no previous measurement by the dielectric fixture had such an outcome.

A comparison of the two-electrode and four-electrode methods is shown in Figure 137. The two-electrode measurement was not performed by dielectric fixture, but by using copper sheet electrodes. The dielectric constants measured using both methods show the same value, while the conductivity for four-electrode method was smaller. The FF for the four-electrode and two-electrode methods was 17.7 and 13.3, respectively.

A comparison of measurements by two-electrode, four-electrode, and dielectric fixture is shown in Figure 138, Figure 139, and Figure 140. The conductivities using the three methods (Figure 138) show a good match for all three measurements from 1 kHz to 2 MHz. The deviations at both the high and low frequency range are different in all three methods. The dielectric constant comparisons (Figure 139 and Figure 140) show few differences with the exception of the four-electrode analyzed by inverse length adjustment. It is also noticeable that the dielectric constant by the four-electrode method has a slightly different slope at low frequency.

7.4.3 Berea Measurements with Large Cylindrical Sample

The four-electrode method was also attempted on large cylindrical Berea samples. The sample used was 2 inches in diameter and 3 inches in thickness (height). The current electrodes were copper sheet electrodes placed on the top and bottom of the Berea sample. The voltage electrodes were wires tightened around the circumference of the sample. This setup is sketched at the bottom of Figure 141. This figure also shows the dielectric constant of the dry Berea cylinder.

The Berea cylinder was later fully saturated in de-ionized water and measured. The result of the single measurement is shown in Figure 142. This result shows some dispersion in addition to the dielectric enhancement in the kHz frequency range, but the data was unavailable below 1 kHz. The conductivity is slightly higher than the past measurements.

7.4.4 Discussion of Method 4

Method 4 covers measurements made with the four-electrode method. The four-electrode method did not eliminate any dielectric enhancement caused by electrode polarization. The measurements on the electrical circuit suggested a more accurate setup when the four-electrode method is used, which is to place the largest sample in between the two electrodes. The measurement setup on a large Berea cylinder was not a good experimental setup because the measured values were higher than previous measurements.

7.5 METHOD 5: NON-CONTACTING METHOD (REVISITED)

The non-contacting method was first attempted in Method 1. A variation on this method using plastic wrap was used in Method 2. Another variation using non-conducting disks is discussed in the sandwich method. The results from these experiments showed dispersions in the kHz to MHz frequency range but the actual value was unreasonable. This section revisits the non-contacting method and some variations to this method and attempts to justify the validity of the experimental results.

7.5.1 Air Gap Method

The air gap method has the same experimental setup as the non-contacting method, but reduces Equation (17) used in the non-contacting method to the following:

$$\epsilon_{\text{sample}} = \frac{d_{\text{sample}}}{\frac{\epsilon_0 A}{C_{\text{total}}} - \frac{d_{\text{air}}}{\epsilon_{\text{air}}}}, \quad (19)$$

where ϵ_{sample} is the dielectric constant of the sample, ϵ_{air} is the dielectric constant of air, ϵ_0 is the permittivity of free space, A is the area of the electrode, C_{total} is the measured capacitance, d_{sample} is the thickness of the sample, and d_{air} is the thickness of the air gap. One immediate benefit from the equation reduction is that only one measurement is required, rather than two measurements as in the non-contacting method. Equation 19 can be further reduced by assuming the dielectric constant of air is 1.

A sensitivity analysis on the air gap thickness d_{air} of equation (19) is shown in Figure 143. A Berea sample of 5.1 mm thickness was measured by dielectric fixture with air gap thickness d_{air} around 0.07 mm, with a resolution of 0.01mm. From the figure it is clear that the calculated dielectric constant changes dramatically with the changes in air gap thickness at a value below the available resolution.

Figure 144 and Figure 145 show the measurement results for Berea and Texas cream samples, respectively. Both calculated dielectric constants have been manipulated by changing d_{air} in Equation (19) so that the values overlap at 50 kHz. The dispersion frequency for Berea sample measurements seems to follow the sample thicknesses but the same effect is not shown in the Texas cream samples.

7.5.2 Discussion of Method 5

The sensitivity analysis of Figure 143 shows the limitations of the air gap method. In order to acquire accurate air gap measurements, both the sample and air gap thicknesses have to be obtained to a resolution of microns (which is usually not possible).

7.5 DISCUSSION OF METHODS

Five major methods were attempted for impedance measurements on fluid saturated cores and they are summarized below:

Method 1 used a dielectric fixture and its electrode in its original configuration. This method worked perfectly on insulated materials such as dry Berea samples and air. However measurements on conductive materials such as fully saturated Berea samples resulted in poor and sometimes inaccurate results. Electrical shorting from the guard electrode to electrode-A of the fixture was found to be the cause.

Method 2 eliminated the electrical leakage problem occurring in Method 1, but as a result of the change, Method 2 enhanced the stray capacitance effect. Another problem with Method 2 was that chemical reactions took place at the surface of the electrodes, causing extra impedances and limiting the accuracy of the measurements.

Method 3 focused on the coating material used on the electrode surfaces. Three approaches were used: gold sputter coating, gold physical vapor deposition, and silver plating powder application. The three approaches showed similar results. The silver powder application was chosen for use in all future experiments because it can be applied easily without complicated instrumentation.

Method 4 covers measurements made with the four-electrode method. The four-electrode method did not eliminate any dielectric enhancement caused by electrode polarization. The measurements on a RC electrical circuit suggested more accurate measurements were obtained when the largest impedance is placed between the two measuring electrodes.

Method 5 revisited the non-contact method and performed a sensitivity analysis that clearly showed the limitations of this method. In order to obtain accurate results, both the sample and air gap thicknesses have to be obtained to a micron resolution, which is not possible with the configuration discussed in this thesis.

Overall, the most convenient method with an acceptable level of accuracy would be Method 3 which uses the Cool-amp silver plating powder.

7.6 DISCUSSION OF RESULTS

With the experimental procedure finalized (Method 3), measurements were made on samples with different salinity and grain size to see how these variables influenced the dielectric properties of rocks. This discussion will focus on changes in electrical properties with two major experimental variables: grain size and saturating fluid salinity.

7.6.1 Changing Grain Size

Seven rock samples were measured. The conductivity measurement results for samples fully saturated with de-ionized water are shown in Figure 146 and Figure 147, where the latter figure displays the de-ionized water saturated shale conductivity. The reason for using de-ionized water as saturating fluid is because the measured result experiences less dielectric enhancement. The figures show that the measured conductivity appears to be increasing with decreasing grain size. The large sintered beads sample has the lowest conductivity while the fine grained Arco-China Shale has the highest conductivity. It makes sense for a larger grain size sample to have lower conductivity because most of the contribution to conductivity comes from surface conduction (which is larger for smaller grain size). The conductivity for limestone (Texas cream) seems to be the exception. This is likely because of the micro porosity of the grains.

The dielectric constant measurement results are displayed in Figure 148 and Figure 149, whereas the second figure is a zoomed-in version of the first one. As grain size increases, the frequency at where the dielectric enhancement ends decreases. In another words, the large and medium sintered beads samples show dielectric enhancement below 1 kHz while the smaller grain size samples show enhancement below 10 kHz. A closer look at the dielectric response from 10 kHz to 10 MHz shown in Figure 149 shows some dispersion responses. This response is more apparent for sintered beads, mainly because the sintered beads are composed of perfectly spherical grains of the same size. If we omit the dielectric enhancement at lower frequencies, then this dispersion might be caused by Maxwell-Wagner polarization.

An Argand diagram is shown in Figure 150. As expected, for de-ionized water saturated samples, the Argand circle decreases in size as grain size decreases. The only exception is the limestone.

An interesting discovery is shown in Figure 151 and Figure 152. Both the reactance and loss tangent reveal a peak in the kHz frequency and this peak appears to be shifting with changing grain size. Except for Texas Cream, the only limestone used in our experiments, the frequency where a peak is observed shifts to a higher frequency as grain size decreases.

The loss tangent peak frequency versus grain size (Figure 153) and permeabilities (Figure 154) clearly show the peak frequency increases as grain size and permeability decreases for sintered bead samples. This response agrees with the following equation derived by Lima and Sharma (1992):

$$\tau = a^2/2D_1, \quad (20)$$

where τ is the relaxation time of the charged particle, a is the grain diameter, and D_1 is the diffusion coefficient of the counterion in the charge layer. If the diffusion coefficient in Equation (20) stays constant (which is the case in this experiment) decreasing the grain size will decrease the relaxation time and increase the peak (relaxation) frequency. The relaxation time is inversely proportional to the peak frequency. Berea and Texas Cream samples also follow the general trend observed for the sintered samples. However, since these natural sandstones have a range of grain size distributions and the grains are cemented together, they do not lie exactly on the trend line observed for the uniform sintered beads.

7.6.2 Changing Saturating Fluid Salinity

To show the effect of changes in saturating fluid salinity, only Berea samples were used. The increase in salinity of the saturating fluid raises both the conductivity and dielectric constant in Berea (shown in Figure 155 and Figure 157). A plot of saturating fluid resistivity (R_w) versus bulk resistivity (R_o) (Figure 156) shows the formation factor is reasonable (15.83) for Berea sandstone.

Figure 158 displays the Argand diagram of the measurements. Dashed lines were drawn to complete the Argand circle. As the saturating fluid becomes more conductive, the

Argand circle becomes smaller and the tail becomes more pronounced. The increase of the tail suggests that the electrode polarization becomes more dominant as the saturating fluid becomes more saline.

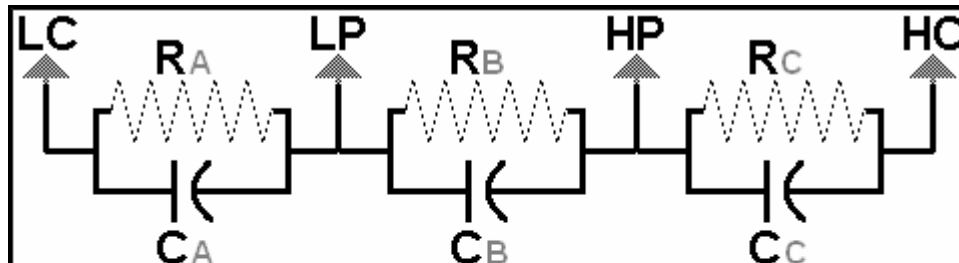
Figure 159 shows the reactance versus frequency at different saturating fluid salinity. The peak reactance- m value shifts to a higher frequency and decrease in value as the saturating fluid becomes more saline. This effect due to changes in fluid salinity can be explained by the double layer model. The increase in salinity of the saturating fluid causes the double layer thickness on the grain surface to decrease. As the size of the double layer thickness decreases, the space for the ions within the double layer also decreases. The size of the double layer changes the frequency while the number of mobile ions within the double layer changes the value of the peak in Figure 159.

A similar trend is also shown in Figure 160 (loss tangent versus frequency). The loss tangent peak increases in both frequency and magnitude as fluid salinity increases. The salinity versus peak frequency obtained from Figure 160 is cross-plotted in Figure 161 to show the effect more clearly. The higher loss at higher salinity is not caused by the double layer, but by the conduction in the bulk fluid outside of the double layer. In another words, the higher salinity causes the sample to be more conductive and prone to electrical energy loss through the conductive paths.

Table 1 Measurement on two different thicknesses Berea samples fully saturated with 3% NaCl brine. The negative dielectric constant for the second table suggested faulty experiment procedures were used and the higher conductivity compared to the first table suggested the some leakage currents were in effect.

| Berea sandstone, fully saturated with 3% brine, 2 inch diameter, 3.18 mm thickness | | | | | | |
|---|---------------|---------------|-------------|------------------|---------------------|----------------------------|
| <i>Freq[kHz]</i> | <i>R[ohm]</i> | <i>X[ohm]</i> | <i>G[S]</i> | <i>B[S]</i> | <i>Conductivity</i> | <i>Dielectric Constant</i> |
| 5 | 4.22E+01 | -2.56E+00 | 2.36E-02 | 1.43E-03 | 6.61E-02 | 1.44E+04 |
| 10 | 3.13E+01 | -1.23E+00 | 3.19E-02 | 1.26E-03 | 8.94E-02 | 6.32E+03 |
| 20 | 2.99E+01 | -7.30E-01 | 3.35E-02 | 8.18E-04 | 9.37E-02 | 2.06E+03 |
| 50 | 2.95E+01 | -3.70E-01 | 3.39E-02 | 4.25E-04 | 9.49E-02 | 4.28E+02 |
| 100 | 2.93E+01 | -2.50E-01 | 3.41E-02 | 2.91E-04 | 9.55E-02 | 1.46E+02 |
| 200 | 2.93E+01 | -2.20E-01 | 3.42E-02 | 2.57E-04 | 9.56E-02 | 6.46E+01 |
| 500 | 2.93E+01 | -3.00E-01 | 3.42E-02 | 3.50E-04 | 9.57E-02 | 3.53E+01 |
| 1000 | 2.92E+01 | -5.00E-01 | 3.42E-02 | 5.86E-04 | 9.58E-02 | 2.95E+01 |
| 2000 | 2.92E+01 | -9.10E-01 | 3.42E-02 | 1.07E-03 | 9.59E-02 | 2.69E+01 |
| 5000 | 2.85E+01 | -1.97E+00 | 3.49E-02 | 2.41E-03 | 9.77E-02 | 2.43E+01 |
| 10000 | 2.67E+01 | -2.81E+00 | 3.71E-02 | 3.90E-03 | 1.04E-01 | 1.96E+01 |
| 13000 | 2.57E+01 | -2.76E+00 | 3.84E-02 | 4.12E-03 | 1.08E-01 | 1.60E+01 |
| Berea sandstone, fully saturated with 3% brine, 2 inch diameter, 3.76 mm thickness | | | | | | |
| 5 | 1.58E+01 | -7.00E-01 | 6.32E-02 | 2.80E-03 | 2.10E-01 | 3.34E+04 |
| 10 | 1.50E+01 | -3.60E-01 | 6.68E-02 | 1.61E-03 | 2.21E-01 | 9.57E+03 |
| 20 | 1.49E+01 | -2.00E-01 | 6.72E-02 | 9.03E-04 | 2.23E-01 | 2.69E+03 |
| 50 | 1.48E+01 | -8.00E-02 | 6.74E-02 | 3.64E-04 | 2.24E-01 | 4.34E+02 |
| 100 | 1.48E+01 | -3.00E-02 | 6.74E-02 | 1.36E-04 | 2.24E-01 | 8.13E+01 |
| 200 | 1.48E+01 | 3.00E-02 | 6.74E-02 | -1.36E-04 | 2.24E-01 | -4.06E+01 |
| 500 | 1.49E+01 | 1.30E-01 | 6.73E-02 | -5.89E-04 | 2.23E-01 | -7.02E+01 |
| 1000 | 1.49E+01 | 2.90E-01 | 6.69E-02 | -1.30E-03 | 2.22E-01 | -7.74E+01 |
| 2000 | 1.50E+01 | 5.80E-01 | 6.64E-02 | -2.56E-03 | 2.20E-01 | -7.64E+01 |
| 5000 | 1.54E+01 | 1.40E+00 | 6.46E-02 | -5.89E-03 | 2.14E-01 | -7.01E+01 |
| 10000 | 1.58E+01 | 2.61E+00 | 6.17E-02 | -1.02E-02 | 2.05E-01 | -6.08E+01 |
| 13000 | 1.63E+01 | 3.24E+00 | 5.90E-02 | -1.17E-02 | 1.96E-01 | -5.38E+01 |

Table 2 List of electrical circuit measurement combinations. The measured data are displayed in Figure 124 to Figure 134.



| Experiment # | Ra | Ca | Rb | Cb | Rc | Cc |
|--------------|-------------------------------|-------|------|-------|------|-------|
| 1 | 50Ω | 50nF | 50Ω | 50nF | 50Ω | 50nF |
| 2 | 50Ω | 50nF | 50Ω | 1nF | 50Ω | 50nF |
| 3 | 500Ω | 50μF | 500Ω | 50μF | 500Ω | 50μF |
| 4 | 50Ω | 50nF | 50Ω | 100pF | 50Ω | 50nF |
| 5 | 5kΩ | 50nF | 50Ω | 100pF | 5kΩ | 50nF |
| 6 | Same as #5 grounded at LP | | | | | |
| 7 | Same as #5 grounded at LP, LC | | | | | |
| 8 | 500Ω | 100pF | 500Ω | 50nF | 500Ω | 100pF |
| 9 | 50Ω | 1nF | 5kΩ | 1nF | 50Ω | 1nF |
| 10 | 500Ω | 50nF | 500Ω | 50nF | 50Ω | 1nF |
| 11 | 0Ω | 0F | 500Ω | 50nF | 0Ω | 0F |
| 12 | Same as #8 grounded at LP | | | | | |
| 13 | Same as #8 grounded at LP, LC | | | | | |

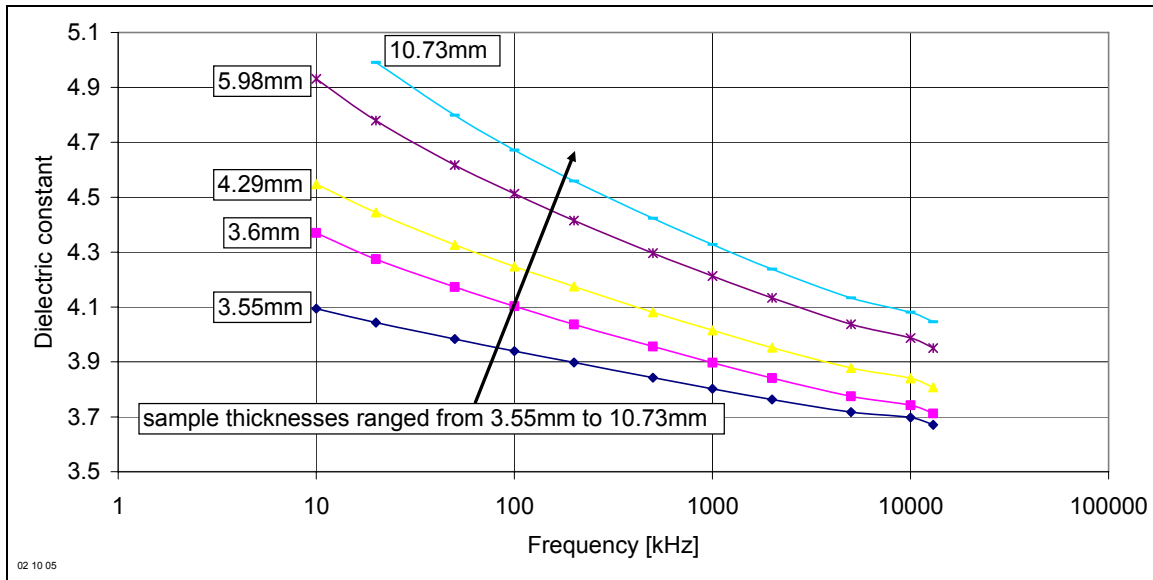


Figure 1 Dielectric constant of dry Berea disks of different thicknesses (Method 1). Sample disks in the experiments were prepared by circular saw and the faces of the sample are less smooth than that prepared by Hillquist thin section machine. The change of dielectric constant with frequency was likely to be caused by limitations of the instrument. The change with sample thickness was caused by parasitic impedances at electrode/sample interface.

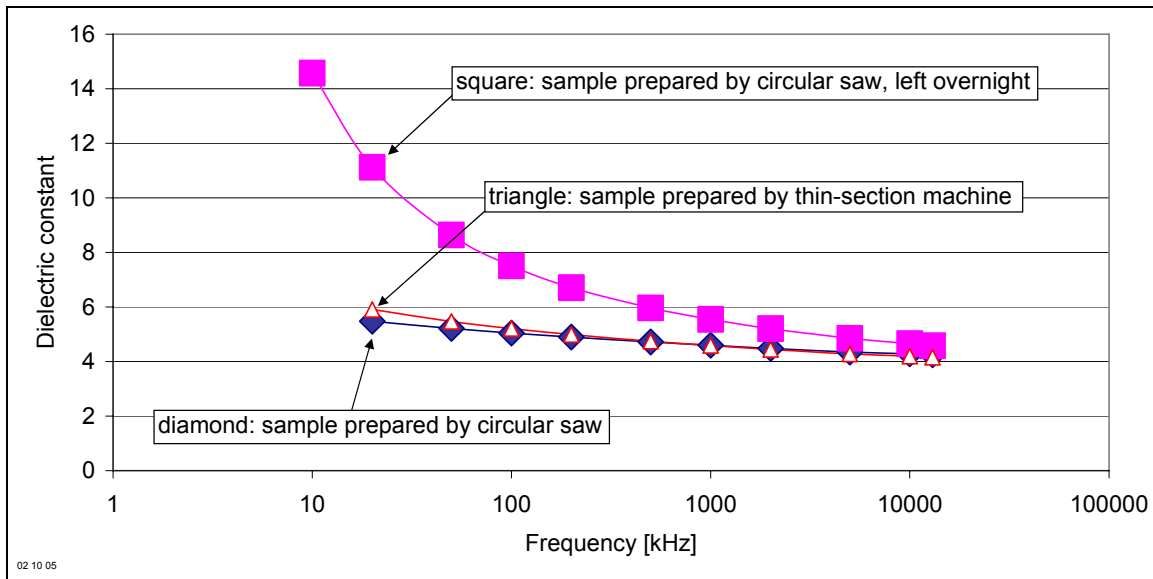


Figure 2 Dielectric constant of dry Berea samples in three different conditions corrected by linear adjustment (Method 1). Sample prepared by circular saw and thin section machine show similar results although sample surface treated by the thin section machine was smoother to the touch. Square data points showed the measured result of samples that were left overnight in open air and likely to have absorbed some moisture.

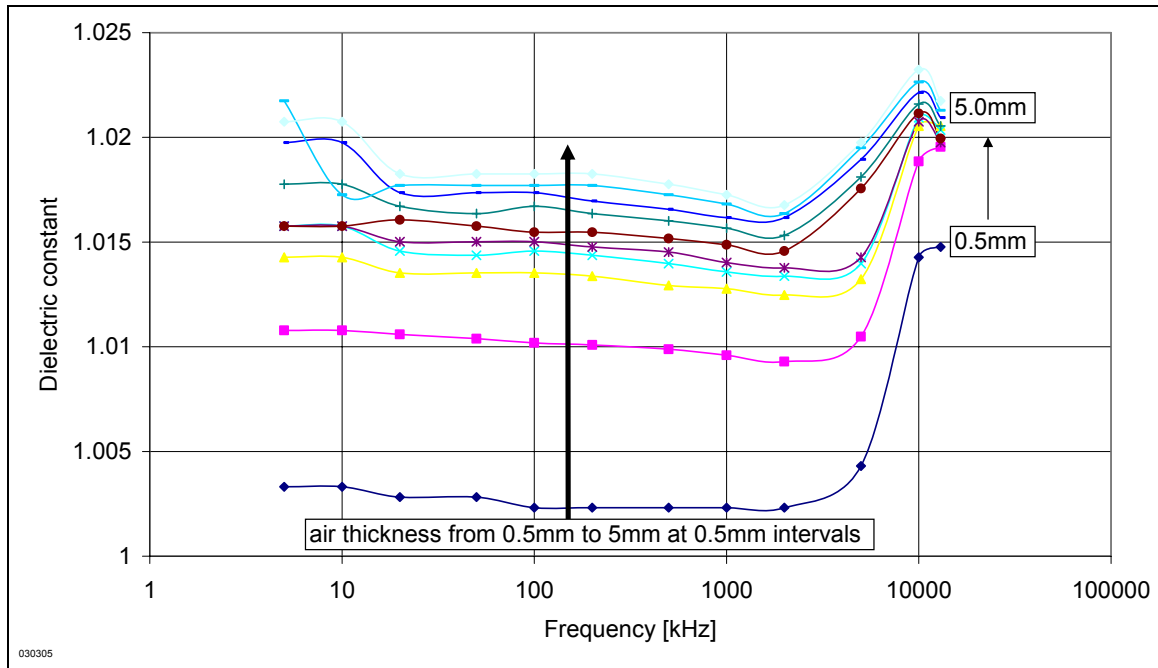


Figure 3 Air dielectric measurements by Method 1 showed a relationship of the measured value correlated with air gap thickness. The increase in dielectric constant value with increasing air gap thicknesses suggested that stray capacitances was more pronounced at larger air gap thickness.

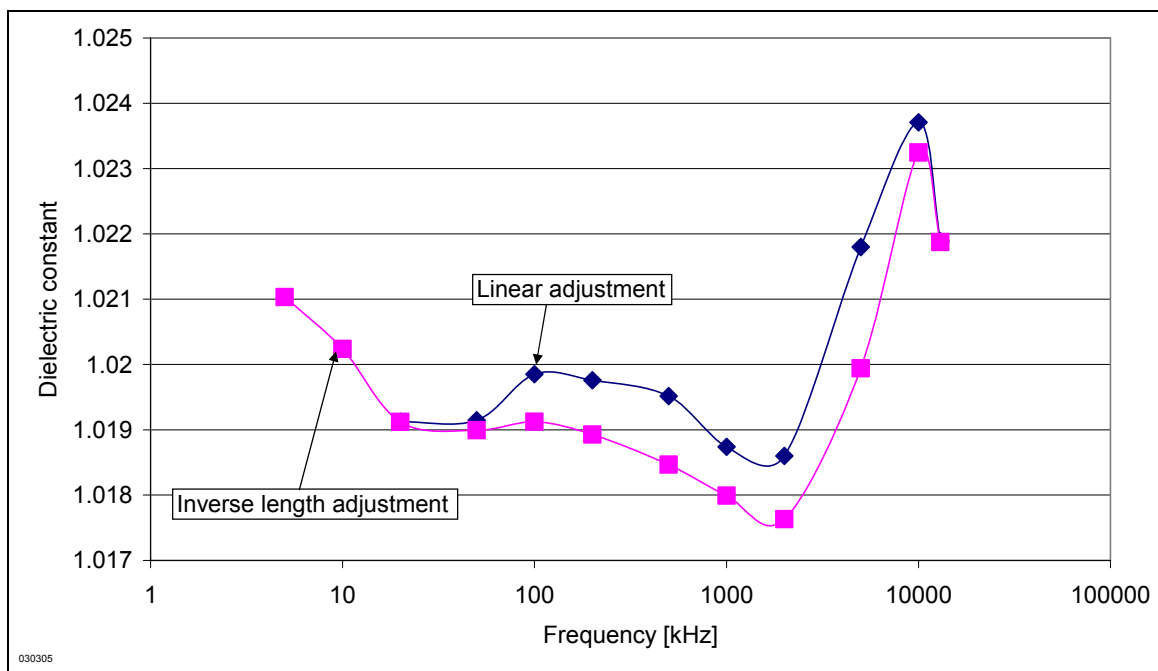


Figure 4 Air dielectric measurements by Method 1 analyzed by both linear adjustment and inverse length adjustment. Both adjustments lead to a close result. The calculated value was within 3% of the known dielectric constant of air of 1.

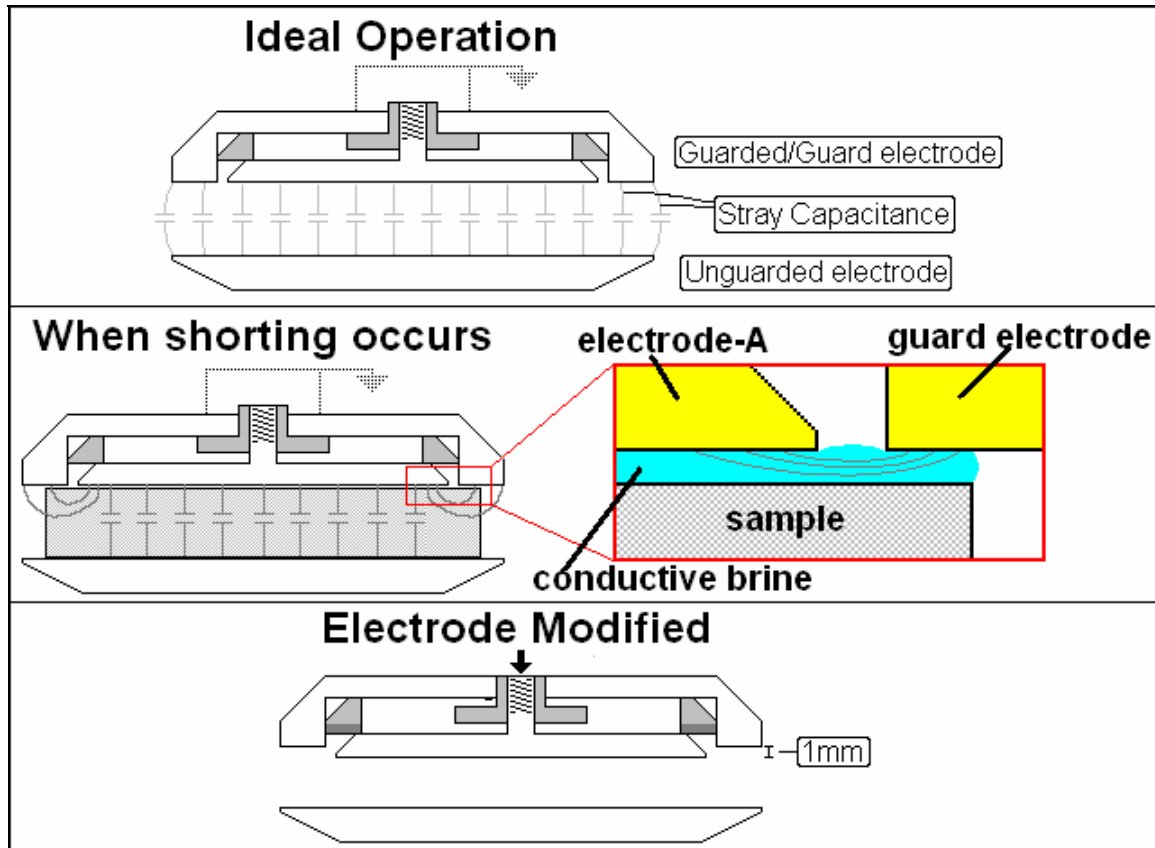


Figure 5 (Top) Ideal operation from the dielectric fixture with guard electrode properly installed. The stray capacitance is eliminated by the guard electrode. (Middle) Electrical shorting occurred when a higher conductive medium existed in between electrode-A and guard electrode. In this case, thin layer of conductive brine at the sample/electrode interface assisted in electrical shorting. (Bottom) Electrode modified by raising the guard electrode to prevent electrical shorting from electrode-A to the guard electrode.

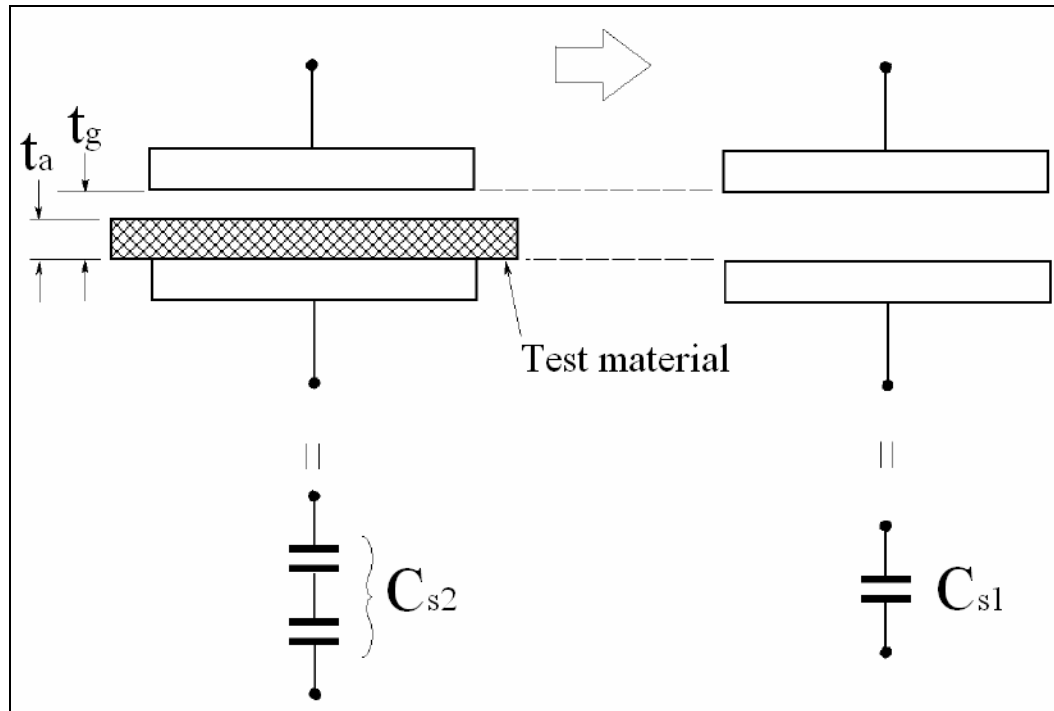


Figure 6 Non-contacting method schematic (Agilent 16451B Manual, 1989). Two measurements are required to find the two capacitances to be used in the calculation.

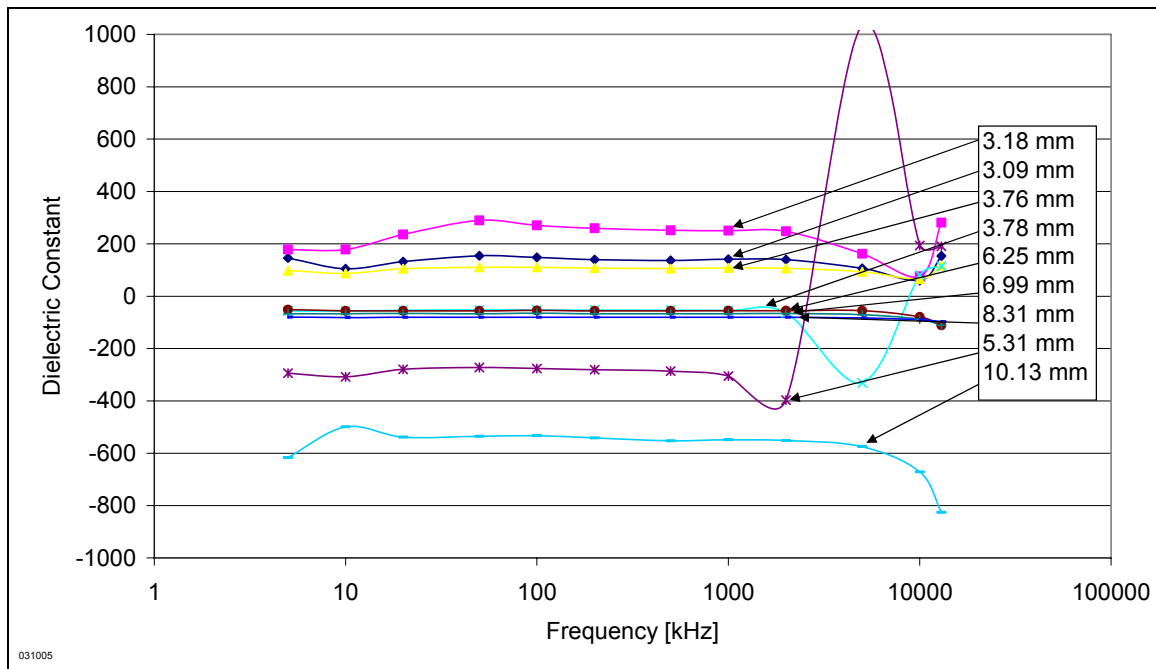


Figure 7 Dielectric constant of Berea samples fully saturated with 3% NaCl brine measured by non-contacting method (Method 1). Result showed no correlation to sample thickness and some measured values were negative. The cause was likely to be the extreme contrast of the capacitances measured with and without the sample.

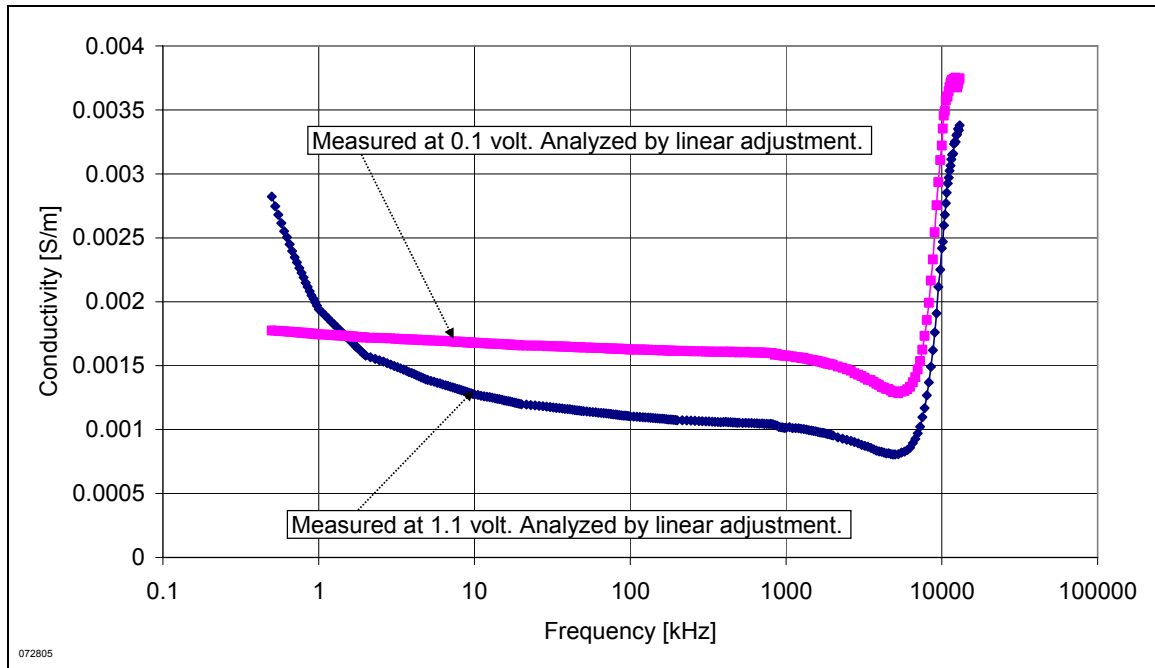


Figure 8 Conductivity of de-ionized water measured by modified dielectric fixture (Method 2). The conductivity should stay constant throughout the frequency and any deviation suggested the presence of parasitic impedances.

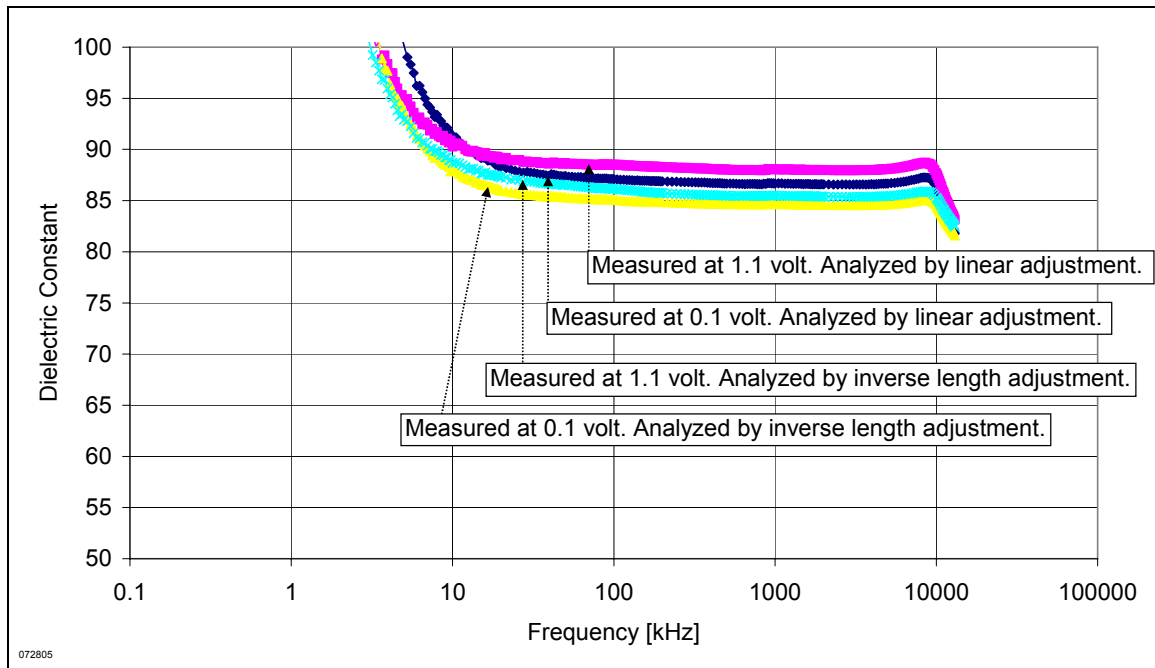


Figure 9 Dielectric constant of de-ionized water (Method 2) showed dielectric enhancement below 10 kHz. The change in applied electrode voltage does not effect this measurement. The deviation at 10 MHz suggested a linkage to the conductivity of the same frequency in Figure 8.

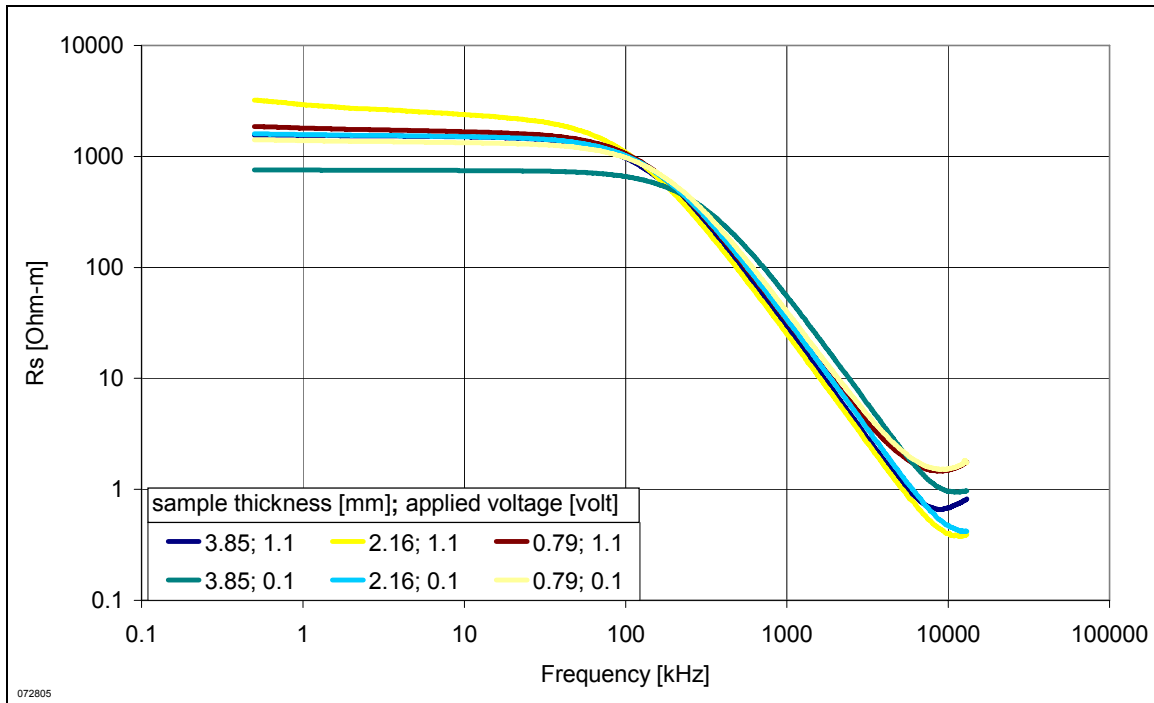


Figure 10 (Raw data) Resistivity of a series equivalent circuit. De-ionized water measurement from Figure 8 and Figure 9.

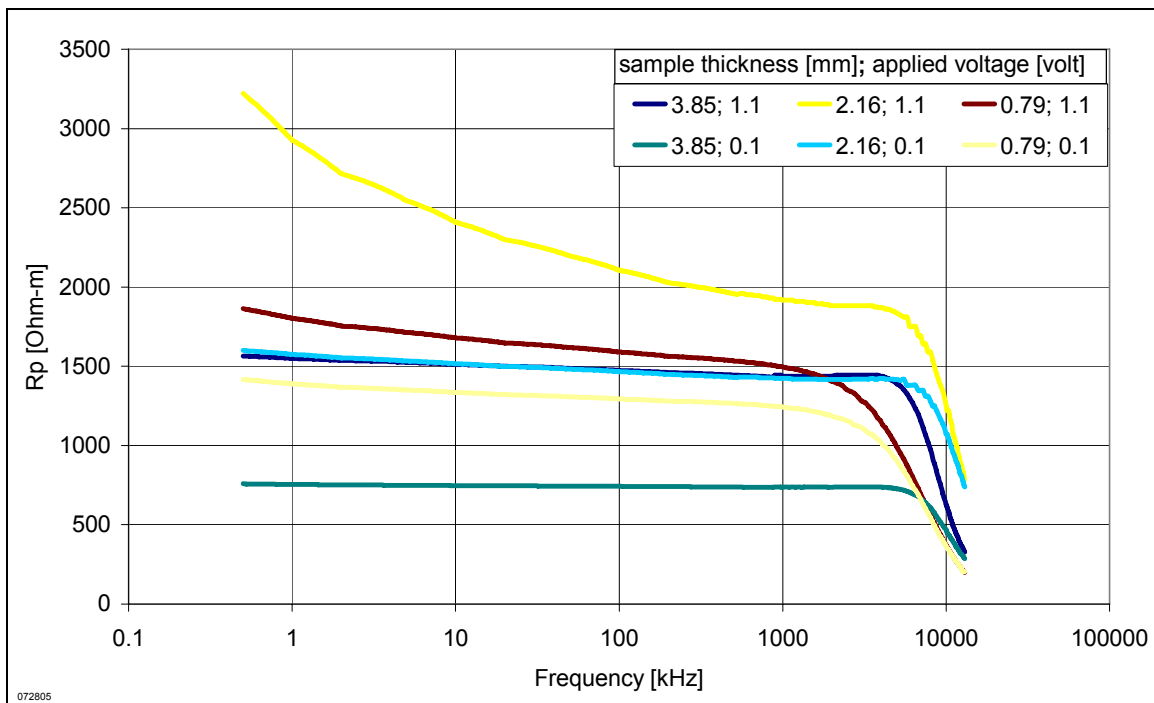


Figure 11 (Raw data) Resistivity of a parallel equivalent circuit. De-ionized water measurement from Figure 8 and Figure 9.

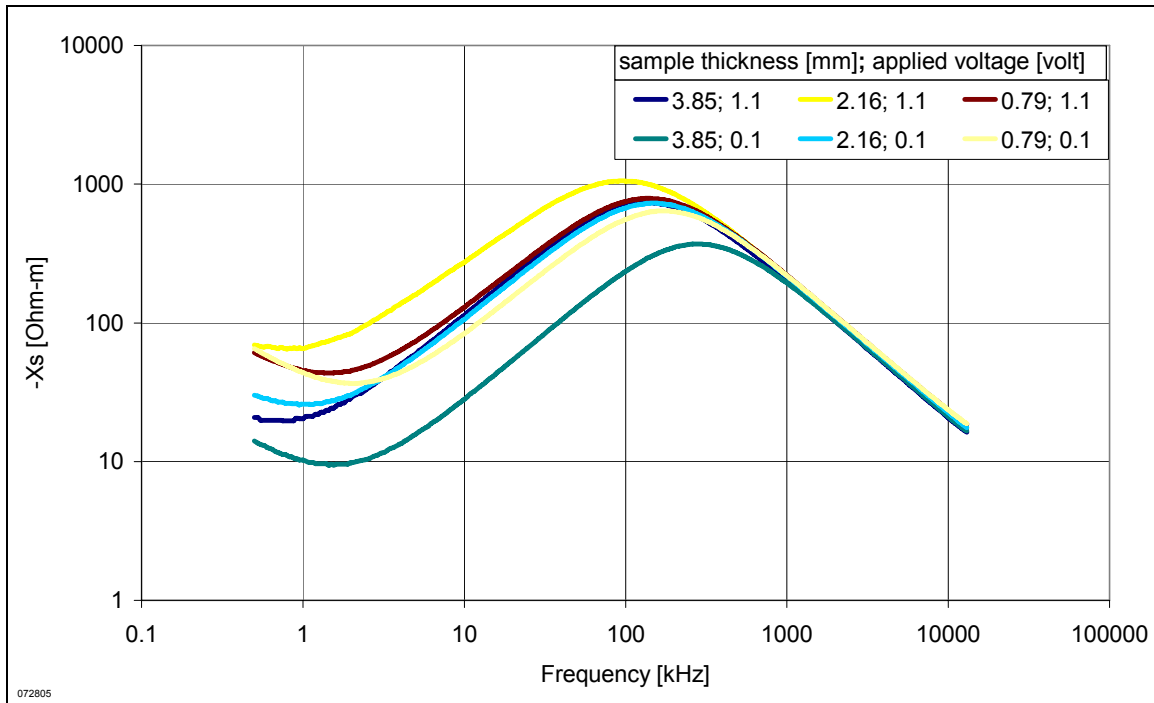


Figure 12 (Raw data) Negative reactance-m of a series equivalent circuit. De-ionized water measurement from Figure 8 and Figure 9.

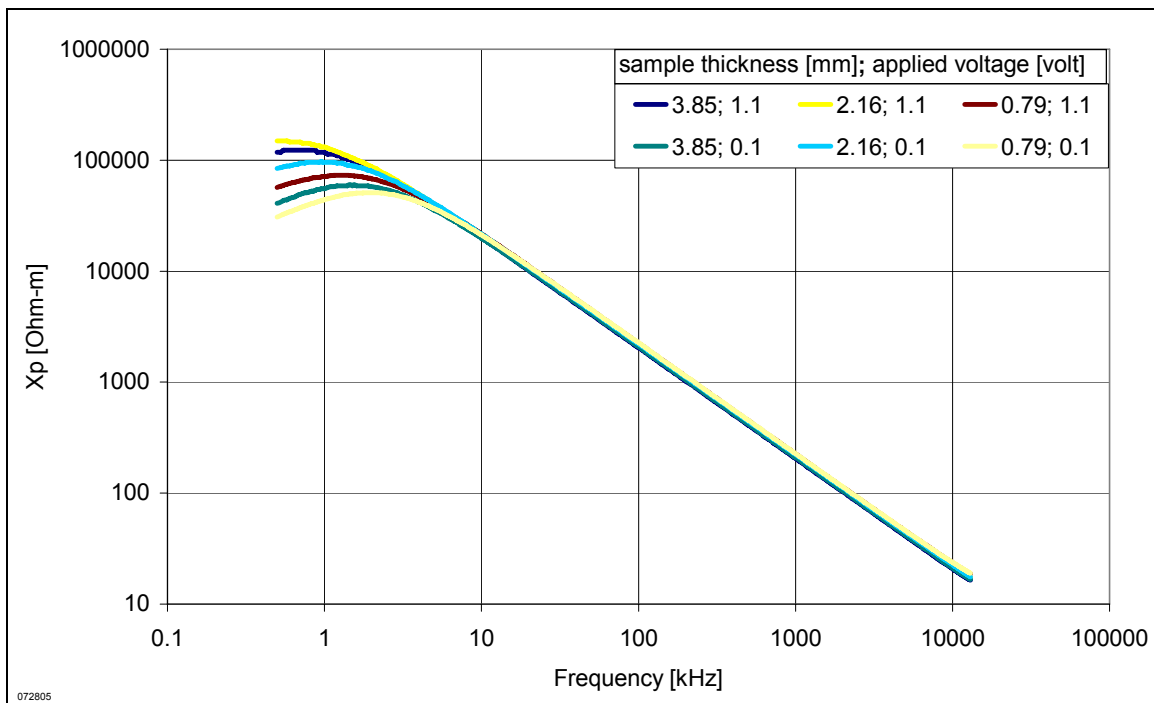


Figure 13 (Raw data) Reactance-m of a parallel equivalent circuit. De-ionized water measurement from Figure 8 and Figure 9.

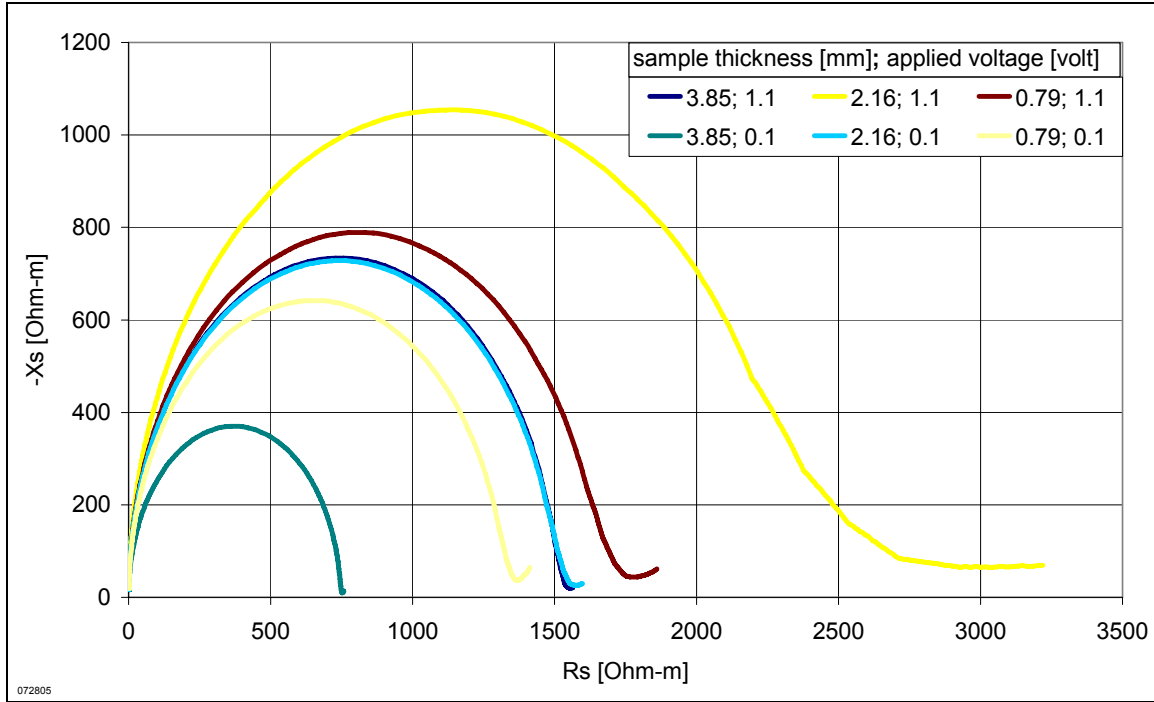


Figure 14 Argand plot of de-ionized water measurement from Figure 8 and Figure 9.

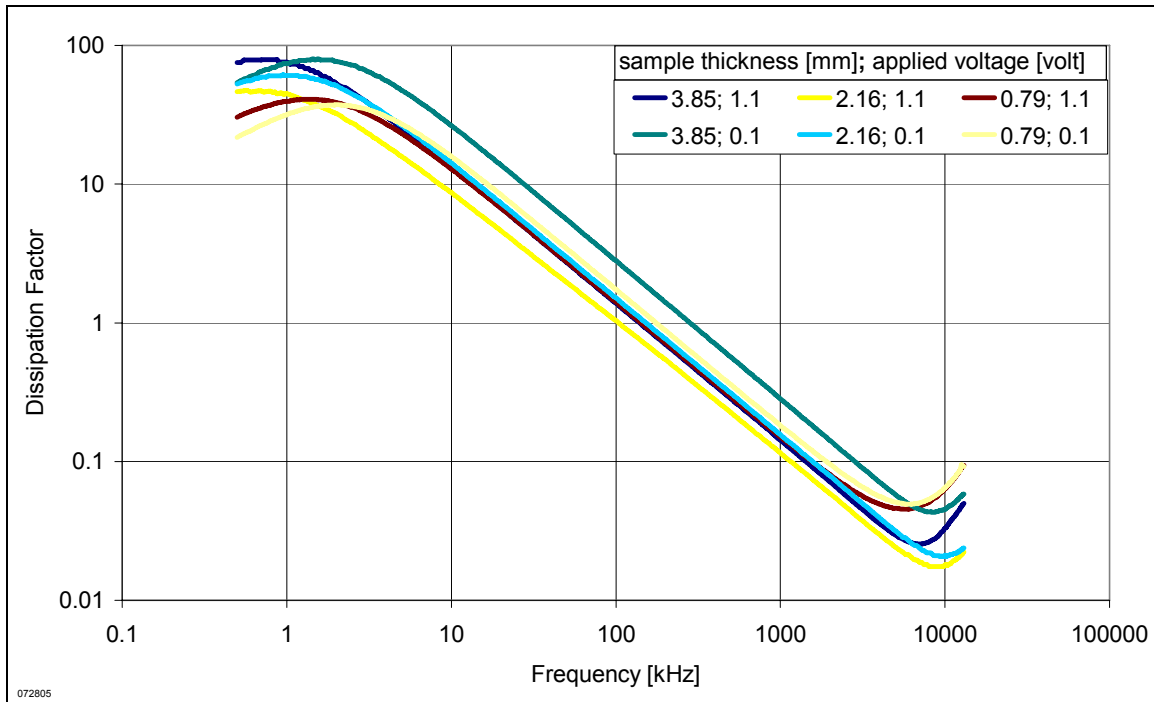


Figure 15 Dissipation factor of de-ionized water measurement from Figure 8 and Figure 9.

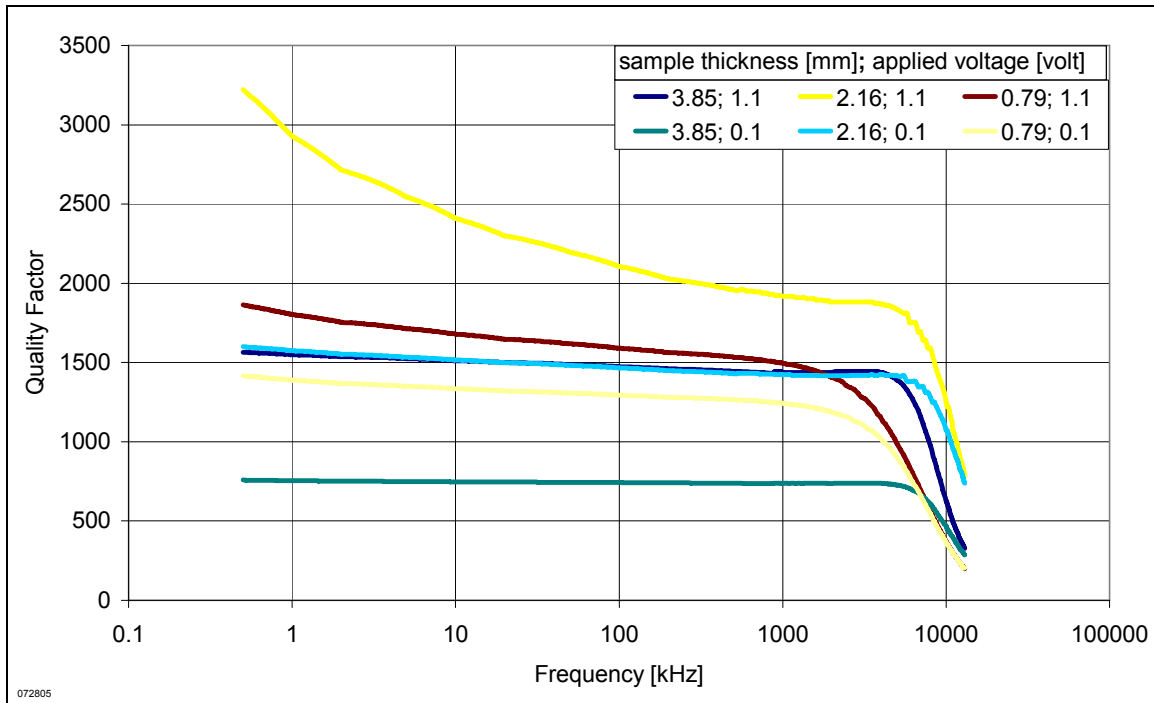


Figure 16 Quality factor of de-ionized water measurement from Figure 8 and Figure 9.

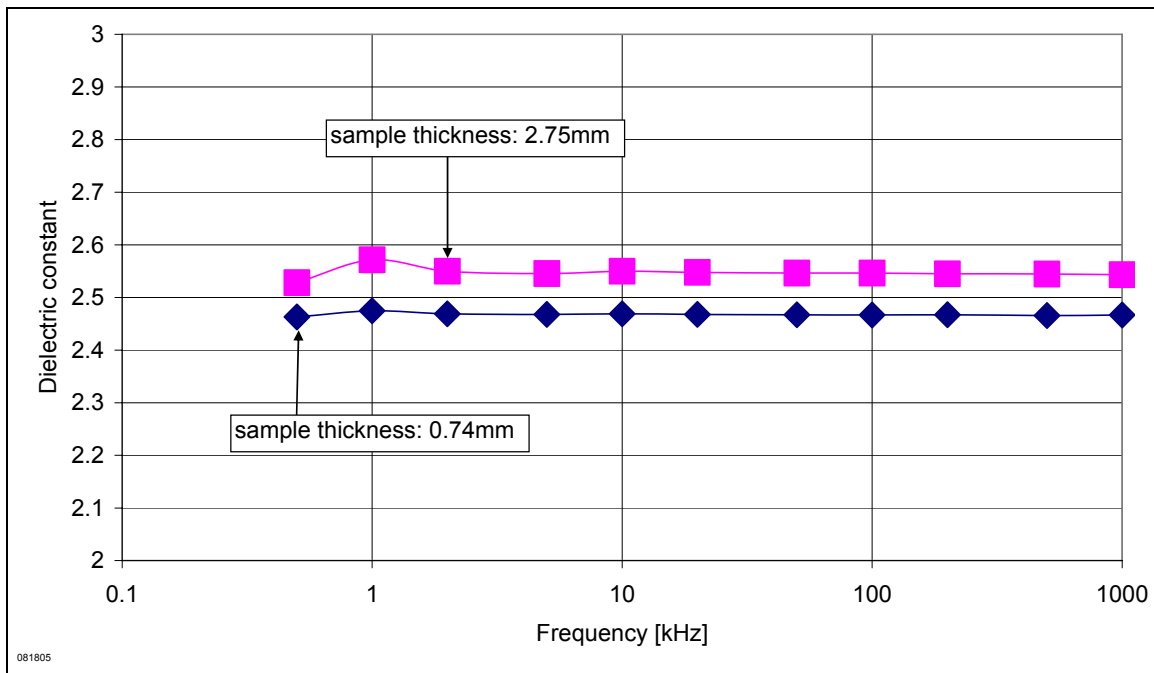


Figure 17 Dielectric constant of toluene (methylbenzene) in single measurements (Method 2). Toluene has a known dielectric constant of 2.4. Toluene is an insulator and therefore, no dielectric enhancement is shown.

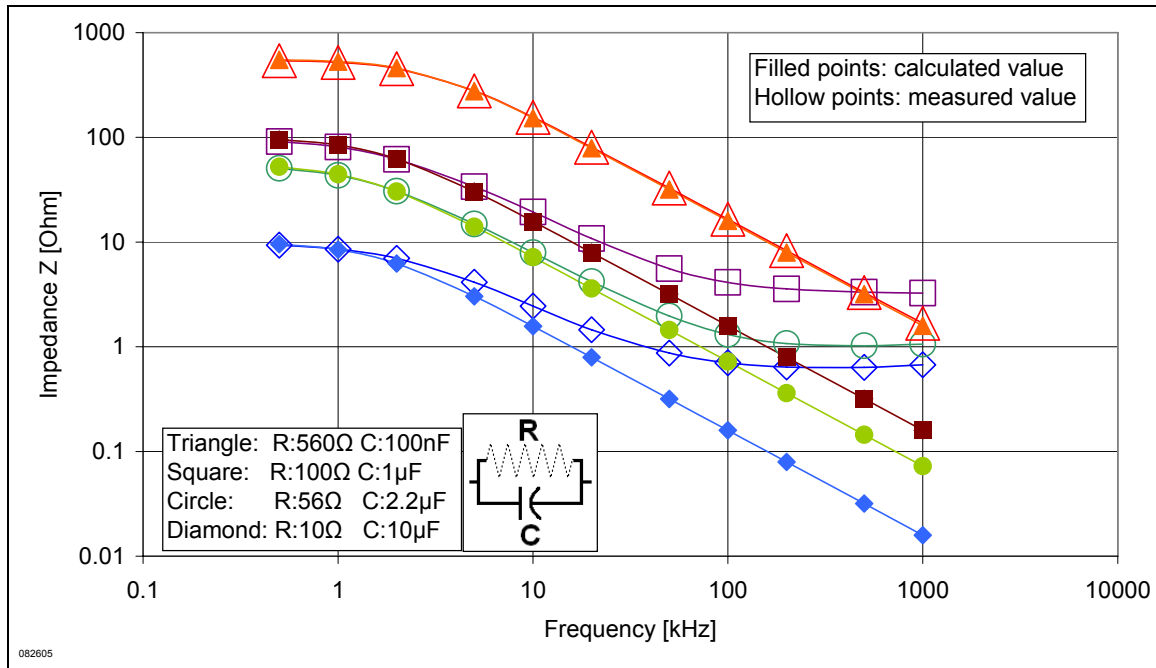


Figure 18 Measurement on electrical circuit of parallel capacitor and resistor connected to the electrode fixture without the electrodes (Method 2). Only the triangular data points matched the calculated values. The mismatch caused by the limitations of the capacitor at high frequency and was not caused by the fixture or 4192A.

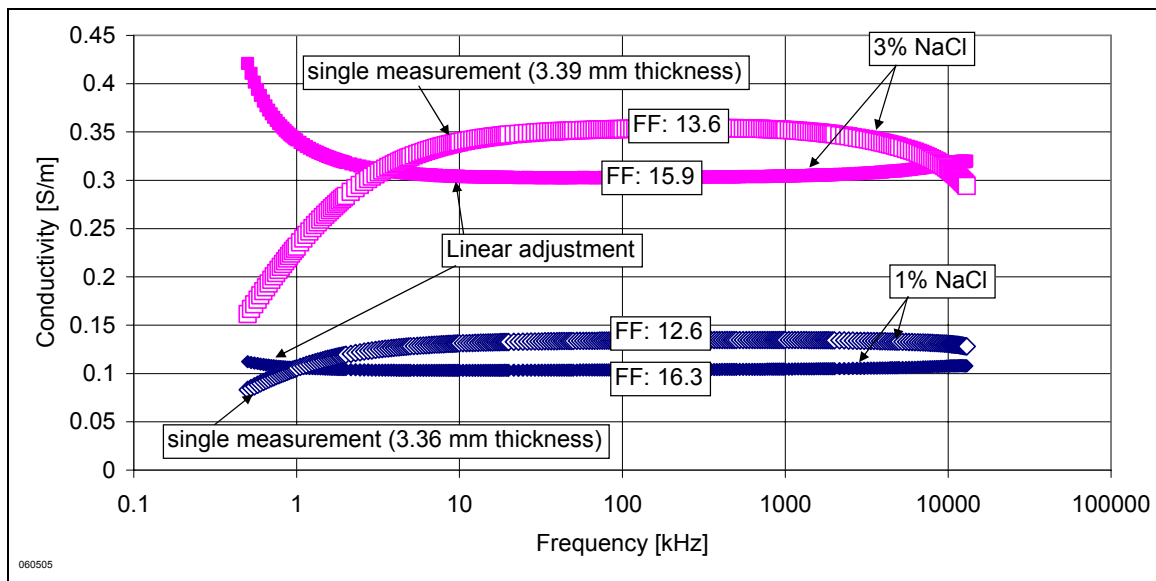


Figure 19 Conductivity measurement by Method 2 on Berea samples fully saturated with 1% and 3% brine. The decrease in conductivity at the low frequency in single measurement increases after linear adjustment was performed. This conductivity change occurs only on measurements with coffee filter and was likely to be caused by parasitic impedances. The formation factor (FF) suggested the adjusted results were inaccurate.

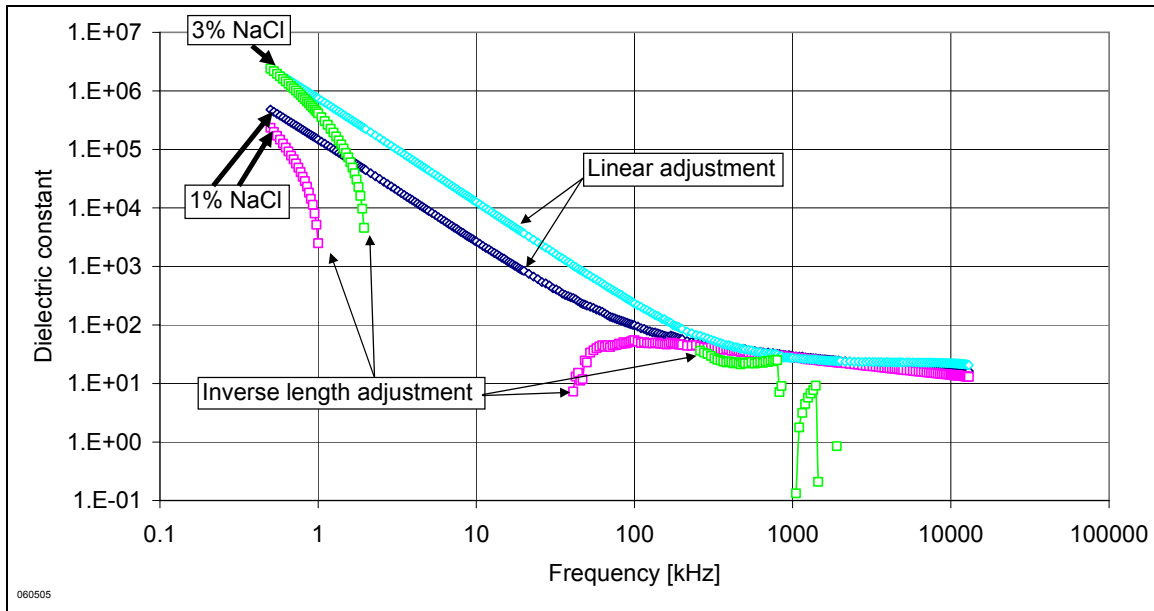


Figure 20 Dielectric constant measured by method 2 on Berea samples fully saturated with 1% and 3% brine. Dielectric enhancement occurred below 1 MHz. Inverse length adjustment showed negative results and suggested the presence of stray capacitance in the measurement.

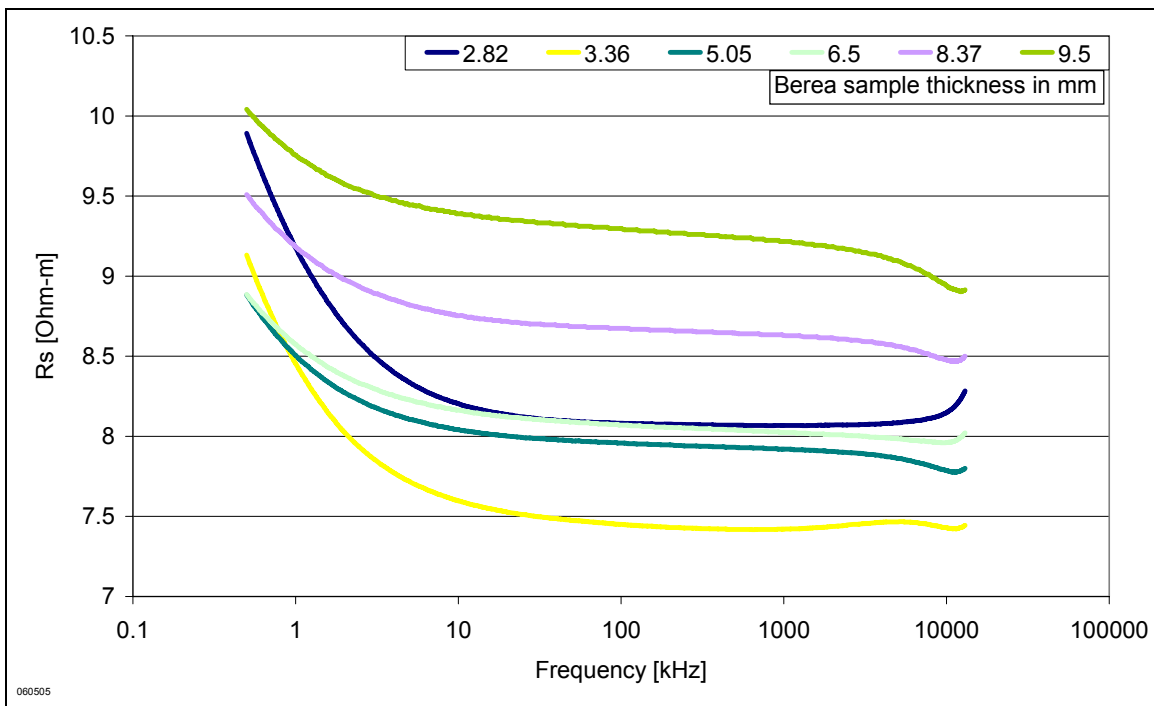


Figure 21 (Raw data) Resistivity of a series equivalent circuit. Berea in 1% brine from Figure 19 and Figure 20.

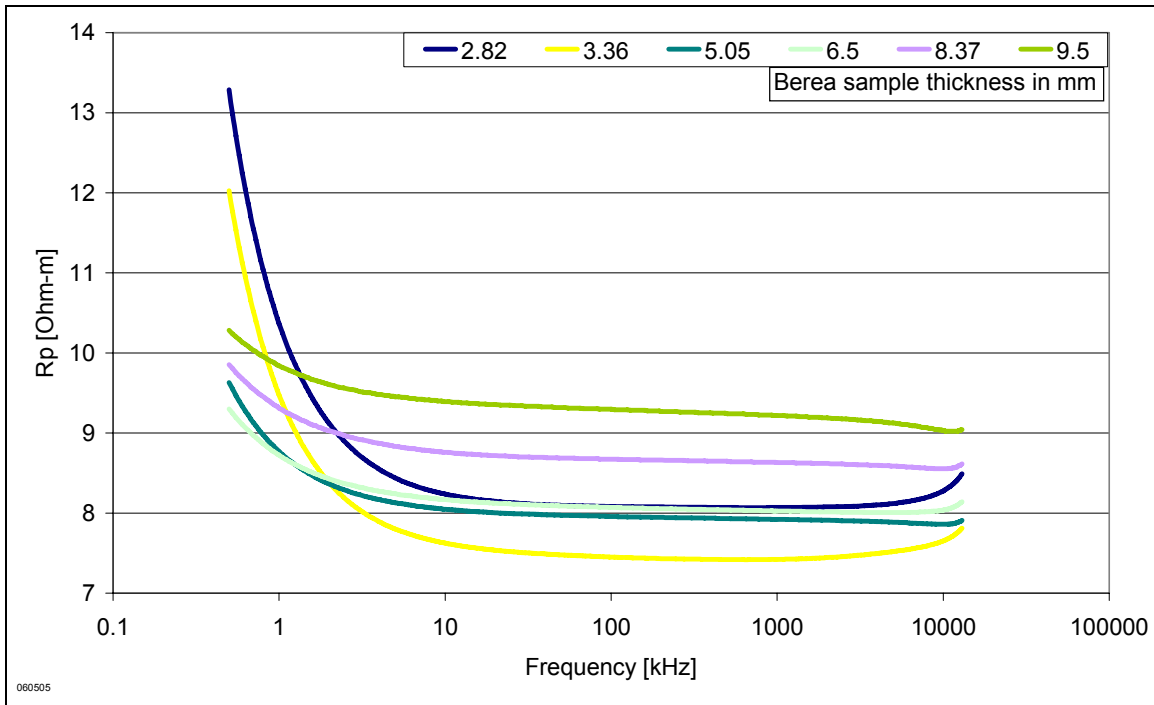


Figure 22 (Raw data) Resistivity of a parallel equivalent circuit. Berea in 1% brine from Figure 19 and Figure 20.

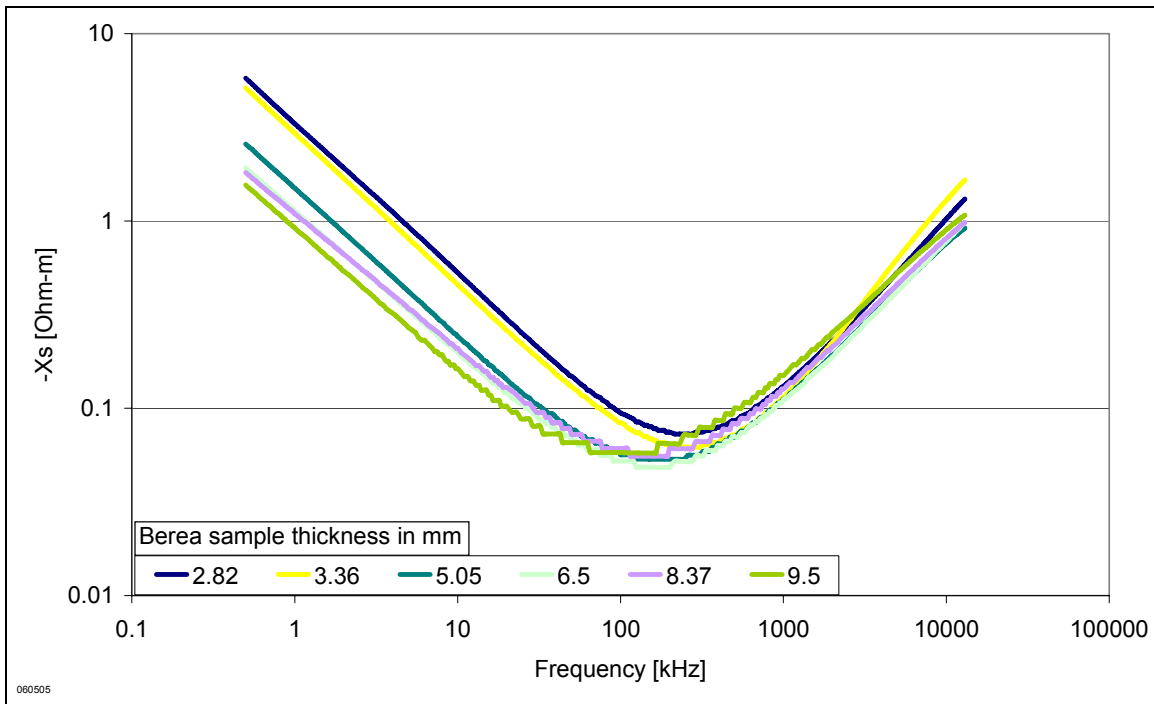


Figure 23 (Raw data) Negative reactance-m of a series equivalent circuit. Berea in 1% brine from Figure 19 and Figure 20.

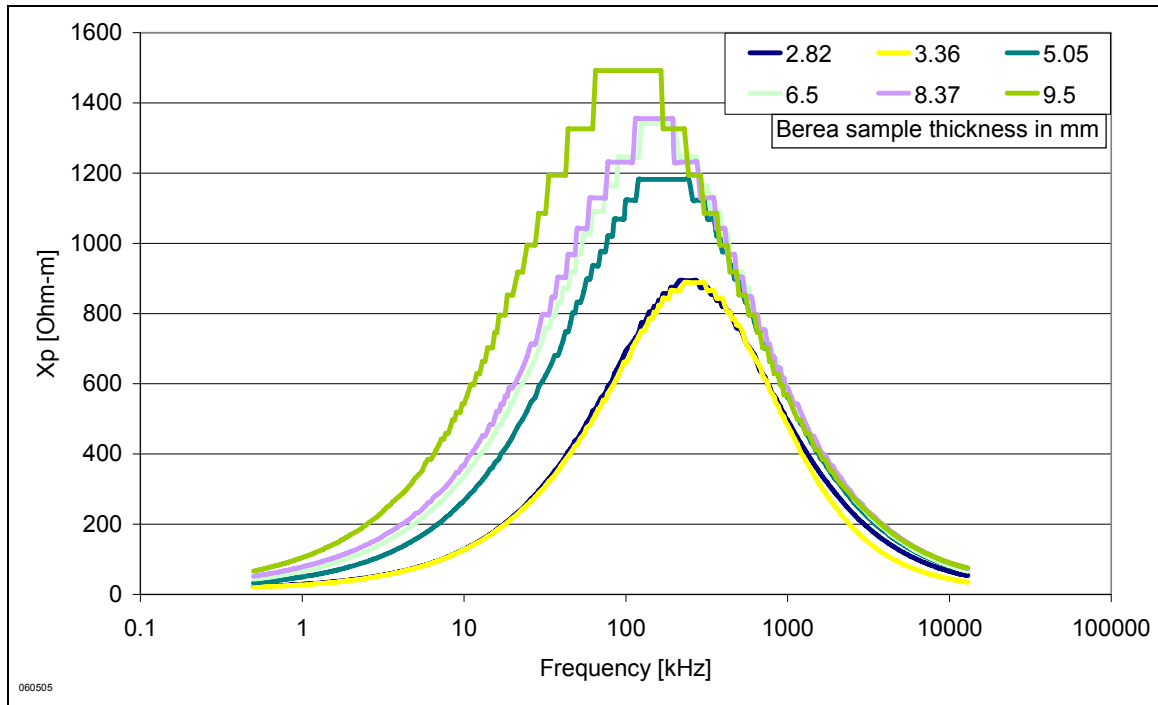


Figure 24 (Raw data) Reactance-m of a parallel equivalent circuit. Bera in 1% brine from Figure 19 and Figure 20.

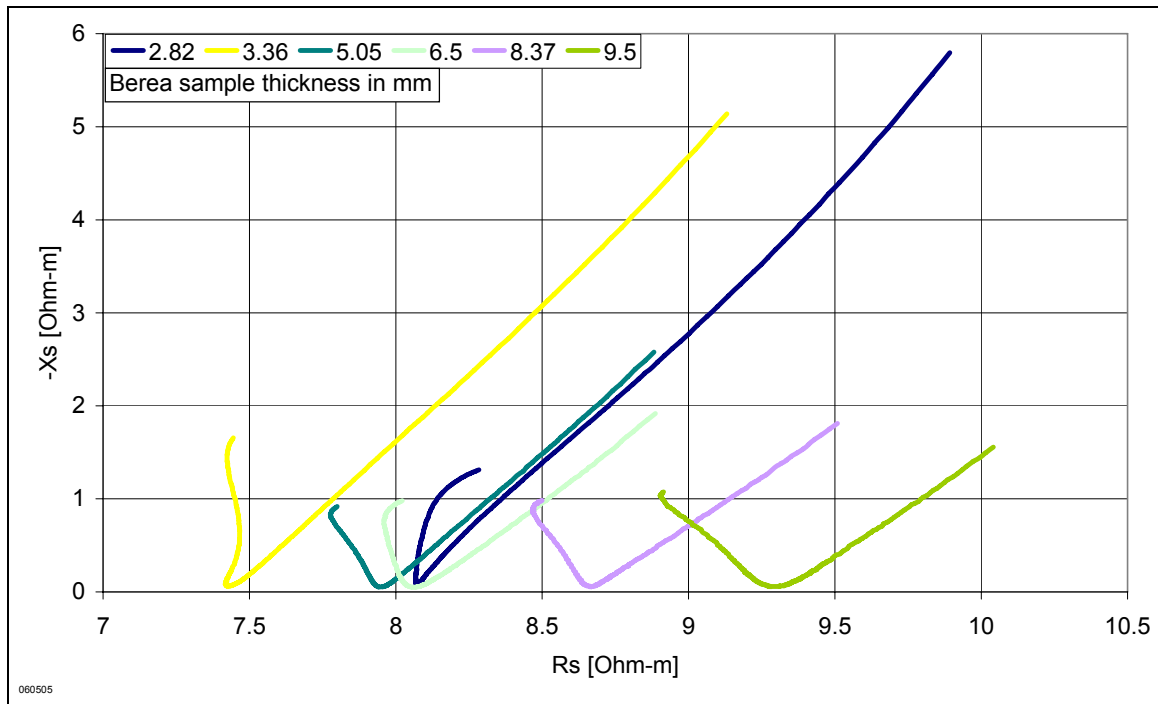


Figure 25 Argand plot of Bera in 1% brine from Figure 19 and Figure 20.

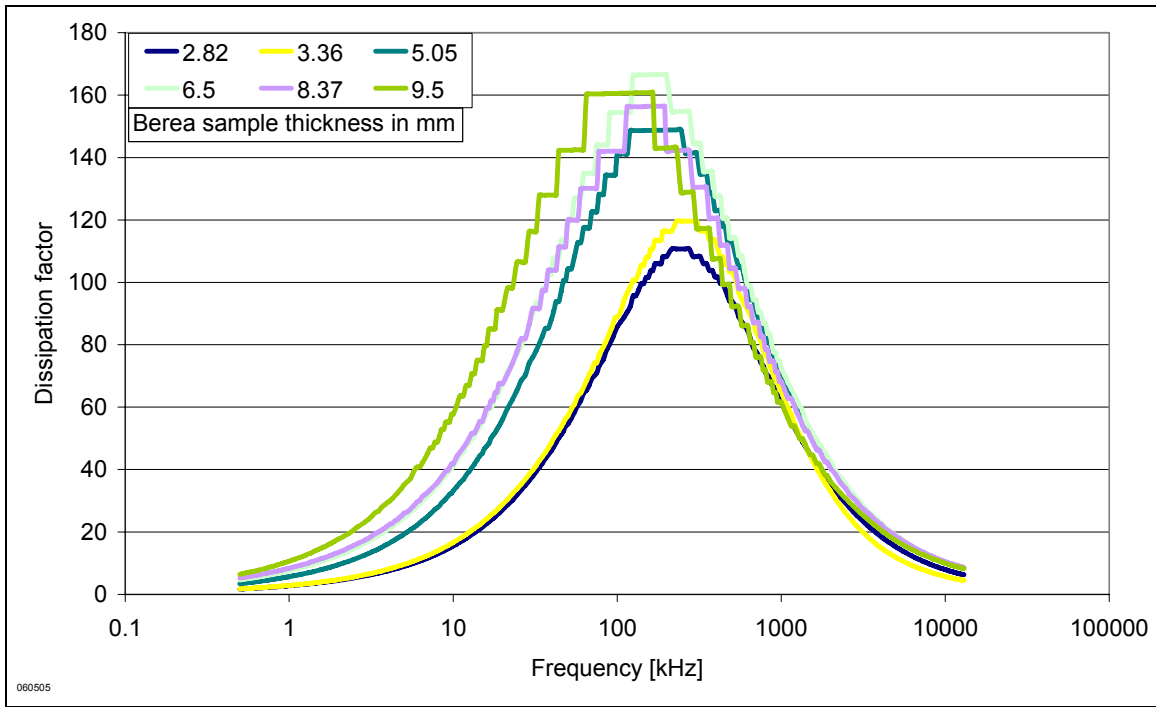


Figure 26 Dissipation factor of Berea in 1% brine from Figure 19 and Figure 20.

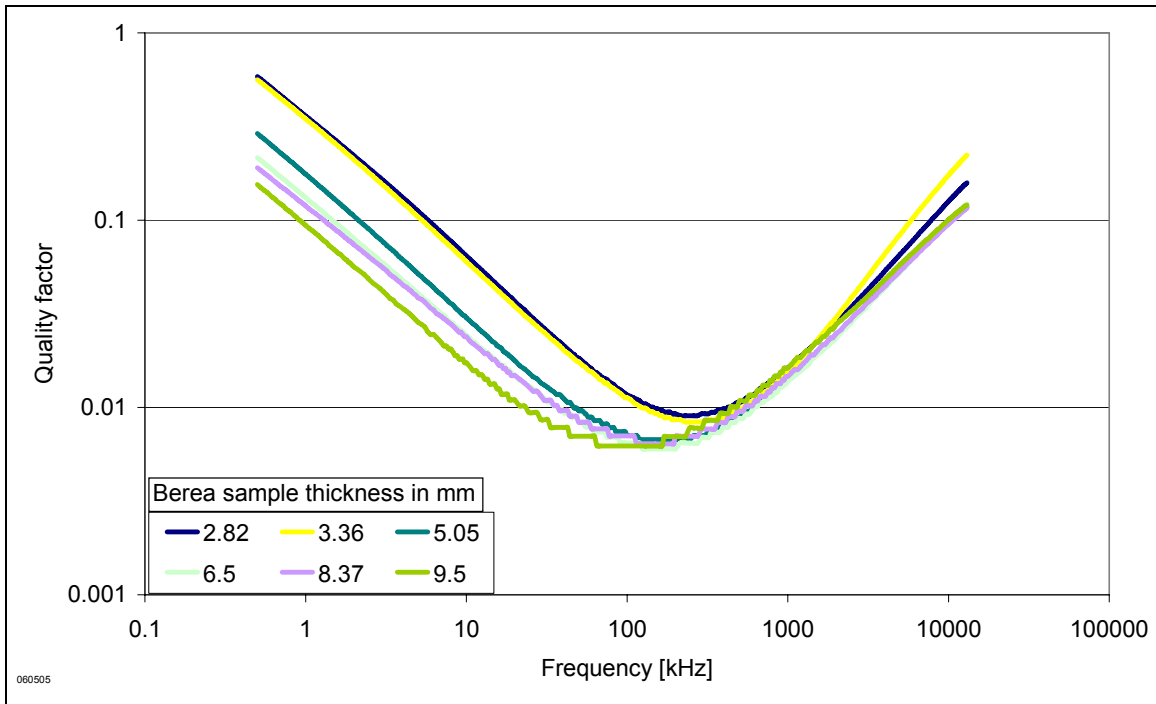


Figure 27 Quality factor of Berea in 1% brine from Figure 19 and Figure 20.

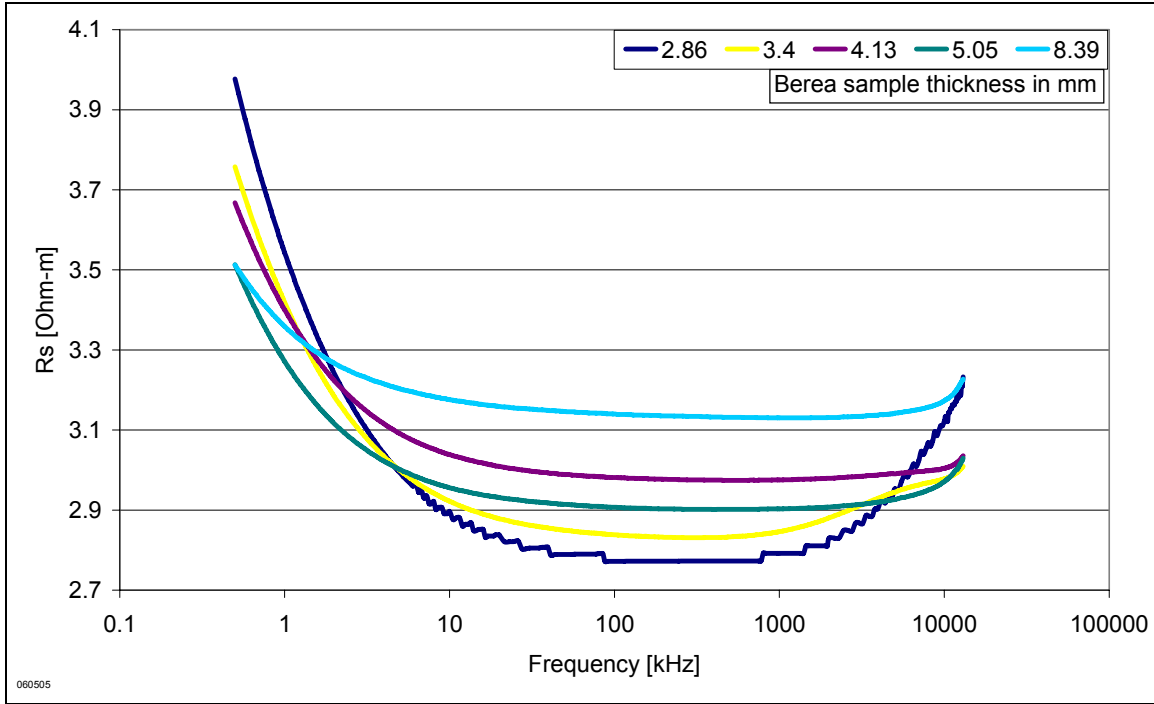


Figure 28 (Raw data) Resistivity of a series equivalent circuit. Berea in 3% brine from Figure 19 and Figure 20.

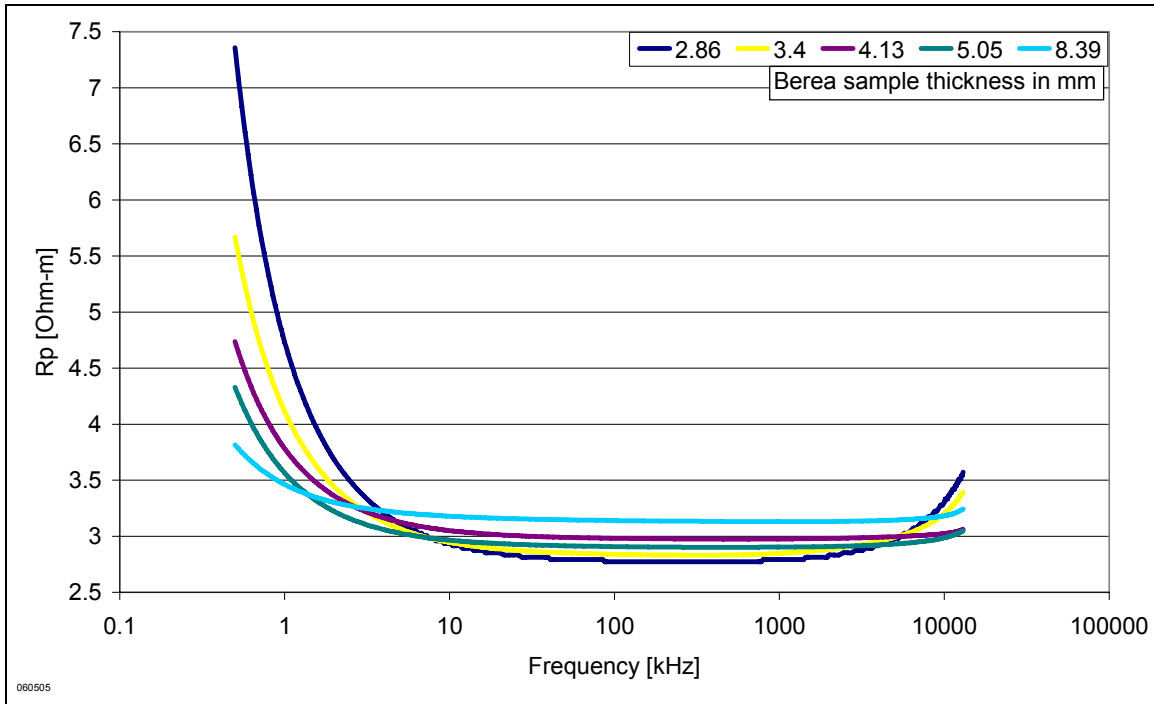


Figure 29 (Raw data) Resistivity of a parallel equivalent circuit. Berea in 3% brine from Figure 19 and Figure 20.

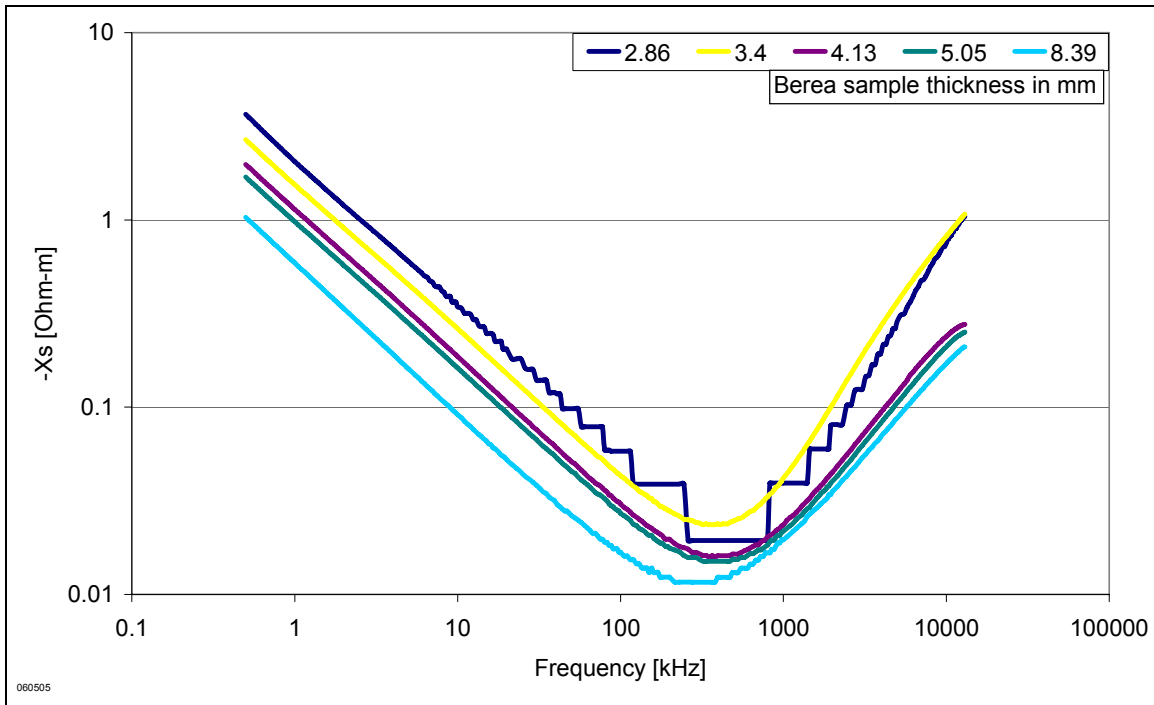


Figure 30 (Raw data) Negative reactance-m of a series equivalent circuit. Berea in 3% brine from Figure 19 and Figure 20.

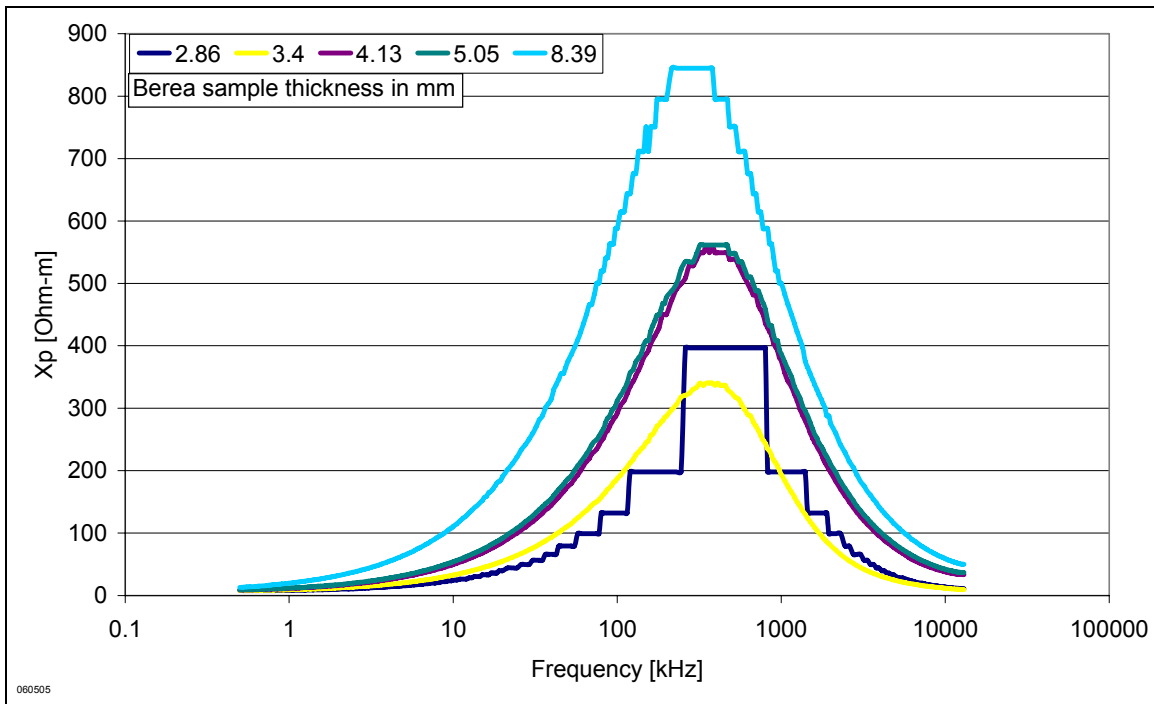


Figure 31 (Raw data) Reactance-m of a parallel equivalent circuit. Berea in 3% brine from Figure 19 and Figure 20.

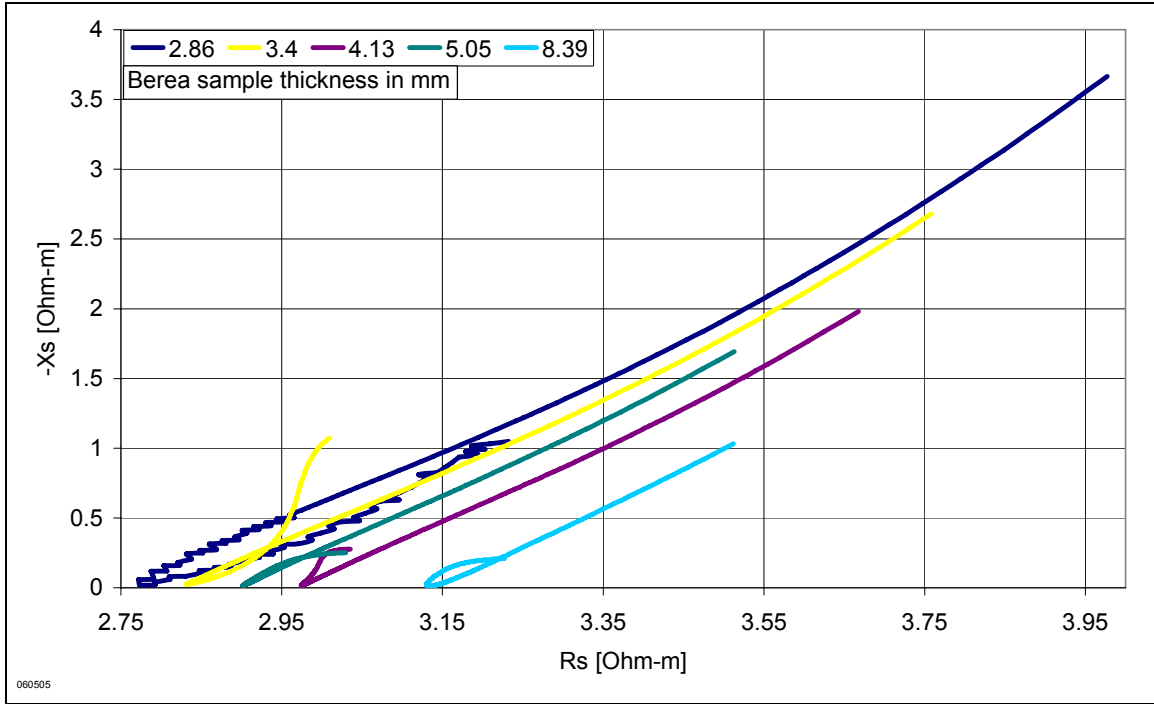


Figure 32 Argand plot of Berea in 3% brine from Figure 19 and Figure 20.

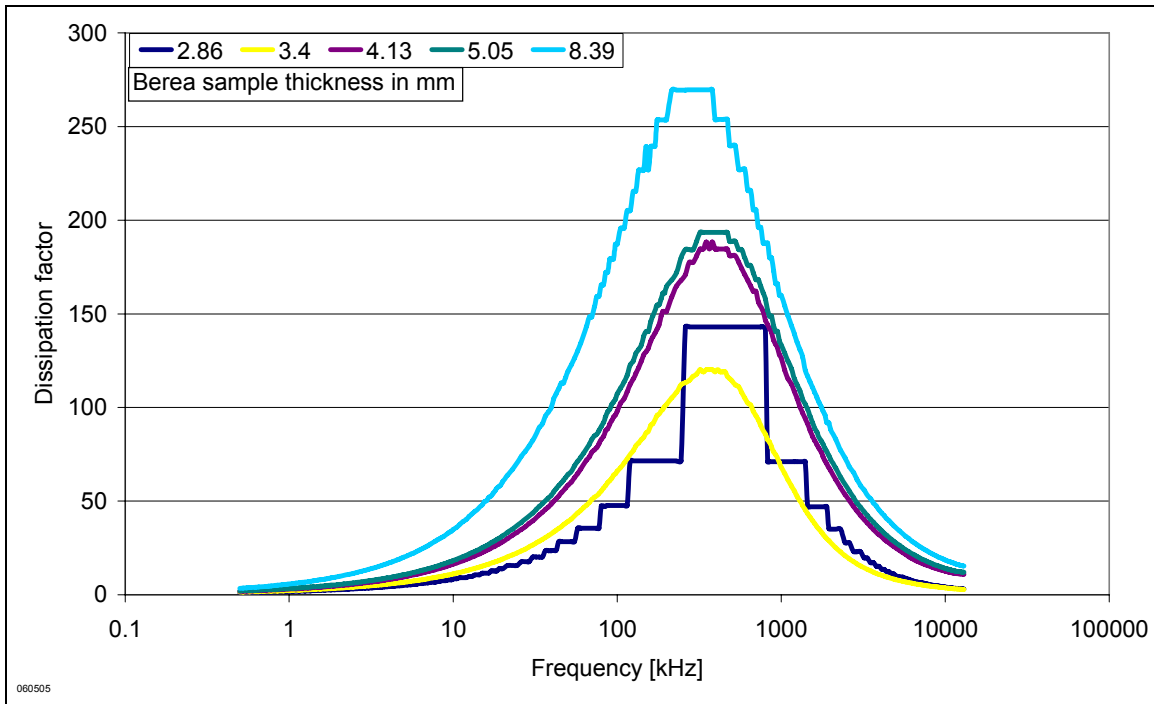


Figure 33 Dissipation factor of Berea in 3% brine from Figure 19 and Figure 20.

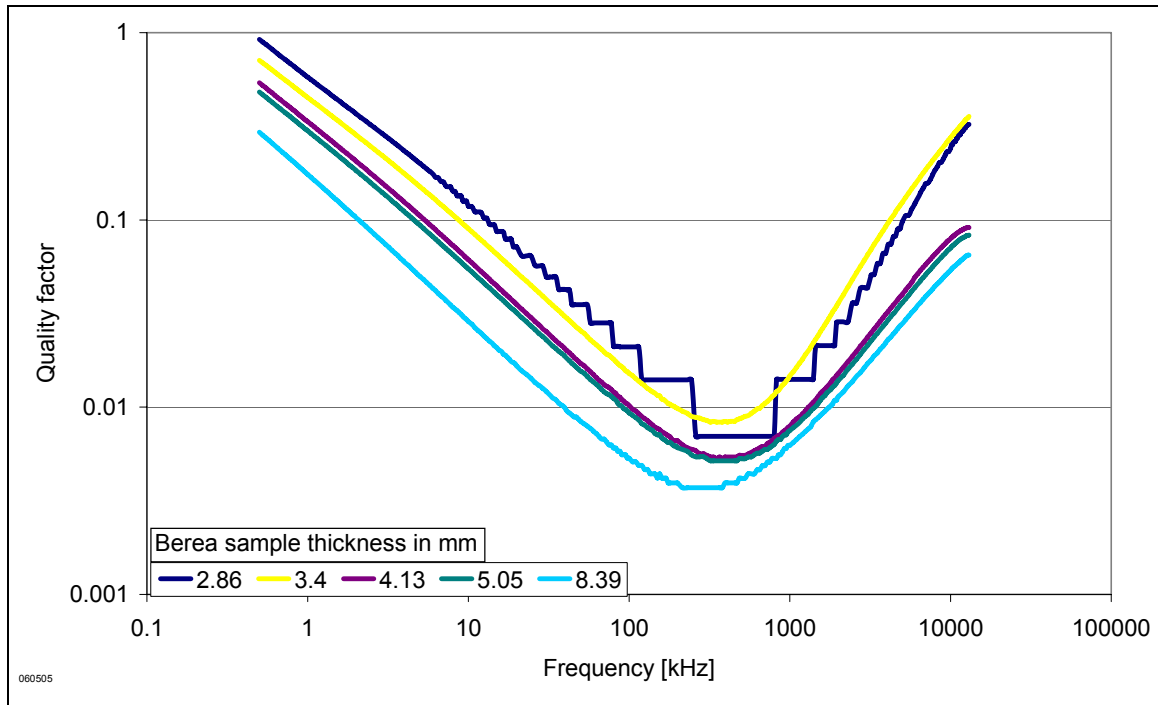


Figure 34 Quality factor of Berea in 3% brine from Figure 19 and Figure 20.

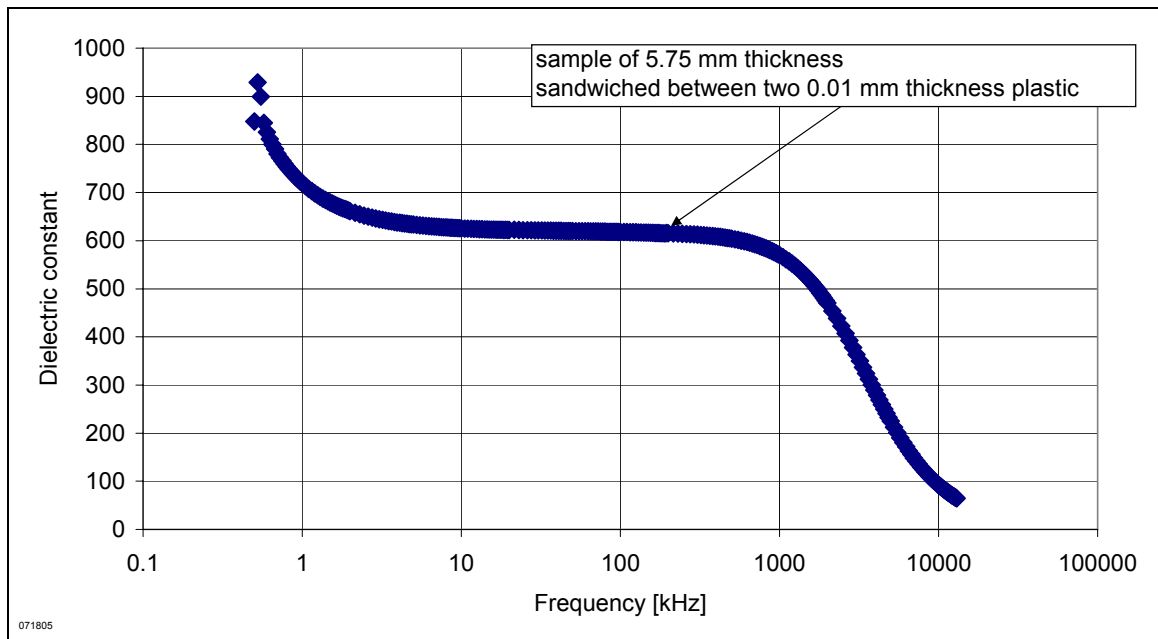


Figure 35 Dielectric constant of Berea sample fully saturated with 1% NaCl brine measured with plastic wrap placed between the sample and the electrodes (Method 2). Dielectric constant of 600 was very unlikely and the calculated result was very sensitive to the plastic wrap thicknesses. Notice the dispersions in the kHz and MHz frequency.

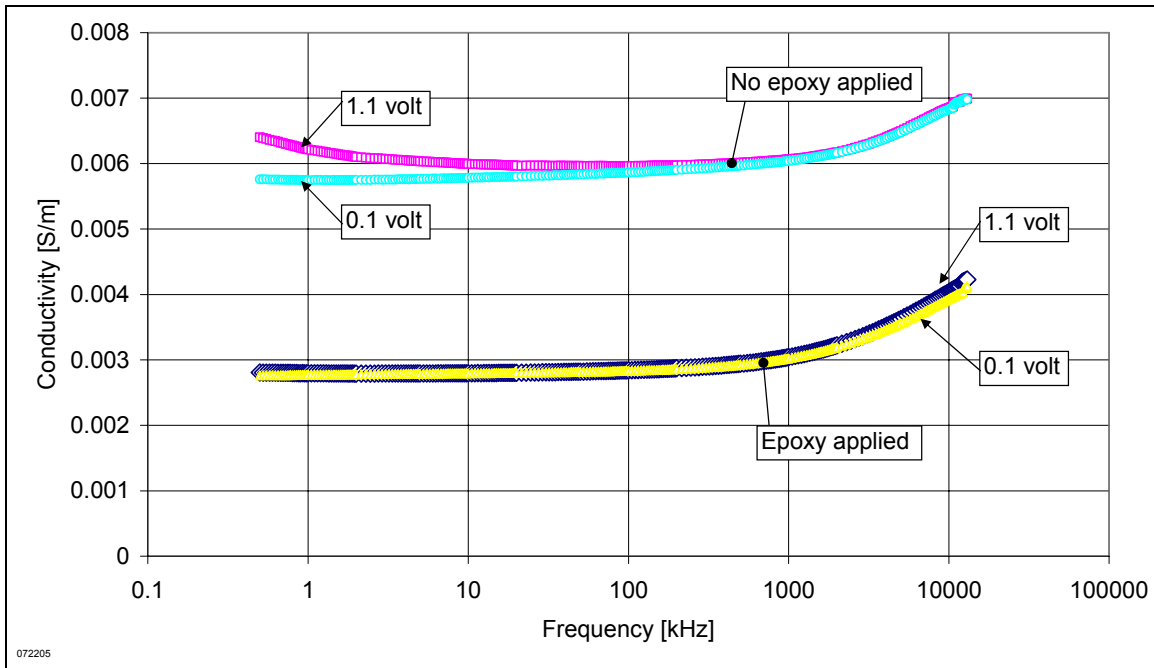


Figure 36 Conductivity of de-ionized water saturated Berea samples corrected by linear adjustment (Method 2). The applied voltage differences does not affect greatly to measurement outcome. Epoxy used on the sample caused the conductivity to decrease.

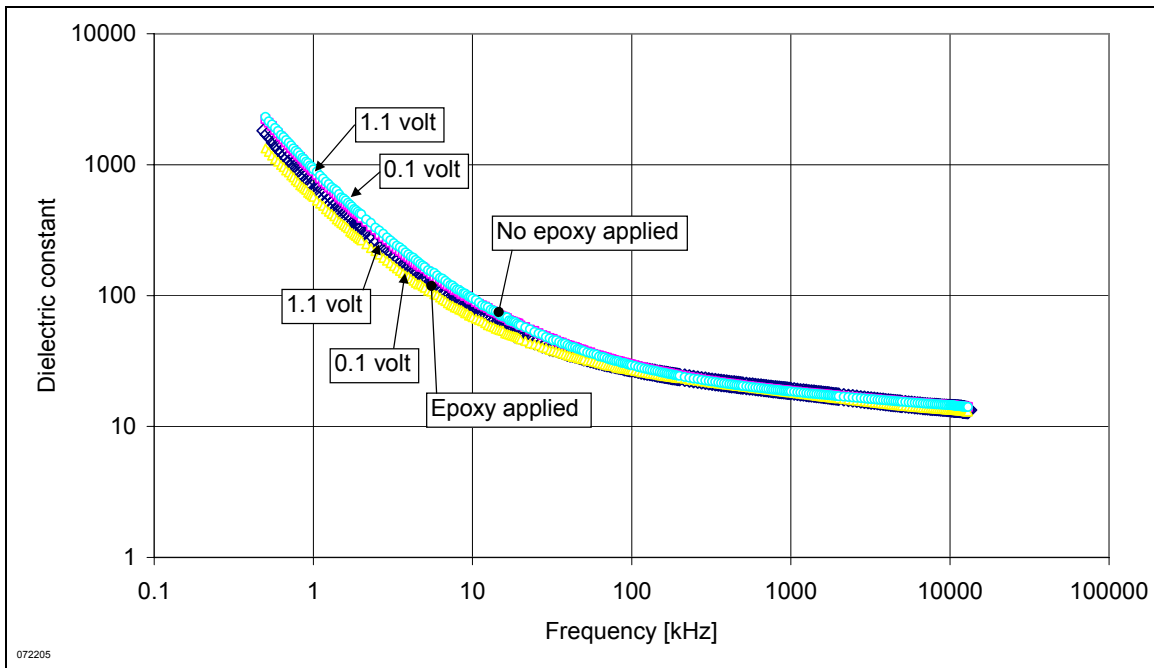


Figure 37 Dielectric constant of de-ionized water saturated Berea samples corrected by linear adjustment (Method 2). The change in applied voltage and application of Epoxy did not change the result after corrections by linear adjustment. Enhancement occurred at lower frequency at a slope of -1 to -1.5 on a log-log scale.

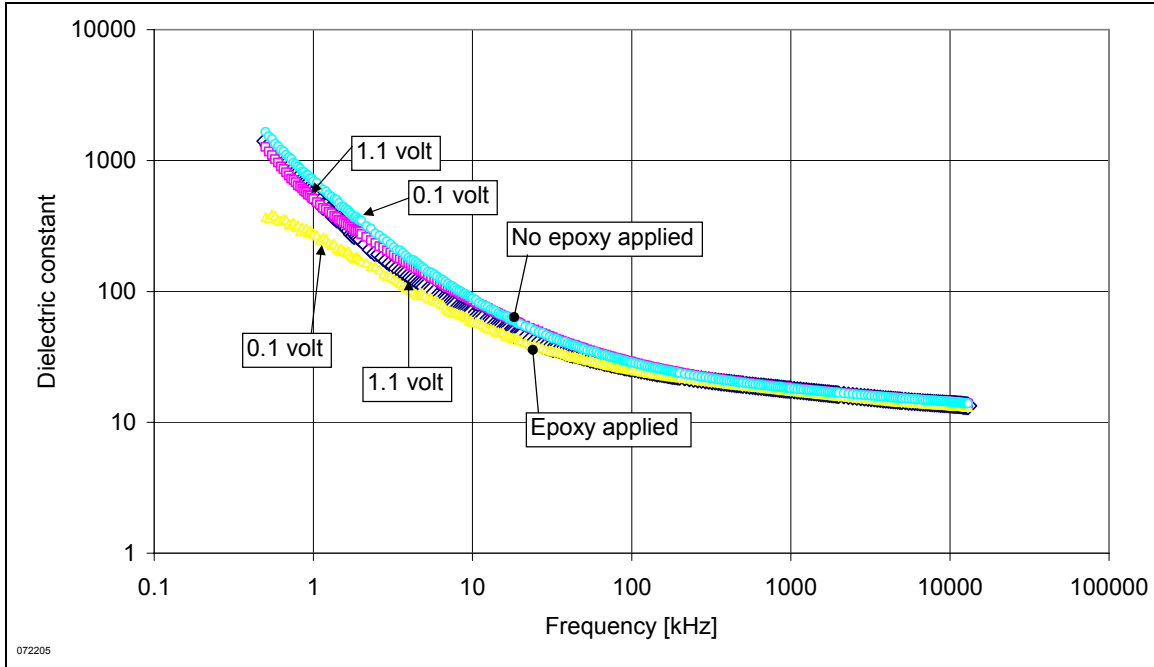


Figure 38 Dielectric constant of de-ionized water saturated Berea samples corrected by inverse length adjustment (Method 2). The results are similar to the ones shown in Figure 37.

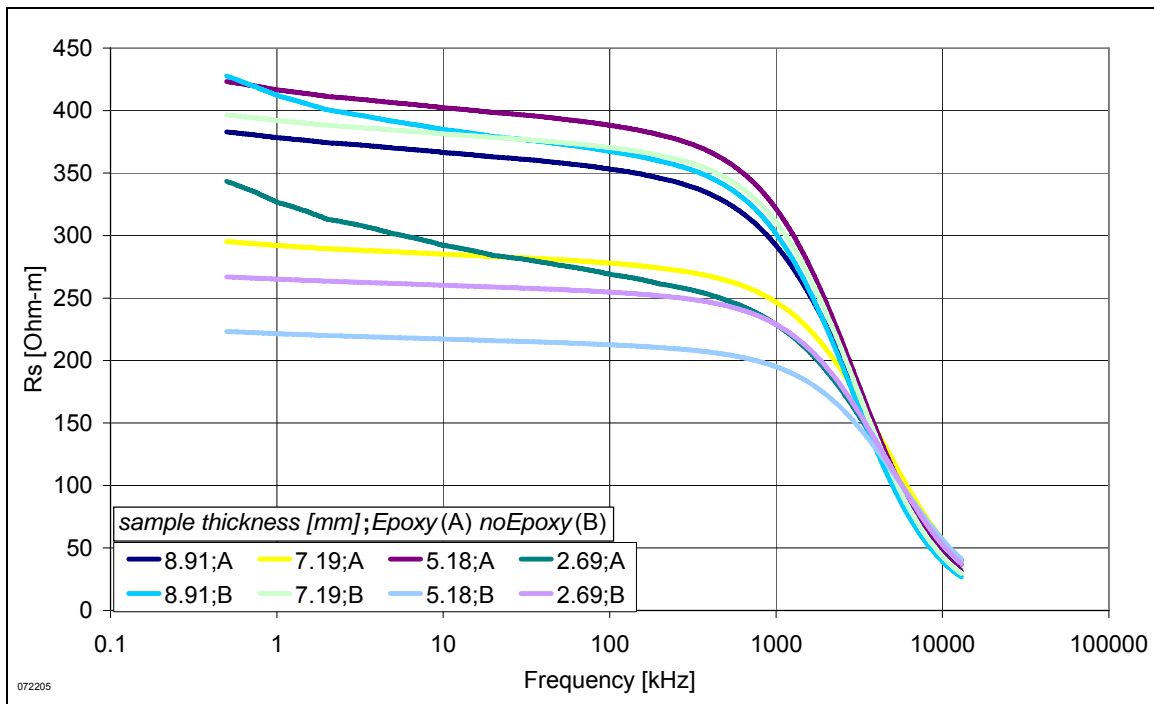


Figure 39 (Raw data) Resistivity of a series equivalent circuit measured at 1.1 applied volts. Berea sample measurement from Figure 36, Figure 37, and Figure 38.

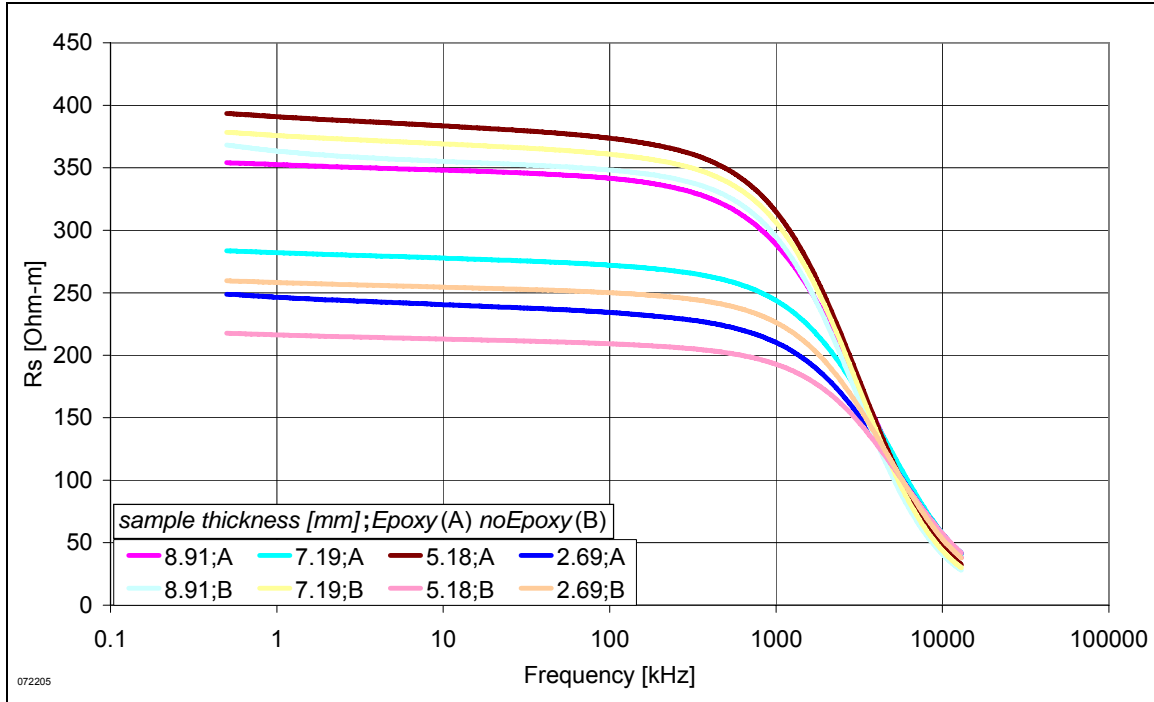


Figure 40 (Raw data) Resistivity of a series equivalent circuit measured at 0.1 applied volts. Berea sample measurement from Figure 36, Figure 37, and Figure 38.

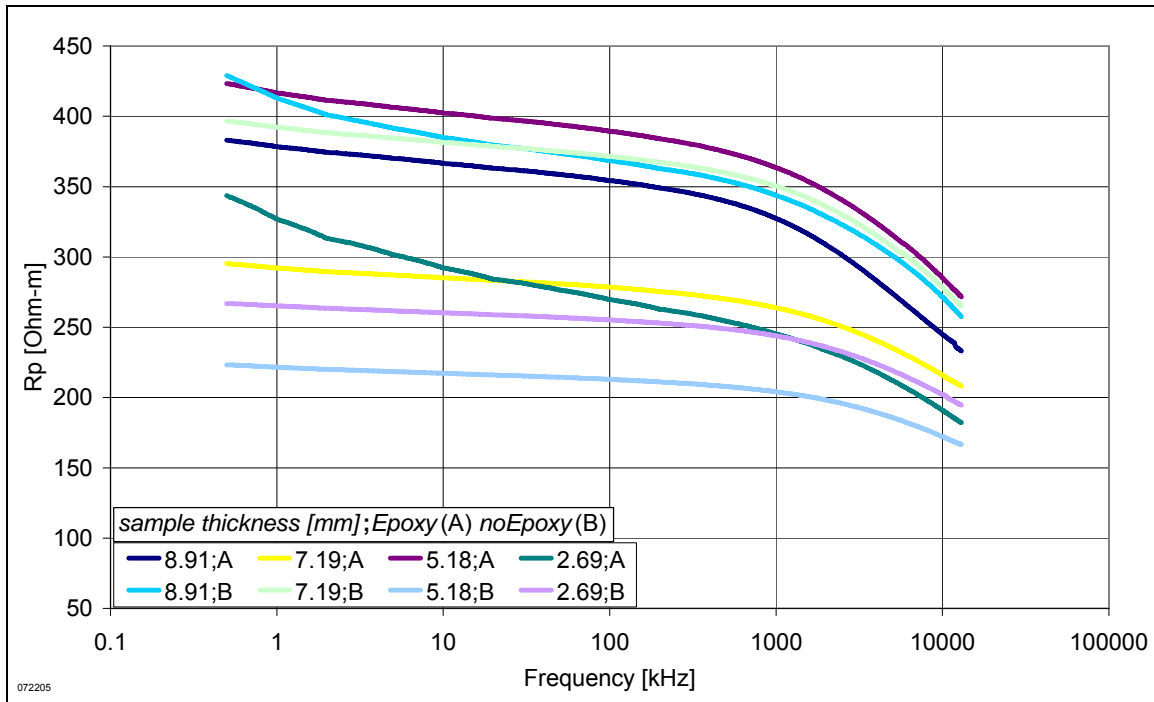


Figure 41 (Raw data) Resistivity of a parallel equivalent circuit measured at 1.1 applied volts. Berea sample measurement from Figure 36, Figure 37, and Figure 38.

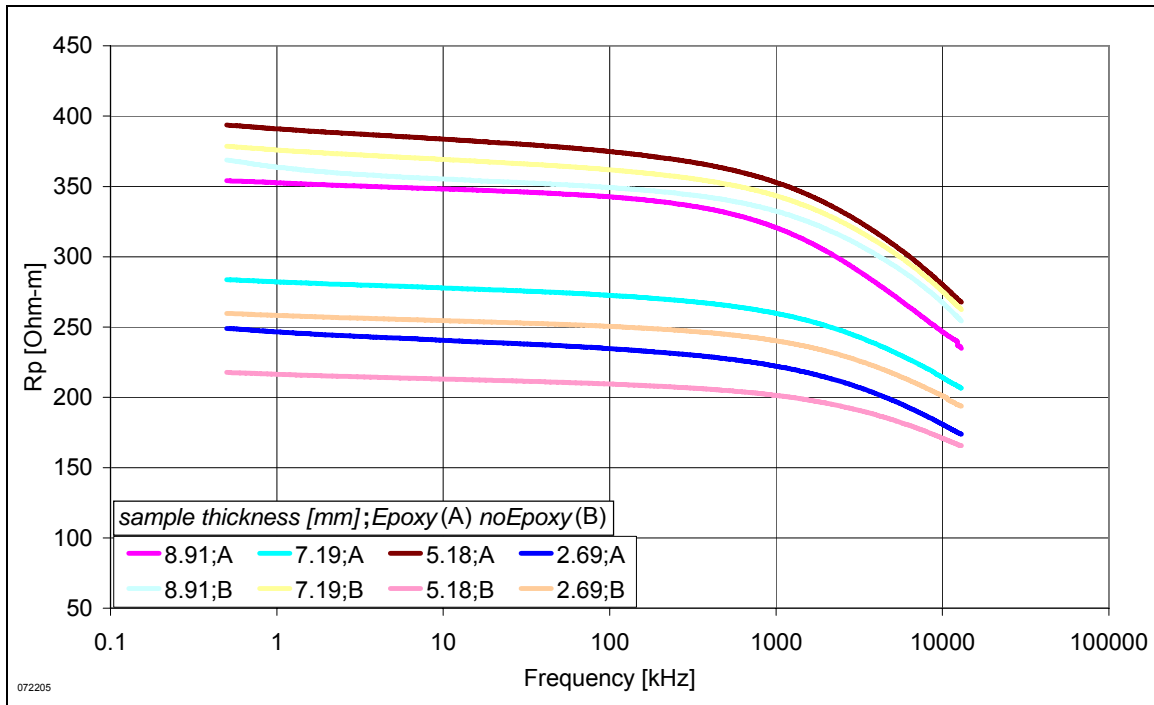


Figure 42 (Raw data) Resistivity of a parallel equivalent circuit measured at 0.1 applied volts. Berea sample measurement from Figure 36, Figure 37, and Figure 38.

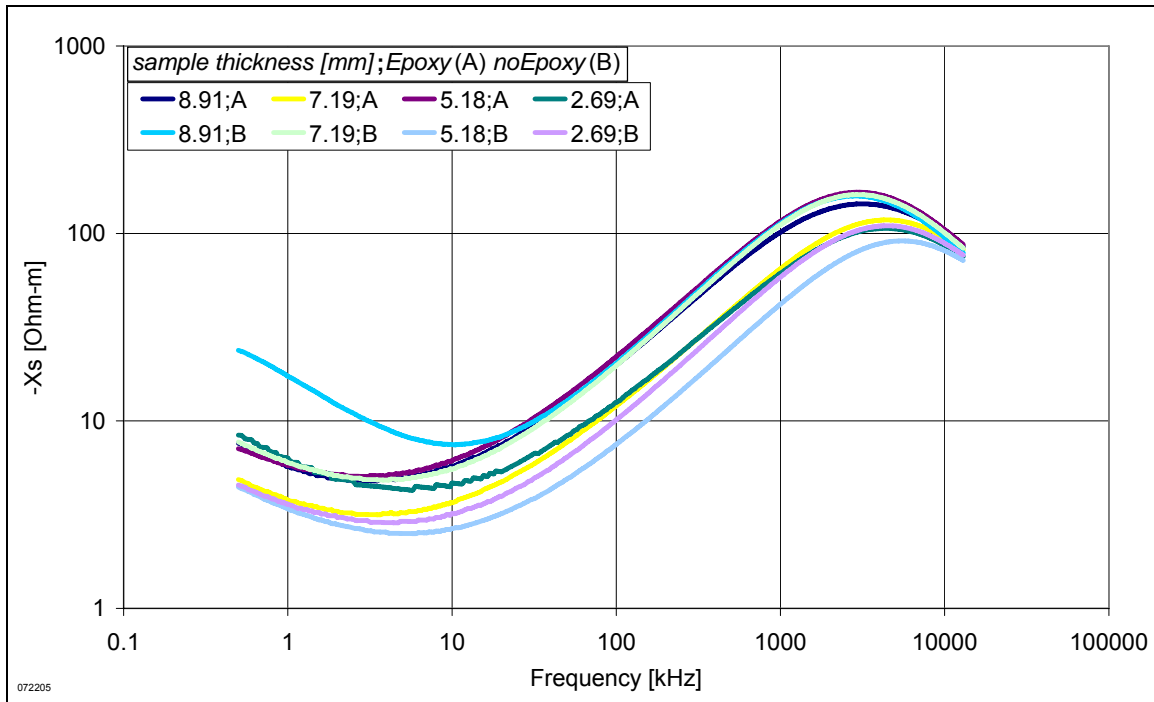


Figure 43 (Raw data) Negative reactance-m of a series equivalent circuit measured at 1.1 volts. Berea sample measurement from Figure 36, Figure 37, and Figure 38.

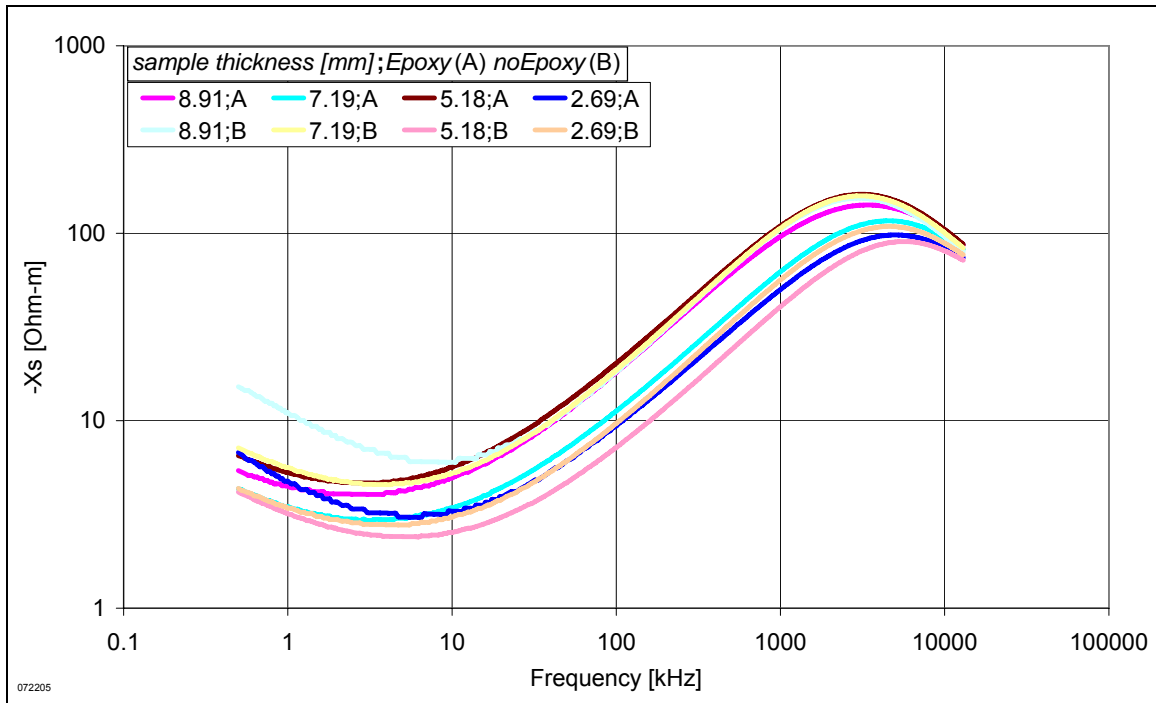


Figure 44 (Raw data) Negative reactance-m of a series equivalent circuit measured at 0.1 volts. Berea sample measurement from Figure 36, Figure 37, and Figure 38.

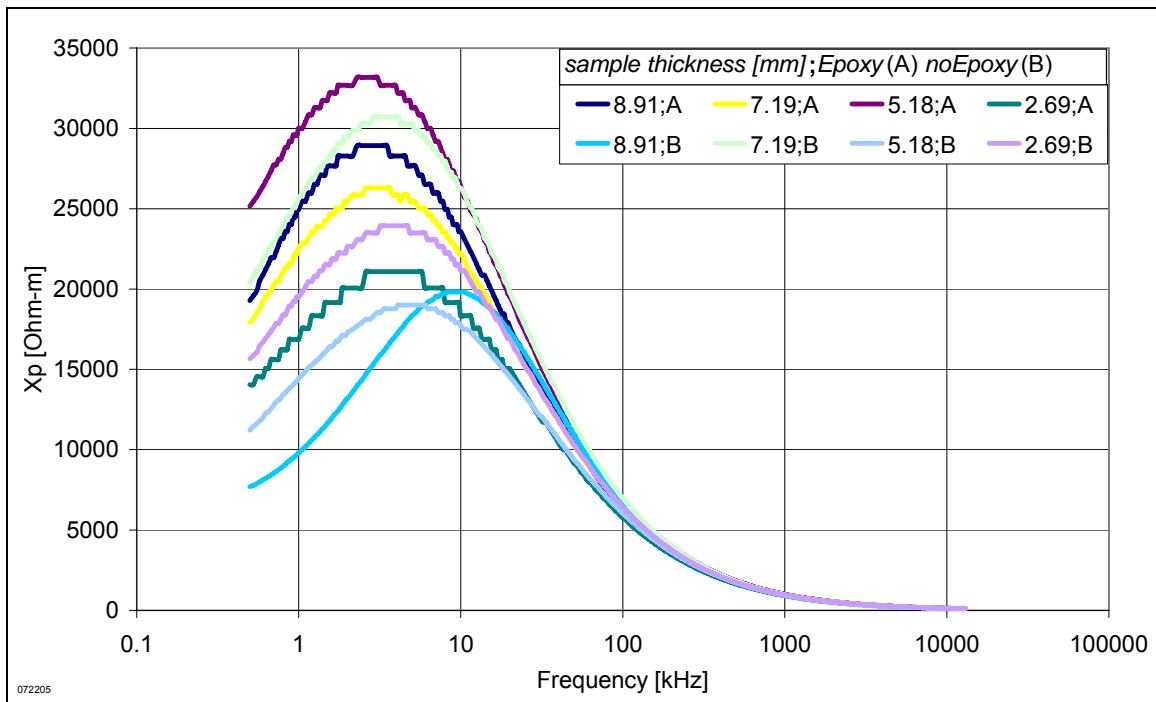


Figure 45 (Raw data) Reactance-m of a parallel equivalent circuit measured at 1.1 applied volts. Berea sample measurement from Figure 25, Figure 26, and Figure 27.

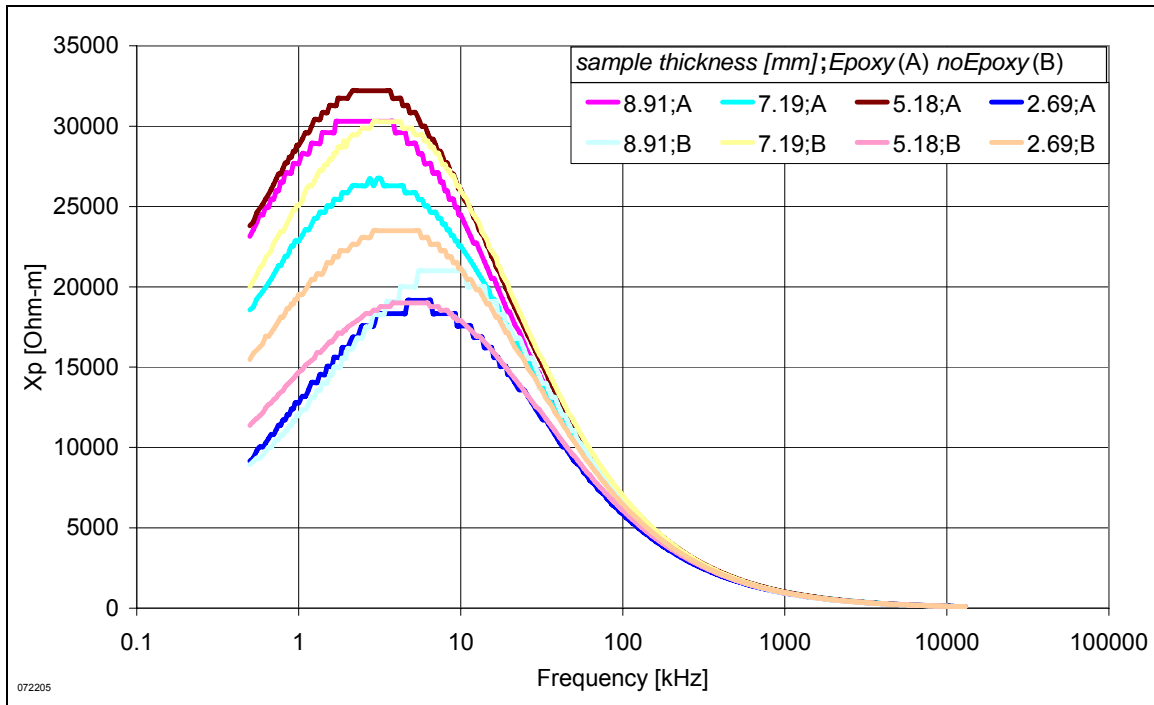


Figure 46 (Raw data) Reactance-m of a parallel equivalent circuit measured at 0.1 applied volts. Berea sample measurement from Figure 25, Figure 26, and Figure 27.

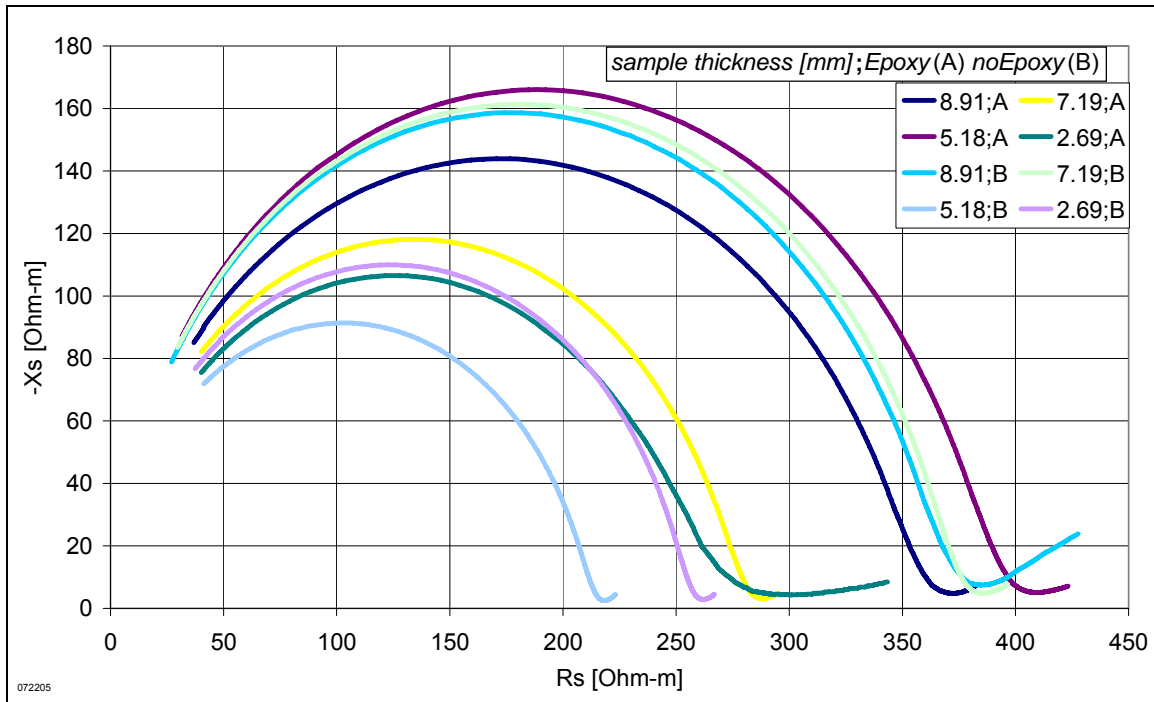


Figure 47 Argand plot of Berea sample measured at 1.1 applied volts from Figure 25, Figure 26, and Figure 27.

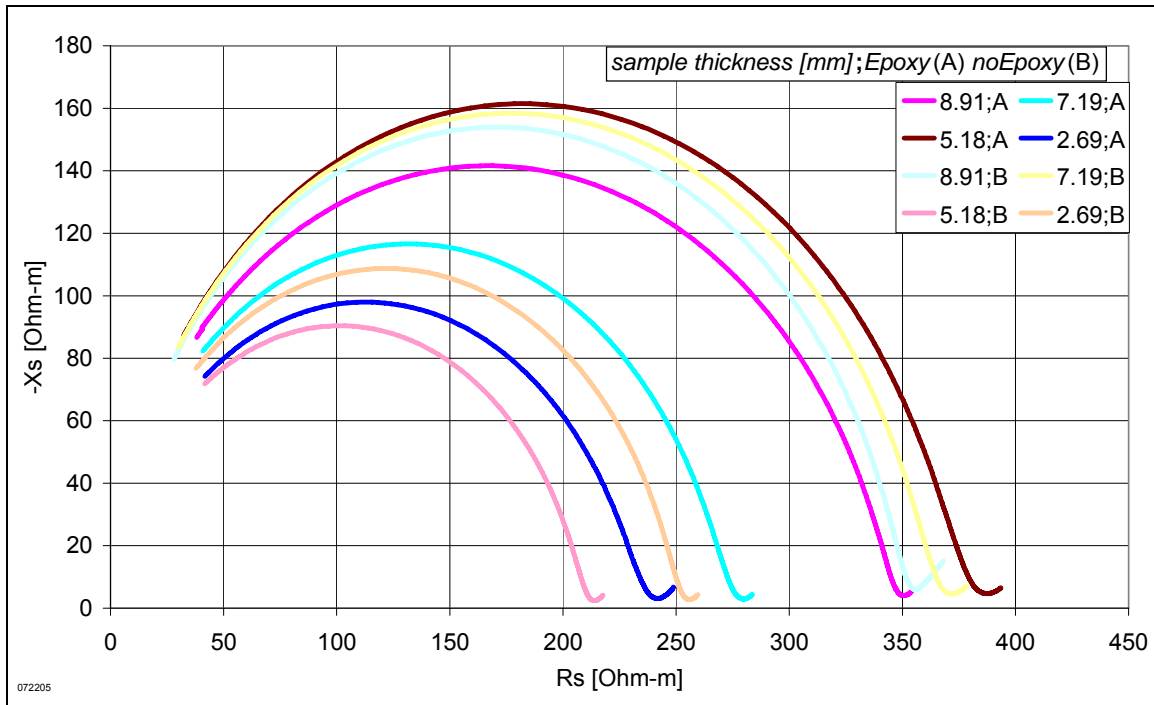


Figure 48 Argand plot of Berea sample measured at 0.1 applied volts from Figure 25, Figure 26, and Figure 27.

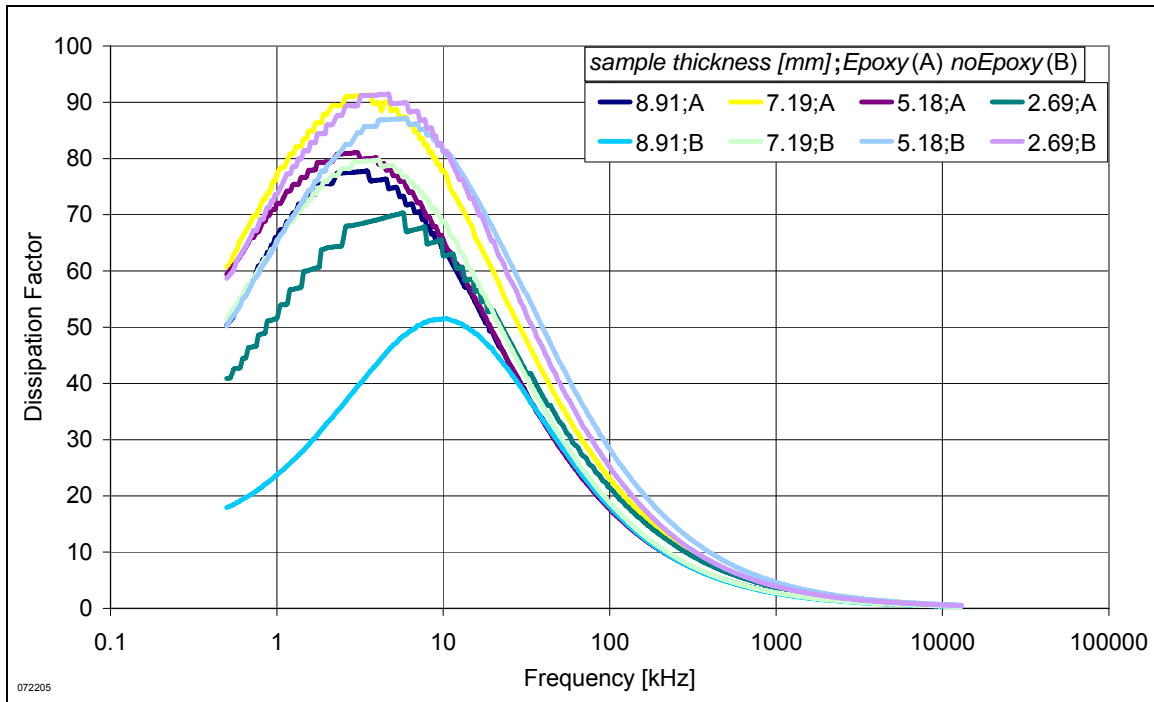


Figure 49 Dissipation factor of Berea sample measured at 1.1 applied volts from Figure 25, Figure 26, and Figure 27.

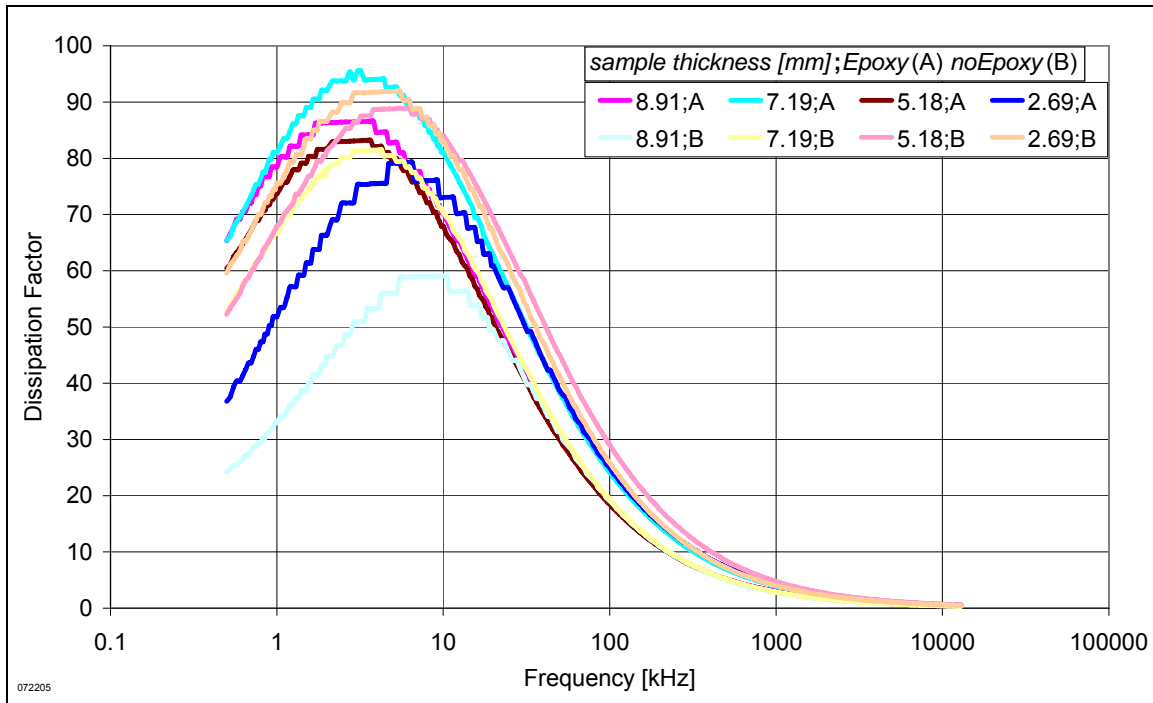


Figure 50 Dissipation factor of Berea sample measured at 0.1 applied volts from Figure 25, Figure 26, and Figure 27.

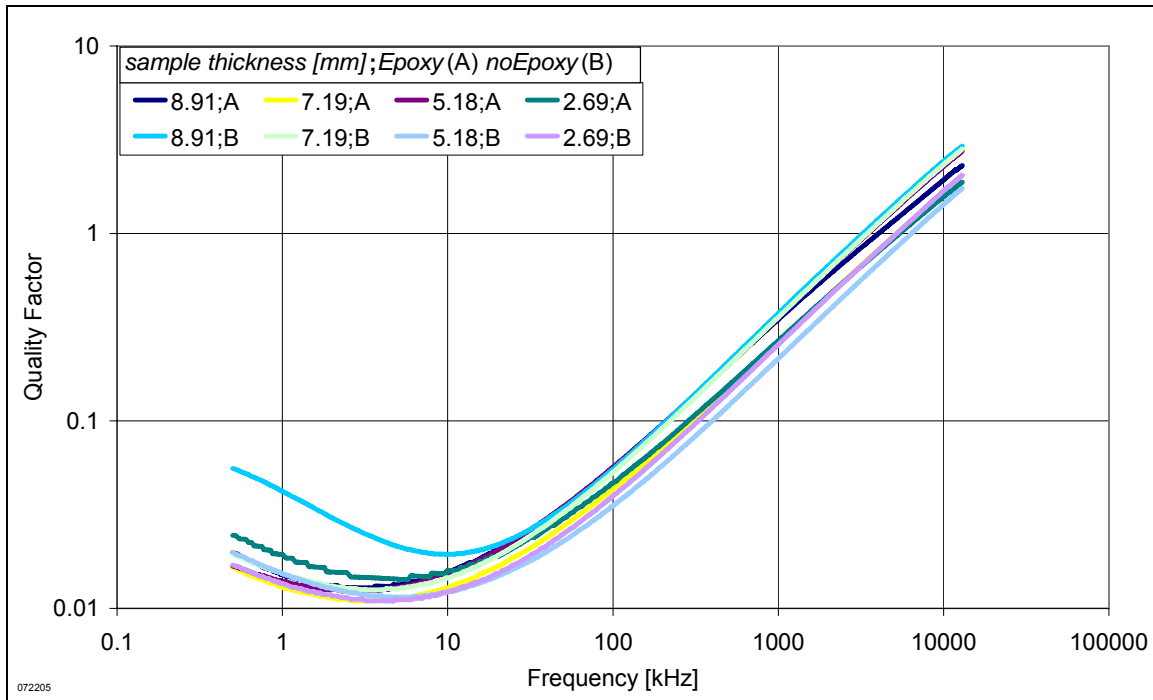


Figure 51 Quality factor of Berea sample measured at 1.1 applied volts from Figure 25, Figure 26, and Figure 27.

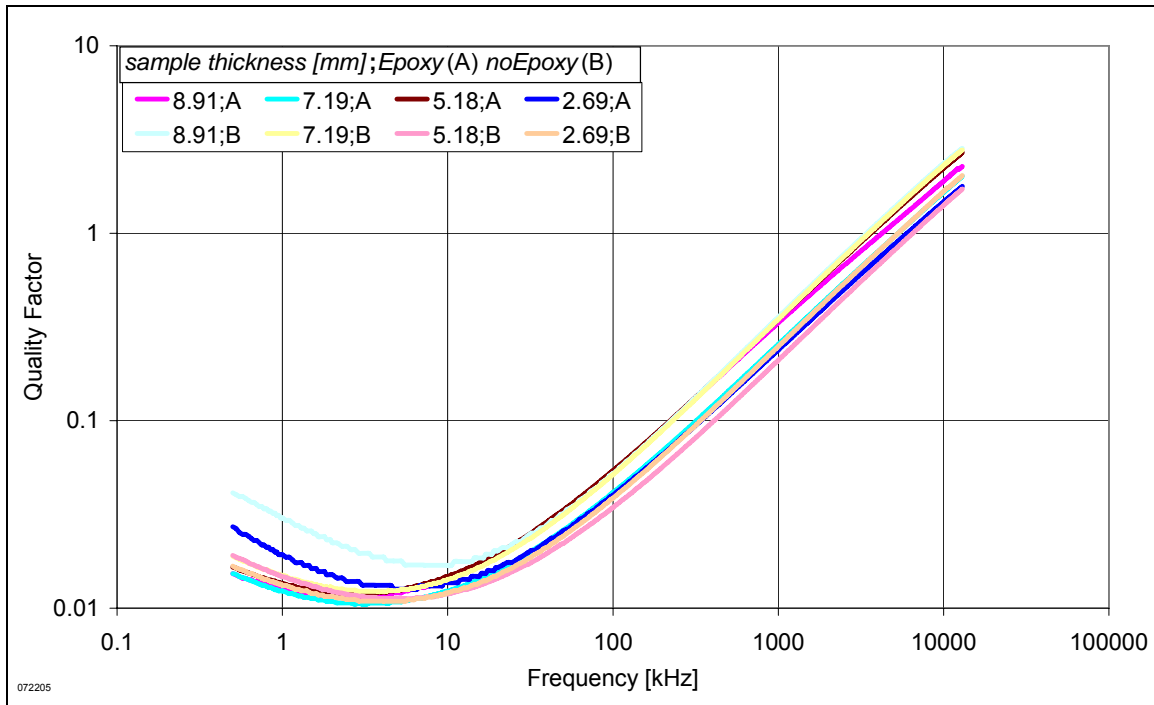


Figure 52 Quality factor of Berea sample measured at 0.1 applied volts from Figure 25, Figure 26, and Figure 27.

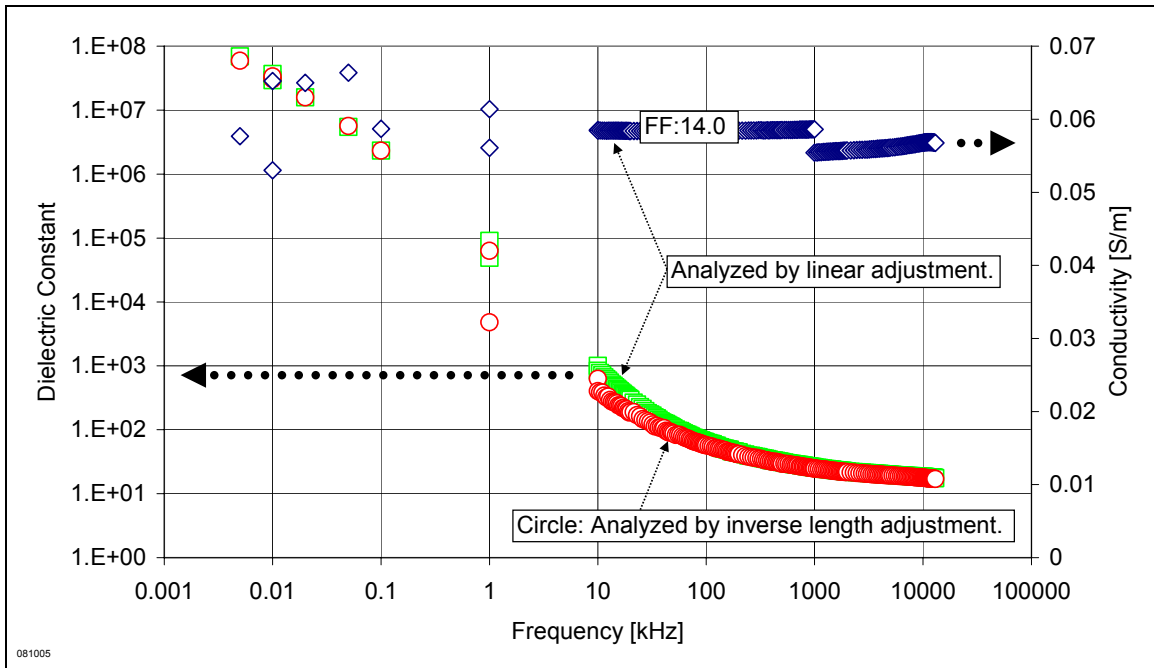


Figure 53 Dielectric constant (green squares and red circles) and conductivity (blue diamonds) measurement on Berea fully saturated with 0.45% NaCl brine (Method 2). Epoxy was applied on the samples.

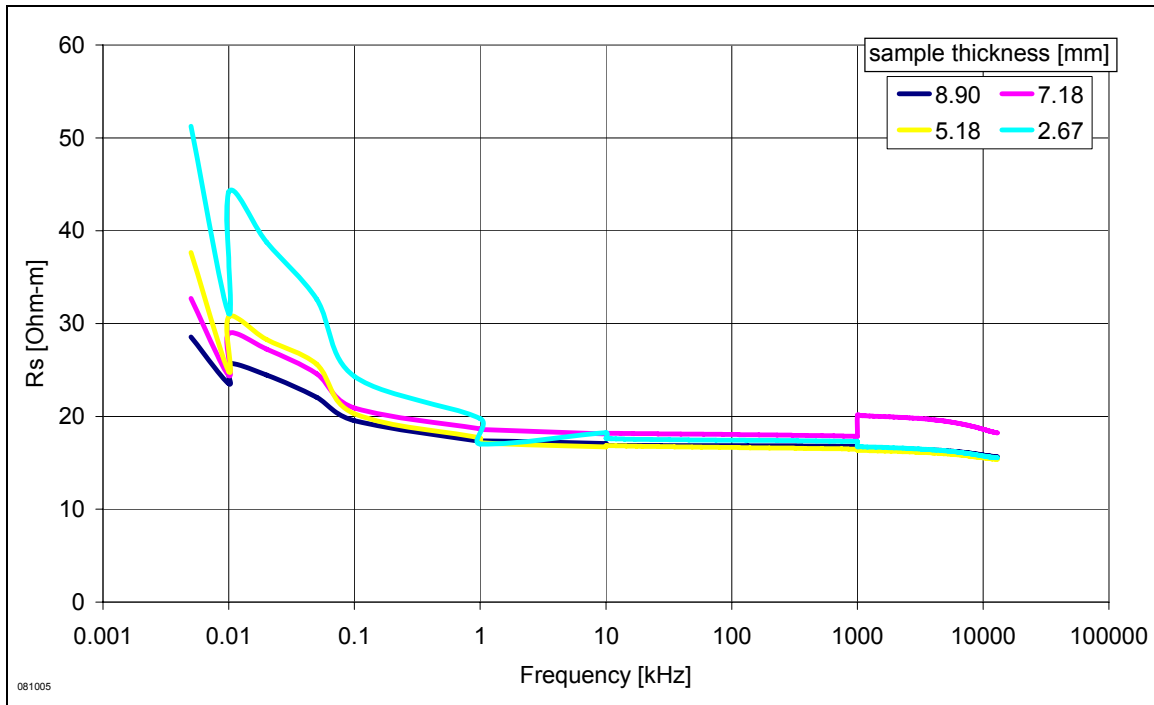


Figure 54 (Raw data) Resistivity of a series equivalent circuit. Berea sample measurement from Figure 53.

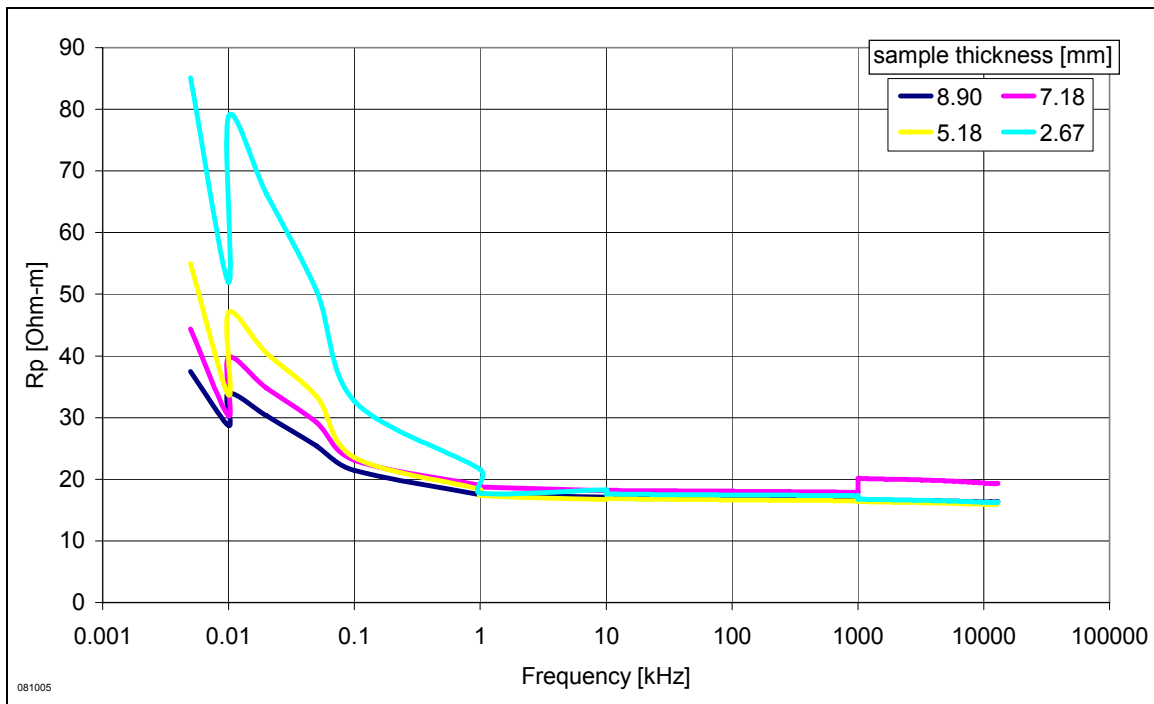


Figure 55 (Raw data) Resistivity of a parallel equivalent circuit. Berea sample measurement from Figure 53.

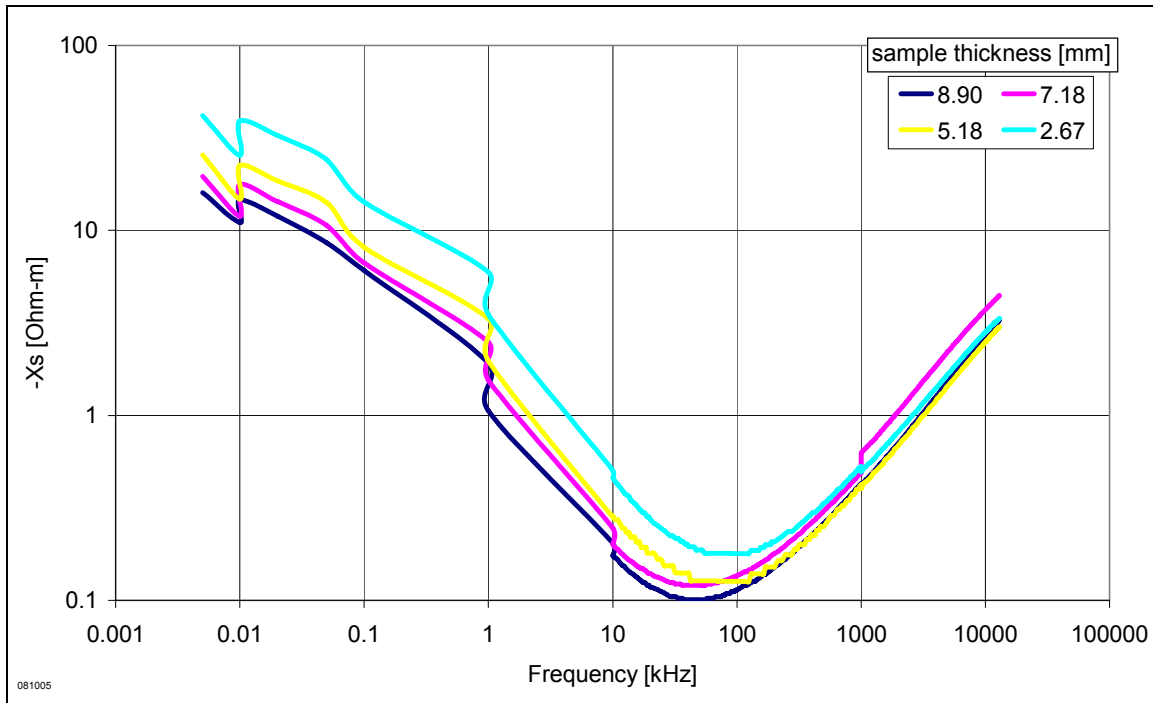


Figure 56 (Raw data) Negative reactance-m of a series equivalent circuit. Berea sample measurement from Figure 53.

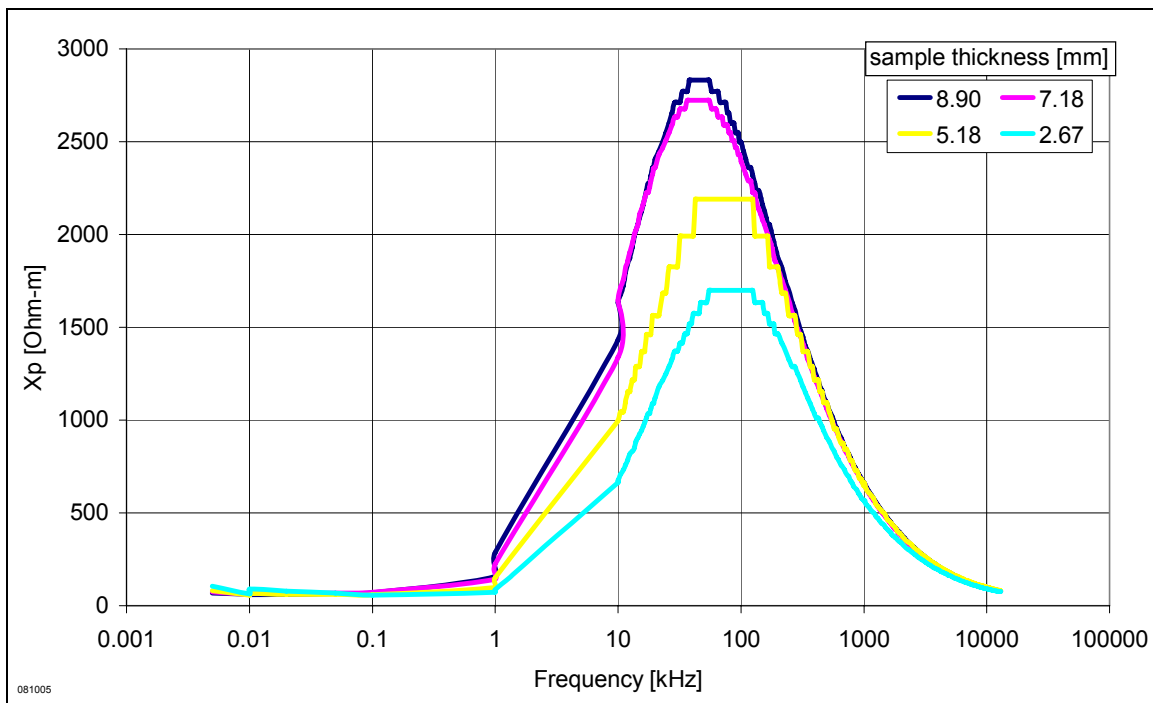


Figure 57 (Raw data) Reactance-m of a parallel equivalent circuit. Berea sample measurement from Figure 53.

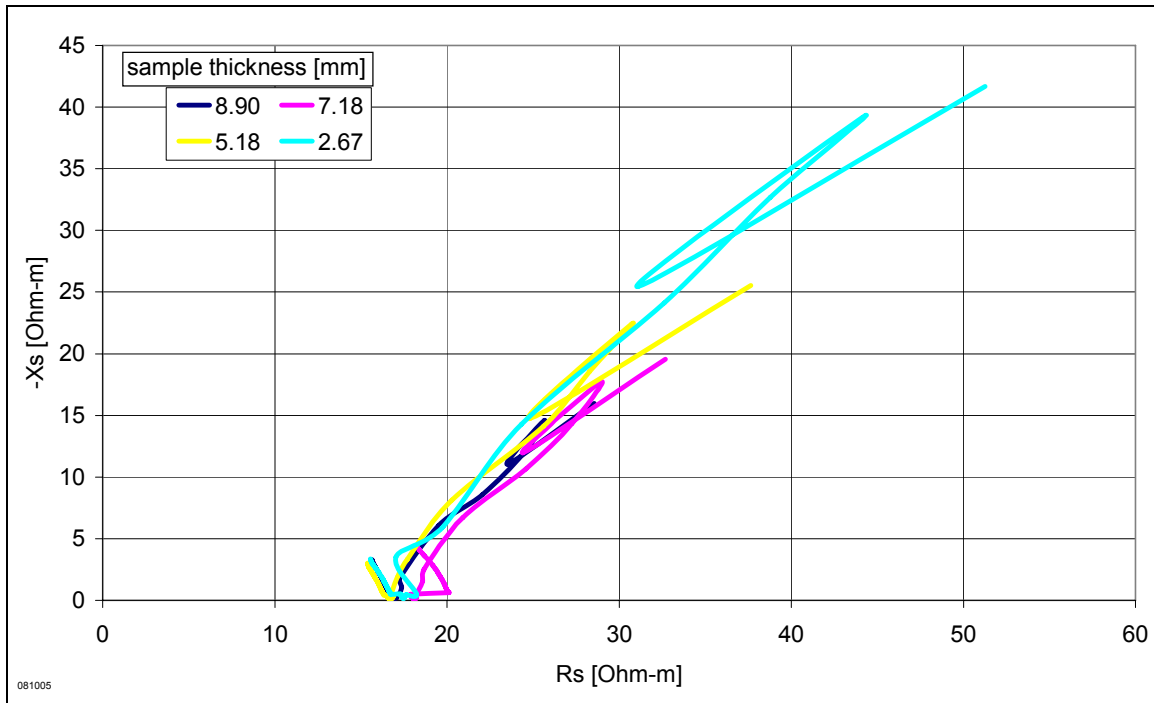


Figure 58 Argand plot of Berea sample measurement from Figure 53.

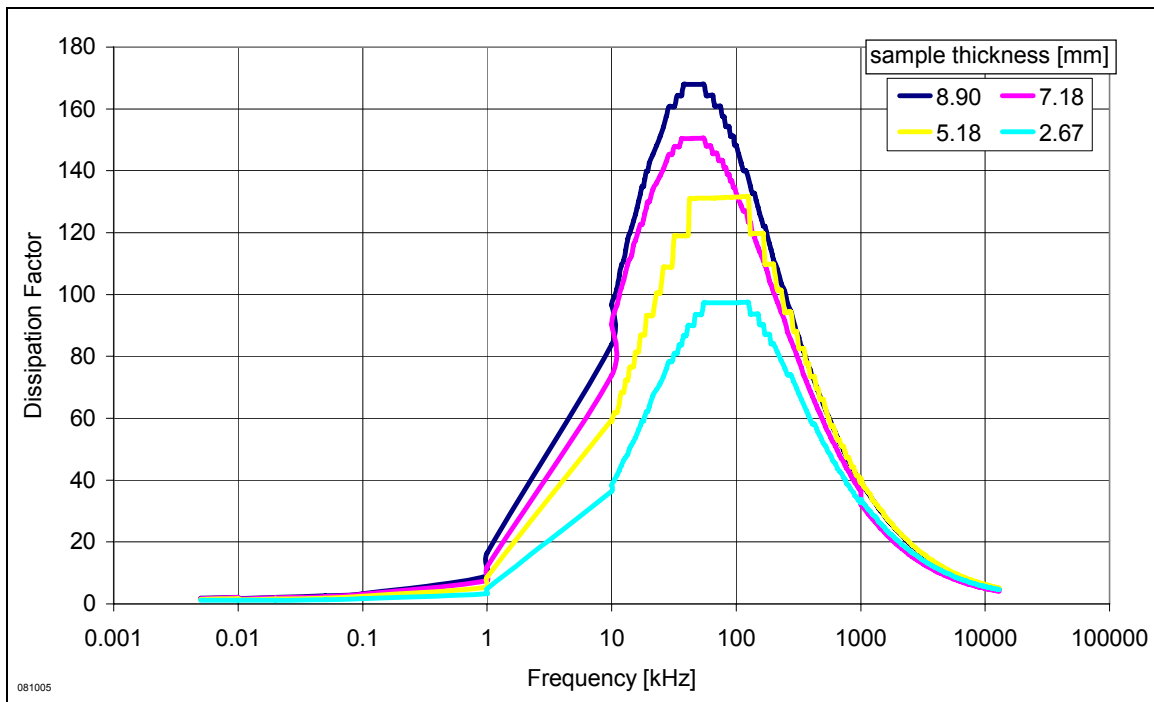


Figure 59 Dissipation factor of Berea sample measurement from Figure 53.

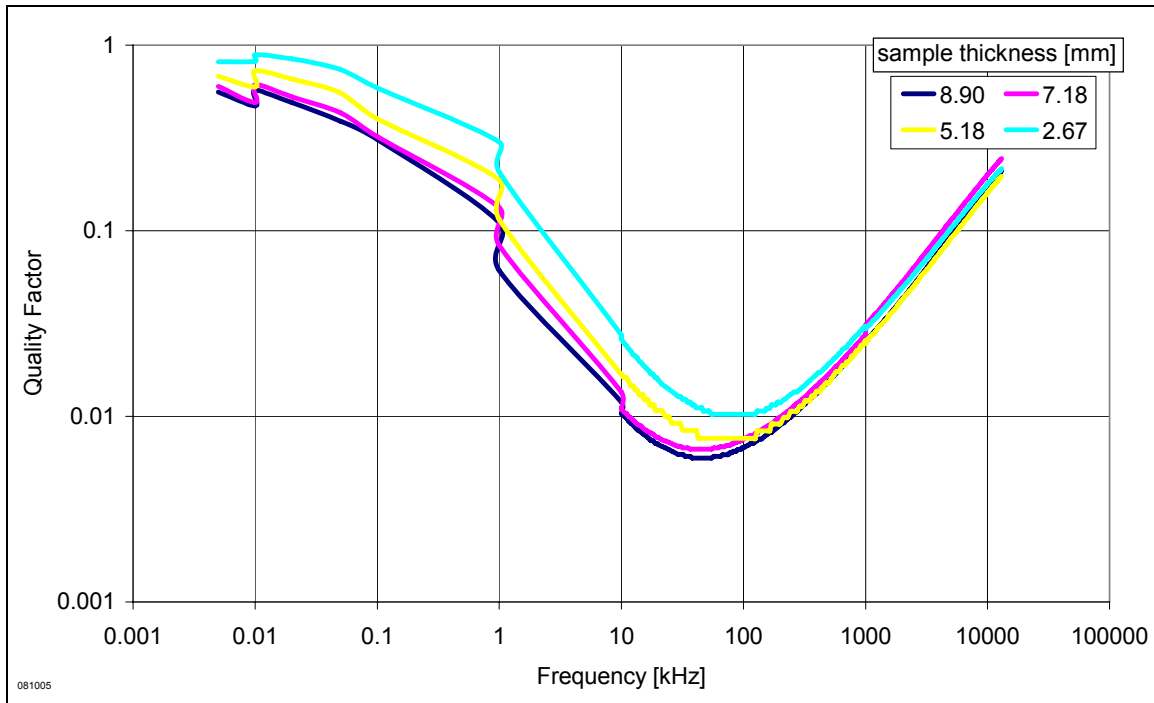


Figure 60 Quality factor of Berea sample measurement from Figure 53.

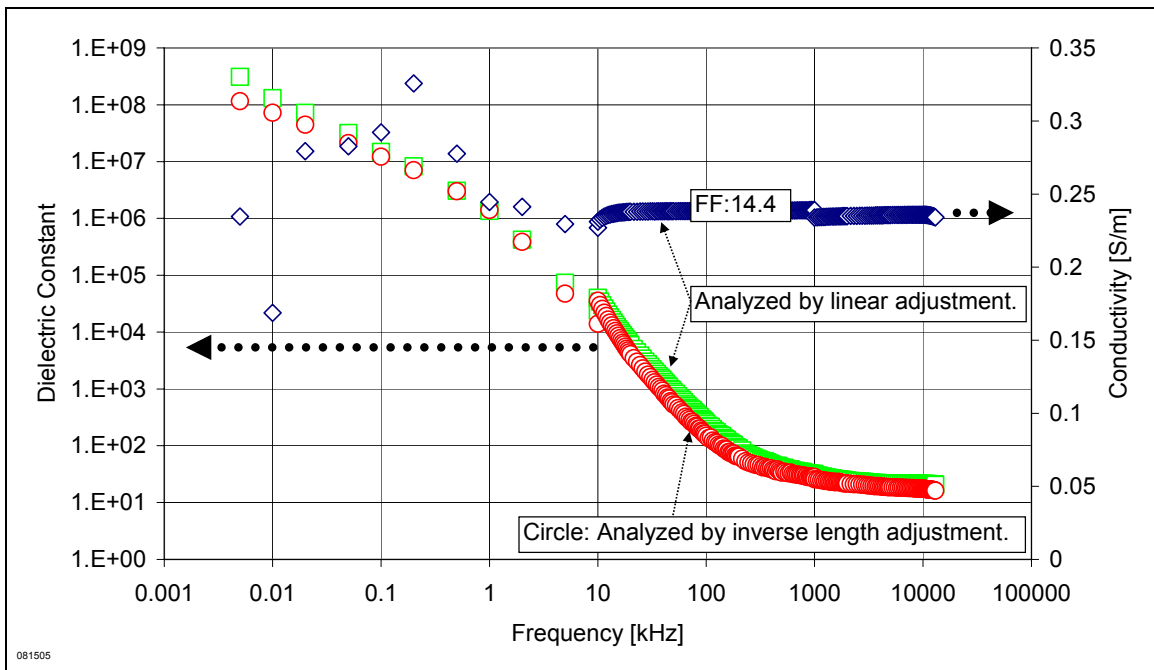


Figure 61 Dielectric constant (green squares and red circles) and conductivity (blue diamonds) measurement on Berea fully saturated with 2.15% NaCl brine (Method 2). Epoxy was applied on the samples. There is a slight deviation to the dielectric constant slope in log-log scale at 1 kHz suggesting a change in one of the parasitic effects.

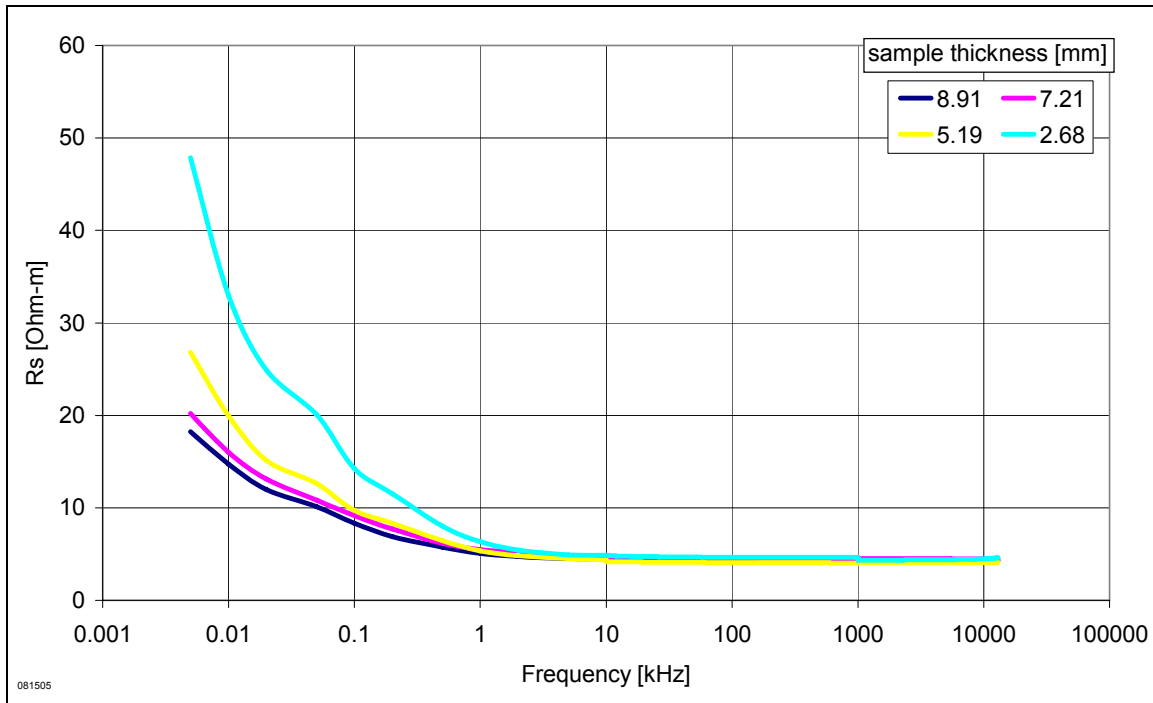


Figure 62 (Raw data) Resistivity of a series equivalent circuit. Berea sample measurement from Figure 61.

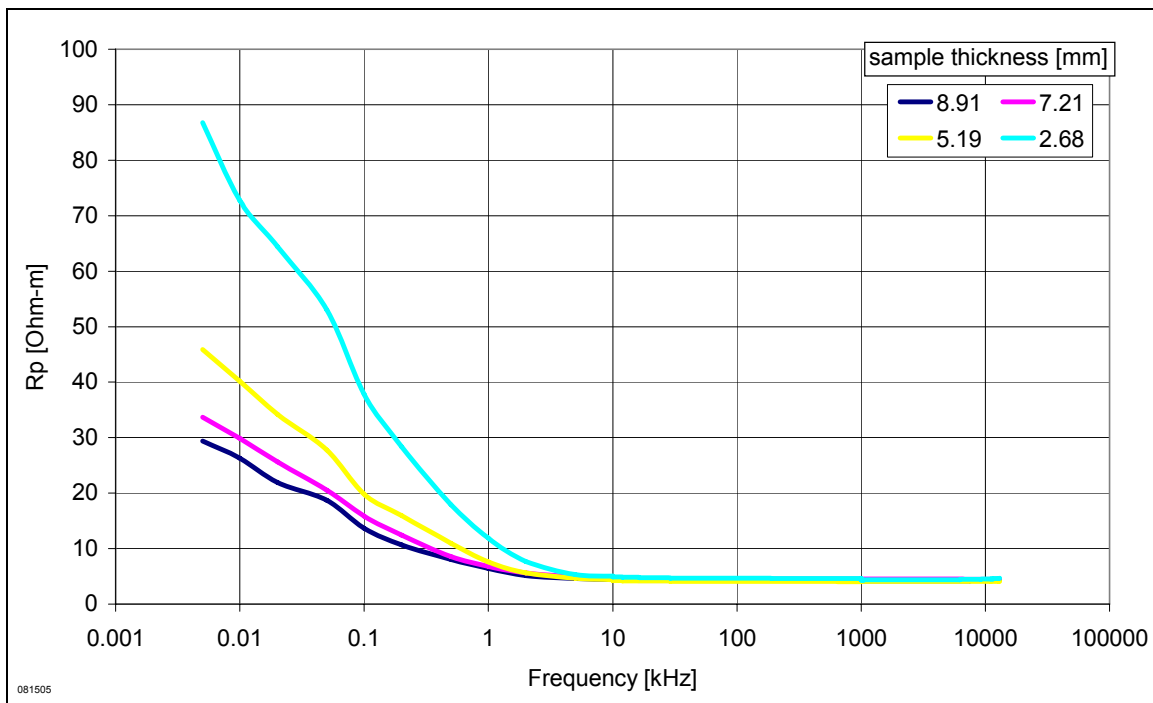


Figure 63 (Raw data) Resistivity of a parallel equivalent circuit. Berea sample measurement from Figure 61.

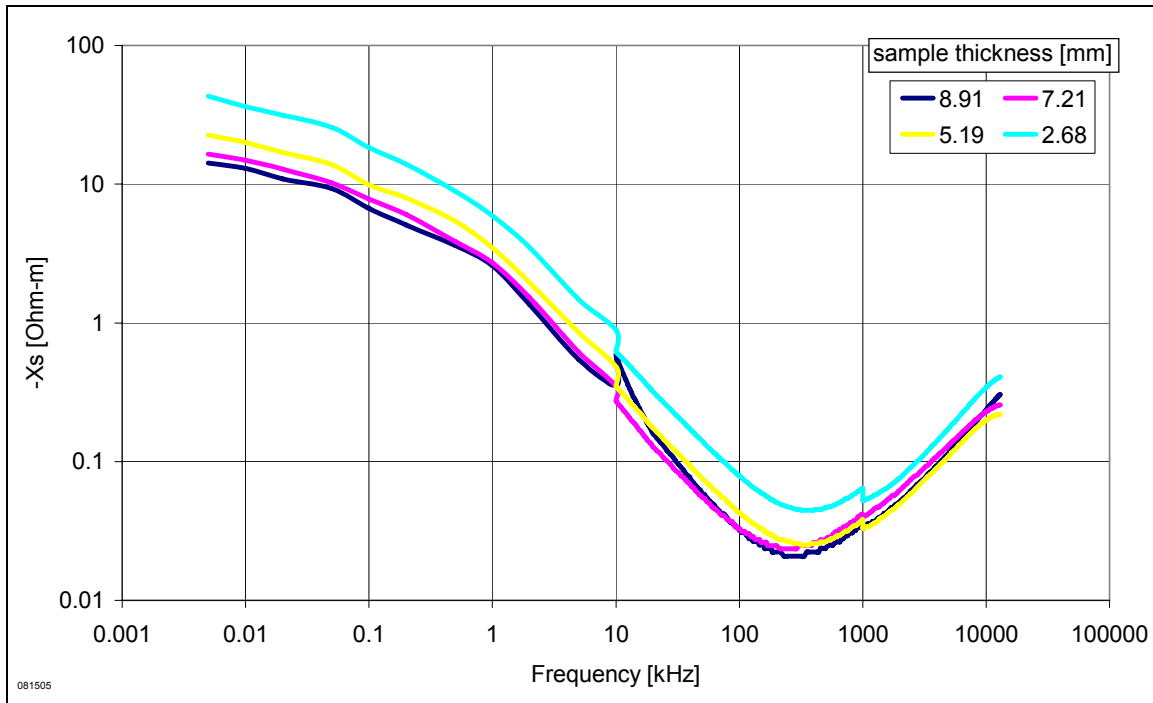


Figure 64 (Raw data) Negative reactance-m of a series equivalent circuit. Berea sample measurement from Figure 61.

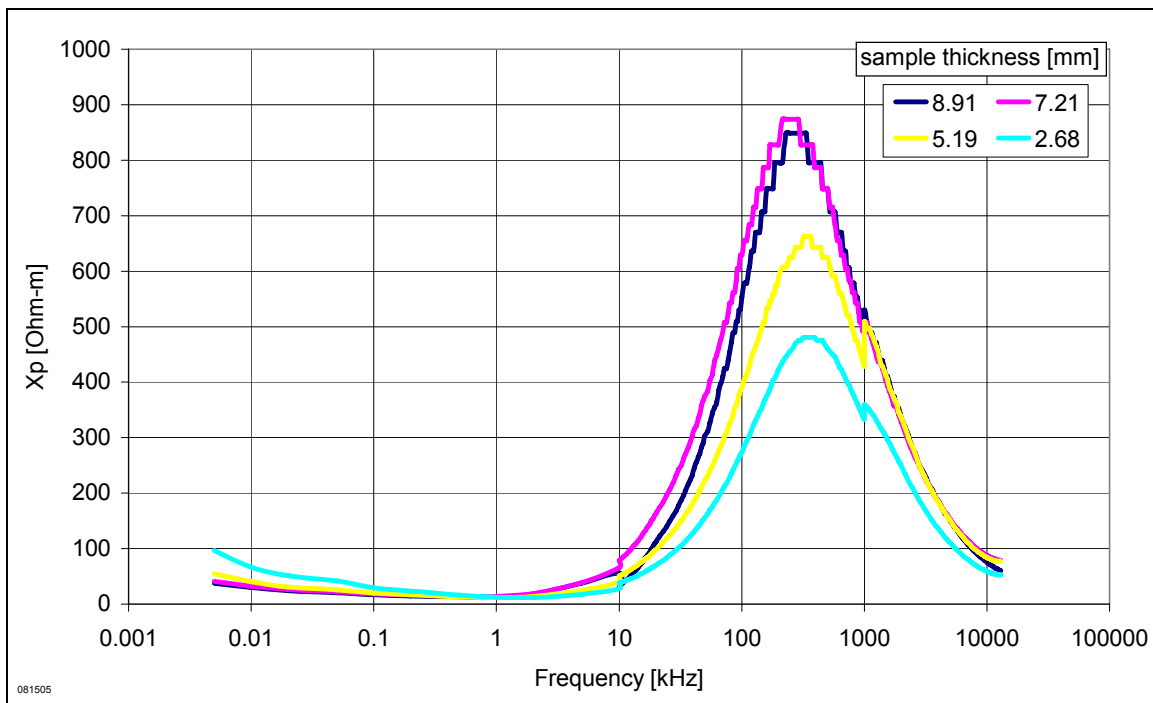


Figure 65 (Raw data) Reactance-m of a parallel equivalent circuit. Berea sample measurement from Figure 61.

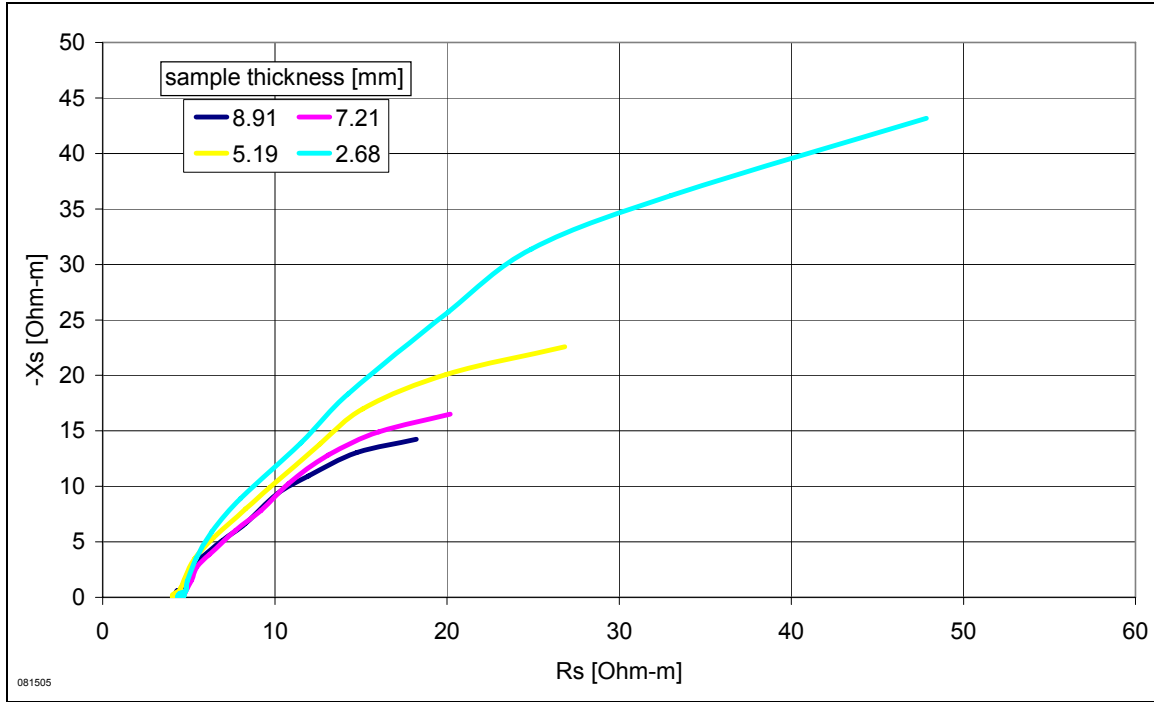


Figure 66 Argand plot of Berea sample measurement from Figure 61.

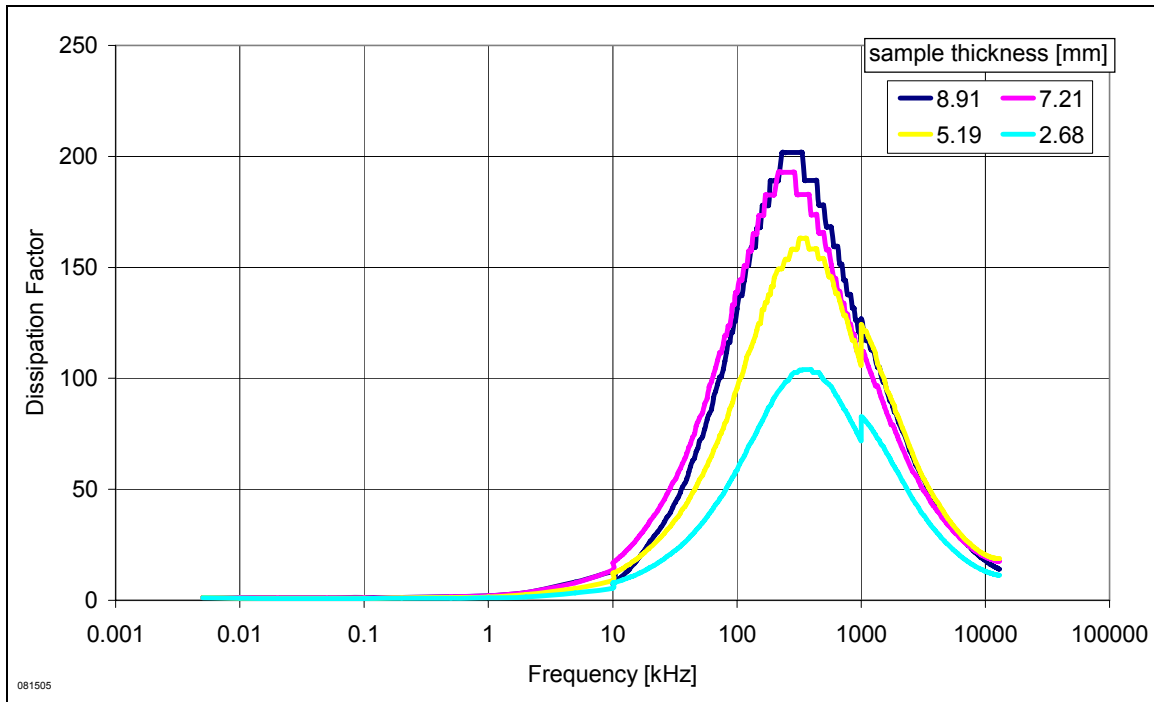


Figure 67 Dissipation factor of Berea sample measurement from Figure 61.

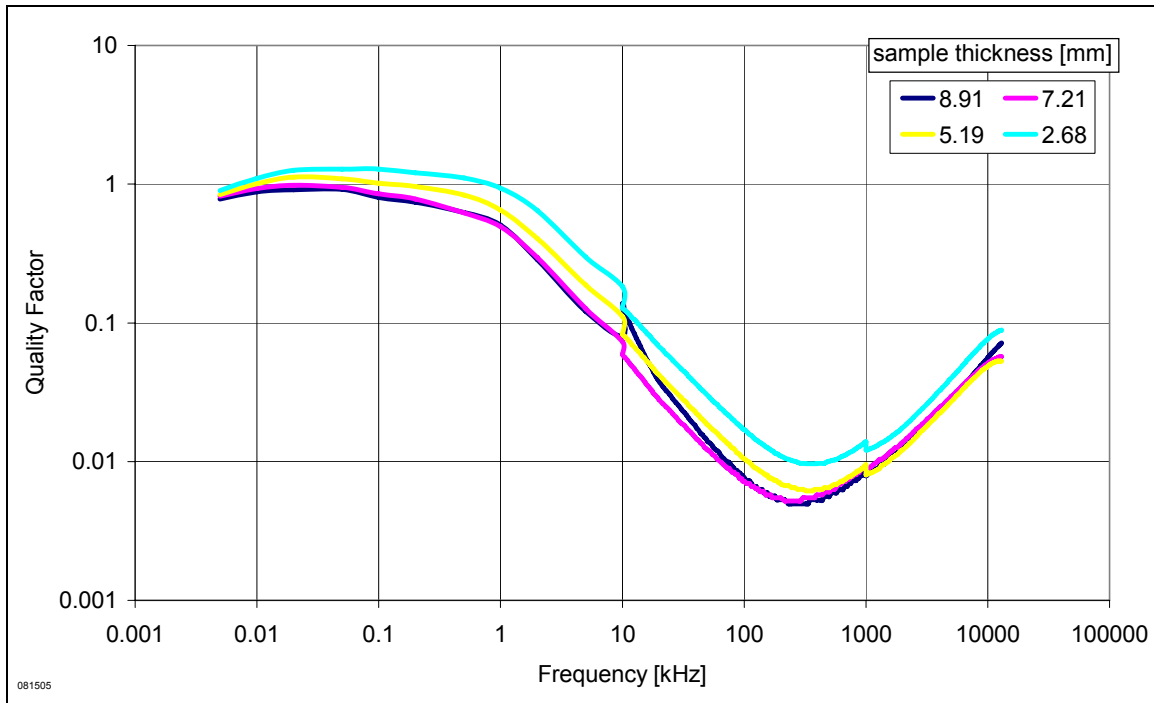


Figure 68 Quality factor of Berea sample measurement from Figure 61.

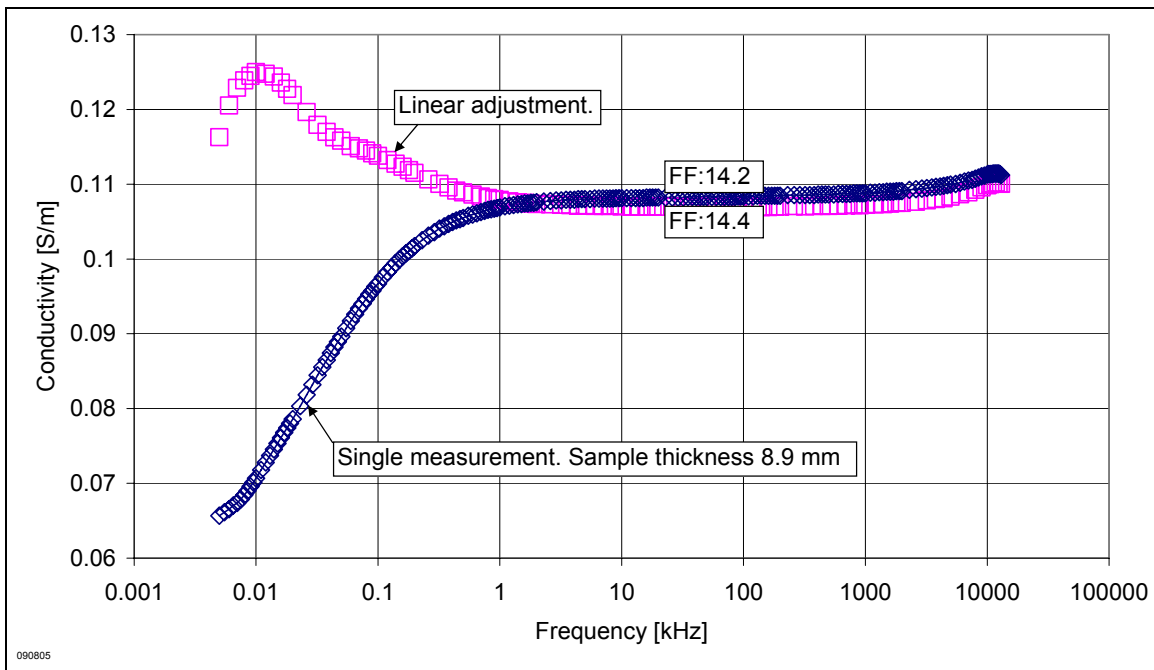


Figure 69 Conductivity on Berea sample fully saturated with 0.9% NaCl brine (Method 3). Experiment from electrode sputter coated with gold for 50 seconds. Parasitic impedances still exist below 1 kHz and linear method analysis eliminated some of the impedances.

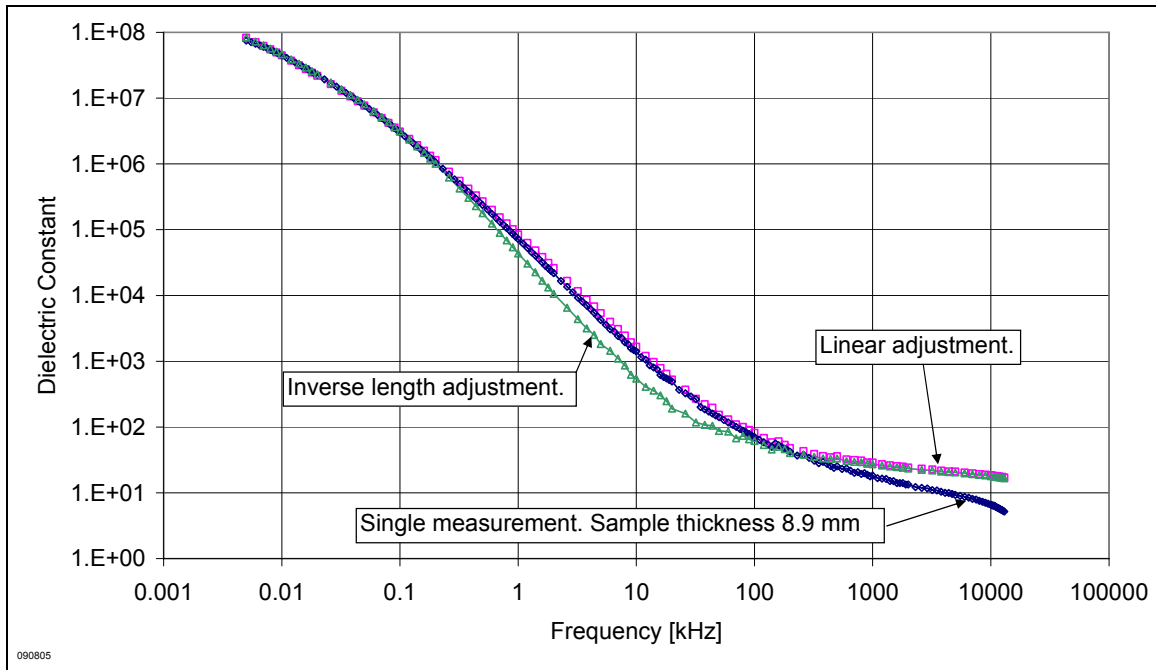


Figure 70 Dielectric constant on Berea sample fully saturated with 0.9% NaCl brine (Method 3). Experiment from electrode sputter coated with gold for 50 seconds. Dielectric enhancement still existed at the low frequencies.

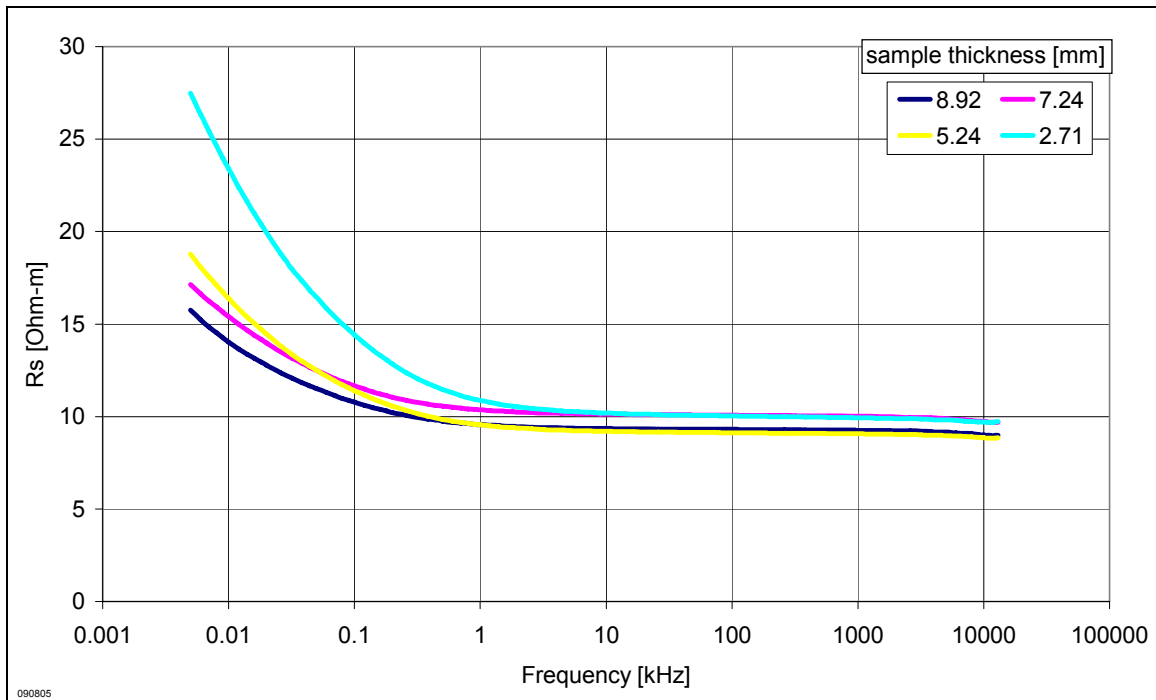


Figure 71 (Raw data) Resistivity of a series equivalent circuit. Berea sample measurement from Figure 69 and Figure 70.

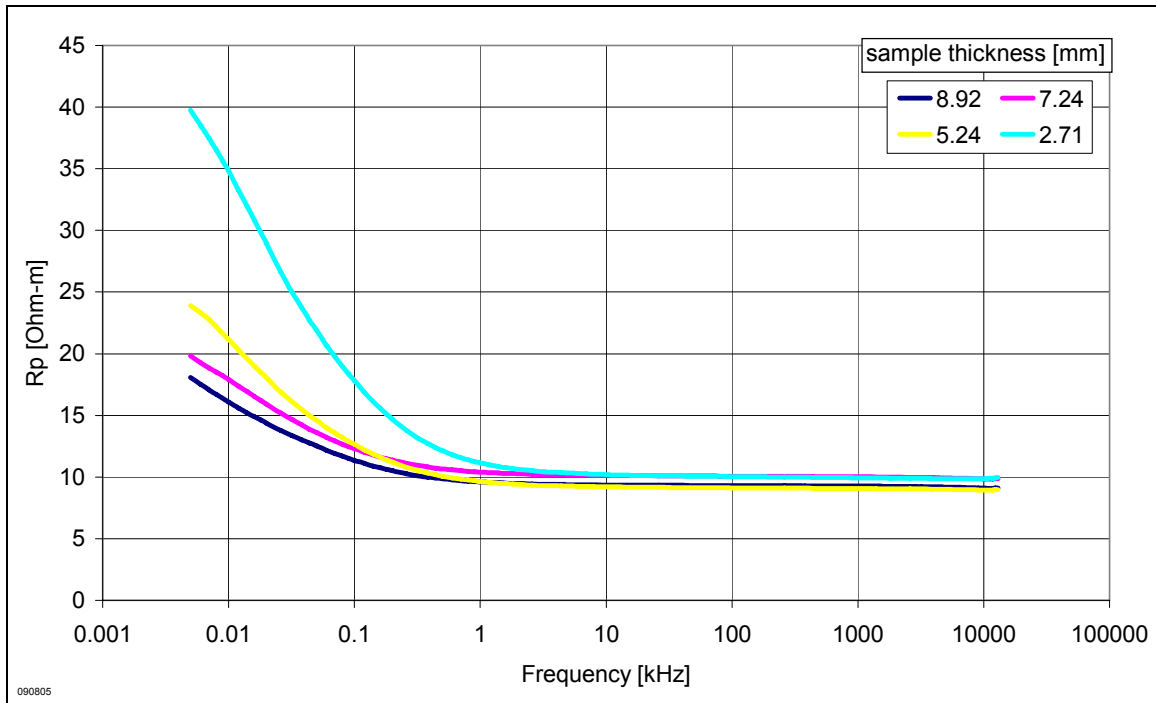


Figure 72 (Raw data) Resistivity of a parallel equivalent circuit. Berea sample measurement from Figure 69 and Figure 70.

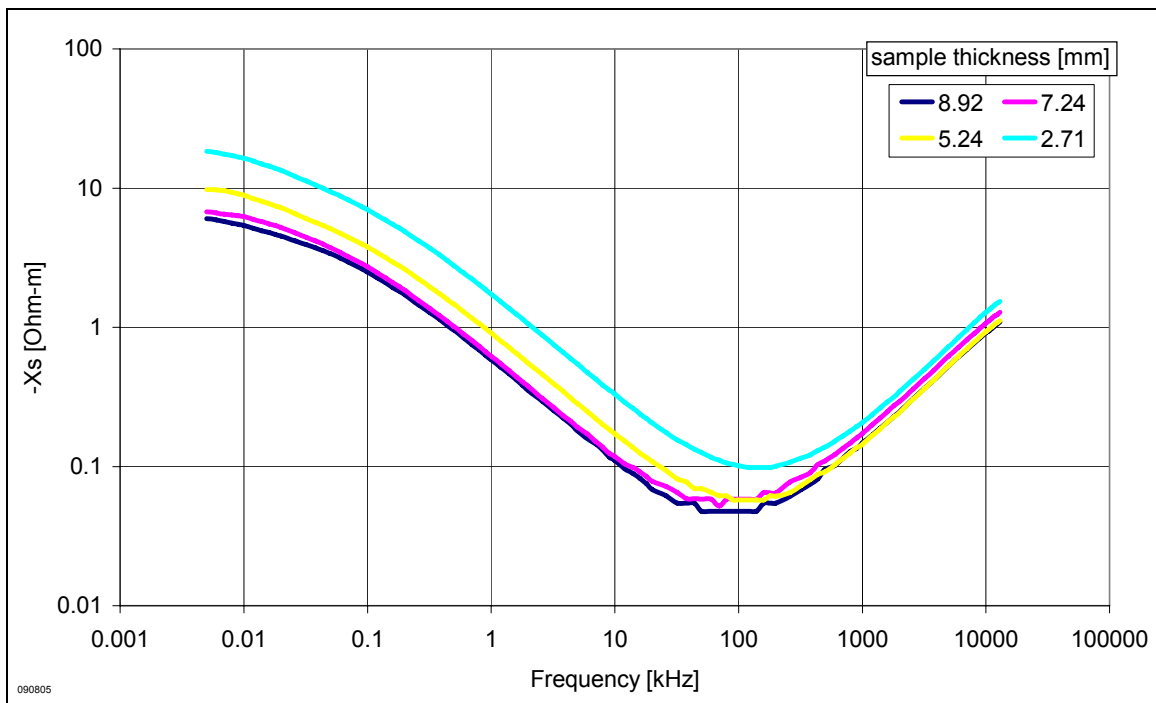


Figure 73 (Raw data) Negative reactance-m of a series equivalent circuit. Berea sample measurement from Figure 69 and Figure 70.

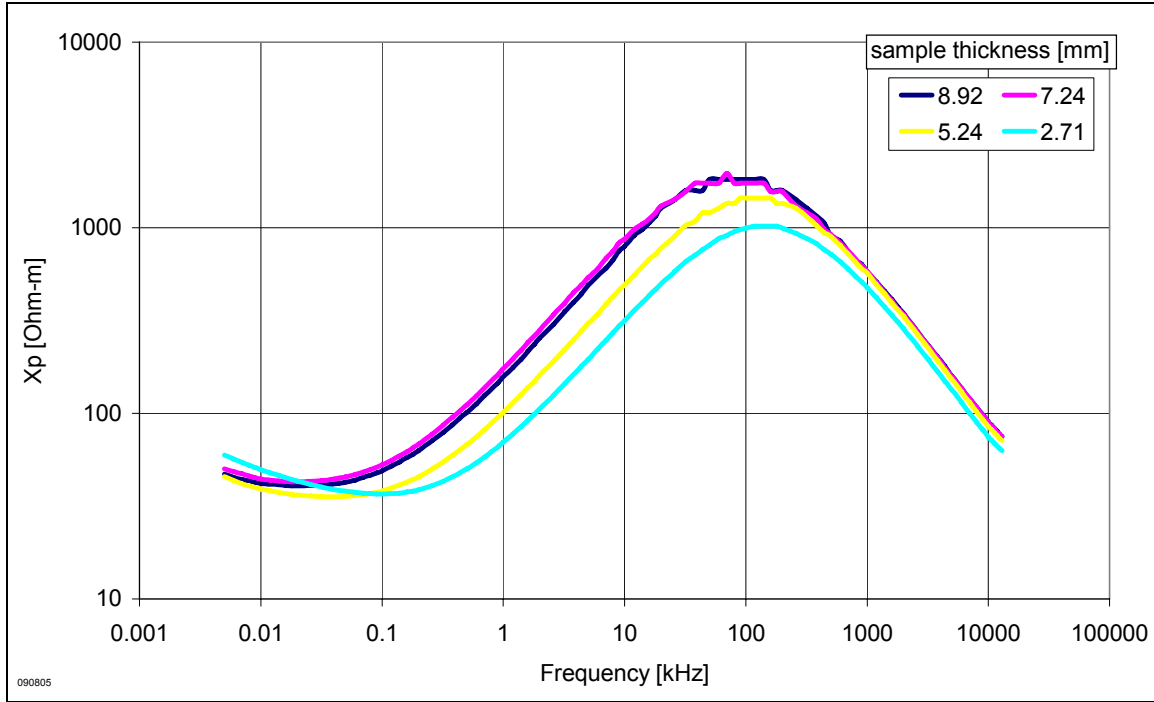


Figure 74 (Raw data) Reactance-m of a parallel equivalent circuit. Berea sample measurement from Figure 69 and Figure 70.

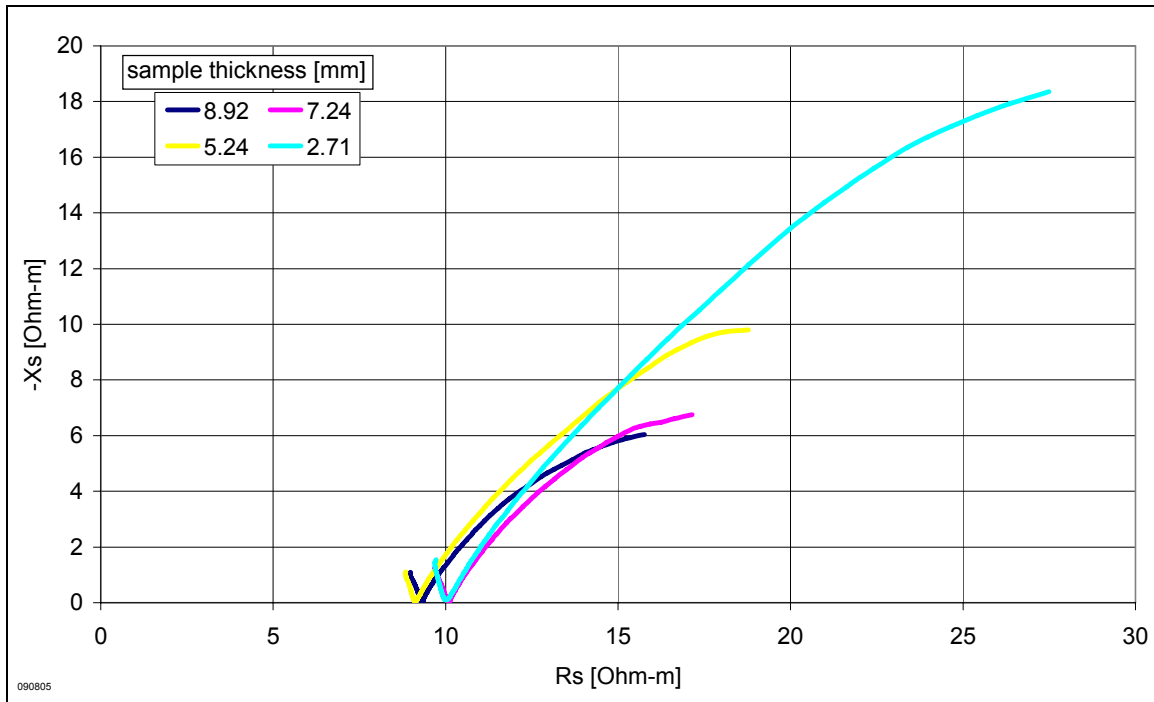


Figure 75 Argand plot of Berea sample measurement from Figure 69 and Figure 70.

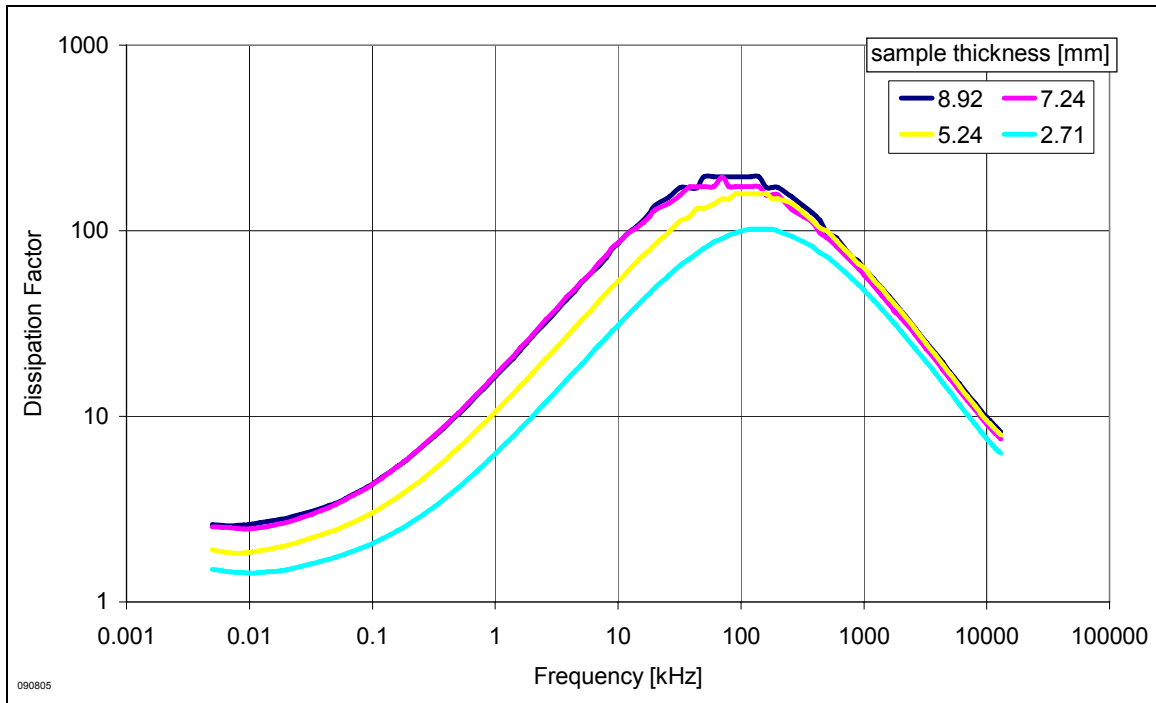


Figure 76 Dissipation factor of Berea sample measurement from Figure 69 and Figure 70.

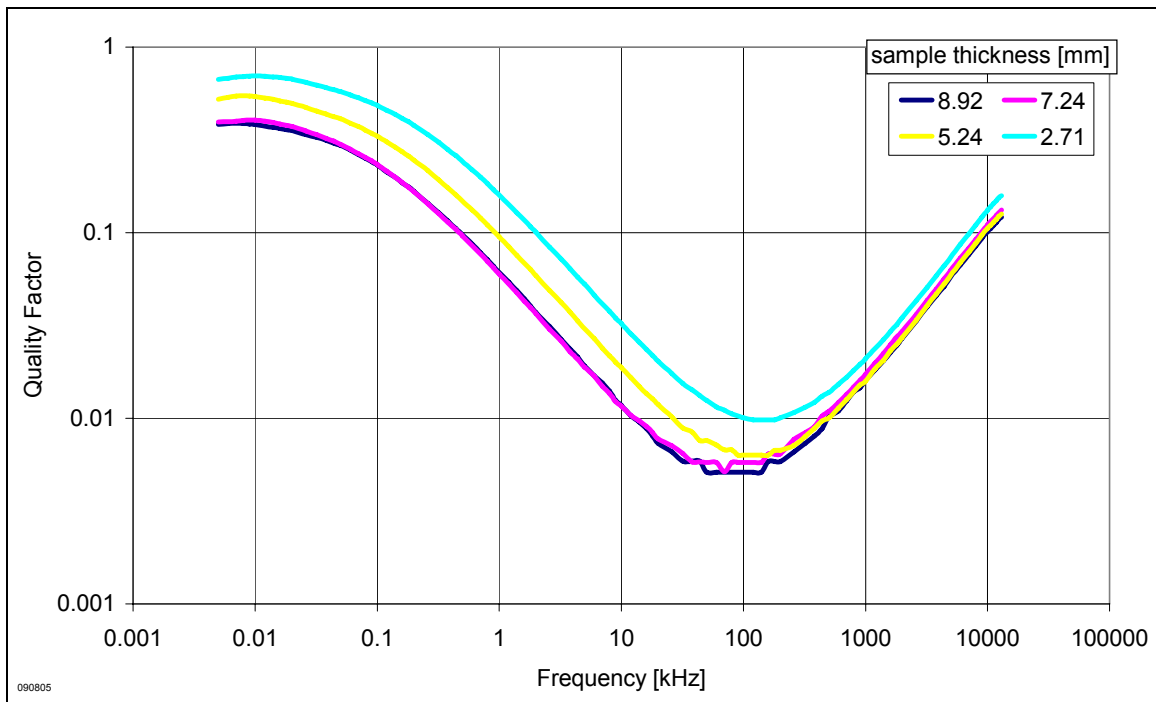


Figure 77 Quality factor of Berea sample measurement from Figure 69 and Figure 70.

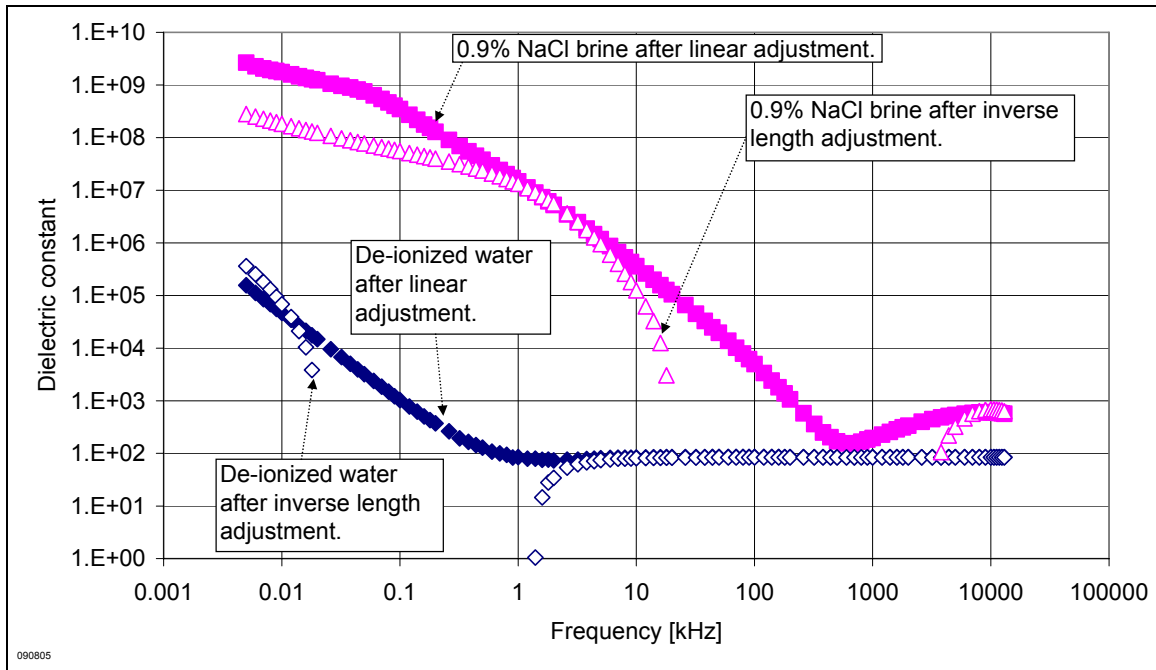


Figure 78 Dielectric constant on de-ionized water and 0.9% NaCl brine (Method 3). Experiment from electrode sputter coated with gold for 50 seconds. The dielectric enhancement was more pronounced and extended to a higher frequency for more conductive samples.

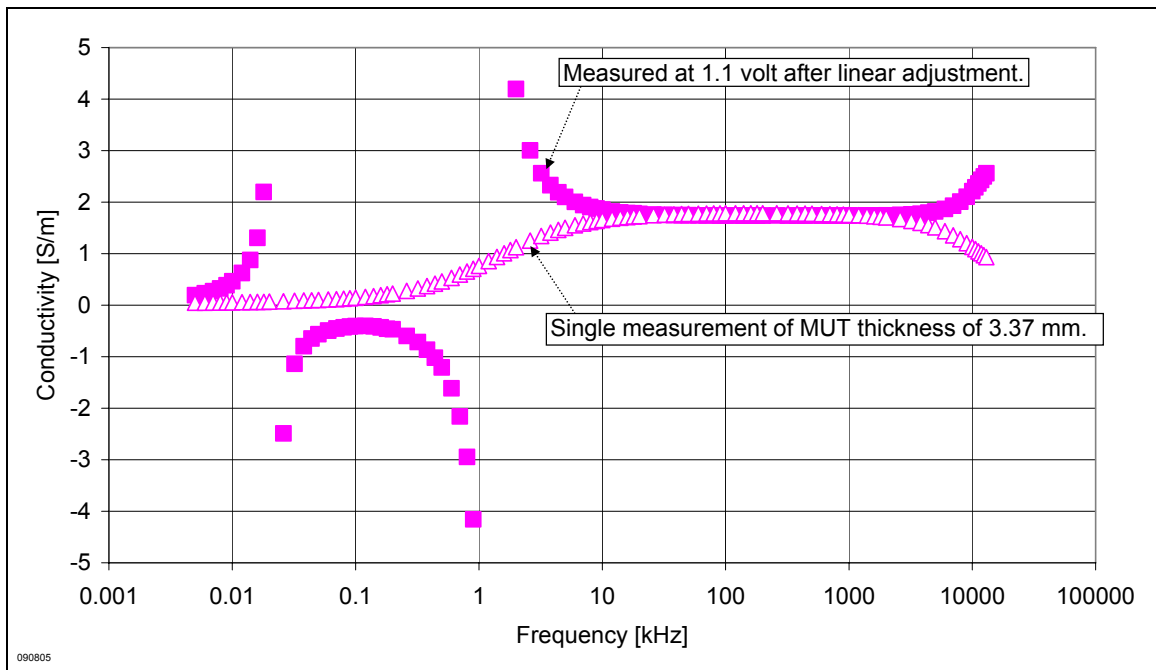


Figure 79 Conductivity on 0.9% NaCl brine (Method 3). Experiment from electrode sputter coated with gold for 50 seconds. The conductivity below 10 kHz was influenced by parasitic impedance effects, and was also suggested by the linear adjustments.

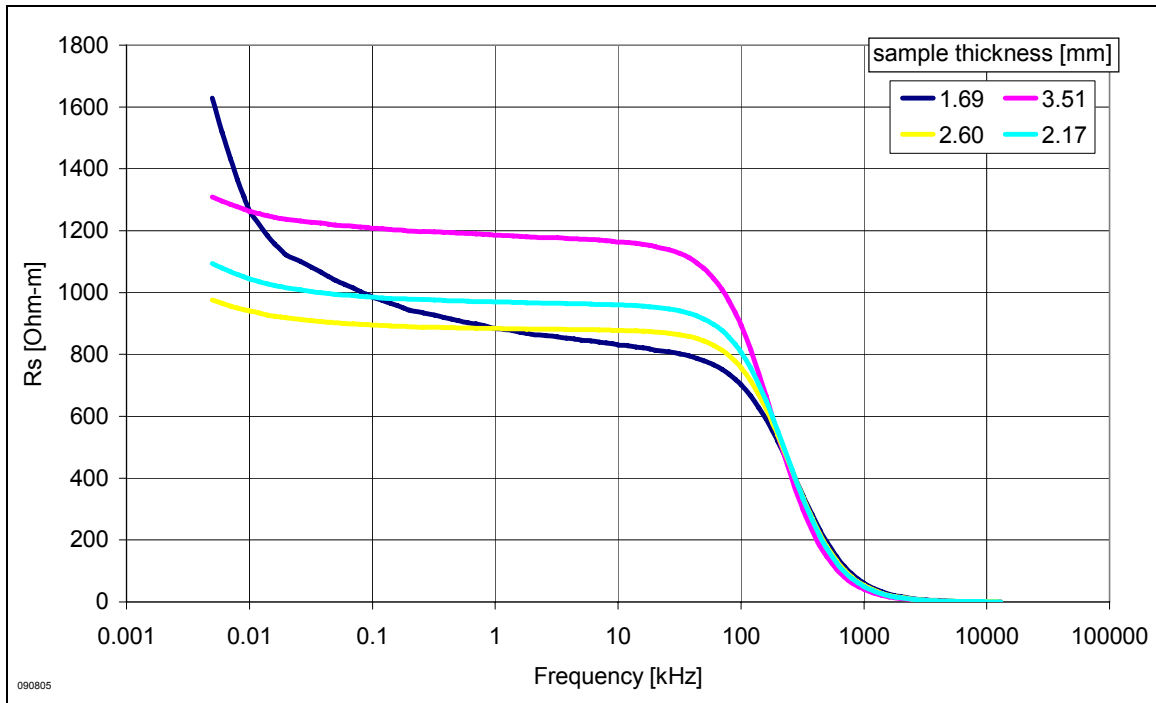


Figure 80 (Raw data) Resistivity of a series equivalent circuit. De-ionized water measurement from Figure 78.

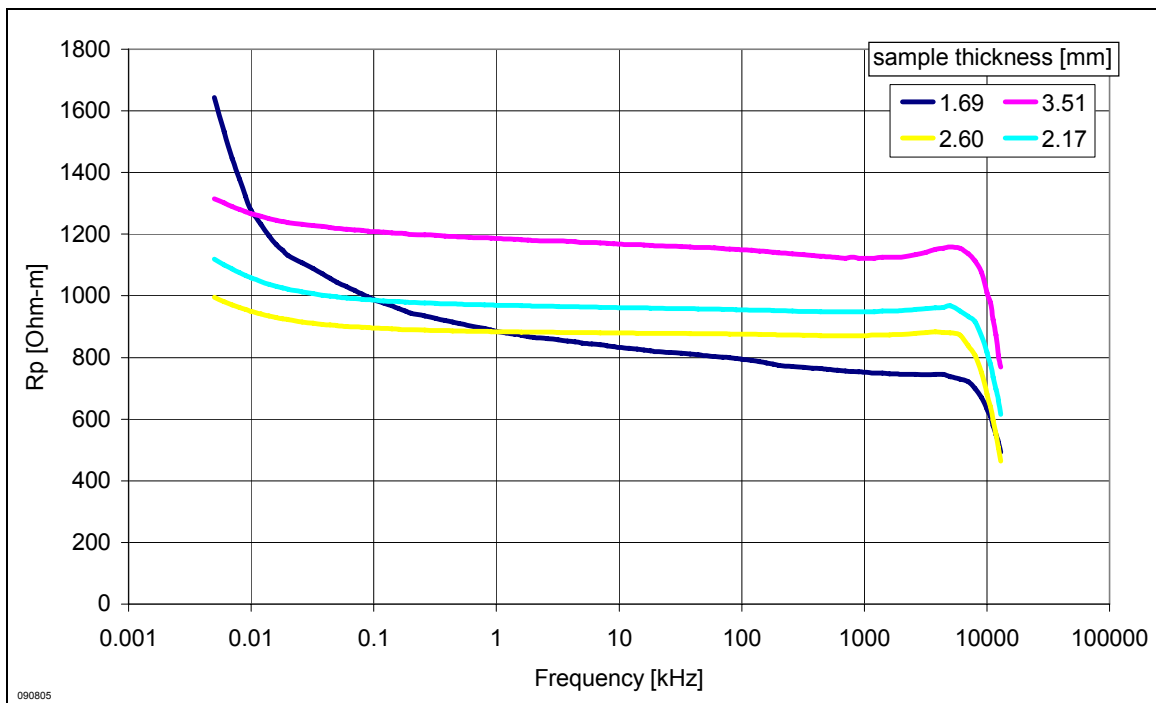


Figure 81 (Raw data) Resistivity of a parallel equivalent circuit. De-ionized water measurement from Figure 78.

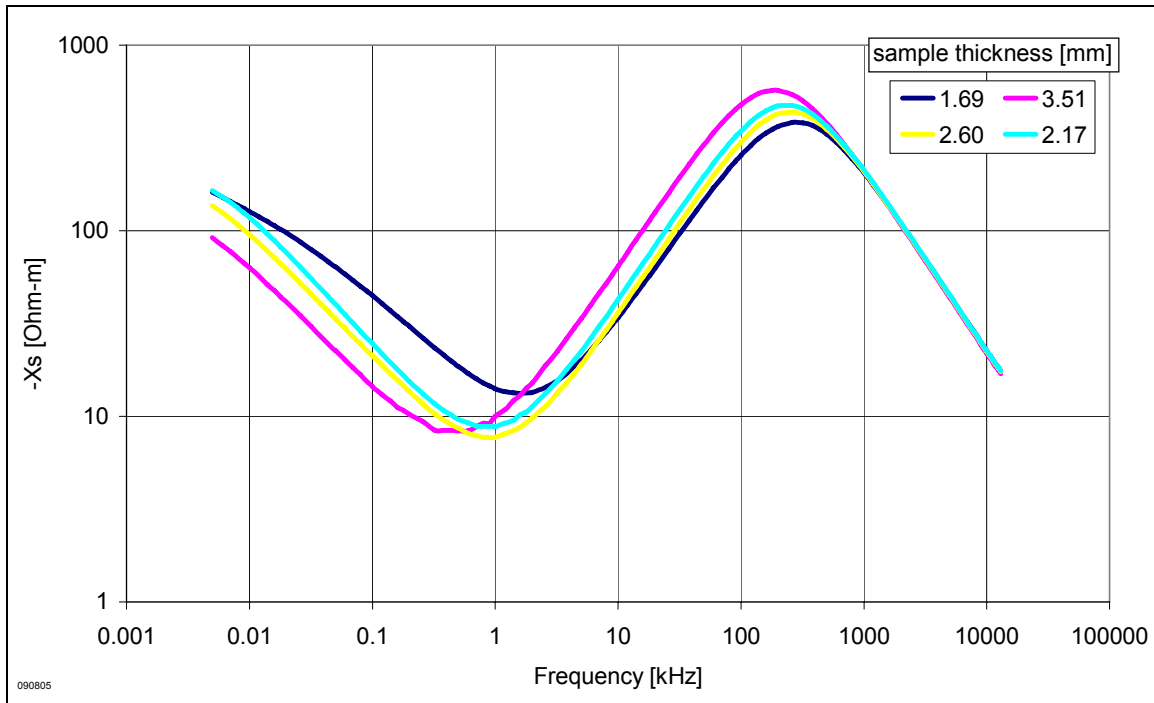


Figure 82 (Raw data) Negative reactance-m of a series equivalent circuit. De-ionized water measurement from Figure 78.

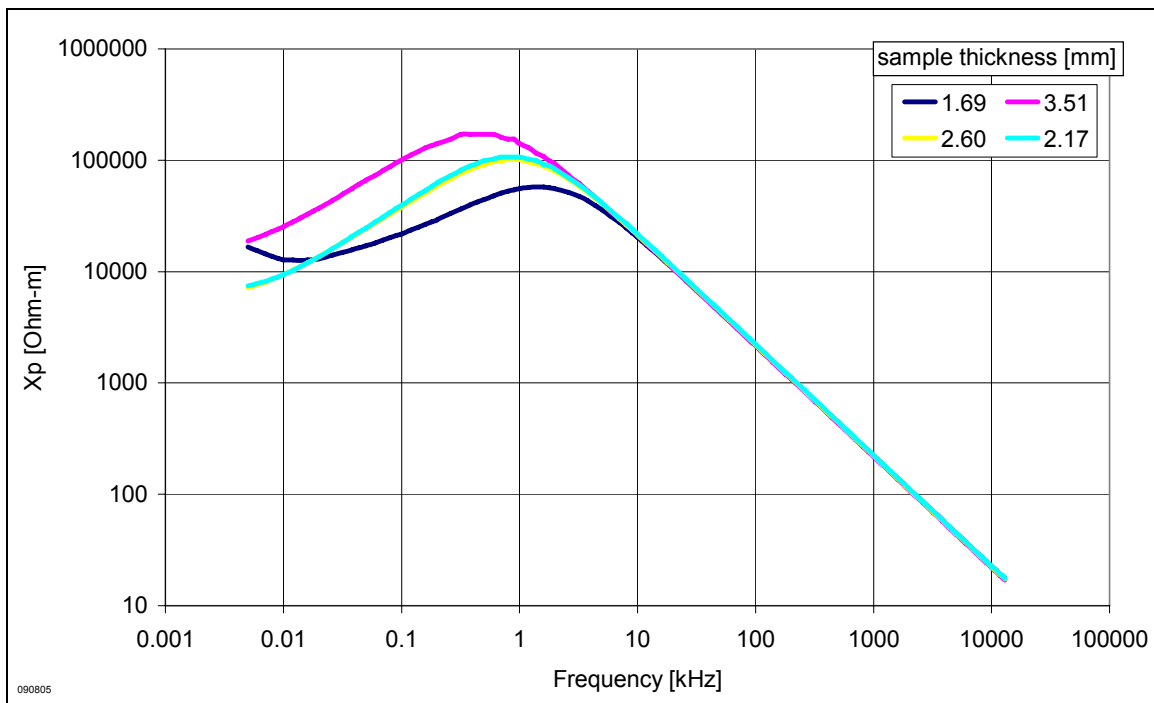


Figure 83 (Raw data) Reactance-m of a parallel equivalent circuit. De-ionized water measurement from Figure 78.

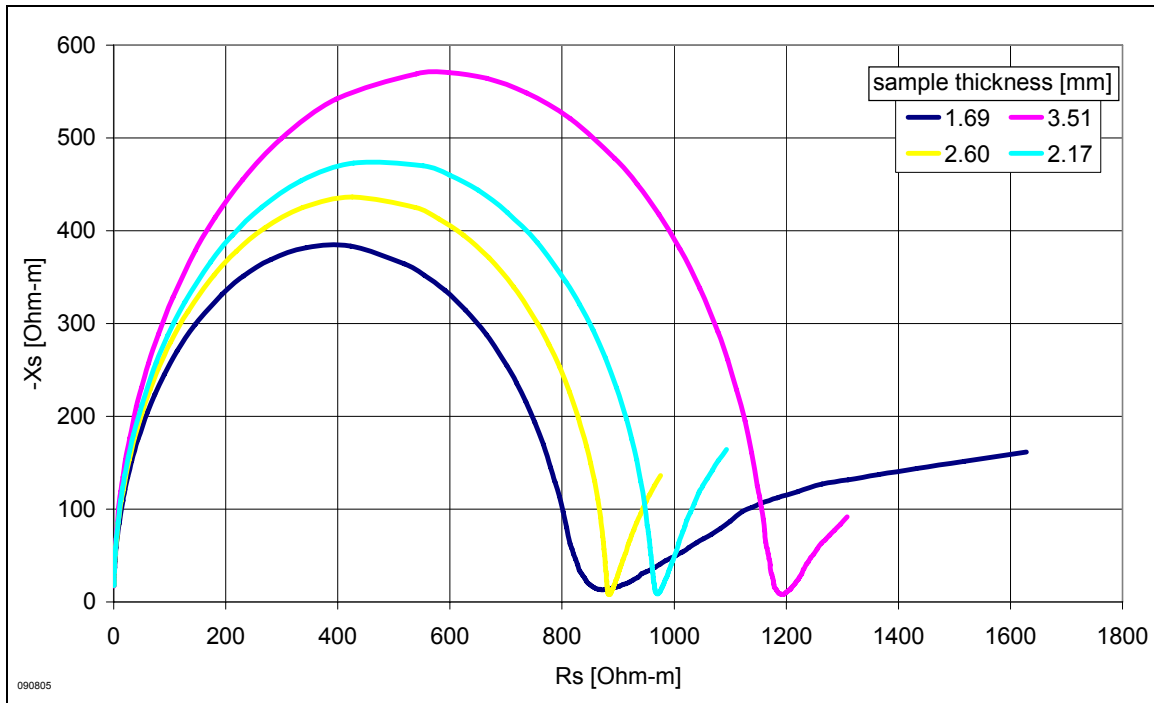


Figure 84 Argand plot of de-ionized water measurement from Figure 78.

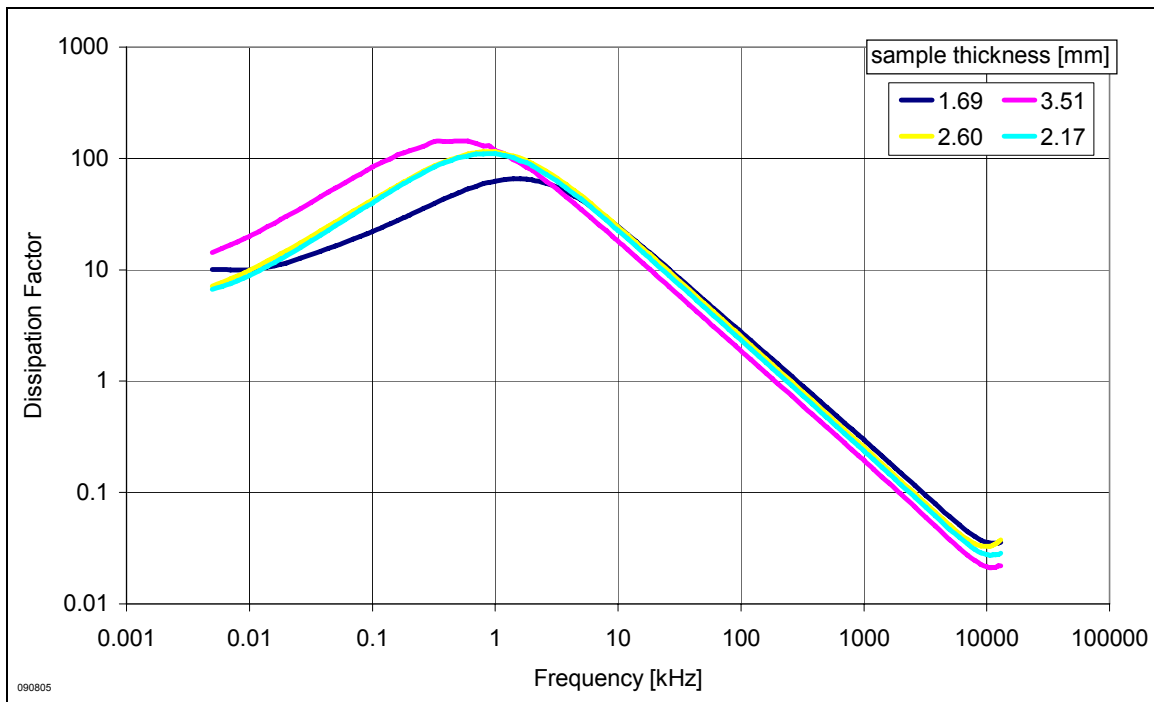


Figure 85 Dissipation factor of de-ionized water measurement from Figure 78.

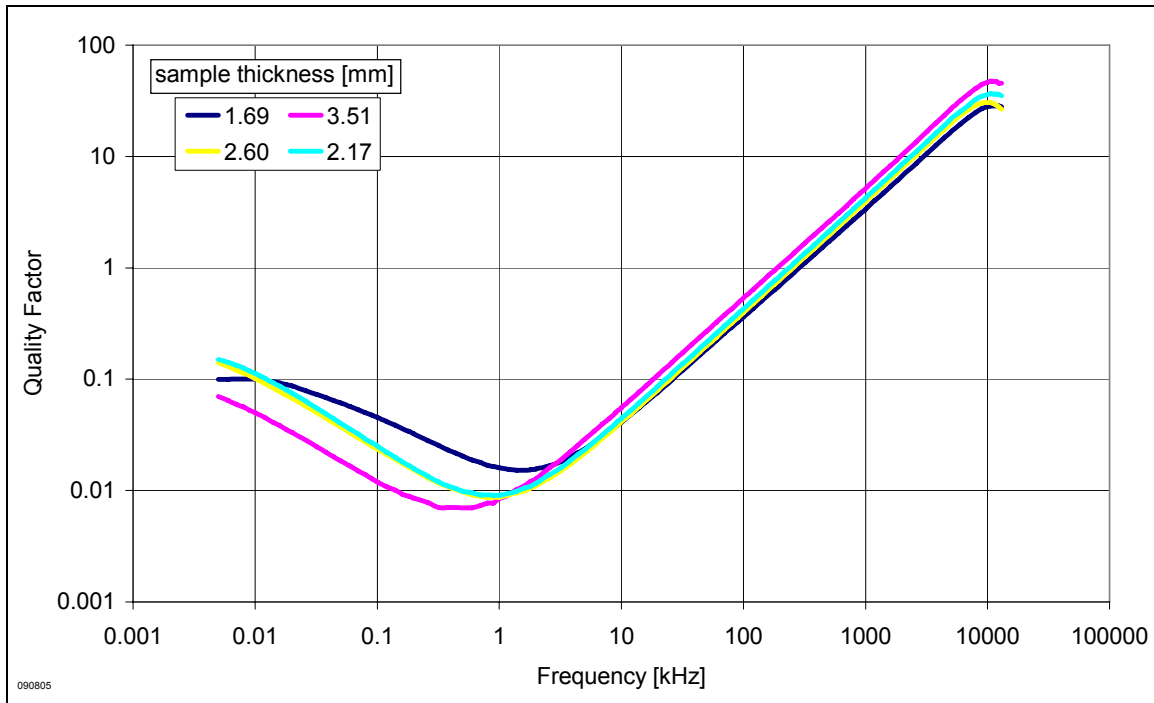


Figure 86 Quality factor of de-ionized water measurement from Figure 78.

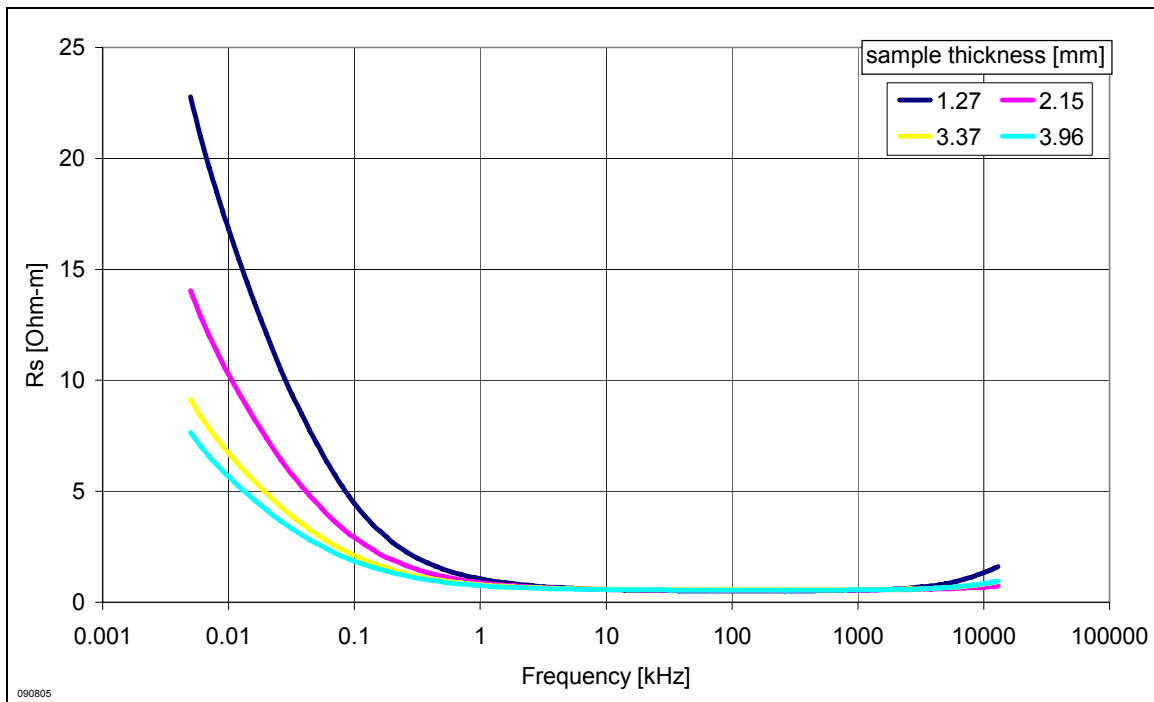


Figure 87 (Raw data) Resistivity of a series equivalent circuit. 0.9% brine measurement from Figure 78 and Figure 79.

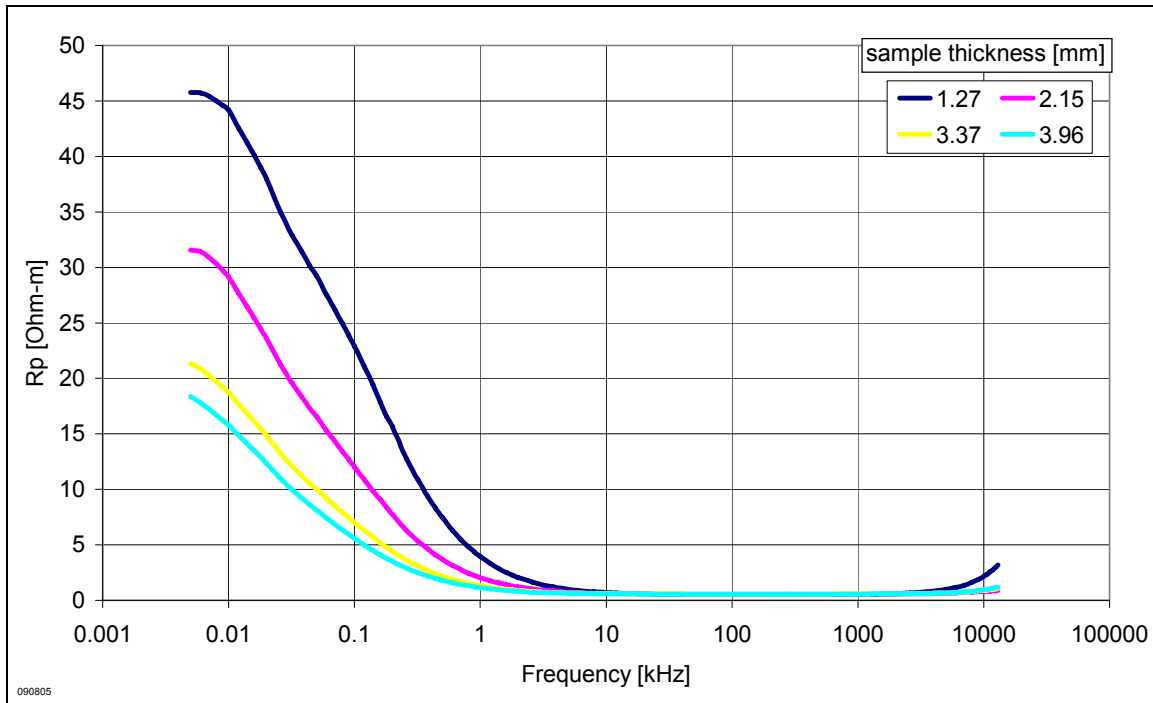


Figure 88 (Raw data) Resistivity of a parallel equivalent circuit. 0.9% brine measurement from Figure 78 and Figure 79.

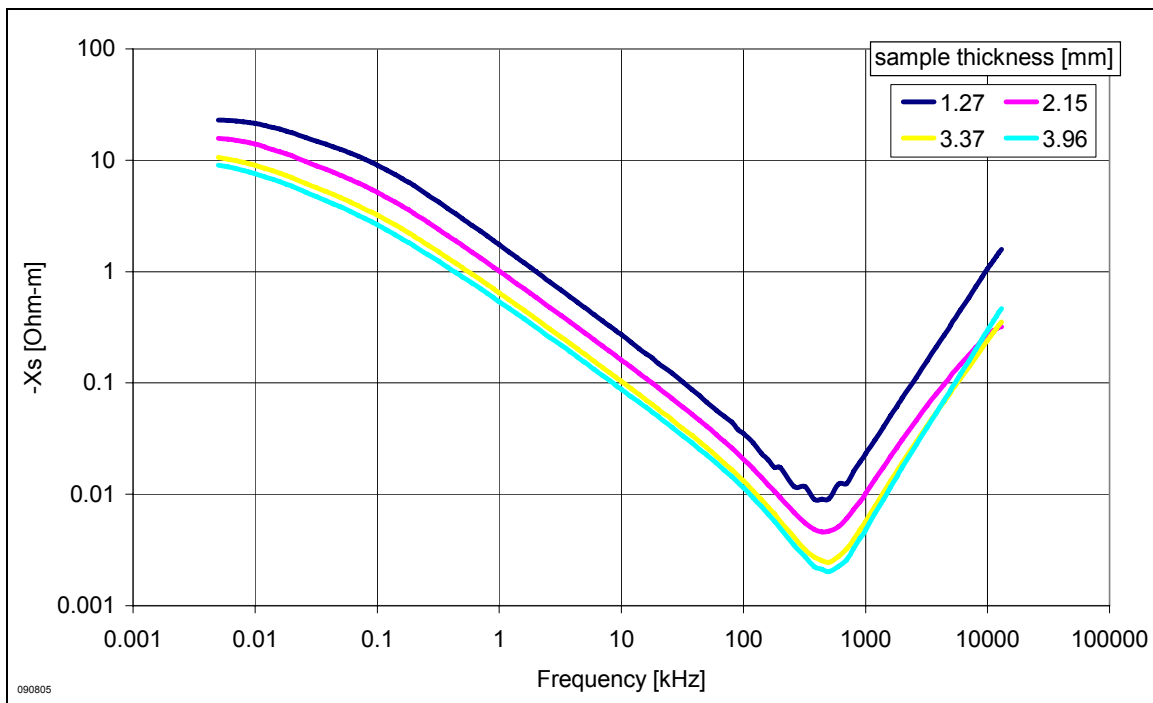


Figure 89 (Raw data) Negative reactance-m of a series equivalent circuit. 0.9% brine measurement from Figure 78 and Figure 79.

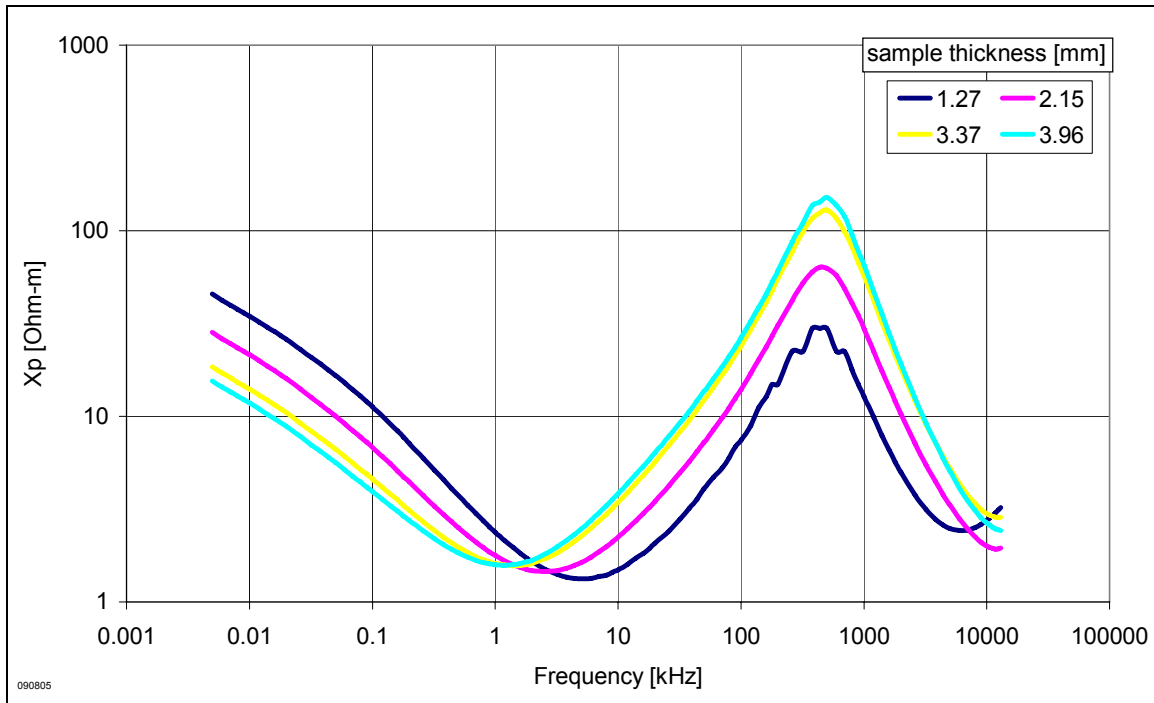


Figure 90 (Raw data) Reactance-m of a parallel equivalent circuit. 0.9% brine measurement from Figure 78 and Figure 79.

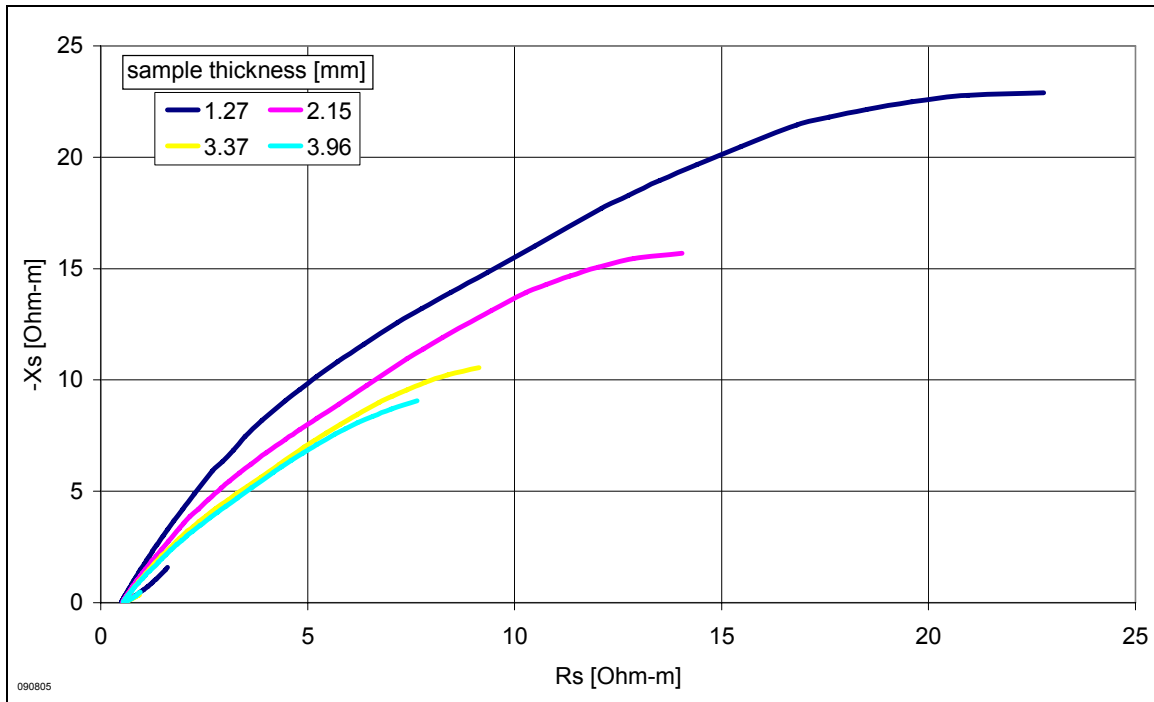


Figure 91 Argand plot of 0.9% brine measurement from Figure 78 and Figure 79.

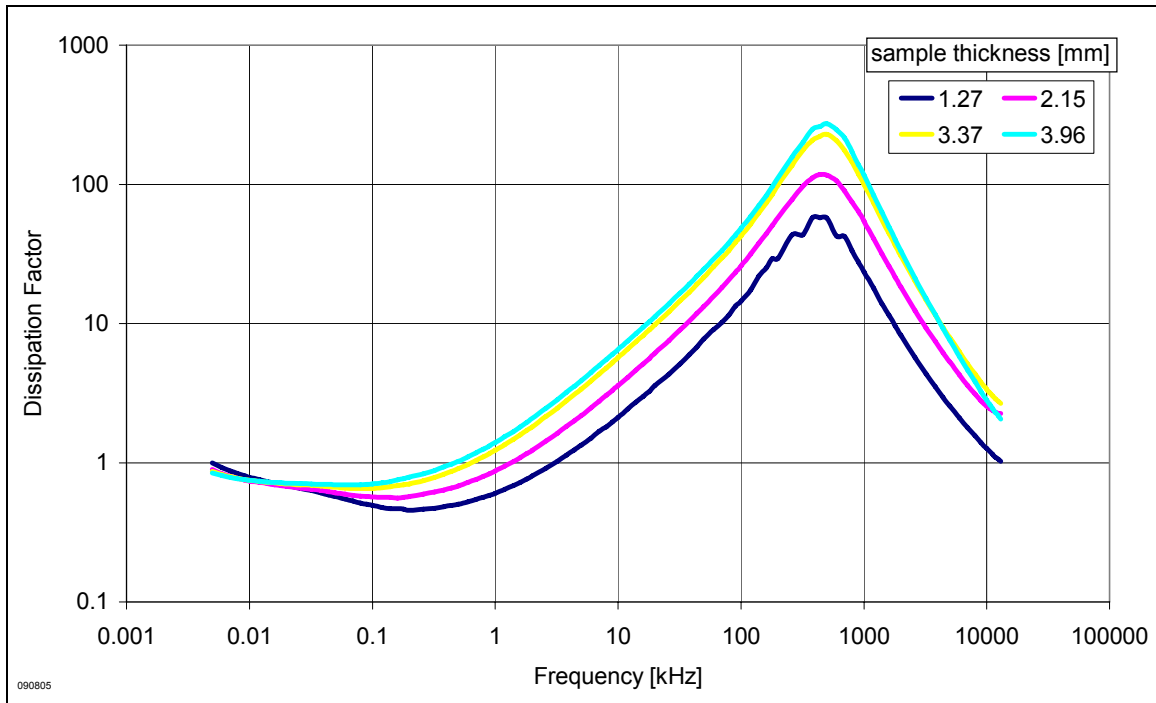


Figure 92 Dissipation factor of 0.9% brine measurement from Figure 78 and Figure 79.

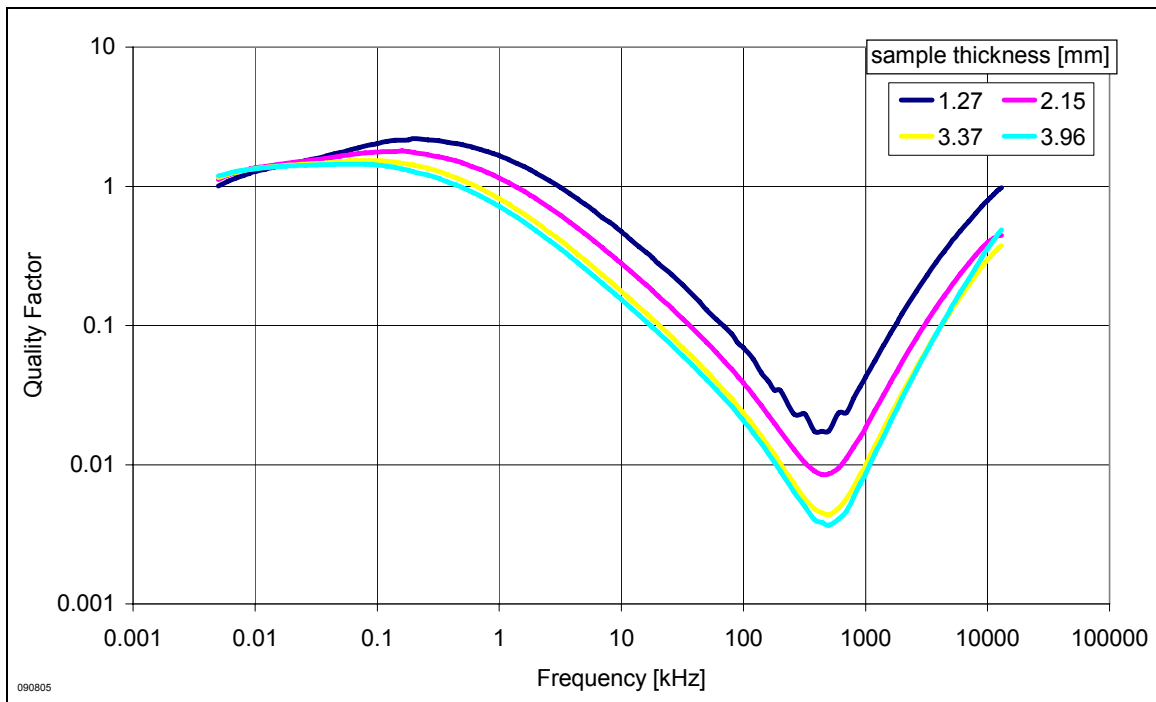


Figure 93 Quality factor of 0.9% brine measurement from Figure 78 and Figure 79.

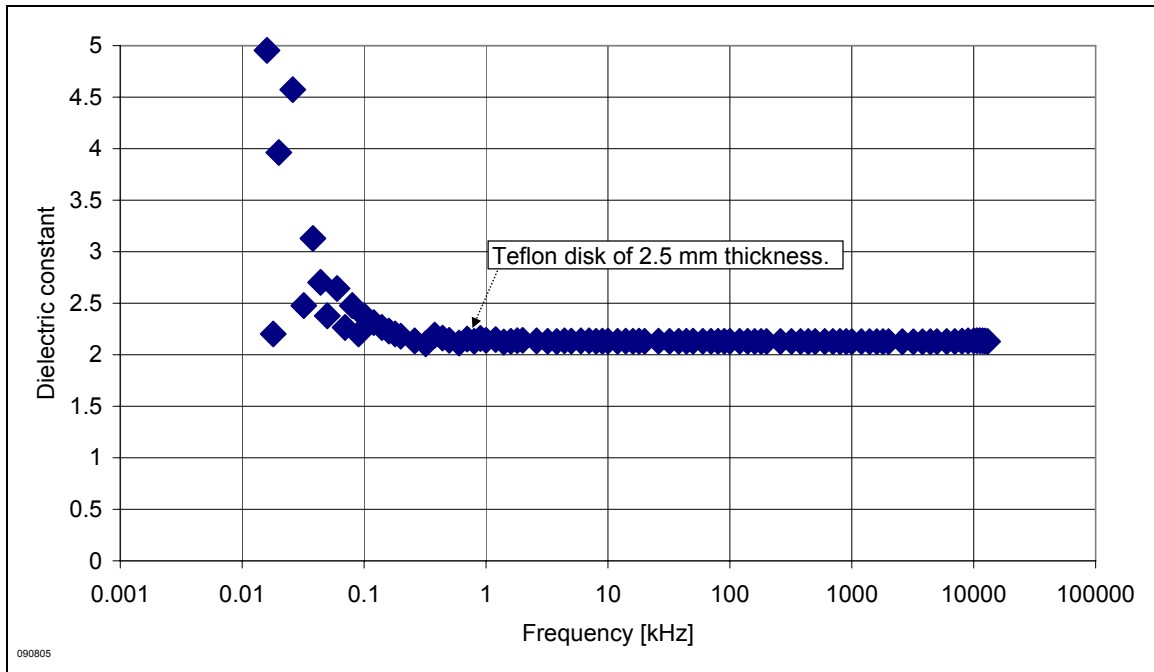


Figure 94 Dielectric measurement on a 2.5 mm thick Teflon disk (Method 3).

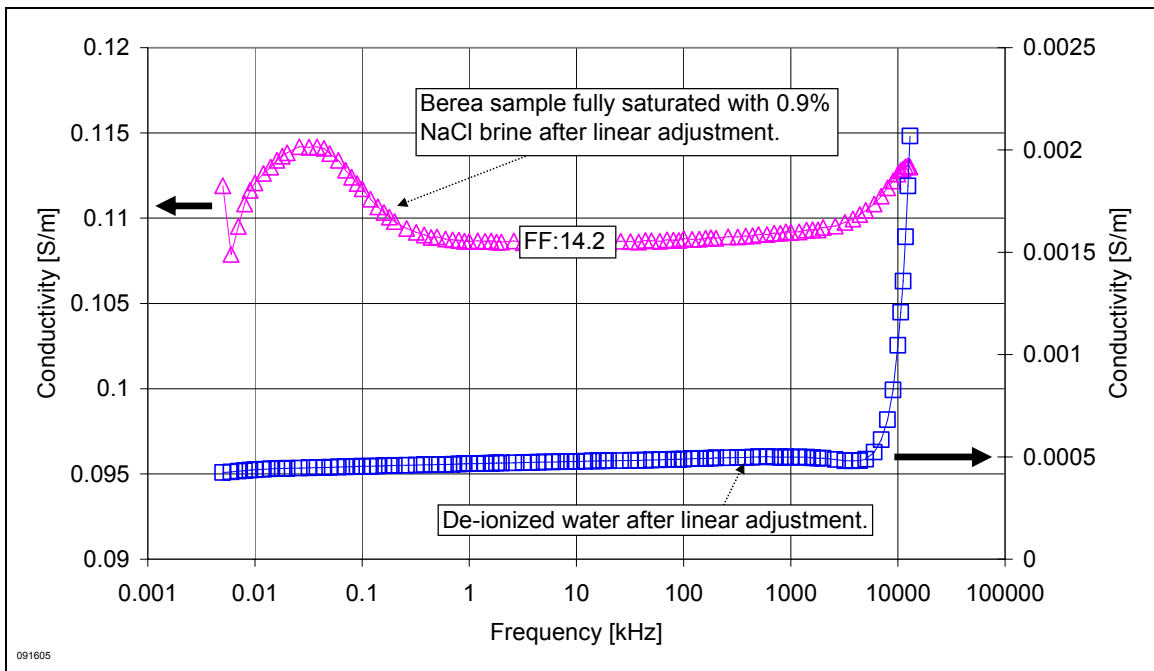


Figure 95 Conductivity measurement on de-ionized water and Berea sample saturated with 0.9% NaCl brine after second gold coating on the electrodes (Method 3).

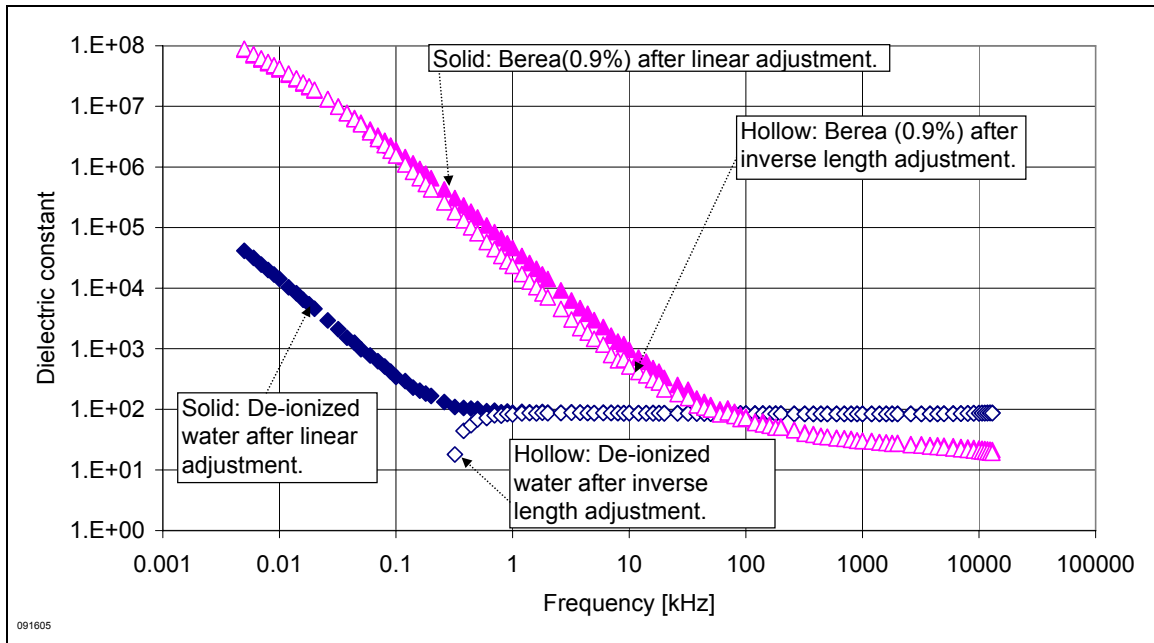


Figure 96 Dielectric constant measurement on de-ionized water and Berea sample saturated with 0.9% NaCl brine after second gold coating on the electrodes (Method 3). The results are very similar to measurements made after the first gold coating in Figure 70 and Figure 78.

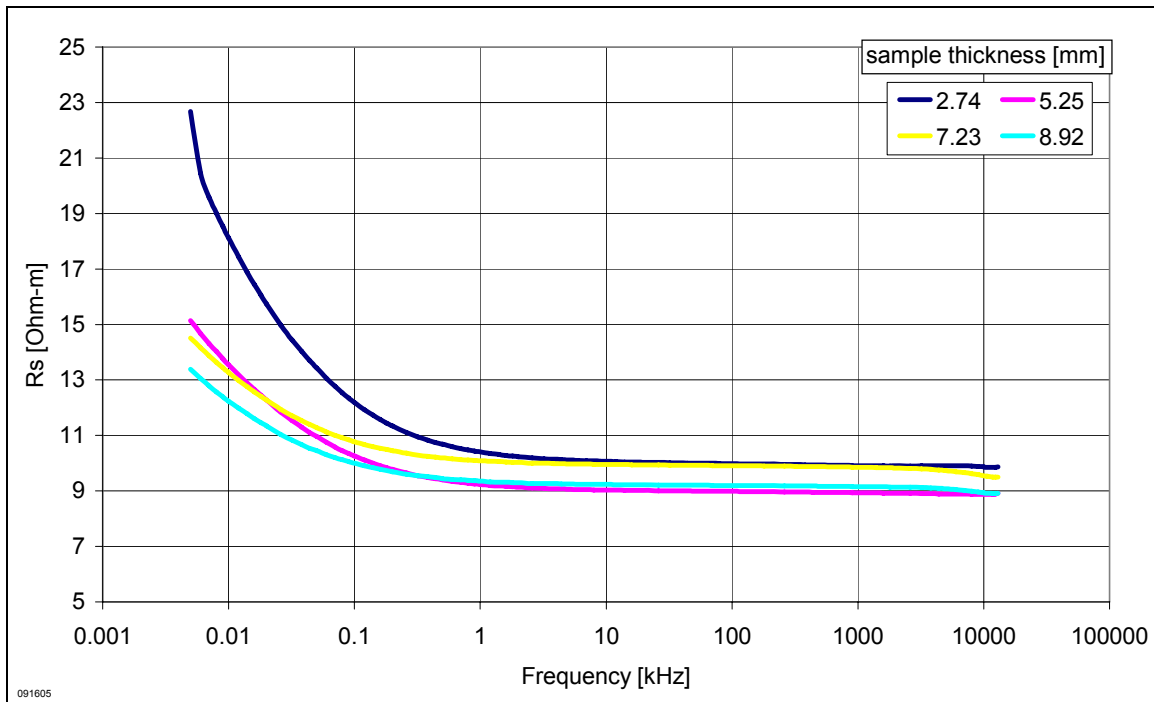


Figure 97 (Raw data) Resistivity of a series equivalent circuit. Berea sample measurement from Figure 95 and Figure 96.

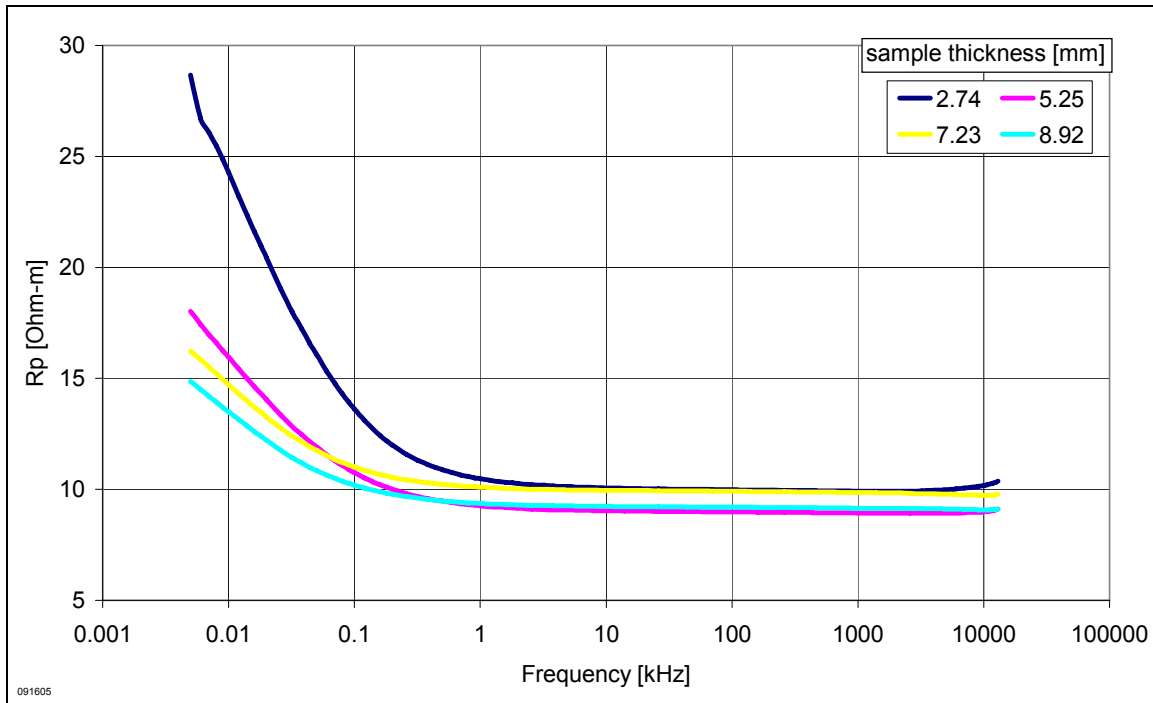


Figure 98 (Raw data) Resistivity of a parallel equivalent circuit. Berea sample measurement from Figure 95 and Figure 96.

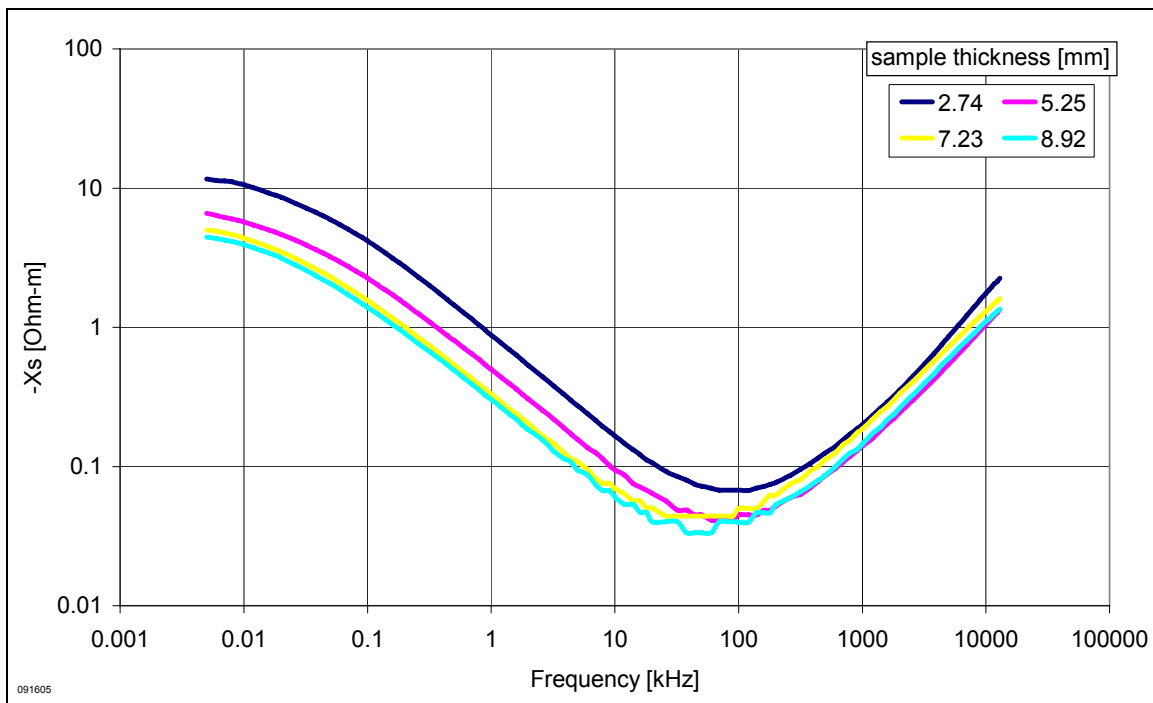


Figure 99 (Raw data) Negative reactance-m of a series equivalent circuit. Berea sample measurement from Figure 95 and Figure 96.

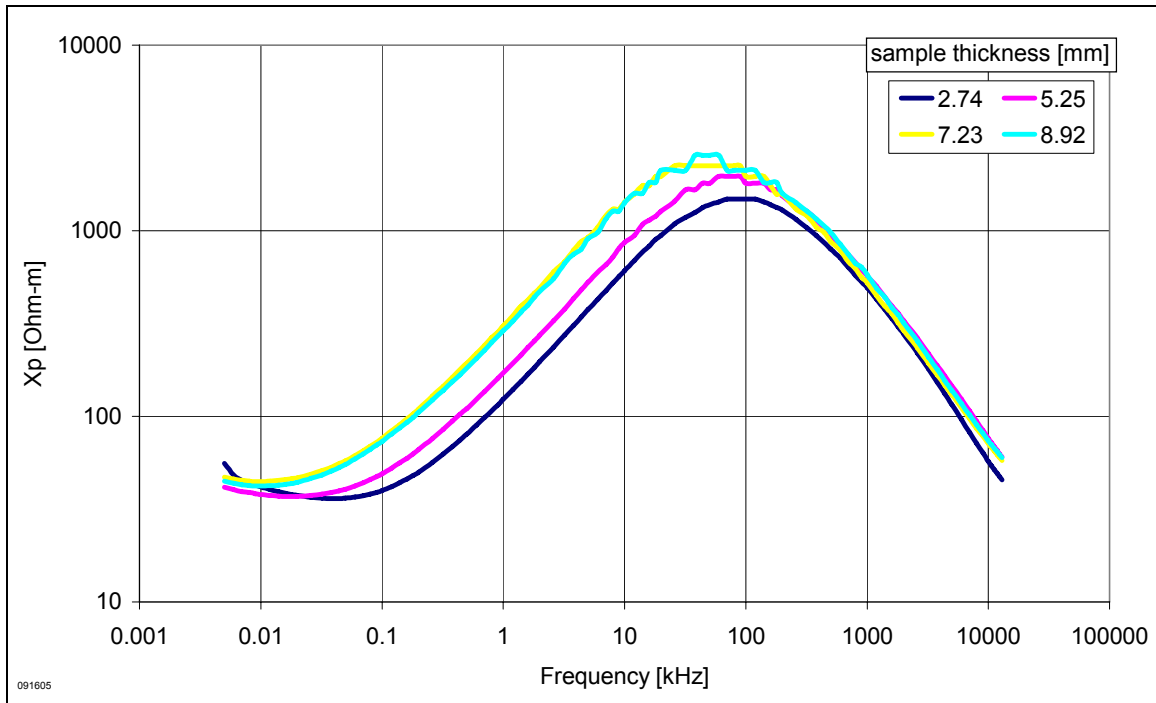


Figure 100 (Raw data) Reactance-m of a parallel equivalent circuit. Berea sample measurement from Figure 95 and Figure 96.

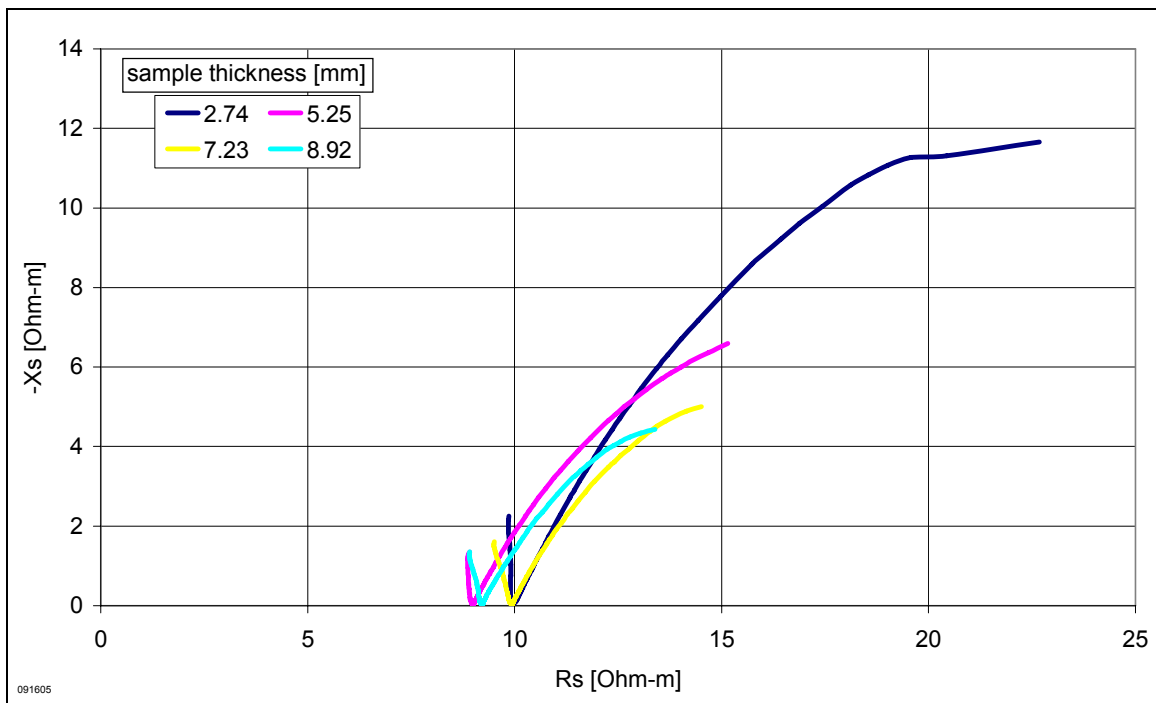


Figure 101 Argand plot of Berea sample measurement from Figure 95 and Figure 96.

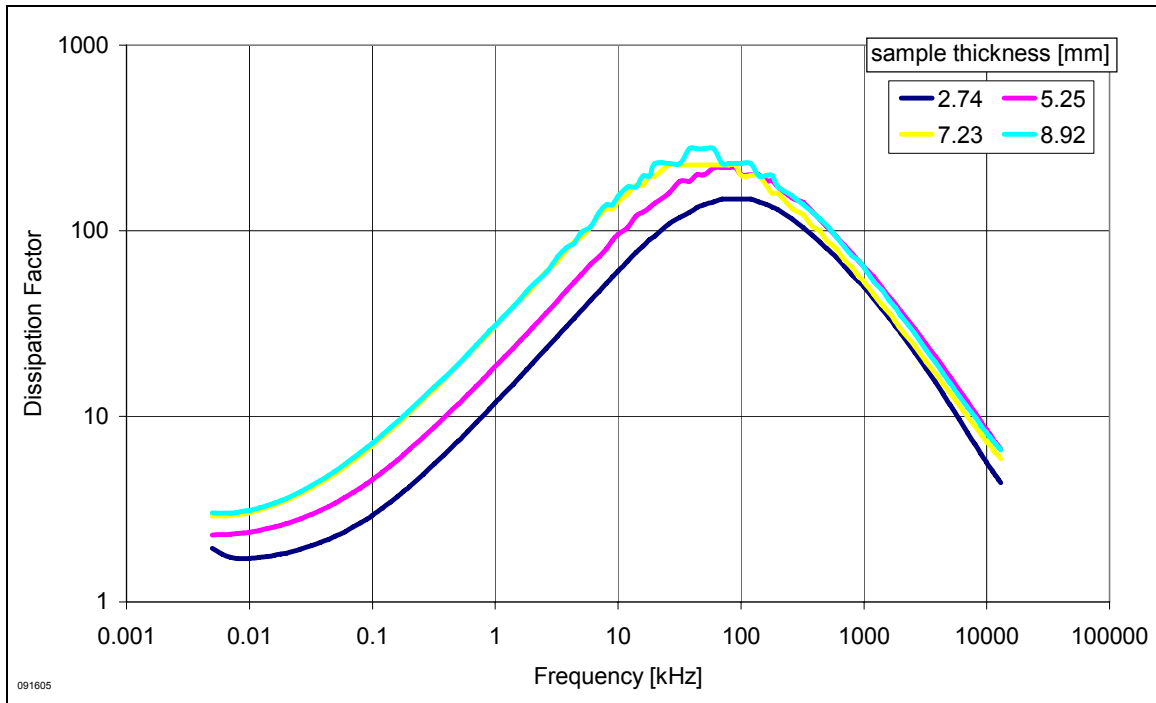


Figure 102 Dissipation factor of Berea sample measurement from Figure 95 and Figure 96.

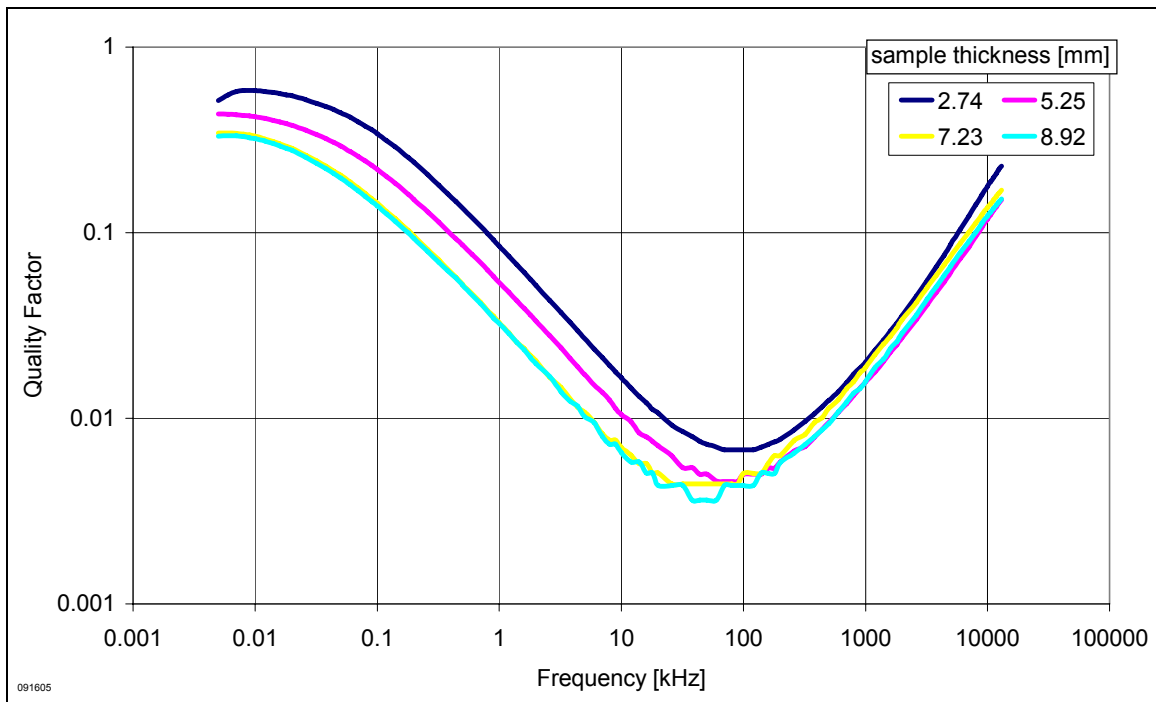


Figure 103 Quality factor of Berea sample measurement from Figure 95 and Figure 96.

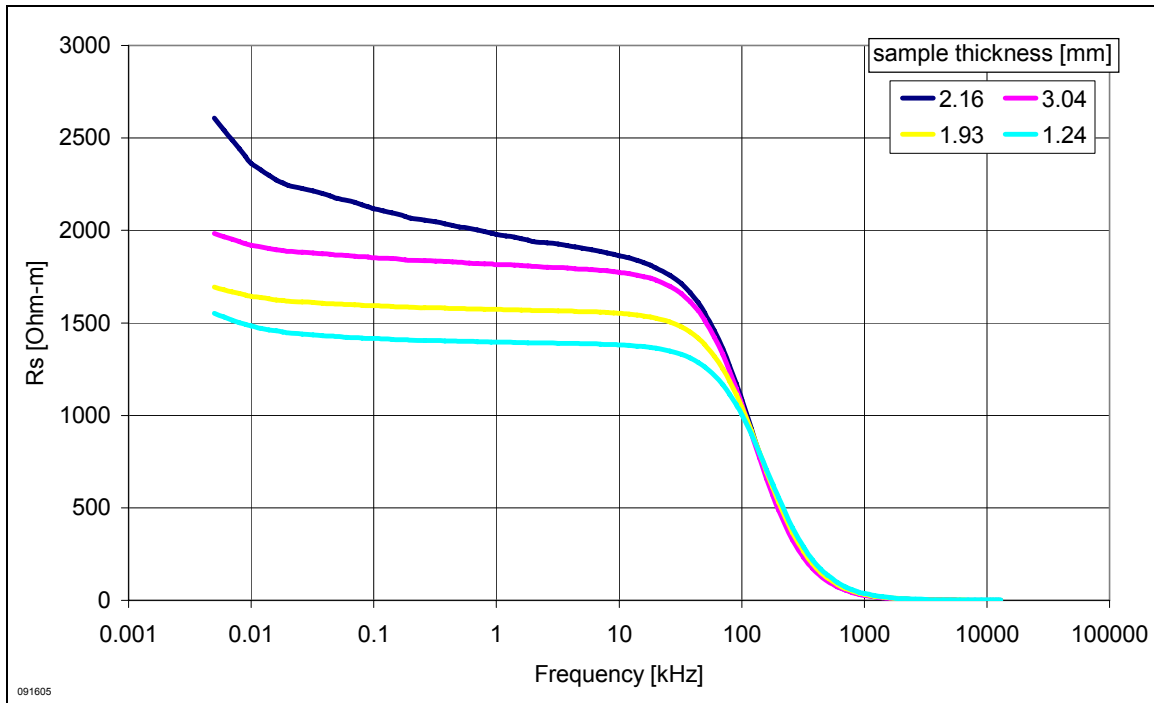


Figure 104 (Raw data) Resistivity of a series equivalent circuit. De-ionized water measurement from Figure 95 and Figure 96.

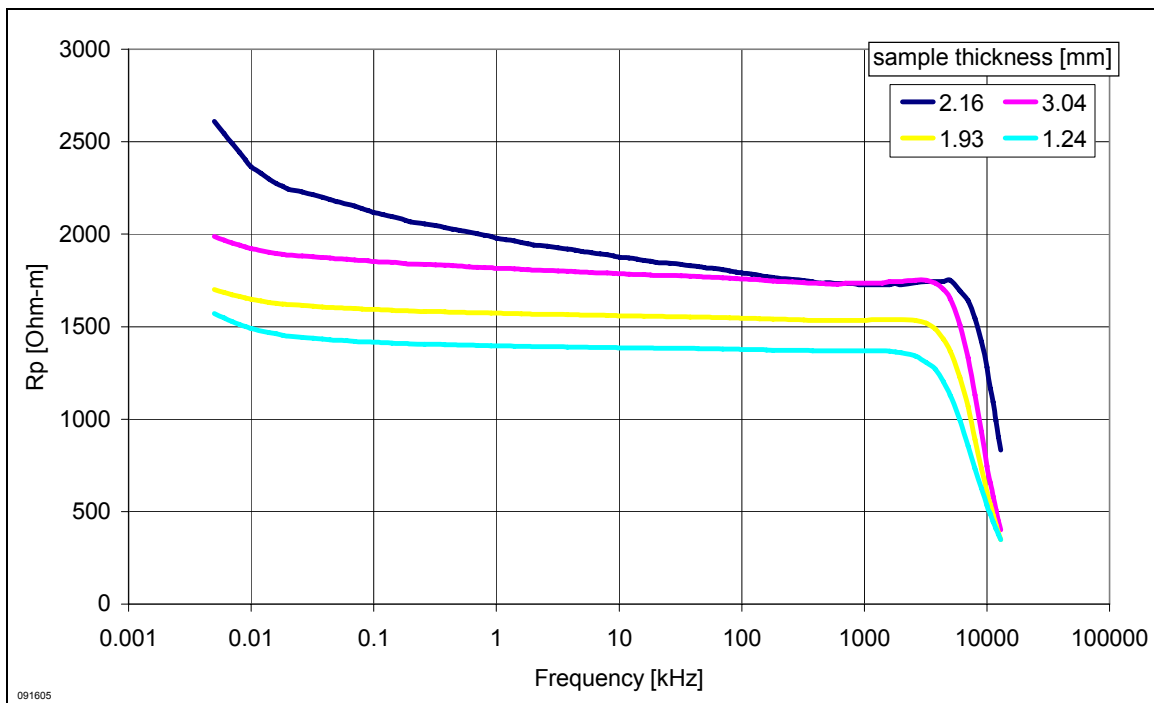


Figure 105 (Raw data) Resistivity of a parallel equivalent circuit. De-ionized water measurement from Figure 95 and Figure 96.

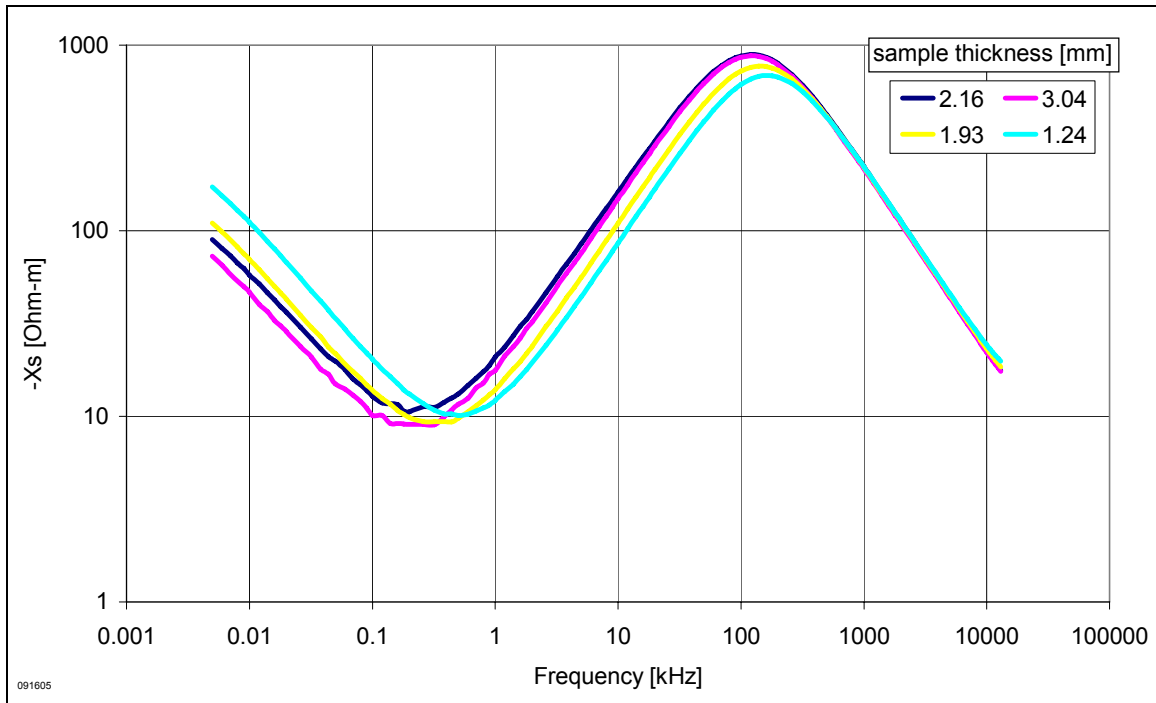


Figure 106 (Raw data) Negative reactance-m of a series equivalent circuit. De-ionized water measurement from Figure 95 and Figure 96.

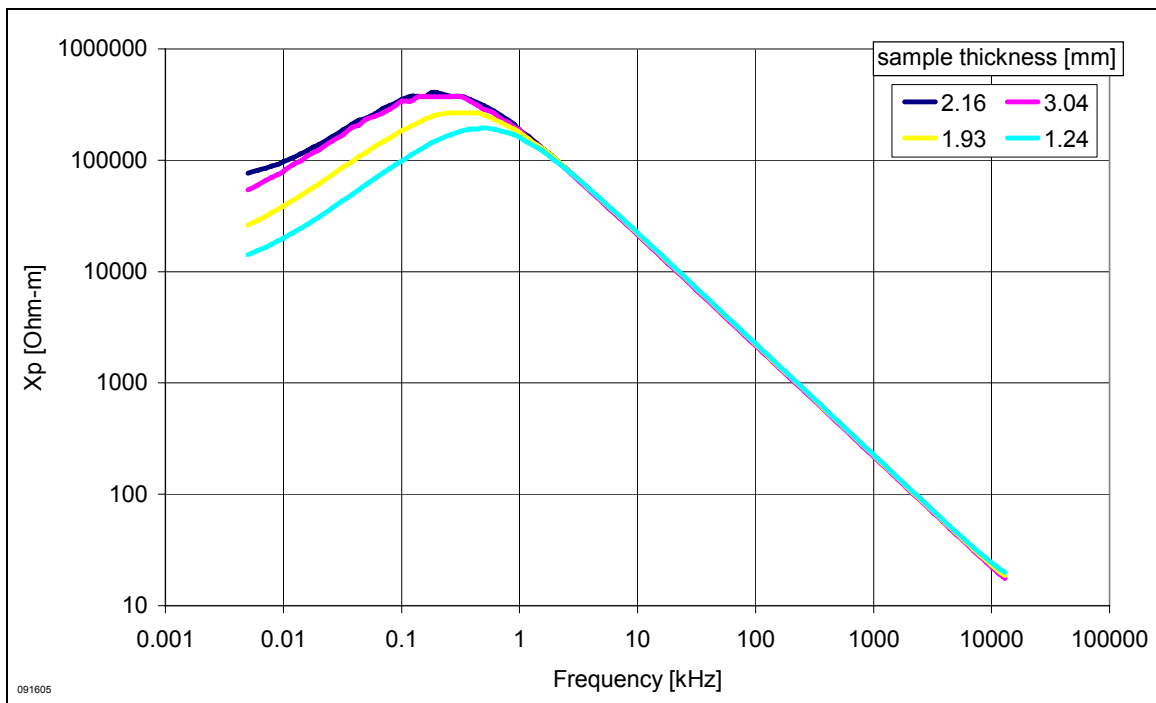


Figure 107 (Raw data) Reactance-m of a parallel equivalent circuit. De-ionized water measurement from Figure 95 and Figure 96.

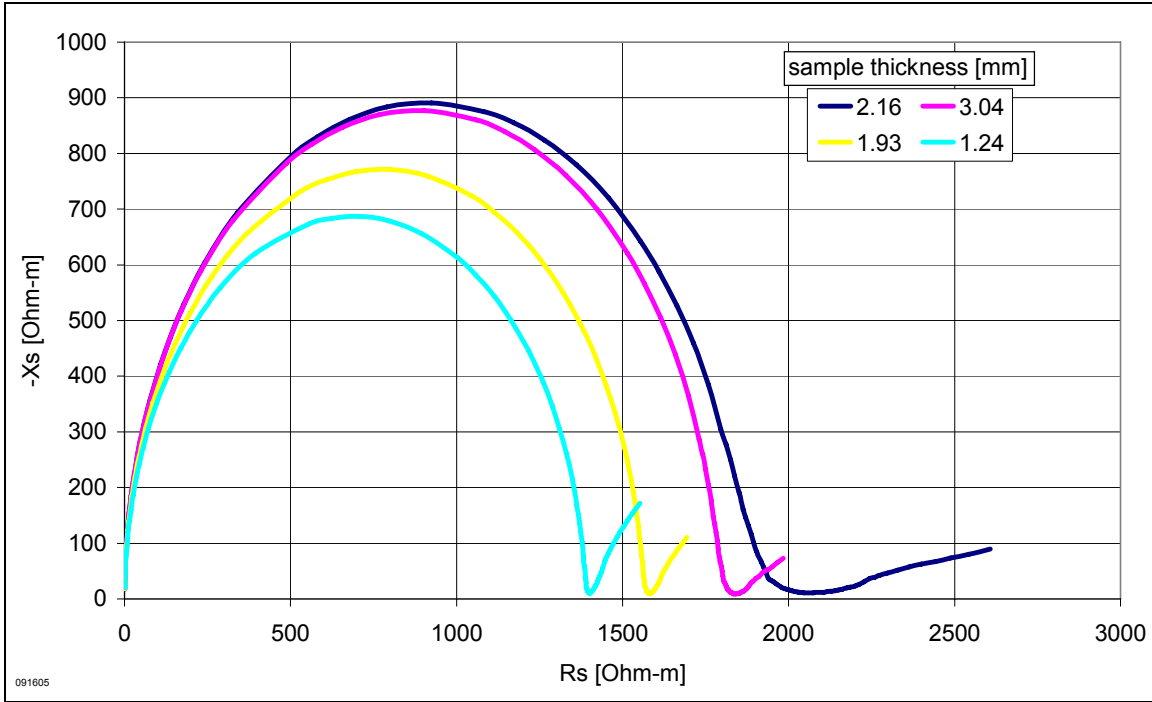


Figure 108 Argand plot of de-ionized water measurement from Figure 95 and Figure 96.

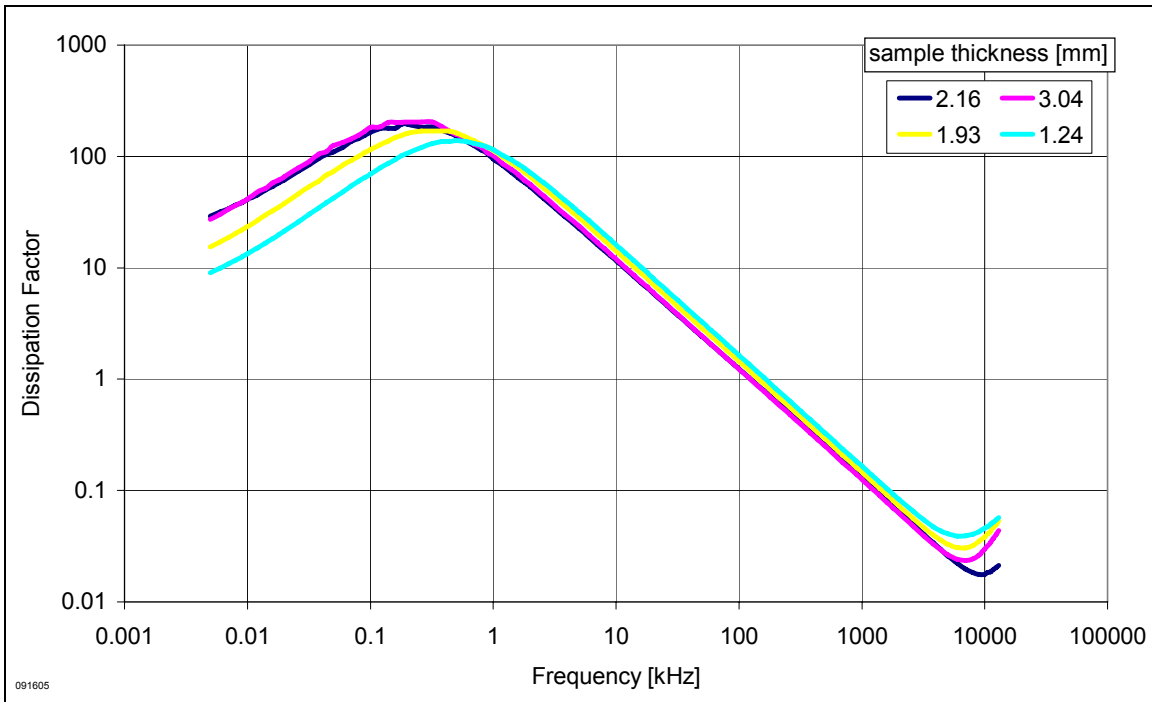


Figure 109 Dissipation factor of de-ionized water measurement from Figure 95 and Figure 96.

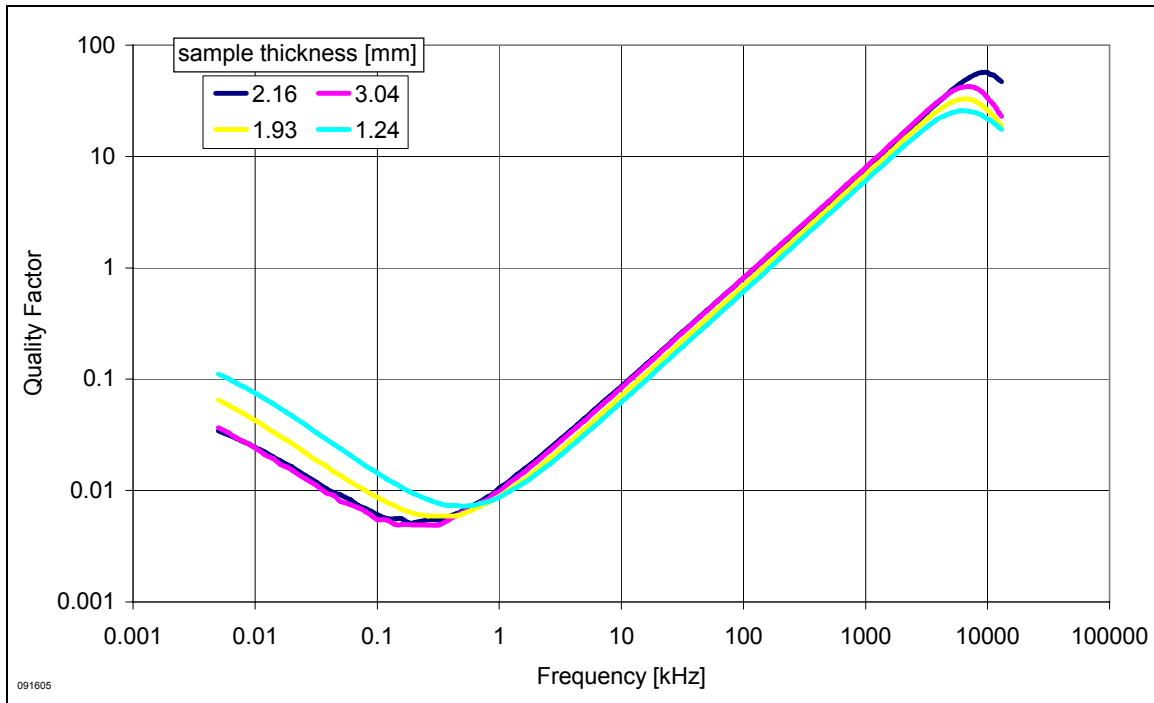


Figure 110 Quality factor of de-ionized water measurement from Figure 95 and Figure 96.

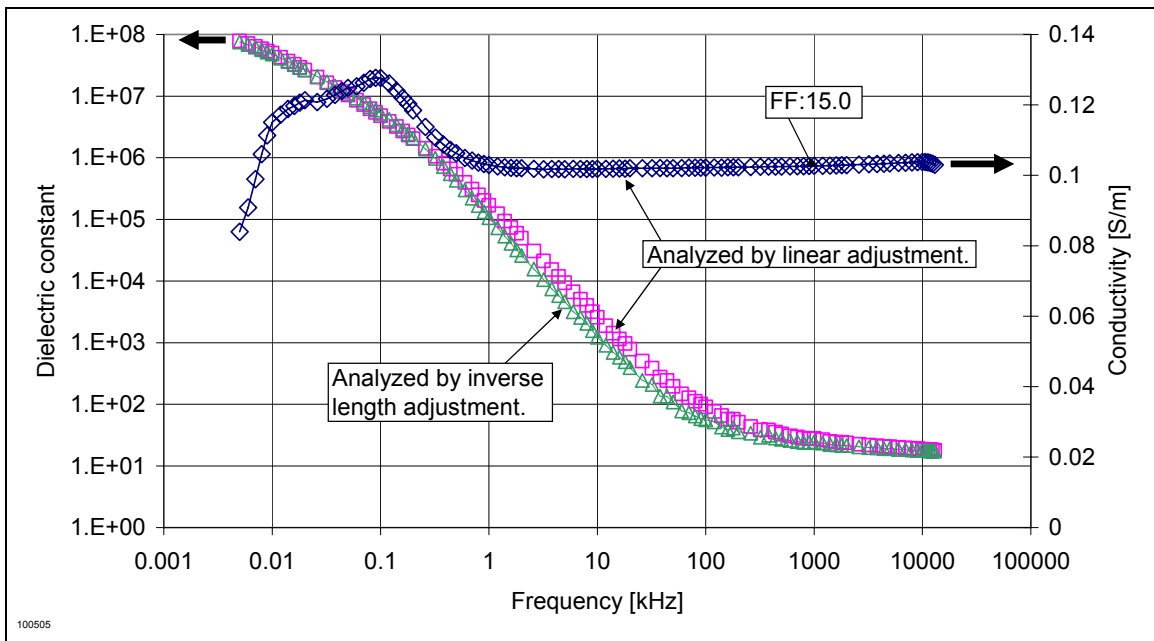


Figure 111 Measurements by partially PVD coated electrodes made on same Berea samples used in sputter coated experiments (Berea fully saturated with 0.9% NaCl brine. Method 3). The outcome was very similar to previous experiments with sputter coated electrodes shown in Figure 95 and Figure 96.

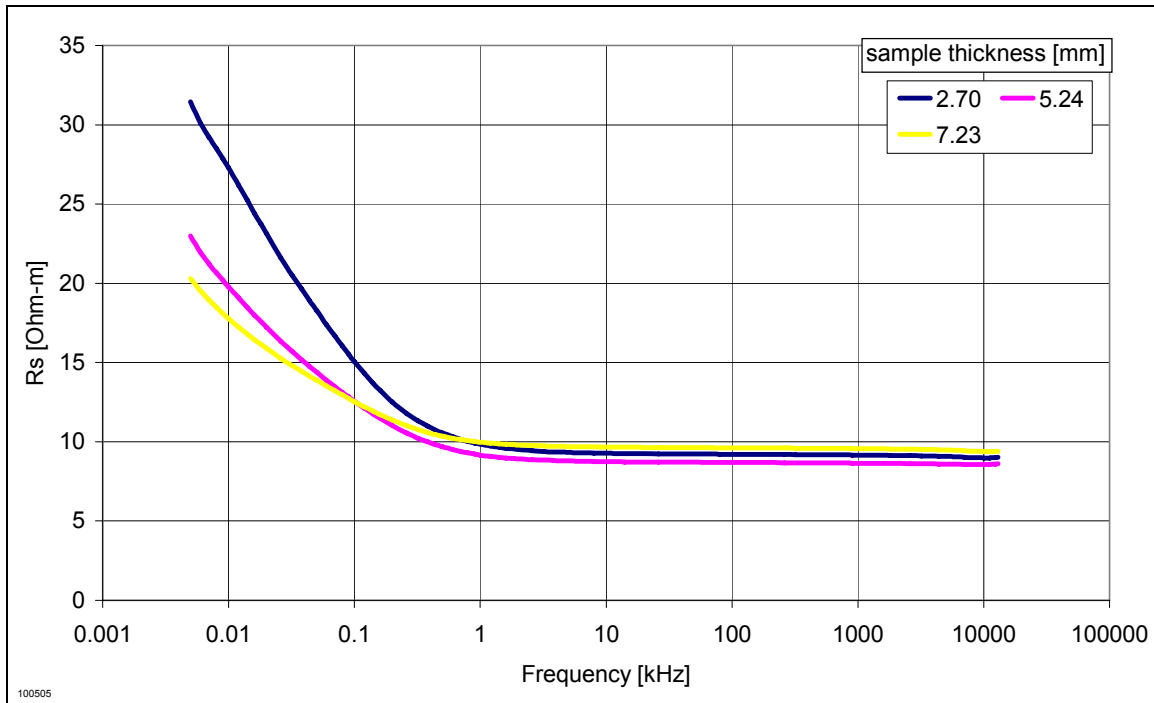


Figure 112 (Raw data) Resistivity of a series equivalent circuit. Berea sample measurement from Figure 111.

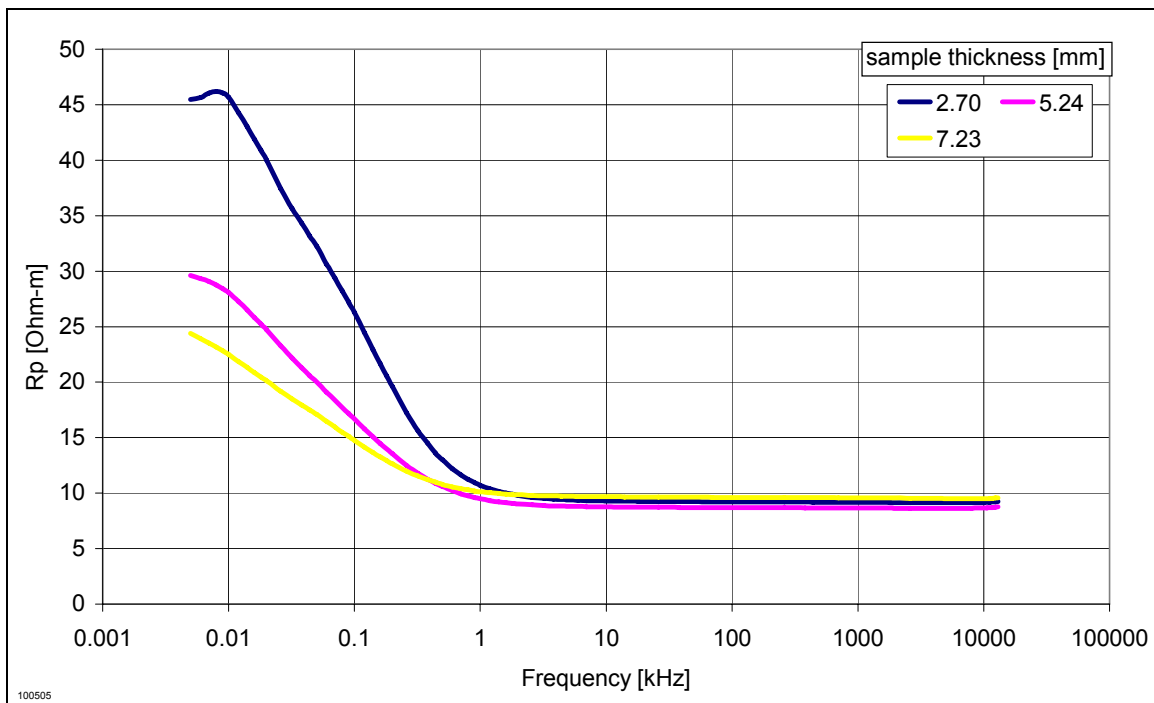


Figure 113 (Raw data) Resistivity of a parallel equivalent circuit. Berea sample measurement from Figure 111.

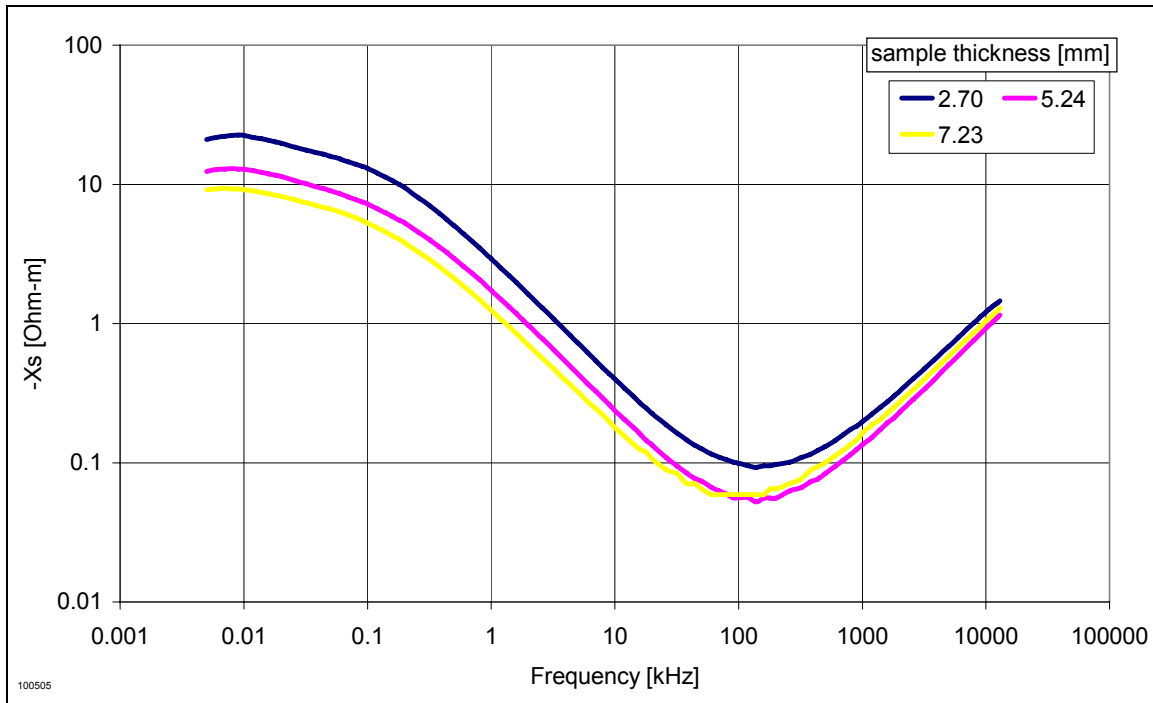


Figure 114 (Raw data) Negative reactance-m of a series equivalent circuit. Berea sample measurement from Figure 111.

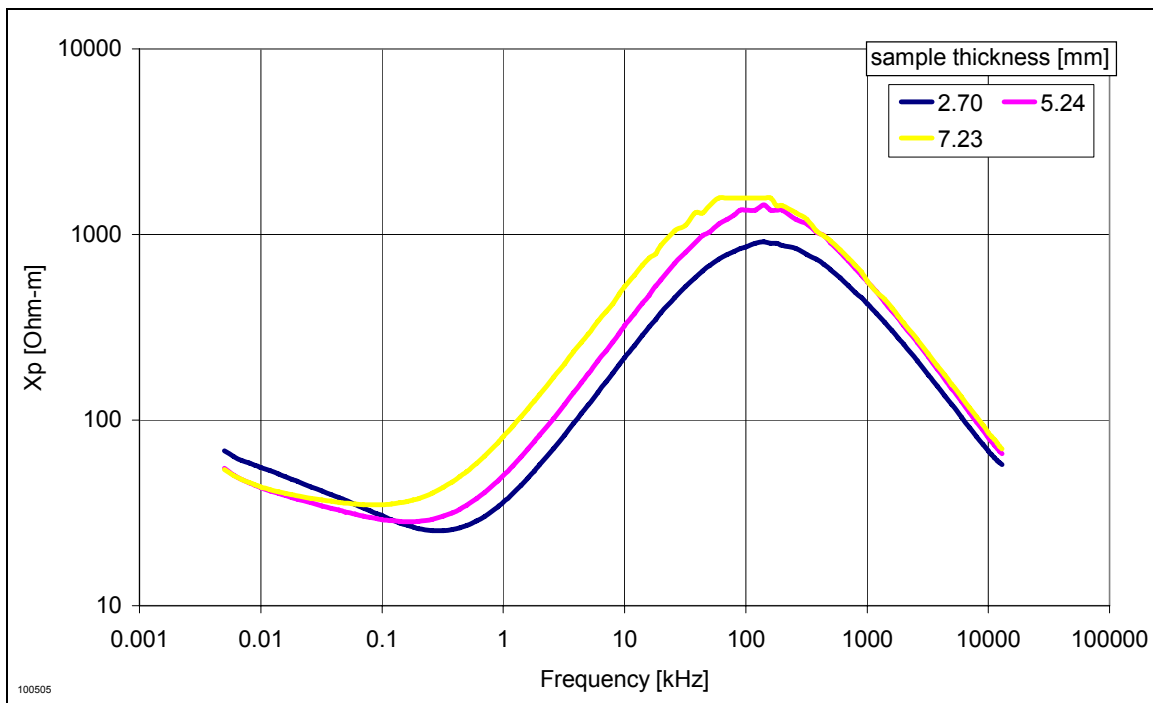


Figure 115 (Raw data) Reactance-m of a parallel equivalent circuit. Berea sample measurement from Figure 111.

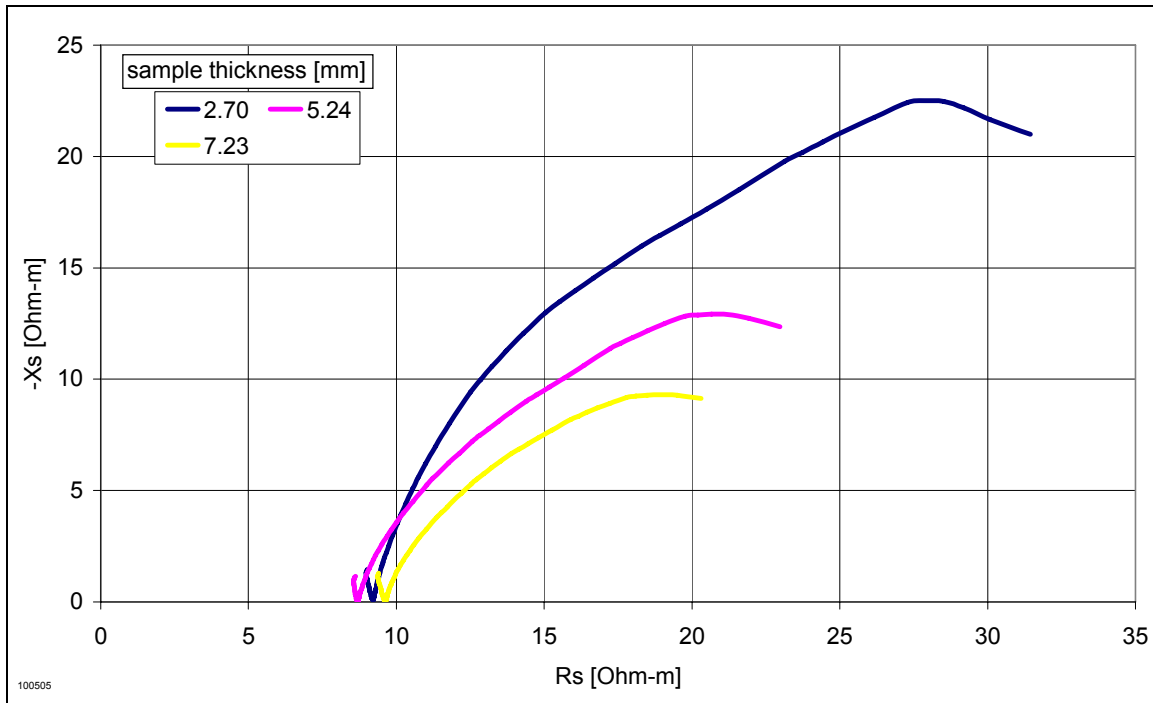


Figure 116 Argand plot of Berea sample measurement from Figure 111.

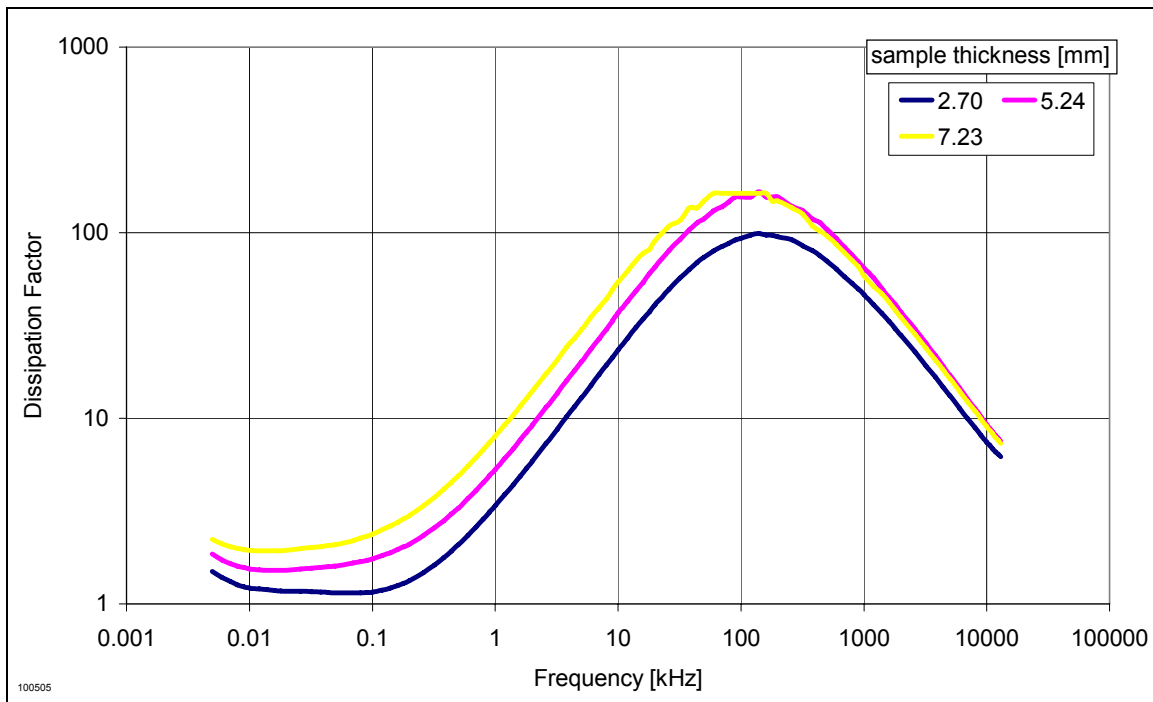


Figure 117 Dissipation factor of Berea sample measurement from Figure 111.

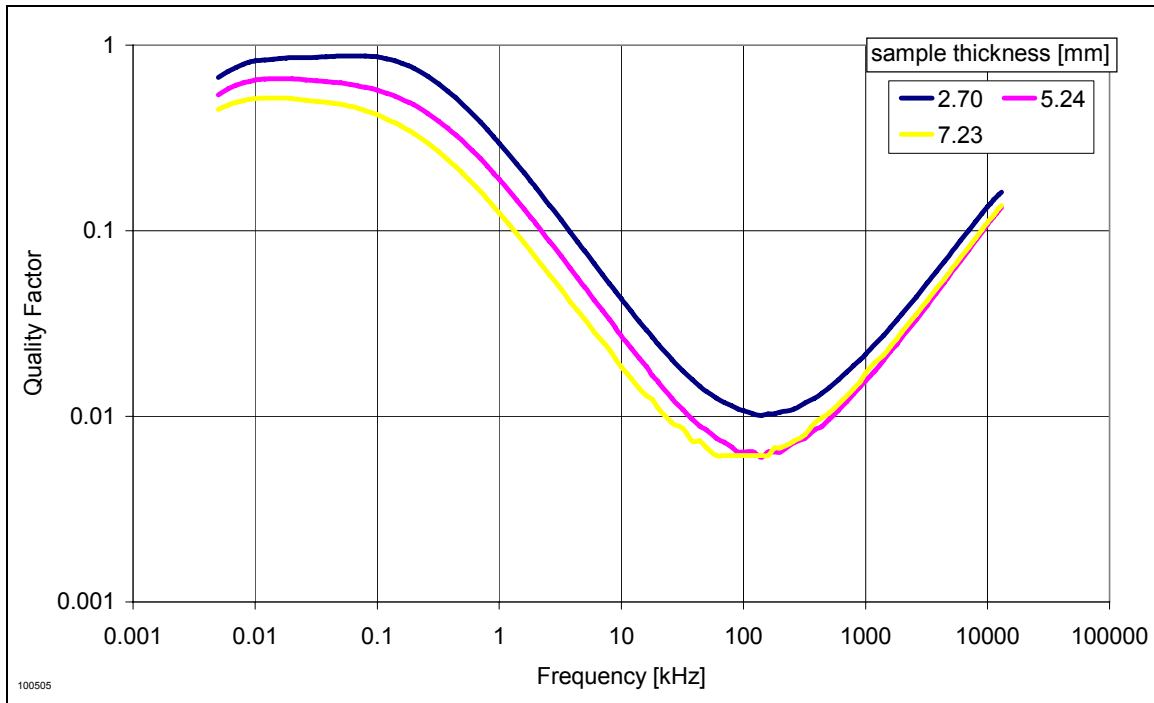


Figure 118 Quality factor of Berea sample measurement from Figure 111.

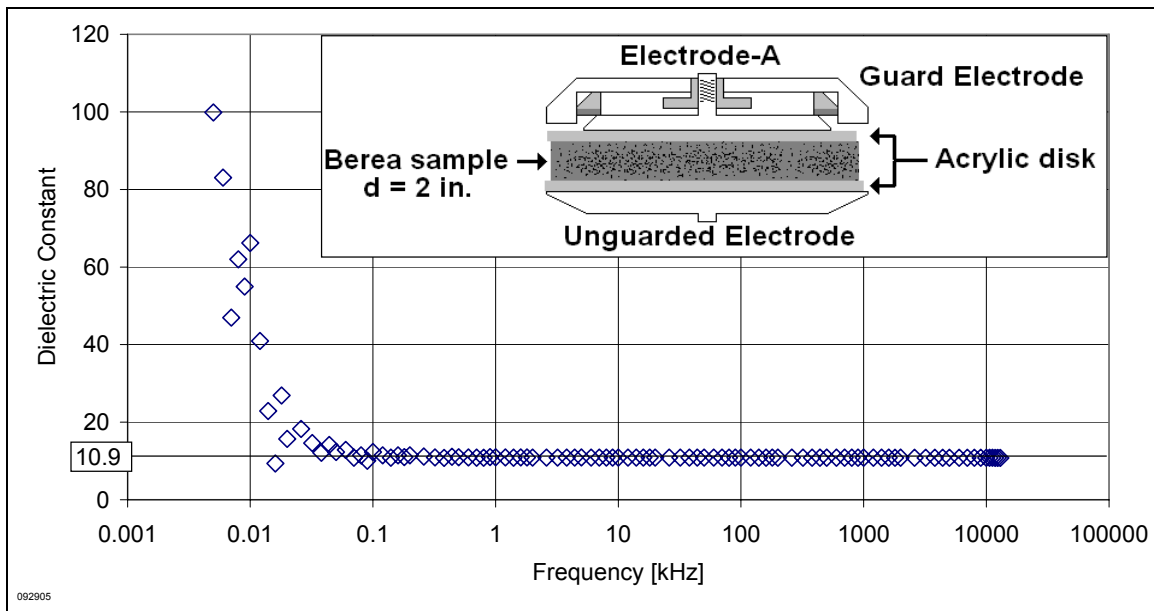


Figure 119 Dielectric constant of Berea sample fully saturated with 0.9% NaCl brine measured by sandwich method depicted in the figure (Method 3). A constant dielectric value was measured above 100 Hz, but the value was too low to be the volume average of water and Berea rock of known porosity.

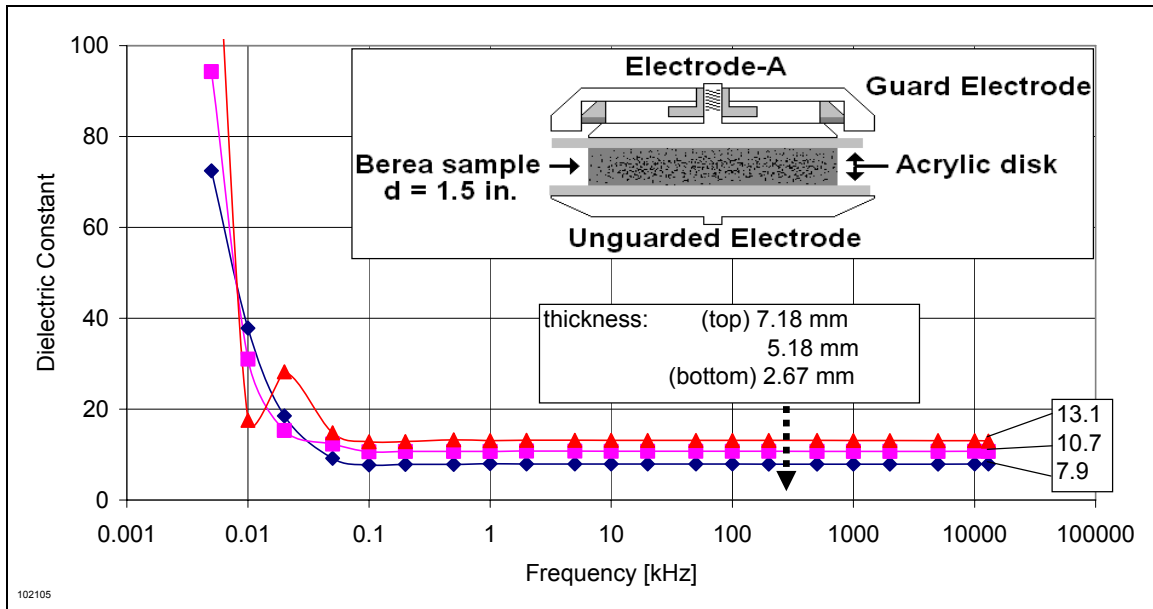


Figure 120 Dielectric constant of Berea sample fully saturated with 0.9% NaCl brine measured by sandwich method depicted in the figure (Method 3). Strong correlation of dielectric value with sample thickness suggests the effect of stray capacitance. Similar to the result in Figure 119, the dielectric values were too low to be the volume average of Berea and water.

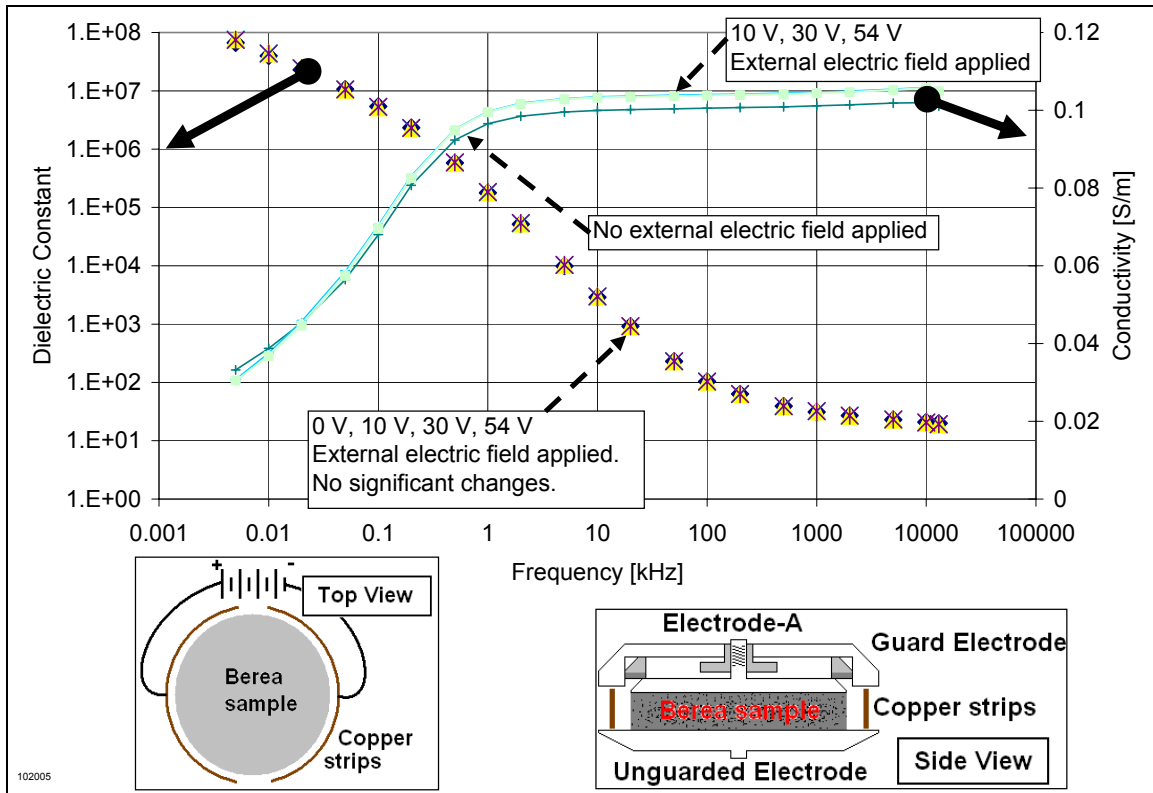


Figure 121 External electrical field was applied at the circumference of the Berea sample attempting to eliminate free moving ions in the sample (Method 3). Diagram at the bottom shows the top and side view of the setup. There were no significant changes due to the changes in external electric field.

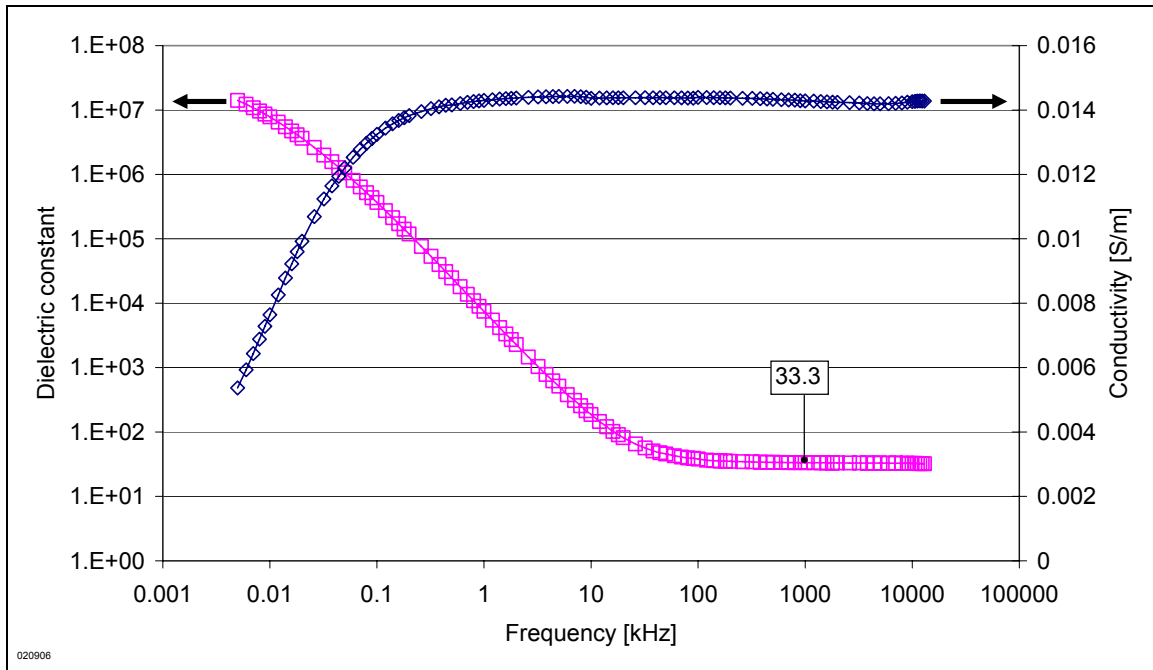


Figure 122 Single measurement on methanol of 3.68 mm thickness by silver plating powder treated electrodes (Method 3). Dielectric enhancement exists below 20 kHz and low conductivity shows below 500 Hz. The dielectric constant measured at 1 MHz is 33.3.

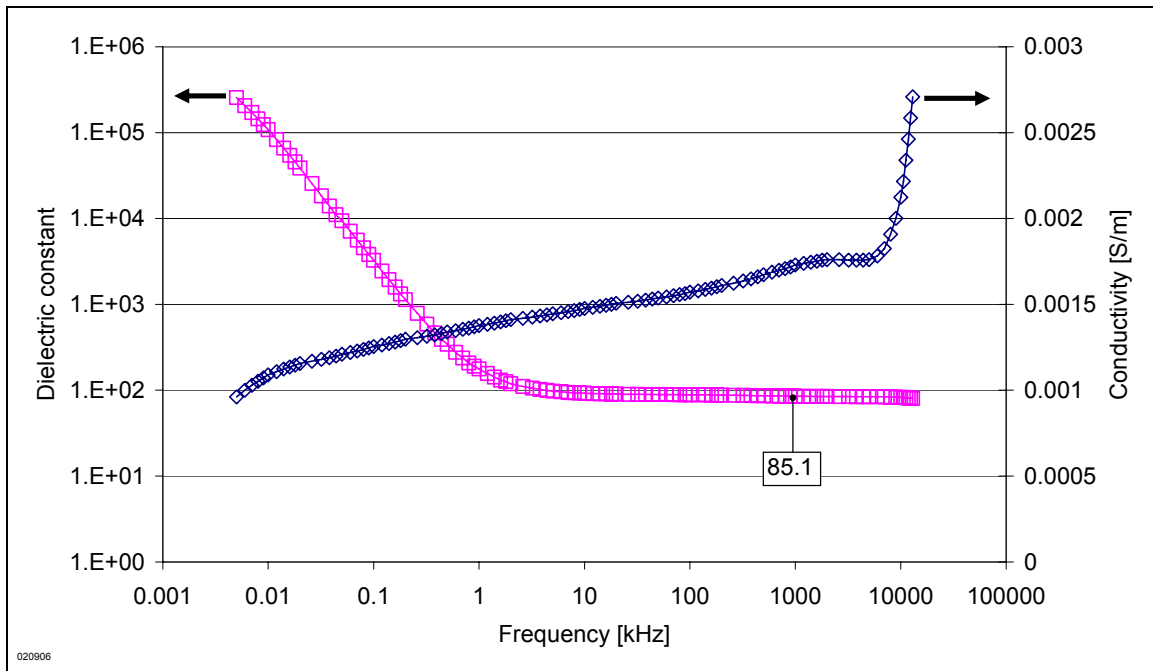


Figure 123 Single measurement on de-ionized water of 3.49 mm by silver plating powder treated electrodes (Method 3). The dielectric constant is similar to the one shown in Figure 78. The increase in conductivity could be measurement error. The dielectric constant measured at 1 MHz is 85.1, which is higher than normal.

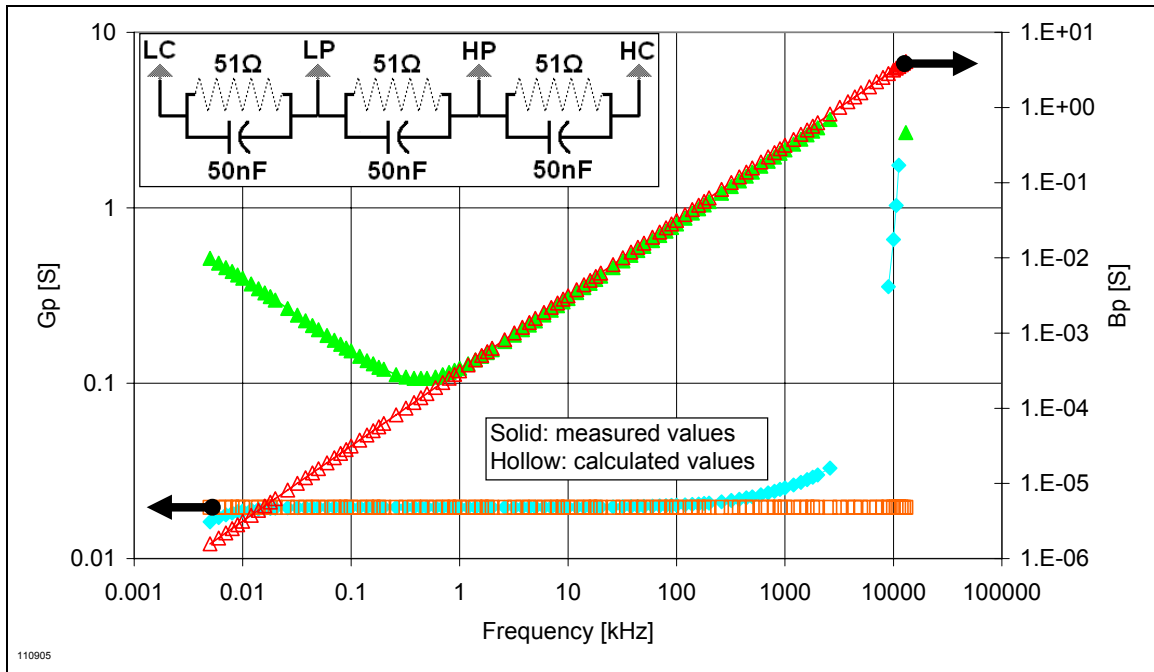


Figure 124 Four-electrode circuit measurement #1 of Table 2 (Method 4).

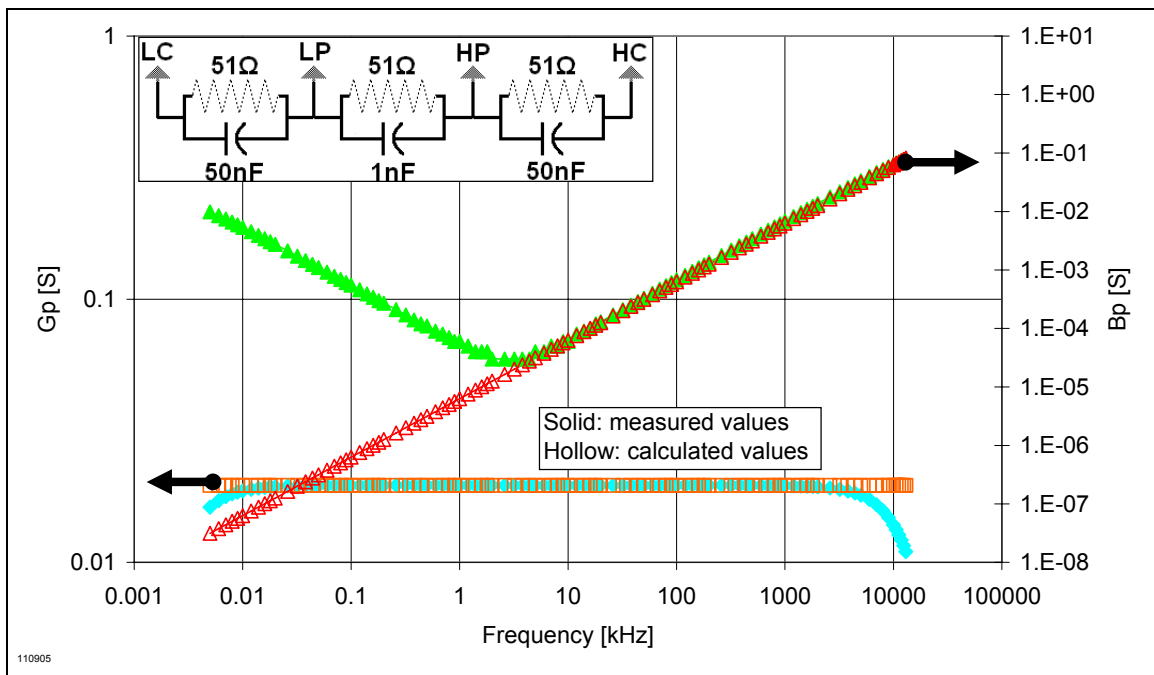


Figure 125 Four-electrode circuit measurement #2 of Table 2 (Method 4).

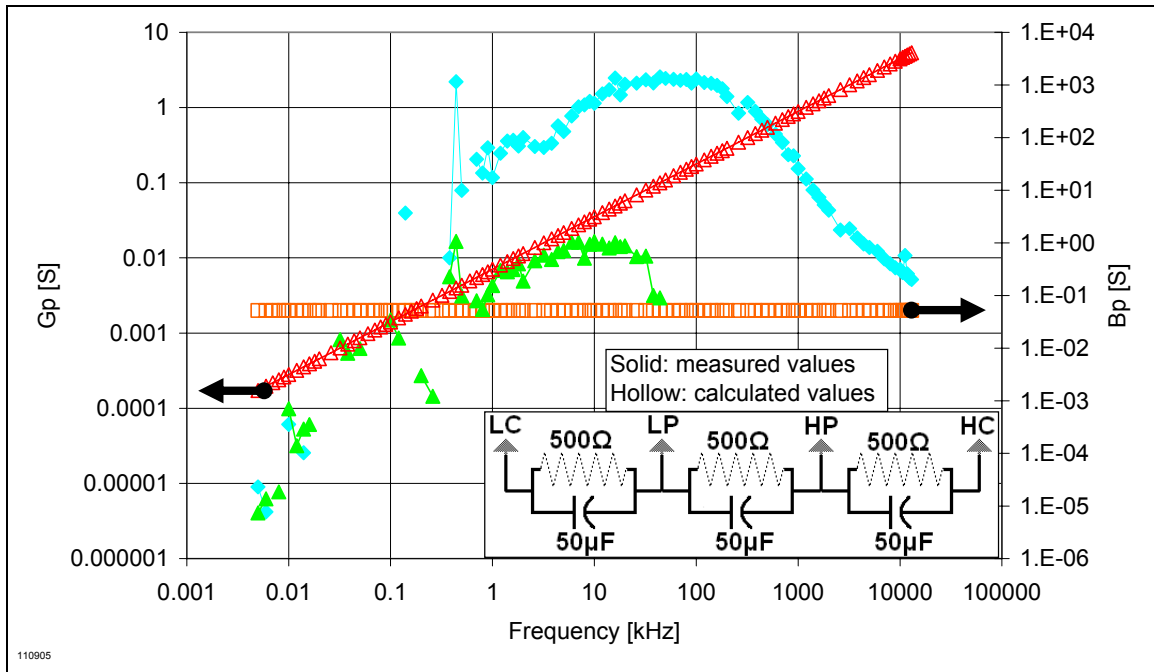


Figure 126 Four-electrode circuit measurement #3 of Table 2 (Method 4).

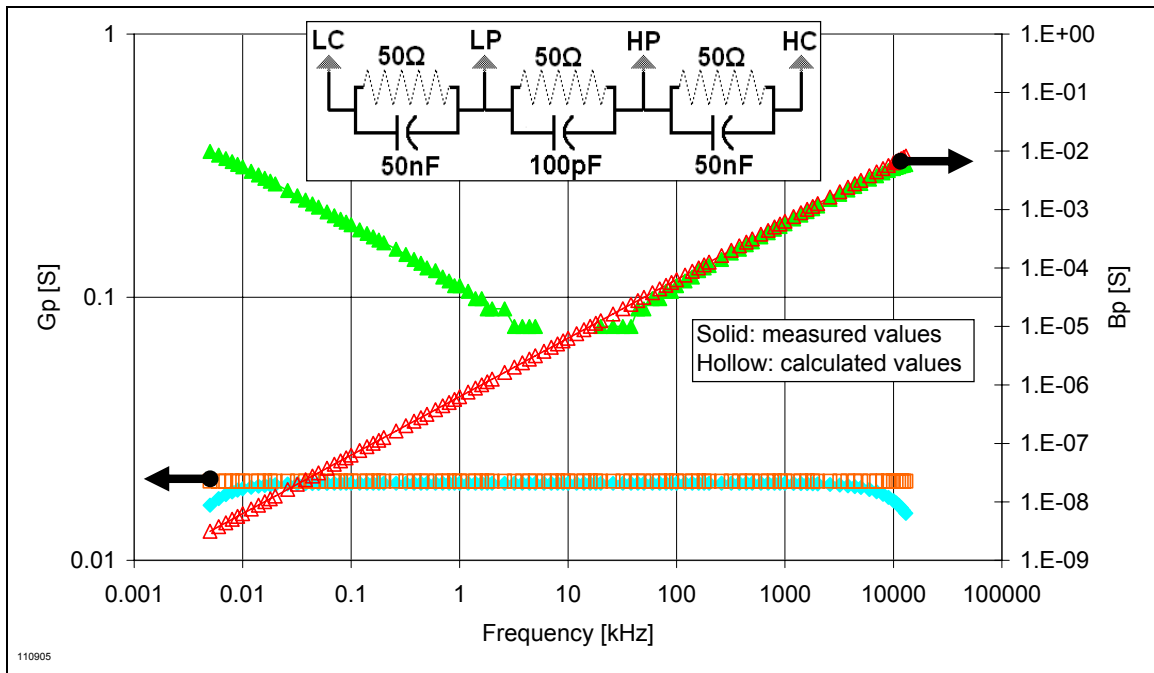


Figure 127 Four-electrode circuit measurement #4 of Table 2 (Method 4).

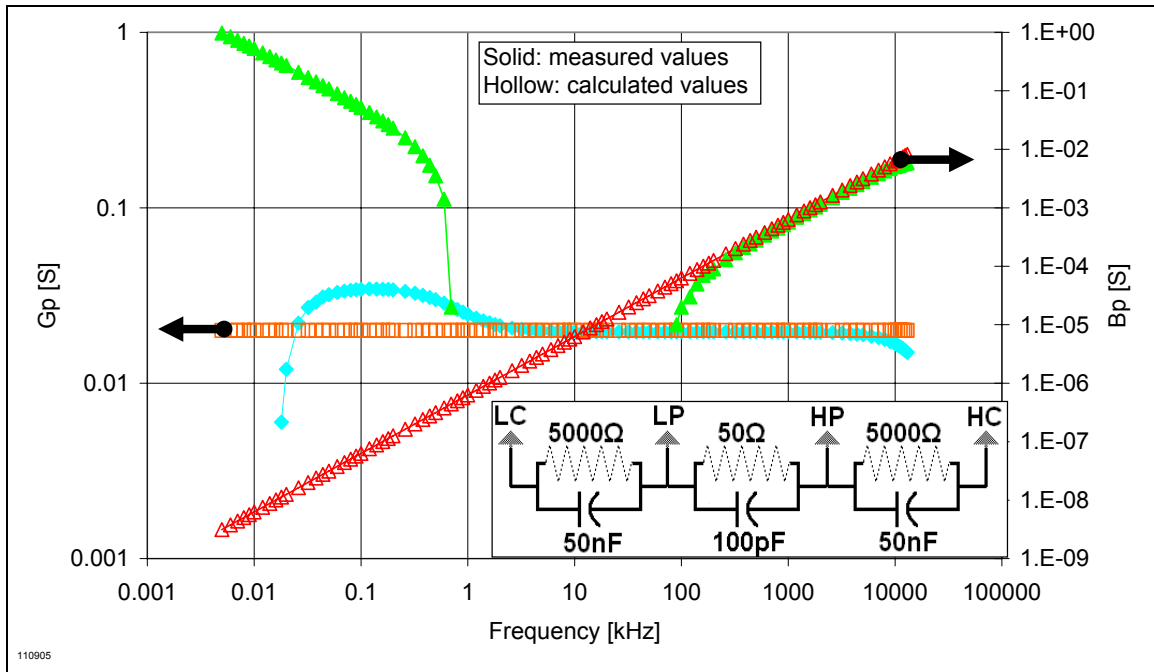


Figure 128 Four-electrode circuit measurement #5 of Table 2 (Method 4).

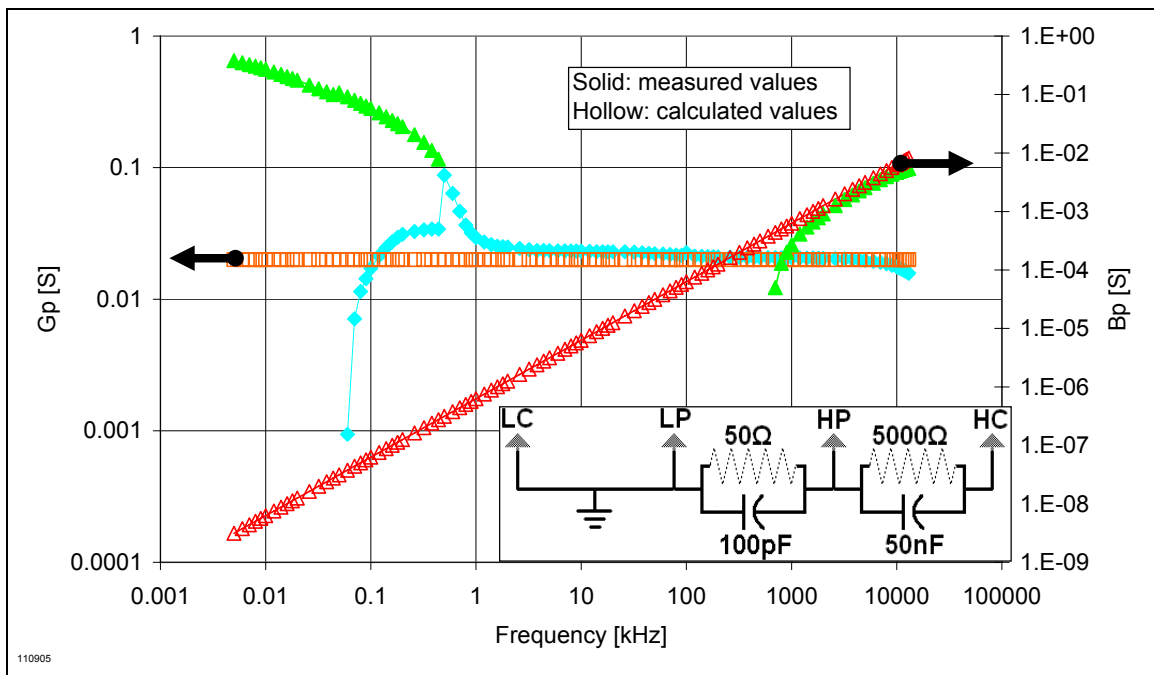


Figure 129 Four-electrode circuit measurement #6 of Table 2 (Method 4).

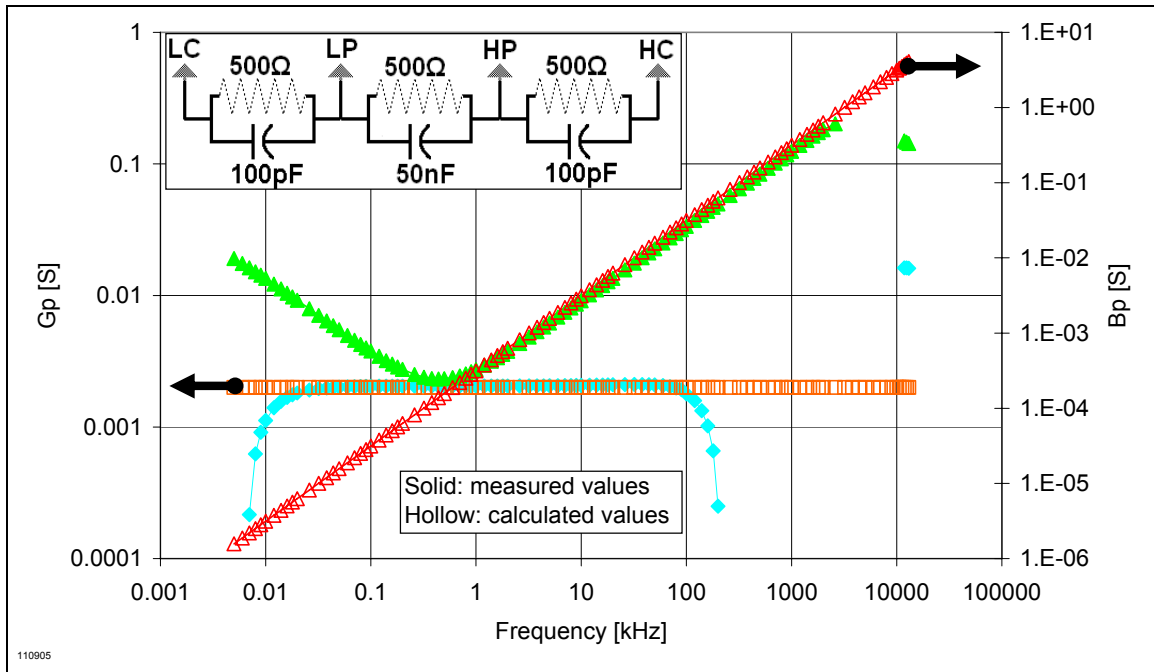


Figure 130 Four-electrode circuit measurement #8 of Table 2 (Method 4).

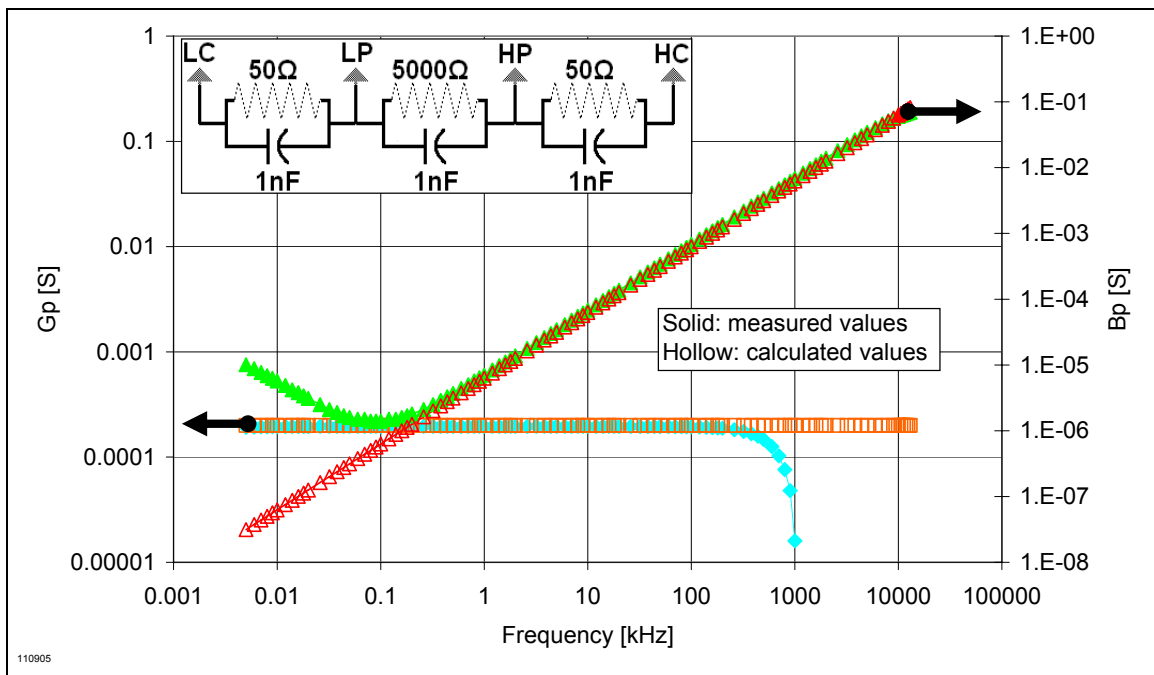


Figure 131 Four-electrode circuit measurement #9 of Table 2 (Method 4).

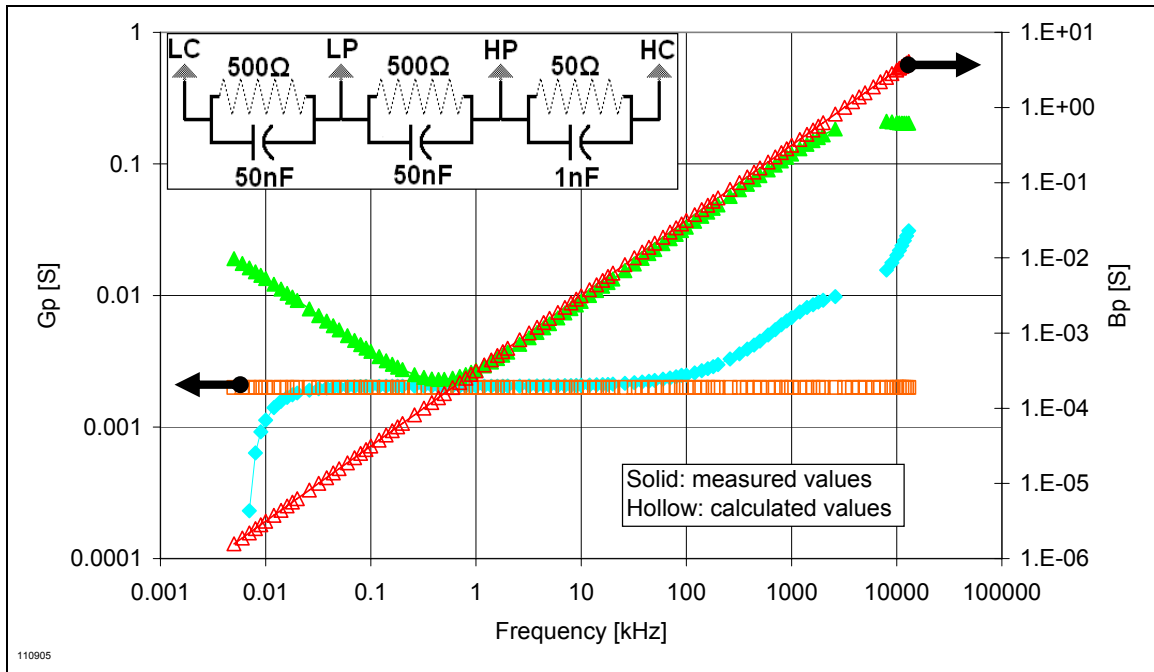


Figure 132 Four-electrode circuit measurement #10 of Table 2 (Method 4).

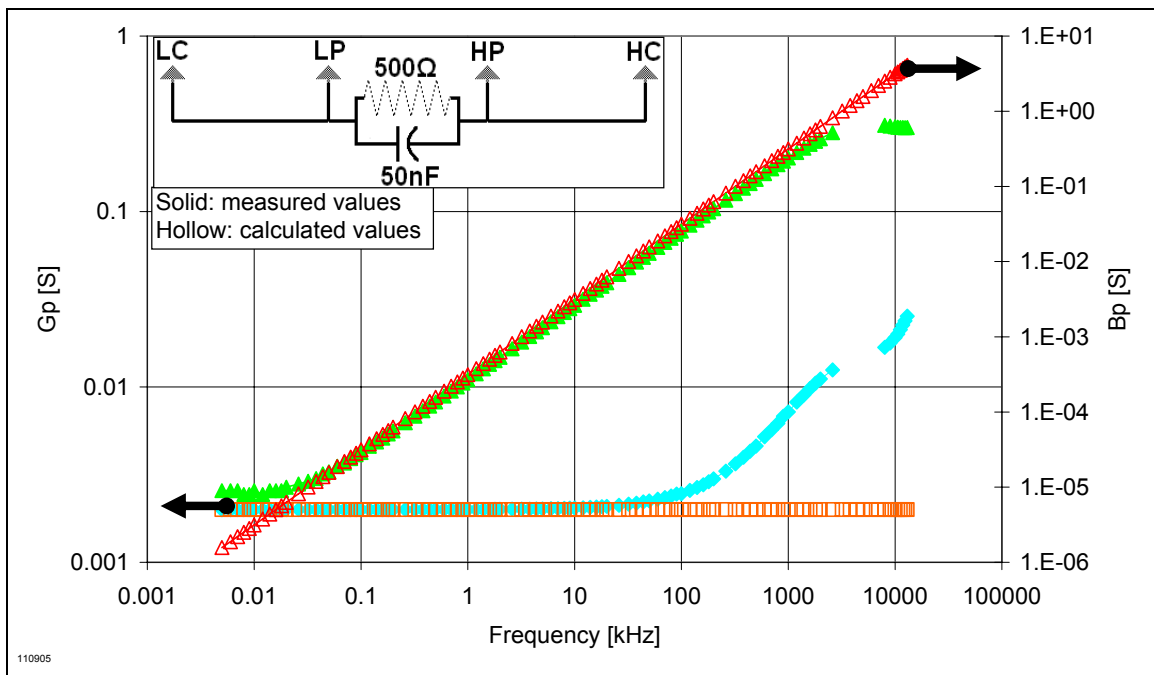


Figure 133 Four-electrode circuit measurement #11 of Table 2 (Method 4).

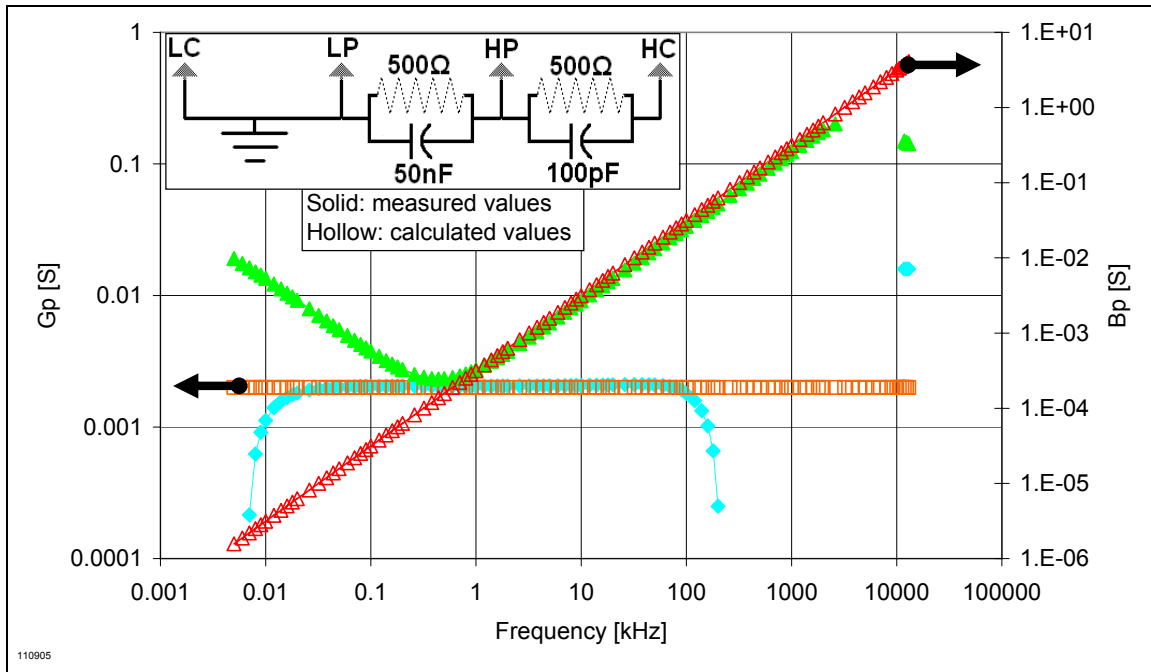


Figure 134 Four-electrode circuit measurement #12 of Table 2 (Method 4).

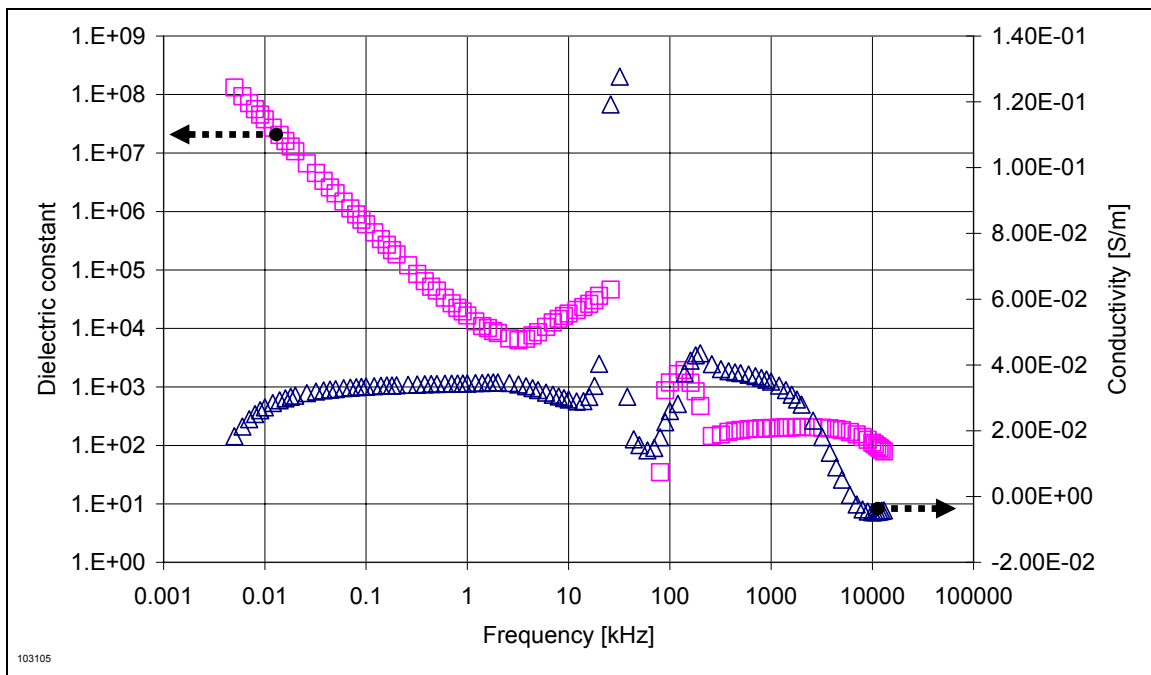


Figure 135 Measurement on Berea sample fully saturated with 0.9% NaCl brine by four-electrode method (Method 4). The result shows very strange values between 5 kHz to 200 kHz of frequency range. Dielectric enhancement still exists even though four-electrode method supposed to be able to eliminate them.

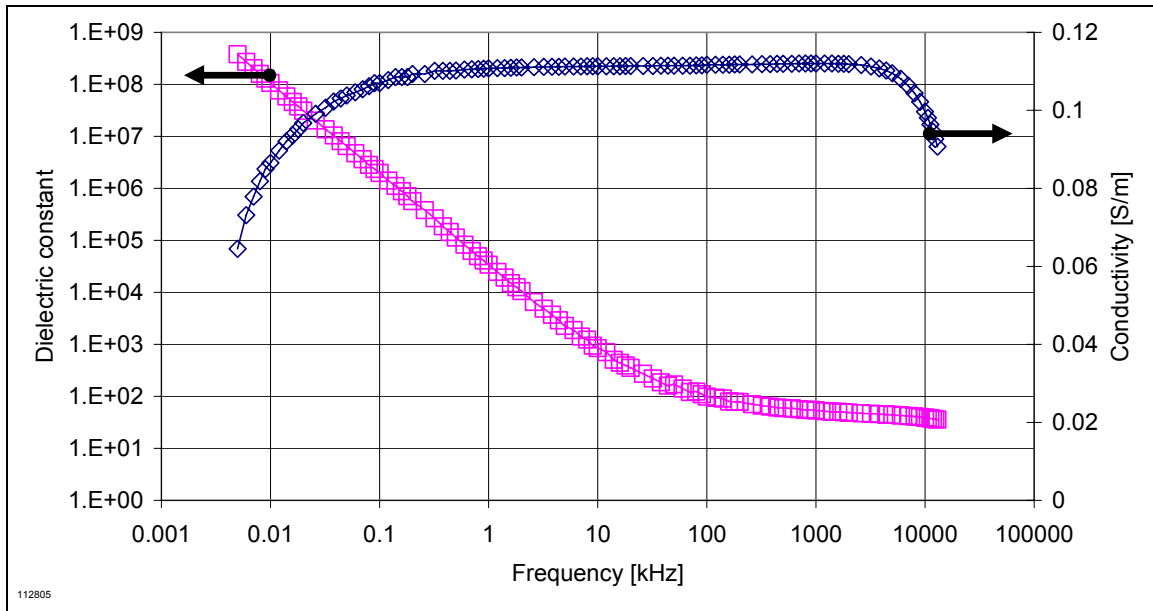


Figure 136 Measurement on Berea sample fully saturated with 0.9% NaCl brine by four-electrode method (Method 4). The experiment was performed after electrical circuit measurement. The result in general is very similar to experiments by dielectric fixture on the same Berea sample.

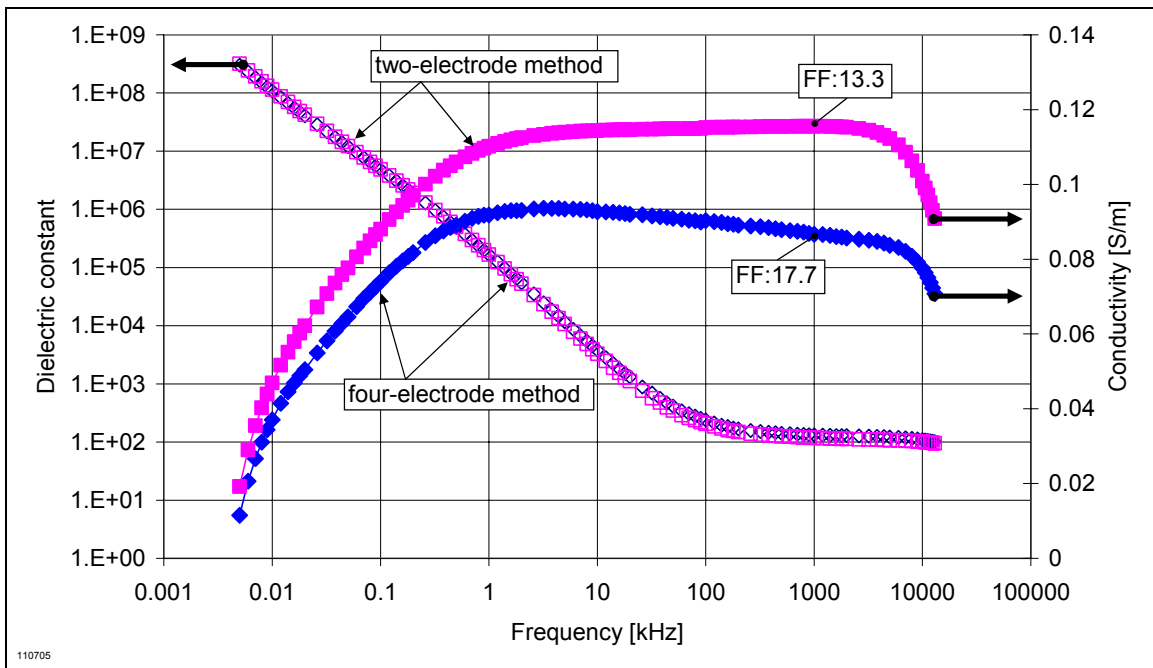


Figure 137 Comparison of two-electrode and four-electrode method by copper sheet electrodes measured on Berea sample fully saturated with 0.9% NaCl brine (Method 4). The dielectric constant for both methods shows the same result while the conductivity for four-electrode method was lower than the two-electrode method.

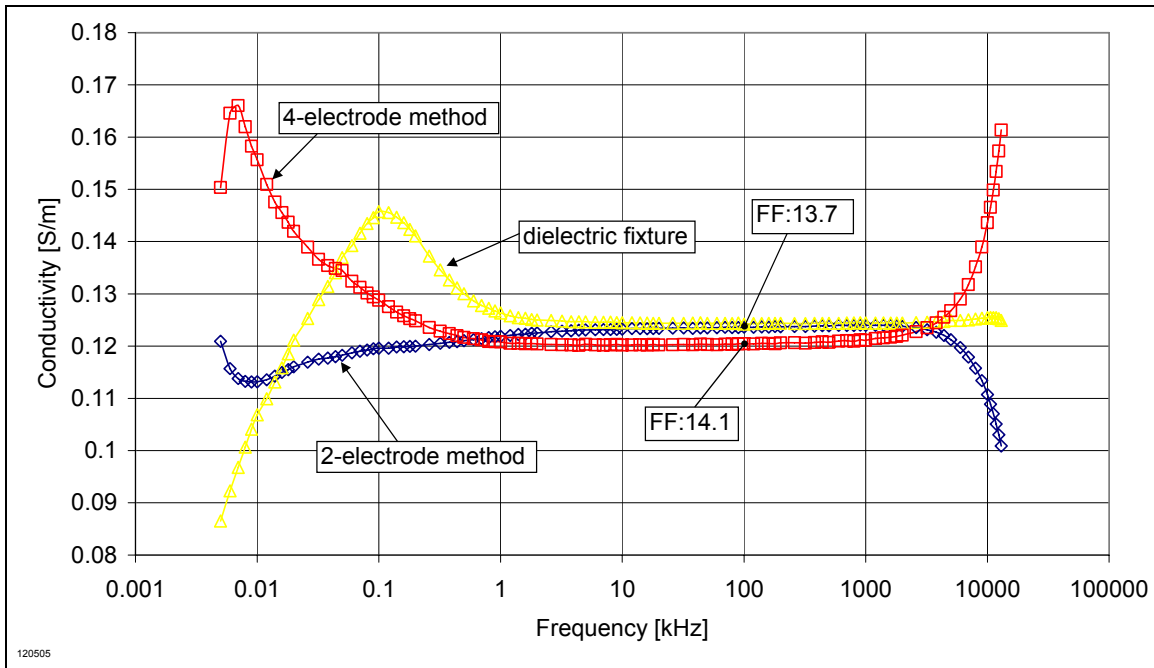


Figure 138 Conductivity of Berea sample fully saturated with 1% NaCl brine measured by dielectric fixture, two-electrode, and four-electrode. The data has been analyzed by linear adjustment.

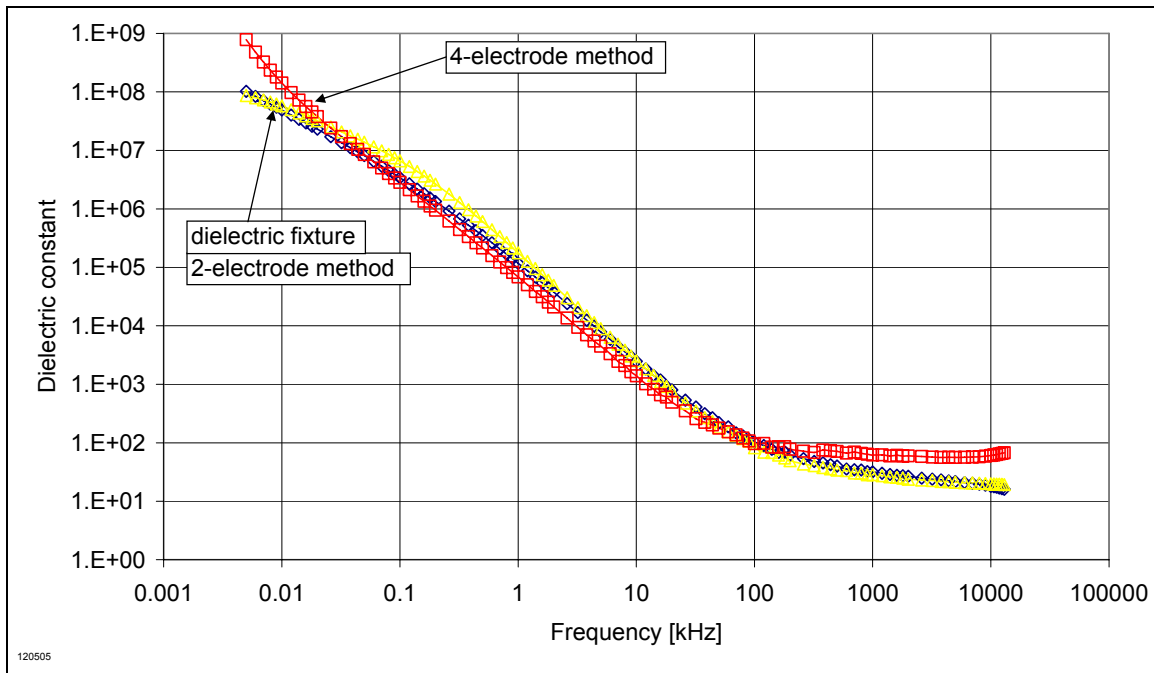


Figure 139 Dielectric constant of Berea sample fully saturated with 1% NaCl brine measured by dielectric fixture, two-electrode, and four-electrode. The data has been analyzed by linear adjustment.

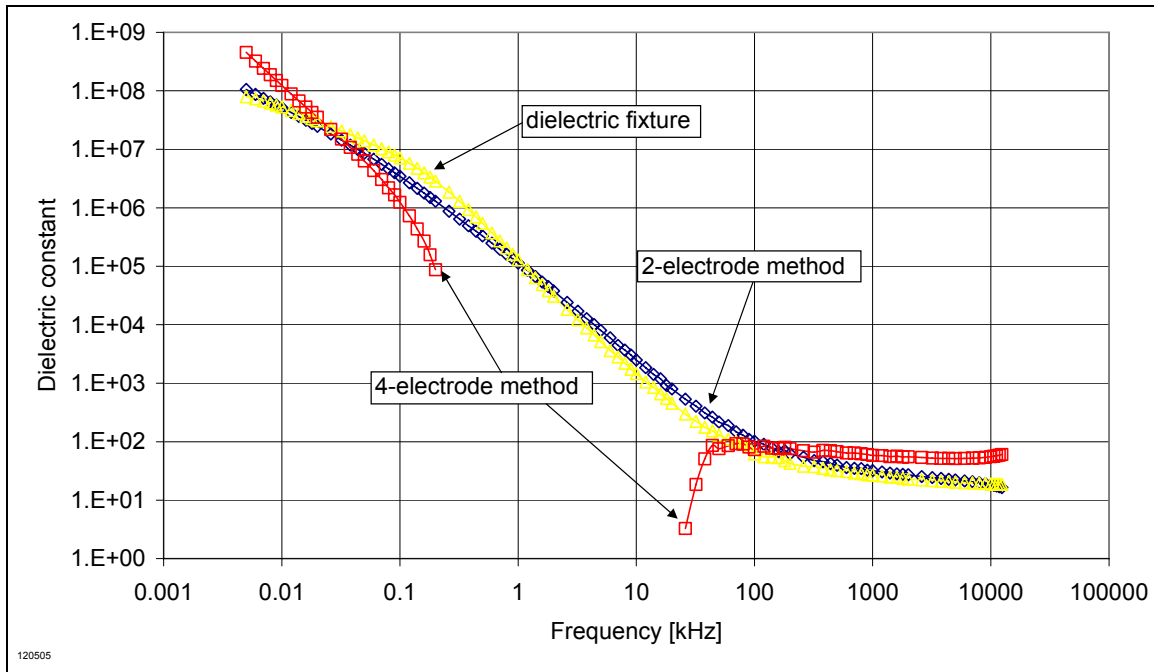


Figure 140 Dielectric constant of Berea sample fully saturated with 1% NaCl brine measured by dielectric fixture, two-electrode, and four-electrode. The data has been analyzed by inverse length adjustment.

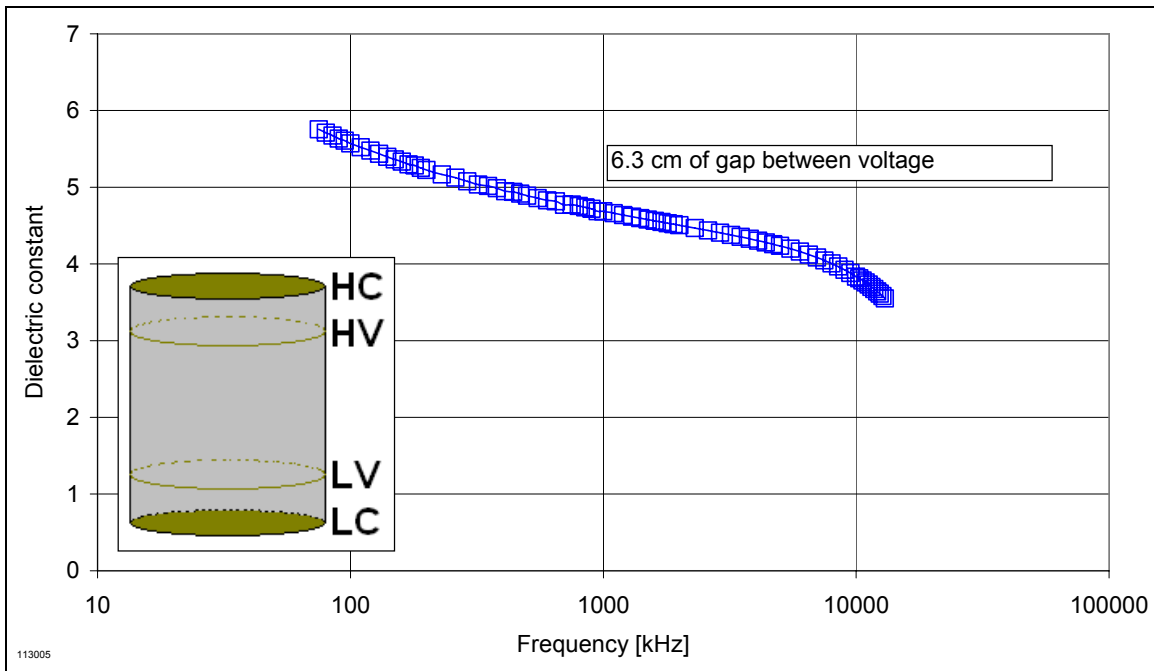


Figure 141 Four-electrode method made on dry Berea cylinder (Method 4). The setup of the measurement is sketched at the bottom. The dielectric constant for the dry Berea is in agreement with the measurement made with dielectric fixture on Figure 1.

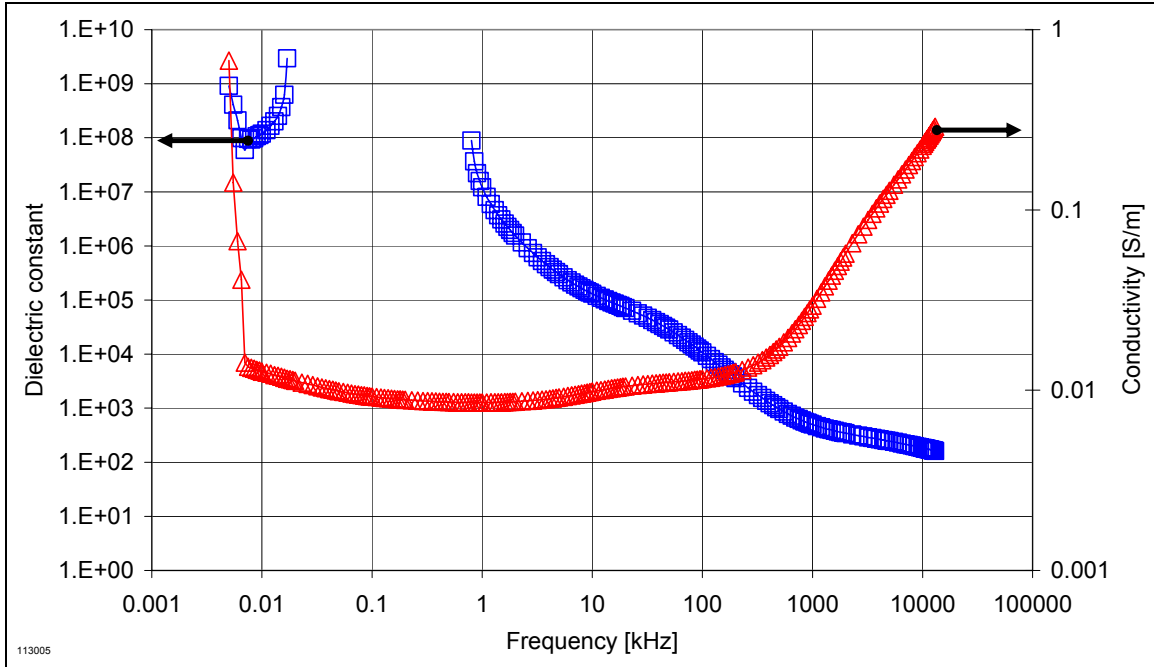


Figure 142 Four-electrode method made on Berea cylinder fully saturated with de-ionized water (Method 4). Both the conductivity and dielectric constant are slightly higher than previous results on same types of samples. There appears to be some dispersion and dielectric enhancement in the kHz frequency range.

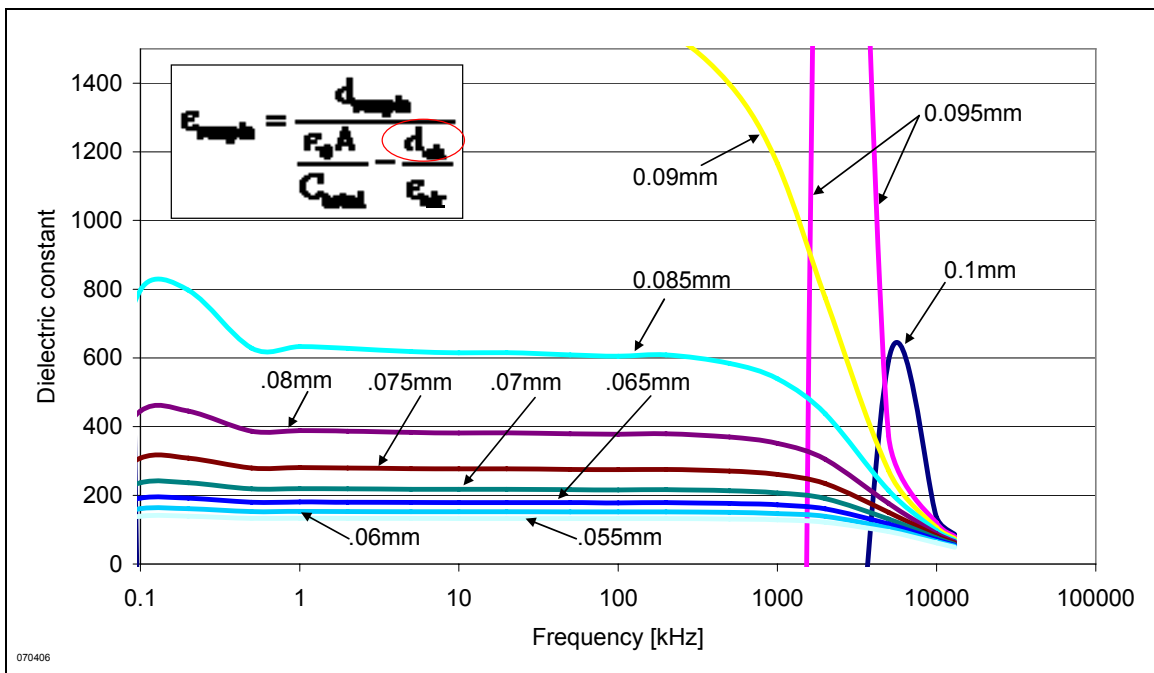


Figure 143 Sensitivity analysis of air gap method (Method 5).

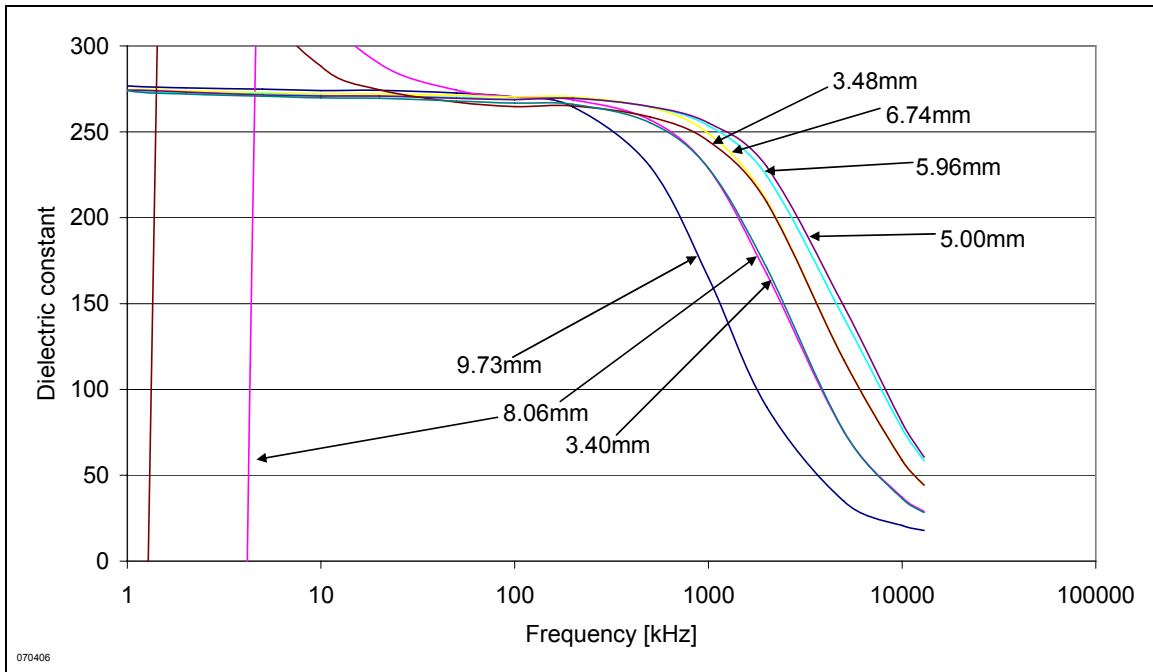


Figure 144 Berea samples of 2 in. diameter fully saturated with 1% NaCl brine. The calculated dielectric constant is manipulated by changing the air gap thickness so that all thickness overlaps at 50 kHz (Method 5).

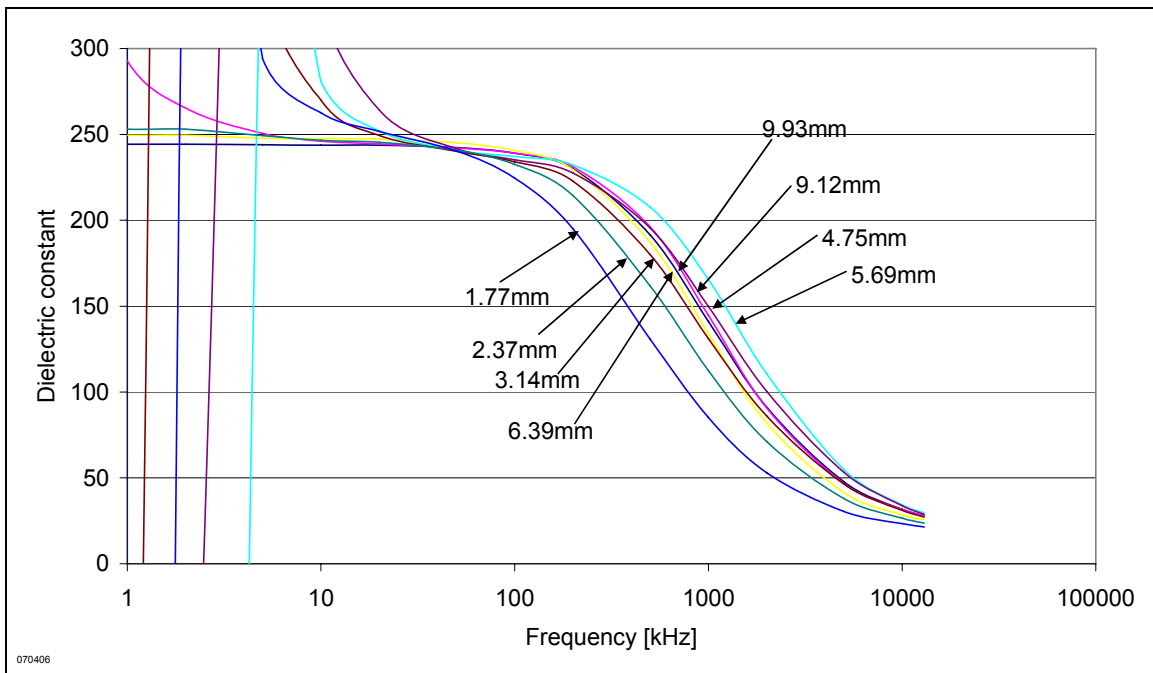


Figure 145 Texas cream samples of 2 in. diameter fully saturated with 1% NaCl brine. The calculated dielectric constant is manipulated by changing the air gap thickness so that all thickness overlaps at 50 kHz (Method 5).

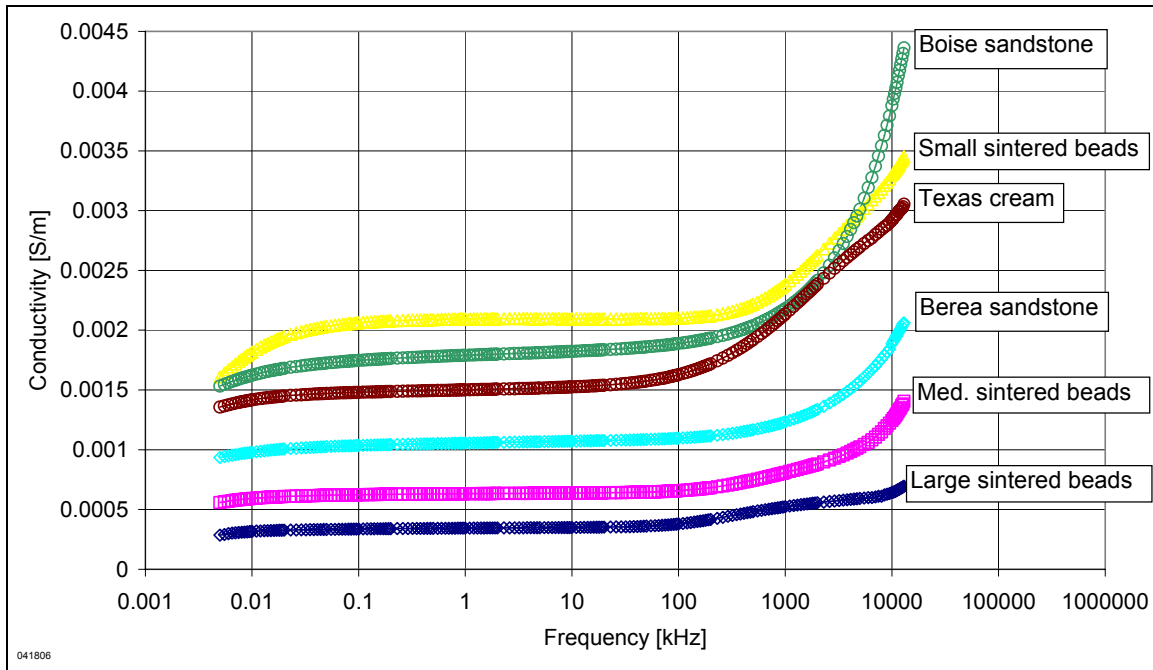


Figure 146 Single measurements of conductivity of samples fully saturated in de-ionized water measured by silver powder plated electrodes (Method 3). The conductivity appears to be correlated with grain size with the exception of Boise sandstone.

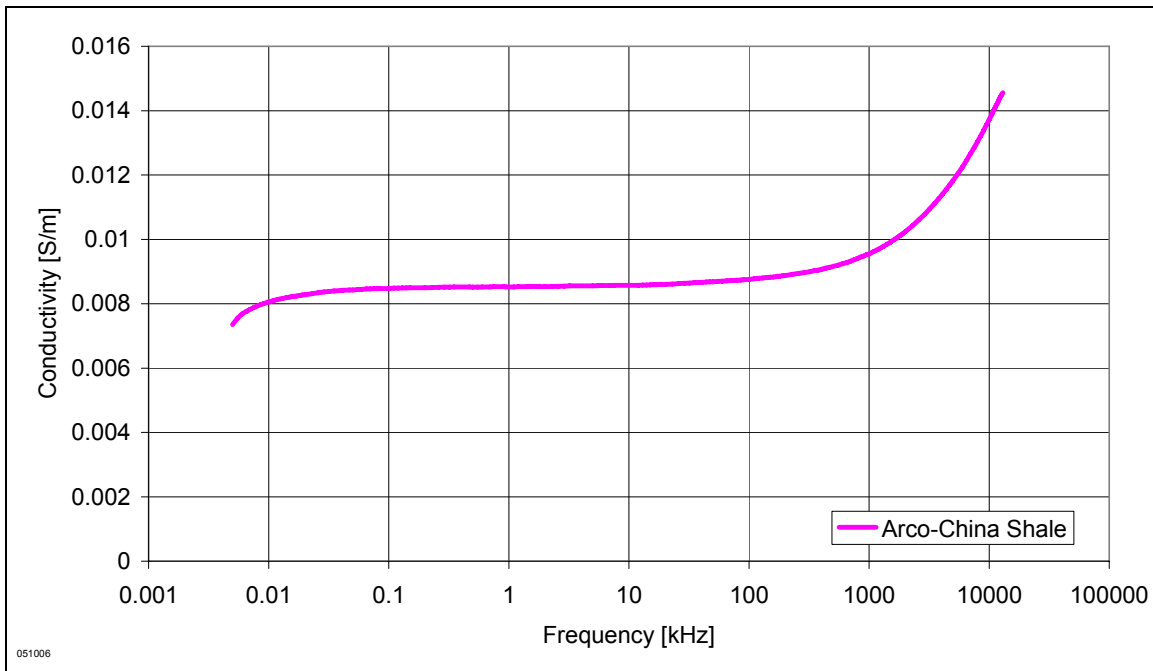


Figure 147 Conductivity measurement of shale fully saturated with de-ionized water (Method 3). The conductivity measured shows a much higher value than samples in Figure 146.

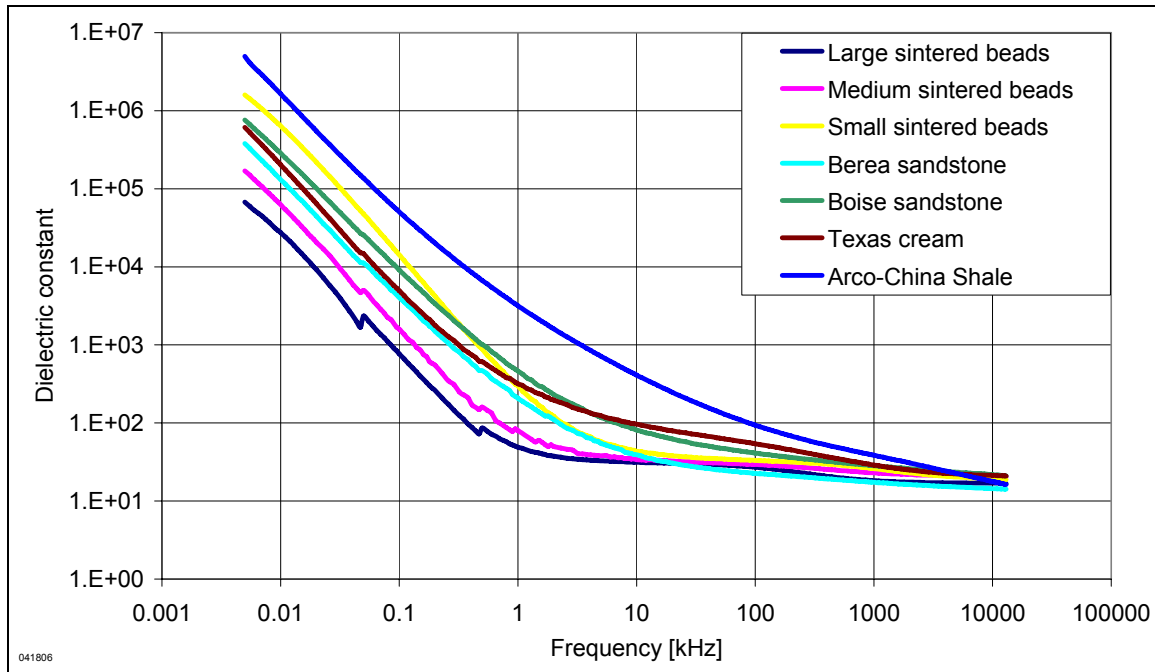


Figure 148 Single measurements of dielectric constant of samples fully saturated in de-ionized water measured by silver powder plated electrodes (Method 3). The frequency where dielectric enhancement terminates seems to be in correlation with the grain size.

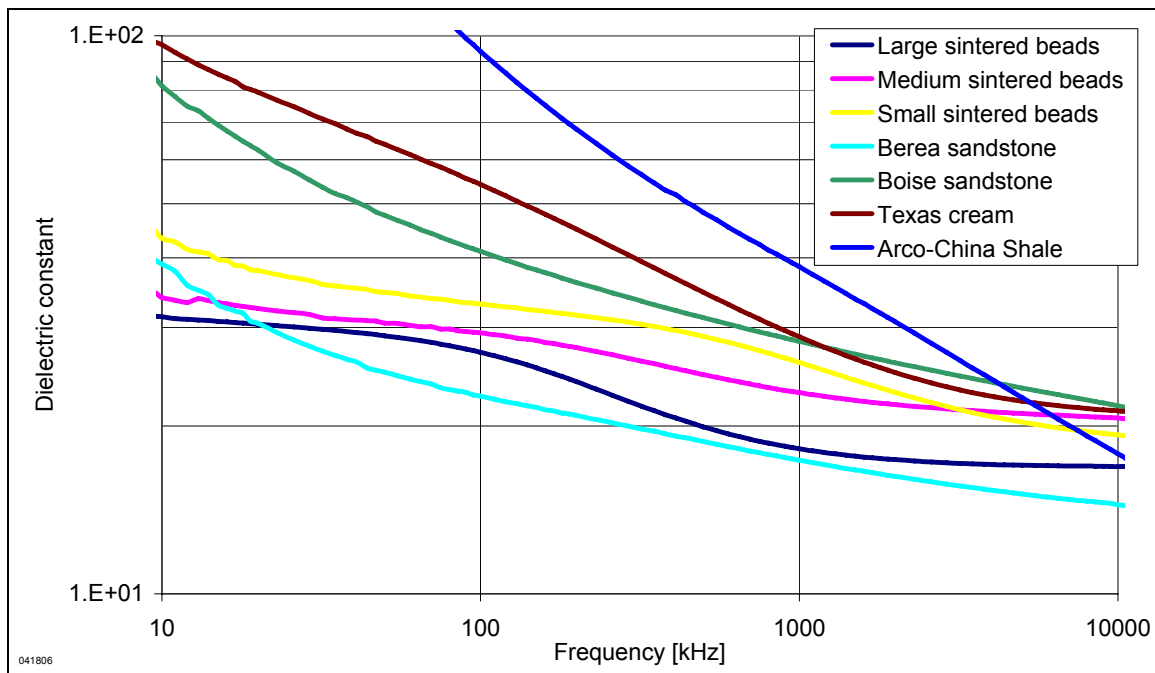


Figure 149 Zoomed in from Figure 148 showed dielectric dispersions presented for all samples. It is more pronounced for sintered beads which are made with perfect spherical grains of the same sizes.

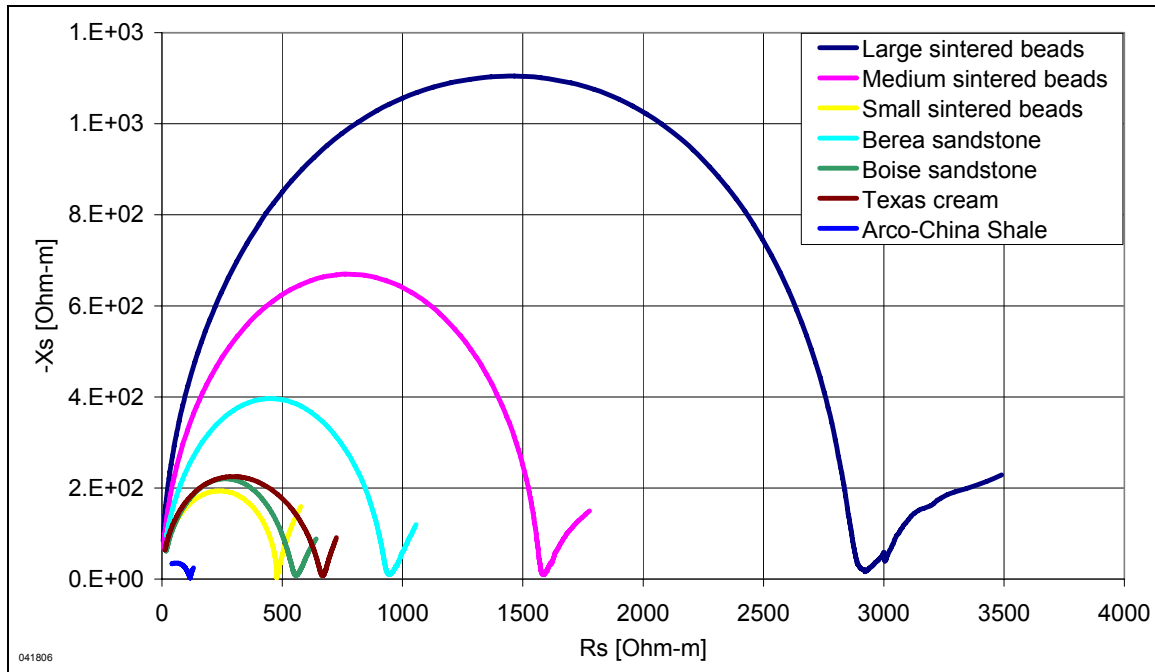


Figure 150 Argand plot of samples fully saturated in de-ionized water measured by silver powder plated electrodes (Method 3). It is clear that smaller grain size samples results in a smaller argand circle.

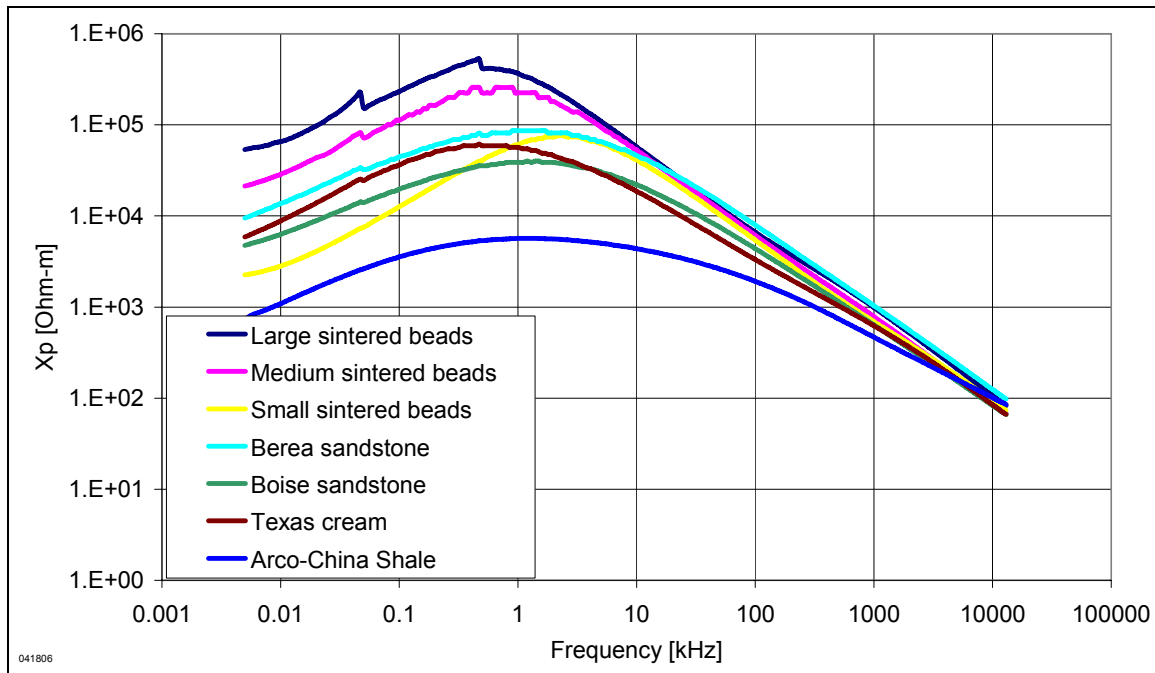


Figure 151 Reactance-m of samples fully saturated in de-ionized water measured by silver powder plated electrodes (Method 3). Except for Texas cream limestone (which contains micro-porous grains), the peak frequency increases as grain size decreases.

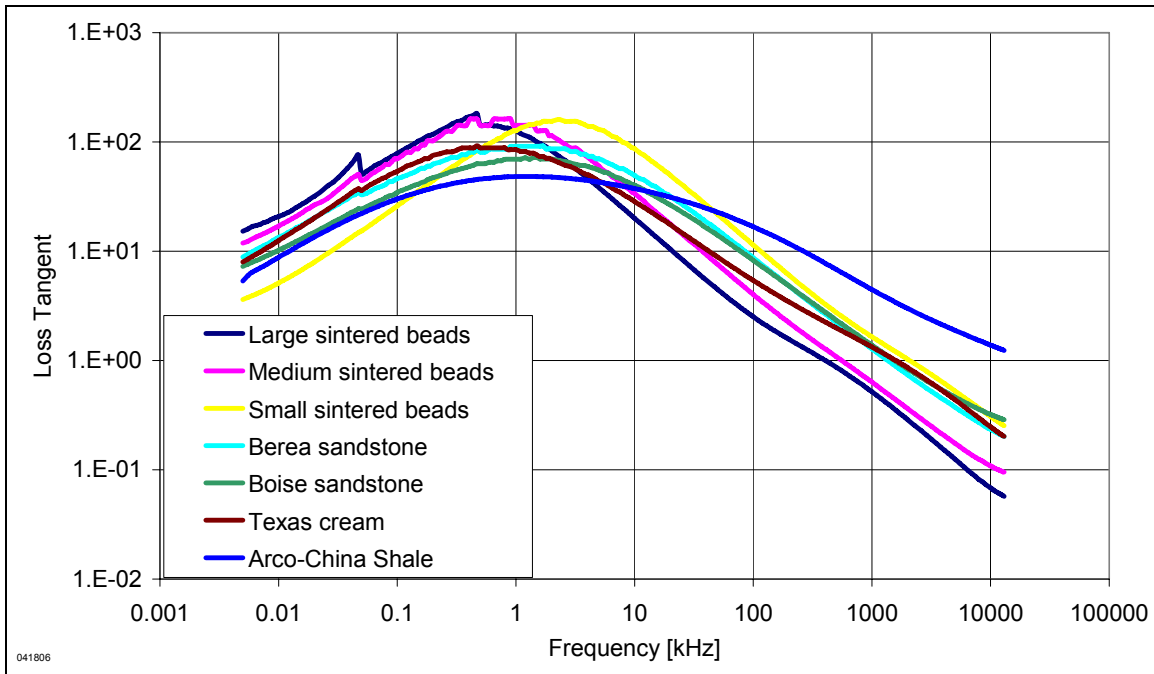


Figure 152 Loss tangent of samples fully saturated in de-ionized water measured by silver powder plated electrodes (Method 3). Except for Texas cream, the frequency where a peak is observed increases as grain size decreases.

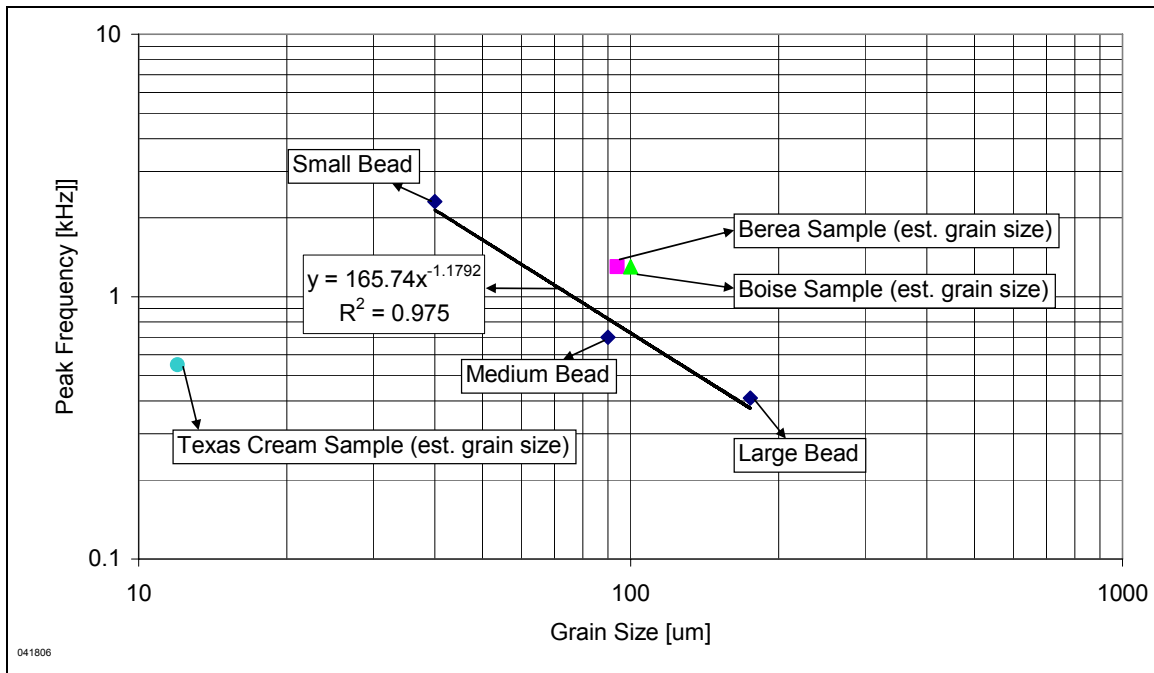


Figure 153 Loss tangent peak frequency (Figure 152) versus the average grain size of the samples.

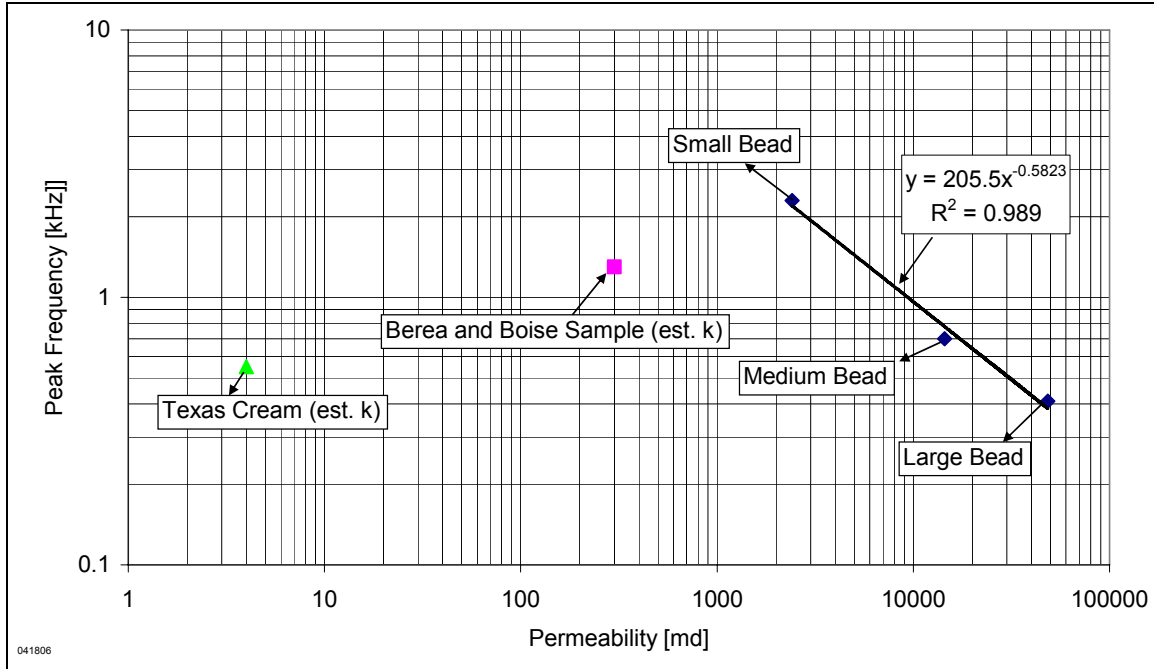


Figure 154 Loss tangent peak frequency (Figure 152) versus the permeabilities of the samples. Permeabilities of Berea and Texas Cream are estimated.

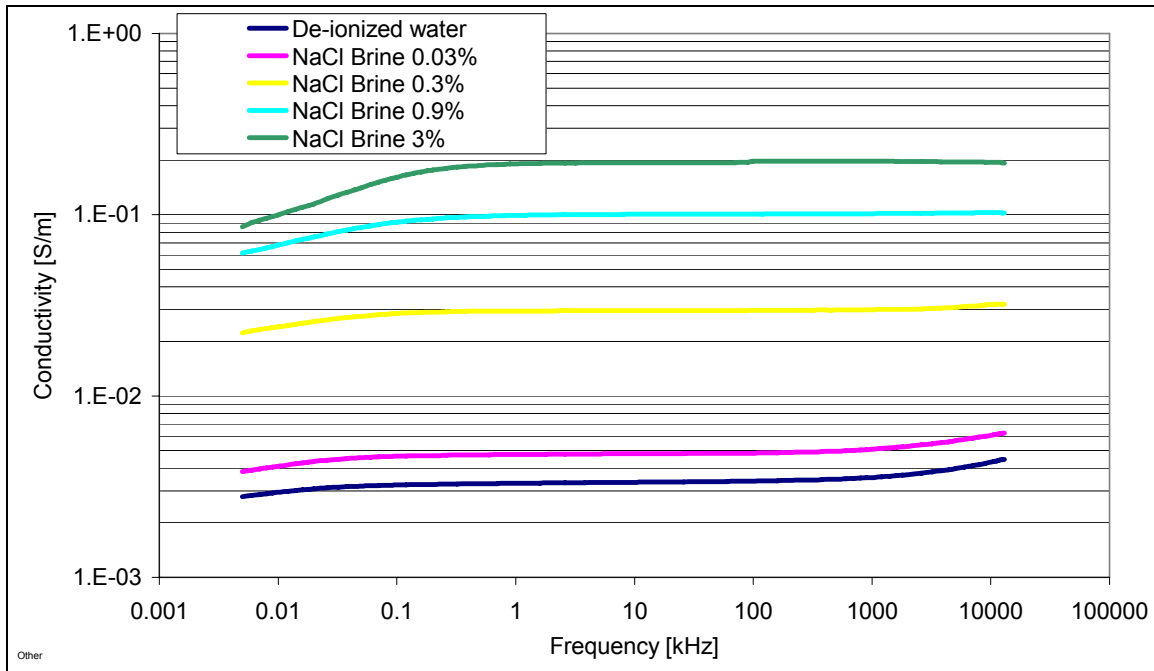


Figure 155 Conductivity of Berea sample of different saturating fluid (Method 3).

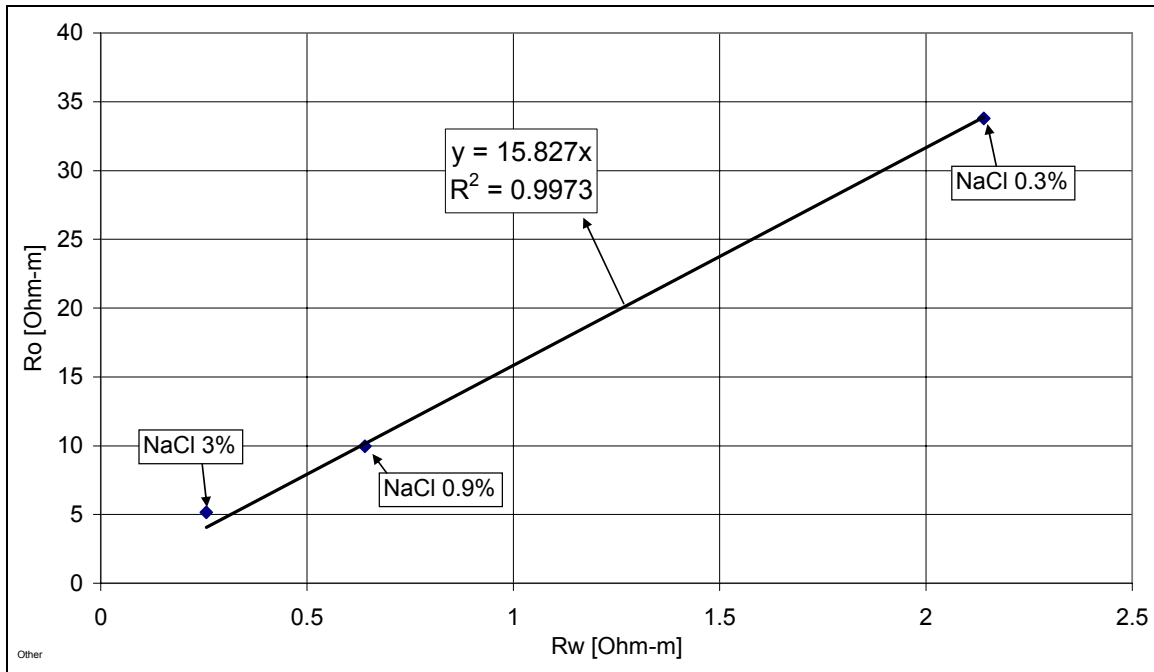


Figure 156 Saturating fluid resistivity versus bulk resistivity of Berea sample at different salinity. The slope of the best fit line shows the formation factor of the sample.

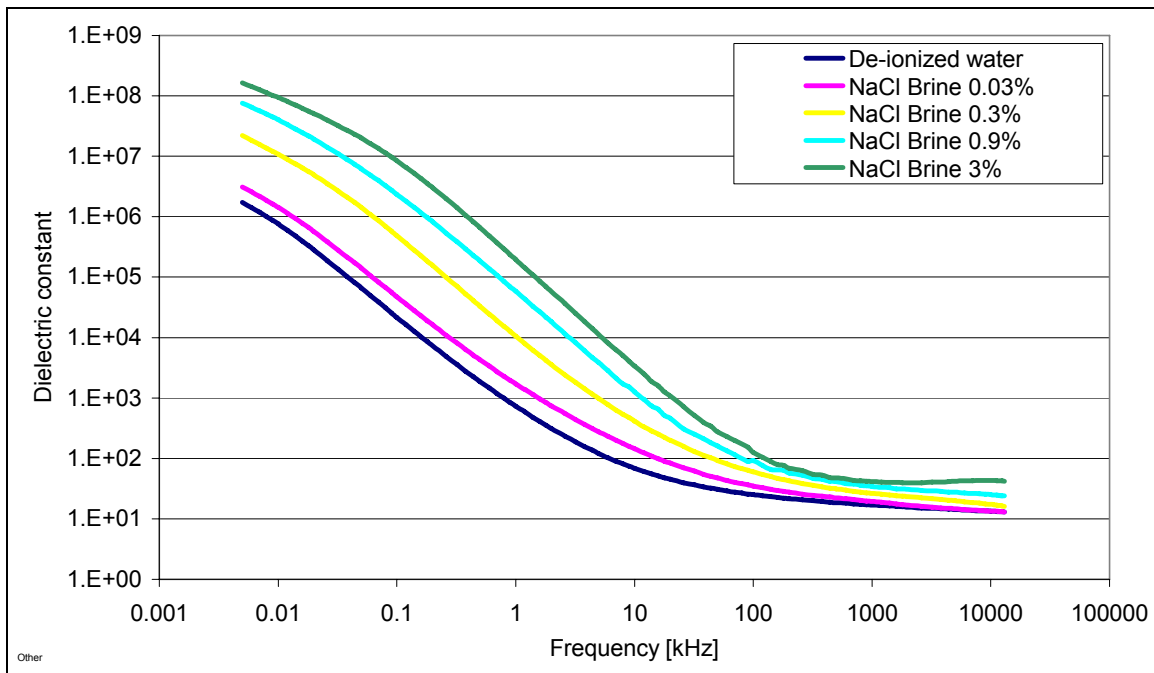


Figure 157 Dielectric constant of Berea sample of different saturating fluid (Method 3).

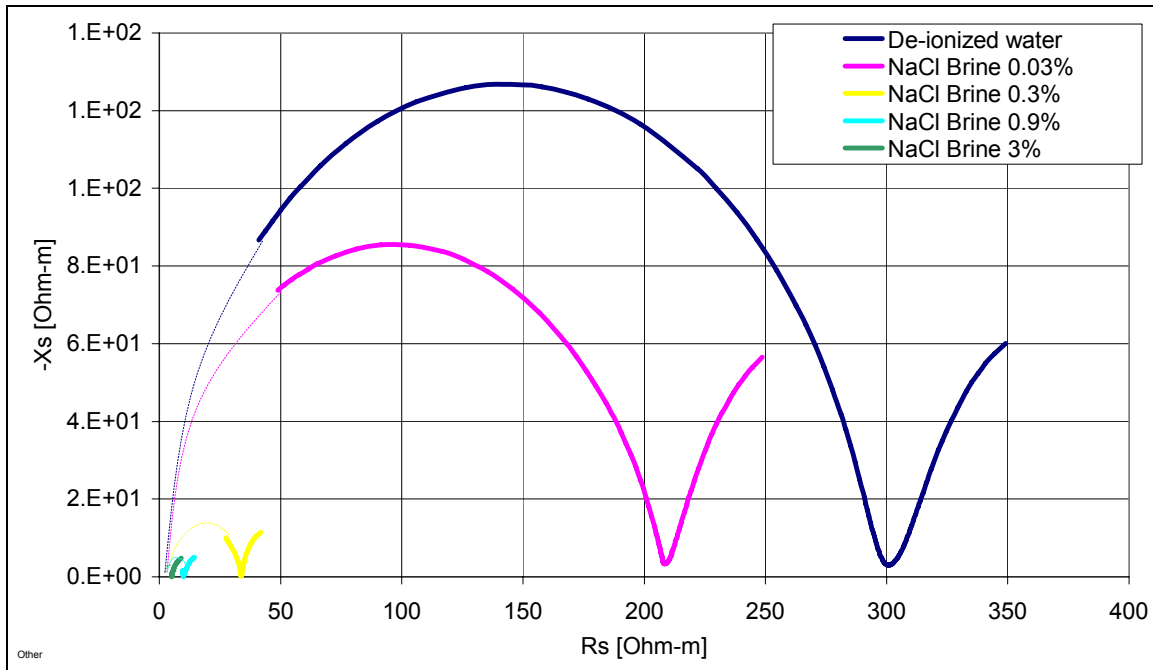


Figure 158 Argand plot of Berea sandstone saturated in water of different salinity. Dashed lines were drawn to complete the Argand circle. The increase in salinity causes the Argand circle to decrease in size and the tail section to increase relatively to the circle.

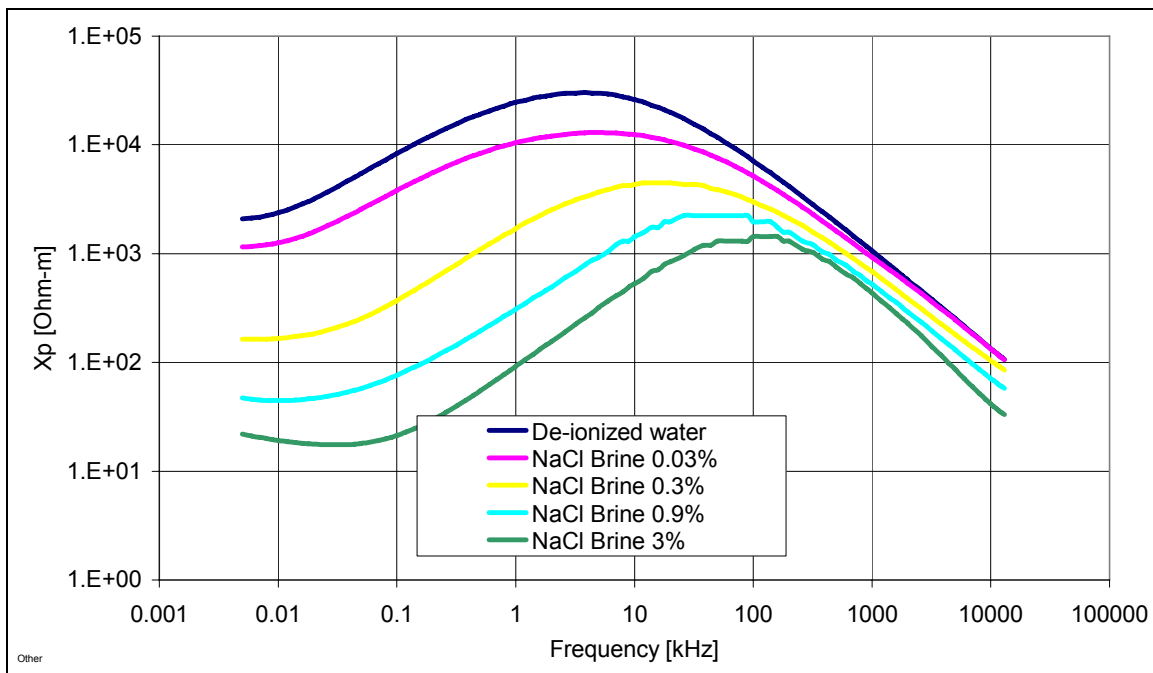


Figure 159 Reactance-m of Berea sandstone saturated in water of different salinity. The peak reactance-m value shifts to a higher frequency and decrease in value as saturating fluid becomes more saline.

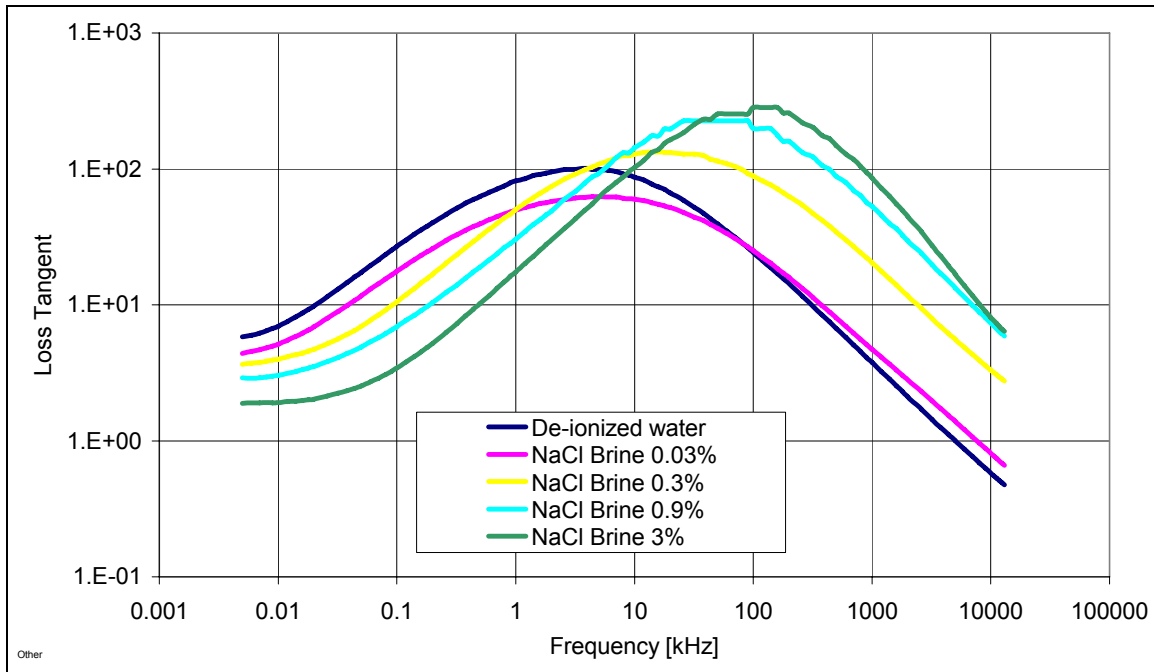


Figure 160 Loss tangent of Berea sandstone saturated in water of different salinity. The peak loss increases both in magnitude and in frequency as the saturating fluid becomes more saline.

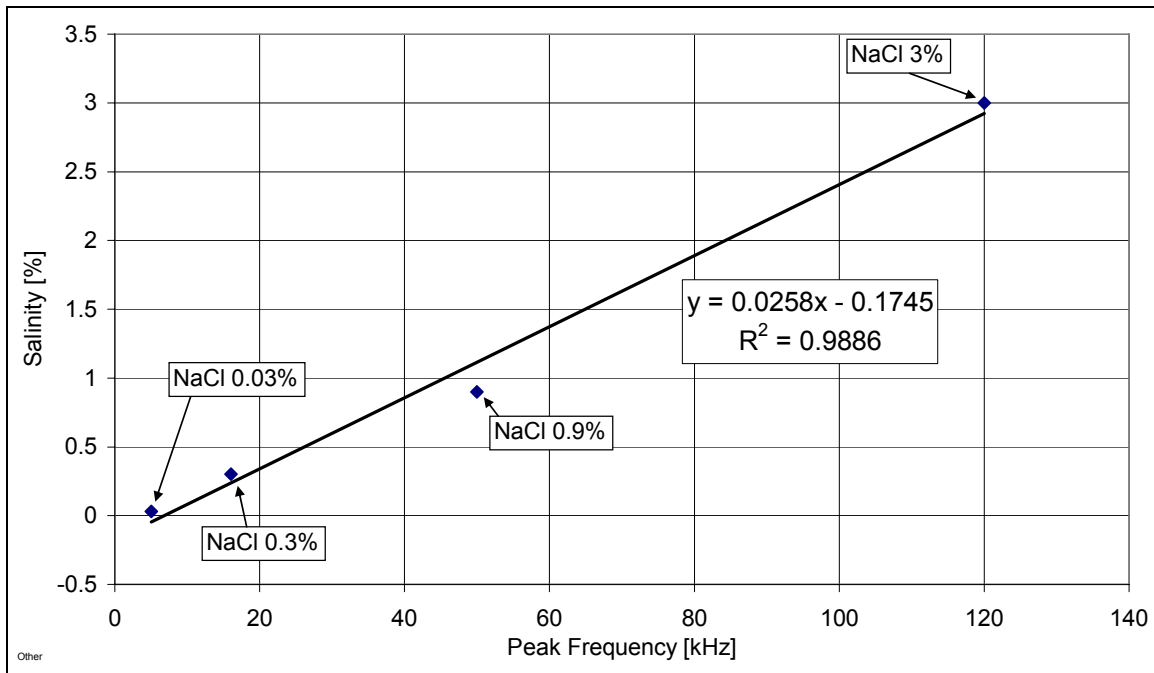


Figure 161 Salinity of the saturating fluid versus the frequency at the value when the loss tangent peaks in Figure 160.

CHAPTER 8. DIELECTRIC MEASUREMENT RESULTS FOR PARTIALLY SATURATED ROCKS

The partial saturation experiments were conducted on six samples of different grain sizes. All samples are flat cylindrical disks 1.5 inches in diameter and 0.7 to 0.9 cm in thickness. Figure 1 shows a simple diagram of the sample dimensions. The sample dimensions were intended to match the requirements for carrying out the tests. The samples were also coated with epoxy at the circumference so that evaporation only takes place at the top and bottom faces.

The first section discusses the procedure and results from the x-ray CT scan experiments. The CT scan provides a visual image of the water saturation profile of the samples as they dry out in open air. The second part covers the experimental results for partially saturated rock samples.

8.1 HIGH RESOLUTION X-RAY CT SCAN

This section describes the high resolution X-ray CT scan procedures and results. The purpose of the scan is to display and analyze the water saturation profile of the rock samples. The water saturation profile provides some indications of the electric field paths.

A holder made of Lexan® designed to grip each sample on three points around the circumference was used and the schematics are shown in Figure 2 through Figure 5. The plastic holder makes minimum contact with the sample and permits evaporation to take place on the top and bottom faces of the samples. The high resolution scans were made at every 0.1 mm interval and each sample takes an average of five minutes to complete. As a result, fully saturated scans were not possible because evaporation took place as soon as the samples were exposed to open air.

An example of a scan slice is shown at the left of Figure 6. The image shows a single 0.1 mm slice of the Berea sample with some high density (bright reddish color) and low density (dark blue color) areas. This image was corrected for water saturation by subtracting

the dried sample image at the same location and the resulting water saturation profile is displayed at the right side of the figure.

MATLAB[®] was used to reconstruct and analyze the scanned image slices. The MATLAB[®] programs performed several operations. *A02SlicingImageALL.m* combined the top-view images and recreated the images in the radial cross-sectional directions. *A03CheckMiddleSlice.m* searched for the center most radial cross-section image of each sample. *A05SaturationProfileTrim.m* loaded and subtracted the radial cross-section image from the dry images and outputted the water saturation images. *A06SaturationCalculation.m* calculated the cross-section water saturation images and presented the results.

8.2 SCAN RESULTS

Figure 7 through Figure 12 shows the water saturation profile of the test samples. In general, the evaporation rate of saturated water in the natural rock samples (Berea, Boise, and Texas Cream) was reasonably constant and uniform in both the cross-sectional and top-bottom directions. The water in the sintered samples (large, medium, and small beads) evaporated non-uniformly in either the cross-sectional and top-bottom directions. The smallest sintered sample, with 40 μ m pore size had the least uniform water saturation profile (Figure 12), shows the water evaporated fastest along the edges of the circumferences that were exposed to air.

Figure 13 and Figure 14 show the water saturation versus time for Berea and Texas Cream. The water saturation was calculated by two methods. The first method was by weighting the sample as time passes. The second method calculated average water saturation from the scanned images in Figure 7 and Figure 8 by adding the intensities of each pixel. As a result, the second method only provides relative saturations. The plot shows a very good linear correlation of the water saturation and drying time in open air. Based on these results, the average water saturation of the sample was calculated from the drying time of the sample as measurements are made.

8.3 PARTIAL SATURATION MEASUREMENT RESULTS

The results of the partial saturation measurements are shown starting from Figure 15. Figure 15 through Figure 23 show results for Berea sandstone, Figure 24 through Figure 32 show the results for Boise sandstone, and Figure 33 through 37 show the results for Texas Cream limestone. All samples were saturated with de-ionized water.

In general, the dielectric constant of Berea sandstone decreases as water saturation decreases; however, at saturations greater than 0.94, the dielectric constant at 1 kHz to 1 MHz is lower than the measurements made at below $S_w = 0.94$ (Figure 15). The reason of this effect is not known, but a possible answer might be the difference of electrode-sample contact at high and low water saturations.

The conductivity measurements (Figure 16) show a significant reduction below 100 kHz when water saturation was less than 0.94. In general, the conductivity decreases as water saturation decreases, as expected. Again, the drop of conductivity below 100 kHz can be caused by electrode-sample contact at high and low water saturations.

The reactance measurements (Figure 17) reveal local maxima in the kHz frequency. The local maxima decrease in frequency but increase in magnitude as water saturation decreases. The loss tangent plot in Figure 18 shows two maxima when water saturation falls below 0.94. A reasonable suggestion for the extra maxima is the creation of an air-water interface at lower water saturations. However, as shown in Figure 19, both loss tangent peaks change very little with water saturation, suggesting the peak frequency is constant with water saturation.

The Argand plot (Figure 20) shows two semi-circles when the water saturation is below 0.94 and the size of the semi-circle increases as water saturation decreases. The resistivity indexes in Figure 21, Figure 22, and Figure 23 are plotted using impedance, resistivity, and reactance respectively. Unfortunately, only the resistivity index plotted by the use of resistivity at high frequency (10 MHz) shows reasonable results while the rest of the plots yielded a best fit line that does not cross the $S_w = 1$ $R_t/R_o = 1$ point and have slope less than 1. It is well known that Berea shows Archie type behavior with a saturation exponent of about 2. Clearly our measurements are affected by non-uniform saturation profiles and yield

resistivities that are too low because conductive pathways of high S_w still exist. As such, these results are not reliable and should not be used.

The measurement results of Boise sandstone are very similar to the results of Berea sandstone. Comparable trends are observed. The only differences are the resultant magnitudes and the effects of water saturation. Similar trends are found in Texas Cream limestone; however, much worse correlations are observed in relation to water saturation for the limestone.

Measurements on sintered beads samples were not performed due to the hydrophobic properties of the samples. Once the sintered beads samples were taken out of the desiccator, the water in the sample began to discharge and drip. The measurement results were inconsistent and, therefore, are not shown here.

8.4 CONCLUSIONS

- For rock samples fully saturated with de-ionized water (or low salinity water), an increase in grain size (or increase in permeability) is reflected in the dielectric measurements as follows:
 - A decrease the bulk conductivity,
 - A decrease the dielectric constant,
 - An increases the size of the Argand circle,
 - A decrease in the peak of the loss tangent plotted against frequency.
- For rock samples saturated with brine, an increase in saturating fluid salinity is reflected in the dielectric measurements as follows:
 - An increase in the rock conductivity,
 - An increase in the dielectric constant,
 - A decrease in the size of the Argand circle,
 - A decrease in the magnitude of the reactance peak value

- An increase in the frequency at when the peak occurs,
 - An increase in the loss tangent peak value
 - An increase in the frequency at when the peak occurs.
- The changes in reactance and loss tangent can be explained by a double layer polarization model.
- For sedimentary rock samples, a decrease in water saturation is reflected in the broadband dielectric measurements in the following ways:
 - A decrease in the bulk conductivity,
 - A decrease in the dielectric constant below 1 kHz and above 1 MHz,
 - An increase in the size of the Argand circle while creating a second semi-circle,
 - An increase in the reactance while creating a second peak,
 - A decrease in the magnitude of loss tangent peak while creating a second loss tangent peak.
- The results presented here suggest that the peak in loss tangent can be used as a wireline derived parameter to obtain an estimate of the grain size (or an indicator of permeability).

Table 1 Sample used for partial saturation experiments.

| Name | Sample Description |
|-------------|--|
| berea | Berea Sandstone |
| texascrm | Texas Cream Limestone |
| boise | Boise Sandstone |
| sinteredL | Sintered Bead of Large 175 μ m pore size |
| sinteredM | Sintered Bead of Medium 90 μ m pore size |
| sinteredS | Sintered Bead of Small 40 μ m pore size |

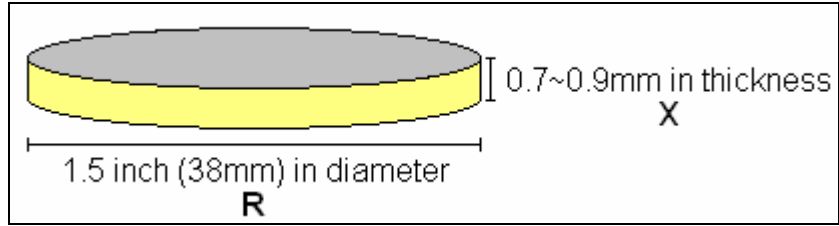


Figure 1 Dimensions and notation of the samples.

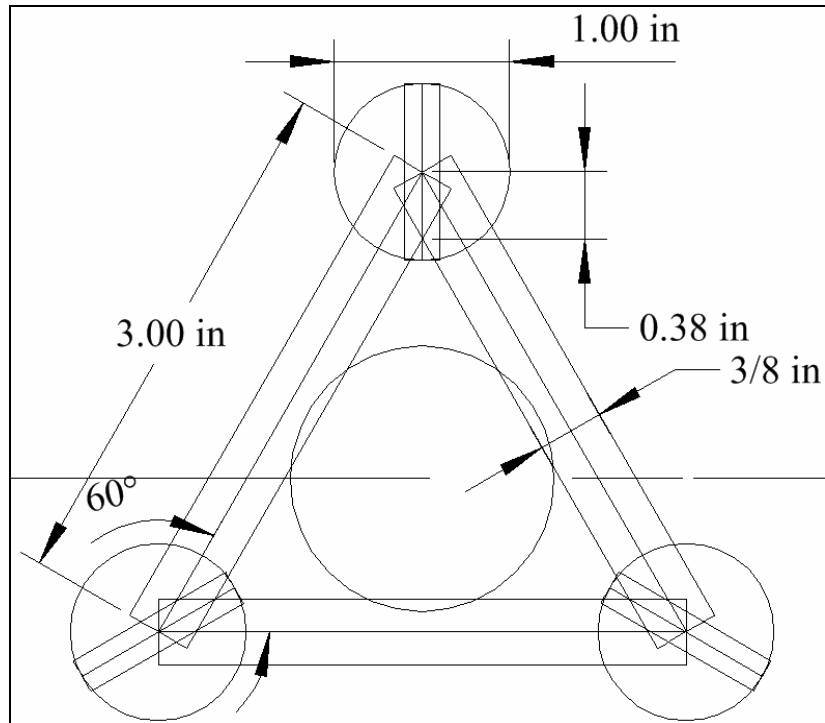


Figure 2 Top view of the schematic of Lexan holder. The rock sample of 1.5 inches in diameter is placed in the middle.

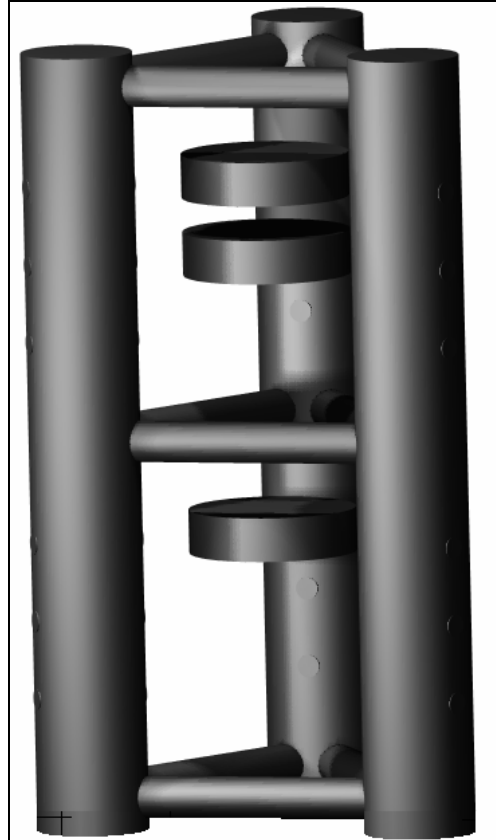


Figure 5 Colored view of the schematic of Lexan holder. The sample disk are pinned in the middle from three sides by plastic screws (not shown).

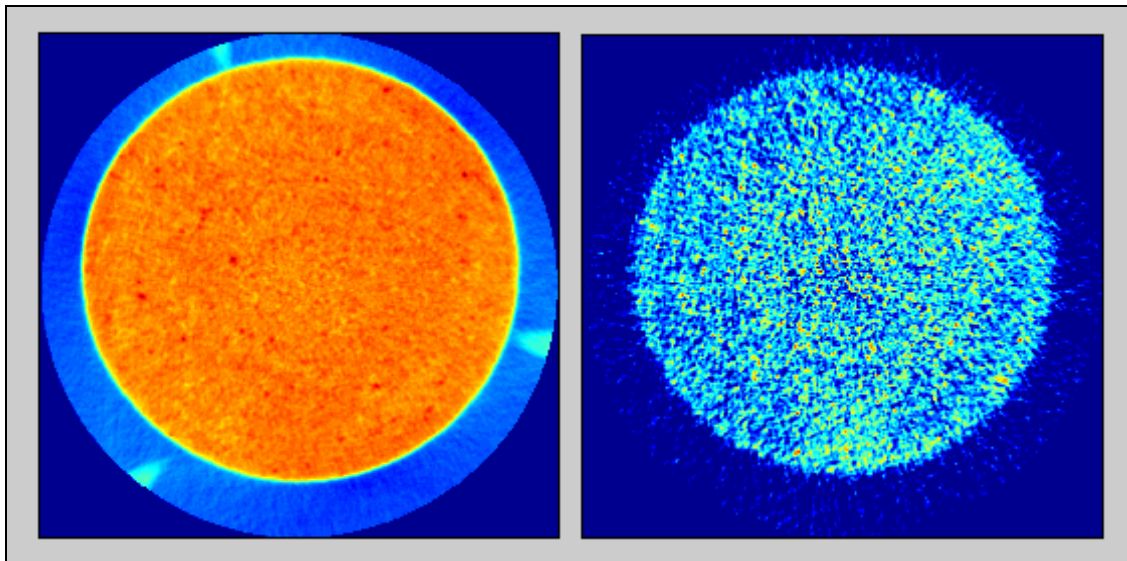


Figure 6 (LEFT) Scan of slide #70 of Berea Sandstone after 47 minutes of drying. The three spikes that hold the sample is visible. (RIGHT) Water saturation profile taken from the difference between the image on the left and fully dried sample of the same position.

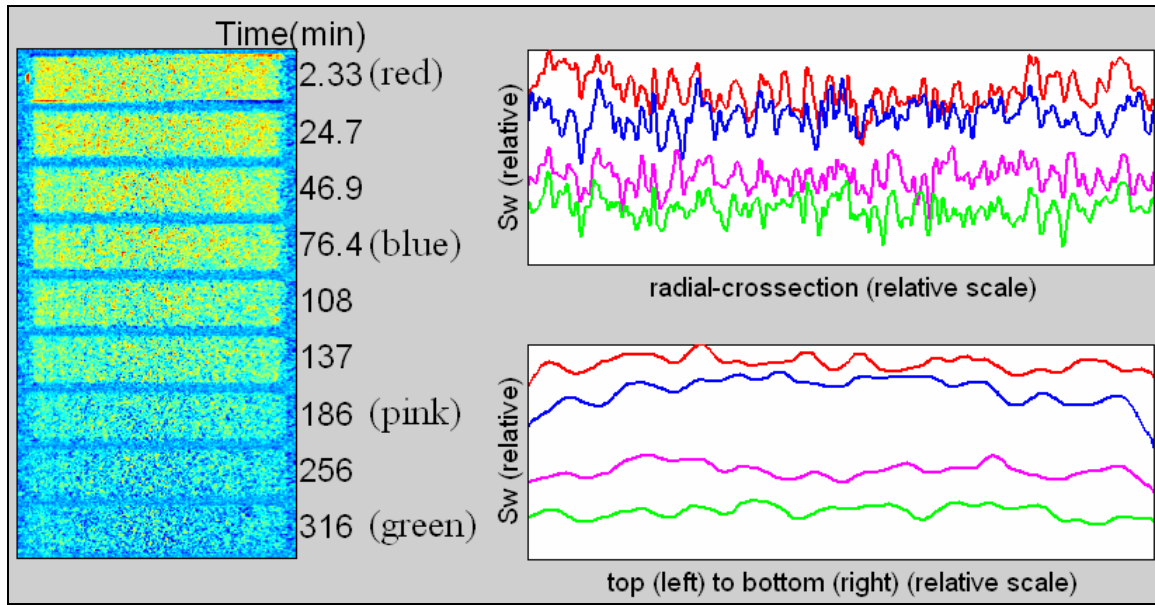


Figure 7 Water saturation profile of Berea sample. (left) radial cross-section view of the water saturation as time passes. (top right) saturation profile in the x-direction in relative scale. (bottom right) saturation profile in the z-direction in relative scale.

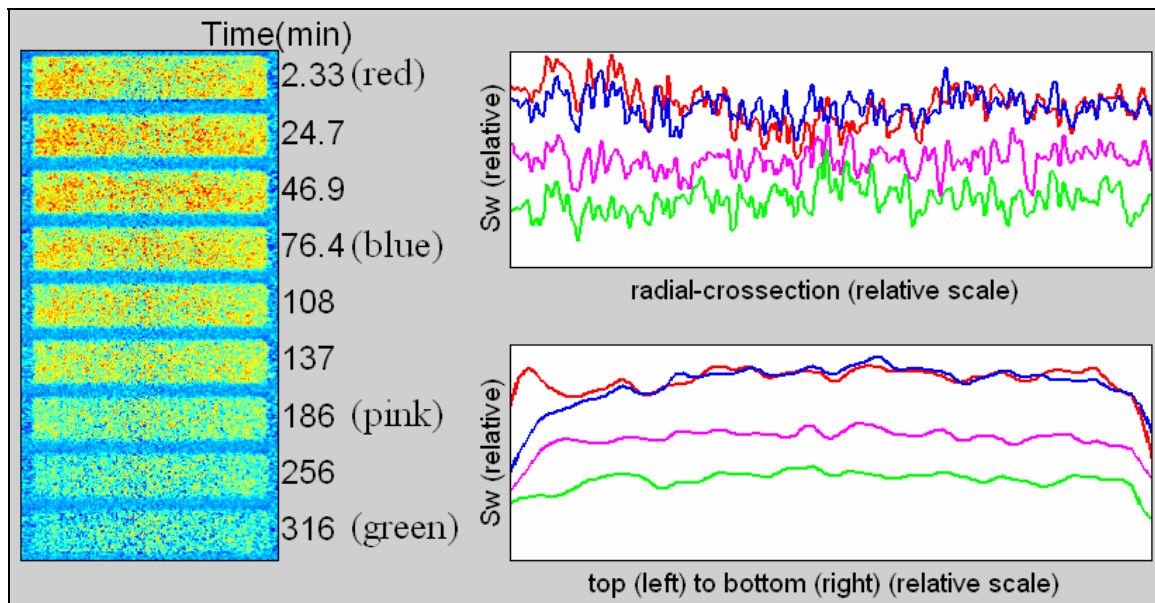


Figure 8 Water saturation profile of Texas Cream sample. (left) radial cross-section view of the water saturation as time passes. (top right) saturation profile in the x-direction in relative scale. (bottom right) saturation profile in the z-direction in relative scale.

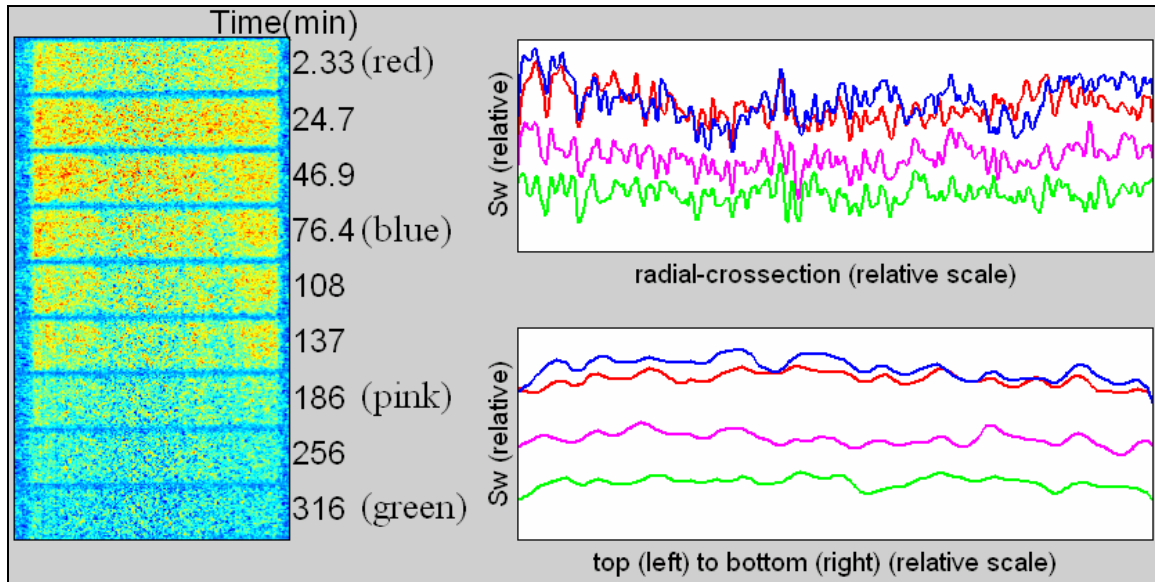


Figure 9 Water saturation profile of Boise sample. (left) radial cross-section view of the water saturation as time passes. (top right) saturation profile in the x-direction in relative scale. (bottom right) saturation profile in the z-direction in relative scale.

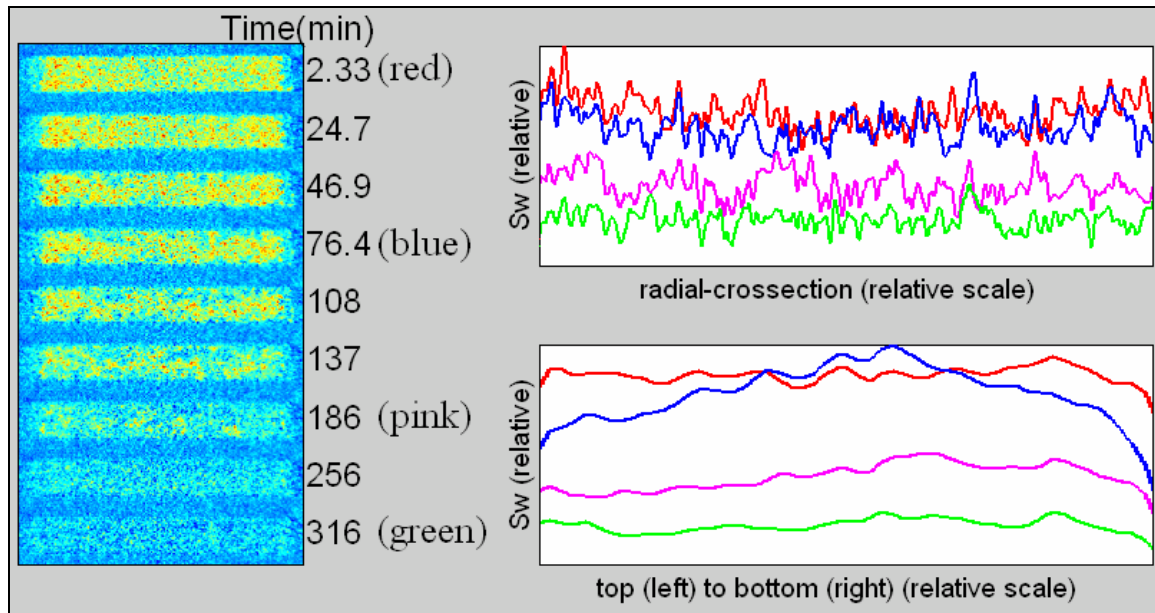


Figure 10 Water saturation profile of large sintered bead sample. (left) radial cross-section view of the water saturation as time passes. (top right) saturation profile in the x-direction in relative scale. (bottom right) saturation profile in the z-direction in relative scale.

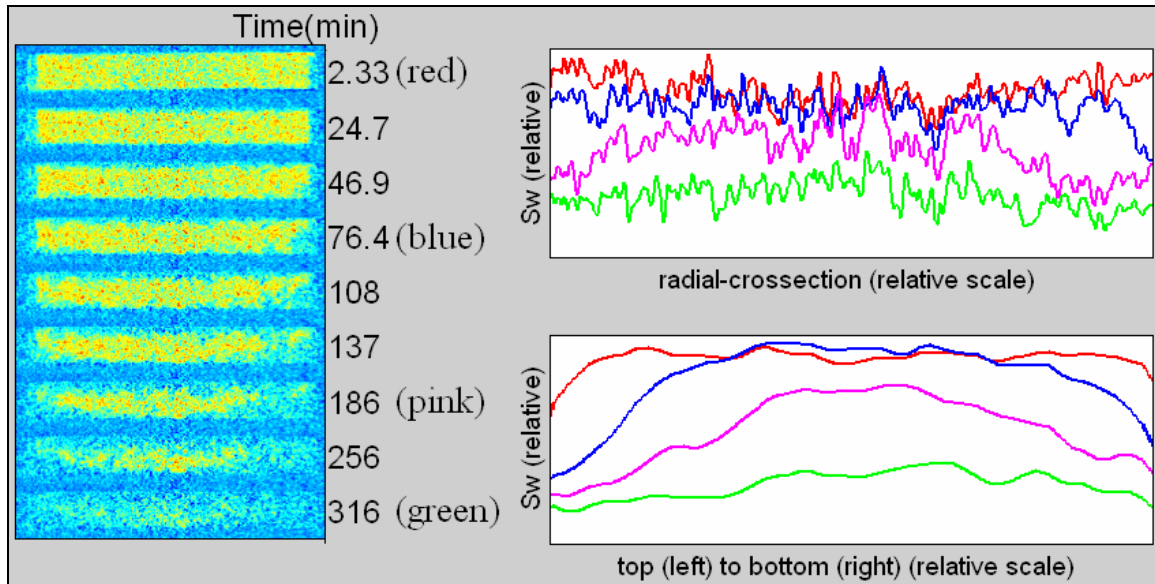


Figure 11 Water saturation profile of medium sintered bead sample. (left) radial cross-section view of the water saturation as time passes. (top right) saturation profile in the x-direction in relative scale. (bottom right) saturation profile in the z-direction in relative scale.

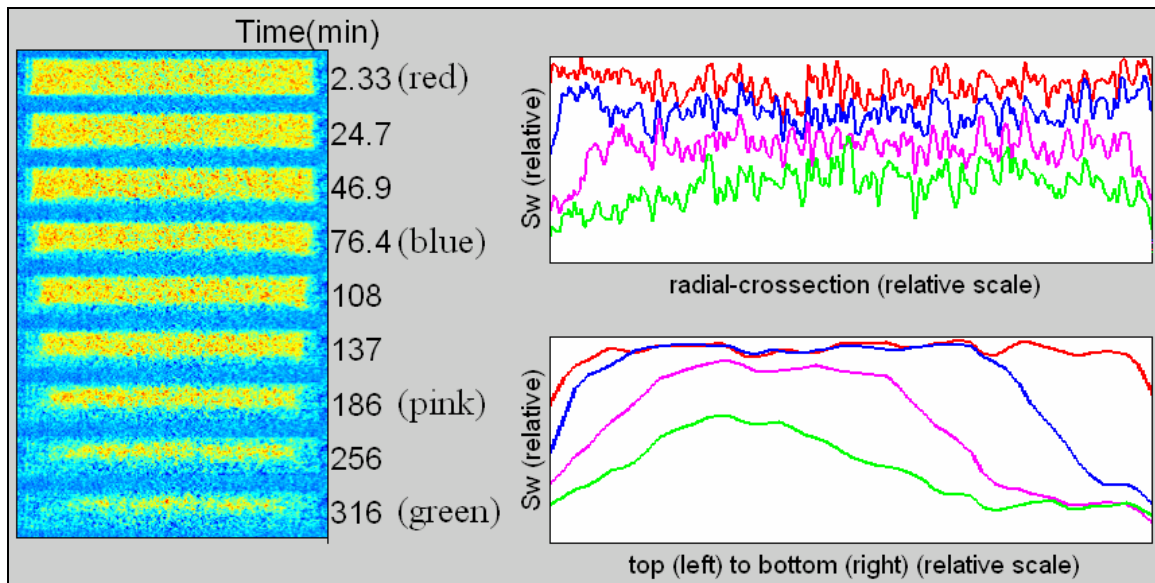


Figure 12 Water saturation profile of small sintered bead sample. (left) radial cross-section view of the water saturation as time passes. (top right) saturation profile in the x-direction in relative scale. (bottom right) saturation profile in the z-direction in relative scale.

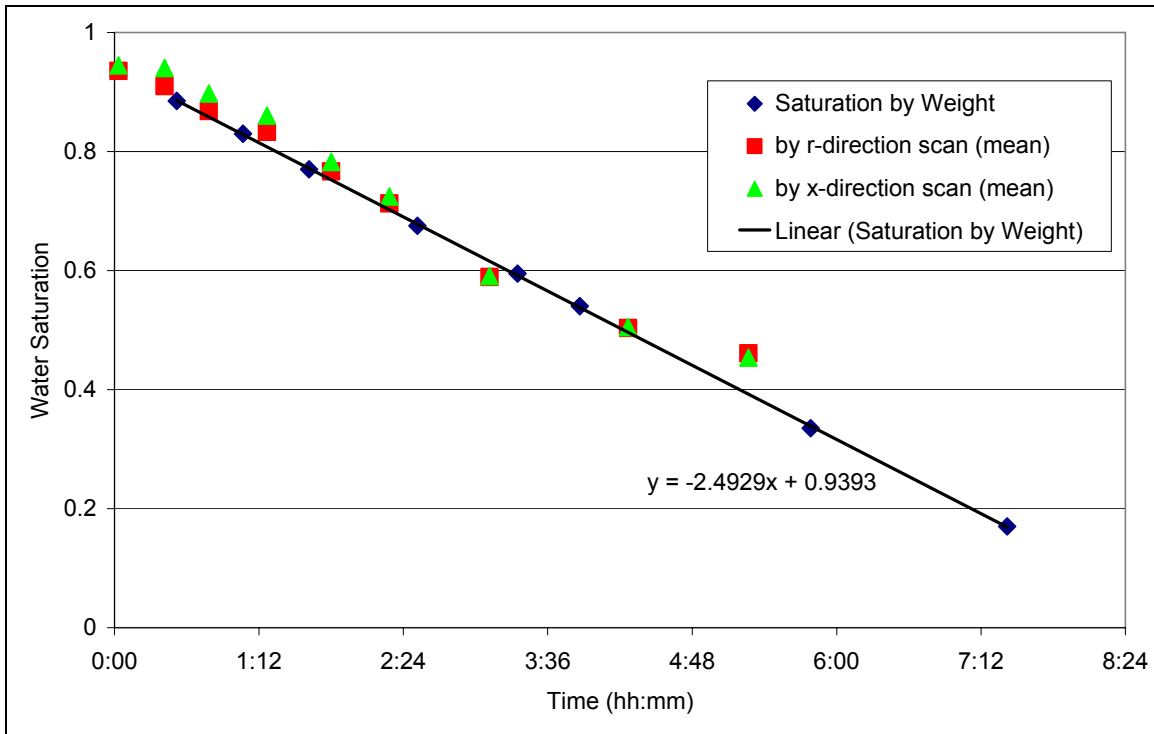


Figure 13 Berea sandstone water saturation by weight and by CT scan vs. Time.

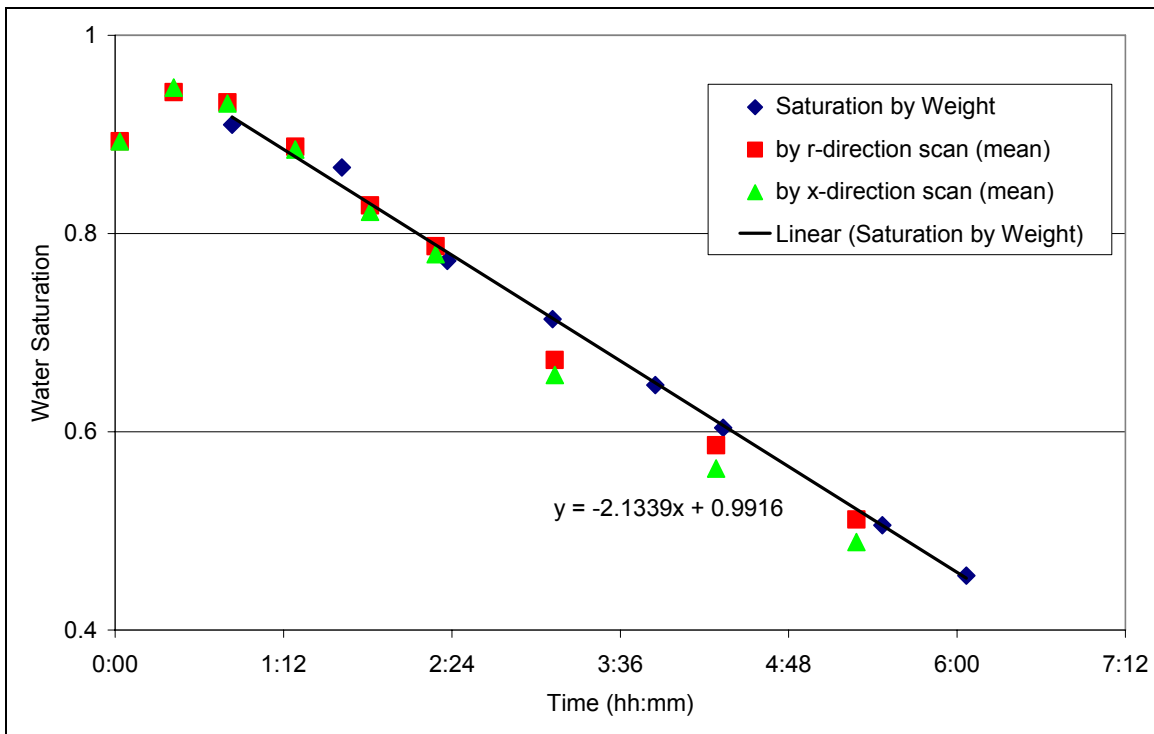


Figure 14 Texas cream water saturation by weight and by CT scan vs. Time.

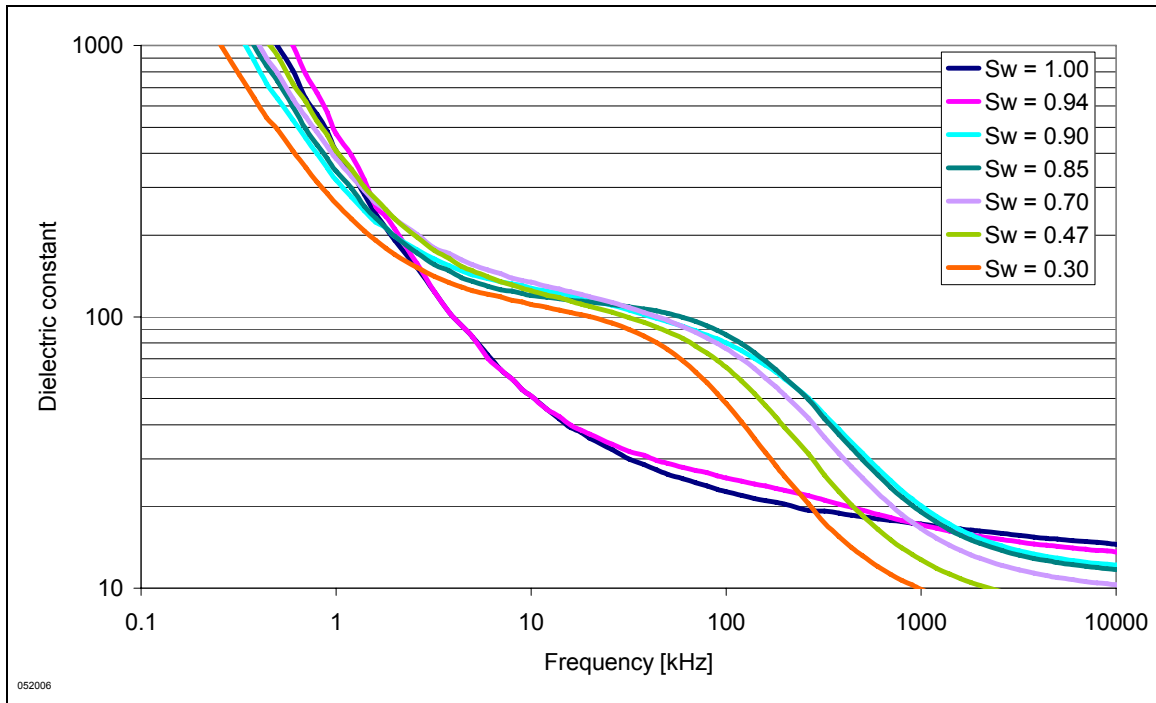


Figure 15 Dielectric constant of partially saturated Berea sandstone samples.

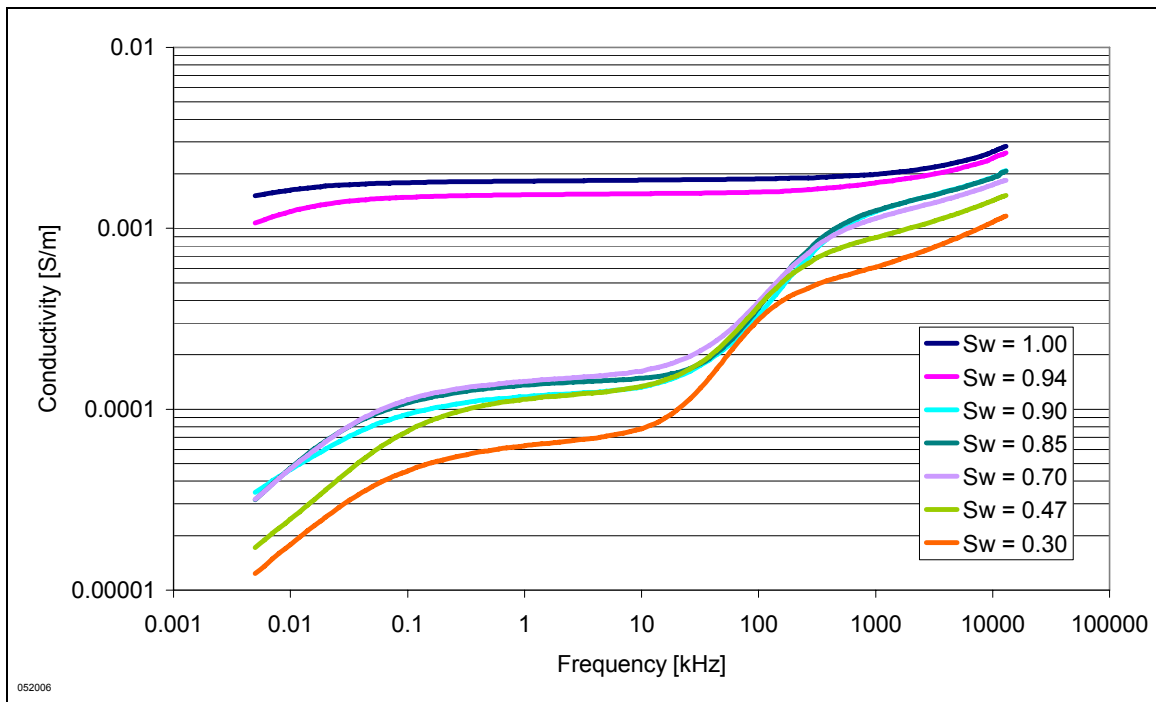


Figure 16 Conductivity in parallel equivalent circuit on Berea samples.

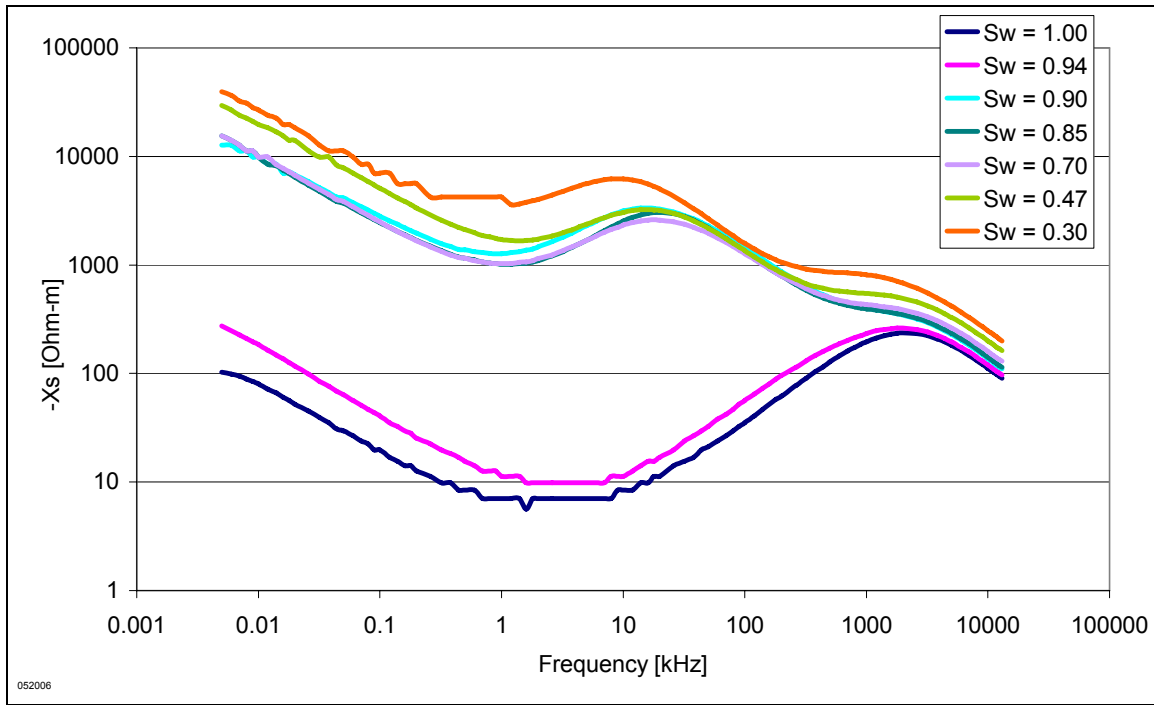


Figure 17 Reactance-m in series equivalent circuit on Berea samples at different S_w .

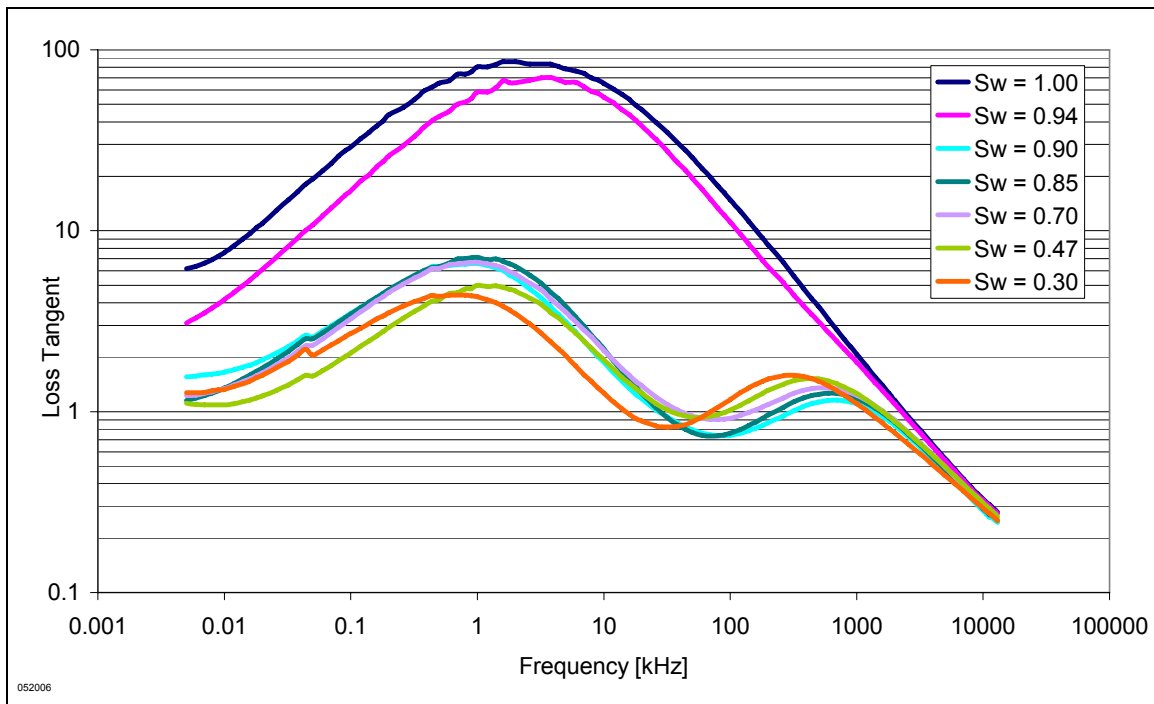


Figure 18 Loss tangent versus frequency of Berea samples at different S_w .

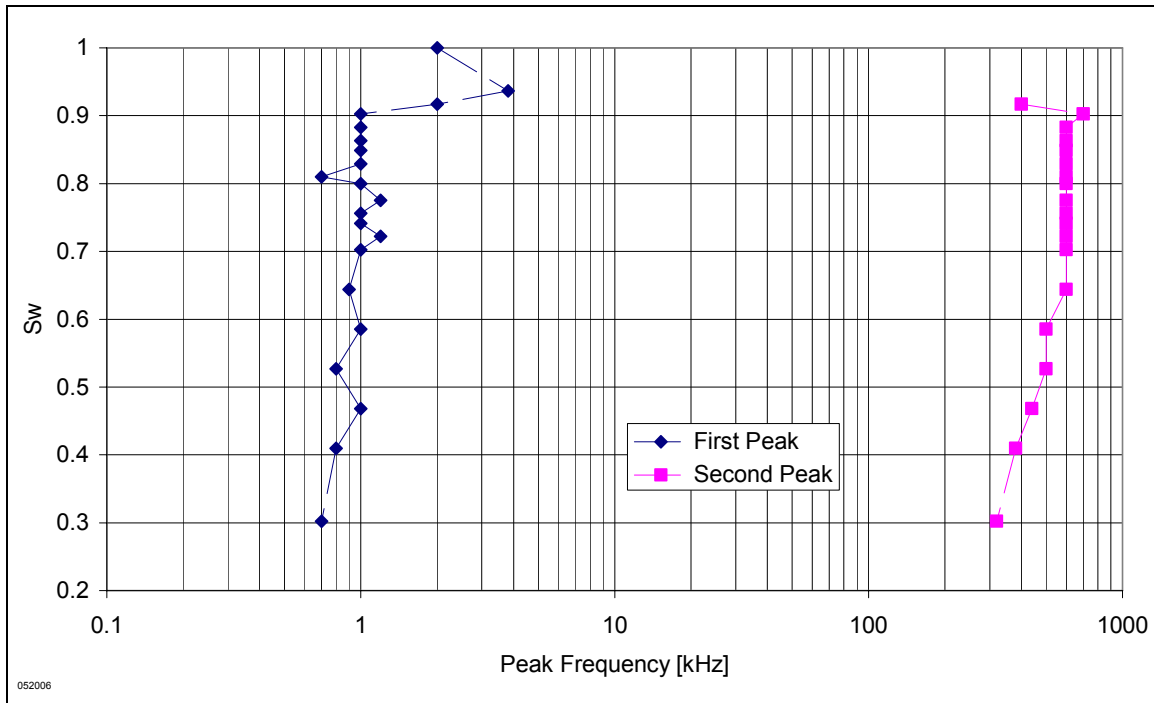


Figure 19 Berea sample measurements. The two frequencies at the two peaks of loss tangent plotted against S_w . The frequencies stays relatively constant with changes in S_w . At lower S_w , the two peaks appears to decrease in frequency.

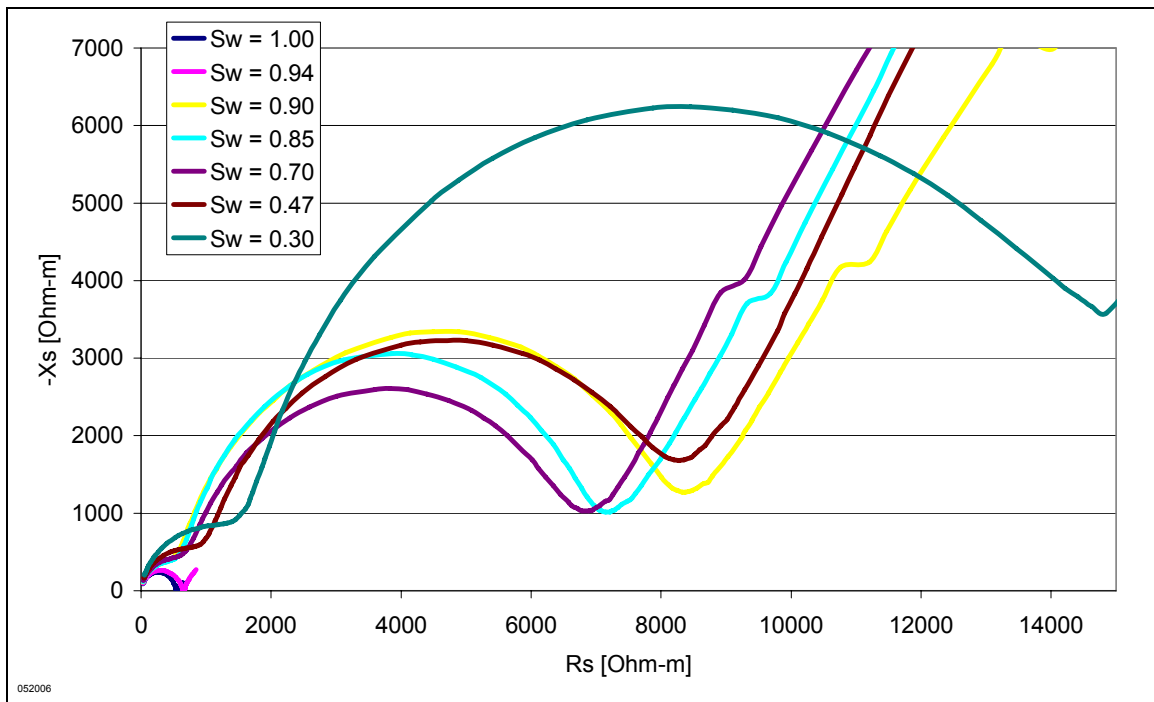


Figure 20 Argand plot of Berea samples at different S_w .

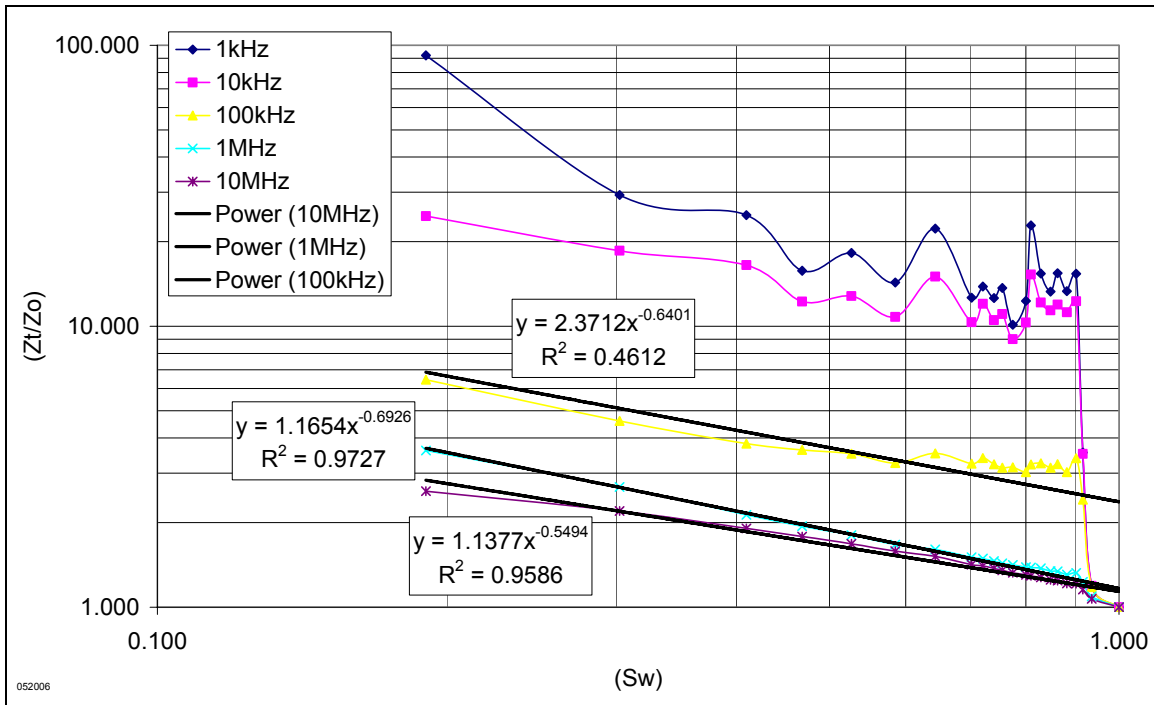


Figure 21 Resistivity index calculated from the Berea sample impedance.

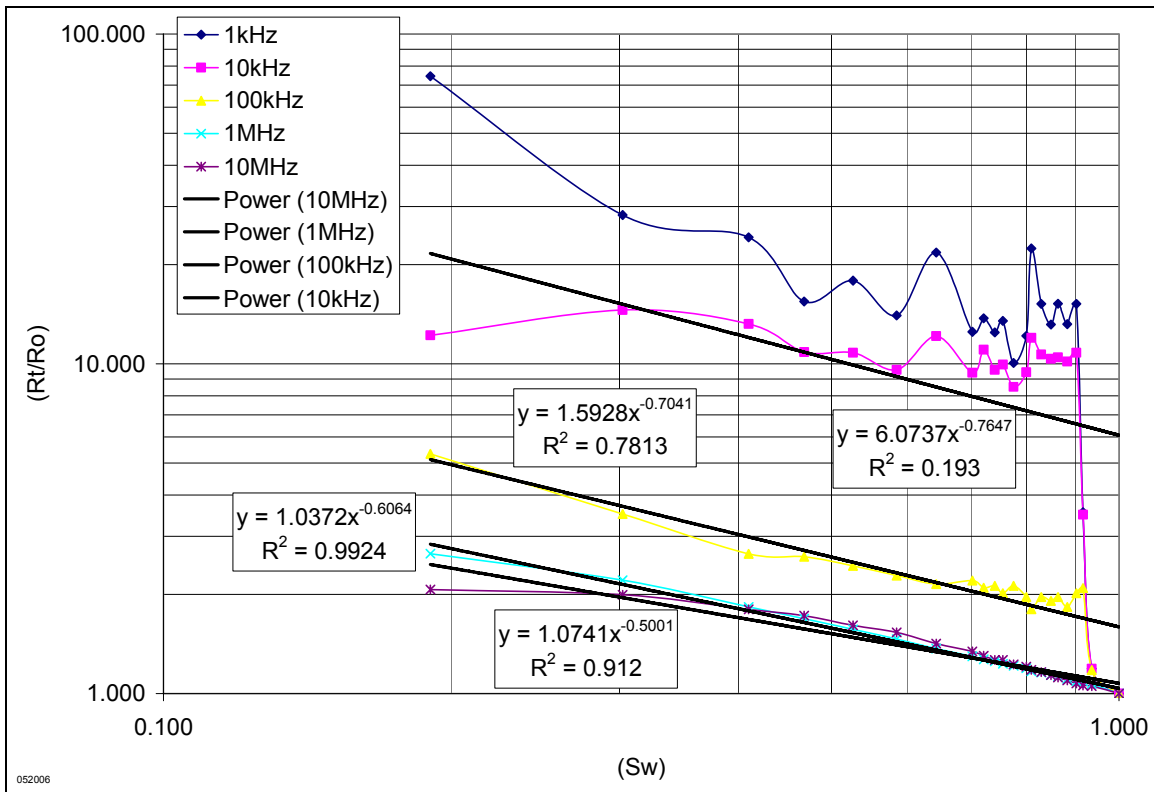


Figure 22 Resistivity index calculated from the Berea sample resistivity.

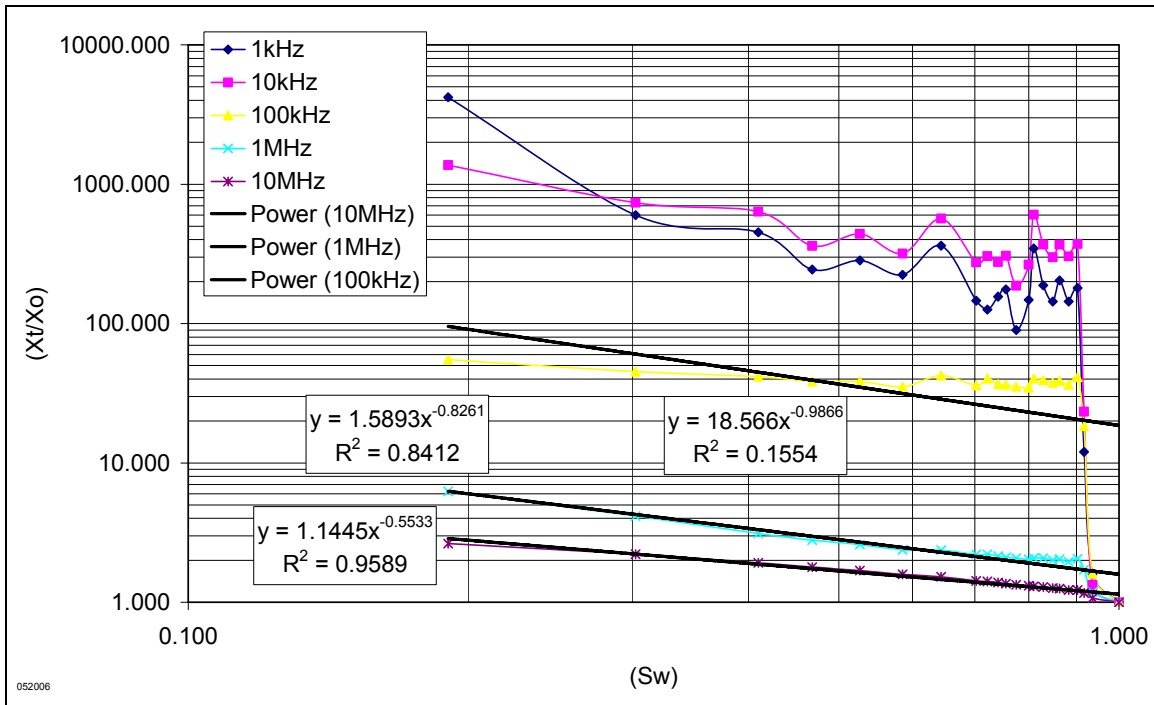


Figure 23 Resistivity index calculated from the Berea sample reactance-m.

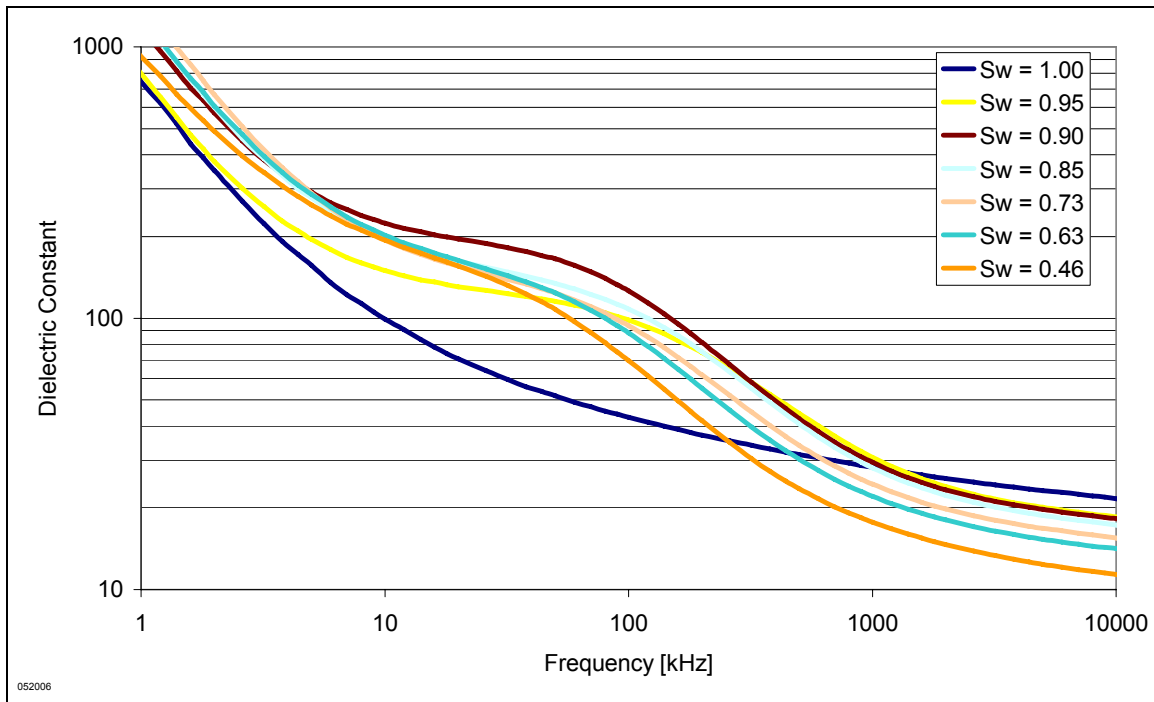


Figure 24 Dielectric constant of partially saturated Boise sandstone samples.

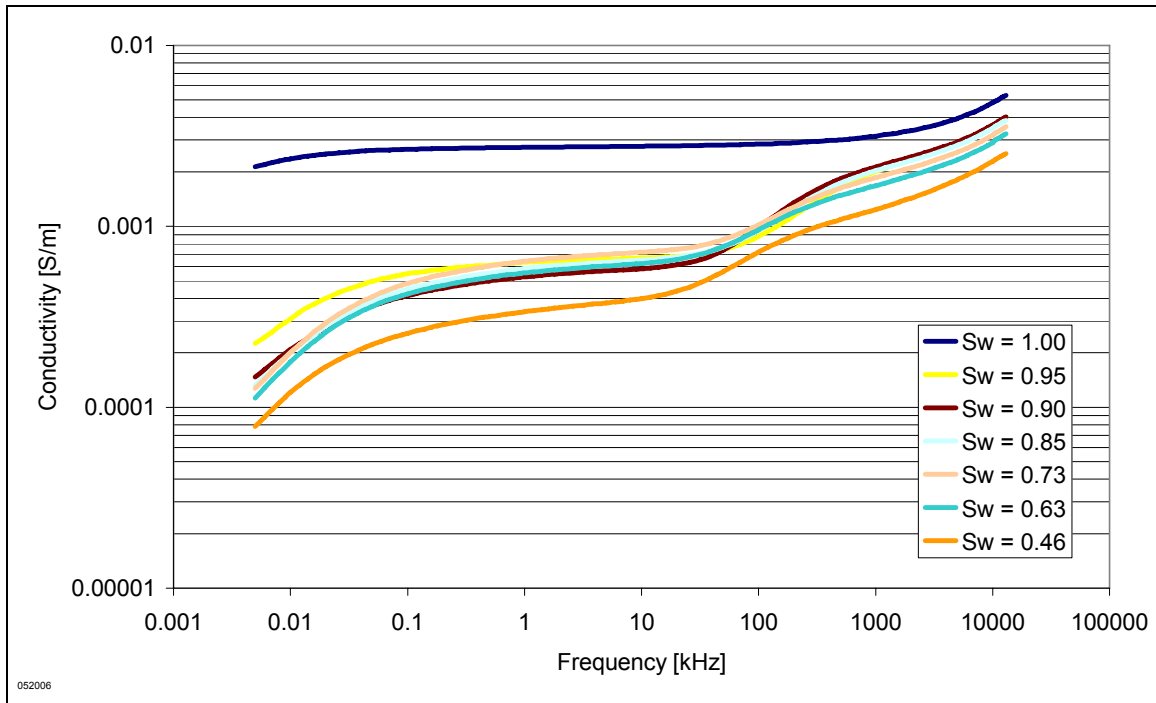


Figure 25 Conductivity in parallel equivalent circuit on Boise samples.

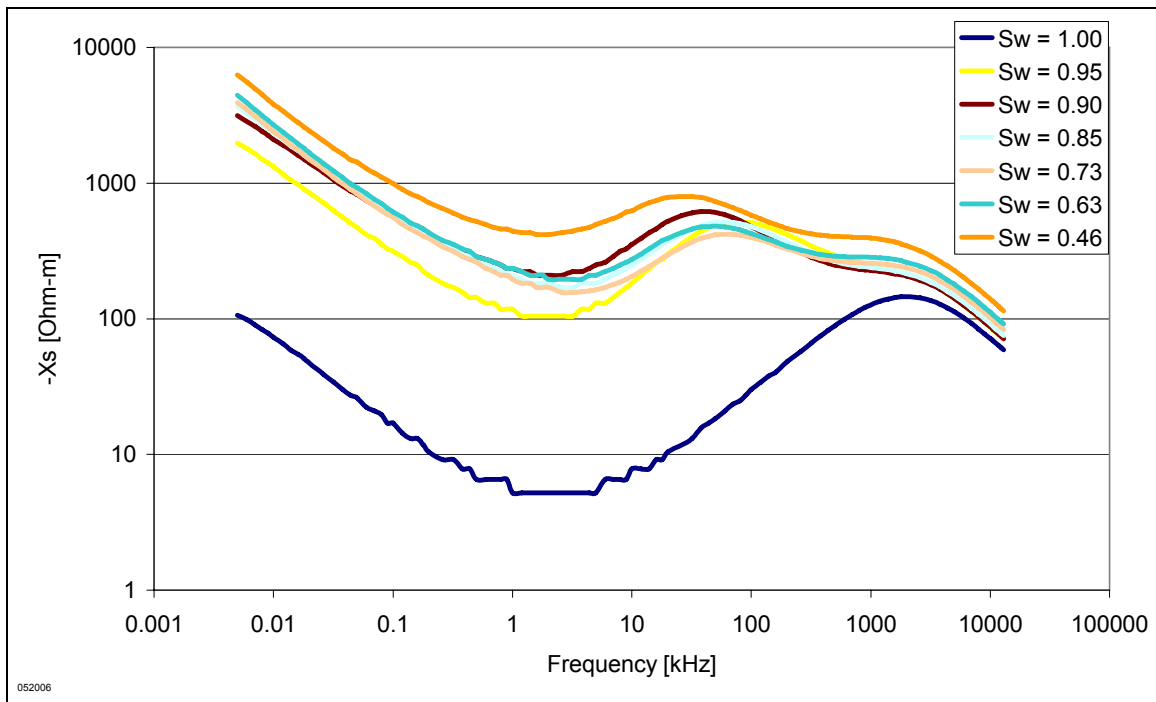


Figure 26 Reactance-m in series equivalent circuit on Boise samples at different S_w .

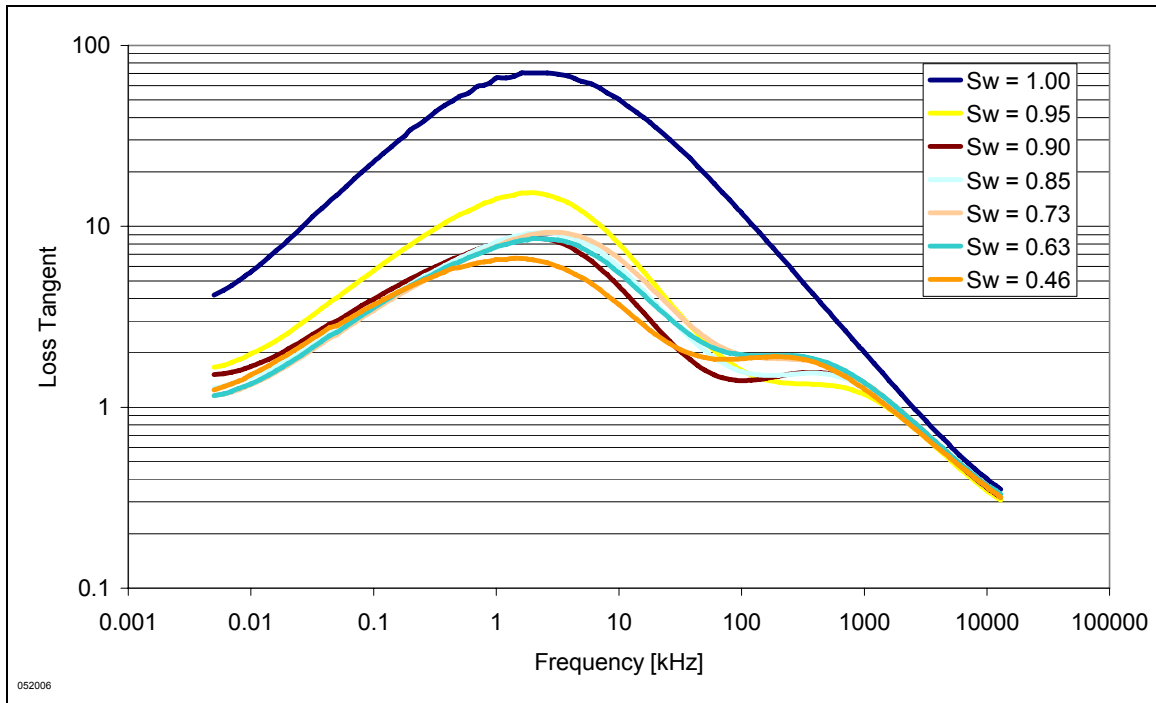


Figure 27 Loss tangent versus frequency of Boise samples at different S_w .

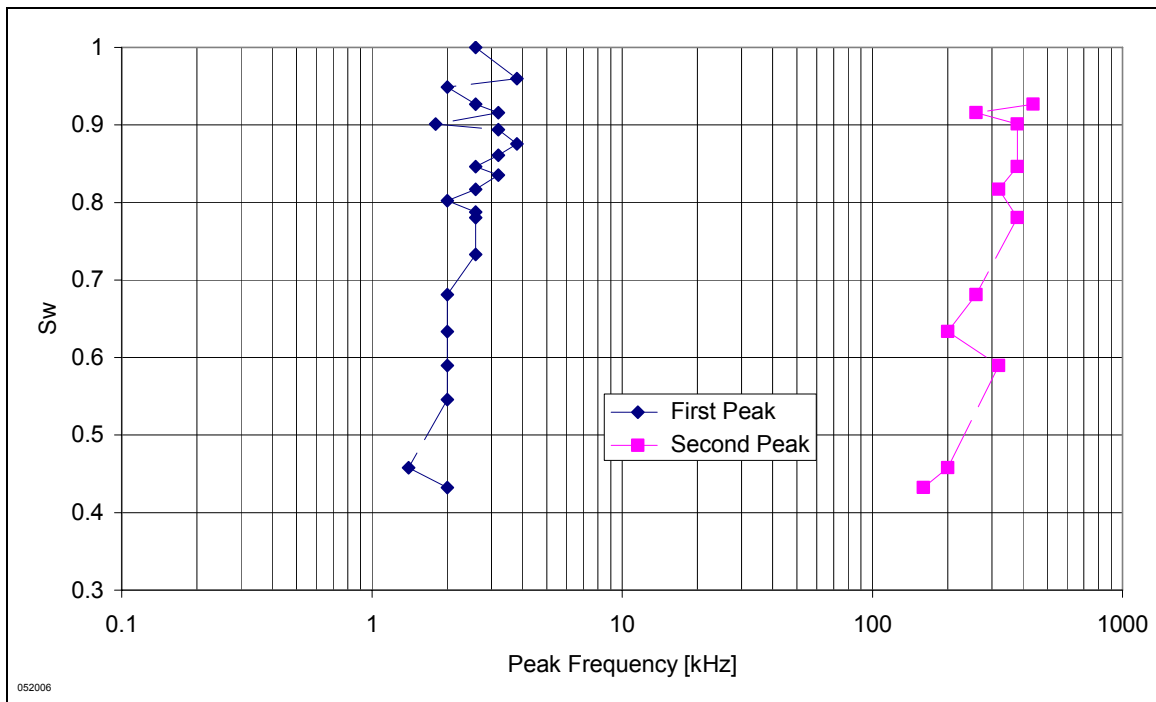


Figure 28 Boise sample measurements. The two frequencies at the two peaks of loss tangent plotted against S_w . The frequencies stays relatively constant with changes in S_w . At lower S_w , the two peaks appears to decrease in frequency.

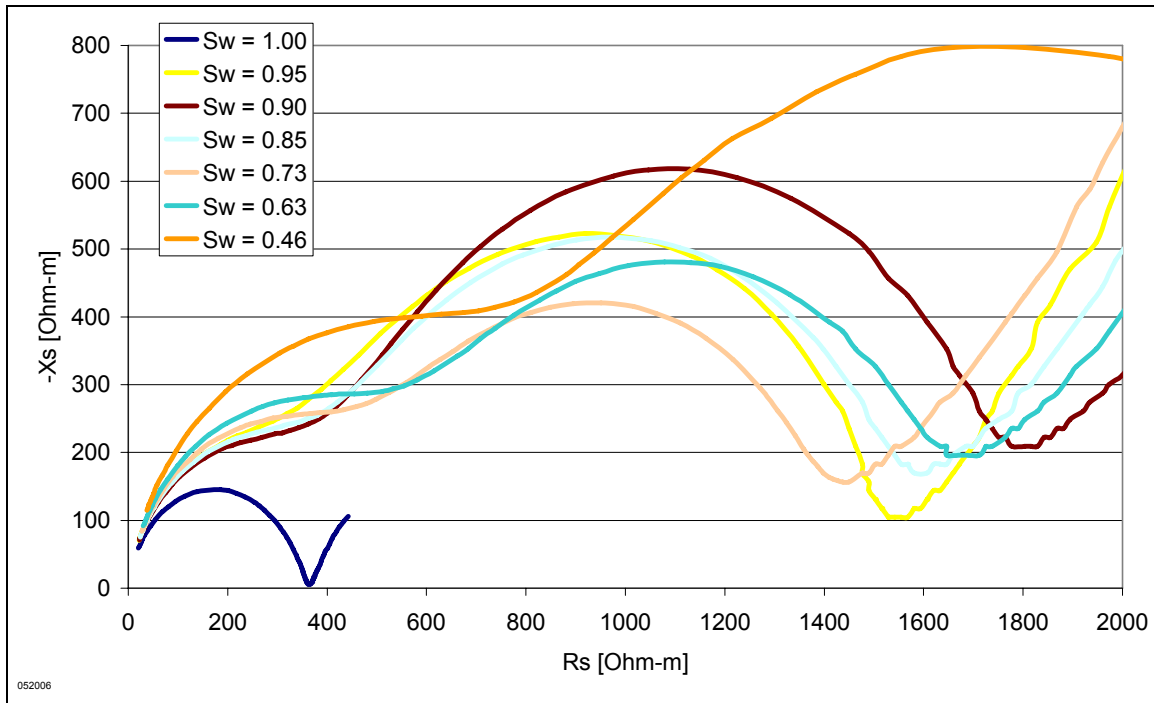


Figure 29 Argand plot of Boise samples at different S_w .

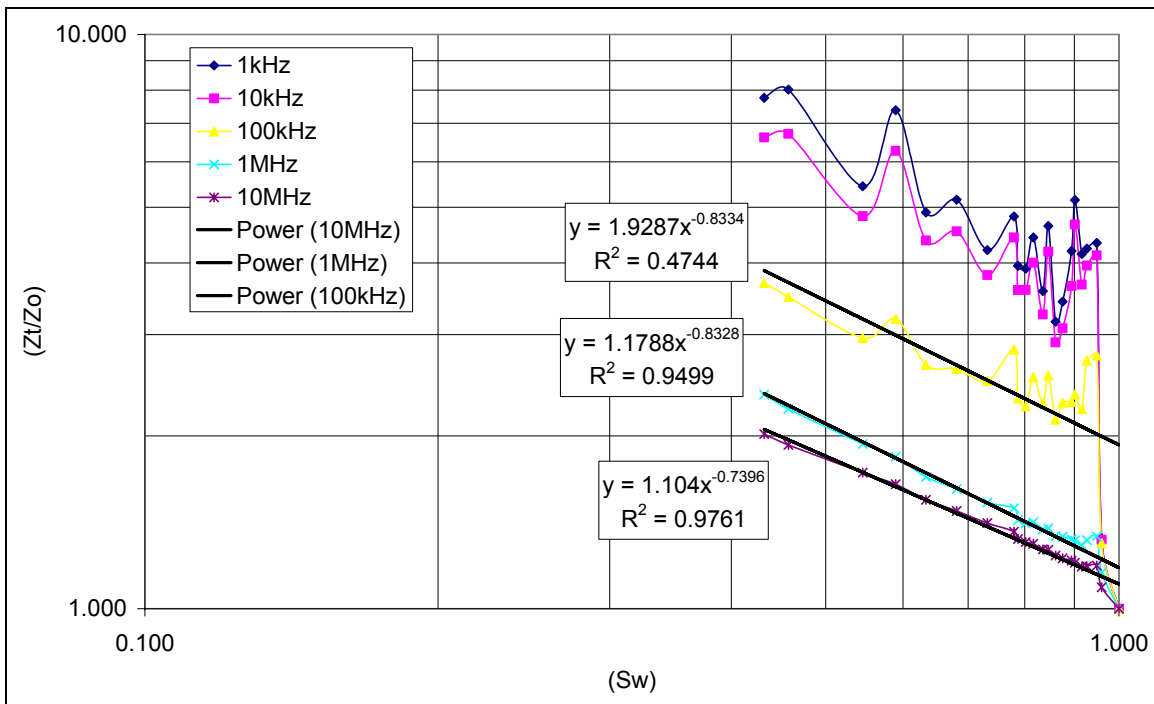


Figure 30 Resistivity index calculated from the Boise sample impedance.

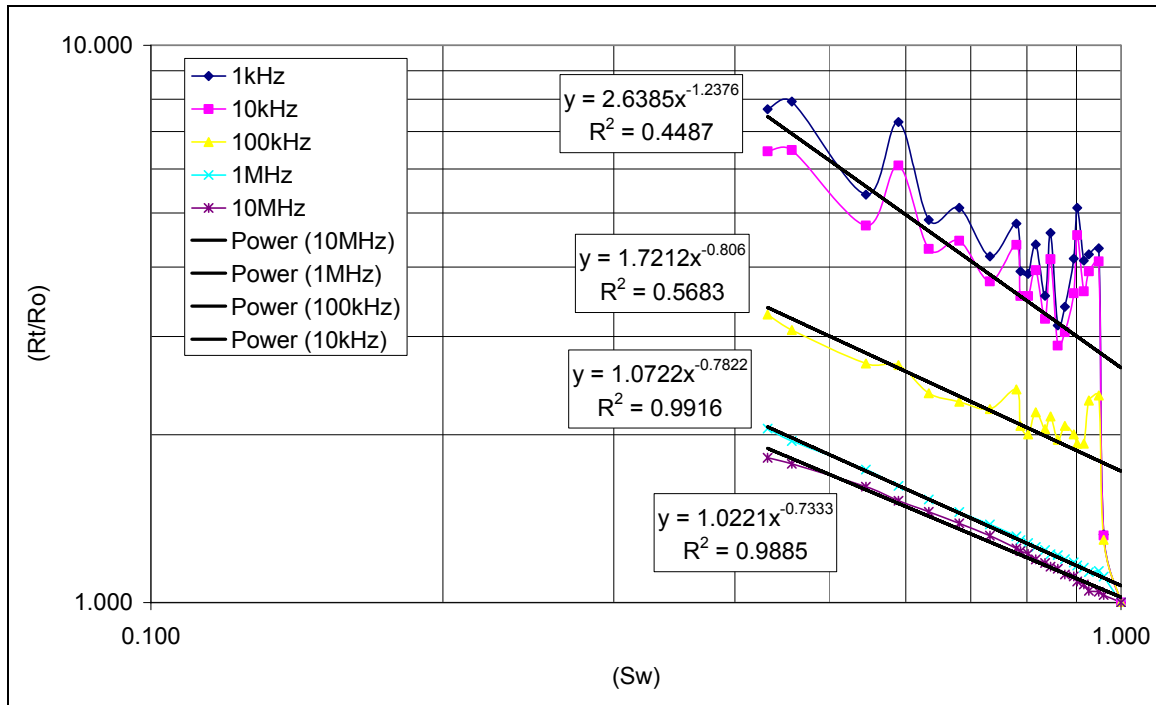


Figure 31 Resistivity index calculated from the Boise sample resistivity.

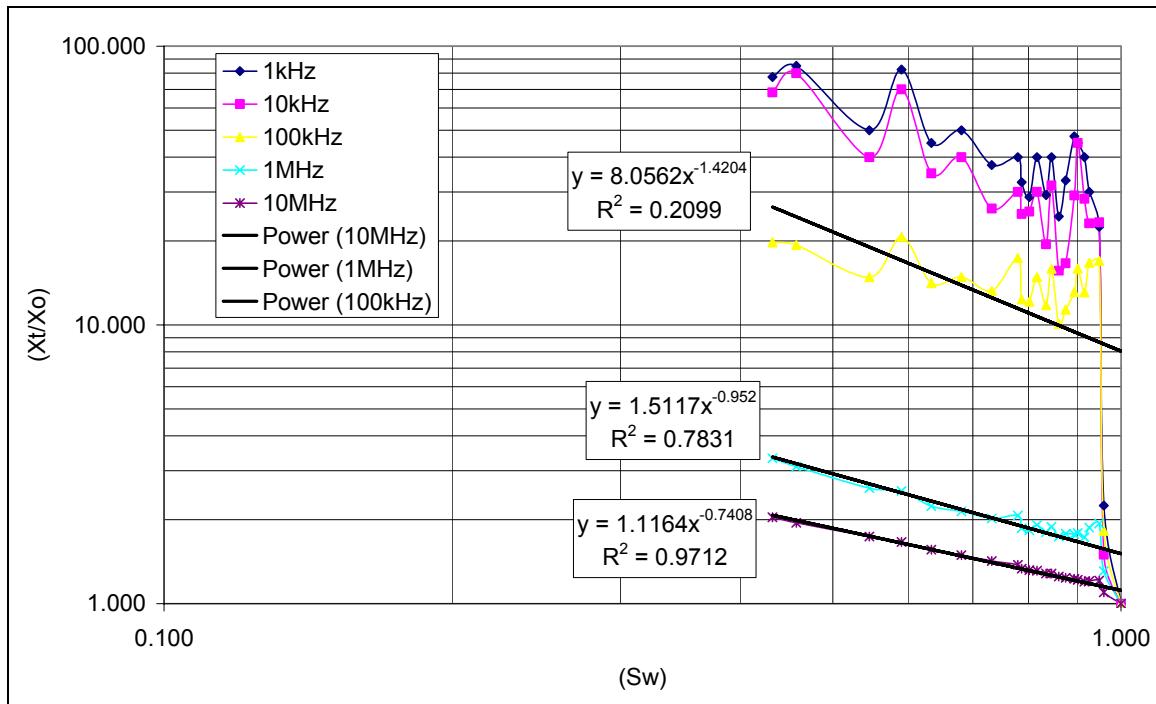


Figure 32 Resistivity index calculated from the Boise sample reactance-m.

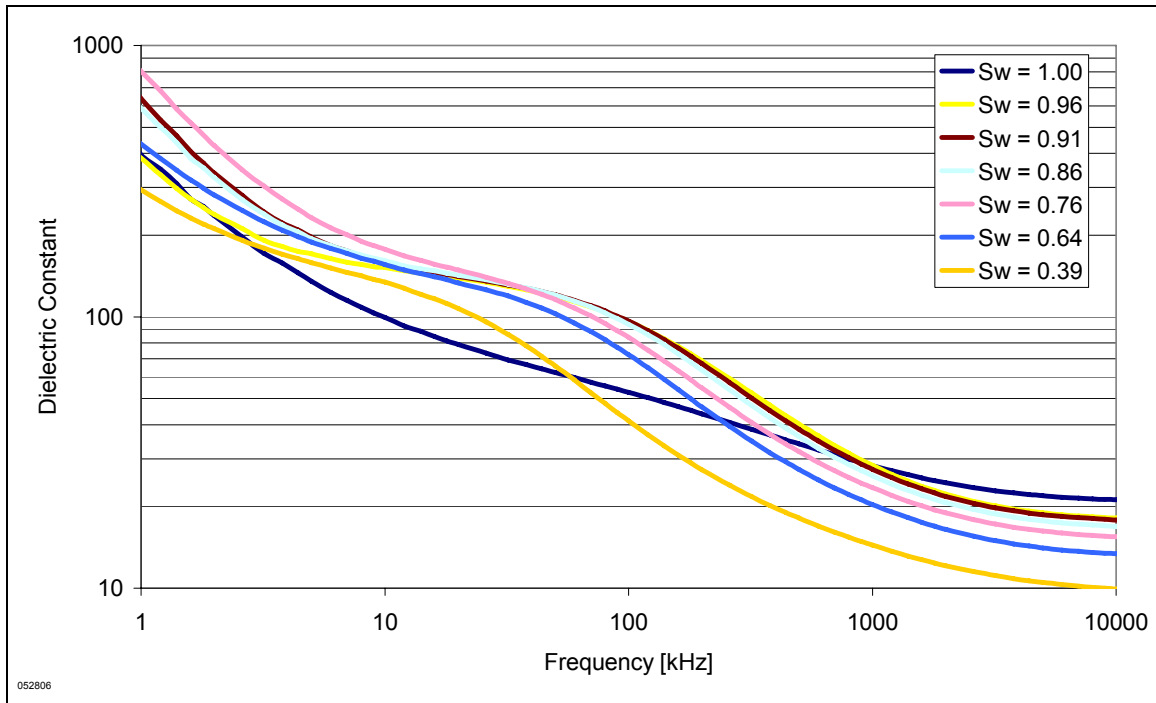


Figure 33 Dielectric constant of partially saturated Texas Cream limestone samples.

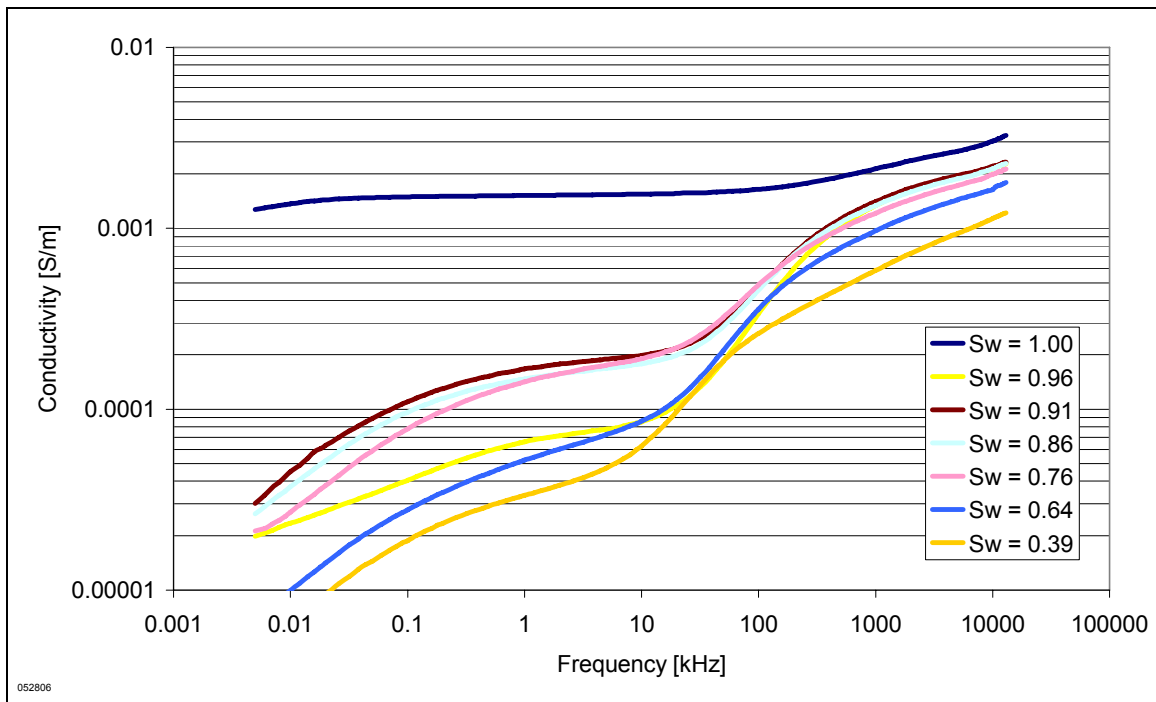


Figure 34 Conductivity in parallel equivalent circuit on Texas Cream samples.

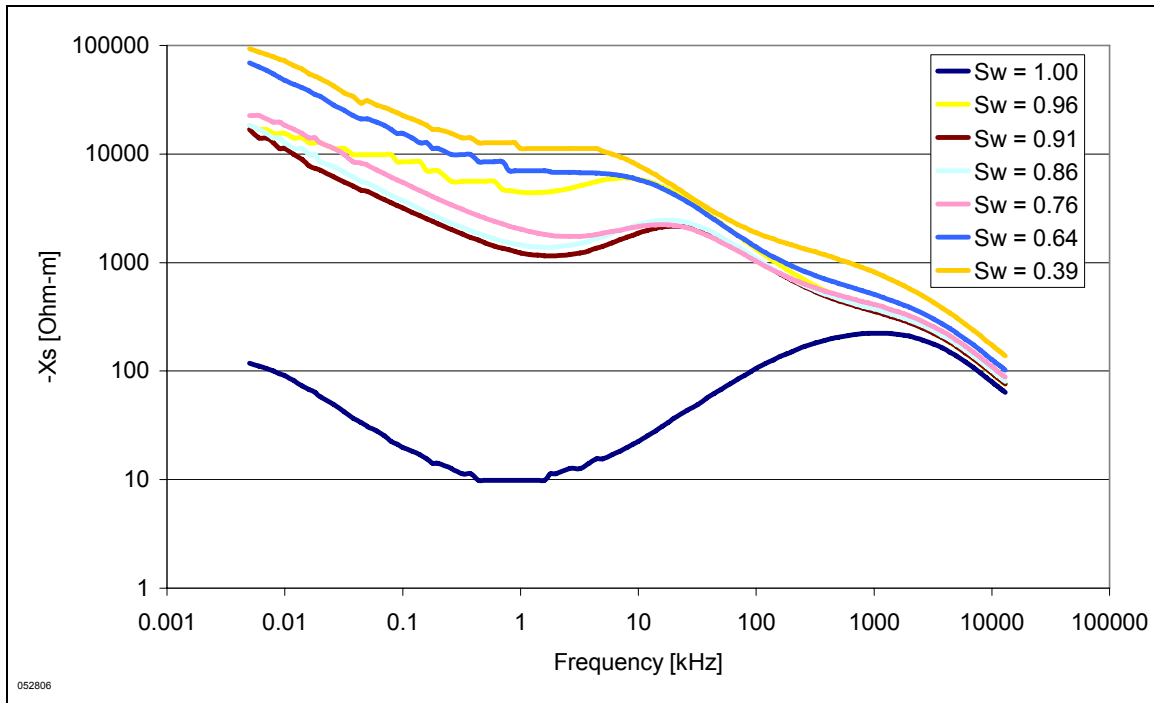


Figure 35 Reactance-m in series equivalent circuit on Texas Cream samples at different S_w .

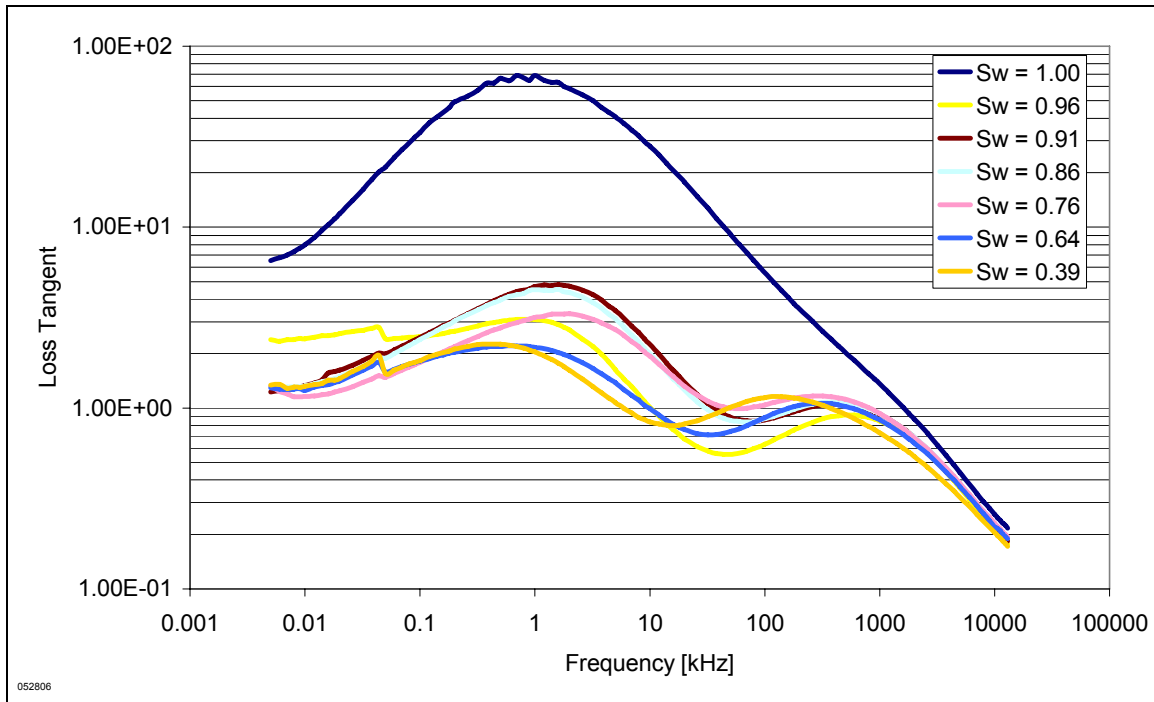


Figure 36 Loss tangent versus frequency of Texas Cream limestone samples at different S_w .

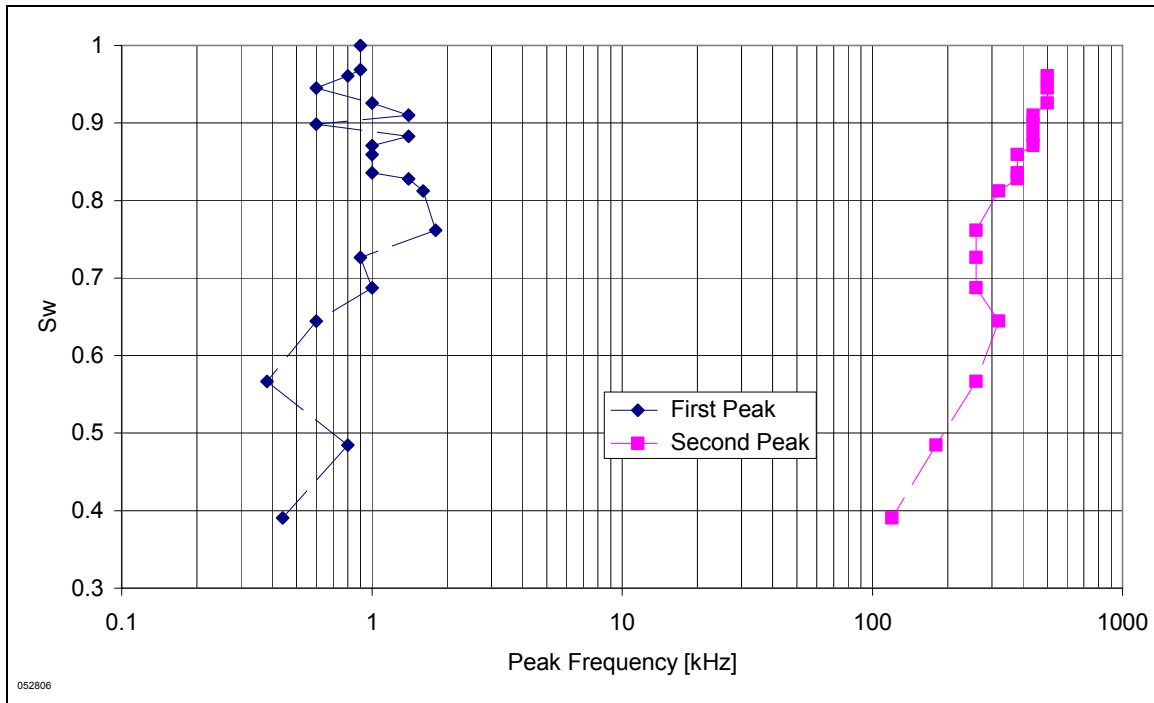


Figure 37 Texas Cream sample measurements. The two frequencies at the two peaks of loss tangent plotted against S_w . The frequencies stay relatively constant with changes in S_w . At lower S_w , the two peaks appear to decrease in frequency.

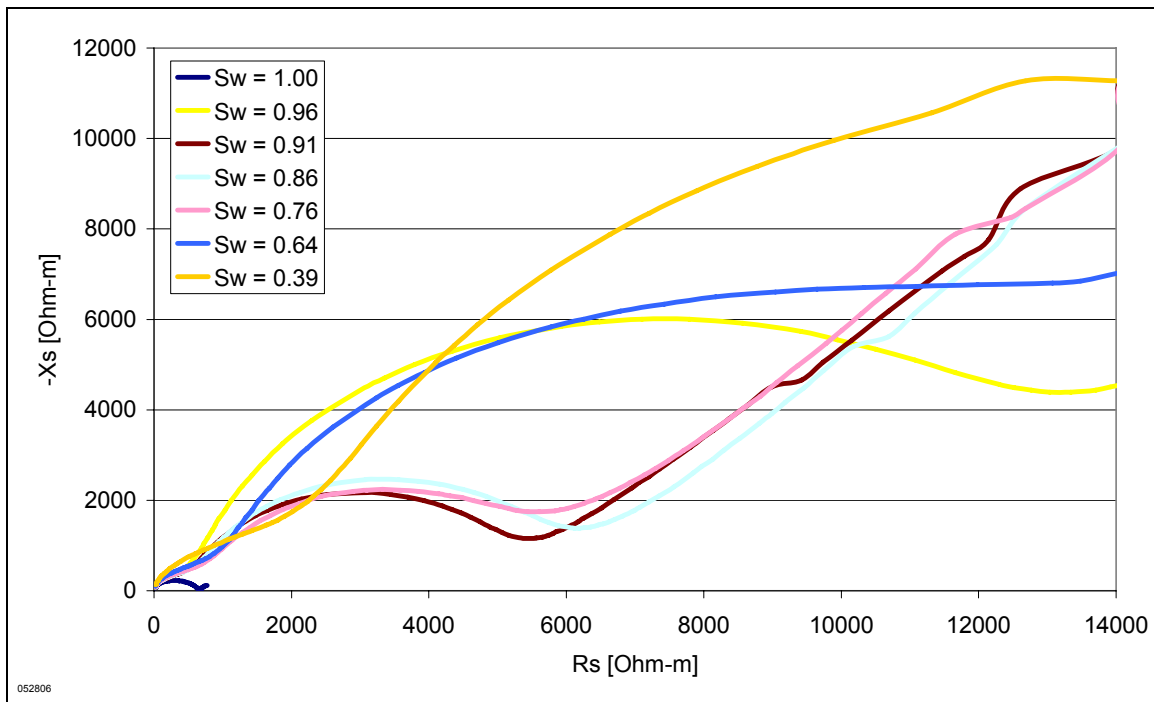


Figure 38 Argand plot of Texas Cream samples at different S_w .

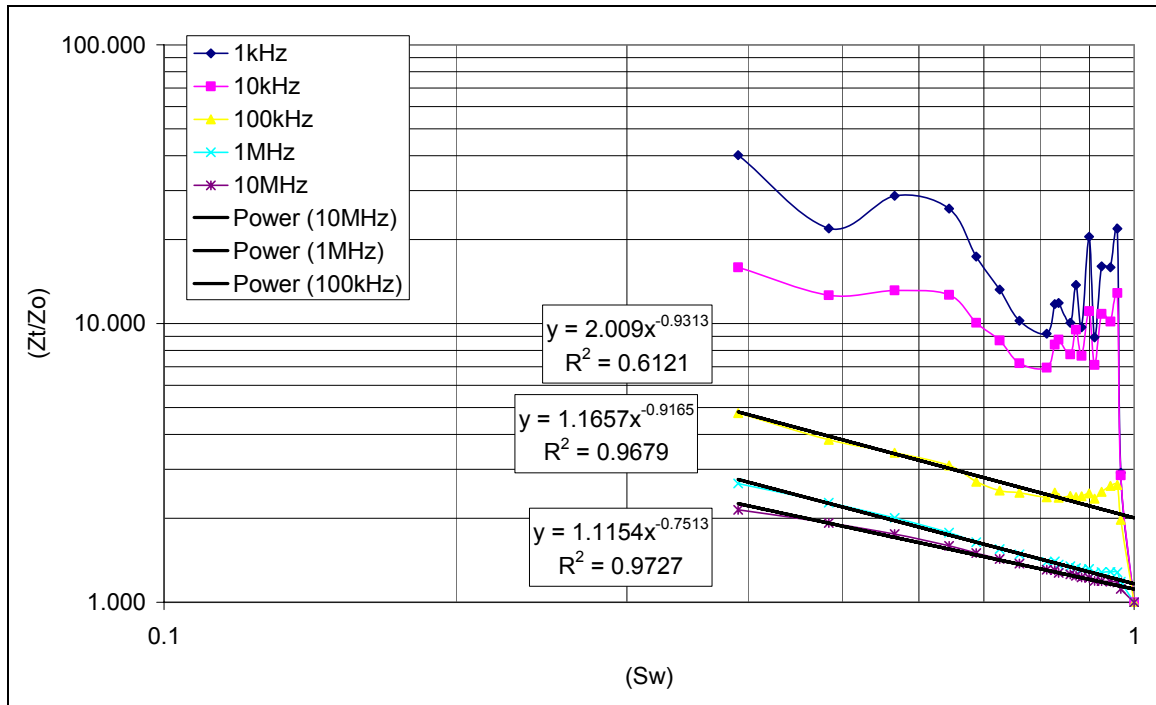


Figure 39 Resistivity index calculated from the Texas Cream sample impedance.